2015

Flaring and pollution detection in the Niger Delta using Remote Sensing

Morakinyo, Barnabas Ojo

COPYRIGHT STATEMENT

FLARING AND POLLUTION DETECTION IN THE NIGER DELTA USING REMOTE SENSING

by

BARNABAS OJO MORAKINYO

A thesis submitted to the Plymouth University

in partial fulfilment for the degree of

DOCTOR OF PHILOSOPHY

School of Marine Science and Engineering

Faculty of Science and Engineering

In collaboration with

ARGANS Limited, Plymouth Science Park, Plymouth, UK

Pixalytics Ltd, Plymouth Science Park, Plymouth, UK

December 2015

Flaring and pollution detection in the Niger Delta using Remote Sensing

Barnabas Ojo Morakinyo

Abstract

Through the Global Gas Flaring Reduction (GGFR) initiative a substantial amount of effort and international attention has been focused on the reduction of gas flaring since 2002 (Elvidge et al., 2009). Nigeria is rated as the second country in the world for gas flaring, after Russia. In an attempt to reduce and eliminate gas flaring the federal government of Nigeria has implemented a number of gas flaring reduction projects, but poor governmental regulatory policies have been mostly unsuccessful in phasing it out. This study examines the effects of pollution from gas flaring using multiple satellite based sensors (Landsat 5 TM and Landsat 7 ETM+) with a focus on vegetation health in the Niger Delta.

Over 131 flaring sites in all 9 states (Abia, Akwa Ibom, Bayelsa, Cross Rivers, Delta, Edo, Imo, Ondo and Rivers) of the Niger Delta region have been identified, out of which 11 sites in Rivers State were examined using a case study approach. Land Surface Temperature data were derived using a novel procedure drawing in visible band information to mask out clouds and identify appropriate emissivity values for different land cover types. In 2503 out of 3001 Landsat subscenes analysed, Land Surface Temperature was elevated by at least 1 ℃ within 450 m of the flare. The results from fieldwork, carried out at the Eleme Refinery II Petroleum Company and Onne Flow Station, are compared to the Landsat 5 TM and Landsat 7 ETM+ data.

Results indicate that Landsat data can detect gas flares and their associated pollution on vegetation health with acceptable accuracy for both Land Surface Temperature (range: 0.120 to 1.907 K) and Normalized Differential Vegetation Index (sd $\pm$ 0.004). Available environmental factors such as size of facility, height of stack, and time were considered. Finally, the assessment of the impact of pollution on a time series analysis (1984 to 2013) of vegetation health shows a decrease in NDVI annually within 120 m from the flare and that the spatio-temporal variability of NDVI for each site is influenced by local factors. This research demonstrated that only 5 % of the variability in δLST and only 12 % of the variability in δNDVI, with distance from the flare stack, could be accounted for by the available variables considered in this study. This suggests that other missing factors (the gas flaring volume and vegetation speciation) play a significant role in the variability in δLST and δNDVI respectively.

List of contents

List of Tables

Chapter 2

Chapter 3

Chapter 4

List of Figures

Chapter 2

Chapter 3

Chapter 4

Chapter 5

Nomenclature

AATSR	=	Advanced Along Track Scanning Radiometer
AG	=	Associated Gas
ARGANS	=	Applied Research in Geomatics, Atmosphere, Nature and Space
ASAR	=	Advanced Synthetic Aperture Radar
ATMCORR	=	Atmospheric correction
AVHRR	=	Advanced Very High Resolution Radiometer
CEOI-ST	=	Centre for Earth Observation Instrumentation and Space Technology
CO	=	Carbon monoxide
CO_2e	=	Carbon dioxide emission
CH_4	=	Methane
DIAL	=	Differential Absorption LIDAR
DMCii	=	Disaster Monitoring Constellation International Imaging
DPR	=	Department of Petroleum Resources
DSMP	=	Defense Satellite Meteorological Program
ENVISAT	=	Environmental satellite
EO	=	Earth Observation
E & P	=	Exploration and Production
EOSDIS	=	Earth Observing System Data and Information System
EROS	=	Earth Resources Observation and Science
ESA	=	European Space Agency
ESMAP	=	Energy Sector Management Assistance Programme
ETM+	=	Enhanced Thematic Mapper Plus
FEPA	=	Federal Environmental Protection Agency
FIRMS	=	Fire Information for Resource Management System
GGFR	=	Global Gas Flaring Reduction
GIS	=	Geospatial Information System
GOES	=	Geostationary Operational Environmental Satellite
LC	=	Land Cover
LNG	=	Liquefied Natural Gas
LPG	=	Liquefied Petroleum Gas
LST	=	Land Surface Temperature
MIR	=	Mid Infra-Red
MODIS	=	MODerate-Resolution Imaging Spectroradiometer

MODTRAN	=	MODerate-Resolution Atmospheric Radiance and Transmittance
MSG	=	Meteosat Second Generation
NASA	=	National Aeronautics and Space Administration
NASRDA	=	National Space Research and Development Agency
NCEO	=	National Centre for Earth Observation
NDES	=	Niger Delta Environmental Survey
NDVI	=	Normalised Difference Vegetation Index
NERC	=	Natural Environment Research Council
NNPC	=	Nigerian National Petroleum Corporation
NOAA	=	National Oceanic and Atmospheric Administration
NO	=	Nitrogen Oxide
OPEC	=	Organization of Petroleum Exporting Countries
PAH	=	Polycyclic Aromatic Hydrocarbon
POP	=	Persistent Organic Pollutants
RADAR	=	Radio Detection and Ranging
RSPSoc	=	Remote Sensing and Photogrammetry Society
SAR	=	Synthetic Aperture Radar
SAVI	=	Soil Adjusted Vegetation Index
SCHIAMACHY	=	SCanning Imaging Absorption spectrometer for Atmospheric CartograpHY
SEVIRI	=	Spinning Enhanced Visible and Infrared Imager
SLIM-6	=	Surrey Linear Imager-6 Channel
SSTL	=	Surrey Satellite Technology Ltd
SVOC	=	Semi-volatile Organic Compound
SWIR	=	Short Wave Infra-Red
SO	=	Sulphur oxide
SO_2	=	Sulphur di-oxide
TIR	=	Thermal Infra-Red
USGS	=	United States Geological Survey
VOC	=	Volatile Organic Compound
WFA	=	World Fire Atlas

Acknowledgements

This thesis is the climax of three years of work at Plymouth University. First and foremost, I would like to express my deepest gratitude to the Almighty God, Jesus Christ, my Saviour, my Lord, my Permanent Solution (Jh. 3 v 16); my Owner (1 Cor. 6 v 19-20); my Redeemer (Gal. 3 v 13-14); in Him I live, I move, and have my being (Acts 17 v 28). Many thanks go to Federal Government of Nigeria, through Tertiary Education Trust Fund (TETFund) who sponsored this study for two years. Also, my thanks go to Professor Akaneren Essien (former Vice-Chancellor, University of Uyo, Uyo) for the approval of my study leave and Surveyor M. A. Isong (former Head of Department, Geoinformatics and Surveying, University of Uyo, Uyo) for his support and encouragement throughout this programme.

From an individual and academic view, I have been supported and helped by numerous individuals who have provided indispensable assistance. First, I am extremely indebted to my supervising team Dr Victor Abbott (Director of Studies), Dr Samantha Lavender and Dr Jill Schwarz for their time, support, motivating me, pushing me, always encouraging investigation into ideas and offering thought-provoking view points throughout my PhD. Special thanks goes to Dr Abbott who created an atmosphere with encouragement, faith, freedom and inspiration (and involved me with Hydrography Society, UK activities); even outside the scope of this thesis, he has been a great source of motivation to me.

Dr Sam, I appreciate you for providing me with countless opportunities over the past three years, taken me to ARGANS Limited and later, to Pixalytics Ltd (remote sensing companies) being the Managing Director, which earned me industry based experience in UK; getting me involved with external activities (RSPSoc, UK), and providing guidance, support and much of your time teaching me to become a remote sensing and computer programming (IDL) expert. Dr Jill, like Dr Sam, I cannot thank you enough for the acceptance to join my supervising team when Dr Abbott discussed this with you. Dr Jill, I thank you for being positive and confident in my ability which has helped me get through the PhD. With much time and patience you have helped me to become an expert in remote sensing and computer programming (MATLAB). I have been enormously blessed to have all of you as supervisors.

In addition to my supervisors, I am indebted to Professor Mick Fuller (Head of Graduate School); Professor Neil James (Head of School of Marine Science and Engineering); Mr John Popplestone (Finance and sustainability); Sarah Kearns (Graduate School); Nina George (International Student Advisory Service) and Francesca Niedzielski (Doctoral Training Centre) for your support to overcome the challenge of funding this PhD.

I would also like to personally thank the Chairman of Board of Directors of ARGANS Limited, Dr Francois-Regis Martin-Lauzer for his support; staff of ARGANS Limited for a favourable atmosphere to have a full practical experience on my Doctoral research; they are Rabiah Habeeb, Jan Jackson, John Hedley, Kathryne Baker, Alexa Borg, Paul Spurgeon and Suzie Bone. I would also thank the Director of Corporate Services of Pixalytics Ltd, Mr Andrew Lavender for his

contribution and support toward the success of my PhD. With regard to data used in this thesis, big thanks to NASA/USGS for the provision of Landsat data, and MODTRAN ATMCORR Calculator; ESA for the provision of ATSR-WFA and (A)ATSR data; DMC International Imaging through Kataryzna Wisniewska for providing me with UK-DMC (SLIM-22) imagery; Federal Ministry of Petroleum Resources, Abuja (Department of Petroleum Resources, Lagos) for fieldwork data from Shell Petroleum Development Company and Eleme Refineries I and II Petroleum Companies gas flaring sites; and Federal Ministry of Aviation, Abuja (Nigerian Meteorological Agency, Lagos) for the provision of meteorological data. Julia Barsi (Landsat Project Science Office, Science Systems and Applications Inc. Greenbelt MD 2077, USA) who is the Web Curator for the MODTRAN ATMCORR Calculator is acknowledged for her support and help.

I am indebted to the Geomatics Research Group and Centre for Marine and Coastal Policy (MarCoPol) team for the support they gave through opportunities to present the progress of my work and their inputs to the completion of this study.

I would also like to acknowledge my Father in the Lord, Pastor E. A. Adeboye, General Overseer of The Redeemed Christian Church of God Worldwide (RCCG), Lagos, Nigeria for his prayers and support. My thanks go to my mentors, pastors, teachers and helpers of destiny; they are Evangelist Esther Benjamin, Founder of The Lord Our Rock Ministry, Abuja, Nigeria; Pastor Benjamin Tunku of Nassarawa Intercessors, Lafia, Nassarawa State, Nigeria; Pastor Johnson Oale of Dominion International Chapel, Mararaba, Presbytery,

Nassarawa State, Nigeria; Dr and Pastor (Mrs) E. E. Abia of RCCG, Uyo, Akwa Ibom State, Nigeria; Deacon and Mrs John Odoemelem of RCCG, Abuja, Nigeria; Pastor and Deaconess Gideon Ademola of RCCG, Abuja, Nigeria and Mr Alfred Alademomi of Deeper Life Christian Ministry Lagos, Nigeria, for their prayers, encouragement and support. My thanks and appreciation goes to Pastor Alfred Sunday Alademomi, every member of Deeper Life Bible Church, Plymouth, UK and every member of Deeper Life Bible Church, Bristol Region, Bristol, UK, for the privileges to fellowship with them. God bless you all in Jesus name. Amen.

Also, a big thank to my friend, Surv. Kehinde Sunmonu for being there at all times and for your financial support toward this study. Mrs Faosat Sanni, Mr Akin Olukiran, Mr Opeyemi Adeyemi, Mr Israel Etobro, Mr Mohammed Chaander, Mr Ayodeji Adeoye, Dr Kayode Owa, Mr and Mrs Ikenna Ubadigha, Dr and Mrs Habeeb Nasiru, Mr Nelson Musana, Surv. Tunji Egberinde and Mrs Sussan White (my landlady), you have sown into my life; your unborn generation will reap the fruits of your labour in Jesus name. Amen. Many thanks to all who generously gave up their time to contribute to the success of my study particularly Mr Shaun Lewin of Geomapping Unit, School of Geography, Earth and Environmental Sciences for his help in the aspects of Geospatial Information System (GIS) analysis; and to my office mates, Carlos Perez Collazo, Javier Abanades Tercero, Rzgar Abdalrahman, Jamie Cross, Abdulla Abo and Dr Adi Kurniawan.

Finally, I can’t thank my immediate family enough. My wife, Pharm (Mrs) R. E. Morakinyo, Our children (Faith and Elijah), Peace Oyekemi Tiamiyu, Mr and

Mrs Samuel Bolaji, Mrs Serah Alao, Mr Omotayo Akanbi Ande, Morufat Alake, my mother (Mrs) Abike Morakinyo, my siblings and my in-laws for their support throughout my study. God's grace upon your life has brought it to pass. I am grateful to you all. May The Almighty God's blessings be constantly abundant upon you in Jesus name. Amen.

Finally, now unto the King eternal, immortal, invisible, the only wise God, be honour and glory, for ever and ever (1 Tim. 1 v 17). Amen.

Author's declaration

At no time during the registration for the degree of Doctor of Philosophy has the author been registered for any other University award without prior agreement of the Graduate Committee. This study was funded for two years with support from the Nigerian Tertiary Education Trust Fund, Federal Ministry of Education, Abuja, Nigeria. It was carried out in collaboration with ARGANS Limited, Plymouth and Pixalytics Ltd, Plymouth.

A programme of advanced study was undertaken, which included: four taught modules at the Plymouth University, Research skills (IMS 5101), Research methods (EAR 5101), Methods of Hydrography (IMS 5104), and Geographical Information System and Remote Sensing (IMS 5109) October, 2011; General Teaching Associate (GTA) course, Plymouth University, November, 2011; Postgraduate Certificate in Academic Practice (PGCAP 600), Plymouth University, June, 2014; and fifty one of the various courses supplied by the Graduate Training School including, introduction to 'R', May, 2011; Preparing to transfer, November, 2011; Geographic Information System (GIS) I and II, November, 2011 and December, 2011; LaTEX, May and June, 2012; SPSS, May, 2012, NVIVO, June, 2012; MATLAB, April, 2013; Ipad Workshop, April, 2013; preparing for viva, March, 2014 and Meet the Editors – Science, Technology, Engineering, Mathematics, Medicine and Dentistry, May, 2014.

Relevant scientific seminars and conferences were regularly attended at which work was often presented; external institutions were visited for consultation purposes and several papers prepared for publications. A list of oral and poster presentations, and workshop attended are outlined below.

Presentations, conferences and workshops attended

Oral presentations

- Morakinyo, B. O., Abbott, V. J., Lavender, S. J. and Schwarz, J. (2014). Land cover classification and changes at gas flaring sites in the Niger Delta using Landsat satellite data. The Postgraduate Society Conference Series, Plymouth University, Plymouth, UK, 17th June.
- Morakinyo, B. O., Abbott, V. J., Lavender, S. J. and Schwarz, J. (2013). The methodology and results from ground truthing satellite observations at gas flaring sites in Nigeria. Remote Sensing and Photogrammetry Society (RSPSoc) Wavelength Conference, Glasgow, Scotland, UK, 11th-13th March.
- Morakinyo, B. O., Abbott, V. J., Lavender, S. J. and Schwarz, J. (2013). Flaring and pollution detection in the Niger Delta using Remote Sensing: Research aim, objectives and methods. Geomatics Research Group, Plymouth University, Plymouth, UK, 9th January.
- Morakinyo, B. O., Abbott, V. J. and Lavender, S. J. (2012). Detection of gas flares locations in the Niger Delta using Remote Sensing. Remote Sensing and Photogrammetry Society (RSPSoc) Annual Students Meeting, Falmouth, Cornwall, Devon, UK, 12th-14th March.
- Morakinyo, B. O., Abbott, V. J. and Lavender, S. J. (2011). Flaring and pollution detection in the Niger Delta using Remote Sensing: Introduction and research questions. Post Graduate Research Skill Session (Presenting to an Audience Part 1), Plymouth University, Plymouth, UK, 9th November.
- Morakinyo, B. O., Abbott, V. J. and Lavender, S. J. (2011). Nigeria, Niger Delta and its natural resources. A seminar presented in partial fulfilment of

the requirement for the General Teaching Associates (GTA) Course, Plymouth University, Plymouth, UK, 13th October 2011.

Poster presentations

- Morakinyo, B. O., Abbott, V. J., Lavender, S. J. and Schwarz, J. (2014). Retrieval of Land Surface Temperature from Landsat 7 ETM+ data: A case study of gas flaring sites in Nigeria. Remote Sensing and Photogrammetry Society (RSPSoc) Wavelength Conference, Great Malvern, Worcester, UK, 16th-18th April.
- Morakinyo, B. O., Abbott, V. J. and Lavender, S. J. (2011). Flaring and pollution detection in the Niger Delta using Remote Sensing: Aim, research questions and objectives. Marine and Coastal Policy Research Group (MarCoPol), Plymouth University, Plymouth, UK, 20th September.

Conferences attended

- Plymouth University Student's Union (UPSU) Climate Change Conference. (2015). Plymouth University, Plymouth, UK, 5th-6th November.
- RSPSoc, NCEO and CEOI-ST Joint Annual Conference. (2015). Earth Observation in the Sentinel Era. University of Southampton, Southampton, UK, 8th-11th September.
- Pollution and the Marine Environment: An English Channel Perspective. (2014). Plymouth University, Plymouth, UK, 2nd September.
- 2nd Marine and Coastal Policy Forum (MarCoPol) Conference. (2014). Plymouth University, Plymouth, UK, 18th-20th June.

- Remote Sensing and Photogrammetry Society Annual Conference (RSPSoc). (2013). Earth Observation for Problem Solving. University of Glasgow, Glasgow, UK, 4th-6th September.
- Vice-Chancellor's Teaching and Learning Conference. (2013). Excellence in Learning, Teaching and Student Experience, Plymouth University, Plymouth, UK, 28th June.
- Making the most of research systems conference: Funding, managing information and networking, Plymouth University, Plymouth, UK, 6th June 2013.
- Vice-Chancellor's Teaching and Learning Conference. (2012). Excellence in Learning, Teaching and Student Experience, Plymouth University, Plymouth, UK, 6th July.
- Plymouth University Marine Institute Spring Term Public Event: Our Past … Our Future! Celebrating 150 years of Marine and Maritime Education at Plymouth University, Plymouth University, Plymouth, UK, 29th February 2012.
- 4th Annual Plymouth Marine Science Education Fund Conference: Blue Horizons Conference. Plymouth Marine Laboratory, Plymouth, UK, 14th December 2011.
- The Postgraduate Society Conference Series (7th Edition), Plymouth University, Plymouth, UK, 23rd November 2011.
- Remote Sensing and Photogrammetry Society Annual Conference (RSPSoc). Earth Observation in a Changing World. University of Bournemouth, Bournemouth, UK, 12th-15th September 2011.
- The Postgraduate Society Conference Series (6th Edition), Plymouth University, Plymouth, UK, 29th June 2011.

- 1st Marine and Coastal Policy Forum (MarCoPol) Conference. (2011). Plymouth University, Plymouth, UK, 22nd-24th June.
- Plymouth University International Students Conference (2011). Next steps to further success. Plymouth University, Plymouth, UK, 27th May.
- 2nd Plymouth University Marine Institute Conference, University of Plymouth, Plymouth, UK, 5th May 2011.

Workshops attended

- Land Cover Land Use (LCLU) focused on the Copernicus Land Services (http://land.copernicus.eu/). Organised by RSPSoc Land Cover Land Use Special Interest Group (LCLUSIG) at RSPSoc, NCEO and CEOI-ST Joint Annual Conference. Earth Observation in the Sentinel Era. University of Southampton, Southampton, UK, 8th September, 2015.
- Subsea UK: Workshop on Oil and Gas and Subsea Technologies, Plymouth University, Plymouth, UK, 19th November 2013.
- Natural Environment Research Council (NERC), UK, Biennial Airborne Research and Survey Facility Workshop at RSPSoc Annual Conference, University of Glasgow, Glasgow, UK, 3rd September, 2013.
- Use of Terrestrial Laser for the Monitoring of Coastal Morphology, The Hydrography Society, UK (SW) and Royal Institution of Chartered Surveyors (RICS) Geomatics (SW), Plymouth, UK, 1st May 2012.
- 2nd ARGANS Limited Innovation Workshop, Plymouth, UK, 19th January 2012.
- Natural Environment Research Council (NERC), UK, Biennial Airborne Research and Survey Facility Workshop at RSPSoc Annual Conference, University of Bournemouth, Bournemouth, UK, 12th September, 2011.

- Calibration of Optical & Medium Resolution Sensors Using (DIMITRI Software V2.0), ARGANS Limited, UK, 6th September 2011.
- ARGANS Limited Away Day: Leadership, management and team working, Boringdon Park, Plymouth, UK, 13th June 2011.

Word count of main body of thesis: 68,604

Signed……

Date…7th December 2015…

Chapter 1
Introduction

1.1 Gas flaring

Gas flaring is widely used to dispose of dissolved natural gas present in petroleum; it emerges from crude oil when it's brought to the surface and separated from the oil prior to transport in the production and processing facilities (Elvidge et al., 2009; Bruno, 2007). The gas flare is a high temperature oxidation process (Kimberly et al., 2007), used to burn combustible components, with volatile organic compounds (VOCs) piped to a remote, usually elevated, location and burned in an open air flame using a specially designed burner tip, auxiliary fuel, and steam or air to promote mixing for nearly complete (> 98 %) VOC destruction (Stone et al., 2000).

Industrial flares may be broadly classified as emergency flares, process flares, or production flares (Johnson and Coderre, 2011; Leahey and Davies, 1984; Brzustowski, 1976). Emergency flaring is by definition intermittent and typically involves large, very short duration, unplanned releases of flammable gas that is combusted for safety reasons. Flare stack exit velocities during emergency flaring can approach sonic. Process flaring may involve large or small releases of gas over durations ranging from hours to days, as is encountered in the upstream oil and gas industry during well testing to evaluate the size of a reservoir, or at downstream facilities during blow-down or evacuation of tanks and equipment. Production flaring typically involves smaller, more consistent gas volumes and much longer durations that may extend indefinitely during oil

production, in situations where associated gas (a.k.a. solution gas) which is the primary contributor (Johnson and Coderre, 2011) is not being conserved.

The composition of flared gas can vary significantly, within the upstream oil and gas (UOG) industry, generally, the major constituent is methane (McEwen and Johnson, 2012). Since methane has a 25 times higher global warming potential (GWP) (on a 100 year time-scale) than CO_2 on a mass basis (IPCC, 2007), flaring can prevent significant greenhouse gas emissions that would occur if the gas were simply vented into the atmosphere (McEwen and Johnson, 2012).

The usual assumption is that combustion processes associated with flares efficiently convert HCs and sulphur compounds to relatively harmless gases such as CO_2, SO_2 and H_2O (Leahey et al., 2001). However, it has been shown that theses processes can be efficient only at low wind speeds because the size of the flame, which is an indicator of flame efficiency, decreases with increasing wind speed (Leahey et al., 2001). Therefore, the flaring process could routinely results, during periods of moderate to high wind speeds, in appreciable quantities of products of incomplete combustion such as anthracene and benzo(a)pyrene, which can have adverse implications with respect to air quality (Leahey et al., 2001).

The design of a flare can also vary significantly, ranging from simple pipe flares (essentially an open-ended vertical pipe) that are common in the UOG industry, to flares with engineered flare tips that can include multiple fuel nozzles and multipoint air and/or steam injection for smoke suppression (Brzustowski, 1976). Estimates of emissions from flaring are complicated by the large diversity

of flare designs, applications, and operating conditions encountered (McEwen and Johnson, 2012). In terms of emissions, key factors that can affect flare performance include the exit velocity of gas from the flare, the flare gas composition, ambient wind conditions, flare stack diameter, and flare tip design (Johnson and Kostiuk, 2000, 2002).

In evaluating the use of flare stacks, safety and environmental concerns should be addressed (Brzustowski, 1976). Safety problems are primarily involved with the flaring of larger volumes of gas and the consequent effects of radiation on plant personnel and structures. Environmental concerns are usually associated with the continuous flaring of gas streams that contain potentially harmful components (Leahey and Davies, 1984).

Wendisch et al. (2004) and Gillespie et al. (1998) stated that in most cases land surfaces are more reflective than water over the range of Operational Linescan System (OLS) wavelengths (~450-850 nm) of Defense Meteorological Satellite Program (DMSP) when used for mapping of flares on land and offshore. The analysis of Ziskin et al. (2011) on gas flare brightness on land and offshore is in agreement with them. Their result shows that land flares appear ~3 % brighter than offshore flares to the OLS instrument but this bias is within the limits of their detection errors. Therefore, they concluded that no correction for this effect is recommended.

Gas flaring is widely recognised as a waste of energy, increases atmospheric carbon emissions (McEwen and Johnson, 2012) and is a significant environmental hazard (Azibaolanri, 1997). Therefore, it's responsible for a vast

amount of both wasted energy and greenhouse gas emissions. For example, over the fifteen year record of worldwide natural gas flaring that was observed by Elvidge et al. (2009), it was estimated that 2.4×10^{12} m^3 of gas was flared creating 5,000 Mt (mega metric tons) of CO_2 equivalent (CO_2e) or roughly 70 % of the total annual greenhouse gas emission of the United States in 2007 (NOAA, 2011; Elvidge et al., 2009). Despite this recognition, there is substantial uncertainty regarding the magnitude of gas flaring. Current volume estimates rely on voluntary reporting by corporations and individual countries, and it's known that some of the reported volumes are unexpectedly low. Furthermore, there are a large number of countries with no publicly reported gas flaring volumes (NOAA, 2011).

Through the Global Gas Flaring Reduction (GGFR) initiative a substantial amount of effort and international attention has been focused on the reduction of gas flaring since 2002 (Elvidge et al., 2009). The World Bank in cooperation with the Government of Norway launched the GGFR initiative at the World Summit on Sustainable Development in August, 2002; the ultimate goal is the elimination of most gas flaring and venting. The GGFR is a public-private partnership with participation from governments of oil-producing countries, state-owned companies and major international oil companies. It identifies areas where gas flaring occurs and works with the countries and companies to promote regulatory frameworks and infrastructure investment to bring flared gas to markets. GGFR country partners include Algeria, Angola, Azerbaijan, Cameroon, Ecuador, Equatorial Guinea, Gabon, Indonesia, Kazakhstan, Khanty-Mansiysk (Russian Federation), Nigeria, Norway, Qatar, United States of America and Uzbekistan. The participating oil companies include BP

Chevron, ConoPhillips, eni, ExxonMobil, Marathon Oil, Shell, Statoil and TOTAL. OPEC and the World Bank Group are also partners. Donor countries are Canada, the European Union, France, Norway, the UK and the United States of America (Elvidge et al., 2009).

1.2 Thesis research questions, aim and objectives

The three primary research questions for this thesis are:

1. How accurately can we detect gas flares from satellite based sensors?
2. Can satellite data be used to detect the impact of gas flaring on vegetation health/land cover?
3. What is the spatial and temporal variability in satellite detectable flare impact on vegetation health and land cover?

Based on these research questions, the primary aim of this thesis is to create a Nigeria-focused methodology for determining the effects of pollution from burning gas using Landsat 5 Thematic Mapper (TM) and Landsat 7 Enhanced Thematic Mapper Plus (ETM+) satellite based sensors.

In order to answer the above research questions, specific objectives have been set:

1. Introduction to oil production in Nigeria as a means to identify the significant gas flaring sites;
2. Detection of oil production-linked polluting sources using public domain remote sensing data;
3. Comparison of spatial variability in air temperature and satellite derived Land Surface Temperature;
4. Detection of environmental impact of gas flaring;

5. Preliminary evaluation of the environmental impact of gas flaring related pollution within Nigeria from 1984 to 2013.

1.3 Thesis structure

This thesis starts with a literature review of the current state of knowledge in gas flaring and environmental pollution in Chapter 2. The various environmental settings in the Niger Delta are first discussed and then the chapter reviews the history of oil exploration, exploitation and production in Nigeria. In addition, there is a review of the Nigerian institutional framework for oil exploration and production; petroleum hydrocarbon industry in Nigeria; and refineries and petrochemical companies in Nigeria. Following this is a review of oil and gas processing; types of flare; gas flaring in Nigeria; Nigerian policies and legislation on gas flaring; gas flaring reduction projects in Nigeria; and factors responsible for continuous gas flaring in Nigeria. Assessing the environmental impact of gas flaring is the goal; hence there was a detailed review of the environmental, economic and health implications of gas flaring in Nigeria. The Chapter concludes with an overview of the remote sensing technology, its various applications, its observables and its specific applications to forest fire and gas flare detection. The last part deals with a review of literature on the remote sensing for oil and gas and environment in the Niger Delta.

Chapter 3 gives a detailed explanation of the research methods. The processes of detecting oil production-linked polluting sources in the Niger Delta using public domain remote sensing data are presented. Three types of data namely optical or visible-thermal infrared (VIS-TIR) satellite, fieldwork and meteorological data were used for the analysis. The processing of satellite data was carried out

using BEAM VISAT, SeaDAS, ArcGIS and MATLAB software. One major problem with optical satellite data is that of cloud cover, where the impacts were reduced by masking the cloud covered locations. MATLAB scripts were written for the processing of satellite data to get the results on radiance, surface reflectance, NDVI, brightness temperature and LST. The method of dark pixel atmospheric correction was employed for the reflective bands of Landsat 5 TM and Landsat 7 ETM+, whilst the atmospheric correction parameter calculator was used to get the atmospheric correction parameters for their single thermal band (band 6-high gain). The ancillary atmospheric data are required to make the correction from Top-of-Atmosphere (TOA) radiance or temperature to surface-leaving radiance or temperature. The Chapter ends with the methods adopted for the fieldwork activities at Eleme Refinery II and Onne Flow Station gas flaring sites. The parameters measured on sites are air temperature, relative humidity and the coordinates of the measurement points.The fieldwork data were used for the comparison of spatial variability in air temperature and satellite derived LST.

Chapter 4 titled 'Multi-satellite mapping of oil production-linked polluting sources' presents the detailed characteristics of the gas flaring case study sites, qualitative analysis of the detection of flare signature, Landsat reflective bands signature and NDVI, quantitative analysis of the detection of flare signature, spatial analysis of LST through ArcGIS, four cardinal directional analyses of results (LST and NDVI), characterisation of spatial variability in LST, significance of LST spatial variability, investigation of potential prevailing wind impact on LST, evaluation of factors influencing change in LST, results of the

fieldwork activities, comparison of spatial variability in air temperature and satellite derived LST. The Chapter ends with a summary and conclusions.

Chapter 5 titled 'Evaluation of environmental impacts of gas flaring on vegetation cover and health' presents a detailed methodology for data analysis, quantitative analysis of a change in vegetation health potentially related to flare pollution at a given time, relationships between the spatial gradient in LST and the spatial gradient in NDVI around flare sites, the influence of environmental factors on vegetation cover and health, and change in vegetation from 1984 to 2013.

Chapter 6 is a synthesis of the results obtained from Chapters 4 and 5 with existing research and the discussion of the major findings of the thesis. The Chapter also outlines future research.

Chapter 7 provides the overall conclusions relevant to each research question and draws out recommendations on how to solve problems relating to gas flaring in Nigeria. The Chapter also identifies the contribution of this research to knowledge and potential areas for development.

Chapter 2
Nigeria, the hydrocarbon industry and remote sensing technology

This Chapter gives an overview of the environmental setting in the Niger Delta, processes for oil exploration and exploitation, oil and gas policy and legislation in Nigeria, flaring and its practice and reasons for the failure to stop it. It also reviews previous literature on the significant impacts of gas flaring and hydrocarbon pollution and concludes with the remote sensing technology that can be used to detect flaring and its effects remotely, some of its general applications, its specific applications to gas flaring and forest fire detection and its importance to this study.

2.1 Nigeria and the Niger Delta

The Federal Republic of Nigeria, one of Africa's largest countries and its most populous, is situated in West Africa between the Latitudes of 4 ° to 14 ° North and Longitudes of 2 ° 2 ' to 14 ° 30 ' East. The country covers an area of 923,768 km², with an estimated 4,049 km of land boundaries, shared with Benin in the west, the Republic of Niger in the north, Chad in the north-east and Cameroon in the east. In the south, Nigeria's 853 km long coastline opens onto the Atlantic Ocean (Figure 2.1) (UNEP, 2011). The southern lowlands merge into the central hills and plateaus, with mountains in the south-east and plains in the north. The country's largest river is the Niger, which joins with the Benue River to form a confluence at Lokoja.

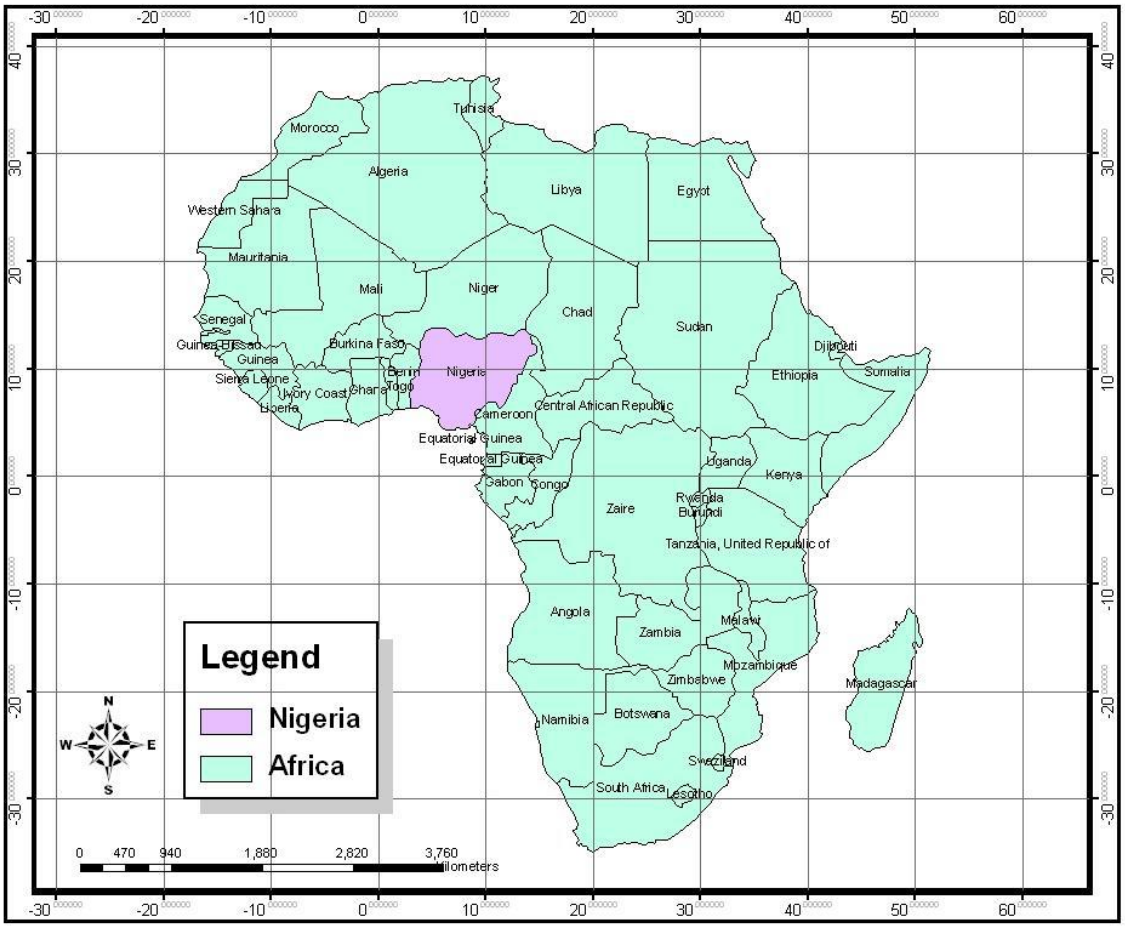

Figure 2-1: Map of Africa showing Nigeria
Adapted from ESRI (2009)

The Niger Delta, located in the southernmost part of Nigeria and covering an area of some 70,000 km², is the largest river delta in Africa and the second largest in the world (Figure 2.2). From a coastal belt of swamps, stretching northwards the land becomes a continuous rainforest which gradually merges with woodland and savannah grasslands in central Nigeria. The swamp, forest and woodland areas occupy about 12 % of the delta's land surface. Nigeria is rich in natural resources, including natural gas, petroleum, tin, iron ore, coal, limestone, niobium, lead, zinc, timber, bitumen and extensive arable land (UNEP, 2011).

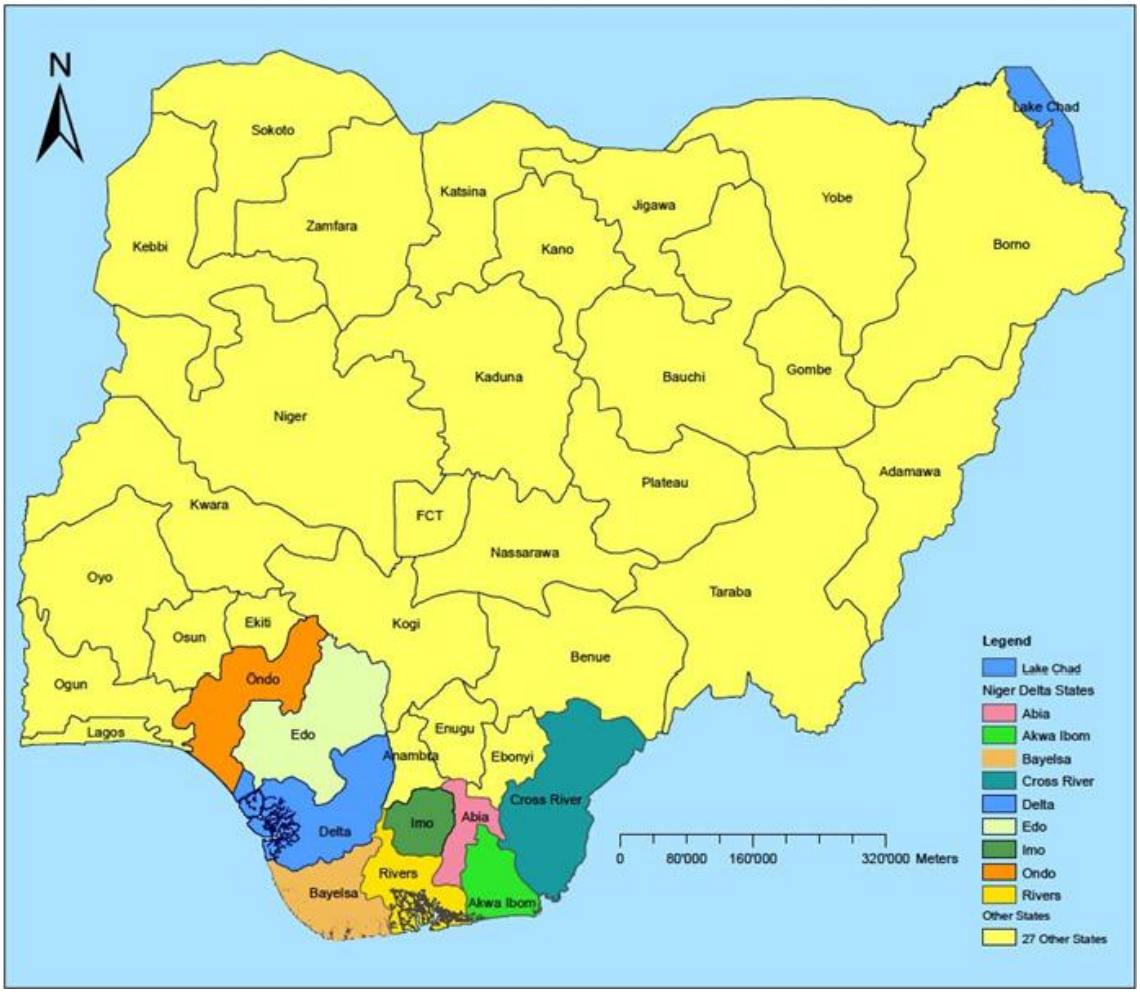

Figure 2-2: Figure 2-2: Map of the Niger Delta States
Source: Ite et al., 2013

2.2 Environmental setting in the Niger Delta

2.2.1 Geographical location

The Niger Delta region which forms part of the coastal zone extends over 450 km from West to East, thus constituting about 60 per cent of the 853 km Nigerian coastline. The region, as cartographically defined in the NDES programme, lies North at Aboh, where the River Niger splits into the Nun and Forcados Rivers, the Benin River estuary to the West and the Imo River estuary to the East (Onosode, 2003). The Niger Delta region traverses nine out of the thirty six states of the Federal Republic of Nigeria; the states of Abia, Akwa Ibom, Bayelsa, Cross River, Delta, Edo, Imo, Ondo and Rivers (Figures 2.2 and 2.3).

2.2.2 Population/demography

The Niger Delta region has an estimated population of about 27 million (2002, projection by the Nigerian Population Commission). It consists of 185 local government areas with 40 ethnic groups and 250 dialects spreads across 5,000 communities (NDDC, 2004). The predominant occupations in the area are fishing and farming.

2.2.3 Natural endowment

The Niger Delta has large deposits of mineral resources and the most important of these are oil and gas which form the economic base of the nation. Also, the biological diversity of the Niger Delta is the richest in the country; its distinct ecological framework offers a diversity of settings for ecological resources. Timber resources serve as a source of construction material and non-timber resources are used for food, spices, condiments, medicines, tannins and dyes. Also, there are agricultural resources in the region such as the significant raffia palms from which oil, palm wine and other palm products are obtained. Other products include rubber, cocoa, cassava, coconut, yam, cocoyam, maize, cowpeas, plantain and rice (Onosode 2003).

The Niger Delta has wetlands of about 20,000 km^2 and this provides home and shelter for a wide variety of wildlife. It harbours extensive water resources through a braided system of eight major rivers, twenty one estuaries and a dense network of tributaries which makes it a major drainage system in Nigeria, emptying into the Atlantic Ocean. Consequently, there is an abundance of fishing resources, marine and aquatic life (NDDC, 2004; Onosode, 2003).

2.2.4 Geology and geomorphology

The Niger Delta is the product of both fluvial and marine sediment build-up since the upper Cretaceous period, some fifty million years ago. Over time, up to 12,000 m of shallow marine sediments and deltaic sediments have accumulated, contributed mainly by the Niger River and its tributaries. The main upper geological layers consist of the Benin Formation, Agbada Formation and Akata Formation. The Benin Formation is comprised of multiple layers of clay, sand, conglomerate, peat and/or lignite, all of variable thickness and texture and covered by overlying soil. Clay beds are discontinuous and groundwater is therefore present both as localized aquifers and in hydraulically interconnected aquifers. The ground characteristics are consistent with deltaic environments, where erosion and deposition of sediments constantly shift the course of channels, tributaries and creeks (UNEP, 2011).

The geomorphology of the Niger Delta is divided into three main environments namely continental, transitional and marine. Five major geomorphological units have been recognized (Short and Stauble 1967; Allen 1965) (see Figure 2.3), which includes:

- Active and abandoned coastal beaches;
- Salt water mangrove swamps;
- Freshwater swamps, back swamps deltaic plain, alluvium and meander belt;
- Dry deltaic plain with abundant swamp zones, Sombreiro Warri plain;
- Dry flat land and plain.

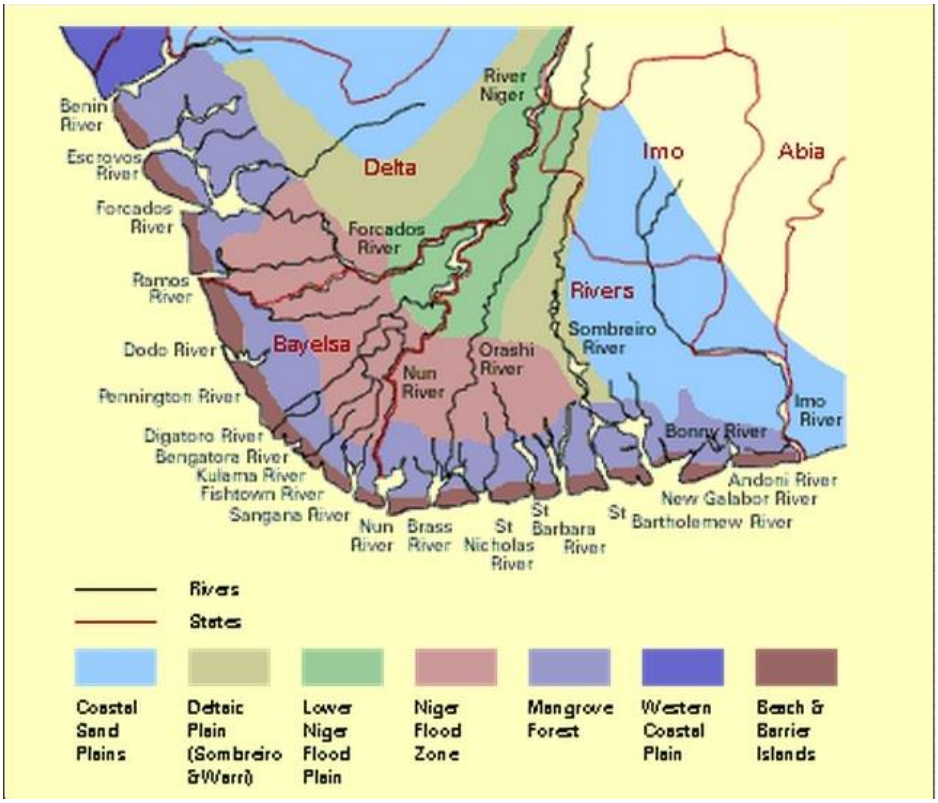

Figure 2-3: Landforms of the Niger Delta
Source: http://tortilla-soup.blogspot.co.uk/2012/11/usa-africa-dialogue-series-point.html

2.2.5 Topography

The Niger Delta is generally low-lying with heights of not more than 3 m above sea level and is generally covered by fresh water swamp, mangrove swamp, lagoonal marshes, tidal channels, beach ridges and sand bars. A topographic survey of the onshore area of the muddy coast revealed heights of 0.8-1.8 m above sea level; with tidal ranges of 1.5 m, making a large portion of the area prone to flooding at high tide; especially during spring tides (Dublin-Green et al., 1999).

2.2.6 Vegetation

The Niger Delta is an arcuate shaped basin with diverse vegetation. It is characterized by four distinct ecological zones: coastal ridge barriers,

brackish/freshwater swamp forests, mangrove forests and lowland rain forests, each of which offers diversity of setting for ecological resources and human activities. The region is home to the world's third largest mangrove forest, the largest mangrove swamp in Africa and the second largest delta in the world, West and Central Africa's most extensive freshwater forest and Nigeria's last remaining rain forest and one of the continents remaining sanctuaries of unique wildlife (Odukoya, 2006; Onosode, 2003).

2.2.7 Climate

The Niger Delta area is dominated by the hot and humid equatorial climate. The annual temperature range is between 22 and 37 °C with the highest temperatures occurring during the dry season (November-March). The total annual rainfall averages between 3,500 and 6,000 mm. More than 80 % of the rainfall occurs in the rainy season (April-October) when the tropical storm conditions are frequent; rainfall is usually heavy and occasionally may last for over 24 hours. Rainfall of 50 mm/hr is common between July and August and often results in flash floods which destabilise soil and enhance erosion. The hottest months are February and March, with high relative humidity throughout the year, decreasing slightly in the dry season (UNEP, 2011). Table 2.1 provides meteorological information on temperature, precipitation and sunshine obtained from satellite for the Niger Delta.

Table 2-1: Monthly average of the minimum and maximum daily temperatures (˚C), monthly precipitation (mm) and monthly average number of hours (hrs) of sunshine per day in the Niger Delta

Months	Temperatures (˚C) Minimum values	Maximum	Precipitation (mm)	Sunshine (hrs)
January	22.5	32.5	27	4.4
February	25.0	37.0	75	4.3
March	26.1	32.6	136	3.8
April	27.0	32.4	175	4.3
May	26.0	31.3	237	4.4
June	24.9	30.0	280	3.5
July	24.7	28.8	345	2.8
August	24.7	28.8	300	2.7
September	24.7	29.0	363	2.9
October	24.7	30.1	247	3.5
November	24.7	32.0	75	4.4
December	22.8	32.5	18	5.0

Source: http://www.allmetsat.com

2.3 Oil exploration, exploitation and production in the Niger Delta

In 1937 Shell had the whole of Nigeria as a concession block and it carried out preliminary subsurface geological investigations. In 1956 the first successful well, Oloibiri 1 was drilled and it attained a production capacity of 6000 barrels per day in 1958. This put the Niger Delta firmly on the path of oil production and it became the prime basin of exploration and production for both oil and gas. In order to create a more competitive base for this development of oil and gas, 50 % of the concession granted Shell was statutorily relinquished in 1958. Subsequently, between 1960 and 1963, Mobil, Texaco, Gulf (now Chevron), Agip, Esso and Safrap (now Elf) were allotted concessions including offshore blocks. In 1963, the first offshore oil discoveries were made by Gulf (Okan 1), Mobil (Ata 1) and Texaco (Koluama 1). Deep water and inland searches for oil and gas intensified and these set the stage for the large scale expansion in exploration and production activities (NNPC, 2012).

Exploration for petroleum uses an interdisciplinary approach which depends extensively on scientific investigations of a site and on the use of sophisticated instruments. There are three sub-stages involved in oil or petroleum exploration (Imaduddin, 2008):

- Geological requisites for an oil or gas field;
- Geological exploration;
- Seismic network and exploratory drilling.

Today, there are up to 606 oil fields in the Niger Delta region, out of which 355 are on-shore and 251 are offshore (Egbogah, 2012; U.S.A, 2005). Figure 2.4 shows oil/gas fields, pipelines, oil refineries, oil tanker terminals (Escravos, Forcados, Pennington, Brass River, Bonny and Qua Iboe), gas processing plant and Liquefied Natural Gas (LNG) terminal in the Niger Delta (African Continental, 2008).

Figure 2-4: Oil fields, pipelines, oil refineries, oil tanker terminals, gas processing plant and LNG terminal in the Niger Delta
Source: African Continental, 2008.

The oil and gas sector accounts for 90-95 % of Nigeria's export revenues, about 90 % of foreign exchange earnings, 80 % of all government revenues, 40 % of GDP, 95 percent of the national budget and 4 percent of employment (Usman, 2007; PEFS, 2005; Olukoju, 1996). Nigeria's natural gas reserve is estimated at over 185 trillion cubic foot (TCF) making the country the eighth largest natural gas reserve holder in the world and the largest in Africa (U.S.A, 2010).

2.3.1 Institutional framework for oil exploration and production in Nigeria

Three major stakeholders are concerned with oil exploration and production in Nigeria; these are government institutions, multi-national oil companies and communities from where the oil is extracted (Omokaro, 2009). Government institutions are the major institutional structures involved in the regulation of oil exploration and production. The key institutions charged with this responsibility are;

- **Federal Ministry of Petroleum Resources (FMPR); Department of Petroleum Resources (DPR):** This ministry is responsible for formulating oil and gas policies and regulating oil exploration and production (E&P) activities by granting flaring permissions and monitoring E&P activities (World Bank, 2011; DPR, 1991).
- **Federal Environmental Protection Agency (FEPA):** The FEPA Environmental Impact Assessment (EIA) Guidelines for E&P project were established in 1994, Decree No. 58/88. FEPA also has the right to grant flaring permission (World Bank, 2011).

- **Nigerian National Petroleum Corporation (NNPC):** This was established by the Nigerian National Petroleum Corporation Decree No. 33 of 1973 (Laws of The Federation of Nigeria (LFN) (LFN, 1990).

These government institutions are not discharging their assigned responsibilities as expected (World Bank, 2011) because of lack of a clearly defined long-term vision for the natural gas sector, lack of the political will to formulate and enforce coherent policies because of political instability and corruption and failure of the government to redeem its financial obligation under the existing joint venture. In addition, the overlapping responsibilities and jurisdictional conflicts especially between the FEPA and DPR has been a major setback in the implementation of gas flaring policies (World Bank, 2011; World Bank, 2002). The oil companies take advantage of these loopholes and this has resulted in the non-implementation of anti-flaring policies.

2.3.2 Petroleum hydrocarbons industry in Nigeria

The oil and gas industry is comprised of two parts: 'upstream' – the exploration and production sector of the industry; and 'downstream' – the sector which deals with refining and processing of crude oil and gas products, their distribution and marketing. Companies operating in the industry may be regarded as fully integrated, (i.e. have both upstream and downstream interests), or may concentrate on a particular sector e.g. an E&P company, or one just focusing on refining and marketing (R&M Company) (NNPC, 2012).

In Nigeria, the NNPC is vested with the exclusive responsibility for upstream and downstream development, which entails exploiting, refining, and marketing Nigeria's crude oil. All NNPC upstream operations i.e. crude oil production, are currently managed under the Exploration and Production Directorate which consists of the following Strategic Business Units (SBUs) that operate directly under the NNPC:

- National Petroleum Investment Management Services (NAPIMS);
- Crude Oil Sales Division (COSD);
- Integrated Data Services Limited (IDLS);
- Nigerian Petroleum Development Company (NPDC);
- Nigerian Gas Company (NGC).

These SBUs are collectively responsible for surveys, seismic data collation and interpretation, crude oil exploration, production, transportation, storage and marketing (NNPC, 2012). The downstream operations cover crude oil/gas conversion into refined and petrochemical products and finer chemicals, and gas treatment as well as transportation and marketing of the petroleum products (NNPC, 2012).

There are eighteen international oil companies operating within the vicinity of the local communities in the Niger Delta (Table 2.2); some have an interest in the deep offshore blocks in partnership with other operators, and the oil majors account for about 99 % of crude oil production in Nigeria (NNPC, 2006).

Table 2-2: The International Oil Companies operating in Nigeria and their time of establishment

Company	Year established in Nigeria
Shell Petroleum Development Company Ltd	1937
Mobil Producing Nigeria Unlimited	1955
Chevron Nigeria Ltd	1961
Texaco Overseas Nigeria Petroleum Co. Unltd	1961
Elf Petroleum Nigeria Limited	1962
Philip	1964
Pan Ocean Oil Corporation	1972
Ashland Oil Nigeria Limited	1973
Agip Energy & Natural Resources	1979
Statoil/BP Alliance	1992
Esso Exploration & Production Nigeria Ltd	1992
Texaco Outer Shelf Nigeria Limited	1992
Shell Nigeria Exploration & Production Co.	1992
Total (Nig.) Exploration & Production Co. Ltd.	1992
Amoco Corporation	1992
Chevron Exploration & Production Co.	1992
Conoco	1992
Abacan	1992

Source: NNPC, 2006

Nigeria's oil industry is dominated by the Nigerian National Petroleum Corporation (NNPC) founded in 1977, which is a major partner in the upstream component with the seven major multinational petroleum exploration and production companies as joint ventures. These are the largest and oldest in Nigeria, Shell Petroleum Development Company (SPDC), Mobil Producing Nigeria Unlimited, Chevron Nigeria, Elf Petroleum Nigeria, Nigerian Agip Oil Company (NAOC) and affiliate, Agip Energy and Natural Resources (AENR).

These oil companies encompass the basic six stages involved in the production and distribution of oil throughout the world (NNPC, 2012):

- Exploring;
- Drilling;
- Production/Recovery;

- Transportation;
- Refining;
- Marketing.

2.3.3 Refineries and petrochemicals in Nigeria

The downstream industry in Nigeria is well established. NNPC has four refineries that are:

- **Port Harcourt I Refinery:** Built and commissioned by Shell BP in 1965 with a processing capacity of 60,000 barrels per day. It is a hydro-skimming refinery and it was acquired by the Nigerian government in 1983 to become the country's first refinery. It was damaged by fire in 1988 but was rehabilitated and put back into production in the 1990s (NNPC, 2012).
- **Port Harcourt II Refinery:** Built in 1988 and commissioned in 1989 with a processing capacity of 150,000 barrels of crude oil per day. It is a complex conversion refinery and the most modern in the country. It was designed as an export and import refinery, hence its location at the coastal village of Eleme, near the older first refinery (NNPC, 2012).
- **Warri Refinery and Petrochemical Plant (WRPP):** It has installed processing capacity of 125,000 barrels per day, built and commissioned in 1978 as 100,000 barrels per day refinery of moderate complexity. A bottleneck was removed in 1982 to increase the processing capacity to 125,000 barrels per day. It has an adjoining petrochemical plant with the production capacity for Carbon check (NNPC, 2012).
- **Kaduna Refinery and Petrochemical Company (KRPC):** This refinery was built and commissioned in 1980 to supply petroleum products to Northern Nigeria with a capacity of 50,000 barrels per day. In 1993 the

capacity was expanded to 100,000 barrels per day by adding a second 50,000 barrels per day crude train designed to process both domestic and imported crude used for the production of Lube oil. The refinery has an adjoining petrochemical plant which can produce asphalt, benzene and heavy paraffin-d base oils used in the manufacture of vehicular lubricants and oils (NNPC, 2012).

The breakdown of refineries, poor management and lack of Turn Around Maintenance (TAM) between 1996-1998 reduced local processing of crude oil to about 75,000 barrels per day. Warri and Port Harcourt refineries presently operate at 30 % capacity. Kaduna refinery was shut down in 1998 due to unsuccessful Turn Around Maintenance (Okon, 2006; U.S.A, 2005). Presently, excess crude oil is being transported by the Nigerian government to other countries for refining.

2.3.4 Oil and gas producing in Nigeria

NNPC upstream operations are carried out in joint partnerships with the major oil companies. These multinational E&P companies are operating predominantly in the on-shore Niger Delta, coastal offshore areas and lately in the deep waters. NNPC is also responsible for the management of the exploration bidding rounds for oil and gas (NNPC, 2012).

With a maximum crude oil production capacity of three million barrels per day, Nigeria ranks as Africa's largest producer of oil and the sixth largest oil producing country in the world. Nigeria appears to have a greater potential for gas than oil. Nigeria's natural gas reserves are bigger, estimated at over 185

trillion cubic foot (TCF) making the country the eighth largest natural gas reserve holder in the world and the largest in Africa (U.S.A, 2010). Nigeria's gas production in the year 2000 was approximately 1,682 billion standard cubic foot (SCF), of which 1,372 billion (SCF) was associated gas and the rest (310 billion) was non associated gas. Nigeria produces only high value, low sulphur content, light crude oils - Antan Blend, Bonny Light, Bonny Medium, Brass Blend, Escravos Light, Forcados Blend, IMA, Odudu Blend, Pennington Light, Qua-Iboe Light and Ukpokiti (NNPC, 2012).

Generally, there are three basic stages for oil and gas production (Imaduddin, 2008):

- Primary production;
- Secondary production;
- Tertiary production.

Primary production: Once oil or gas is discovered and accessed, production engineers begin the task of maximizing the amount that can ultimately be recovered. Oil and gas are contained in the pore spaces of reservoir rock and some rocks may allow the oil and gas to move freely, making it easier to recover. Other reservoirs do not part with the oil and gas easily and require special techniques, e.g. in some reservoirs more than two-thirds of the oil may not be recoverable (Imaduddin, 2008).

There are two mechanisms for oil recovery, namely the dissolved gas drive mechanism and the water drive mechanism. In the dissolved gas drive mechanism, an average of about 20 % of the original oil is recovered. The water drive mechanism is much more efficient facilitating recovery of 50-80 % of the

original oil. However, if the oil-bearing rock is both very permeable and steeply inclined, the oil will run down because of gravity. Gas is collected at the top of the reservoir when wells are drilled down deep, which is called gravity drainage. If the produced gas is re-injected into the top of the reservoir, it is called the gas cap production mechanism and its efficiency is comparable to that of water drive. Some wells may stop producing in economic quantities in only a few years (Imaduddin, 2008).

Secondary production: Many oil fields that were produced by the dissolved gas drive mechanism until they became uneconomical are revived by using the water flooding technique. Water is injected into specially drilled wells forcing the oil out of the pores in the rock. After water flooding, about 50 % of the original oil still remains in the place thereby increasing production from the well (Imaduddin, 2008).

Tertiary production: Depending on reservoir conditions various substances will recover most of the residual oil when injected into the rock. These include solvents such as propane and butane; gases such as CO_2, N_2 and CH_4; and surfactant (soap) all of which will dissolve in the oil and form a bank of lighter liquid which picks up the oil droplets left behind in the rock and drives them to the producing wells. The only commercially successful enhanced recovery method to date is steam injection. Two methods of re-injecting steam are cyclic and in-situ combustion (Imaduddin, 2008).

Offshore facilities are different from those on land and the contributing factors are the type of platform, weight and space limitations, environmental

conditions, government regulations, drilling support, enhanced recovery, logistics of supply and market factors (they all have major impacts on the design) (Sen, 1988). There are six major different types of platforms for oil and gas exploitation and processing (Villasenor, 2003). They are:

- Drilling platform
- Crude oil recovering platform
- Crude oil measurement platform
- Transportation platform
- Flaring platforms
- Linking platform

Presently, there are over a thousand producing wells in the Niger Delta producing about three million barrels of oil per day from the numerous oil fields. Nigeria has an estimated 30 billion barrels of oil reserves. Oil and gas are produced from the same reservoir. Many Nigerian oil fields are saturated and have primary gas caps. The gas deposits outweigh oil by far. This makes the country more of a gas producer than oil producer (NNPC, 2012).

2.3.5 Types of flare

Gas flares are produced in the exploration, primary, secondary and tertiary stages of oil and gas production. Flares are generally categorized in two ways (Stone et al., 2000):

- By the height of the flare tip (i.e. ground or elevated)
- By the method of enhancing mixing at the flare tip i.e. steam-assisted, (Kalcevic, 1980); air-assisted, (McCartney, 1990); pressure-assisted, (Stone et al., 2000); non-assisted, (Shore, 1990) and enclosed ground, (Kalcevic, 1980).

Elevating the flare can prevent potentially dangerous conditions at ground level where the open flame (i.e. an ignition source) is located near a process unit. Further, the products of combustion can be dispersed above working areas to reduce the effects of noise, heat, smoke, and objectionable odours. In most flares, combustion occurs by means of a diffusion flame (Stone et al., 2000).

Cracking can occur with the formation of small hot particles of carbon that gives the flame a characteristic luminosity. If there is oxygen deficiency and if the carbon particles are cooled to below their ignition temperature, smoking occurs. In large diffusion flames, combustion product vortices can form around burning portions of the gas and shut off the supply of oxygen. This localized instability causes flame flickering, which can be accompanied by soot formation. As in all combustion processes, an adequate air supply and good mixing are required to complete combustion and minimize smoke. The various flare designs differ primarily in their accomplishment of mixing (Stone et al., 2000).

2.4 The gas flaring process

On oil production wells, rigs, in refineries and chemical plants, the primary purpose of gas flaring is to act as a safety device to safely dispose of gas during emergencies or during the breakdown of machinery (Edino et al., 2010; World Bank, 2003) and to protect vessels or pipes from over-pressuring due to unplanned upsets. Pressure control valves are set at predetermined pressures to release excess gas, thus allowing continued operation. Whenever plant equipment is over-pressured, the pressure relief valves on the equipment automatically release gases (and sometimes liquids as well) which are routed through piping runs called flare headers to the flare stacks. The gases and/or

liquids are separated in a flare knock out drum with the gas piped to the flare stacks for burning or for venting of lighter gas. The size and brightness of the resulting flame depends upon how much flammable material is released. Typically there may be more than one flare system handling high pressure gas, low pressure gas, sour or corrosive gas, cold gas and wet gas (Bruno, 2007).

In addition, vents (un-ignited flares) are used typically on gas plants for emergency gas disposal (Johnson et al., 2001). Flare gas recovery systems are occasionally used to collect low flows of waste gas and return it to the process plant as opposed to burning. Steam can be injected into the flame to reduce the formation of black smoke, but this does make the burning of gas sound louder, which can cause complaints from nearby residents (Bruno, 2007). Compared to the emission of black smoke, it can be seen as a valid trade off.

Furthermore, in order to keep the flare system functional, a small amount of purge gas flows continuously, whilst there are continuously burning pilots, so that the system is always ready for its primary purpose of burning as an over-pressure safety system. Enclosed ground flares are engineered to eliminate toxic and corrosive components, reduce smoke, and contain the flame within the enclosure. Burn pits are used to dispose of waste hydrocarbon liquids and are increasingly being designed out due to their unacceptable dirty appearance (Bruno, 2007).

Many flare systems are currently operated in conjunction with base-load gas recovery systems. These systems recover and compress the waste VOC for use as a feedstock in other processes or as fuel. When base-load gas recovery systems are applied, the flare is used in a backup capacity and for emergency releases.

Depending on the quantity of usable VOC that can be recovered, there can be a considerable economic advantage over the operation of a flare alone. Also, streams containing high concentrations of halogenated or sulphur containing compounds are not usually flared due to corrosion of the flare tip or formation of secondary pollutants (such as SO_2). If these vent types are to be controlled by combustion, thermal incineration, followed by scrubbing to remove the acid gases, is the preferred method (McCartney, 1990).

The emissions from gas flaring are referred to as hydrocarbon pollutants (Alakpodia, 1989). It is expected that gas flaring in the Niger Delta is the major single contributor to the emissions of these pollutants into the atmosphere with concentrations largely dependent on the extent of oil production at each location (Johnson et al., 2001).

2.5 Gas flaring in Nigeria

In Nigeria, gas flaring started since the discovery of crude oil in the late 1950s and has not stopped. This flaring activity is a constant phenomenon that occurs in all oil exploration, exploitation and production locations in all the nine states of the Niger Delta region of Nigeria (Odukoya, 2006; Dupont et al., 2000), with a total of 131 gas flaring sites (NASRDA, 2005). Figure 2.5 shows gas flaring at Eleme Petroleum Refinery Company II, Eleme in Rivers State.

Figure 2-5: Gas flaring at Eleme Refinery II, Eleme, Rivers State
Source: UNEP, 2009

Standard gas flaring sites in Nigeria are located at ground level and surrounded by thick mangrove vegetation, arable land and rural housing (Abdulkareem, 2005). The gas is sometimes burnt directly from flare pits or from flare stacks (Ekpoh and Obia, 2010). Figure 2.6 (A and B) shows typical gas flaring sites in the Niger Delta. Figure 2.6 (A) shows a gas flare burning at the horizontal level on the ground during the day and Figure 2.6 (B) is an example of gas flares burning vertically at night.

A B

Figure 2-6: (A and B): Gas flaring sites in the Niger Delta
Source: Social Action, 2009

The UNDP/World Bank in 2004 estimated Nigerian flaring at close to 2.5 billion cubic feet daily (over 70 million cubic metres daily), amounting to about 70 million tonnes of carbon dioxide (World Bank, 2004) and that the volume of gas flared in Nigeria was equivalent to one-sixth of total gas flared in the world (Kimberly et al., 2007). Flaring in Nigeria contributes a measurable percentage of the world's total emissions of greenhouse gases; due to the low efficiency of many of the flares (as demonstrated in Figure 2.5) much of the gas is released as CH_4 (which has a high global warming potential), rather than CO_2 (Dung et al., 2008; Malumfashi, 2007; ICF, 2006; World Bank, 2002).

As a result, Nigeria is rated as the second country in the world for gas flaring after Russia (Table 2.3); estimated for individual countries based on the sum of light index values with Russia and Nigeria accounting for 40 % of global flaring and the top twenty countries accounting for 85 % (Eseoghene, 2011; Ziskin et al., 2011; Elvidge et al., 2009; Kimberly et al., 2007). However, Nigeria is among other 16 countries that exhibit a downward trend in gas flaring from 1995 to 2006. Nigerian gas flaring has had several ups and downs – but the overall

reduction in gas flaring as at 2006 is in the range of 10 Billion Cubic Metres (BCM) (Kimberly et al., 2007). Shell, Mobil and Chevron Petroleum Companies of Nigeria are the three biggest flarer in the country (Table A-1 in Appendix A). Figure 2.7 below shows the network of Shell's oil and gas pipelines in the Niger Delta region.

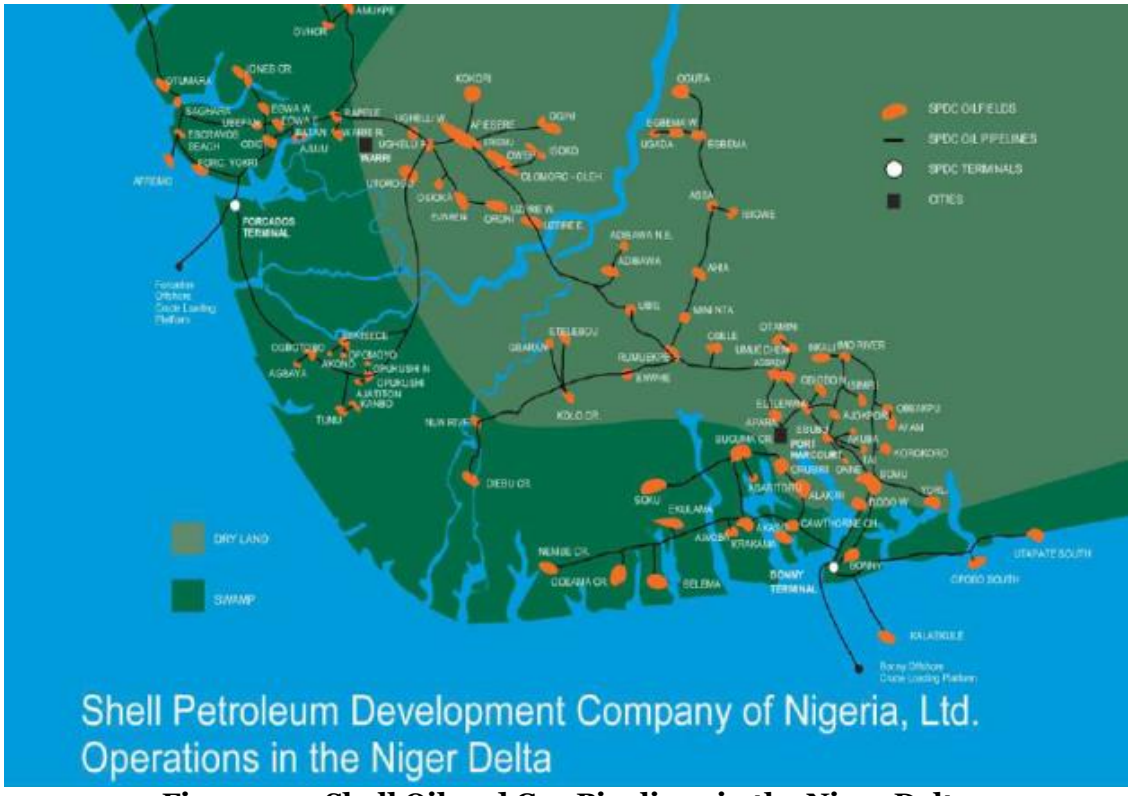

Figure 2-7: Shell Oil and Gas Pipelines in the Niger Delta
Source: Shell Annual Report, 2002 (SPDC, 2002)

Not all the AG produced in Nigeria is flared. The gas is either used as fuel, sold to third parties, converted to Liquefied Natural Gas (LNG) or re-injected to enhance oil recovery (NNPC, 2012; NNPC, 2009; NNPC, 1997). Table 2.4 shows Nigerian gas production and flare volumes for the past 50 years (1961-2010). Although there has been a remarkable decline in the volume of % of gas flared, from over 95 % in the 1960s to approximately 24 % in 2010, the remaining economic loss, environmental degradation and health hazard cannot be ignored.

Table 2-3: Estimated flared volumes from satellite data (2006–2010) for top six countries

Countries	2006 volume (BCM)	2007 volume (BCM)	2008 volume (BCM)	2009 volume (BCM)	2010 volume (BCM)	Changes from 2009 to 2010
Russia	50.0	52.3	42.0	46.6	35.2	11.4
Nigeria	18.6	16.3	15.5	14.9	15.2	0.3
Iran	12.2	10.7	10.8	10.9	11.3	0.4
Iraq	7.2	6.7	7.1	8.1	9.1	1.1
Algeria	6.4	5.6	6.2	4.9	5.4	0.5
Angola	4.0	3.5	3.5	3.4	4.1	0.7
Total top 6	98.4	95.1	85.1	88.8	80.3	8.5
Rest of the world	62.6	58.9	61.9	58.2	53.7	4.5
Global flaring level	161.0	154.0	147.0	147.0	134.0	13.0

Source: NOAA, 2011.

Table 2-4: 1961, 1971, 1981, 1991, 2001 and 2010 gas flaring volumes for Nigeria (Million Cubic Metres)

Year	Gas produced	Gas flared	% of gas flared
1961	310	N/A	N/A
1971	12996	12790	98.41
1981	17113	13470	78.71
1991	31460	24660	78.39
2001	52453	26759	51.02
2010	67758	16468	24.30

Source: NNPC, 2012; NNPC, 2009; NNPC, 1997

In Table 2.3, the estimated flared volume from satellite data for Nigeria in 2010 is 15.2 Billion Cubic Metres (BCM) (NOAA, 2011) while in Table 2.4, 16.5 Billion Cubic Metres (BCM) was reported by NNPC (NNPC, 2012) as the flared volume for the same year 2010. The difference in the result could be attributed to the availability of uncertainties. This is supported by NOAA (2011) that there is substantial uncertainty regarding the magnitude of gas flaring and that the current volume estimates rely on voluntary reporting by corporations and individual countries.

2.5.1 Policies and legislation on gas flaring in Nigeria

The Nigerian government in the pursuit of phasing out gas flaring has enacted a number of regulations for monitoring flaring volumes and enforcing operational procedures. Despite the introduction of these regulations more than 40 years ago, these regulatory policies have mostly been unsuccessful. According to Abdulkareem (2005), these policies and regulations are very poor and inefficient due to the fact that the government puts profit maximisation ahead of the environment and the wellbeing of its citizens. Another factor is the insignificant fines imposed as a penalty for gas flaring, which the multi-national oil companies are willing to pay as it is more economical to flare and pay fines than to stop flaring (Ishisone, 2004). Several regulations on gas flaring from its inception till 2014 are stated overleaf;

- **1969 - Petroleum (Drilling and Production) Act and Regulations:** This encouraged the use of associated gas, by exempting multi-national oil companies from the payment of royalties (ICF, 2006).
- **1979 - Associated Gas Re-injection Act (AGRA):** This act prohibited flaring of AG after January 1, 1984 without the permission from the Minister of Petroleum. Since about 90 % of Nigeria's foreign exchange comes from oil revenue, the government failed in implementing the 1984 deadline (Aghalino, 2009; Sonibare and Akeredolu, 2006).
- **1985 - Associated Gas Re-injection Act Amendment Decree 7:** As a result of the failure of the 1979 AGRA, the 1985 AGRA amendment decree was promulgated which provides for exemption to the 1979 AGRA and permits a company engaged in the production of oil or gas to continue to flare gas in a particular field or fields on the payment of a fee set by the Minister of Petroleum. The fine was 2 kobo (0.0009 US$ equivalence) per 1000 SCF of

gas flared. This rose to 50 kobo (0.03 US$ equivalence) in 1992 and further to N10.00 (0.46US$ equivalence) in 1998. This policy was also unsuccessful as fines were insignificant and did not provide any incentive to encourage the multi-national oil companies to reduce flaring of AG (Aghalino 2009; Malumfashi, 2007; Sonibare and Akeredolu, 2006).

- **1992 - Associated Gas Framework Agreement (AGFA):** This is a form of fiscal incentives for companies involved in gas utilization (Aghalino 2009; ICF, 2006).
- **1988/92 - The Federal Environmental Protection Agency (FEPA) Act**: This act is principally for environmental management (Malumfashi, 2007).
- **1998 - Finance (Miscellaneous Taxation Provision) Decree:** This is also a form of fiscal incentives for companies involved in downstream and upstream gas utilization, by reducing their tax burden (Sonibare and Akeredolu, 2006).
- **2004 - Associated Gas Re-Injection Act and the Associated Gas Re-Injection (Amendment) Act**: This also prohibited flaring of AG without the permission from the Minister of Petroleum. It obligated all oil producing companies in the country to submit detailed plans for gas utilisation (Malumfashi, 2007).
- **Petroleum Industrial Bill (PIB):** At the time of writing, this bill is yet to be passed by the Nigeria government. The initial PIB draft (2008), had provisions to enforce multi-national oil companies to comply with international standards on integrated health, safety and environmental quality management systems by specifying quality, effluent and emission targets (Legall, 2009). However, this draft according to a joint position paper

by three Civil Society Organizations in Nigeria [Social Action, Environmental Rights Action (Friends of the Earth Nigeria) and Civil Society Legislative Advocacy Centre, 2011], have been adjusted, deleting the clauses that have to do with the prohibition of gas flaring and the imposition of penalties for gas flaring. This new PIB draft (2010), unfortunately has given absolute legality to the flaring of gas.

2.5.2 Gas flaring reduction projects in Nigeria

In an attempt to reduce and eliminate gas flaring the federal government of Nigeria has implemented a number of gas flaring reduction projects. These are;

- **The Nigeria Liquefied Natural Gas (NLNG) Limited:** This is the largest natural gas utilization project in Nigeria, located in Bonny Island in the Niger Delta region of Nigeria. It is jointly owned by Agip (10.4 %), Nigeria National Petroleum Corporation (NNPC) (49 %), Shell (25.6 %), and TotaFinaElf (15 %) (Sonibare and Akeredolu, 2006).
- **Brass River LNG:** This is the third LNG plant to be developed by the Federal Government of Nigeria, Philips and Agip (Sonibare and Akeredolu, 2006).
- **Escravos gas-to-liquid projects (EPG):** This project is being developed by Chevron and will involve the exploitation of technologies to convert gas to synthetic fuels (diesel, kerosene, jet fuel, and naphtha) (Malumfashi, 2007; Sonibare and Akeredolu, 2006).
- **West Niger Delta LNG:** This is the second LNG plant to be developed by Chevron, Texaco, Conoco, and ExxonMobil (Sonibare and Akeredolu, 2006).
- **The West African Gas Pipeline (WAGP):** This is a 617 km pipeline designed to transport Nigerian natural gas from the Niger Delta region of

Nigeria to power generation and industrial customers in Benin, Togo and Ghana. This project is being developed by Chevron Nigeria Limited, Shell Development of Nigeria Limited, NNPC, The Volta River Authority (Interests formally held by Ghana National Petroleum Corporation), SobeGas of Benin Republic, and SotoGas of the Republic of Togo. The World Bank estimated that the amount of flaring would be reduced by 78 million tonnes of carbon dioxide equivalent (tCO_2e) (Sonibare and Akeredolu, 2006; World Bank, 2003).

There are other gas flaring reduction projects and development in Nigeria. For example, the fourth LNG plant by Shell, Norway Statoil, and NNPC, Compressed Natural Gas (CNG) sponsored by SPDC in Warri and Nigeria Gas Company (NGC) (Malumfashi, 2007; Sonibare and Akeredolu, 2006).

Notwithstanding all these gas flaring reduction projects, the deadlines to eliminate gas flaring in Nigeria are still not being met. The presence of large amounts of natural gas reserves for both associated gas and non-associated gas, have been identified as one of the major reasons for this setback. This can be seen when Sonibare and Akeredolu (2006) noted that only 30 % of the gas utilized in the first LNG plant (NLNG) comes from AG, therefore flaring reduction measures implemented here would not significantly contribute to phasing out of gas flaring.

2.5.3 Factors responsible for continuous gas flaring in Nigeria

There have been several attempts to stop gas flaring in Nigeria and despite regulations introduced more than 40 years ago to prohibit flaring, associated

gas is still being flared. Several studies have been conducted to identify the factors responsible for its continuous practice. These include:

- Lack of a strong and consistent fiscal, legal and regulatory framework and institutions to interface with international investors (ICF, 2006; ESMAP, 2004).
- Lack of the political will to formulate and enforce coherent policies because of political instability and corruption (Edino et al., 2010; Ishisone, 2004).
- Lack of a clearly defined long-term vision for the natural gas sector due to the inadequate capabilities and overlapping responsibilities of government institutions (Omakaro, 2009; ESMAP, 2004; Gerner et al., 2004; Ishisone, 2004).
- Failure of the government to redeem its financial obligation under the existing joint venture (Ishisone, 2004).
- Inadequate or lack of necessary technology for gathering and harvesting associated gas (ICF, 2006; ESMAP, 2004).
- Low demand for gas in both the domestic and regional markets because of reduced industrial activities and low domestic oil price (Sonibare and Akeredolu, 2006).
- The presence of an enormous amount of natural gas deposits makes it more economical for the government to use non-associated gas as an energy source rather than harvesting the associated gas (Ishisone, 2004).
- The short-term profit maximisation of multi-national oil companies (Omakaro, 2009; Ishishone, 2004).
- Limited studies and low level of environmental awareness of the cost and impacts of gas flaring in the country (Ishisone, 2004).

In addition, the report on Strategic Gas Plan for Nigeria concluded that apart from eliminating all the above factors, the Nigerian government needs to overhaul its power sector, in order to create an avenue for the utilization of the AG produced (ICF, 2006; ESMAP, 2004).

2.6 Environmental pollution

Pollution is the introduction of contaminants into a natural environment that causes instability, disorder, harm or discomfort to the ecosystem i.e. physical systems or living organisms. It can take the form of chemical substances or energy such as heat, light or noise. Pollutants (the components of pollution) can be either foreign substances or energy or naturally occurring contaminants (Ja Eun et al., 2010). It is often classified as point source or non-point source and it is a serious problem for the environment. Point emission sources are generally considered to be fixed facilities that produce waste products such as gaseous, liquid and particulate atmospheric pollutants. Non-point pollution generally comes from many diffuse sources such as land runoff, precipitation, atmospheric deposition, drainage, seepage or hydrological modification. Pollution alters the natural environment, adversely affecting its use by environmental receptors such as plants, animals, and humans (Djoundourian et al., 2007). The natural environment includes three environmental media: air, land, and water. Water includes wetlands, rivers, lakes, oceans and groundwater aquifers which flow underground. Pollution contaminates these environmental media, which may then serve as pathways that transfer contaminants to other media or to receptors (Mucahit, 2011).

The term environmental pollution is more often used to describe the direct or indirect impacts of human activities. The cumulative effects of concentrated human activities can create large-scale or long-term environmental consequences beyond the assimilative capacity of the environment (Chaerun et al., 2007). Land, water, air and other types of pollution such as radiation, noise, thermal and visual pollution are some direct results of human activities. Indirect pollution like ozone depletion in the atmosphere is also occurring. Indirect effects are more difficult to prove because they can occur over long periods of time and result from complex interactions (Ja Eun et al., 2010).

Manmade pollution is divided into two classes (accidental and chronic). In the case of oil, accidental spills usually result from large volumes of oil escaping from damaged pipes, ships or offshore drilling operations. Chronic pollution comes from industrial sources or intentional dumping, such as gas flaring, oil spills from refineries, industrial chemical wastes, bilge waste from ships. Dock areas and coastal industrial regions with high industrial activity produce waste oils and some of these eventually get into the environment (Roberts et al., 2000).

Thermal (heat) pollution occurs when heat released into air or water produces undesirable effects and it can occur as a sudden or acute event that may result from natural or human processes. Sources of thermal pollution include gas flaring, biomass burning, power plants generating electricity from fossil fuel and water used as a cooling agent. Also, fires of high intensity generate a large amount of smoke that is dispersed depending upon wind direction and speed (Khandewal and Goyal, 2010).

Oil companies in Nigeria are considered to be a source of chronic pollution with continual discharge of gas flaring, oil spillage and waste waters into the environment. Oil production processes generate an important quantity of aqueous effluents that are usually discharged to the recipient environment (Sundt et al., 2011). Pollution resulting from hydrocarbons can be classified according to the three media of environment, therefore producing land or soil pollution, air pollution and water pollution. Hydrocarbons can be gases (e.g. methane and propane), liquids (e.g. hexane and benzene), waxes or low melting solids (e.g. paraffin wax and naphthalene) or polymers (e.g. polyethylene, polypropylene and polystyrene). The pollutants from hydrocarbons include the following: Carbon Dioxide (CO2), Carbon Monoxide (CO), Nitrogen Oxides (N2O), Sulphur Dioxide (SO2), Atmospheric Particulates Matter (APM), and Mercury (Hg) (Schifter, 2005; Silberberg, 2004). Among the pollutants, petroleum hydrocarbons are important due to their high toxicity and carcinogenicity (Schifter, 2005; Silberberg, 2004).

2.7 Environmental, economic and health implications of gas flaring in the Niger Delta

Flaring of natural gas in the Niger Delta and offshore has been identified by several studies as damaging to the environment and people (Azibaolanri, 1997; Alakpodia, 1989); the host communities live and work alongside the flares with no protection (FOE, 2004) and so experience effects such a serious air pollution (Edino et al., 2010; CLO, 2004).

Leahey et al. (2001) found that contrary to the assumption that flaring achieves complete combustion with relatively harmless by-products such as CO_2 and

H_2O, it does not. Moreover a number of carcinogenic by-products are produced from flares which may have harmful effects on the ecosystem. Studies from Sonibare and Akeredolu (2004), Winter et al. (1999) and Obioh et al. (1994) have shown that gaseous pollutants (CO_2, CO, NO, NO_2 and SO_2) are present in combustion reactions from gas flaring and are very harmful to human health causing diseases such as cancer (Majumdar, 2008), asthma, rhinitis and other respiratory health effects (Johnson, 2010), alongside oxidative damage to macromolecules, chromosomal aberrations and changes in gene expression (Rossner, 2011; Alvim et al., 2011). Several studies have linked health issues such as skin disorder, heat irritation, sunstroke, eye conditions and heat exhaustion to the fumes produced by gas flaring (Nwanya, 2011; Effiong, 2010).

The study by the Environmental Rights Action and the Climate Justice Programme in 2005, quantified damage done by the toxic cocktail of pollutants, including benzene and dioxins for the Bayelsa State alone as statistically likely to cause 49 premature deaths, 5,000 cases of child respiratory illness, some 120,000 asthma attacks and 8 additional cases of cancer each year (Utomwen, 2011; Okon, 2006).

Several other studies also point to deterioration of soil structure, loss of organic matter contents, loss of soil mineral nutrients, soil leaching and erosion caused by lead that has been used as a fuel additive, reduced or inhibited soil enzymes activities (Akubugwo et al., 2009). As the plants and vegetative cover dies off (Akeredolu, 1989) and are being harvested for fuel wood (Nwanya, 2011), this ecologically sensitive area is destroyed and so there is lower diversity (Ugochukwu and Ertel, 2008; Ekwekwe, 1981; Fagbade, 1981 and Odu, 1981),

plus there is an increase in surface temperature of about 3.7 °C above the mean normal daily temperature within a radius of 270 m of flare site (Oseji, 2007) and greenhouse gases such as CO_2 and CH_4 hinder the escape of long wave terrestrial radiation into space (Zekai, 2004). Furthermore, the ability of NO_X and SO_2 to react with water to form acidic compounds has implicated gas flaring as being responsible for acid rain in the Niger Delta (Sonibare and Akeredolu, 2004).

Thermal pollution has also disturbed the ecosystem balance and affected aquatic creatures, which can lead to migration and vulnerability to invasive species (Abbaspour et al., 2006). Also, there is growing evidence that regional air pollution can contribute to planetary scale changes in atmospheric precursors for ozone formation and particulate matter (Seinfeld, 2004). The most noticeable effect is light pollution across the oil producing regions that, in the rainy season, reflects luridly from the clouds and lights up the night sky. Villagers close to flares complain that nocturnal animals are disturbed, and leave the area, making hunting more difficult (Ugochukwu, 2008). In a recent study by Nwankwo and Ogagarue (2011), surface and ground water from gas flare regions in Warri, Delta State, was found to have high concentrations of heavy metals beyond the maximum permissible limits specified by the World Health Organization (WHO).

Local farmers have complained about retardation of growth and productivity of farm crops around gas flares (Abdulkareem, 2005; Ologunorisa, 2001). Oluwatimilehin (1981) observed depression in flowering and fruiting in Okro, palm trees and cassava. He found that cassava tubers decreased in length and

weight with decreasing distances from the gas flares. Osuji and Avwiri (2005) also supported Ologunorisa (2001), Abdulkareem (2005) and Oluwatimehin (1981), they reported that heat associated with gas flares has killed vegetation around the flare stack, suppressed the growth and flowering of some plants, and reduced agricultural production. Ukegbu and Okeke (1987) studied the effect of a gas flare on the growth, productivity and yield of selected farm crops in the Izombe flow station, located in Izombe Ohaji/Egbema/Oguta Local Government Area of Imo State. They found an almost 100 % loss in yield in all crops cultivated up to 200 m away, 45 % loss for those up to 600 m and 10 % loss in yield for crops up to 1000 m away from the flare.

The impact of gas flaring on vegetation degradation was studied by Nelson (1997) at four flare sites in Bayelsa and Rivers States. Specifically, the study deals with the thermal impact of gas flaring on plant species frequency, density and leaf scorching relative to distance from some gas flare sites. The study reveals that plant species frequency and density decreased with distance from gas flare sites and that leaf scorching increased around the flare sites. Dung et al. (2008) also discussed the effects of gas flaring on crops and vegetation cover in the Niger Delta. Their study explored the spatial variability effects of gas flaring on the growth and development of cassava (*Manihot esculenta*), waterleaf (*Talinum triangulare*), and pepper (*Piper* spp.). Temperatures of 57 °C were recorded within 40 m of the gas flare and reduced to 32 °C at 100 m. Dung et al. (2008) suggested that a spatial gradient exists for the effects of gas flares on crop development. Retardation in crop development is manifested in decreased dimensions of leaf lengths and widths of cassava and pepper crops closer to the gas flare point. Statistical analysis also confirmed that cassava

yields are higher at locations further away from the flare point. In addition, the amount of starch and ascorbic acid in cassava decreased when the plant is grown closer to the gas flare. High temperatures around the gas flare appeared to be the most likely cause of this retardation (Dung et al., 2008).

Results from Isichei and Sandford (1976), on the influence of gas flaring on vegetation cover and crops show that leaf chlorophyll content and internode length of Eupatorium odoratum plants close to the flares decreased. The flowering of the short-day plant, Eupatorium odoratum was suppressed in the area of the flares. A bare area, 30-40 m in radius, occurred around the flare stacks. Outside this bare area, the species composition of the vegetation was affected by the flares up to a distance of 80 to 100 m from the stacks and the total number of species close to the flares decreased.

Furthermore, Odjugo and Osemwenkhae (2009) reported that with the rise in air and soil temperatures at Ovade flaring site, relative humidity and soil moisture decreased toward the flare. The induced microclimatic condition, which impacted on the soil, reduced the yield of maize by 76.4 %, 70.2 % and 58.2 % at a distance of 500 m, 1 km and 2 km respectively from the flare. Maize production is not economically viable within 2 km distance from the flaring site. Ugochukwu and Ertel (2008) and Ofomata (1997) argued that gas flaring leads to the charring of the mangrove and rainforest vegetation (Ofomata (1997) of the oil region, Niger Delta along with damage to numerous economically and botanically valuable plant species.

In light of the above, the livelihoods of the people, especially fishing and farming communities, have been significantly affected leading to a high level of poverty (Omokaro, 2009; Nduka et al., 2008). In addition, the economic loss to Nigeria as a whole is immense. Gas flaring results in the wastage of large amounts of Nigeria's second most valuable natural resource, estimated by the World Bank to cost between $2.5-$3 US billion annually (Ishisone, 2004; World Bank, 2002). When the wide environmental, economic and social consequences are factored in it could be in the order of $150 billion US per annum (NBS, 2006); part of this cost has been the impact on human health (Okon, 2006). In spite of all these consequences, oil companies will only reduce flaring when the marginal costs of gas utilization exceed the marginal benefits; not considering the cost of its negative externality (Aghalino, 2009). There are limited studies to fully determine the environmental impact of gas flaring over a long period and, as noted by Edino et al., (2010), "the environmental cost of gas flaring is yet to be fully estimated, but anecdotal evidence suggests it is equally colossal". Dung et al., (2008) also noted "the environmental costs are yet to be adequately quantified". Finally, Ofomata (1997) called for intense research in all aspect of environmental impact of gas flaring in the Niger Delta.

2.8 Remote sensing technology for fire and gas flare

Sabins (1978) defined remote sensing as the collection of information about an object without being in physical contact and commonly is restricted to methods that employ electromagnetic energy as a means of detecting and measuring target characteristics. Remote sensing is a tool that can be used to monitor an increasing number of environmental parameters over a range of spatial and temporal ranges (Lavender, 2007). Lavender (2007) also stated that maps will

have inherent biases/errors that must be appreciated if the data are to be used in an appropriate way. She concluded that as remotely sensed products are made available to a wider audience through electronic media such as the World Wide Web (WWW) background information is often lost.

Technological advances have driven all aspects of Earth Observation (EO) data, including improvements in sensor characteristics and capabilities, global data processing, near real-time monitoring, value-added products, and the distribution of global products (Slonecker and Fisher 2011; Philip, 2007). ESA, USGS, NOAA and FIRMS (a NASA-funded application) are examples that illustrate the increasing ease with which EO data are accessible to a broad range of users (Davies et al., 2009). There are three possible sources of the energy that can be received by a remote sensing instrument. They are originated from the Sun and reflected; emitted by the surface being observed; and produced on the satellite by the sensor and then reflected (Amici et al., 2011; Robinson, 2004).

During daylight hours, the Sun's emitted energy (solar irradiance) is transmitted through the atmosphere and a proportion (dependent on whether the wavelength is within a spectral region of low atmospheric absorption) reaches the Earth's surface. At the surface, this radiation is partially reflected and transmitted back up through the atmosphere where it can be detected by a sensor (optical imaging). If the radiation is instead absorbed by the surface and re-emitted as heat this would be thermal imaging (Lavender, 2007).

A wide overview of sensors, missions, agencies and their technical characteristics (Table A-2 in Appendix A) was provided by Spazio (2015). Since

passive sensors depend on solar illumination or emitted radiance, their energy source generates continuous incoherent electromagnetic radiation and there is no chance of obtaining phase information (Robinson, 1995), whereas microwave sensors usually transmit a train of microwave pulses. Also, because active sensors generate their own illumination, these sensors can operate any time of the day and the illumination geometry is selectable and controllable. However, LiDAR is an active sensor and is greatly affected by cloud but > 1 cm wavelength RADAR is unaffected not because it is active, but because the wavelength is much longer than the atmospheric particles that impact optical wavelength electromagnetic radiation.

Passive microwave and thermal infrared sensors are sensitive to the surface thermal properties (Planck Equation) and must account for surface emissivity. Multispectral short and near-infrared sensors are also sensitive to the chemical composition of the surface. All sensors are sensitive to the surface topography and no single sensor can provide a complete description of the surface properties (Colwell, 1983). Use of multiple wavebands/wavelengths can help to diagnose surface type if the object emissivity varies spectrally. High spectral resolution is achieved by narrow bandwidths which collectively are likely to provide a more accurate spectral signature for individual discrete objects than are broad bandwidths (Colwell, 1983).

Remote Sensing has become a widely used tool for applications centred on the monitoring of land, land cover state and changes. In addition, it can be used for geological and hydrological purposes, measurement of surface radiance and emittance, measurement of liquid water content, and the mapping of burned

areas at regional and global scales (Gomez and Martin, 2011). The primary quantities that can be observed from the space are listed in the Table 2.5.

Table 2-5: The primary remote sensing technology observables for land and ocean

S/N	Land remote sensing	Ocean remote sensing
1.	Colour	Apparent water colour
2.	Temperature	Sea surface temperature
3.	Surface roughness	Sea surface roughness
4.	Surface height	Sea surface height, geostrophic currents, bathymetry
5.	Land cover types and land use changes	Chlorophyll-a fluorescence, phytoplankton chlorophyll-a
6.	Vegetation cover, health	Sea surface salinity
7.	Albedo	Sea surface albedo
8.	Pressure and Aerosol are atmospheric quantities that can also be retrieved over water	

Adapted from: **Richter, 2005; Robinson, 2004**

Planetary albedo is simply the fraction of incident light from the sun which is reflected back into space by the earth. It is a sum of reflection by ground surfaces, ocean surfaces, clouds, atmospheric gases, and atmospheric particles, but of these, clouds contribute by far the highest proportion of total reflection (Twomey, 1974). Furthermore, a direct connection exists between pollution and the number of drops in a cloud and hence the optical thickness and reflectance of the clouds. Pollution leads to dirty clouds with lower albedo. Scattering and absorption are higher than in cloud-free air because of the introduction of additional aerosol particles. However, the probable importance of the influence of pollution on cloud reflectance lies in the fact that the process of cloud condensation causes some of the particles in the atmosphere to grow into droplets which have cross-sectional areas typically a hundred thousand times that of the nucleating particles (Twomey et al., 1984).

2.8.1 Satellites and sensors for detection of fire and gas flares

There are a number of different satellite remote sensing platforms with multiple sensors in the TIR spectrum, giving useful datasets to measure LST. Datasets are available for different time periods, at different spatial resolutions, with varying accuracy; therefore this section reviews all possible choices of data that are relevant to this study. Nadir-viewing orbital satellites are limited by image acquisition time which is set by the orbital characteristics of the satellite and means that readings at specific times cannot be obtained or requested unless they match the orbit but those orbital satellites capable of off nadir viewing acquires more images. Geostationary satellites, which stay in the same position relative to the Earth, offer a greatly increased temporal resolution and coverage area at the expense of reducing spatial resolution. Also, not all images may be accurate, as high zenith angles result in a lengthened atmospheric path that can result in less accurate surface temperature values (Streutker, 2003). Choice of image timing is also important. For example, Rigo et al. (2006) found that MODIS LST was more accurate at night compared to the daytime, and the AATSR target accuracy is $\pm$2.5 K for daytime, increasing to $\pm$1 K at night time (Noyes et al., 2007). Similarly, Hartz et al. (2006) found night time ASTER images could better observe neighbourhood climatic conditions. Limitations of spatial resolution are being investigated, and algorithms have been developed to sharpen thermal images to increase the spatial resolution (Dominguez et al., 2011).

2.8.1.1 Landsat series

The Thematic Mapper (TM) on Landsat 4 and 5 that were launched 16th July 1982 and 1st March 1984 respectively had a visible-SWIR resolution of 30 m and

a TIR resolution of 120 m (band 6, 10.4-12.5 μm) but data processed before February 25, 2010 are resampled to 60 m. Products processed after February 25, 2010 are resampled to 30 m (NASA, 2015a). Landsat 4 TM was decommissioned on June 15, 2001 and Landsat 5 TM operational imaging ended in November 2011 and it was decommissioned on June 5, 2013 (USGS, 2015a).

Landsat 7 Enhanced Thematic Mapper (ETM+) that was launched 15th April 1999 collects thermal data at a 60 m resolution (band 6, 10.4-12.5 μm) but products processed after February 25, 2010 are resampled to 30 m (NASA, 2015a). All bands can collect one of the two gain settings (high or low) for increased radiometric sensitivity and dynamic range, while thermal band collects both high and low gain for all scenes. Landsat 7 has a near polar Sun-synchronous orbit with a revisit time of 16 days, meaning that a given point on Earth should be imaged at approximately the same local time (~1000 h) every 16 days. The ETM+ offers some of the highest thermal resolution measurements from space, and data are available freely from the U.S. Geological Survey (USGS) (http://earthexplorer.usgs.gov/or http://glovis.usgs.gov), however data from 2003 onwards are impaired due to failure of the scan line corrector. This result in only ~80 % of each scene being captured (Chen et al., 2012). The Landsat data archive has been freely available since 2008; therefore the number of studies using Landsat 7 ETM+ has increased in recent years. A disadvantage of data from Landsat is that prior to ETM they were not collected at night, and the thermal calibration is limited. More details on the Landsat project are available (http://pubs.usgs.gov/fs/2010/3026) and the Landsat Data Continuity Mission (LCDM) aims to continue the long term Landsat record

(NASA, 2015b). Resampling the thermal band to lower resolutions (e.g. 30 m to match the visible spectrum) is a common technique (Cao et al., 2010; Xian and Crane, 2006; Weng et al., 2004; Weng, 2003) in order to simplify analysis. Table 2.6 show the spectral bands, wavelength and spatial resolution for Landsat 4-5 TM and Landsat 7 ETM+.

Landsat 8 Operational Land Imager (OLI) and Thermal Infrared Sensor (TIRS): Landsat 8 was launched 11th February 2013 and is formerly known as the Landsat Data Continuity Mission (LDCM) (NASA, 2015b). Landsat 8 images consist of eleven spectral bands; nine bands have a spatial resolution of 30 m for bands 1 to 7 and 9. New band 1 (ultra-blue) and new band 9 are useful for coastal and aerosol studies, and for cirrus cloud detection respectively. The spatial resolution for band 8 (panchromatic) is 15 m. Thermal bands 10 and 11 are acquired at 100 m resolution, but resampled to 30 m in the delivered data product and they are useful in providing more accurate surface temperatures. However, the radiometric integrity of the resampled data can be affected. The instruments provide improved signal-to-noise (SNR) radiometric performance quantized over a 12-bit dynamic range (NASA, 2015a). Table 2.7 show the spectral bands, wavelength and spatial resolution for Landsat 8 OLI/TIRS. Landsat 8 has dual window (bands 10 and 11) for thermal bands that allows the application of dual window methods for the correction of atmospheric effects on the acquired thermal data. Hence, it provides more accurate results on emissivity and surface temperatures (Tomlinson et al., 2011). NASA and the USGS began planning Landsat 9 that was announced on April 16, 2015 and planned to launch in 2023. This will provide mission-critical continuity in the Earth-observing program's record of land images (NASA, 2015b).

In the USA, Aniello et al. (1995) used Landsat TM data to help map micro urban heat islands (UHIs) (hot spots within a city) in Dallas, Texas, USA by combining both the thermal band (6) and extracted tree cover data from an unsupervised classification. One satellite image was used and the results showed that micro UHIs were highest in the centre and were generally resulting from a lack of tree cover. Weng (2003) used three Landsat TM images (from 1989, 1996 and 1997) to study the UHI in Guangzhou, China alongside fractal analysis with the result that showed two significant heat islands existed in the city. Weng et al. (2004) use Landsat ETM+ to link LST to Normalized Difference Vegetation Index (NDVI) in Indianapolis, USA which resulted in results linking LST to different land cover types and Xian and Crane (2006) use both Landsat TM and ETM+ to explore the thermal characteristics of urban areas in Tampa Bay and Florida, USA finding that land use and land cover fundamentally affect the thermal results. In Europe, Stathopoulou and Cartalis (2007) used Landsat ETM+ data to explore the daytime UHI across the major cities in Greece using a method that incorporates the CORINE land cover classification to superimpose land cover based emissivity values to create a mean surface temperature by land cover. Landsat has a great strength in terms of spatial resolution, however its 16 day revisit time and lack of night time image acquisition is limiting at the temporal scale.

Table 2-6: Spectral bands, wavelengths and spatial resolution for Landsat 4-5 TM and Landsat 7 ETM+

Bands	Wavelength (μm)	Resolution (m)	Useful for mapping
Band 1 - Blue	0.45-0.52	30	Bathymetric mapping, distinguishing soil from vegetation and deciduous from coniferous vegetation
Band 2 - Green	0.52-0.60	30	Emphasizes peak vegetation, which is useful for assessing plant vigour
Band 3 - Red	0.63-0.69	30	Discriminates vegetation slopes
Band 4 - Near Infrared	0.77-0.90	30	Emphasizes biomass content and shorelines
Band 5 - Short-wave Infrared	1.55-1.75	30	Discriminates moisture content of soil and vegetation; penetrates thin clouds
Band 6 - Thermal Infrared	10.40-12.50	120 (TM), 60 (ETM+) and both resampled to 30	Thermal mapping and estimated soil moisture
Band 7 - Short-wave Infrared	2.09-2.35	30	Hydrothermally altered rocks associated with mineral deposits
Band 8 - Panchromatic (Landsat 7 only)	0.52-0.90	15	15 meter resolution, sharper image definition

Source: USGS, 2015a

Table 2-7: Spectral bands, wavelengths and spatial resolution for Landsat 8 OLI/TIRS

Bands	Wavelength (μm)	Resolution (m)	Useful for mapping
Band 1 - Coastal aerosol	0.43-0.45	30	Coastal and aerosol studies
Band 2 - Blue	0.45-0.51	30	Bathymetric mapping, distinguishing soil from vegetation and deciduous from coniferous vegetation
Band 3 - Green	0.53-0.59	30	Emphasizes peak vegetation, which is useful for assessing plant vigor.
Band 4 - Red	0.64-0.67	30	Discriminates vegetation slopes
Band 5 - Near Infrared (NIR)	0.85-0.88	30	Emphasizes biomass content and shorelines.
Band 6 - Short Wave Infrared 1 (SWIR 1)	1.57-1.65	30	Discriminates moisture content of soil and vegetation; penetrates thin clouds
Band 7 - Short Wave Infrared 2 (SWIR 2)	2.11-2.29	30	Improved moisture content of soil and vegetation and thin cloud penetration
Band 8 - Panchromatic	0.50-0.68	15	15 meter resolution, sharper image definition
Band 9 - Cirrus	1.36-1.38	30	Improved detection of cirrus cloud contamination
Band 10 - Thermal Infrared (TIRS) 1	10.60-11.19	100 resampled to 30	100 meter resolution, thermal mapping and estimated soil moisture
Band 11 - Thermal Infrared (TIRS) 2	11.50-12.51	100 resampled to 30	100 meter resolution, improved thermal mapping and estimated soil moisture

Source: USGS, 2015a

2.8.1.2 AATSR

The Advanced Along Track Scanning Radiometer (AATSR) was carried onboard the European Space Agency (ESA) ENVironment SATellite (ENVISAT) which was launched in March 2002 and ceased operations in April 2012. This was the third instrument and the last in a series (ATSR-1 and ATSR-2) which started with the Along Track Scanning Radiometer (ATSR-1) in 1991. The primary objective of these missions has been for sea surface temperature (SST) collection. ENVISAT is in a Sun-synchronous polar orbit with a 35 day repeat cycle, which means data availability is lower than others (Spazio, 2015; ESA, 2015a). AATSR data have a resolution of 1 km at nadir, and are derived from measurements of reflected and emitted radiation taken at the following wavelengths: 0.55, 0.66, 0.87, 1.60, 3.70, 11.00 and 12.00 μm (ESA, 2015a). Hence, the spectral configuration of this instrument is very similar to the AVHRR. A primary difference is the use of a conical scan to give a dual-view of the Earth's surface, on-board calibration targets, and use of mechanical coolers to maintain the thermal environment necessary for optimal operation of infrared detectors. The swath-width is 500 km and the spatial resolution is 1 km at nadir (Foody, 2002).

The LST product is operational from March 2004 for data from the AATSR, and the TIR bands 11 and 12 μm are used to provide LST at ~1 km resolution and the algorithms developed were applied to data from the previous sensors (ATSR-1 and ATSR-2) resulting in an LST dataset starting in 1991 (Istomina et al., 2010). The AATSR literature is primarily concerned with the theoretical science for algorithm development (Prata, 2002), evaluation of algorithms (Sòria and Sobrino, 2007) or validation (Coll et al., 2009; Noyes et al., 2007; Coll et al.,

2005). AATSR has been used for monthly LST mapping over Europe (Joan and Cesar, 2009) and more broadly for drought prediction (Djepa, 2011), estimating evapotranspiration (Liu et al., 2010) and detection of snow covered areas (Istomina et al., 2010). Table 2.8 show the spectral bands, wavelength and spatial resolution for AATSR.

Table 2-8: Spectral bands, wavelengths and spatial resolution for AATSR

Bands	Wavelength (μm)	Resolution (m)
Band 1 - MWIR	3.7	1000
Band 2 - TIR	10.8	1000
Band 3 - TIR	12	1000
Band 4 - VIS	0.555	1000
Band 5 - VIS	0.659	1000
Band 6 - NIR	0.865	1000
Band 7 - SWIR	1.61	1000

Source: ESA, 2015a

2.8.1.3 MODIS

The MODerate resolution Imaging Spectroradiometer (MODIS) sensor is carried on both NASA's Aqua and Terra satellites that have near polar orbits resulting in two images per satellite per day. Image acquisition on Aqua is ~ 1330 and 0130 h and Terra is ~ 1030 and 2230 h, all local time with a spatial resolution of ~ 1 km (NASA, 2015d). The MODIS instruments were designed to meet the needs of the land, ocean and atmospheres communities and in some case, were a compromise among competing needs. The land requirements for MODIS instrument grew from the experience with daily observations of the Landsat Thematic Mapper instrument (Foody, 2002). Additional bands were added in the middle infrared and thermal regions for land sensing and bands were included to enable atmospheric correction and cirrus cloud detection. MODIS has 36 spectral bands with 12-bit quantization. Two bands are at 250

m spatial resolution, five bands are at 500m spatial resolution and the remaining 29 are at 1 km (NASA, 2015d; Foody, 2002) (see Table 2.9). Bands 1 to 9 are in nm; bands 20 to 36 are in μm; Spectral Radiance values are in (W/m^2-m-sr); SNR = Signal-to-noise ratio and NE(delta)T = Noise-equivalent temperature difference. The higher spatial resolution bands were selected for land remote sensing to improve upon the AVHRR (Salomonson et al, 1989). The Earth Observation Satellite (EOS) Terra and Aqua is at ~ 705 km, and with the MODIS ± 55 degree scan angle, this gives a swath width of 2,330 km and global near-daily coverage (USGS, 2015b). The instrument design is described in detail by Barnes et al. (1998), calibration and early performance is described by Guenther et al. (2002) and the instrument geolocation by Wolfe et al. (2002).

MODIS data are available from the USGS Land Processes Distributed Active Archive Center (https://lpdaac.usgs.gov/) and useful LST products include MYD11A1 (Aqua) and MOD11A1 (Terra) which are the daily LST and emissivity at 1 km. These LST products primarily use Thermal Infrared (TIR) bands 31 (10.78-11.28 μm) and 32 (11.77-12.27 μm) combined with split window algorithms (Wan and Dozier, 1996) which multiple studies have tested (Wan, 2008; Coll et al., 2005; Wan et al., 2004; Wan, 2002) with results suggesting accuracies greater than 1 K over homogeneous surfaces. A useful tool for processing MODIS data in ESRI ArcMap is the Marine Geospace Ecology Tools (MGET) plugin (Roberts et al., 2010), or the standalone MODIS Reprojection Tool (https://lpdaac.usgs.gov/lpdaac/tools/modis_reprojection_tool). The MODIS Land products provide a major advance over those available from the AVHRR in both spatial resolution and quality, and include surface reflectance

corrected for aerosols (Vermote et al., 2002), snow cover (Hall et al., 2002), land surface temperature (Wan, 2002), active fire, and burned area (Roy et al., 2005; Giglio et al., 2003; Justice et al., 2002), leaf area index (Myneni et al., 2002), albedo (Schaaf etal., 2002), land cover (Friedl etal., 2002), vegetation continuous fields (Hansen et al., 2002), and vegetation continuous (Zhan et al ., 2002). The NDVI for MODIS was augmented with the Enhanced Vegetation Index which built on a large body of research investigating indices designed to reduce the effects of soil background and atmospheric effects (Huete et al., 2002).

Rapid delivery of MODIS products within a few hours of acquisition has led to near real time applications of the data (Justice et al., 2002). There are a number of studies that use MODIS LST data, for example, Pongrácz et al. (2010) explored the UHI of nine central European cities and find that the most intense UHI occurs during daytime in the summer. Work has looked at the 10 most populated cities of Hungary (Pongrácz et al., 2006). Studies in Bucharest used MODIS to calculate the UHI in summer months (Cheval and Dumitrescu, 2009) and under heatwave conditions (Cheval et al., 2009). Globally, Hung et al. (2006) quantified the UHI in eight Asian mega-cities using MODIS data. Jin et al. (2005) analysed various cities including Beijing and New York, and Imhoff et al. (2010) used MODIS data averaged over 3 years to calculate UHIs across the United States. A strength of the MODIS sensor is the compromise between regular image acquisition and reasonable spatial resolution, in comparison to other sensors that offer higher spatial resolution but lower temporal resolution (e.g. Landsat), or higher temporal resolution but lower spatial resolution (e.g. SEVIRI). However, problems with early calibration

adjustments render the MODIS Terra data prior to November 2000 largely unusable for land studies.

Table 2-9: MODIS spectral bands with their bandwidth and primary uses

Bands	Bandwidth	Spectral Radiance	Required SNR	Primary use
1	620-670	21.8	128	Land/Cloud/Aerosol boundaries
2	841-876	24.7	201	
3	459-479	35.3	243	
4	545-565	29.0	228	
5	1230-1250	5.5	74	
6	1628-1652	7.3	275	
7	2105-2155	1.0	110	
8	405-420	44.9	880	Ocean colour/Phytoplankton/Biogeoch-emistry
9	438-448	41.9	838	
10	483-493	32.1	802	
11	526-536	27.9	754	
12	546-536	21.0	750	
13	662-672	9.5	910	
14	673-683	8.7	1087	
15	743-753	10.2	586	Atmospheric water vapour
16	862-877	6.2	516	
17	890-920	10.0	167	
18	931-941	3.6	57	
19	915-965	15.0	250	
			Required NE [delta] T (K)[4]	
20	3.660-3.840	0.45 (300 K)	0.05	Surface/cloud temperature
21	3.929-3.989	2.38 (335 K)	2.00	
22	3.929-3.989	0.67 (300 K)	0.07	
23	4.020-4.080	0.79 (300 K)	0.07	
24	4.433-4.498	0.17 (250 K)	0.25	Atmospheric temperature
25	4.482-4.549	0.59 (275 K)	0.25	
26	1.360-1.390	6.00	150 (SNR)	Cirrus clouds water vapour
27	6.535-6.695	1.16 (240 K)	0.25	
28	7.175-7.475	2.18 (250 K)	0.25	
29	8.400-8.700	9.58 (300 K)	0.05	Cloud properties
30	9.580-9.880	8.94 (300 K)	0.25	Ozone
31	10.780-11.280	9.55 (300 K)	0.05	Surface/cloud temperature
32	11.770-12.270	8.94 (300 K)	0.05	
33	13.185-13.485	4.52 (260 K)	0.25	Cloud top altitude
34	13.485-13.785	3.76 (250 K)	0.25	
35	13.785-14.085	3.11 (240 K)	0.25	
36	14.085-14.385	2.08 (220 K)	0.35	

Source: USGS, 2015b

2.8.1.4 AVHRR

The Advanced Very High Resolution Radiometer (AVHRR) is a radiation detection imager for remotely determining cloud cover and the surface temperature. AVHRR sensor has been on a number of National Oceanic and Atmospheric Administration (NOAA) satellites and Meteorological Operational Polar Satellites (MetOps) and is currently operational on NOAA-15,-16,-17,-18 and 19; and MetOps-1 and 2 offering at least daily coverage, but restricted to daytime images (NASA, 2015). The European Meteorological Operation satellites, MetOp-1 and MetOp-2 have been flying AVHRR instruments in near-polar orbits providing global 1 km data with an orbital repeat time of 29 days. Also, MetOp-3 has been approved (NOAA, 2015). AVHRR was configured originally with four channels (0.55-0.90 μm, 0.73-1.1 μm, 3.5-3.9 μm, and 10.5-11.5 μm) for meteorological applications (NOAA, 2015; Foody, 2002) that were expanded to five channels (by including an 11.5-12.5 μm channel) with the launch of NOAA-7 in June 1981. A sixth channel (1.5-1.7 μm) was added with the launch of NOAA-15 in May 1998. AVHRR was modified and the first channel was narrowed to 0.55-0.70 μm. The principal reason for confining channel 1 to the visible part of the spectrum was to increase AVHRR effectiveness for snow mapping and vegetation monitoring (Schneider and McGinnis, 1977). Table 2.10 show AVHRR/3 band characteristics.

The NOAA-series of Sun-synchronous near-polar-orbiting meteorological satellites orbit at an altitude of ~ 830 km. One half of these satellites in this series have a daytime overpass time suitable for obtaining AVHRR data for global vegetation studies while the other satellites in NOAA series have equatorial overpass time of 0730 and 1930 hours, that precludes global

vegetation studies (Foody, 2002). The AVHRR sensor scans ~ ±55 ° from nadir and complete coverage of the earth is available at least twice daily with two spatial resolutions at the satellite subpoint: 1.1 km, and a spatially degraded resolution representing ~ 5.5 ° × 3.3 km, called Global Area Coverage (GAC). The GAC data are formed as a partial average of a 5 by 3 element block of 1.1 km pixels. The first four 1.1 km pixels in the first scan line of the block are averaged, and the fifth pixel is skipped, as well as the next two rows of five pixels. Thus, the GAC data represent a 4/15 sample reduction in data volume compared to the original 1.1 km data (Cracknell, 1997). NOAA National Environmental Satellite Data Information Service (NESDIS) collected the AVHRR global area coverage (GAC) at a spatial resolution of approximately 4 km (600 megabytes/da) and selected local area coverage at a spatial resolution of 1.1 km. Because of constraints of limited on-board storage capability, 1.1 km AVHRR data were only collected by direct transmission to line-of-sight around receiving stations or for a limited number of areas using the on-board tape recorder as requested (Foody, 2002).

The spatial resolution of AVHRR is ~ 1.1 km and LST is derived from TIR channels 4 (10.3-11.3 μm) and 5 (11.5-12.5 μm), with a global dataset provided through the Sun-synchronous orbit. Data are available from the NOAA Comprehensive Large Array Stewardship System (http://www.nsof.class.noaa.gov/saa/) and the High Resolution Picture Transmission Software (http://www.satsignal.eu/software/hrpt.htm) can be useful for analysis. Comparative studies of AVHRR algorithms exist which offer more details (Vázquez et al., 1997; Ottle and Vidal-Madjar, 1992). Most of the vegetation indices derived from NOAA AVHRR data use the normalized

difference vegetation index (NDVI), which is calculated from channels 1 (0.55-0.70 μm and 2 (0.73-1.1 μm) (Foody, 2002). The requirement for products of improved spatial resolution was identified by scientists of the International Geosphere Biosphere Program (IGBP) (Townshend et al., 1994). In response to this requirement, the IGBP-DIS developed an international effort to compile a global 1 km AVHRR data set from different ground stations for 1992 (Eidenshink and Faundeen, 1994). This product was eventually used to generate global 1 km land cover and active fire products (Dwyer et al., 2000; Loveland et al., 2000). The in-depth research associated with utilizing these data sets led to a better characterization of the instruments and identification of the limitations of the products (Csiszar and Sullivan, 2002; Giglio et al., 1999). The poor geolocation and resulting spatial registration problems of AVHRR data, the broad band widths and lack of calibration in the visible and near infrared channels, and the orbital drift during lifetime of each satellite, were early limitations to using AVHRR data for land studies that were overcome as the time span of the data increased (Foody, 2002).

Table 2-10: AVHRR/3 band characteristics

Bands	Resolution at Nadir (km)	Wavelength (μm)	Primary use
1	1.09	0.58-0.68	Daytime cloud and surface mapping
2	1.09	0.725-1.00	Land-water boundaries
3A	1.09	1.58-1.64	Snow and ice detection
3B	1.09	3.55-3.93	Night cloud mapping, sea surface temperature
4	1.09	10.30-11.30	Night cloud mapping, sea surface temperature
5	1.09	11.50-12.50	Sea surface temperature

Source: NOAA, 2015

The strength of the AVHRR sensor is that there is a relatively long historical record of data, and correspondingly a significant body of research that has used

the sensor for many different uses. A notable use of AVHRR data has been in the creation of an 18 years (1981-1998) diurnal LST dataset (Jin, 2004) at 8 km resolution globally for snow free land surfaces. It gives monthly diurnally averaged, minimum and maximum skin temperatures. This long term record is not possible with most other sensors as the historical data are not available, as the satellites and sensors were not developed or in space. Studies using AVHRR include Gallo et al. (1993) who investigated the surface temperature and vegetation index for 37 cities in the United States, particularly noting the consistent nature of the data when studying UHI. Also, AVHRR data have been used to study the growth of the UHI in Houston, Texas, USA between 1985-1987 and 1999-2001, with the results showing a growth in magnitude of 35 %, and a growth in area between 38 and 88 % depending on method (Streutker, 2003). Stathopoulou and Cartalis (2009) used AVHRR data from Greece and applied downscaling techniques to increase the output resolution (1 km > 120 m), helping to address the inevitable balancing between spatial and temporal resolution. A significant weakness of AVHRR includes the lack of availability of night time images (Tomlinson et al., 2011).

It is remarkable that more than 20 AVHRR instruments have been flown since the launch of NOAA in 1979. However, although obvious and significant improvements to the AVHRR instruments have been recommended, such as improved spectral bandwidths for channels 1 and 2, on-board calibration of channels 1 and 2, routine global 1 km data acquisition (only 16 gigabits/day), and full-time operation of all six channels, changes to operational instruments have been extremely difficult for NOAA to implement for reasons not apparent to the user community (Cracknell, 2001).

2.8.1.5. ASTER

The Advanced Spaceborne Thermal Emission and Reflection Radiometer (ASTER) is an advanced multispectral imager that was launched on board NASA's Terra spacecraft in December, 1999. ASTER covers a wide spectral region with 14 bands from the visible to the thermal infrared with high spatial, spectral and radiometric resolution (SIC, 2015). An additional backward looking near-infrared band provides stereo- coverage (USGS, 2015c). ASTER consists of three different subsystems: the Visible and Near-infrared (VNIR) has three bands with a spatial resolution of 15 m, and an additional backward telescope for stereo; the Shortwave Infrared (SWIR) has 6 bands with a spatial resolution of 30 m; and the Thermal Infrared (TIR) has 5 bands with a spatial resolution of 90 m (see Table 2.11) (USGS, 2015c). Each subsystem operates in a different spectral region, with its own telescope(s). In addition, one more telescope is used to view backward in the near-infrared spectral band (band 3B) for stereoscopic capability. Each ASTER scene covers an area of 60 x 60 km (USGS, 2015c) and calculates surface temperature (AST08product – http://asterweb.jpl.nasa.gov/content/03_data/01-Data_ Products/SurfaceTemperature.pdf) using the Temperature Emissivity Separation (TES) algorithm (Gillespie et al., 1998).

ASTER can acquire data over almost the entire globe with an average duty cycle of 8 % per orbit. This translates to acquisition of about 650 scenes per day that are processed to Level-1A; of these, about 150 are processed to Level-1B. All 1A and 1B scenes are transferred to the EOSDIS archive at the EROS Data Center's (EDC) Land Processes Distributed Active Archive Center (LP-DAAC), for storage, distribution, and processing to higher-level data products.

All ASTER data products are stored in a specific implementation of Hierarchical Data Format called HDFEOS (USGS, 2015c).

Table 2-11: Characteristics of the ASTER sensor systems.

Subsystem	Bands	Spectral range (μm)	Spatial resolution (m)	Bits
VNIR	1	0.52-0.60	15	8
	2	0.63-0.69	15	8
	3N	0.78-0.86	15	8
	3B	0.78-0.86	15	8
SWIR	4	1.60-1.70	30	8
	5	2.145-2.185	30	8
	6	2.185-2.225	30	8
	7	2.235-2.285	30	8
	8	2.295-2.365	30	8
	9	2.360-2.430	30	8
TIR	10	8.125-8.475	90	12
	11	8.475-8.825	90	12
	12	8.925-9.275	90	12
	13	10.25-10.95	90	12
	14	10.95-11.65	90	12

Source: USGS, 2015c

ASTER full technical details are available in USGS (2015c) and Yamaguchi et al. (1998). ASTER is fundamentally different from other sensors discussed in this review in that it is request only, with fees payable for data. Hence, data are only acquired if a specific request has been detailed and paid for, and therefore the historical data are limited and costly. This is a significant restriction, given the difficulties of ensuring suitable atmospheric and weather conditions for a specific future request, and obviously limits historical studies (Tomlinson et al., 2011). However, the 90 m thermal resolution is high, only comparable with Landsat when considering the spatial scale. Comparison of spectral bands between ASTER and Landsat 7 ETM+ show that their bands 1-3 are equivalent, ASTER band 4 is equivalent to band 5 of Landsat 7, ASTER bands 5-7 is equivalent to band 7 of Landsat 7 and ASTER bands 12-14 is equivalent to band

6 of Landsat 7 (USGS, 2015c). ASTER images have been used for a number of studies. They were used to compare LST to urban biophysical descriptors (such as impervious surface, green vegetation and soil) in Indianapolis, USA through linear spectral mixture analysis and multiple regression models, with the results that impervious surfaces and hot objects were positively correlated with LST, whereas vegetation and cold objects were negatively correlated (Lu and Weng, 2006). An ASTER image was used alongside a 148 km vehicle traverse of Hong Kong in order to compare air and remotely sensed temperatures (Nichol et al., 2009) and ASTER (for thermal use) and IKONOS data (for high resolution (4 m) visible and near infrared use) were combined to explore the cooling effect of urban parks in Nagoya, Japan (Cao et al., 2010). There are frequent comparisons between ASTER and MODIS data, for example in verification. This is because ASTER and MODIS are complementary in scale (90 m and ~1 km) and based on the same satellite platform, so image acquisition occurs at the same time, height and location which aid comparison (Tomlinson et al., 2011). Land surface emissivity and radiometric temperatures have been compared with good agreement over desert in the USA and savannah in Africa (Jacob et al., 2004). Direct comparisons between three correction approaches over the Loess Plateau in China have reduced the discrepancies between ASTER and MODIS data (Liu et al., 2007). Long term ground based long wave radiation between 2000 and 2007 has been compared to ASTER and MODIS images for both LST and emissivity (Wang and Liang, 2009).

2.8.1.6 GOES

The Geostationary Operational Environmental Satellite (GOES) system is a network of geostationary satellites (status available:

http://www.oso.noaa.gov/goesstatus/) carrying the GOES Imager, a multispectral instrument. Currently, the United States is operating GOES-13 and GOES-15. (GOES-12, which is partially operational, supports Central and South America to prevent data outages during the GOES-13 rapid scan operations). GOES-14 is being stored in orbit as a replacement for either GOES-13 or GOES-15, in the event of failure (NASA, 2015d). The United States normally operates two meteorological satellites in geostationary orbit over the equator. Each satellite views almost a third of the Earth's surface: one monitors North and South America and most of the Atlantic Ocean, the other North America and the Pacific Ocean basin. GOES-13 (or GOES-East) is positioned at 75 °W longitude and the equator, while GOES-15 (or GOES-West) is positioned at 135 °W longitude and the equator. The two operate together to produce a full-face picture of the Earth, day and night. Coverage extends approximately from 20 °W longitude to 165 °E longitude (NASA, 2015d).

Changes to the GOES Imager from GOES-8 through GOES-15 were carried out (NOAA, 2011b). The differences in spectral bands between the two versions of the GOES Imager (Schmit et al., 2002) are explained in Table 2.12. Each version has five bands. The Imagers on GOES-8 through GOES-11 contain bands 1 through 5. The Imagers on GOES-12, 13, 14, and 15 contain bands 1 through 4 and band-6 (NOAA, 2011b).

Table 2.12: GOES Imager band nominal wavelengths (GOES-8 through GOES-15)

GOES Imager band	Wavelength range (μm)	Central wavelength (μm)	Meteorological objective
1	0.53-0.75	0.65 (GOES-8/12) 0.63 (GOES-13/15)	Cloud cover and surface features
2	3.8-4.0	3.9	Low cloud/fog and fire detection
3	6.5-7.0 5.8-7.3	6.75 (GOES-8/11) 6.48 (GOES-12/15)	Upper level water vapour
4	10.2-11.2	10.7	Surface or cloud-top temperature
5	11.5-12.5	12.0 (GOES-8/11)	Surface or cloud-top temperature and low-level water vapour
6	12.9-13.7	13.3 (GOES-12/15)	CO_2 band: Cloud detection

Source: NOAA, 2011b

The differences in the nominal spatial resolution between the GOES-12 through GOES-15 Imager are explained in Table 2.13. The increased resolution of band 6 necessitated a change in the GOES Variable (GVAR) format to include an additional block of data associated with two detectors instead of only one detector (NOAA, 2011b).

Table 2.13: GOES Imager band nominal spatial resolution (GOES-12 through GOES-15).

GOES Imager band	Central wavelength (μm)	Spatial resolution (km)	Number of detectors
1	0.65	1	8
2	3.9	4	2
3	6.48	4	2
4	10.7	4	2
6	13.3	8 (GOES-12/13) 4 (GOES-14/15)	1 (GOES-12/13) 2 (GOES-14/15)

Source: NOAA, 2011b

GOES imager offers two channels in the TIR, 10.2-11.2 and 11.5-12.5 μm for GOES-8 to 11; and 10.2-11.2 and 12.9-13.7 for GOES 12 to 15 with an at nadir

resolution of ~4 km. GOES related studies discussed algorithm development for dual thermal channel sensors (e.g. on GOES-8 and -10) (Sun, 2003) and single thermal channel sensors (e.g. GOES 12-15) (Sun et al., 2004). An evaluation of GOES LST retrievals over the USA is given by Pinker et al. (2009). An illustration of an advantage of geostationary satellites is shown by Sun et al. (2006), which measures the diurnal temperature range across the USA, possible due to the high temporal availability of data. An interesting study links MODIS data as a calibration source for GOES data, resulting in a 1 km LST dataset at 30 minutes temporal resolution and a measured accuracy better than 2 °C (Inamdar et al., 2008).

2.8.1.7 SEVIRI

The primary mission of the geostationary Second-Generation Meteosat (MSG) satellites is the continuous observation of the Earth's full disk with a multi-spectral imager (ESA, 2015c; Aminou, 2002). The Spinning Enhanced Visible and Infrared Imager (SEVIRI) is an instrument on Meteosat-8 which provides image data in 4 Visible and Near-InfraRed (VNIR) channels and 8 InfraRed (IR) channels with 11 narrow-bandwidth channels and 1 high spatial-resolution broad-bandwidth visible channel. A key feature of SEVIRI is its continuous imaging of the Earth in 12 spectral channels with a baseline repeat cycle of 15 minutes. The imaging sampling distance is 3 km at the sub-satellite point for standard channels, and down to 1 km for the high resolution visible channel (see Table 2.14) (ESA, 2015). SEVIRI uses a generalized split window algorithm (detailed in Sobrino, 2004) to calculate LST from two thermal channels (10.8 and 12 μm). The satellite application facility on land surface analysis

(http://landsaf.meteo.pt/) is responsible for generation and archiving of the data.

Table 2-14: Spectral bands, their wavelengths range and spatial resolution for SEVIRI

Bands	Spectral range (μm)	Spatial resolution (km)
1 (Broad band VIS)	0.6-0.9	1
2	0.56-0.71	3
3	0.74-0.88	3
4	1.50-1.78	3
5	3.48-4.36	3
6	5.35-7.15	3
7	6.85-7.85	3
8	8.30-9.10	3
9	9.38-9.94	3
10	9.80-11.8	3
11	11.0-13.0	3
12	12.4-14.4	3

Source: ESA, 2015c

Though it has a very high temporal resolution of 15 min (theoretical maximum of 96 images per day) the area covered is constant and not global. All the land pixels within the Meteosat disc that are below a 60 ° viewing angle are processed for LST measurements, to avoid excessive atmospheric attenuation and reduced accuracy at higher angles. This results in a spatial pixel resolution of 3 km at nadir (increasing to ~ 6 km at > 60 °) (Tomlinson, et al., 2011). The high temporal resolution of MSG (SEVIRI) has a number of advantages, namely it has a much greater chance of acquiring cloud free images of a study area due to the number that are taken and it enables the potential to study the diurnal LST pattern. MSG data have been available since July 2005 for the complete Meteosat disc (February 2005 for Europe) (Schmetz et al., 2002). Trigo et al. (2008) compare Meteosat LST with MODIS LST over three locations and find that Meteosat temperatures are warmer than MODIS, particularly in the

daytime. A comparison between MODIS and Meteosat LST has also been carried out focussing on the heatwave in Athens, Greece during July 2007 (Retalis et al., 2010) and the results show significant correlation both between each other and between air temperature measurements, which agrees with other air temperature and Meteosat LST comparisons that also perform well (Nieto et al., 2011). High temporal resolution of the instrument is also useful for hazard modelling such as near real time forest fire monitoring (Umamaheshwaran et al., 2007).

2.8.1.8 TRMM-VIRS

The Visible and Infrared Scanner (VIRS) instrument on board the Tropical Rainfall Measuring Mission (TRMM) satellite that was launched in 1997 is designed primarily to study precipitation; it offers an opportunity for the remote sensing of tropical and sub-tropical fires (NASA, 2015c**;** WDC, 2015). The platform provides day and night time coverage of regions at latitudes within $\pm$ 40 ° of the equator, and carries five separate instruments intended for rainfall related observations (Kummerow et al., 1998; Simpson et al., 1996). Some of these instruments are useful for the monitoring of biomass burning. Of particular interest is the VIRS, a five band radiometer with bands ranging from 0.6 to 12 μm similar to the AVHRR (see Table 2.15). The similarity of the VIRS infrared bands, in particular, to those of AVHRR provides a foundation for fire detection, which has been clearly demonstrated for AVHRR (Kummerow et al., 1998).

The TRMM satellite maintains a 350 km circular orbit inclined at 35 ° (NASA, 2015c; Kummerow et al. 1998), allowing the local overpass time to drift over the

entire 24 hours of a day roughly once each month. While intended to allow observations over the prominent diurnal rainfall cycle, this orbit characteristic allows observation of the well-documented diurnal burning cycle as well. The 90 minutes orbital period results in a total of 16 orbits each day. The five VIRS bands have central wavelengths of 0.63, 1.61, 3.75, 10.8, and 12.0 μm (WDC, 2015). With the exception of band 2, these are identical to the AVHRR. At a nominal orbit altitude of 350 km, the VIRS has an instantaneous field of view (IFOV) of 2.11 km at nadir. The $\pm$ 45 ° scan angle limits produce a 720 km swath (WDC, 2015; Giglio et al., 2000). As with the AVHRR, the thermal bands saturate at equivalent blackbody temperatures of approximately 322 deg K. Although the low saturation temperature can cause problems for AVHRR fire detection, the larger sampling area of VIRS is expected to reduce the likelihood of saturation by hot subpixel targets. Unlike the AVHRR, post-launch calibration of the VIRS reflective bands is possible using an on-board solar diffuser (Kummerow et al. 1998).

Table 2-15: TRMM-VIRS bands, spectral region and wavelengths

Bands	Spectral region	Wavelength (μm)
1	Visible	0.63
2	Near Infrared	1.60
3	Near Infrared	3.75
4	Near Infrared	10.8
5	Thermal	12.0

Source: NASA, 2015c

The VIRS is clearly useful for fire detection in tropical and sub-tropical areas, allowing full coverage of two critical regions in terms of biomass burning: Southern Africa and the Amazon (Kummerow et al., 1998). Additionally, the orbit inclination enables observations throughout the entire diurnal burning cycle over the course of each month. In addition to its demonstrated utility for

burned area detection (Eva et al. 1998), the inclusion of the 1.6 μm band also allows discrimination between very hot (and/or large) fires and hot surfaces (e.g. deserts) which confound fire detection for AVHRR-based contextual fire detection algorithms due to saturation (Giglio et al., 2000). Data from all of the TRMM instruments is available from the Goddard Distributed Active Archive Centre (DAAC) web site (http://daac.gsfc.nasa.gov/) (NASA, 2015c). Table 2.16 Show data characteristics for pre-boost and post-boot for TRMM-VIRS.

Table 2-16: Data characteristics for pre-boot and post-boot for TRMM-VIRS.

Characteristics	Pre-boot (before 08/07/2001)	Post-boot (After 08/24/2001)
Temporal coverage	Start date: 12/20/1997 Stop date: 08/07/2001	Start date: 08/24/2001 Stop date: - Ongoing
Geographic coverage	Latitude: 38 °S-38 °N Longitude: 180 °W-180 °E	Latitude: 38 °S-38 °N Longitude: 180 °W-180 °E
Temporal resolution	About 91.5 minutes per orbit About 16 orbits per day	About 92.5 minutes per orbit About 16 orbits per day
Spatial resolution	2.2 km	2.4 km
Scan characteristics	Swath width: 720 km Pixels/Scan: 261 Scans/Second (SS): 2×98.5/60 Seconds/Orbit (SO): 5490 Average Scans/Orbit: nscan = SS×SO = 18026	Swath width: 833 km Pixels/Scan: 261 Scans/Second (SS): 2×98.5/60 Seconds/Orbit (SO): 5550 Average Scans/Orbit: nscan = SS×SO = 18223
Average file size	Original: ~ 137 MB	Original: ~ 138 MB
File type	HDF	HDF

Source: NASA, 2015c

Table 2.17 shows a summary of LST sensors, their satellites' information, number of thermal band channels for each sensor and websites to access the specification documents of individual sensors and satellites.

2.8.1.9 Future developments

The future for remote sensing of LST retrievals is focussed on two main areas, that of improved or replacement of physical sensors and platforms, and that of

improvements in data manipulation of current, historical and future data (Tomlinson et al., 2011). In terms of data manipulation there is potential for improved algorithms, for example improved cloud masking or emissivity calculations. These will rely on ongoing validation and testing across a variety of landscapes and sensors, and could improve existing and future data (Tomlinson et al., 2011). Regarding the near future of sensors and satellite platforms, a number of relevant projects are in development. To start with, ESA Sentinel-1A and Sentinel-2A are in orbit. Sentinel-1A was launched on 3 April 2014 while Sentinel-2A was launched on 23 June 2015, for mapping of changing land cover, water bodies, disaster mapping and plant health (ESA, 2015d). Data acquired from Sentinel-1 and Sentinel-2 are presently undergoing calibration and validation processes before they can be released to the user community (ESA, 2015d). Sentinel-3A was designed specifically to measure biomass burning events including small fires from oil and gas facilities, and has been planned to be launched late 2015 (ESA, 2015d) (See section 2.9.2.1). NASA and the U.S. Geological Survey (USGS) have started planning the Landsat 9 mission, planned to launch in 2023, which will extend the Earth-observing program's record of land images to half a century (NASA, 2015b). The approved geostationary GOES-R, S, T and U satellites are scheduled to launch in the near future with GOES-R and GOES-S to be launch in October 2015 and February 2017 respectively (NOAA, 2015a). The National Polar-orbiting Operational Environmental Satellite System (NPOESS) is due to launch in 2016, designed to replace NASA's Aqua, Terra and Aura satellites and offering the Visible and Infrared Imagery Radiometer Suite (VIIRS) sensor for LST. An interesting sensor in development is the Hyperspectral InfraRed Imager (HyspIRI) from NASA that is provisionally planned for launch in 2020, offering a ~ 60 m spatial

resolution in the thermal bands and a repeat cycle of 5 or 16 days. This is still in a planning phase and more details are available online (http://hyspiri.jpl.nasa.gov/) but this offers the next generation of space based thermal sensors (ESA, 2015c). In the future there is likely to be an increase in the number of small satellites that enable relatively quick and inexpensive missions, which could for example help to observe dynamic weather systems (Sandau et al., 2010) (See Table A-2 in Appendix A). Future increases in spatial resolution of sensors combined with the high temporal resolution that geostationary platforms can provide is likely to offer the most useful data; however this offers considerable scientific challenges (Tomlinson et al., 2011).

For this study, Landsat 5 TM and Landsat 7 ETM+ were used because of their higher spatial resolution, accessibility to data without payment of fees and time span.

Table 2-17: Summary of Land Surface Temperature sensors and satellite information.

Sensor	Satellite	Spatial resolution	Orbital frequency	TIR spectral bands (µm)	Image acquisition (local time)	Data available since	Website
Landsat ETM+	Landsat 7	60 m (resampled 30 m)	16 days	(6) 10.4-12.5	~ 10:00	1999	http://pubs.usgs.gov/fs/ ETM+ 7 2010/3026/ http://landsat.gsfc.nasa.gov/
Landsat OLI/TIR	Landsat 8	100 m	16 days	(10) 10.60-11.19 (11) 11.50-12.51	~ 10:00	2014	http://landssat.usgs.gov/landsat8 .hph
MODIS	Aqua	~ 1 km	12 hours	(31) 10.78-11.28 (32) 11.77-12.27	~ 13:30 ~ 01:30	2002	http://modis.gsfc.nasa.gov/ https://lpdaac.usgs.gov/lpdaac/p roducts/modis overview
MODIS	Terra	~ 1 km	12 hours	(31) 10.78-11.28 (32) 11.77-12.27	~ 10:30 ~ 22:30	2000	http://modis.gsfc.nasa.gov/ https://lpdaac.usgs.gov/lpdaac/p roducts/modis overview
AATSR	Envisat	~ 1 km	35 days	11 12	~ 10:00	2004	http://envisat.esa.int/instrument s/aatsr/
ASTER	Terra	90 m	12 hours	(10) 8.125-8.475 (11) 8.475-8.825 (12) 8.925-9.275 (13) 10.25-10.95 (14) 10.95-11.65	On request only	1999	http://asterweb.jpl.nasa.gov/ index.asp
AVHRR	Multiple NOAA	~ 1.1 km	12 hours	(4) 10.3-11.3 (5) 11.5-12.5	See http://ivm.cr.usgs. gov/tables.php for full orbital details of each.	1979	http ://noaasis.noaa.gov/ NOAASIS/ml/avhrr.html http ://eros.usgs.gov/#/Find_Dat a/Products_and_Data_ Available/AVHRR
AVHRR	MetOP	~ 1.1 km	29 days	(4) 10.3-11.3 (5) 11.5-12.5	~ 0930	2006	http://www.esa.int/esaLP/ESA7U SVTYWC LPmetop 0.html
VIRS	TRMM	~ 2.1 km	30 days	(4) 10.8 (5) 12	Drift over the entire 24 hours of a day	1998	http://daac.gsfc.nasa.gov/
SEVIRI	Meteosat-8	~ 3.0 km	Geostationary	10.8 12	Every 15 minutes	2005	http://landsaf.meteo.pt/
GOES Imager	GOES network	~ 4.0 km	Geostationary	(4) 10.2-11.2 (5) 11.5-12.5	30 minutes	1974	http://goespoes.gsfc.nasa.gov/ goes/index.html

Source: ESA, 2015a-c; NASA, 2015a-e; NOAA, 2015; USGS, 2015a-c

2.9 Applications of remote sensing technology relevant to gas flaring and oil pollution

SCIAMACHY on ENVISAT was used to measure the concentration changes of CO_2 and CH_4 and the authors concluded, using three years (2003-2005) of data, that the emission of anthropogenic CO_2 and CH_4 can be detected from space (Khlystova, 2010; Schneising, 2008); Grutter and Flores (2004) also mapped and monitored air quality by taking a measurement of O_3 and SO_2 with Fourier Transform Infrared (FTIR) and Differential Optical Absorption Spectrometer (DOAS). In addition, remote sensing using the thermal infrared (TIR) has demonstrated an ability to sound the troposphere and provide global distributions for some of the key atmospheric species (Clerbaux et al., 2010; Aqishev and Bajazitov, 1996). Therefore, remote sensing techniques can significantly improve our understanding of the global CH_4 and CO_2 budget (Leifer et al., 2006).

Several studies were also carried out to: evaluate air pollution control strategies using Landsat and MODIS data (Feldman, 2010); evaluate the impacts of fire on the landscape and biodiversity and fire management in term of risk estimation, detection and assessment (Gomez and Martin, 2011); and provide useful information on marine environment processes such as eutrophication or the air-sea exchange of CO_2, that are important in determining the distribution and fate of pollutants (Park et al., 1991). Also, satellite remote sensing has been applied to geochemical prospecting and seismic exploration of oil and gas seeps (Kenneth et al., 2002). In the oceans, floating oil forms slicks that are detectable from space (MacDonald et al., 2002).

Visible and near infrared data, for example from Landsat ETM+, can be useful when assessing the thickness of hydrocarbon spills as the areas of thicker oil may be slightly brighter because they suppress the signal from the underlying seawater (Howari, 2004). Ud et al. (2008) mapped hydrocarbon polluted sites using data from Landsat TM and Landsat ETM+; emissivity, transmittance and mean atmospheric temperature were used to estimate land surface temperature (LST). The authors concluded changes in the surface emissivity, due to oil pollution after the derivation of the apparent temperature, was a recognition element for mapping out oil polluted surfaces.

Hyperspectral remote sensing has also been a valuable tool for habitat mapping and oil detection (Evans et al., 2002), including the investigation and detection of hazardous gas leakage from pipelines and tanks through the analysis of Hymap hyperspectral imagery (Van der Werff et al., 2007), and post-closure monitoring of hazardous waste sites (Slonecker and Fisher, 2011). LIDAR Systems with the DIAL Principle, which includes a mobile multi-wavelength-LIDAR, were developed for monitoring trace gases that absorb light between 255 and 290 nm and around 400 nm using up to 16 different wavelengths (Moreno et al., 2004).

2.9.1 Fire detection

The most effective sensors for fire detection were already discussed in section 2.8.1. A major goal in satellite remote sensing of fire is to derive globally accurate measurements of the spatial and temporal distribution of burning (Fuller, 2000). Various satellite systems (as discussed in section 2.8.1) with different sensing capabilities are being used to research different aspects of fire

with the effectiveness being strongly related to satellite observation overpass time, sensor spatial resolution, geometry and detector saturation levels. The processing and analysis procedures have been sufficiently well-developed that since 2000 satellite fire data has been routinely used for resource management applications (Fuller, 2000).

The demand for improved information on regional and global fire activity in the context of land use/land cover change, ecosystem disturbance, and climate modelling and natural hazards has increased efforts to improve Earth-observing satellite sensors and associated methods for fire information retrieval. Despite the considerable headway, retrieval of fire properties from satellites remains problematic (Giglio and Kendall, 2001). These problems are uncertainties in the measurements of fire size and temperature that strongly influences how fires spread (Pyne et al., 1996), the amount and chemistry of their gas and aerosol emissions (Andrea and Merlet, 2001) and their impacts on ecosystems (Hanley and Fenner, 1998). However, as a more complete global picture of biomass burning emerges, this information, combined with detailed data from field experiments, can help provide reliable budgets of trace gases and particulate species that affect the global energy balance and climate (Fuller, 2000).

Active fire remote sensing relies on the detection and measurement of electromagnetic energy released by combustion processes; explainable at the molecular level as a set of exothermic chemical reactions. Combustion reactions release thermally emitted radiation according to Planck's Radiation Law, with the wavelength of peak emission typically lying within the Short Wavelength Infra-Red (SWIR) (1.6-2.5 μm), Mid Infra-Red (MIR) (3-5 μm) or Long

Wavelength Infra-Red (LWIR) (8-14 μm) atmospheric windows; dependent upon whether the fire is strongly flaming, smouldering at typically lower temperatures, or has burnt out and is simply emitting radiant energy from areas of cooling ash, soil and partly burned fuel. All LST sensors as previously discussed in section 2.8.1 have channels covering some or all of in these infrared domains. In addition, airborne and spaceborne microwave K-emission signature detection complements the more common thermal remote sensing approaches (Amici et al., 2011).

Multi-spectral thermal infrared image data can also assist in the mapping of different phases of volcanic activity by combining the thermal characteristics with textural and short-wave spectral information (Smith et al., 2009). Thermal infrared radiation is affected by the thermal emission from surface materials; the amount of radiation that is emitted by a material is controlled by the efficiency of a material to absorb and re-radiate radiation, known as the emissivity (Price, 1977). An emission, or emissivity, spectrum at TIR wavelengths represents the signature caused by variation of processes between molecules (Smith et al., 2009).

The AATSR basic objective of determining surface temperature accurately enough allows quantitative investigations of climatic behaviour (Llewellyn-Jones and Remedios, 2011). AATSR measures the radiance in similar wavebands to MODIS but from both forward and nadir viewing angles, providing improved atmospheric correction (Ghent, 2009). Comparisons between MODIS and AATSR indicate that AATSR gives the higher temperature of the satellite LST products (Noyes et al., 2006). The larger MODIS viewing

angles yield correspondingly larger daytime discrepancies; due perhaps to the difference in sunlit and shadow areas (Goward et al., 2002). The higher sensitivity of AATSR LST retrieval to atmospheric conditions achieved due to its two-angle viewing method could also contribute to the disparity between model simulations and this satellite product (Noyes et al., 2006). In addition, variations in the thermal properties can be a useful complement to reflectance measures in distinguishing some land cover and soil types (Lovett and Turner, 2009). Soil moisture and downward radiation are two of the most significant factors in non-fire related surface temperature changes.

The Along Track Scanning Radiometer World Fire Atlas (ATSR-WFA) products have been shown to be well correlated with the TRMM-VIRS and MODIS-Aqua/Terra monthly night-time fire counts (Amici et al., 2011). MODIS was found to be better for detecting fires than AVHRR for near real-time monitoring because of rapid delivery of MODIS products within a few hours of acquisition (Justice et al., 2002): AVHRR detected 37 % of the total fire count while MODIS achieved 64 % (Philip, 2007). Complementing the near-polar orbiting platforms discussed so far, geostationary imagers such as meteosat offer important temporal advantages when studying rapidly changing phenomena such as vegetation fires (Xu et al., 2010). However, since they are always positioned above the equator they are of limited use for latitudes greater than 60-70 °North or South. Also, the further the site from the equator the lower the spatial resolution of each pixel and the greater the possibility of fire hot spots being hidden by the earth's curvature. So, for a typical Meteosat image, a pixel near the equator may represent a 2.5 km square on the ground, while a pixel positioned for example in Northern Europe may represent 10 km on the ground

and therefore provides less information (such as temperature, vegetation, wind speed, albedo, etc.) per m^2 (Xu et al., 2010).

Satellite imagery (Satellite Pour l'Observation de la Terre [SPOT2]) and Landsat 7 ETM+ can detect and map fire severity patterns in a rugged landscape with variable vegetation. The relationships between field severity class and NDVI difference values revealed that vegetation type does influence the detection of fire severity using these types of satellite data. The effect of vegetation type on areas mapped in each fire severity class was examined but found to be minimal in the study due to the uneven distribution of vegetation types in the study area (Hammill and Bradstock, 2006). The interactions between fire severity (plant damage) and plant regeneration after fire by means of remote sensing imagery and a field fire severity map was studied by Díaz-Delgado et al. (2003) using 8 Landsat TM (post fire) and 10 MSS and 1 TM (pre fire) images. Plant regeneration was monitored using NDVI measurements; average class values standardized with neighbour unburned control plots. Pre-fire NDVI decline due to fire was positively correlated with field fire severity class. Results show different patterns of recovery for each dominant species, severity class and combination of both factors. For all cases a significant negative correlation was found between damage and regeneration ability.

Fire Radiative Power (FRP) is the emitted radiant energy released per unit time by burning fuel (Sperling et al., 2009). Fire Radiative Energy (FRE) is established by temporally integrating FRP over the course of a burning event, and it is this measure that is proportional to the fuel mass combusted and carbon released (Sperling et al., 2009). Paugman et al. (2013) studied to

demonstrate an approach that can accurately and semi-automatically geo-reference thermal imagery using a handheld thermal camera operated by pointing it out of the door or window of a standard helicopter. They used these data to accurately map spatio-temporal variations in flame front rate of spread (ROS) and fire radiative power (FRP) on a series of experimental fires, including a 945 m^2 open vegetation fire conducted in Northumberland, U.K, particularly by enabling the effective and efficient geometric correction of thermal imagery collected from such devices, even when viewing far off-nadir (e.g., out of a side door or window). The approach is based on the automated detection of a set of fixed thermal "ground control points," with the use of a linear transformation matrix for warping the raw infrared imagery to a fixed coordinate system. The spatially explicit data on fire radiative power (FRP), fire radiative energy (FRE), and ROS captured by this remote sensing approach provide more information with regard to the variability of fire energy release and fire front behaviour than the more commonly used point-based approaches long employed by the fire science community (e.g., Stephens et al., 2008 and Jacoby et al., 1992). The spatially explicit maps of FRP provide the detail necessary to study the effects of varying sensor view angle, and address the issue (when coupled with visible imagery) of the impact of direct v.s. indirect flame radiation. They also allow the derived maps of FRE to be related to the spatial variability of fuel consumption (Wooster et al., 2005; Freeborn et al., 2008). In terms of ROS, their method allows this important parameter to be mapped and its variability across the burning plot to be examined and related to driving parameters such as wind speed, fuel availability, and the coalescing of separate fire fronts.

Remote sensing of fire is growing rapidly, for example with the design of Sea and Land Surface Temperature Radiometer (SLSTR) sensor which is to be operated from Sentinel-3 satellite from October 2015. The fire-related capabilities of the planned (SLSTR), a new dual-view EO instrument was explained by Wooster, et al. (2012). They describe in detail the pre-launch active fire product algorithm, which uses data from the SLSTR near-nadir scan. The algorithm detects pixels containing actively burning fires, and uses the MIR radiance method to estimate their fire radiative power (FRP). They tested the algorithm using a series of EOS MODIS scenes covering a range of fire-affected forest and savannah environments, comparing performance to that of the existing MODIS MOD14 'Fire and Thermal Anomaly' products (Giglio et al., 2003). Across 385 scenes covering Africa, South America and Australia, they find that the SLSTR algorithm applied to MODIS data detects in total 20 % more fire pixels than does the MOD14 algorithm applied to the same data. Some scenes show very large differences, while others showed no differences, and some of the extra detections made by SLSTR may be false alarms. For a better evaluation, they use the simultaneous high spatial resolution active fire detections made from ASTER to provide an independent accuracy assessment. Across 45 separate geographical regions covered simultaneously by ASTER and MODIS, they found that the SLSTR algorithm detected 13 % more correctly identified clusters of active fire pixels than the MOD14 algorithm, and that these contained 36 % more active fire pixels. They concluded that the SLSTR algorithm shows increased detection probabilities at small/low FRP fires, mainly due to the more liberal characteristics of its potential fire pixel detection stage. This performance enhancement comes, however, at the expense of a small (<2 %) increase in commission error (i.e. false alarm rate) when compared to

MOD14. The SLSTR algorithms ability to better detect low FRP fires may be important, since these are usually the most common component of a region's fire regime.

The effects of fire on vegetation, soil and the atmosphere are strongly associated with fire regimes; the average fire conditions occurring over a long period of time (Morgan et al., 2001). Fire intensity and severity are associated with fire behaviour characteristics (mainly fire duration and radiative power). In addition, seasonality, along with severity, is closely related to weather conditions and vegetation fire resistance and resilience (Amici et al., 2011; Amici et al., 2009).

An instrument such as MODIS, operating at 1 km spatial resolution, is limited in the smallest fires that may be detected and hence in the measured FRP (Sperling et al., 2009). Fires can also remain undetected because they are simply too small and/or cool to produce a measurable fire signature at the sensor, or because they were not burning at the time of the satellite overpass. In addition, wind direction and speed have a profound effect on fire thermal pollution (Khandewal and Goyal, 2010). Therefore, it is recommended that users of the active fire data perform individual validations to ensure that all relevant fires are included (Giglio et al., 2003).

In summary, there are two types of errors that affect the fire product namely, undetected fires (omission errors) and false alarms (commission errors). Undetected fires can occur, as previously discussed, due to spatial resolution and timing and because they occur under forest canopy or during periods of

persistent cloud cover. False alarms are caused by sun glint and desert boundaries, and along coastlines (Hawbaker et al., 2008). Therefore, the effects of the errors of omission and commission present in hot spot data can potentially introduce errors in fire classification (Giglio et al., 2003).

2.9.2 Gas flare detection

None of the available EO sensors were designed and flown specifically for the observation of gas flaring. In reviewing the available sources, it is evident that several satellite systems have a capability to detect gas flares based on the radiative emissions from flames. However, given the wide spatial distribution and possibility that gas flaring activity fluctuates over time, particular attention has to be given to sensors that collect data globally on a frequent basis and have a capability to readily detect gas flaring (Giglio and Kendall, 2001).

All instruments that are capable of fire detection that were discussed in section 2.8.1 can be applied to flare detection. In order to monitor gas flaring on a global scale a new active flame detection scheme from satellite night-time SWIR, 1.6 μm, has been developed and tested using the AATSR family of measurements (Casadio et al., 2011). Flaring sites have been discriminated according to time persistency criteria, i.e. locations for which hot spots are found at frequencies higher than four times a year are assumed to be industrial settlements. Validation of flaring sites can be performed by the visual inspection of high spatial resolution optical imagery.

Gas flares have also been identified visually in the Defence Meteorological Satellite Program-Operational Linescan System (DMSP-OLS) night-time light

composites; DMSP-OLS was designed to collect global cloud imagery using a pair of broad spectral bands placed in the visible and thermal waveband. Gas flares are detected, and easily identified, when they are offshore or in isolated areas not impacted by urban lighting (Elvidge et al., 2009). There are three general characteristics for gas flares that provide the visual clues for their identification (Figure 2.8) (Ziskin et al., 2011; Xu et al., 2010):

- Very bright point sources of light with no shielding to the sky, and with circular lighting features with a bright centre and wide rims;
- Most are active for a period of years and;
- Tend to be in remote locations, outside of urban centres.

In Figure 2.8, imagery from 1995 is blue, 2000 is green and 2006 is red. The vector polygon drawn around the gas flares associated with Nigeria is shown in white. In both Russia and Nigeria, DMSP-OLS data show some flares going out and new flares being established in other locations on an annual basis. This turnover in the spatial location of active flares suggests the tapping of new reservoirs for crude oil production (Elvidge et al., 2009).

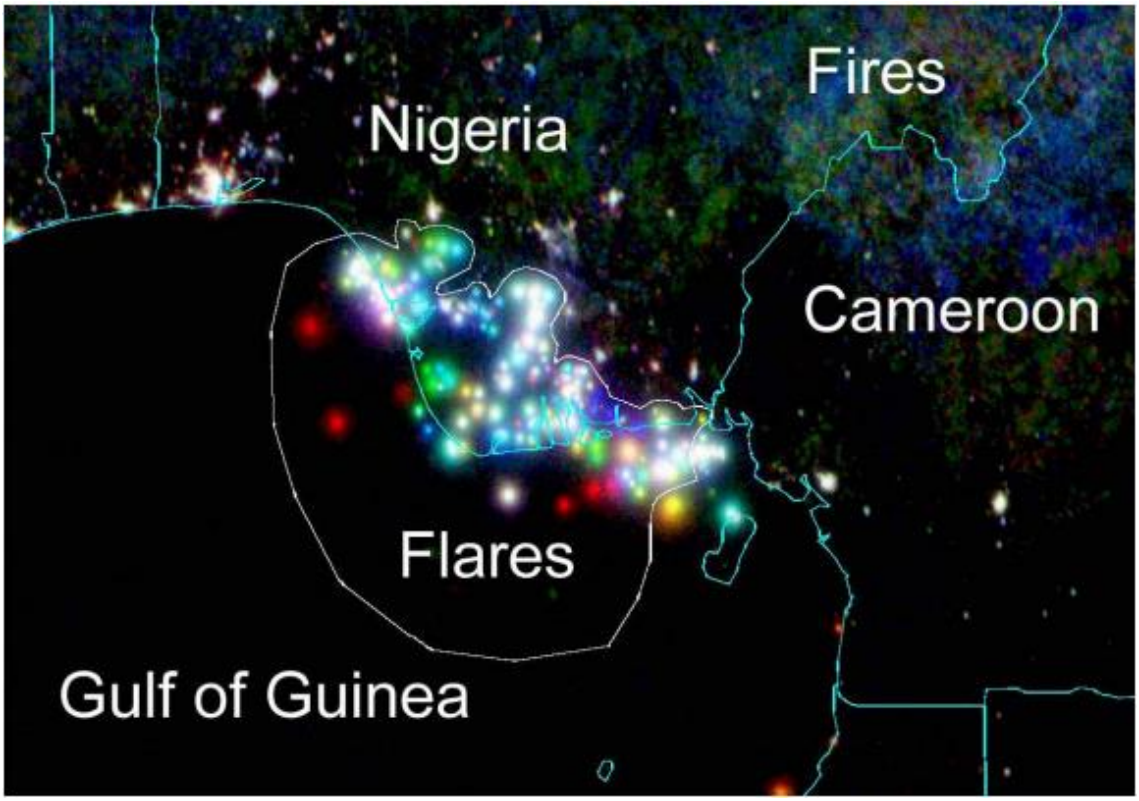

Figure 2-8: Colour composite image from DMSP-OLS showing flare locations in the Niger Delta.
Source: Kimberly et al., 2007

2.9.2.1 Minimum sensor specifications for flare detection

Flare design is influenced by several factors, including the availability of space, the characteristics of the flare gas (namely composition, quantity, and pressure level) and occupational concerns. The sizing of flares requires determination of the required flare tip diameter and height (Stone et al., 2000). The minimum flare height normally used is 9.144 m (Shore, 1990). The minimum flare size is 0.0254 m; larger sizes are available in 0.0508 m increments from 0.0508 to 0.610 m and in 0.152 m increments above 0.610 m. The maximum size commercially available is 2.286 m (Shore, 1990). Hence, the author suggests the minimum sensor specifications needed for flare detection to be:

- Spatial resolution: 5 m;
- Temporal resolution: Daily;
- Coverage: Global;

- Thermal Infrared band: Multiple bands (minimum of 2 bands);
- High radiometric calibration.

Among the future sensors for LST previously mentioned in section 2.8.1.9, some aspects of the SLSTR instrument for Sentinel-3 were designed specifically to target biomass burning events, including operation of the SWIR channels at night and the inclusion of low-gain middle infrared and thermal infrared channels that will minimise saturation over even high intensity fires. F1 and F2 bands are based on the same detector as S7 and S8 but with an increased dynamic range (Wooster et al., 2012). The high precision, rapidly disseminated radiometry provided by Sentinel-3 SLSTR will allow delivery of an operational Active Fire and FRP dataset having global day/night coverage (Kaiser et al., 2012). The SLSTR instrument is a conical scanning imaging radiometer employing the along track scanning dual-view technique to provide robust atmospheric correction over a dual-view swath and has two new channels at wavelengths of 2.25 and 1.375 μm in support of cloud clearing for surface temperature retrieval (ESA, 2015b). Also, the SLSTR active fire detection algorithm perfomed well when it was tested in SWIR channels (S5 and S6) for detection of gas flares. Further development of SLSTR active fire algorithms for identification of sites of natural gas flaring from oil and gas exploration zones have been considered (ESA, 2015b; Wooster et al., 2012). These features of Sentinel-3 SLSTR and its active fire algorithm with a consideration to the detection of flares are breakthroughs to the remote sensing of flares. Tables 2.18 and 2.19 shows specifications for Sentinel-3 SLSTR and its radiometric bands.

Table 2.18: Specifications for Sentinel-3 SLSTR

	Capability	SLSTR Specifications
Swath	Nadir view Oblique	> 1400 km > 740 km
Global Coverage Revisit Times	1 Satellite (dual view) 2 Satellites (dual view) 1 Satellite (nadir view) 2 Satellites (nadir view)	1.9 days (mean) 0.9 days (mean) 1 day (mean) 0.5 day (mean)
Spatial Sampling interval at Sub-satellite point (km)		0.5 km: VIS-SWIR 1 km: IR-Fire
Spectral channel centre (μm)	VIS SWIR MWIR/TIR Fire 1/2	0.55; 0.659; 0.865 1.375; 1.610; 2.25 3.74; 10.85 3.74; 10.85
Radiometric Resolution	VIS (Albedo = 0.5 %) SWIR (Albedo = 0.5 %) MWIR (T = 270 K) TIR ((T = 270 K) Fire 1(< 500 K) Fire 1(< 400 K)	SNR > 20 SNR > 20 SNR = Signal-to-Noise-Ratio NEΔT < 80 mK NEΔT < 50 mK NEΔT < 1 K NEΔT < 0.5 K NEΔT = Noise-Equivalent Temperature Difference (270 K)
Radiometric Accuracy	VIS-SWIR (Albedo = 2-100 %	< 2 % (Beginning of Life) < 5 % (End of Life)
	MWIR-TIR (265-310 K)	< 2 K (0.1 K gola)

Source: ESA, 2015b

Table 2.19: The radiometric bands for Sentinel-3 SLSTR

Band	λ centre (μm)	Width (μm)	Function	Comments		Res. (m)
S1	0.555	0.02	Cloud screening, vegetation monitoring, aerosol	Visible Near IR	Solar reflectance bands	500
S2	0.659	0.02	NDVI, vegetation monitoring, aerosol			
S3	0.865	0.02	NDVI, cloud flagging, Pixel co-registration			
S4	1.375	0.015	Cirrus detection over land	Short-Wave IR		
S5	1.61	0.06	Cloud clearing, ice, snow, vegetation monitoring			
S6	2.25	0.05	Vegetation state and cloud clearing			
S7	3.74	0.38	SST, LST, Active fire	Thermal infra-red Ambient bands (200 K - 320 K)		1000
S8	10.85	0.9	SST, LST, Active fire			
S9	12	1	SST, LST			
F1	3.74	0.38	Active fire	Thermal infra-red fire emission bands		
F2	10.85	0.9	Active fire			

Source: ESA, 2015b

2.9.3 Remote sensing for oil and gas and environment in the Niger Delta

Africa is one of the world largest oil producers after the Middle East. The frantic search for hydrocarbons in Africa has become so intense and wide ranging that there is planned or ongoing oil and gas exploration in at least 51 of the continent's 54 countries (Brown, 2013). The top ten oil producing countries in Africa are Nigeria, Algeria, Angola, Libya, Egypt, Sudan, Equatorial Guinea, The Republic of Congo, Gabon and South Africa. Also, Ghana started producing oil and natural gas in commercial quantities in 2011 (Brown, 2013). Remote

sensing technology has been applied in Africa for mapping of oil and gas geological structures. For example, Peňa and Abdelsalam (2006) used multi-spectral optical and radar remote sensing data combined with Digital Elevation Models (DEMs) extracted from the Shuttle Radar Topography Mission (SRTM) data for mapping lithological units and geological structures in Southern Tunisia. They used Landsat 7 ETM+ and ASTER (Red, Green and Blue) colour combination images (both band and band-ratio images) for the identification of various lithological units when they are exposed on the surface and RADARSAT images for tracing geological formations and geological structures that are buried under thin (~1 m) sand. Colour Normalization Transformation (CNT) method was adopted for the fusion of optical and radar remote sensing data. Hill-shading techniques are applied to SRTM DEMs to enhance terrain perspective views and to extract geomorphological features and morphologically defined structures through the means of lineament analysis. Their results show (1) the validity of applying visible and near infra red (VNIR) and short wave infra red (SWIR) bands of Landsat 7 ETM+ and ASTER data for lithological mapping through the identification of subtle spectral differences between different rock types, especially carbonates and shales. (2) The effectiveness of radar data for mapping near surface geological structures on the basis of their morphological expression and surface roughness. They concluded that identifying lithological and structural features using remote sensing studies incorporated with surface and sub-surface geological investigations in Southern Tunisia can aid exploration for new oil and gas fields and such an approach can be successfully adopted in other parts of North Africa and arid regions in general.

In a similar study, Thurmond et al. (2006) integrated Landsat 7 ETM+, ASTER, Synthetic Apperture Radar (SAR) data and DEMs from Shuttle Radar SRTM for geological mapping in arid regions of Afar Depression in Ethiopia. The Afar Depression is a natural laboratory for studying processes of sea-floor spreading and the transition from rifting to true sea-floor spreading. It is ideal for geological remote sensing because of its vastness, remoteness and inaccessibility together with almost continuous exposure, and lack of vegetation and soil cover (Thurmond et al., 2006). They employed band-ratios of ASTER thermal infrared (TIR) data with Landsat 7 ETM+ VNIR and SAR (L-band) (k = 24 cm) data with horizontally transmitted and horizontally received (HH) polarization. The results obtained distinguished between spatial and temporal distribution of individual lava flows in the Quaternary Erta 'Ale Volcanic Range in the Northern part of the Afar Depression. The results also, help to visualize and interpret extensional imbrication fans that constitute part of the Dobe Graben in the central part of the Afar Depression. Finally, mapping of 3D morphologically defined structures (Gani and Abdelsalam, 2006) in rhyolite flows that exposed on the flanks of the Tendaho Rift was possible (Thurmond et al., 2006). They stated that optical-radar-DEM data integration proved to be an effective approach for aiding geological mapping and structural analysis in arid regions such as the Afar Depression.

The integration of Geospatial Information System (GIS) with Global Navigation Satellite System (GNSS) and Remote Sensing can effectively and efficiently handle the upstream, midstream and downstream activities of oil and gas industry in Ghana (Quaye-Ballard et al., 2013). Remote Sensing devices employed for such activities include infrared video and photography from

airborne platforms, thermal infrared imaging and airborne and space borne SAR. They also, stated that Remote Control Vehicles (RCV) operating on land or in the air fitted with radio control device, cable between control and vehicle, or an infrared controller; and Remotely Operated Vehicles (ROV) fitted with thrusters, video and still cameras, lights, and sensors can be employed for oil and gas research and exploration. ROV aids in conducting undersea surveys, searching for mineral deposits and monitoring installed oil rigs and dams; data is amalgamated with GIS (Quaye-Ballard et al. (2013).

Some methods to use SAR imagery to monitor oil spills have been proposed for West African sub-region (Klogo, et al., 2013) and its prospects for monitoring and detecting oil spill in Ghana were explained by Bonsu and Yankey (2014). They explained two types of approaches to oil spill detection on SAR images as manual, where the operators are trained to analyse images for detecting oil spills; and semi-automatic or fully automatic approaches, where automations are inserted. Kostianoy et al. (2014) also employed Advanced Synthetic Aperture Radar (ASAR) data and historical information to study Bonga oil spill pollution in the coastal water of Nigeria which occurred on 20 December 2011. ASAR data was used to determine spill location, size and extent of the spill, direction and magnitude of oil movement, and wind, current and wave information for predicting future oil movement. Furthermore, Balogun (2015) used SAR data acquired on 22 December 2012 for mapping of oil spill on water and land in the mangroves of Rivers State of the Niger Delta successfully. In a similar study, Ajide and Isaac (2013) studied oil spillage that occurred at Jesse village in Delta State and their findings revealed that oil spillage is increasing unabated in the study area. However, despite the advances in performance of

SAR, oil spill detection efficiency would still be low without complementary processing techniques to effectively analyse and interpret the data from these sensors (Bonsu and Yankey, 2014; Lavender, 2007).

Furthermore, Balogun (2015) stated that one of the problems of SAR is that it could not discriminate between backscatter of oil on land and that of soil with high water content. Another problem of SAR that was stated by Klogo, et al. (2013) is the presence of speckle noise. In order to overcome these problems, advanced computing techniques such as pattern recognition and parallel programming (Bonsu and Yankey, 2014) and the use of mean and median filters (Klogo, et al., 2013) were employed to interpret these data to greatly improve the efficiency of oil spill detection. For example, Klogo, et al. (2013) compared the mean and median filters to evaluate their performance in reduction of speckle noise. The simulation results show that the median filters performs better for high levels of speckle noise in the SAR image. The mean filter performs very well in terms of Mean Square Error (MSE) when the noise levels are low. They concluded that designing an adaptive algorithm which will take advantage of the strengths of both the mean and median filters should be considered (Klogo, et al., 2013).

Wireless sensor networks are useful for pipeline monitoring (Yoon et al., 2011) and topological changes (Jawhar et al., 2006). Nweke and Ogbu (2015) explained the benefits of wireless sensor network for pipeline vandalisation, oil spillage detection and monitoring to Nigerian oil and gas sector. These includes the use of inexpensive and low-powered micro-controllers and transceivers that makes it affordable to many organisations; better coverage (Chanin and

Hollaran, 2009); ad-hoc nature of the network allow addition of wireless nodes when required (Bhattacharyya et al., 2010); negative environmental condition can not affect pipeline monitoring; allows many user and sensor nodes are self-healing, nodes can be added or removed without bringing the network to a halt. The network can re-configure itself and determine the best route to the base station (Huen and Sohu, 2007).

Omodanisi et al. (2010) integrated remote sensing and geoinformation techniques with the use of Landsat 7 ETM+ data and 1: 25,000 topographic map to identify vulnerable settlements within crude oil pipeline corridor at Amuwo-Odofin Local Government Area, Lagos State, Nigeria. The selected communities had been affected by conflagration from bust pipeline in 1990. The study showed that the oil pipeline in the study area is exposed, hence its vulnerability to vandals, whose activities resulted in the conflagration. Their results also revealed that a number of settlements exist within the oil pipeline corridor that probably increased the casualties in the previous disaster. In a similar study, Omodanisi (2013) used Landsat 7 ETM+ (2005) and Ikonos (2007), orthophoto map and fieldwork data to evaluate the impact of oil spill, explosion and fire at the same Amuwo Odofin Local Government Area. She used ERDAS Imagine 9.2 for image processing and a Bayesian classifier for classification of land cover. Her results show that vegetation cover was high in 2005 but has been replaced by light forest in 2007 and that the changes in land use and land cover could be as a result of the oil spill and explosion that occurred and had decimated the mangrove vegetation. Finally, the proximity of the mangrove vegetation to oil spill increased the rate at which the vegetation decayed and dies. She concluded that land use and land cover of the study sites has been changed by human

activities through oil spill that had occurred and polluted the vegetated land cover.

Anejionu et al. (2014) used the Landsat Flare Detection Method (LFDM), that was based on the combination of the near, shortwave, and thermal infrared bands of Landsat imagery (bands 4, 7, and 6) to develop the multi-band flare detection technique for detection of gas flare in the Niger Delta. The technique was validated using a reference data set of flares locations interpreted from aerial photographs, achieving a user accuracy of 86.67 %. The LFDM was applied to a time series of imagery (1984-2012) to obtain a long-term flaring history of the region; 303 flares (251 onshore and 52 offshore) were detected over the study period. The use of the spectral characteristics and relatively high spatial resolution of Landsat imagery enables the LFDM to overcome many of the limitations of techniques that have used MODIS imagery for flare detection (Anejionu et al., 2015).

A second gas flare detection approach by the same authors (Anejionu et al., 2015) was based on MODIS-acquired night-time thermal imagery of the Niger Delta region for gas flare detection and estimation of flaring volumes at 29 flow stations. They developed the MODIS flare detection technique (MODET) and the MODIS flare volume estimation technique (MOVET) that exploit the absolute and contextual radiometric response of flare sites. The MODIS flare detection technique (MODET) utilised the radiometric and spatial properties of gas flares for detecting flares and discriminating them from other features with high thermal emissions. The MOVET is based on the concept that the volume of gas flared at each flow station for any given time period (i.e. the combustion

rate) would determine the intensity of fire at that location, and by extension the magnitude of the spectral radiance emitted at the location, captured by the MODIS sensor (Anejionu et al., 2015). The levels of detection accuracy and estimation error were quantified using independent observations of flare location and volume. MODIS data (588 images) from December to January for the period 2000 to 2014 were used. Their results demonstrate the substantial spatial and temporal variability in gas flaring across the region, between states and between onshore and offshore sites. The estimated total volume of gas flared in the region over the study period is 350 Billion Cubic Metres; the heterogeneity in the flaring indicates that the impacts of such flares will be highly variable in space and time (Anejionu et al., 2015). However, they stated that it is important that the robustness and transferability of the LFDM, MODET and MOVET techniques is evaluated in other oil-producing regions of the world to enable the methods to make a key contribution to monitoring the compliance of countries to the Global Gas Flaring Reduction initiative and for modelling the health and environmental impacts of flaring (Anejionu et al., 2015).

Several authors used remote sensing data to assess the environmental impact of oil and gas exploitation in the Niger Delta region. Twumasi and Merem (2006) used Landsat data from 1985 to 2000 to study the consequence of several severe oil spills on land cover change in the Eastern subset of the Niger Delta. In a similar study, land cover change was analysed for a selected area of the Niger Delta between 1986 and 2008 using Landsat and Nigeriasat-1 imagery (Abbas and Fasona, 2012). Uchegbulam and Ayolabi (2013) employed one Landsat TM scene for 1987 and the same frame covered in 2002 by Landsat 7 ETM+, to

study the impact of hydrocarbon exploration on vegetation cover in the Western part of the Niger Delta. The NDVI results show decreasing NDVI values between 1987 and 2002 and they concluded that the results obtained occurred due to the negative effect of hydrocarbon exploration on vegetation. James et al. (2007) used Landsat data to assess the alteration of mangrove forest ecosystems between the mid-1980s and 2003. The results indicate that the spatial extent of mangrove loss summed up to 21,340 ha and was primarily caused by deforestation due to dredging activities and oil exploration.

In addition, Fabiyi (2011) utilized Landsat 7 ETM+ satellites images from two dates (31 December 2000 and 22 December 2006) and other auxiliary data on oil activities to examine the main drivers of change and vegetation loss in the Niger Delta. His results showed that anthropogenic activities such as oil and gas exploration and refining processes were responsible for the major changes in the vegetation cover within the study area. Also, Olusola and Okoroige (2010) used Landsat 5 TM of 3 November 2001, 15 November 1986 and 7 November 1992 for land use and land cover evaluation analysis of a part of Rivers State and Omo-Irabor and Oduyemi (2012) also employed Landsat 5 TM scene of 1987 and a Landsat 7 ETM+ scene of 2002 to study land cover changes of a part of Bayelsa State. They concluded that the effects of oil exploration and exploitation have caused land resource degradation and that some of these problems include agricultural land degradation, deforestation, mangrove degradation, biodiversity, fisheries depletion, coastal erosion etc. Hamadina and Anyanwu (2012) reviewed the consequences of oil exploitation and exploration and land use changes in the Niger Delta. A mixed scale approach was adopted involving literature review, land use and land cover change detection using two Landsat

dates (1985 and 2005), and sampling and analysis of soil from four variables. Their results show that oil spills had damaged the ecosystems and changed land cover from forest to sparse vegetation. They concluded that these are long term environmental problems that have grievous consequences.

Furthermore, Kuenzer et al. (2014) analysed land surface dynamics and environmental challenges of the Niger Delta from 1986 to 2013 using 15 dates of data. The results of the analysis show the impact of the oil exploiting industry, manifested in the expansion of access canal networks within mangrove areas and that of gas flare activity with a clear increase in flares from 1986/87 to 2002/2003. They concluded that the activities of the international oil industry are seriously impacting the ecological system of the Niger Delta. Onojeghuo and Blackburn (2011) used Landsat TM data for 19/12/1986 and NigeriaSat-1 for 20/01/2007 to investigate the spatial extent and rates of forest transition in the Niger Delta region taking into consideration the patterns, causes and implications of the landscape dynamics. They concluded that the influence of oil and gas exploration in the Niger Delta has intensified logging of trees and has negatively impacted the once flourishing and ecologically diverse forest system of the Niger Delta region.

Adamu et al. (2015) investigated the potential for using broadband multispectral vegetation indices to detect impacts of oil pollution on vegetation conditions using twenty vegetation indices. Landsat TM and ETM+ imagery, acquired on 17 January 1986, 19 December 1986, 29 November 1999, 17 December 2000 and 8 January 2003 (path 188, row 57) and the ancillary data (oil pipeline maps, spill records from 1985 to 2000 and geographical

coordinates of spill points) were analysed. The indices use data at the visible, near infrared and shortwave infrared wavelengths. Comparative index values from 37 oil polluted and non-polluted (control) sites show those 12 broadband multispectral vegetation indices (BMVIs) indicated significant differences (p-value < 0.05) between pre- and post-spill observations. The 12 BMVI values at the polluted sites before and after the spill are significantly different to the ones obtained on the spill event date. The result at the non-polluted (control) sites show that 11 of the 20 BMVI values did not indicate significant change and remained statistically invariant before and after the spill date (p-value > 0.05) (Adamu et al., 2015). They stated that oil spills result in biophysical and biochemical alteration of the vegetation, leading to changes in reflectance signature detected by these indices. The evaluation of their results showed that the best performing indices in detecting and monitoring vegetation affected by oil pollution were those derived using a combination of reflectance at the visible and NIR wavelengths (Adamu et al., 2015). They are Normalized Difference Vegetation Index (NDVI), Soil Adjusted Vegetation Index (SAVI), Adjusted Resistant Vegetation Index (ARVI2), Green Near Infrared (G/NIR) and Green Shortwave Infrared (G/SWIR). It is known that the reflectance signatures of vegetation in these bands are sensitive to any changes in vegetation conditions. Therefore, any changes in vegetation biophysical and biochemical characteristics induced by oil pollution would affect the reflectance signature of vegetation in these bands, which can be detected by indices derived using these bands (Adamu et al., 2015). These five indices were found to be consistently sensitive to oil pollution effects as shown by their significant temporal changes between pre- and post-spill events. Therefore, these indices could be used for

monitoring oil pollution in vegetated areas (Adamu et al., 2015; Veraverke et al., 2012).

In summary, limited research into gas flare detection in the Niger Delta has been published to date, and no studies relating gas flaring to environmental impact on vegetation have been published (or at least this research has not been found within the peer-reviewed literature). Furthermore, when the spatial nature of many environmental impacts are considered, remote sensing becomes an appropriate tool that can be used to detect, map and estimate flaring and pollution and its impact on the Niger Delta environment with respect to the vegetation and land cover over time. Therefore, this research aims to provide evidence-based information to aid Nigerian government policy and an implementation mechanism to tackle gas flaring.

Chapter 3
Data sources and methodology

This Chapter describes the research methods adopted to fulfil the research aim and objectives. The research approach, specific methods, research stages, type of data used and reasons for data choices, the programming code development, the data processing methods, and finally the limitations are presented. This comprises an approach to using Landsat 5 TM and Landsat 7 ETM+ to detect gas flaring and its effects on the environment of the Niger Delta with a focus on vegetation cover and health.

3.1 Methodological approach and design

Collis and Hussey (2003) stated that the purposes of research include to review or synthesize existing knowledge; investigate existing situations or problems; provide solutions to problems; explore and analyse more general issues and to construct or create new procedures or systems. Neville (2007) and Creswell (2003) identified various methodological approaches to research such as quantitative/qualitative, applied/basic and deductive/inductive approaches. This study adopts a quantitative approach because it establishes statistically significant conclusions about a population by studying a representative sample of the population (Lowhorn, 2015; Berry, 2006). Quantitative research is generally associated with the positivist/post-positivist paradigm and large data sets and statistical analyses are often used and conclusions drawn (Neville, 2007). This research employs various methods at different stages to enhance the usefulness of the research end results.

3.2 Research stages

This study is divided into two major research stages. The first is to find out if gas flares and their pollution can be detected by satellites, because none of the satellite instruments were designed primarily for the purpose of flare detection and measurement. Next, a method was sought by which the impacts of gas flaring pollution on the environment with respect to the vegetation cover and health could be determined. The case study approach is adopted for this study. This was done using fieldwork observations, acquisition of satellite data, applying remote sensing software (BEAM VISAT and SeaDAS) and developing MATLAB software for visual display of data, processing and analysis. The following is the breakdown of the stages involved.

Stage one: Detection, mapping of flares and associated environmental impact

This required the development and use of MATLAB programming code for the detection of the thermal signatures of flares from gas flare sources, mapping of oil and gas facilities, and the evaluation of the environmental impacts of gas flares with a particular focus on vegetation cover and health.

Stage two: Fieldwork activities

Fieldwork activities were carried out to collect data for a ground validation exercise. It involved physical inspection and fieldwork measurements at the two gas flare sites in the Niger Delta. The variables measured were the coordinates of ground points within 480 m^2 around the flare at 30 m intervals; the parameters measured included air temperature and relative humidity, plus photographs were taken of identified locations with evidence of the impacts of the gas flares.

Stage three: Meteorological effects

This stage is where the phenomena of the atmosphere, especially weather and weather conditions of the Niger Delta, were considered in relation to the acquired study data.

3.3 Stage one: Detection, mapping of flares and associated environmental impact

This stage comprised three major activities: Determining the location of the oil producing facilities that produce gas flares, detailed mapping of the land around these oil producing facilities and, finally, evaluation of the impacts of the gas flares on the environment. The MATLAB programming tool was used for the processing of Landsat 5 TM and Landsat 7 ETM+ data to produce relevant products - land surface temperature, vegetation index (NDVI) and land surface cover.

3.3.1 Detection of the gas flare sites linked to oil production using public domain remote sensing data

The first question for this research is: Where are the gas flare sources in the Niger Delta? Terrestrial surveying methods are not suitable to solve this problem due to the topography of the area, inaccessibility (most of the locations are at the coastal boundaries and some are offshore), security, the political situation of Nigeria and the spatial scale of this research. This makes remote sensing a valuable technique and indispensable tool. The public domain remote sensing data employed are discussed in sections 3.3.1.1 to 3.3.1.4.

3.3.1.1 ATSR-World Fire Atlas

The World Fire Atlas consists of a global collection of "hot spots", i.e. the locations from which emitted radiances exceed predefined thresholds, and forms a unique time series of global fire locations and timing. Data are available from 1995 and the processing is ongoing, with the first full year of data being available for 1997 (ESA, 2015a). The data used are those recorded at night-time by the ATSR-2 and since 2003 the follow-on AATSR. Each record comprises the detection date, time, latitude and longitude of a 1 km by 1 km pixel when the brightness temperature in the 3.7 μm channel exceeds either 312 K (algorithm 1) or 308 K (algorithm 2) with pixels being revisited on average every 3 days. These records are available as monthly ASCII files direct from the World Fire Atlas (WFA) website (http://dup.esrin.esa.it/ionia/wfa/index.asp) (Arino et al., 2012; Arino et al., 2005).

It should be noted that the records represent all pixels exceeding these thresholds with no subsequent elimination quality control, thus the interpretation of these records in terms of cause is for the user to perform. The archive should be used with caution for the detection of small fires (including gas flares), agricultural fires, savannah fires and boreal forest fires (Arino et al., 2005).

For this research, both algorithms 1 and 2 of the ATSR-WFA were examined on a monthly basis using data from 1997 to 2011. The seasonality of the WFA hotspots was used to determine which are flares, and which are agricultural. It was found that the hotspots (gas flares) detected in the WFA were present every month of the year throughout the time period. In the case of agricultural fires, hotspots were not repeated for more than three to four months and their

appearance is seasonal i.e. during the end of dry season and approaching the rainy season in Nigeria; this is the period when farmers clear land by burning in order to prepare the ground for planting crops. The WFA results were used to identify 65 hotspots of which 52 were determined to be gas flare sites. These sites were characterised in the next analysis step (see section 3.3.2). The availability and the use of the ATSR-WFA archive helped to differentiate gas flare sites from forest fires in other locations within the Niger Delta.

3.3.1.2 Google Earth

'Virtual globe' software is growing rapidly in popularity as a way to visualise and share 3D environmental data. Google Earth "A 3D Interface to the Planet" (Google Corporation, 2006) was publicly released in June 2005 and has attracted widespread public use and attention due to its ability to view landscapes in a fairly realistic 3D view using a combination of digital elevation models, satellite imagery, and 3D building envelopes (in some selected cities). Google Earth grew to over 100 million users on the internet within one year of its release (Google Corporation, 2006), and in the United Kingdom, it is reported that "Google Earth" became the eighth most popular search term during the month of January 2006 (Hopkins, 2006). For example Edward et al. (2013) developed a public open space desktop auditing tool (POSDAT) using Google Earth for Perth, Western Australia and Taylor et al. (2011) also measured the quality of public open space (50 parks) in Southwest part of Sydney, Australia using Google Earth. They concluded that remote assessment method provides the capacity to assess the quality of large number of parks and other green spaces without the need for in-person visits, dramatically reducing the time required for environmental audits of public open space. Other software that is available with some similar capabilities includes Microsoft Virtual Earth

(a.k.a. Bing), World Wind (NASA, 2006) and ESRI's ArcGIS Explorer (ESRI, 2006).

Google Earth was employed for the searching and identification of oil and gas producing facilities sites with flares (hotspots) that were already identified with WFA data in the Niger Delta. Google Earth provided visual confirmation and geographical coordinates for the locations of gas flaring sources such as refineries, oil wells, flow stations, terminals and Liquefied Natural Gas (LNG) plant. Figures 3.1 (A) and (B) from Google Earth show the locations of Eleme Petroleum Refinery II Company at Eleme and Alua Flow Station, Alua, which are both in the Rivers State of the Niger Delta region, Nigeria.

A: Eleme Refinery II Petroleum Company (Google Earth, 2015)

B: Alua Flow Station (Google Earth, 2015)

Figure 3-1: (A) Eleme Petroleum Refinery II Company (Google Earth, 2015) (B) Alua Flow Station (Google Earth, 2015)

3.3.1.3 GeoEye I, Quickbird, WorldView-1 and WorldView-2 browse images

Due to failure of several attempts made to gain access to Shell Petroleum Development Company, Nigeria to obtain data (oil processing related and satellite), the author is left with the alternative of using browse images instead

of full resolution images such as Ikonos and SPOT to examine changes at the flaring sites. According to Wolf (2012) the multispectral imagery such as that from GeoEye I, Quickbird, WorldView 1 and 2 provides information for public, commercial and intelligence uses to support decision making across a growing number of private and industrial applications such as land mapping, terrain classification and feature extraction. These multispectral images allow the use of non-traditional means of measuring the differences which exist in the features, artefacts, and surface materials in the data. In order to examine various developments at gas flaring sites in the Niger Delta region GeoEye I, Quickbird, WorldView-1 and WorldView-2 browse images obtained from http://browse.digitalglobe.com/imagefinder/public.do were employed. Also, these browse images were used to check and compare to those browse images obtained from Google Earth. This gives a visual history of the sites and helps in qualitative analysis. Figure 3.2 (A) and (B) are browse images from Quickbird and WorldView-2 for Eleme Petroleum Refinery II Company on June 12, 2010 and January 13, 2014 respectively.

A: Eleme Petroleum Refinery II Company (June 12, 2010 (Quickbird)

B: Eleme Petroleum Refinery II Company January 13, 2014 (WorldView-2)

Figure 3-2: Eleme Petroleum Refinery Company II in (A) June 12, 2010 (Quickbird) and (B) January 13, 2014 (WorldView-2) Source: http://browse.digitalglobe.com/imagefinder/public.do

3.3.1.4 UK-DMC (SLIM 6–22)

A single image from the UK-DMC (SLIM 6-22) sensor for January 18, 2011 that was acquired free from DMCii was employed for further identification and confirmation of oil and gas facilities, gas flares sources and the surrounding features. The visible spectral region of UK-DMC imagery is not particularly useful for the study of fires, and indeed is more commonly used to discriminate fires from sun glint, since these two phenomena can look rather different in the visible spectrum but rather similar in the mid infra-red (Zhukov et al., 2005). Also, it is used to provide a detailed record of fire scars i.e. for burn scar mapping, accurate measurement of the extent of fires and their validation, and their environmental impact (Levin and Heimowitz, 2012). Its was chosen over Landsat imagery because its spatial resolution (22 m) made it possible to clearly discriminate and identify different features such as oil facilities, buildings and roads on the ground that might not be apparent in 30 m Landsat TM/ETM+.

The geographical coordinates of the gas flare sources obtained from Google Earth were used to ascertain the exact positions of gas flare sources and the surrounding features in UK-DMC imagery. BEAM VISAT, an open source remote sensing image processing software was used to enable an open source solution to complement the freely available Landsat imagery and the pixel coordinates for each flare location were extracted. Figure 3.3 shows the UK-DMC image used for the study.

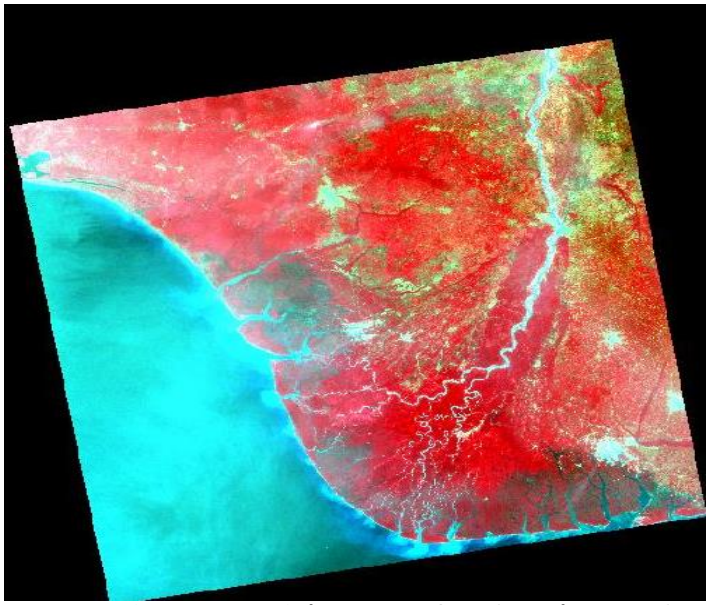

Figure 3-3: UK-DMC (SLIM 6-22) imagery for the Niger Delta (January 18, 2011)

3.3.2 Mapping of flare sites and associated environmental impacts

Diverse oil facilities serve different purposes in the processing stages involved in oil and gas production from exploration to transportation. These facilities are oil wells, flow stations, refineries, liquefied natural gas plants and terminals. In all these facilities, gas flaring is used continuously in the Niger Delta as a safety mechanism. This section discusses the survey of the gas flare sites and their surrounding environment. The following are the criteria used for the selection of the flare sites used for this study:

- Availability of Landsat data in the USGS/NASA Archive;
- Function of the oil and gas facilities e.g. refineries, flow stations, terminals, oil wells;
- Coverage i.e. availability of data covering the facility throughout the study period;
- Variety of size/capacity i.e. spatial dimensions of the facility (i.e. both large and small facilities in order to compare their results);
- Accessibility;

- Location i.e. both coastal and inland facilities in order to compare results.

Each flare site was investigated as a 12 by 12 km area (400 × 400 Landsat pixels); this size was chosen in order to include sufficient area for the analysis of the impacts of gas flaring. This is based on previous literature by Dung et al. (2008) and Isichei and Sandford (1976), that the spatial extent of primary gas flare impacts was expected to be much less than 2 km in any direction.

3.4 Data used and sources

In order to carry out detailed mapping of the gas flares sites, to detect and evaluate the effects on the environment with the focus on vegetation cover and health, the three key data required for this study are satellite data, ground validation/fieldwork data and meteorological data. The quality of the data used for this study is of varying standard e.g. during the fieldwork activities the maximum effort was taken at Eleme Refinery II and Onne Flow Station gas flaring sites to ensure that the acquired data were measured with precautions.

3.4.1 Satellite data

The minimum available satellite data requirements for this study are:

- Parameters: VIS-TIR for derivation of Land surface temperature (LST) and Normalized Difference Vegetation Index (NDVI);
- High spatial resolution sensor;
- Medium temporal resolution sensor;
- Availability of data;
- Time span;
- Number of low cloud images for the Niger Delta.

Based on the above listed data requirements, the satellite imagery employed for mapping of gas flare sites were Landsat 5 TM and Landsat 7 ETM+. Both Landsat 5 TM and Landsat 7 ETM+ scenes are geo-referenced to Worldwide Reference System -2 (WRS-2) (USGS, 2011). Landsat 5 TM and Landsat 7 ETM+ were chosen for this study in preference to other available sensors (see section 2.8.1) because of the following reasons: (1) All available Landsat 4 TM data for Niger Delta were covered with cloud. (2) Though Landsat 8 OLI/TIR has spatial resolution of 100 m and its data resampled to 30 m, it was not considered for this study because the author has completed data analysis at the time it was launched. However, both Landsat 5 TM and Landsat 7 ETM+ have a single thermal band that prevents the use of split window algorithms which is the robust method for the correction of atmospheric effects for thermal bands. The available Landsat 5 TM and Landsat 7 ETM+ scene used were from month of October to April of the year which is dry season in Nigeria except only one scene dated 12 August 2012 which is the only available scene that was used for ground validation (see sample dates in Table A-7 in Appendix A).

The effects of cloud cover on Landsat 5 TM and Landsat 7 ETM+ data acquired over the Niger Delta is enormous. The archives for both data sets were systematically searched and scenes with < 30 % cloud contamination were selected for analysis. See Table 2.19 for the summary of Landsat 5 TM and Landsat 7 ETM+ data characteristics and their applications.

For this study, the key parameters to address the research question one and objective two were the LST and land surface cover (LSC). LSC was used to select appropriate surface properties in the LST calculation (see section 3.5.2). For the

research questions one and three and for objectives four and five, the key remote sensing parameter was LSC to identify areas of vegetation and an indicator for vegetation health. The calculation of these parameters is described in sections 3.5 to 3.6.2.

3.4.2 Ground validation/fieldwork data

In remote sensing, ground validation (through the collection of field data) is especially important to relate image data to real features and materials on the ground (Brown, 1996). More specifically, ground validation may refer to a process in which a pixel on a satellite image is compared to what is on the ground in reality (at a matching time) in order to verify what the pixel is showing. Ground-based data will always be required for validation of any remote sensing technique, whether it is for land surface or seabed mapping, no matter the spatial resolution or source (Serpetti et al., 2011). Furthermore, remote sensing instruments may not be able to identify all the features at the time the satellite passes over a given area due to for example spectral ambiguity or cloud cover. Therefore, ground validation can also be an effective means to fill in the features that were missing or could not be easily identified through the imagery (Vega et al., 2011).

Ground validation usually involves performing surface observations and measurements of various properties of the features that are being studied. It also involves taking the coordinates of features and comparing those with the coordinates of the corresponding pixel being studied to understand and analyse the location errors and how these may affect a particular study (Vega et al., 2011). It is also important in the initial supervised classification of an image and helps with validation of the atmospheric correction. Since the signal acquired by

satellites has to pass through the atmosphere, it can be attenuated and distorted by absorption and scattering. Other purposes of acquiring ground validation data are for the calibration of remote sensing sensors; developing new methods, improving and testing existing algorithms for geophysical parameter retrieval; development of multi-satellite remote sensing interpretation; complex exploration of natural objects, among them ecologically dangerous regions, by integrating information, obtained from different sensors at different levels with different temporal, spectral and spatial resolutions (Pressler and Walker 1999).

It is difficult to make in-situ measurements coincident with image acquisition, and the measurement scales and properties of the surface recorded are fundamentally different. Therefore, relationships developed between in-situ and remotely sensed measurements often come with extensive sets of qualifiers or more usually are specific to a particular image acquisition (Smith et al., 2009).

For this research fieldwork activities were carried out with the aim of ground validation at two gas flaring sites; namely Eleme Petroleum Refinery Company II and Onne Flow Station both in Rivers State. See section 3.7 for more details on the fieldwork activities and section 4.7 for the results.

3.4.3 Meteorological data

The minimum data requirements for analysis of the meteorological effects in the Niger Delta are daily observation of the meteorological parameters. The meteorological data available for the study were collected from the Nigerian Meteorological Agency, Lagos. These data are provided on monthly basis and includes minimum and maximum air temperature, solar radiation, wind speed,

wind direction, rainfall, relative humidity, sunshine and air temperature (dry bulb).

3.4.4 Summary of data sources

The list of data used in this study and their sources are summarised in Table 3.1.

Table 3-1: Summary of Data Sources

Type of data	Name of data	Sources	Time
Satellite	ATSR-World Fire Atlas	ESA	1997-2011
Satellite	UK-DMC (SLIM 6-22)	DMCii, UK	18/1/2011
Satellite	Landsat 5 TM	USGS	1984-1991
Satellite	Landsat 7 ETM+	USGS	1999-2013
Fieldwork	Air temperature, relative humidity, geographical coordinates of points and photographic pictures of selected points.	Eleme Refinery II Petroleum Company and Onne Flow Station.	4/8/2012-9/8/2012 and 8/9/2012-13/9/2012
Meteorological	Temperature, solar radiation, wind speed, wind direction, rainfall, relative humidity, sun shine and air temperature (dry bulb).	NMA, Lagos.	2000-2013

3.5 Parameters investigated for mapping of flare sites and environmental impacts of gas flaring

Radiance is the total amount of energy that flows from the light source in a given direction, and it is usually measured in watts per steradian per square metre ($Wsr^{-1}m^{-2}$) (Gonzalez and Woods, 2008). Then, reflectance is the ratio of the radiant energy reflected by a body to that incident upon it. In general, reflectance is a function of the incident angle of the energy, viewing angle of the sensor, spectral wavelength and bandwidth, and the nature of the object (NASA, 2002; Markham and Barker 1986). The reflectance for band wavelength (λ) is computed by the equation 3.1 which assumes Lambertian surface reflectance:

$$\rho_p = (\pi \times L_\lambda \times d^2) \div (ESUN_\lambda \times \cos \theta s) \qquad (3.1)$$

Where:

ρ_p = Unitless effective at-satellite planetary reflectance;

L is measured per unit solid angle;

πL = Upwelling radiance over a full hemisphere;

d = Earth-Sun distance in astronomical units interpolated from values listed in Tables A-5 and A-6 in Appendix A, for Landsat 5 TM and Landsat 7 ETM+ respectively;

$ESUN_\lambda$ = Mean solar exoatmospheric irradiances. See Tables A-3 and A-4 in Appendix A, for Landsat 5 TM and Landsat 7 ETM+ respectively;

θs = Solar zenith incident angle in degrees (Chander and Markham, 2003).

3.5.1 Vegetation indices

Vegetation indices have been developed for qualitatively and quantitatively evaluating vegetation cover using spectral measurements; the spectral response of vegetated areas presents a complex mixture of vegetation, soil brightness, environmental effects, shadow, soil colour, moisture and viewing angle effects. Moreover, the vegetation indices are affected by spatial-temporal variations of the atmosphere. As a result, over 100 vegetation indices have been developed in order to enhance the sensitivity of algorithms to the vegetation response and minimize the effects of the factors stated above (Adamu et al., 2015; Veraverke et al., 2012; Bannari et al., 1995).

Vegetation affected by oil production related pollution experiences changes in the biophysical and biochemical characteristics, which can be detected in changes in reflectance measured using satellite sensors (Adamu et al., 2015; van der Meer et al., 2000). This is because vegetation spectral reflectance is

dependent on the chlorophyll and water absorption in the leaves, which get altered by hydrocarbon pollution. Therefore, vegetation indices derived from satellite data can be used to determine the health of vegetation in areas affected by hydrocarbon pollution (Adamu et al., 2015). Several researchers (Khanna et al., 2013; Zarco-Tejada et al., 2005; Li et al., 2005; Peñuelas et al., 1993) have used vegetation indices as the main method for assessing various biophysical and biochemical properties of plants such as chlorophyll concentration, water content and vegetation structure. Broadband multispectral vegetation indices (BMVIs) are mathematical combinations of reflected energy recorded at various wavelengths (Jensen, 2014; Teillet et al., 1997) and have been used to monitor and characterize Earth's vegetation cover from space (Saleska et al., 2007; Myneni et al., 2002).

Several studies have been carried out on comparison of vegetation indices by researchers. For example, the results obtained from vegetation indices calculated using all the mixed three visible bands (i.e. Red, Green and Blue bands) which includes the Green Leaf Index (GLI), and Normalized Difference 550/450 Plant Pigment Ratio (PPR) indicated significant differences in vegetation before and after oil pollution at the polluted sites in the Niger Delta (Adamu et al., 2015). However, these indices performed poorly by indicating significant difference in temporal changes in vegetation conditions at the non-polluted control sites (Adamu et al., 2015). The results of indices that combined the SWIR with the NIR band and that of SWIR band with the visible (Green) band did not indicate any temporal changes in vegetation conditions at the non-polluted sites i.e. vegetation conditions before and after pollution at these sites remain relatively the same (García and Caselles, 1991).

Soil Adjusted Vegetation Indices (SAVIs) outperformed the Normalized Difference Vegetation Index (NDVI) in environments with a single vegetation type (Veraverke et al., 2012). Logically, the sensitivity to vegetation variability increased with increasing vegetation cover. However, this increase was clearly more explicit for the SAVI compared to the NDVI and the Transformed Vegetation Index (TVI) (Veraverke et al., 2012). The NDVI more accurately estimated vegetation cover in environments with heterogeneous vegetation layers and a single soil type and in overall, when both vegetation and background variability is incorporated in the model, the NDVI was the most optimal index because its strong normalizing capacity minimizes the impact of vegetation variability on fractional cover estimates (Veraverke et al., 2012). Illumination differences due to topography for example, result in clearly different reflectance values for the same amount of vegetation, whereas the normalizing property of the NDVI is known to minimize the difference in index values along an illumination gradient (Song and Woodcock, 2003).

The patchiness in vegetation cover, related to landscape heterogeneity and high species richness, can be measured as variability in NDVI (Gould, 2000). The NDVI is more stable than SAVIs against the variability in spectral response of different vegetation types (Veraverke et al., 2012; Gao et al., 2000) and it is the most widely used vegetation greenness measure (Heumann et al., 2007; Myeni et al., 1997; Reed et al., 1994). At moderate resolution scale the Landsat-derived NDVI is the most widely used method to assess post-fire vegetation recovery (Clemente et al., 2009; Malak and Pausas, 2006; McMicheal et al., 2004).

Also in the mixed environments background such as char and ash in the post-fire and vegetation spectral properties result in mixed background-vegetation

signals at the scale of moderate spatial resolution sensors (Veraverke et al., 2012). NDVI is sensitive to the optical properties of the soil background (Baret and Guyot, 1991), which is particularly important when vegetation cover is sparse (Purevdorij et al., 1998). Numerous studies have denoted that the NDVI has higher values for a given amount of vegetation with a dark background than with a bright background (Gao et al., 2000; Huete, 1988). Several modifications to the NDVI have been proposed in order to account for these background effects (Richardson and Wiegand, 1997; Rondeaux et al., 1996; Qi et al., 1994). The physical basis of these modifications relies on the fact that vegetation greenness isolines do not converge in the origin of the Red–NIR bi-spectral space (Richardson and Wiegand, 1997 and Huete, 1988).

Soil Adjusted Vegetation Indices (SAVIs) were developed to account for the optical properties of the background in an attempt to align the index isolines with the isolines of the biophysical variables (e.g. fractional cover, Leaf Area Index). Therefore SAVIs typically include an adjustment factor which is related to the direction of the soil line, i.e. the regression line of soil reflectance in the Red–NIR space (Richardson and Wiegand, 1997; Rondeaux et al., 1996; Huete, 1988). The theoretical improvements of the SAVIs do not consistently outperform the NDVI (Clemente et al., 2009; Carreiras et al., 2006). Several empirical studies indicated that the SAVIs did not result in more reliable estimates of vegetation cover compared to the NDVI (Baugh and Groeneveld, 2006; Schmidt and Karnieli, 2001; Purevdorj et al., 1998; Leprieur et al., 1996). Purevdorj et al. (1998) assessed the relationship between several R – NIR vegetation indices (VI) over a wide range of grass densities in Mongolia and Japan. The grasslands consisted of a plethora of species. Although they acknowledged the capability of the SAVIs to reduce the influence of soil

variation, they concluded that overall the NDVI was the best index, outperforming the SAVIs.

Carreiras et al. (2006) estimated tree canopy cover in heterogeneous Mediterranean shrubland. They assumed that the partition between the tree overstorey and shrub understorey was constant over the full density range and as such they could use the mixed overstorey-understorey signal to estimate oak tree coverage. Regression equations between vegetation indices and estimates of tree coverage retrieved from aerial photographs were calculated. The NDVI also obtained higher R^2 values than the SAVIs. Clemente et al. (2009) and Vila and Barbosa (2010) represent two studies in a post-fire recovery environment. Clemente et al. (2009) contrasted the NDVI with the SAVIs for estimating post-fire vegetation regrowth 7 and 12 years after a fire in Spain. The vegetation layer was highly diverse and varied from shrublands to woodlands. The NDVI had higher correlations with field estimates of vegetation cover than any other index. Vila and Barbosa (2010) drew the same conclusion as Clemente et al. (2009). They also found that the NDVI was most accurately related to field data 8 years after a fire in Italy. Also, Gao et al. (2000) explained that different canopy types can produce different VI values while having an identical fractional cover or Leaf Area Index (LAI). They demonstrated that NDVI values were fairly uniform across vegetation types, whereas the SAVI exhibited pronounced differences among canopy types.

3.5.1.1 Normalized Difference Vegetation Index (NDVI)

The NDVI was first formulated by Rouse et al. (1974) and applied to a wide range of practical remote sensing applications in a series of studies by Tucker

and other researchers in the 1970s and 1980s, e.g. (Tucker et al., 1985). The mathematical algorithm for NDVI is:

NDVI = (NIR − Red) ÷ (NIR + Red) (Huete, 1988) (3.2)

Where:

NIR = Reflectance from Near Infra-Red (NIR) channel, band 4 for Landsat TM and ETM+;

Red = Reflectance from Red channel, band 3 for Landsat TM and ETM+

The NDVI is built on the assumption that chlorophylls a and b in green leaves strongly absorb light in the Red, with maximum absorption at about 690 nm, while the cell walls strongly scatter (reflect and transmit) light in the NIR region (about 850 nm) (Tucker, 1979). This result in a strong absorption contrast across a narrow wavelength band of 650-850 nm captured by the NDVI and other vegetation indices (Glenn et al., 2008). A defining characteristic of the NDVI is that it limits are bound from −1 to 1 (Veraverke et al., 2012). However Huete et al. (1997) showed that the structure of the NDVI equation, a non-linear transformation of the simple ratio (Near-infrared/Red), is the major cause for non-linearity and saturation in high biomass situations. This constraint, called saturation, is often found in tropical forests (Huete et al., 1997).

NDVI is useful for measuring relative changes in the condition of vegetation over time and across the same area of landscape (Sader et al., 1989; Maxwell, 1981). It is an indicator usually used to assess the spatial distribution of vegetation and photosynthetic activity (Basith et al., 2010). Rouse et al. (1974) first used it to monitor and distinguish vegetated areas from other land cover types (Lyon et al., 1998). Many other studies have found correlations of NDVI with leaf area (Curran et al., 1992). Healthy vegetation absorbs most of the

reflectance from the red band, and reflects a large portion of the near-infrared light. Unhealthy or sparse vegetation reflects more visible light and less near-infrared light (Curran et al., 1992) (i.e. healthy vegetation 'regulates' heating by scattering strongly in the near-infrared). The amount of red light backscattered by healthy vegetation also depends on leaf pigmentation, i.e. species, as well as health or physiological state.

Positive NDVI values (NIR > RED) indicate green, vegetated surfaces, and higher values indicate increases in green vegetation (Weiss et al., 2004). Reflectance of the red portion of the spectrum decreases as solar radiation is absorbed, largely by chlorophyll, whereas reflectance of the near infrared portion is caused by leaf mesophyll structure (Kremer and Running, 1993). Negative NDVI values indicate non-vegetated surfaces such as water, ice, and snow. Studies have related NDVI to biophysical variables such as leaf area, canopy coverage, productivity, and chlorophyll density as well as to vegetation phenology (Goward et al., 1985; Justice et al., 1985; Tucker et al., 1985; Townshend and Justice, 1986; Spanner et al., 1990; Yoder and Waring, 1994; Peters and Eve, 1995; Prince et al., 1995). Low values of NDVI result from sparse vegetation and little photosynthetic activity. Surface heterogeneity also complicates interpretation of NDVI (Weiss et al., 2004).

In general, the calculations of NDVI values for a given pixel result in a number that ranges from −1.0 to 1.0, with negative values indicating clouds, water and ocean, positive values near zero indicating bare soil and sparse vegetation (0−0.01), and increasingly higher positive values indicating sparse vegetation (0.1−0.5) through to dense green vegetation (0.6 and above). Indirectly, NDVI has been used to estimate and assess the quality of the environment as a habitat

for various animals, pests and diseases, vegetation over a certain period of time, rangeland carrying capacity, and crop yields for different crop types. Healthy green plants exhibit high NDVI values while diseased vegetation or non-vegetated areas feature low or even negative NDVI values (Williams, 2012; Julien et al., 2011).

However, Williams (2012), Julien et al. (2011) and Gamon et al. (1995) showed a non-linear relationship between NDVI and vegetation measurements (leaf area index, green biomass and chlorofila) in temperate forest. However, they pointed out the restrictions of using NDVI as an indicator of canopy structure and chemical contents for well-developed canopies. They considered that beyond a certain canopy density, the addition of more canopy layers make little difference in the relative reflectance of Red and Near-infrared radiation, and thus little difference in NDVI. This constraint caused by saturation was also noted by Shimabukuro et al. (1998) in Amazonian regenerating forests, and by Bawa et al. (2002) in Indian evergreen forests. However, NDVI showed good results in a study on vegetation at early successional stages in Amazonian Forest, establishing relationships to basal area and leaf area index (Amaral et al., 1997). Similarly, studies in drier forests did not find constraints due to saturation in NDVI, such as deciduous tropical forest in India (Bawa et al., 2002), and dry tropical forest in Costa Rica (Arroyo-Mora et al., 2003). NDVI is a good indicator of green biomass in deciduous and dry forests (Veraverke et al., 2012).

Another constraint of visible and near-infrared bands usage is the asymptotic behaviour of reflectance with a biophysical parameter of vegetation increases continuously that is, the sensitivity of the NDVI to biophysical properties declines at large vegetation amounts (Freitas, et al., 2005; Carlson and Ripley,

1997: Ripple, 1985; Tucker, 1977). So at very high NDVI values, a small change in NDVI may actually represent a very large change in vegetation and at low NDVI soil, illumination etc. may play a vey large role. Other factors affecting NDVI are environmental stress (Williams, 2012); growth stage and speciation (Julien et al., 2011); the attenuation by the large atmospheric water and aerosol load above tropical forest canopies; the low reflectance of red and NIR wavelengths from tropical forest canopies (Singh, 1987); scale of the imagery, vegetation moisture, vegetation type, photosynthetic activity, soil moisture and differences in soil type (Carlson and Ripley, 1997) and the ecological and physical complexity of tropical forest environments (Sader et al., 1990).

For this research, the only factor that was corrected for was the atmospheric conditions (section 3.6.2); there was not sufficient information about the other factors, which made it impossible to correct for their effects. Hence, NDVI was applied in this study as one means to detect and evaluate the effects of environmental stress caused by gas flaring.

3.5.2 Emissivity

Emissivity (Ɛ) is the ratio of energy emitted from a natural material to that from an ideal blackbody at the same temperature. An accurate value of surface Ɛ is desired in land surface models for better simulations of surface energy budgets from which skin temperature is calculated (Mallick et al., 2012; Jin et al., 1997). Remotely sensing a surface Ɛ is very challenging because of the high heterogeneity of land surfaces and the difficulties in removing atmospheric effects (Liang, 2004; Liang, 2001; Wan and Li, 1997). Current emissivity databases consist of MODIS, ASTER and Landsat products (Mallick et al., 2012).

Researchers have worked on emissivity, for example Pu et al. (2006) used a constant value of emissivity for all materials, although the authors stated that it is not wise decision to use the same value of emissivity (Ɛ) for all types of surfaces i.e. emissivity = 1. Peng et al. (2008) and Xu et al. (2008) retrieved spectral emissivity (Ɛ) over urban areas in a pixel-by-pixel basis. Furthermore, many studies have been carried out in order to retrieve land surface emissivity, such as temperature-independent spectral indices (TISI) methods (Zhu, 2006; Becker and Li, 1995; Li and Becker, 1993). This kind of algorithm combines middle wave infrared data (MWIR: 3.4-5.2 μm) with thermal infrared data (TIR: 8-14 μm) to estimate emissivity. Gillespie et al. (1998) developed this method for ASTER data and estimated emissivity with high accuracy. But the accuracy of this algorithm depends on some assumptions and ties to the atmospheric correction. NDVI methods proposed by Caselles and Sobrino (1989) and developed by van de Griend and Owe (1993) supplied a technique to calculate emissivity, and its successful performance in natural surface. But this method assumes the land surface is mainly made up of two types i.e. vegetations and soil, which is not in agreement with land surface. Jimenez-Munoz et al. (2006) used NDVI based emissivity method to obtain surface emissivities over agricultural areas from ASTER data, and found that band 13 gave most accurate emissivity measurement. Wan and Dozier (1996) utilized a classification-based emissivity method and applied results to split window method, which performed satisfactorily and the accuracy of land surface temperature was ± 1 K. Snyder et al. (1998) also used this method to retrieve global emissivity without considering the complicated urban surface (heterogeneous).

Emissivity has strong seasonality and land use/land cover dependence (Mallick et al., 2012). Specifically, emissivity depends on surface cover type, soil moisture

content, soil organic composition, vegetation density, and structure. For example, the broadband Ɛ is usually around 0.96-0.98 for densely vegetated areas [(leaf area index) LAI > 2], but can be lower than 0.90 for bare soils (e.g., desert) (Jin and Liang, 2006).

For this research, the method used to estimate Ɛ for land cover types at the flaring sites is based on the Ɛ of four land cover types (vegetation, soil, built up areas and water) present at each site and that of gas flare. Each pixel land cover types were considered for the entire site and their emissivity values (both minimum and maximum) were taken from the literature. Mean of Ɛ for land cover types for each single pixel obtained from using their minimum and maximum values from the literature were calculated. Average of these two results of Ɛ values i.e. $Ɛ_{min}$ and $Ɛ_{max}$ were obtained for each pixel and the same procedure was repeated for all pixels in the selected 12 by 12 km area around the gas flare source. Therefore, the value of emissivity used for each 30 m^2 Landsat pixel for the atmospheric correction is a combination of the emissivity for any flare present and that of the other background features within the pixel. The author adopted an independent method of using land cover types at each site for the correction of Ɛ rather than Global Land Cover (GLC) data from USGS in order to ensure quality control primarily. Table 3.2 is the look up table (LUT) for the emissivity of gas flare and land cover types.

Table 3-2: Surface emissivity for gas flare and land cover types

Land cover type	Emissivity (minimum)	Emissivity (maximum)	Reference
Vegetated areas:			
Short grass	0.979	0.983	(Labed and Stoll, 1991)
Bushes (≈ 100 cm)		0.994	(Labed and Stoll, 1991)
Densely vegetated areas	0.960	0.980	(Jin and Liang, 2006)
Soils:			
Bare soil		0.960	(Humes et al., 1994)
Bare soil (desert)		0.900	(Jin and Liang, 2006)
Bare soil (sandy)		0.930	(Hipps, 1989)
Bare soil (loamy sand)		0.914	(van de Griend et al., 1991)
Water body:			
Water body		0.980	(Masuda et al., 1988)
Water body	0.950	0.963	(Engineering Tool Box, 2013)
Water body		0.990	(Stathopoulou and Cartalis, 2007)
Built up areas:			
Medium built		0.964	(Stathopoulou and Cartalis, 2007)
Densely urban		0.946	(Stathopoulou and Cartalis, 2007)
Flare:			
	0.13	0.40	(Shore, 1996)
	0.15	0.30	(PTT, 2008)
	0.18	0.25	(Sáez, 2010)

Variability in ε is a source of error in the brightness temperature (T) calculations. For vegetation, which is the focus of this study, the range of ε values found in the literature would result in an LST range. To quantify this error range, equations 3.5 and 3.6 are used for the computations of brightness temperature (T) and Land Surface Temperature (LST) as an example shown below.

$\varepsilon_{vegminimum} = 0.960$ (extracted from LUT, Table 3.2);

$\varepsilon_{vegmaximum} = 0.994$ (extracted from LUT, Table 3.2);

$L_6 = 100$;

$T_{minimum} = 173.464\ Wm^{-2}sr^{-1}\mu m^{-2}$;

$T_{maximum} = 164.580\ Wm^{-2}sr^{-1}\mu m^{-2}$;

$LST_{minimum} = 809.626$ K;

$LST_{maximum} = 805.124$ K.

Range of $T = T_{minimum} - T_{maximum} = 173.464 - 164.580 = 8.884\ Wm^{-2}sr^{-1}\mu m^{-2}$;

Range of $LST = LST_{minimum} - LST_{maximum} = 809.626 - 805.124 = 4.502$ K.

The results show that the amount of error introduced to Ɛ will affect T, which will also cause the final resulting LST to be in error. Therefore, a careful estimation of Ɛ for land cover types at the flaring sites was undertaken to reduce this error to the minimum.

3.5.3 Land Surface Temperature (LST)

Remote sensing of LST has become an important research area in the past decade (Qin et al., 2011). This can be attributed to the diverse applications of LST, for example, detection of gas flaring or forest fires, land use and land cover change, climatic change analysis, geothermal area detection, weather prediction and analysis of energy and matter exchanges between the atmosphere and surfaces (Qin et al., 2011; Akhoonadzadeh and Saradjian, 2008; Jimenez-Munoz et al., 2003; Valor and Caselles, 1996).

LST can be applied in estimating a critical variable in fire ignition and propagation. Additionally, it is a key component in the derivation of the surface energy balance equation with implications for the partitioning of energy into sensible and latent heat fluxes (Williams et al., 2007). Furthermore, the limitation of traditional in-situ measurements, which are carried out in a few selected weather station points, necessitates new approaches for LST measurement from satellite sensors such as Landsat 5 TM and Landsat 7 ETM+.

While advances have been made in LST estimation from satellite data, there are still some challenges that affect the accuracy of the derived LST values. For example, the satellite systems measure the upwelling thermal radiation which is used as a proxy for estimating the LST. Unfortunately, the measured radiation is affected by atmospheric constituents before reaching the sensors resulting in inaccurate LST estimates if the atmosphere is not correctly accounted for. Moreover, the thermal radiation is detected in only one direction (Otukei and Blaschke, 2012).

Furthermore, although it is possible to make atmospheric corrections for the observed radiation, an additional critical problem is the separation of coupled temperature and emissivity parameters (Inamdar et al., 2008; Sobrino et al., 2002). As a result, given a sensor of N channels, there will be only N observations but N+1 unknowns i.e. N emissivity measurements and 1 temperature measurement (Valor and Caselles, 1996). This makes it difficult to separate temperature from emissivity using passive radiometry since the system of equations has no unique solution.

Several approaches have been developed to handle the N+1 unknown parameter problem. Among these are the single or multi-channel (split window) and dual angle approaches (Jimenez-Munoz et al., 2003; Liang, 2001; Valor and Caselles, 1996). A variety of split-window methods have been developed to retrieve land surface temperature from NOAA/AVHRR data (Mao, et al., 2005). The split-window LST method utilizes the differential absorption in adjacent thermal band to correct the atmospheric effects (Qin et al., 2001; Wan and Dozier, 1996; Prata 1994). Wan and Li (1997) propose a multi-band algorithm to retrieve land surface emissivity and LST from MODIS, which is only influenced by the surface

optical properties and the ranges of atmospheric condition. The accuracy of these two algorithms is less than 1 °C (Wan et al., 2004, Wan, 2002). Gillespie et al. (1998) propose an algorithm to retrieve temperature and emissivity from ASTER. The accuracy of this algorithm output temperature and emissivity images are dependent on the empirical relationship between emissivity values and spectral contrast, compensation for reflected sky irradiance, and ASTER's precision, calibration, and atmospheric compensation. However, the accuracy of most algorithms is very high but they still need to make some assumptions regarding prior knowledge of atmosphere (especially water content). Owing to different considerations of the atmospheric effect on the radiation transfer through the air, the prior knowledge required is different (Mao, et al., 2005). Sobrino et al. (1993) and Harris et al. (1992) conclude that including column water vapour in the split-window algorithms can improve sea surface temperature (SST) accuracy.

Furthermore, Mao et al. (2005) developed a practical split-window algorithm for MODIS which requires two essential parameters (transmittance and emissivity) for LST retrieval. The method was developed to estimate transmittance from water content. They retrieve the water content from the MODIS NIR bands, and then compute the transmittance of MODIS band 31 and band 32 through building the relationship between the water content and the transmittance. LST error is only changed between 0.18 and 1.1 °C when the water content error changes between −80 % and 130 % and the relative transmittance error changes between 0.01 and 0.31. However, they get a similar conclusion through changing the water content retrieved from MODIS band 2 and band 19. They confirm the conclusion by retrieving LST from MODIS image data through changing retrieval water content error. So they concluded that

their algorithm is not sensitive to water content and get higher accuracy if they can reasonably utilize the prior knowledge of water content. On the other hand the emissivity is not sensitive to their algorithm in MODIS band 31 and band 32. Two methods have been used to validate the algorithm: standard atmospheric simulation and MODIS LST product. Validation with standard atmospheric simulation indicates that this algorithm can achieve the average accuracy of this algorithm of 0.32 °C in LST retrieval for the case without error in both transmittance and emissivity estimations. The accuracy of this algorithm is 0.37 °C and 0.49 °C, respectively, when the transmittance is computed from water by exponent fit and linear fit, respectively. Compared with the MODIS LST product, the results from the analysis indicate that the algorithm is able to provide an accurate estimation of LST from MODIS data (Mao et al., 2005).

The most robust algorithm for retrieving LST is the split window algorithm (Zhang et al., 2006; Mao et al., 2005). Unfortunately, the split-window algorithm cannot be applied for the analysis of Landsat 5 TM and Landsat 7 ETM+ data since it requires more than one thermal bands. In this regard, approaches based on single channels were adopted (Qin et al., 2011). The atmospheric correction parameters for the Landsat thermal band, namely upwelling and downwelling radiance, and transmittance were computed using the Atmospheric Correction Parameter Calculator (ATMCORR) (see section 3.6.2); the dark object method was used to correct for the atmosphere for the visible bands data (see section 3.6.2). Land cover types of each site were used to estimate the emissivity value for each site which helped to solve the N+1 problem (see section 3.5.2). The main aim of this study was to provide the LST estimates of gas flaring sites in the Niger Delta using Landsat 5 TM and Landsat

7 ETM+ satellite data. Hence, LST was employed in this study as a parameter used for detection of gas flaring in the Niger Delta.

3.5.3.1 Theoretical basis for Land Surface Temperature measurement

The theoretical basis for the LST measurement is Plank's radiation function, formulated as:

$$B(\lambda, T) = \frac{C_1\lambda^{-5}}{\Pi\,(\exp\,(C_2/\lambda\,T)-1)} \qquad (3.3)$$

Where: $B(\lambda, T)$ is the spectral radiance of a blackbody in units of $Wm^{-2}sr^{-1}\mu m^{-2}$, and in practice, it is the emitted radiance of a ground object. λ is the wavelength in metres, T is temperature in Kelvin, the first spectral constant $C_1 = 3.741775x10^{-22}\ Wm^2$, the second spectral constant $C_2 = 1.4388 \times 10^{-2}$ mK and PI (π) is the constant, and = 3.142 (Qin et al., 2011).

When the emitted radiance of ground object B (λ, T) is measured, generally by a thermal sensor, the temperature T can be computed by inverting the Planck's radiance function as follows:

$$T = \frac{C_2}{\lambda \ln[(C_1/\lambda^5 B(\lambda, T))+1]} \qquad (3.4)$$

As T in equation 3.4 is the "brightness temperature" i.e. temperature corresponding to observed top of atmosphere (TOA) radiation for a black body, measured at TOA, specific algorithms are necessary to convert the value of T to LST as well as to correct for emissivity ≠ 1.

3.5.3.2 Land Surface Temperature Calculation

The approach for the calculation of LST, by first calculating brightness temperature and substituting it into the Planck function and inverting the function to get the LST, was adopted for the study.

The formula for computing brightness temperature is:

$$B(T) = (L_s - L_u)/\varepsilon\tau) - ((1 - \varepsilon)/\varepsilon) \times L_d \quad (3.5)$$

Where,

L_s = at sensor radiance;

L_u = is the upwelling or atmospheric path radiance;

L_d = the downwelling or sky radiance;

τ = the atmospheric transmission;

ε = emissivity.

It worth noting that L_u, L_d and τ are atmospheric correction parameters for the Landsat thermal band.

LST is generated by inverting equation 3.5 above,

$$LST = \frac{K_2}{\ln((K_1/(B(T)) + 1)} \quad (3.6)$$

Where,

$K_1 = 666.09\ W\ m^{-2}\ sr^{-1}\mu m^{-1}$.

$K_2 = 1282.71\ K$,

K_1 and K_2 are thermal band calibration constants calculated for the Landsat sensor characteristics.

3.6 Method of processing satellite data with MATLAB programming tool

This section is divided into two namely: a MATLAB programming tool used to process satellite data and step by step procedures required to process satellite data in order to achieve the aim of the study.

3.6.1 MATLAB programming tool

The primary justification for using a programming tool for this study is because of the number of available useful Landsat 5 TM and Landsat 7 ETM+ scenes used; 11 scenes from Landsat 5 TM and 49 scenes from Landsat 7 ETM+ making 60 days from October 10, 1984 to March 8, 2013 (see Table A-7 in Appendix A). From the available programming languages (such as IDL, C++, OpenGL and MATLAB) MATLAB was chosen because it is similar to FORTRAN 77, with which the author is familiar. Also, its popularity in the academic sector and the availability of extensive support resources were advantageous. MATLAB is a numerical computing environment and fourth-generation programming language. It has several advantages over other languages: Its basic data element is the matrix; vectorised operations i.e. adding two arrays together, needs only one command; the graphical output is optimized for interaction i.e. plotting of data is very easy and changing of colour, sizes, scales etc. by using graphical interactive tools and implementation of algorithms, MATLAB's functionality can be greatly expanded by the addition of toolboxes. For example, the statistics toolbox allows more specialized statistical manipulation of data such as linear regression and correlation coefficient, analysis of variance (ANOVA), multivariate analysis of variance (MANOVA) and curve-fitting. Also, another MATLAB's toolbox (cluster analysis) facilitates creating grouping of data into groups according to similarities on a number of measures, which are useful for

land-cover classification. For example, the k-means approach was used for cluster analysis of land cover types (Vesanto et al., 2000). However, it uses a large amount of memory and this limits the size of images that can be analysed.

3.6.2 Steps used for the processing of Landsat 5 TM and Landsat 7 ETM+ data

The scenes were downloaded from the U.S. Geological Survey Earth Resources Observation and Science (EROS) Data Centre website (http://earthexplorer.usgs.gov/) using the Glovis/Earth Explorer interface. Figure 3.4 shows Landsat 7 ETM+ images overlapping footprints in the Niger Delta from the EarthExplorer website. The processing level for all the scenes is L1T, which means systematic radiometric and geometric correction using ground control points (GCPs), and the digital elevation model has been applied. In 2003, there is a problem of Scan Line Correction (SLC-off mode) with Landsat 7 sensor that causes loss of part of data in the scenes (Chen et al., 2012); and from 2004 onwards scenes are affected with this problem which excludes parts of the scene from this study. This problem was reduced to a minimum by setting one of the criteria for the selection of flare sites as the availability of data covering each facility throughout the study period (see section 3.3.2). The 11 sites used for this study were successfully imaged for up to 96 % of the scenes used.

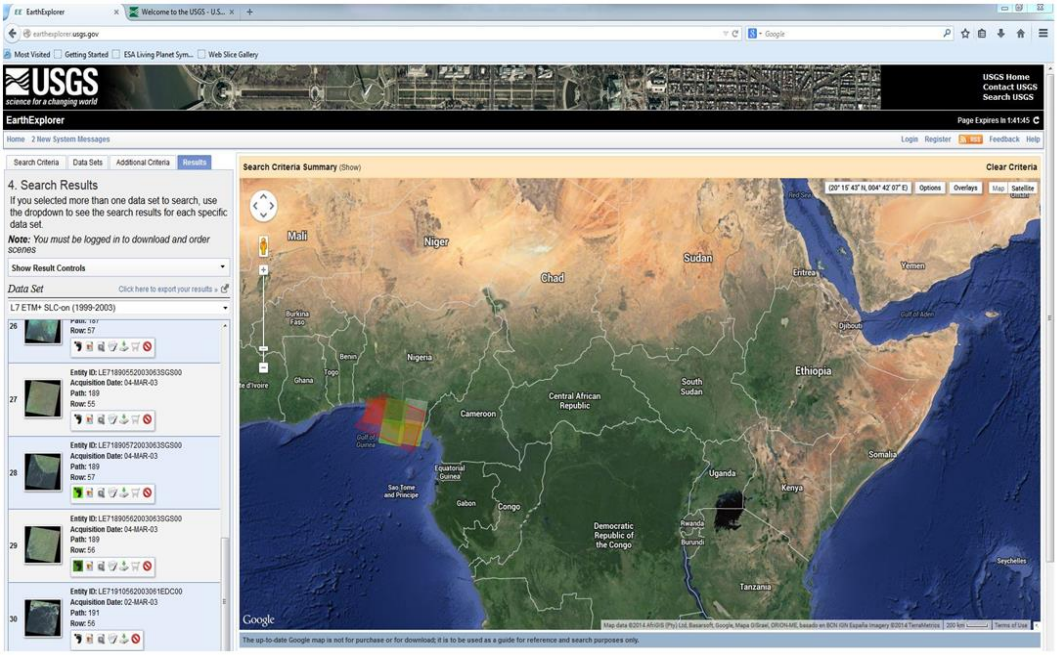

Figure 3-4: EarthExplorer showing Landsat 7 ETM+ images overlapping study sites in the Niger Delta. Sources: USGS (2011)

Step one: The first step in the processing of Landsat 5 TM and Landsat 7 ETM+ data was the verification of geo-location points. Five ground control points were selected over the Niger Delta using Google Earth. Ten images for both Landsat 5 TM and Landsat 7 ETM+ were uploaded into ArcGIS and the selected GCPs were identified. The coordinates of these controls (obtained from both Google Earth and ArcGIS) were compared and a negligible difference found (1.0×10^{-6} to 7.3×10^{-6} m) (see Table 3.3). This was taken as an acceptable error range for the geo-location of the imagery. Table 3.3 shows the coordinates of the selected GCPs from the Google Earth and ArcGIS.

Step two: The second step was the removal of zero or out of range values from the data and their replacement with not a number (nan) in order to avoid divide by zero errors in calculations. MATLAB code was used to process the data and to remove the zero and values at the upper and lower limits of the 8-bit data

range which cannot be distinguished from noise. Noise results when the sensor is not sufficiently sensitive to resolve gradients in reflected or emitted radiation.

Table 3-3: Verification of geo-location points for Landsat 5 TM and Landsat 7 ETM+ data

	Google Earth Latitude (θ) Longitude (λ)	L5 TM & L7 ETM+ Latitude (θ) Longitude (λ)	Google Earth Eastings Northings	L5 TM & L7 ETM+ Eastings Northings	Remarks
1	4.410390 7.164627	4.410391 7.164548	296335 487741	296326 487741	A sharp bend on the ground
2	4.409837 7.139953	4.409910 7.140001	293596 487687	293601 487695	A point on top of the LNG structure
3	4.428572 7.185888	4.428581 7.185897	298700 489746	298701 489747	A junction point on the ground
4	4.382893 7.172327	4.382890 7.172329	297182 484698	297183 484698	An edge of a LNG structure on the ground
5	4.426084 7.144811	4.426079 7.144809	294140 489482	294140 489482	An offshore point on a LNG terminal

Step three: Radiometric calibration of both the multispectral bands and the thermal band of the data is the third step. This was performed by converting the Digital Number (DN) values recorded by the remote sensor into top of atmosphere radiance values based on sensor calibration parameters provided within the metadata files from USGS, and this operation is carried out according to the Landsat 5 TM (Chander and Markham, 2003) and Landsat 7 ETM+ (NASA, 2002) Science Data Users Handbooks using equation 3.7.

$$L_\lambda = G_{rescale} \times QCAL + B_{rescale} \quad (3.7)$$

This is also expressed as;

$$L_\lambda = ((LMAX_\lambda - LMIN_\lambda) / (QCALMAX - QCALMIN)) \times (QCAL\text{-}QCALMIN) + LMIN_\lambda \quad (3.8)$$

Where:

L_λ = Spectral Radiance at the sensor's aperture in $Wm^{-2}sr^{-1}\mu m^{-1}$;

$G_{rescale}$ = Rescaled gain (the data product "gain" contained in the Level 1 product header or ancillary data record) in $Wm^{-2}sr^{-1}\mu m^{-1}$ / DN;

$B_{rescale}$ = Rescaled bias (the data product "offset" contained in the Level 1 product header or ancillary data record) in $Wm^{-2}sr^{-1}\mu m^{-1}$;

QCAL = the quantized calibrated pixel value in DN (Digital Number);

$LMIN_\lambda$ = the spectral radiance that is scaled to QCALMIN in $Wm^{-2}sr^{-1}\mu m^{-1}$;

$LMAX_\lambda$ = the spectral radiance that is scaled to QCALMAX in $Wm^{-2}sr^{-1}\mu m^{-1}$;

QCALMIN = the minimum quantized calibrated pixel value (corresponding to $LMIN_\lambda$) in DN = 1 for LPGS (a processing software version) products;

QCALMAX = the maximum quantized calibrated pixel value (corresponding to $LMAX_\lambda$) in DN = 255

Tables 3.4 and 3.5 give the values for the $LMIN_\lambda$ and $LMAX_\lambda$ for Landsat 5 TM and Landsat 7 ETM+.

Table 3-4: LMINλ and LMAXλ values for Landsat 5 TM

$Wm^{-2}sr^{-1}\mu m^{-1}$								
Band	From March 1, 1984 to May 4, 2003				After May 5, 2003			
	$LMIN_\lambda$	$LMAX_\lambda$	$G_{rescale}$	$B_{rescale}$	$LMIN_\lambda$	$LMAX_\lambda$	$G_{rescale}$	$B_{rescale}$
1	-1.52	152.10	0.602431	-1.52	-1.52	193.0	0.762824	-1.52
2	-2.84	296.81	1.175100	-2.84	-2.84	365.0	1.442510	-2.84
3	-1.17	204.30	0.805765	-1.17	-1.17	264.0	1.039880	-1.17
4	-1.51	206.20	0.814549	-1.51	-1.51	221.0	0.872588	-1.51
5	-0.37	27.19	0.108078	-0.37	-0.37	30.2	0.119882	-0.37
6	1.2378	15.303	0.055158	-1.2378	1.2378	15.303	0.055158	-1.2378
7	-0.15	14.38	0.056980	-0.15	-0.15	16.5	0.065294	-0.15

Source: Chander and Markham (2003)

Step four: Computation of top of atmosphere reflectance for multispectral bands 1 to 4, including the application of simple sun angle correction. See section 3.4 for the equation for the computation of reflectance for band λ.

Table 3-5: LMINλ and LMAXλ values for Landsat 7 ETM+

$Wm^{-2}sr^{-1}\mu m^{-1}$								
Band	Before July 1, 2000				After July 1, 2000			
	Low Gain		High Gain		Low Gain		High Gain	
	$LMIN_\lambda$	$LMAX_\lambda$	$LMIN_\lambda$	$LMAX_\lambda$	$LMIN_\lambda$	$LMAX_\lambda$	$LMIN_\lambda$	$LMAX_\lambda$
1	-6.20	297.50	-6.20	194.30	-6.20	293.70	-6.20	191.60
2	-6.00	303.40	-6.00	202.40	-6.40	300.90	-6.40	196.50
3	-4.50	235.50	-4.50	158.60	-5.00	234.40	-5.00	152.90
4	-4.50	235.00	-4.50	157.50	-5.10	241.10	-5.10	157.40
5	-1.00	47.70	-1.00	31.76	-1.00	47.57	-1.00	31.06
6	0.00	17.04	3.20	12.65	0.00	17.04	3.20	12.65
7	-0.35	16.60	-0.35	10.932	-0.35	16.54	-0.35	10.80
8	-5.00	244.00	-5.00	158.40	-4.70	243.10	-4.70	158.30

Source: NASA (2002)

Step five: The fifth step is the correction of the atmospheric effects for both the multispectral bands (1-4) and thermal band. An atmospheric correction is required to retrieve the real surface parameters by removing the atmospheric effects, such as (potentially) thin clouds (Inamdar et al., 2008), molecular and aerosol scattering, absorption by gases (such as water vapour, ozone, oxygen) and aerosol, and sometime also the correction for cloud shadows, upward emission of the radiation from the Earth surface (Qin et al., 2011), environmental radiance which produces the adjacency effects, variation of illumination geometry including the Sun's azimuth and zenith angles, and ground slope (Mather, 2004).

Atmospheric effects are generally less pronounced for long compared to short wavelength radiation (Otukei and Blaschke, 2012). Accordingly, the visible bands of Landsat 5 TM and Landsat 7 ETM+ are more strongly affected by varying atmospheric conditions than the infrared and mid-infrared bands. Pre-processing of the multispectral bands was therefore necessary to make corrections for the atmospheric and solar illumination effects (Otukei and Blaschke, 2012). Atmospheric correction consists of two major steps: parameter estimation and surface reflectance retrieval (Liang et al., 2001). The most

difficult component of atmospheric correction is to eliminate the effect of aerosols. The fact that most aerosols are often distributed heterogeneously makes this task more difficult (Liang et al., 2001).

There is a relatively long history of the quantitative atmospheric correction of Landsat 5 TM and Landsat 7 ETM+ imagery visible and NIR bands. The methods reported in the literature can be roughly classified into the following groups: Invariant-object, histogram matching, dark object subtraction (DOS), and contrast reduction (Liang et al., 2001). A Dark object subtraction method have a long history (Kaufman et al., 2000; Liang et al., 1997; Kaufman et al., 1997; Popp, 1995 and Teillet and Fedosejevs, 1995) and are probably the most popular atmospheric correction method (Liang et al., 2001) reported in the literature. The basic assumption is that within the image some pixels are in complete shadow and their radiances received at the satellite are due to atmospheric scaterring (path radiance). This assumption is combined with the fact that very few targets on the Earth's surface are absolute black, so an assumed 1 % minimum reflectance is better than 0 % (Chavez, 1996). Both the moderate-resolution imaging spectroradiometer (MODIS) and medium resolution imaging spectroradiometer (MERIS) atmospheric correction algorithms (Santer et al., 1999) are based on this principle. However, this method assumes that this error is the same over the whole image (Liang et al., 2001).

In this study, the dark object subtraction method was used and its principle applied to this study means that pixels corresponding to the darkest location (Atlantic Ocean) were selected for each band 1 to 4. The number of pixels obtained varies depending on the size of the darkest spot (Table 3.6). The

reflectance for these dark pixels was computed for each band and the minimum value obtained for each band was used as an estimate of the atmospheric reflectance for the respective band. These small errors were subtracted from the computed reflectance for each pixel of the whole image to reduce the atmospheric effects.

Table 3-6: Latitude and Longitude of some dark pixels over Atlantic Ocean

Image ID	Band 1 (Lat/Long.)	Band 2 (Lat/Long.)	Band 3 (Lat/Long.)	Band 4 (Lat/Long.)
LT51880571986 017AAA04	4.336699 7.250121	4.332076 7.257068	4.336710 7.254742	4.327437 7.257078
LT51880571987 004XXX04	4.169107 7.074345	3.798029 7.699768	3.792277 7.694059	3.788445 7.690256
LT51880571986 353XXX10	4.281913 7.366087	4.183774 7.659434	4.138324 7.352093	4.076853 7.143137
LE71880571999 333AGS00	3.665176 6.592174	3.665176 6.592174	3.723996 6.567263	3.664760 6.592157
LE7188057200 0352EDC00	4.281250 8.164940	4.282325 8.163866	4.281548 8.164345	4282569 8.163037
LE71880572003 008SGS00	3.591636 7.948805	3.594024 7.948802	3.598809 7.948797	3.596421 7.948800

Removing the effects of the atmosphere in the thermal region is an essential step necessary to use the thermal band imagery for absolute temperature studies. The emitted signal leaving a target on the ground can be both attenuated and enhanced by the atmosphere. Unlike multi-thermal band systems, the Landsat 5 TM and Landsat 7 ETM+ instruments, each with a single thermal band, provide no opportunity to inherently correct for atmospheric effects. Ancillary atmospheric data are required to make the correction from Top-of-Atmosphere (TOA) radiance or temperature to surface-leaving radiance or temperature (Otukei and Blaschke, 2012; Qin et al., 2011; Barsi et al., 2003). With appropriate knowledge of the atmosphere, a radiative transfer model can be used to estimate the transmission, upwelling radiance and downwelling radiance (Barsi et al., 2003; Berk et al., 1999). Once these parameters are

known, it is possible to convert the top of atmosphere radiance to a surface-leaving radiance (see equation 3.9) (Barsi et al., 2005; Barsi, et al., 2003):

$$L_{TOA} = \tau\varepsilon L_T + L_U + \tau(1-\varepsilon)L_d \qquad (3.9)$$

Where,

τ is the atmospheric transmission;

L_T is the radiance of a blackbody target of kinetic temperature T;

L_U is the upwelling or atmospheric path radiance;

L_d is the downwelling or sky radiance;

L_{TOA} is the space-reaching or TOA radiance measured by the instrument.

Radiances are in units of $Wm^{-2}sr^{-1}\mu m^{-1}$ and the transmission and emissivity are unitless.

Atmospheric correction parameter calculator (ATMCORR)

In order to obtain the atmospheric correction parameters for the thermal band imagery, the Atmospheric Correction Parameter Calculator (ATMCORR) was employed. It was developed for Landsat 5 TM and Landsat 7 ETM+ thermal band and has been available to the public at http://atmcorr.gsfc.nasa.gov since 2003 (Coll et al., 2010). Validation of ATMCORR by Barsi et al. (2005) revealed a bias of 0.5 ± 0.8 K for LSTs generated using the correction parameters. ATMCORR uses National Center for Environmental Prediction (NCEP) to provide atmospheric data for 28 altitudes; NCEP has global coverage, but at a coarse $1°$ by $1°$ grid spatial resolution and six hour interval i.e. temporal resolution. Currently, ATMCORR only provides atmospheric correction parameters for dates after 19 January 2000 as this is when that dataset begins (McCarville et al, 2011). This shows that for Landsat 5 TM and Landsat 7 ETM+ contemporary thermal atmospheric correction data are a minimum requirement.

The Calculator requires a specific date, time and location as the input. The web interface for the Calculator is shown in Figure 3.5 and the inputs required by the calculator are listed in Table 3.7. The Calculator provides two methods of resampling the grid for the specific site: “Use atmospheric profile for closest integer lat/long” (Figure 3.6) or “Use interpolated atmospheric profile for given lat/long” (Figure 3.7). The first extracts the grid corner that is closest to the input location for the two time samples bounding the time input, and interpolates between the two time samples to the given time. The second option extracts the profiles for the four grid corners surrounding the location input before and after the time input. The corner profiles are interpolated for each time, and then the resulting time profiles are interpolated resulting in a single profile (Barsi et al., 2003).

Table 3-7: Input data for the computation of Thermal Atmospheric Parameter by the Calculator

Flare station	Latitude (θ)	Longitude (λ)	Acquired date (yr m d)	Acquired time (hr m s)
Eleme Refinery I	4.728772	7.118861	2000/12/17	09:35:36.7
Eleme Refinery II	4.762175	7.111025	2003/01/08	09:33:30.69
Onne Flow station	4.712321	7.141187	2008/01/06	09:35:33.01
Bonny LNG	4.414188	7.139889	2013/01/03	09:41:21.73

The user can select how the modelled atmospheric profile is interpolated. If local surface conditions are available, then the user can enter them. Then, the local conditions will be used instead of the surface layer predicted by the model, and the lower layers of the atmosphere will be interpolated from 3 km above sea level to the surface to remove any discontinuities. Another option is the choice between a summer standard atmosphere and the winter standard atmosphere

for the upper layer (Barsi et al., 2005). The user has the option to select the TM bandpass, the ETM+ bandpass, or no spectral bandpass, in which case, only the interpolated atmospheric profiles for use in a radiative transfer model are output (Barsi et al., 2005). The resulting integrated transmission, upwelling, downwelling radiances and all the atmospheric data used to generate the results are output to the browser and emailed to the user for use in removing the effects of the atmosphere, where the emissivity is specific to each surface cover type.

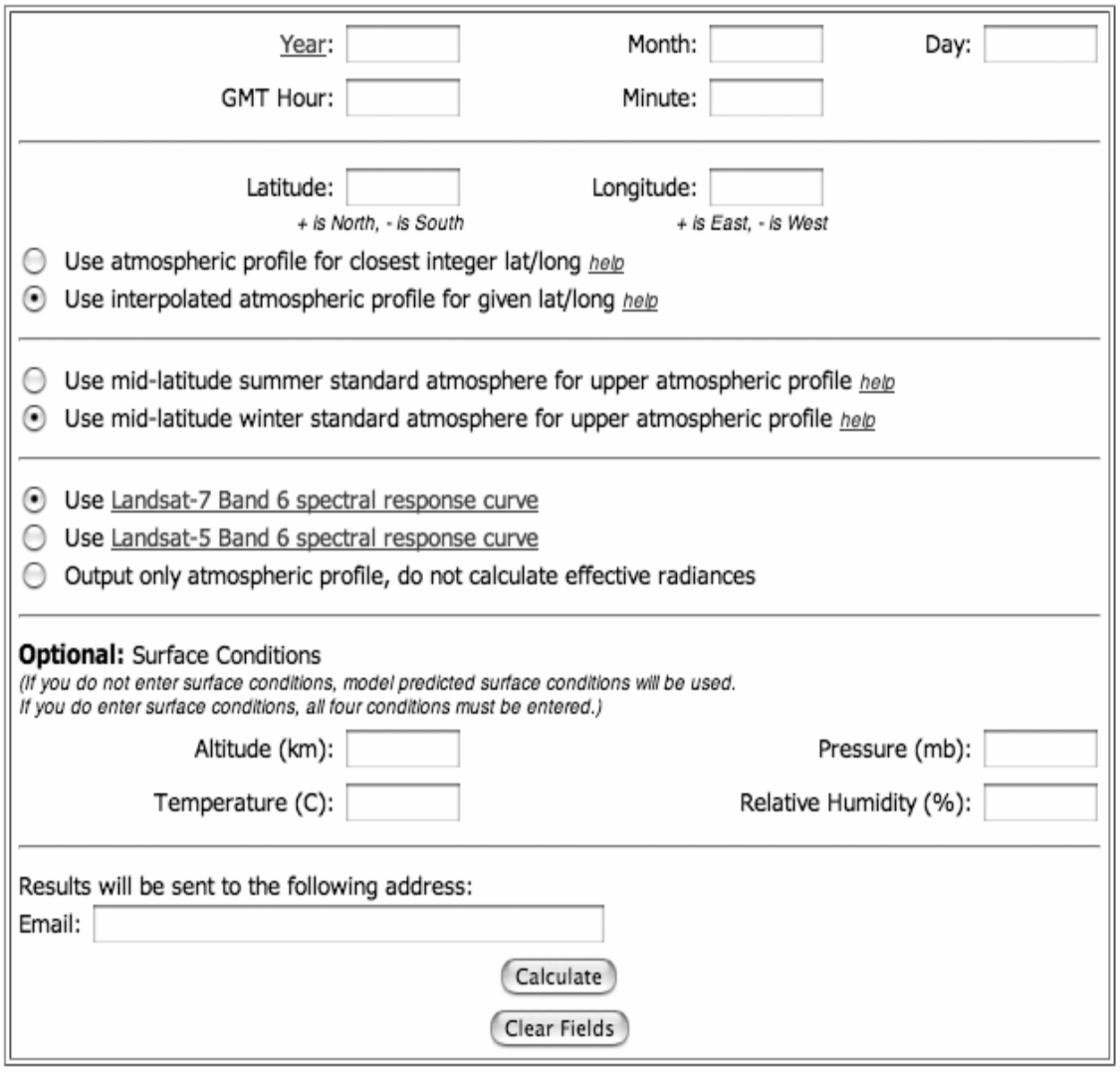

Figure 3-5: The Atmospheric Correction Parameter Calculator Web Interface Source: Barsi et al. (2003)

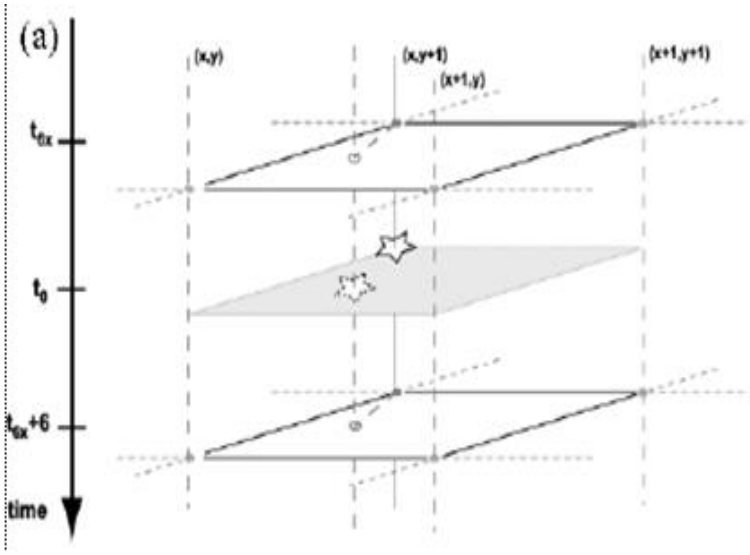

Figure 3-6: Use atmospheric profile for closest integer lat/long
Source: Barsi et al. (2003)

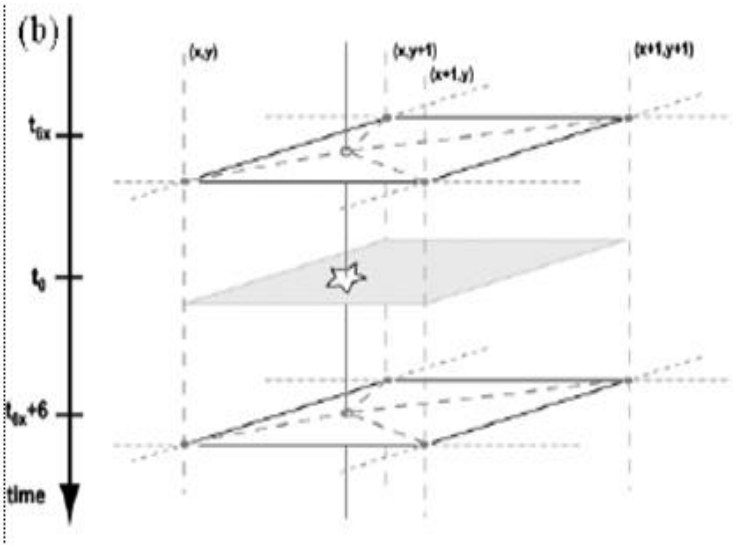

Figure 3-7: Use interpolated atmospheric profile for given lat/long
Source: Barsi et al. (2003)

In light of the above, the author inputted the coordinate of each flare station (latitude and longitude), year, month, date and time of data acquisition (hours and minutes) into the calculator. Option B, which is to use an interpolated atmospheric profile for given latitude and longitude, Landsat 5 band 6 spectral response curves for Landsat 5 TM and Landsat 7 band 6 spectral response curves for Landsat 7 ETM+ and mid-latitude summer standard atmosphere for the upper atmospheric profile were all selected. An e-mail address was provided

and finally the option 'calculate' was selected. In less than four minutes, the data supplied were processed and the result displayed on the computer screen and also to the supplied e-mail address.

For example, Figure 3.8 is an example result. Figure 3.9 is the MODTRAN grid for the flaring sites investigated in this study.

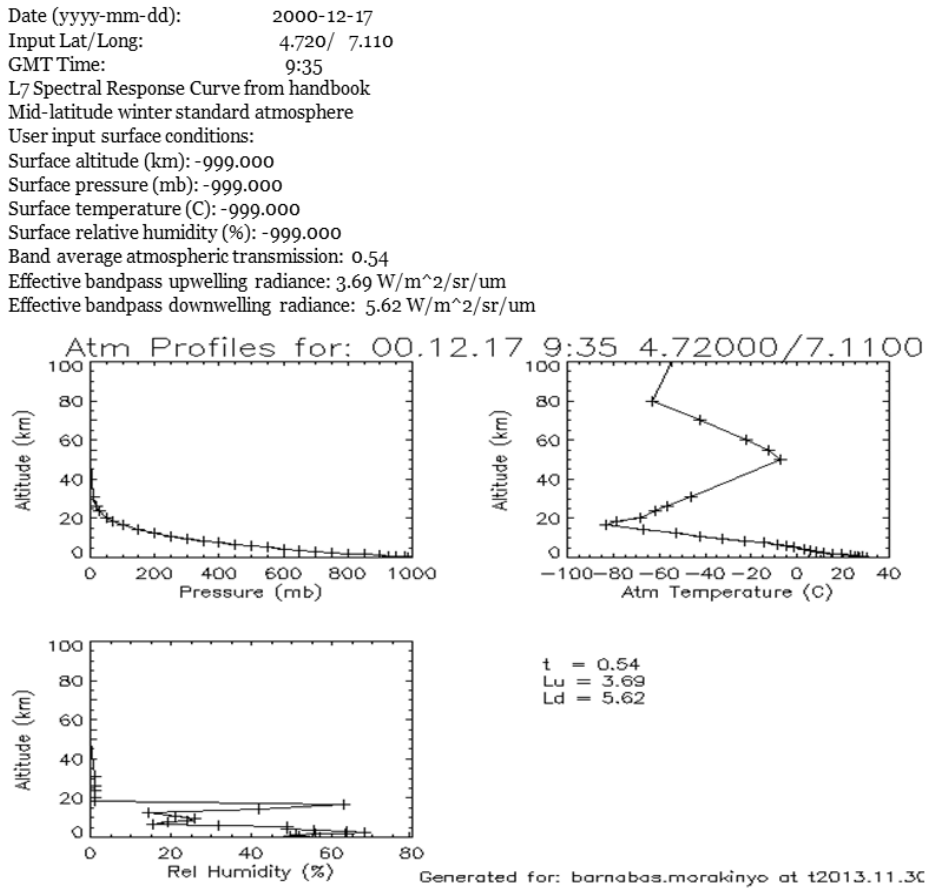

Figure 3-8: Atmospheric Correction Parameter and its Profile from the ATMCORR Calculator

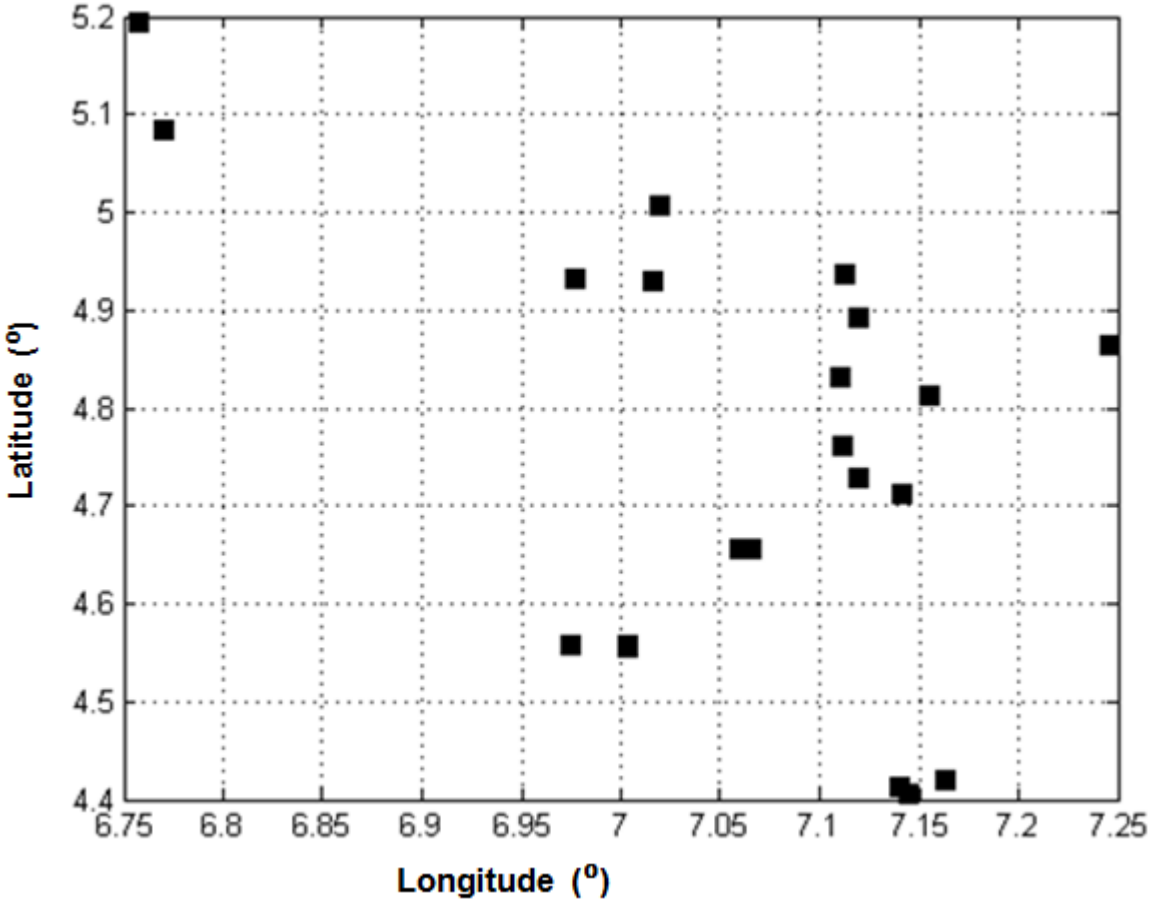

Figure 3-9: The MODTRAN grid cell for gas flare locations studied in the Niger Delta

The atmospheric correction parameters were applied to the calibrated at-sensor radiance of thermal band 6 (high gain) to compute brightness temperature of the station from equation 3.5. The emissivity of the station is estimated from land surface cover i.e. was picked from the LUT shown in Table 3.2. Then, the Planck equation was inverted using the calibration constants to derive LST. Table 3.8 gives the TM and ETM+ thermal band calibration constants.

Table 3-8: ETM+ and TM Thermal Band Calibration Constants

	Constant 1 – K_1 ($Wm^{-2}sr^{-1}\mu m^{-1}$)	Constant 2 – K_2 (Kelvin)
Landsat 7	666.09	1282.71
Landsat 5	607.76	1260.56

Source: NASA (2002)

Limitations of the Atmospheric Correction Parameter Calculator

According to Barsi et al. (2005) the limitations of the atmospheric correction parameter calculator are as follows:

1. The Calculator generates parameters for a single point. In some cases, this may be adequate to describe the atmosphere across a whole Landsat scene. In others, especially where there is considerable elevation change, more than one run of the Calculator may be necessary to characterize the atmosphere over the scene.

   For this research, this was dealt with by running the calculator over each site of interest.

2. There is no automatic check for clouds or discontinuities in the interpolated atmosphere. The user should check the profiles contained in the emailed summary file for problems. At present, however, there are no plans to add the ability to modify such a problem atmosphere.

   For this research when the problem of discontinuities in the interpolated atmosphere was encountered, the profile contained in the emailed summary file was checked to identify the problems. Julia Barsi (Web Curator) from Landsat Project Science Office, Science Systems and Applications, Inc. Greenbelt, United States of America was contacted and she provided a solution that latitude and longitude with more than one decimal place should not be inputted into the Calculator (Barsi, 2014).

3. The user must know the emissivity of the target in order to calculate LST.

   For this research, this was supplied via Table 3.2.

4. NCEP data, in the format currently used, are not available for the entire lifetime of Landsat 7 or Landsat 5. The NCEP holdings include all dates since March 1, 2000.

5. The interpolation in time and space is linear. This may not be the most appropriate method for sampling weather fronts or the diurnal heating cycle

Error analysis for the ATMCORR Calculator

In order to know the amount of error introduced by the atmospheric correction parameters (upwelling and downwelling radiances, and transmittance) into the LST when they are applied, an error analysis was carried out. Fourteen Landsat 7 ETM+ scenes from 4th March 2000 to 8th August 2012 (Table 3.9) were used over the test sites (Bonny Liquefied Natural Gas plant, Eleme Refineries I and II Petroleum Company, and Onne Flow Station).

The atmospheric correction parameters were obtained from the ATMCORR Calculator (previously discussed above) for the four flaring sites and for all fourteen scenes. Table A-8 in Appendix A lists the coordinates for each flare stack at the flaring sites and the upwelling and downwelling radiances, and transmittance obtained.

Table 3-9: Date and time of the Landsat 7 ETM+ scenes used for ATMCORR Calculator error analysis

Scene Identity No.	Date	UTC Time (h:m)	Path /row	Processing Level
LE71880572000064SGS00	March 4, 2000	09:37	188/057	L1T
LE71880572000336AGS00	December 1, 2000	09:35	188/057	L1T
LE71880572002037SGS00	February 6, 2002	09:34	188/057	L1T
LE71880572002325SGS00	November 21, 2002	09:33	188/057	L1T
LE71880572004043ASN01	February 12, 2004	09:34	188/057	L1T
LE71880572004331ASN00	November 26, 2004	09:34	188/057	L1T
LE71880572006016ASN00	January 16, 2006	09:35	188/057	L1T
LE71880572006352ASN00	December 18, 2006	09:35	188/057	L1T
LE71880572008006ASN00	January 6, 2008	09:35	188/057	L1T
LE71880572008326ASN00	November 21, 2008	09:34	188/057	L1T
LE71880572010043ASN00	February 12, 2010	09:37	188/057	L1T
LE71880572010347ASN00	December 13, 2010	09:38	188/057	L1T
LE71880572012017ASN01	January 17, 2012	09:39	188/057	L1T
LE71880572012225ASN00	August 12, 2012	09:40	188/057	L1T

The acquired upwelling and downwelling radiances and transmittance were applied to equation 3.5 (see section 3.5.3.2) for the computation of brightness temperature with the emissivity values estimated from the LUT (Table 3.2) based on land cover type at each site. The difference between the ATMCORR parameters interpolated for each study site and those of the central station of MODTRAN grid cell (Figure 3.9) were calculated and used for this analysis. Four different brightness temperature scenarios were examined with equation 3.6, and they are represented with equations 3.10-3.13.

$$BT_1 = (L_s - (L_{uc} + \Delta L_u)) / (\varepsilon \times \tau_c) - (1 - \varepsilon) / (\varepsilon) \times L_{dc} \quad (3.10)$$

$$BT_2 = (L_s - L_{uc}) / (\varepsilon \times \tau_c) - (1 - \varepsilon) / (\varepsilon) \times (L_{dc} + \Delta L_d) \quad (3.11)$$

$$BT_3 = (L_s - L_{uc}) / (\varepsilon \times (\tau_c + \Delta\tau)) - (1 - \varepsilon) / (\varepsilon) \times L_{dc} \quad (3.12)$$

$$BT_4 = (L_s - L_{uc}) / (\varepsilon + \Delta\varepsilon) \times (\tau_c) - (1 - \varepsilon) / (\varepsilon) \times L_{dc} \quad (3.13)$$

Where,

L_s = Radiometrically corrected Landsat thermal band 6 radiance (high gain);

L_{uc} = Upwelling radiance for the central station of MODTRAN grid;

L_{dc} = Downwelling radiance for the central station of the MODTRAN grid;

τ_c = Transmittance for the central station of the MODTRAN grid;

ΔL_u = Difference between the upwelling radiances for the central station of MODTRAN grid and each study site;

ΔL_d = Difference between the downwelling radiances for the central station of MODTRAN grid and each study site;

$\Delta\tau$ = Difference between the transmittance for the central station of MODTRAN grid and each study site;

ε = Emissivity;

$\Delta\varepsilon$ = Difference between the emissivity for the central station of MODTRAN grid and each study site.

The computed brightness temperature obtained from equations 3.10 to 3.13 for each site were used to compute LST for each site based on equation 3.6. The summary of a range of percentage error introduced to brightness temperature and LST for each study site is presented in Table 3.10.

Table 3-10: Minimum and maximum error introduced to brightness temperature and LST from thermal atmospheric correction parameters obtained from the ATMCORR Calculator

Flaring site	BT (%) Min. error	BT (%) Max. error	LST (%) Min. error	LST (K) Min. error	LST (%) Max. error	LST (K) Max. error
Bonny LNG	0.005	0.191	0.093	9.3×10^{-4}	1.118	0.0112
Eleme Refinery I	0.031	0.169	0.119	1.19×10^{-3}	0.785	7.85×10^{-3}
Eleme Refinery II	0.007	0.128	0.242	2.4×10^{-3}	0.675	6.75×10^{-3}
Onne Flow Station	0.003	0.133	0.062	6.2×10^{-4}	0.769	7.69×10^{-3}

Results from Table 3.10 show that a range of error 9.3×10^{-4}-0.0112, 1.19×10^{-3}-7.85×10^{-3}, 2.4×10^{-3}-6.75×10^{-3} and 6.2×10^{-4}-2-7.69×10^{-3} is introduced to LST retrieved at Bonny LNG, Eleme Refineries I and II, and Onne Flow Station respectively. Bonny LNG is with the highest value of error (0.01025 K) and this can be attributed to its location at the bank of Atlantic Ocean. Onne Flow Station is the next to Bonny LNG with 0.00707 K errors which may result from its location being surrounded by the creek. Eleme Refineries I and II give 0.00660 K and 0.00433 K errors respectively; though to the West Eleme Refinery I shared a boundary with a creek, it is not surrounded by water. Eleme Refinery II is not surrounded by water. The results show that the larger the amount of water body at the site, the higher the error introduced into LST retrieved from Landsat scene and vice versa. In conclusion, the results shows that the amount of water body at each site has a great influence on Landsat thermal atmospheric correction parameters obtained from the ATMCORR Calculator.

Step six: This involves land surface cover classification and computation of NDVI.

Land surface cover classification

Remote sensing of land cover classification is an important research subject globally. Land surface characteristics are primarily represented by land use/cover (Boori et al., 2015; Antonarakis et al., 2008). The accuracy of land cover classification determines the value of the map obtained. However, the assessment of classification accuracy is not a simple task (Foody, 2002). Through visit to the Niger Delta during fieldwork activities for ground validation of Landsat 5 TM and Landsat 7 ETM+, it was confirmed that land cover types at Eleme Refinery II Petroleum Company and Onne Flow Station flaring sites are vegetation, some buildings, open land i.e. bare soil and water bodies. Also, land cover types for other 9 flaring sites are similar to that of Eleme Refinery II Petroleum Company and Onne Flow Station because the topography of the Niger Delta is the same. In addition, qualitative analysis of all the 11 sites was carried out using true colour images from Google Earth, Digital Globe and the plotted Landsat derived parameters (bands 1-4) for the confirmation (see sections 3.6.3 and 4.1). The k-means function (Şatır and Berberoğlu, 2012; Hestir et al., 2008) adopted for the classification of these 4 land cover types is a tool in MATLAB.

The first unsupervised cluster analysis (Alvarez, 2009; Hestir et al., 2008) of the atmospherically corrected reflectance (bands 1-4) using the k-means function was carried out for each. The results obtained give three classes of land cover type with cloud classified as the fourth class. The four classes identified are any of these three: vegetation, water, soil and built up area, and cloud as the fourth class. The next stage was the elimination of the class for the cloud by masking using MATLAB code. The second cluster analysis was performed with the cloud-masked reflectance (bands 1-4) to give 4 (Boori et al., 2015) (vegetation, soil,

built up area and water) land cover types for all flaring sites (see Figure 3.10). Landsat SWIR bands 5 and 7 were also employed for the classification of land cover types but they could not give useful information as bands 1-4 hence, they were dropped for further analysis. The land cover types at these flaring sites change from scene to scene and from site to site (see section 4.1).

Researches on mapping of vegetation and identification of its species using remote sensing requires high spatial resolution imagery and has been carried out by some researchers, for example Underwood et al. (2003) used high spatial resolution hyperspectral data for mapping of iceplant (Carpobrotus edulis) and jubata grass (Cortaderia jubata) in California's coastal habitat. Andrew and Ustin (2008) mapped Lepidium latifolium (perennial pepperweed) with 3 m spatial resolution, 128-band HyMap image data in 3 sites of California's San Francisco Bay/Sacramento-San Joaquin Delta Estuary. Antonarakis et al. (2008) used two methods namely bimodal distribution skewness and kurtosis models, and classification logic excluding the influence of the ground to classify five types of riparian forest using LIDAR and SPOT data. These forest types included planted and natural forest stands of different ages. Accuracies between 66 and 98 % were achieved. However, they stated issues affecting their methods as high elevation for the river surface and different species of woody vegetation were not identified in these methods. Carleer and Wolff (2006) combined spectral information from IKONOS, QuickBird, and OrbView-3 with visual interpretation to study land cover classification. They stated that visual impression is a good means to guide the feature choice for land cover classification, although it does not allow one to choose a specific feature in the main feature types that can contain numerous features. They concluded that contrast between the vegetation and the non-vegetation is lower.

Computation of NDVI

The cloud-masked reflectance (bands 3 and 4) were used to compute NDVI with equation 3.2, as discussed in section 3.5.1.1 (see Figure 3.10).

A summary of stages in the satellite data processing is shown in the schematic diagram (Figure 3.10).

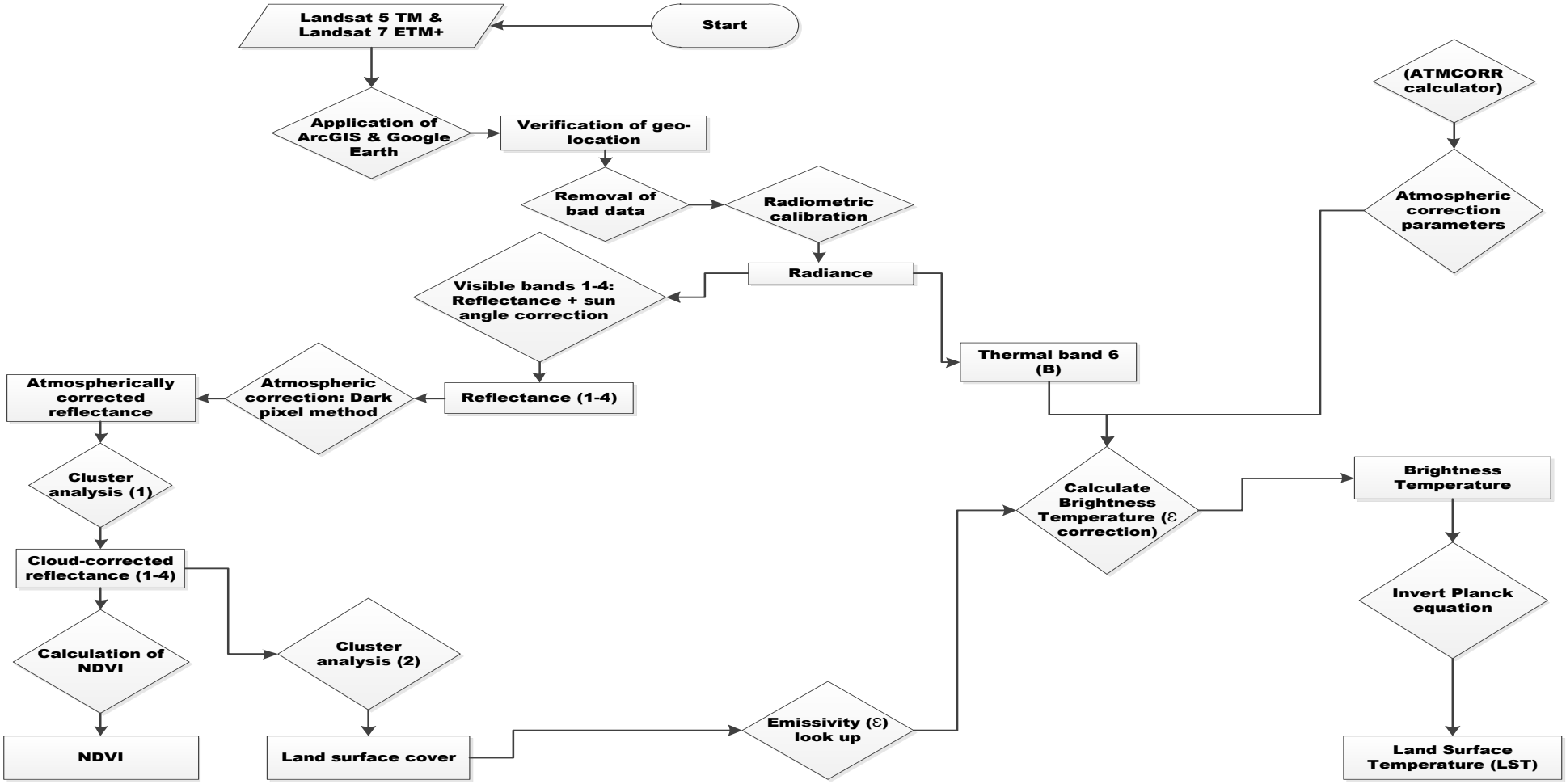

Figure 3-10: Schematic diagram of methods of processing satellite image

3.6.3 Methodology for data analysis

Methods adopted for the analysis of results for this study are the following:

- **Visual overview of the site and derived parameters**: In order to provide a visual overview of the selected flaring sites, true colour images acquired from Google Earth and the plotted Landsat derived parameters (bands 1-4) were used for comparison (see section 4.1).
- **Site characteristics:** Flaring sites used for this study are acquired through Google Earth. An area of 12 km by 12 km was marked out using geographical coordinates of ground features and ruler from the Google Earth for distance measurement with the oil facility at the centre. Also, the size of the oil facility and height of the flare stack were measured using the ruler function in Google Earth. The height (i.e the beginning and the top) of the flare stack were clearly seen in the Google Earth true colour images and they were measured from the beginning to the top in the same way the size of the facility were measured with the ruler function (Edward et al., 2013; Taylor et al., 2011). Also, true colour images such as Quikbird, WorldView-1 and WorldView-2 obtained from Digital Globe were used to check the results obtained from Google Earth. In addition, land cover types for each site were estimated using colour images from Google Earth and the land cover results from classification (see section 4.1). Human habitations within the site were deduced with the help of true colour images from Google Earth. However, high spectral and spatial resolution images are required to differentiate vegetation types (Alvarez, 2009; Carleer and Wolff, 2008).
- **Qualitative analysis of the detection of flare signature:** Spatial analysis of LST through ArcGIS (section 4.4.1.1) and transects of LST in the prevailing wind direction (South-North) (see section 4.2) were used to

distinguish the flare stack position from other parts of the oil and gas facilities at the flaring sites.

- **Landsat reflective bands signature:** Transects of reflectance (bands 1-4) in the prevailing wind direction (South-North) were used to inform the interpretation of NDVI (see section 4.3).
- **Quantitative analysis of the detection of flare signature:** This was achieved using the following: (1) variability in LST with distance (450 m) from the flare as shown in the Type A curve shown in Figures 4.61 and 4.62;
  (2) Four cardinal directional analysis which present the results (LST and NDVI) in the North, East, South and West directions in order to address the possible influence of wind direction on LST; (3) Analysis of variance to test whether LST and NDVI gradients around the flare were statistically significant. Linear regression was used to test relationships between LST gradients and NDVI gradients (see sections 4.4.3, 5.2.2 and 5.3.1).
- **Investigation of potential prevailing wind impact:** This was achieved using spatial analysis of LST through ArcGIS (section 4.4.1.1), linear regression analysis, and by applying geographical symmetry of LST in relation to the flare (see section 4.5).
- **Evaluation of factors influencing δLST:** Factors that can impact δLST at gas flaring sites as follows: rate of burning gas, size of the facility, height of flare stack, vegetation type, vegetation density, and time (month, Julian Day and year) but those that can be derived from satellite data and are therefore available for this study are size of facility, height of flare stack and time. Pairwise linear regression and multiple regression based on the results from the available information were employed for this analysis (see section 4.6).

Similarly, the influences of environmental factors on vegetation health are discussed in section 5.4.

3.7 Fieldwork

This section addresses objective three, which is the comparison of spatial variability in ground air temperature and satellite derived LST using the air temperature measured at two flaring sites and LST obtained in Chapter 4. The fieldwork activities carried out at the Eleme Refinery II Petroleum Company (hereafter called Eleme Refinery II) and Onne Flow Station will be explained in detail so that the results obtained can be compared to the satellite data. Section 3.7.1 describes the location of the field sites, and then an explanation of the reconnaissance surveys is presented in section 3.7.2 with the instruments used for the fieldwork observations and measurements described in section 3.7.3. In section 3.7.4 the actual fieldwork activities are explained while section 3.7.5 explains the problems encountered before and during the fieldwork activities. Section 3.7.6 describes the available meteorological data acquired; the results of the fieldwork are presented in Chapter 4.

3.7.1 Field site descriptions

Eleme Refinery II and Onne Flow Station are located in the Eleme Local Government Area of Rivers State in the Niger Delta (Figure 3.11). Eleme Refinery II complex is situated at about 70 km from the Eastern part of Port Harcourt, Rivers State capital. In the North, Eleme Refinery II is about 2 km from the Bori/Onne road and surrounded by vegetation with a few built up areas; in the East, it is bounded by vegetation/built up areas; in the South it is bounded by built up areas and in the West, it has a boundary with Port Harcourt

Refinery road. The dimensions are 2.25 by 1.40 km. Onne Flow Station is about 20 km away to the South-East.

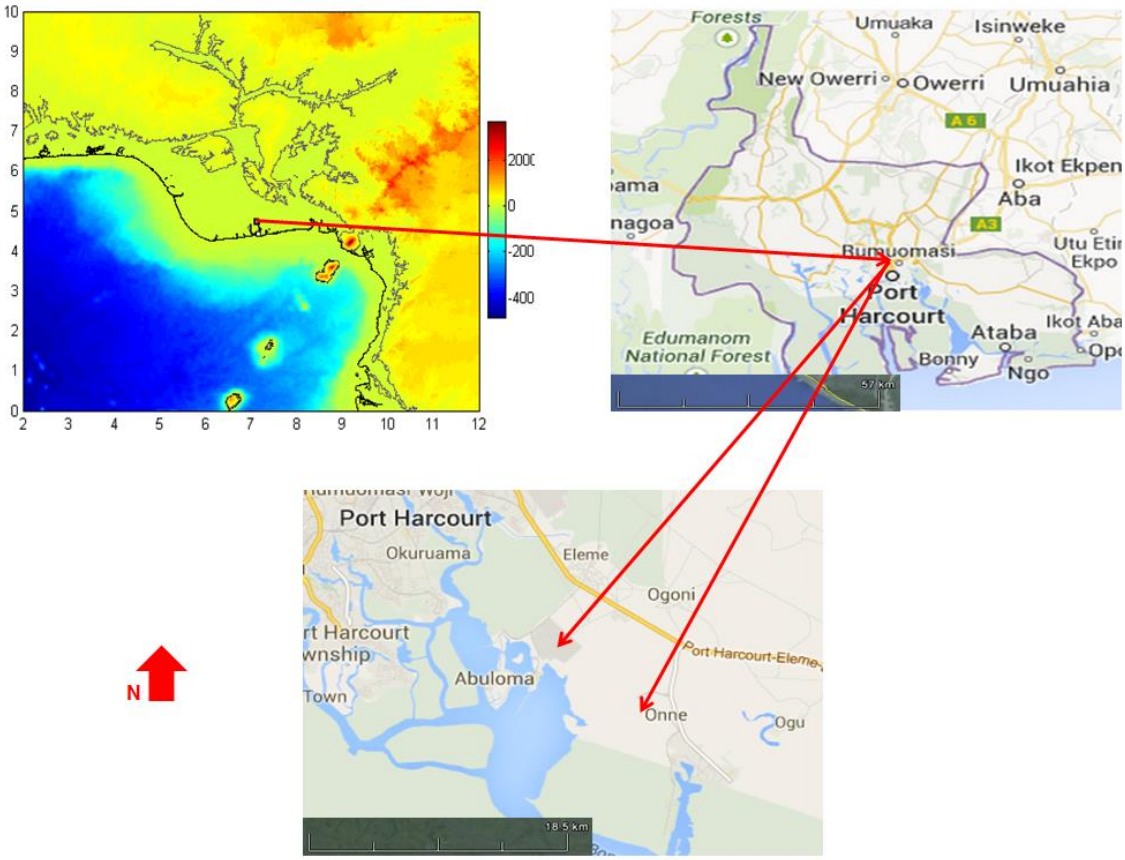

Figure 3-11: Map of the Niger Delta showing Eleme Refinery II Petroleum Company and Onne Flow Station flaring sites in Rivers State Sources: (Upper left: NOAA, 2015; Upper right: Google Earth, 2015; Lower: Google Earth, 2015)

3.7.2 Reconnaissance Survey

Allan (1997) affirmed that reconnaissance is the first and most important stage of survey and that the experience of the full technical and administrative factors of surveying is required to carry out an effective reconnaissance. He stated that this experience includes the whole production chain subsequent to fieldwork so that potential problems and difficulties can be avoided. Reconnaissance involves visiting sites and their physical inspection to decide how to carry out the surveys. The importance of reconnaissance survey to this fieldwork activity cannot be over emphasised. It helps to know the topography of the sites; helps

in the preparation and planning for the real survey such as to know the methods to be adopted for the field observations; the action and reaction of the host communities; the number of personnel required; the choice of the appropriate instruments; to be informed of the expected challenges to be encountered and to know the appropriate time suitable for the commencement of the fieldwork.

On 27 July 2012, both sites were visited for the purposes of a reconnaissance survey and it was discovered that direct or open access would not be allowed into the two flaring sites. Also, the use of surveying instruments openly at both sites would be difficult. Furthermore, the hazards discovered are: Firstly, the local communities could become hostile which can lead to loss of life and of surveying instruments. For example, the court case between Ogoniland (where these sites are located) and Shell Petroleum Development Company was in the court at the time of this reconnaissance and fieldwork. Secondly, some areas within each site are swampy which made them difficult to walk upon.

Eleme Refinery II gas flaring stack is at the extreme North East end of the complex, away from the main gate. It is connected to pipes linked to the crude oil refining facilities located within the complex, and the gas flaring stack is open to the air and about 65 m in height. The surroundings consist of a mixture of oil, water and open ground without grass; especially close to the gas flaring stack. Also, far away from the stack, changes in land cover were noticed. The ground was covered with grass and other vegetation (trees) outside the complex at about 180 m away from the flaring stack.

Onne Flow Station is also located in an enclosed compound. The gas flaring pipe contains three outlet sources connected to a single pipe. The surrounding is not built up but opens with a mixture of soil and water on the ground. The station is about 3 km east of the West Africa Container Terminal complex at Onne Oil and Gas Free Zone. It is bounded in the South and South-East by a creek which causes the ground to the South-East of the station to be swampy and dangerous to walk on. The fence is bounded by swampy vegetation in the South and Western directions. The reconnaissance survey helped to choose Saturday 4 August 2012 as the starting date for the actual fieldwork because it is the date given by the security guards after they had helped concluding the discussion with the host communities. Figures 3.12 and 3.13 are the reconnaissance diagrams for Eleme Refinery II and Onne Flow Station.

3.7.3 Instruments used

The following instruments were employed for measurement during the fieldwork; supported by one Survey assistant (David Peter).

- 1 Handheld GPS, Model Garmin Oregon 600, single frequency, 12 channels (Accuracy: 10-15 m).
- 1 Anemometer, Model AM-4237SD with the following accuracy: Temperature = ± 1.2 °C (± 2.5 °F); humidity: < 70 % RH: ± 4 % of reading, ≥ 70 % RH: ± (4 % reading + 1.2 % RH) and air velocity: ≤ 20 m/s: 3 % FS, > 20 m/s: 4 % FS.
- 150 m Linen measuring tape
- 1 Samsung Digital Camera
- Machetes

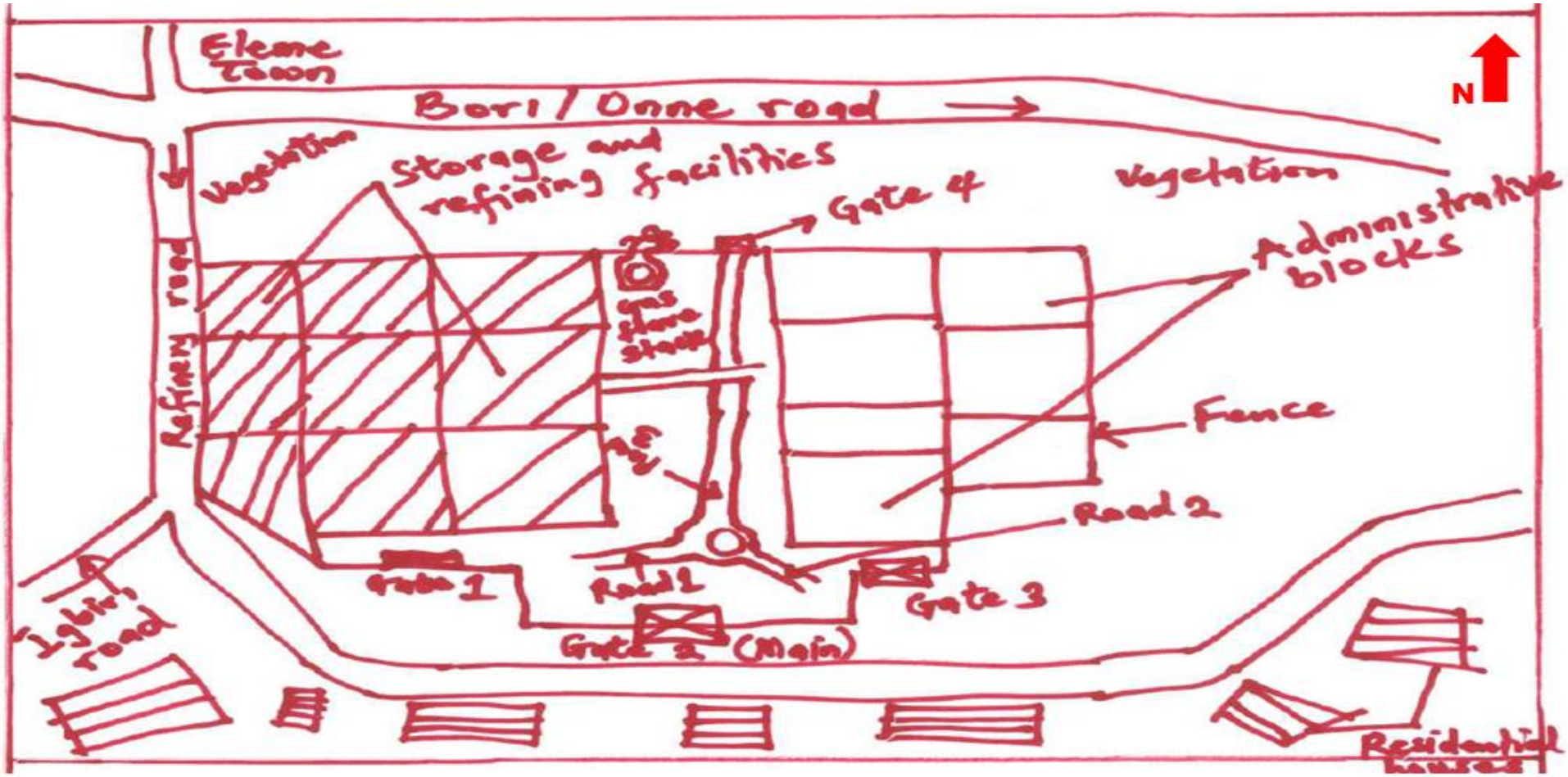

Figure 3-12: Reconnaissance diagram for Eleme Refinery II Petroleum Company's complex (Author original made in the field, 27/7/2012) (Re-drawn from field sketch and not to scale)

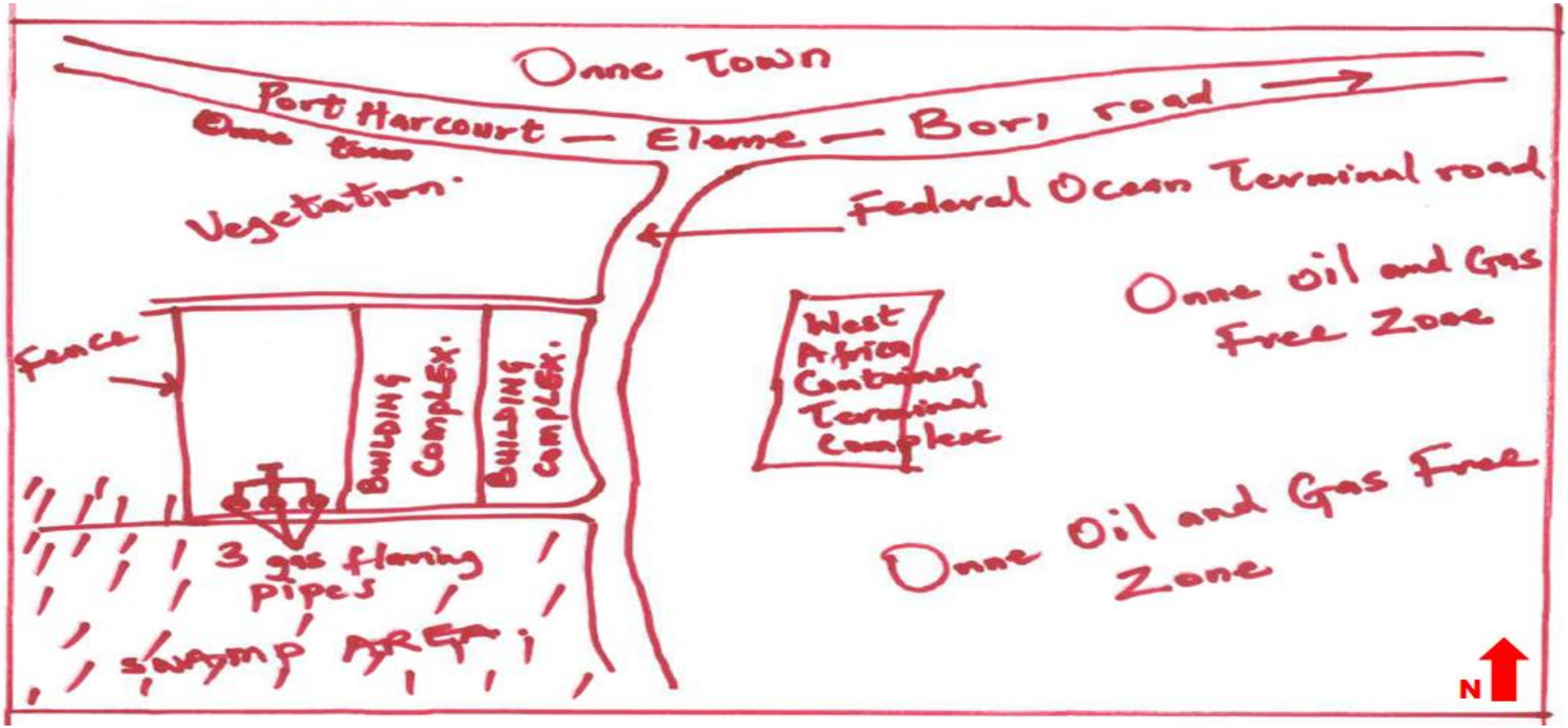

Figure 3-13: Reconnaissance diagram for Onne Flow Station (Author original made in the field, 27/7/2012) (Re-drawn from field sketch and not to scale)

3.7.4 Fieldwork processes

At both sites direct access to the flare sources was not possible for the fieldwork activities despite letters of identification collected from the Federal Ministry of Petroleum Resources Lagos, Nigeria (see Appendix D); due to lack of openness to research data and information, lack of security and political problems in the country. See section 3.7.5 for details on problems encountered and their solutions.

Fieldwork observation and measurements took place at both sites in August and September, 2012, during a period of six weeks. The weather conditions were similar throughout this period being clear sky, dry and air temperatures of around 20 °C. Distance measurement started at 30 m away from the gas flaring source at both sites. Eight lines were projected from both gas flaring sources to enable the author to obtain the detailed features surrounding the flaring sources (see Figures 3.14 and 3.15). The author paced all distances measured because the open use of surveying instruments would have made the fieldwork activities more obvious to the people around; a distance of 30 m was measured with a tape and the author paced it to know the exact number of steps that are equivalent to the 30 m distance measured with the linen tape. The uncertainty in the initial taped 30 m measured is $\pm$ 0.05 m. Each point, measured at every 30 m interval, was marked with a permanent object to enable proper identification during the second visit, and for future reference; each line was made up of eight points with a total distance of 240 m.

The first set of field measurements at Eleme Refinery II commenced on 4 August 2012 and completed on 6 August 2012, while that of Onne Flow Station

started on 7 August 2012, and ended on 9 August 2012. The second set of field measurements took place a month later. Measurement took place at Eleme Refinery II between 8 September 2012 and 10 September 2012 while that of Onne Flow Station was from 11 September 2012 to 13 September 2012. The parameters measured by anemometer were air temperature and relative humidity; a handheld GPS measured coordinates of points, and photographs of features were taken to show the impact of gas flaring on the land and vegetation with a Samsung Digital Camera. The survey assistant helped in giving the direction of lines, marking of points and taking photographs of the selected features. Data collected for each line was obtained in one go, i.e. no measurement for each line was stopped on one day and the rest continue on a different day. The measurements were taken from 09:00 to 15:00 everyday.

In addition, at each point, three sets of temperature and relative humidity readings were recorded at three different heights above the ground in the form of lower (1 m), middle (1.5 m) and upper (2 m) at a minute interval (see Table A-9 in Appendix A for a line readings). The time interval between two sets of observations was five minutes. The whole processes were repeated during the second visit at both sites, and the locations of ground points already used for the first set measurements were maintained.

Furthermore, it was observed during the field observations at both flaring sites that the plume from the flare stacks moves outwardly (Figure 3.16).

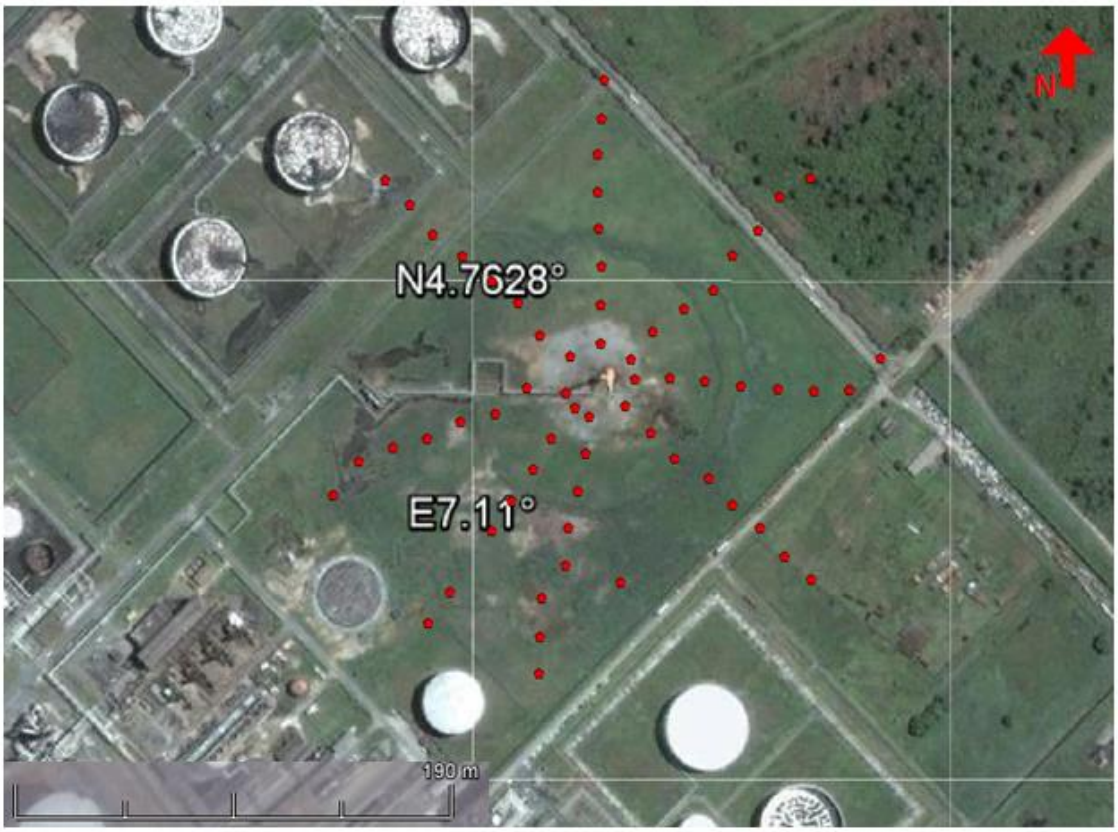

Figure 3-14: Image showing the location of gas flaring stack and field measurements (in red) at Eleme Refinery II Petroleum Company (Google Earth image overlaid with GPS derived points)

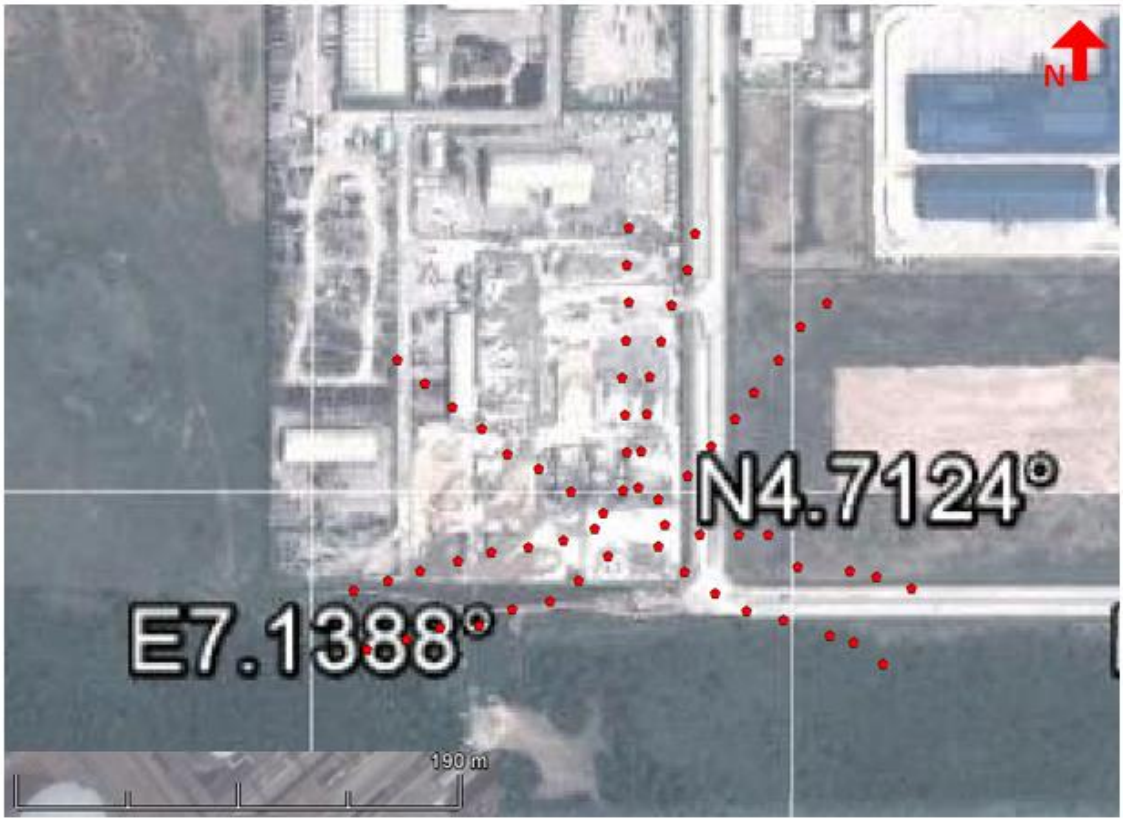

Figure 3-15: Image showing the location of gas flaring pipes and field measurements (in red) at Onne Flow Station (Google Earth image overlaid with GPS derived points)

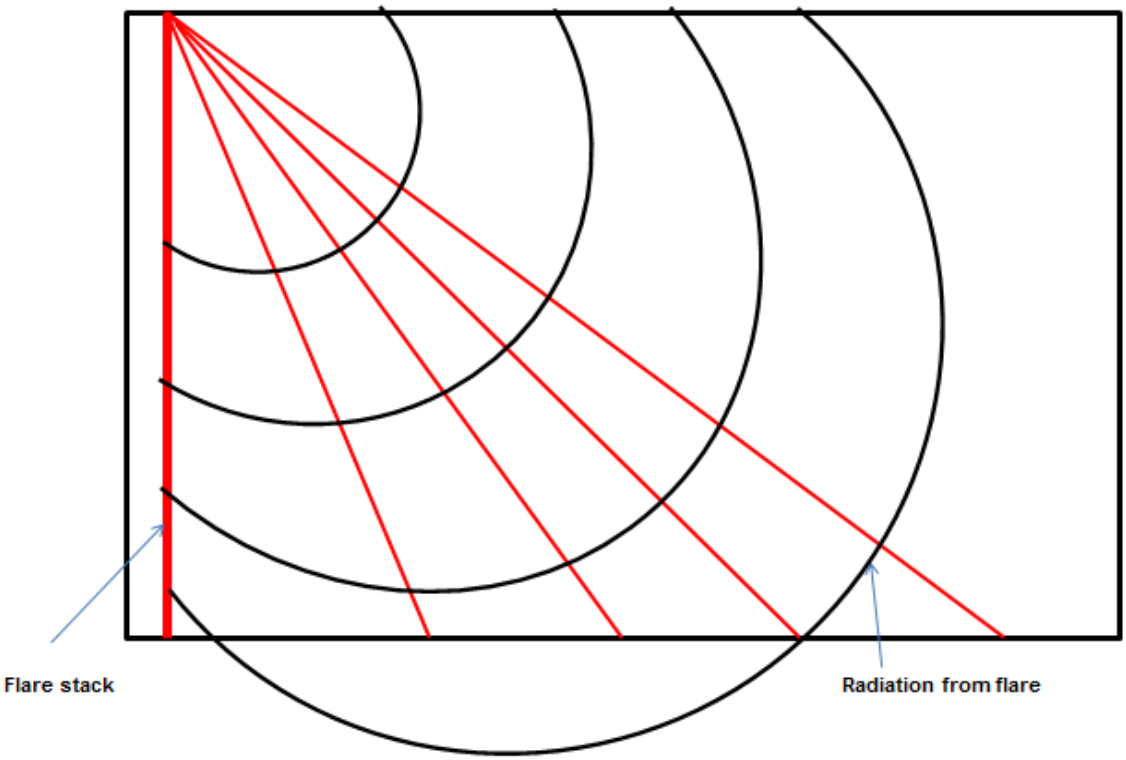

Figure 3-16: Pattern of the plumes at Eleme Refinery II Petroleum Company and Onne Flow Station

3.7.5 Problems encountered

A number of difficulties and challenges were encountered during the fieldwork. First, the letter of notification and permission to carry out the fieldwork at the gas flaring sites in Nigeria written by Plymouth University through my Director of Studies (see Appendix D) posted to the Federal Ministry of Petroleum Resources (Department of Petroleum Resources), Lagos, Nigeria could not be found at the Ministry. Therefore, it was applied for again and the approval was given. Also, the letter of Authorization to study gas flaring sites in the Niger Delta taken from the Federal Ministry of Petroleum Resources, Lagos, Nigeria to Eleme Refinery II and Shell Petroleum Development Company, Headquarters, Lagos, Nigeria did not result in direct access to the gas flaring sites being granted.

Furthermore, due to the political situation in Nigeria, it is very difficult to carry out any surveying fieldwork related to oil and gas production in the Niger Delta region because the local communities could become hostile; several land surveyors have been kidnapped and killed as a result of this. However, access was gained into the two flaring sites on compassionate grounds with help from the security guards and this has allowed limited data collection.

3.7.6 Meteorological data for the site

The nearest meteorological station to the two flaring sites which is about 50 km away and located at Port Harcourt International Airport, Rivers State. The available meteorological data obtained for the two sites were air temperature, relative humidity, wind direction, wind speed, solar radiation, rainfall, and sunshine; covering a period of fourteen years from 2000 to 2013. Figures 3.17 and 3.18 show the pattern of air temperature and relative humidity. The results show that air temperature was at a maximum value in February, which is the month for the peak of the dry season in Nigeria, and then values drop in March because of the rainy season. The rainy season commences in April, and in the month of August the maximum rainfall is recorded resulting in the lowest air temperature values. In the case of the relative humidity, the month of February has the lowest value because the air temperature was the highest implying the lower the relative humidity; the higher the air temperature and the highest values were recorded in the months of July and August.

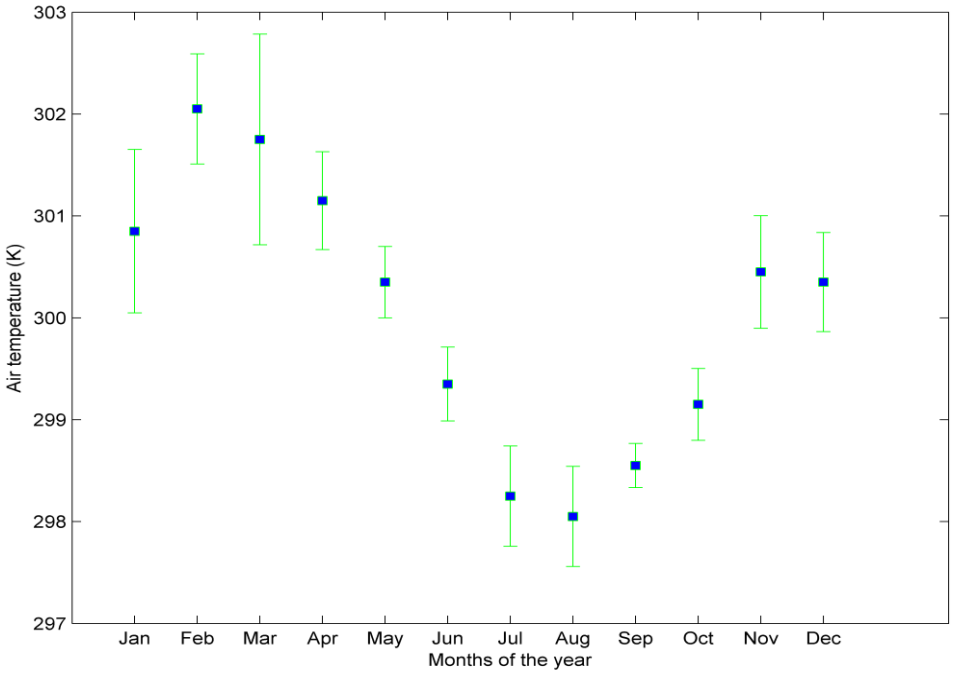

Figure 3-17: Air temperature (2000–2013) at Port Harcourt Airport Meteorological Station

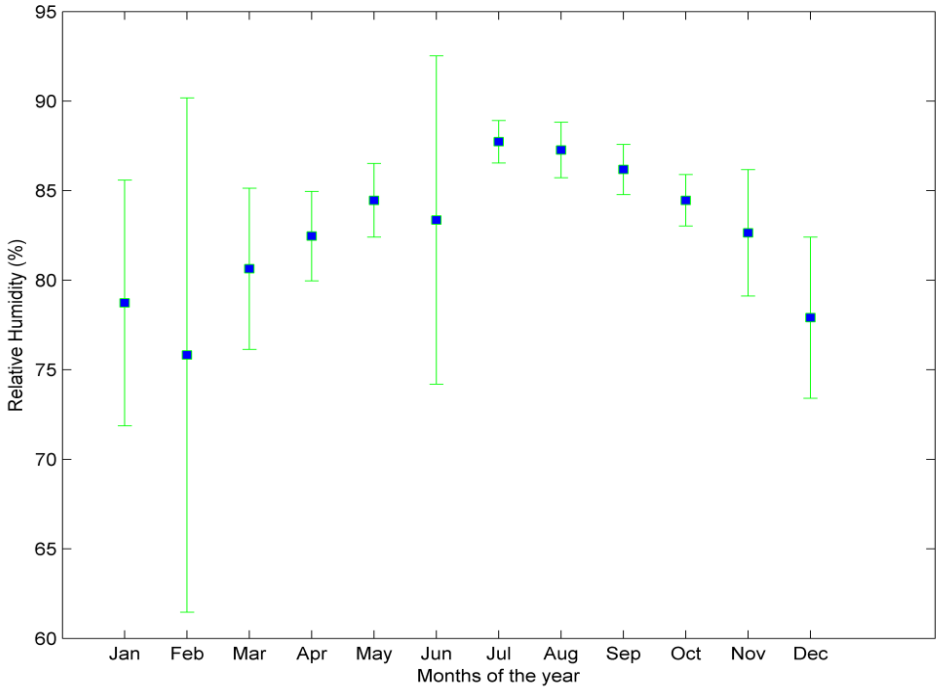

Figure 3-18: Relative humidity (2000–2013) at Port Harcourt Airport Meteorological Station

Chapter 4
Multi-satellite mapping of oil production-linked polluting sources

This chapter addresses research questions one and two and objectives two, three and four. The questions include how accurately can we detect gas flares from satellite based sensors and can satellite data be used to detect the impact of gas flaring on vegetation health and land cover? The objectives are the detection of oil production-linked polluting sources using public domain remote sensing data, comparison of spatial variability in air temperature and satellite derived land surface temperature (LST) and the detection of environmental impact of gas flaring. Qualitative preliminary analysis, including a visual overview of the site, and derived parameters, site characteristics, GIS spatial analysis of satellite derived LST and temperature transects are used to guide the subsequent quantitative analysis of the flare signature, investigation of prevailing wind potential impact on LST, additional factors that influence changes in LST (see section 3.6.3) and comparison of spatial variability in air temperature and satellite derived LST. Table 4.1 summarises the research questions, data sources and analysis presented in this chapter.

Table 4-1: Methodology for data analysis for objectives number two and four

Section	Question/ topic	Data	Analysis
4.1	Overview of study sites	Images held within Google Earth and Digital Globe website, Landsat imagery for bands 1-4 and 6, Landsat RGB pseudo-true colour composite images, Landsat land cover types. Ancillary data: Flare stacks height, facility area and distance from residential areas.	Qualitative: Visual appraisal and summary
4.2	Is there a clear flare signature in LST at the study sites?	Landsat LST	Qualitative: South-North transect through flare location. South is the direction of prevailing wind in the Niger Delta
4.3	Is there a clear flare signature in the colour or vegetation index data at the study sites?	Landsat bands 1-4 and NDVI	Qualitative: South-North transect through flare location
4.4	What is the magnitude of the flare impact on LST at the study sites?	Landsat LST	Qualitative: Characterisation of change in LST with distance from flare into 4 curve types; GIS spatial analysis of LST Quantitative: Parameterisation of flare-related change in LST as δLST; Quality control of δLST using analysis of variance
4.5	Is there a detectable impact of wind direction on the spatial gradients in LST around the flares?	Landsat LST	Qualitative: GIS spatial analysis of LST Quantitative: Linear regression of δLST values with distance North, South, East and West of the flare
4.6	Can LST gradients near the flares be accounted for using public data?	as 4.1	Qualitative: GIS spatial analysis of LST Quantitative: Pairwise linear regression of δLST against factors that might affects temperature; multiple linear regression of δLST against factors that might influence temperature
4.7	Is there a difference in spatial variability of air temperature and satellite derived LST?	Coordinates of locations (Latitude and Longitude), air temperature, relative humidity and Landsat LST.	Qualitative: Plotting of air temperature, relative humidity, and combine plot of Landsat LST and air temperature. Quantitative: Mean and standard deviation of air temperature and relative humidity; parameterisation of change in air temperature as δAT and comparison between air temperature and Landsat LST

Section 4.1 displays the characteristics of the 11 case study sites using images held within Google Earth, Landsat imagery (bands 1-4 and 6), RGB pseudo-true colour composite images, and derived land cover types; section 4.2 presents a qualitative assessment of flare signatures while section 4.3 presents Landsat reflective band signatures, and NDVI results in a qualitative appraisal of potential flare signatures. Quantitative analysis of the detected flare signatures is explained in section 4.4 and section 4.5 describes the investigation of the prevailing wind potential impact on LST. Section 4.6 presents the evaluation of factors influencing change in LST and then in section 4.7 the results of the fieldwork are presented. Section 4.8 compares the air temperature results to the LST values derived from Landsat 5 TM and Landsat 7 ETM+ data and section 4.9 summarizes the Chapter and gives the conclusions.

4.1 Characteristics of gas flaring case study sites

Nigeria has about 131 gas flaring sites in the Niger Delta region (NASRDA, 2005), out of which 11 were selected for this study; see section 3.3.2 for the selection criteria. The flaring sites investigated for this research are all located in Rivers State of the Niger Delta. They are Eleme Refinery I and II Petroleum Companies, Bonny Liquefied Natural Gas Plant, and Onne, Umurolu, Alua, Rukpokwu, Obigbo, Chokocho, Umudioga and Sara Flow Stations. For these flaring sites, the size of the area investigated around the flare stacks with Landsat satellite data is 12 by 12 km i.e. 400 by 400 pixels, in order to include sufficient data for detailed mapping of each site so that processes not related to flaring could also be resolved. The spatial gradients of remotely sensed parameters in the area are analysed in relation to the flare stacks investigated.

Furthermore, in order to answer the research questions and objectives, the following analysis steps were used: an overview of spatial variability in land use that was achieved using simple visual examination of Worldview-1 and 2 and Ikonos pseduo-true colour images accessed through Google Earth and Digital Global (http://browse.digitalglobe.com/imagefinder/public.do); see Chapter 3. The land cover classification results were used to summarise the land cover types around each site. Then, the Landsat reflective bands were examined to identify any unusual ground features associated, and the emissive band was used to show the position of the flare stack (hotspot). Finally, the pseudo-true colour images from the combination of bands 3, 2 and 1 as red, green and blue (RGB) were included as a comparison to the higher spatial resolution WorldView and Ikonos browse images in identifying features at each site (the green features in the Landsat RGB image should correspond to green features in Google Earth); see Figures 4.1-4.22. Other Landsat bands combination such as Red, Green and Near Infrared bands; Green, Blue and Near Infrared; Red, Green and Short Wave Infrared (band 5) and Red, Green and Short Wave Infrared (band 7) were also processed to obtain their pseudo-true colour images. The combination of RGB bands gives the best result and so it was used for the qualitative analysis of this study.

In the location figure for each oil and gas facility, the position of the flare stack was clearly marked with a circle. The information about the closeness of these sites to habitation are provided in order to show development that has taken place around these facilities, and to show whether the impact of flaring affects only the environment or also the livelihood of people.

4.1.1 Eleme Refinery I Petroleum Company

Eleme Refinery I Petroleum Company is located at Eleme town, built and commissioned in 1965 (see section 2.3.3) and is about 1.6 by 1.1 km in size with a flare stack of about 50 m height. The total number of Landsat cloud-free images available for studying this facility is 37. Eleme Refinery I is surrounded by vegetation, but to the west it shares a boundary with a creek. Also, it is about 1.7 km and 1.5 km from the habitation towards the East and North respectively. Figures 4.1-4.2 show the location of the oil facility in relation to the flaring site, the hotspot pixel for the position of the flare stack, towns such as Abuloma, part of Eleme and Onne in Okrika and Eleme Local Government Areas respectively, and four types of land cover at Eleme Refinery I.

A: Eleme Refinery I Petroleum Company, 2000 (Google Earth, 2015)

B: Eleme Refinery I Petroleum Company, 2015 (Google Earth, 2015)

Figure 4-1: Eleme Refinery I Petroleum Company, in 2000 and 2015

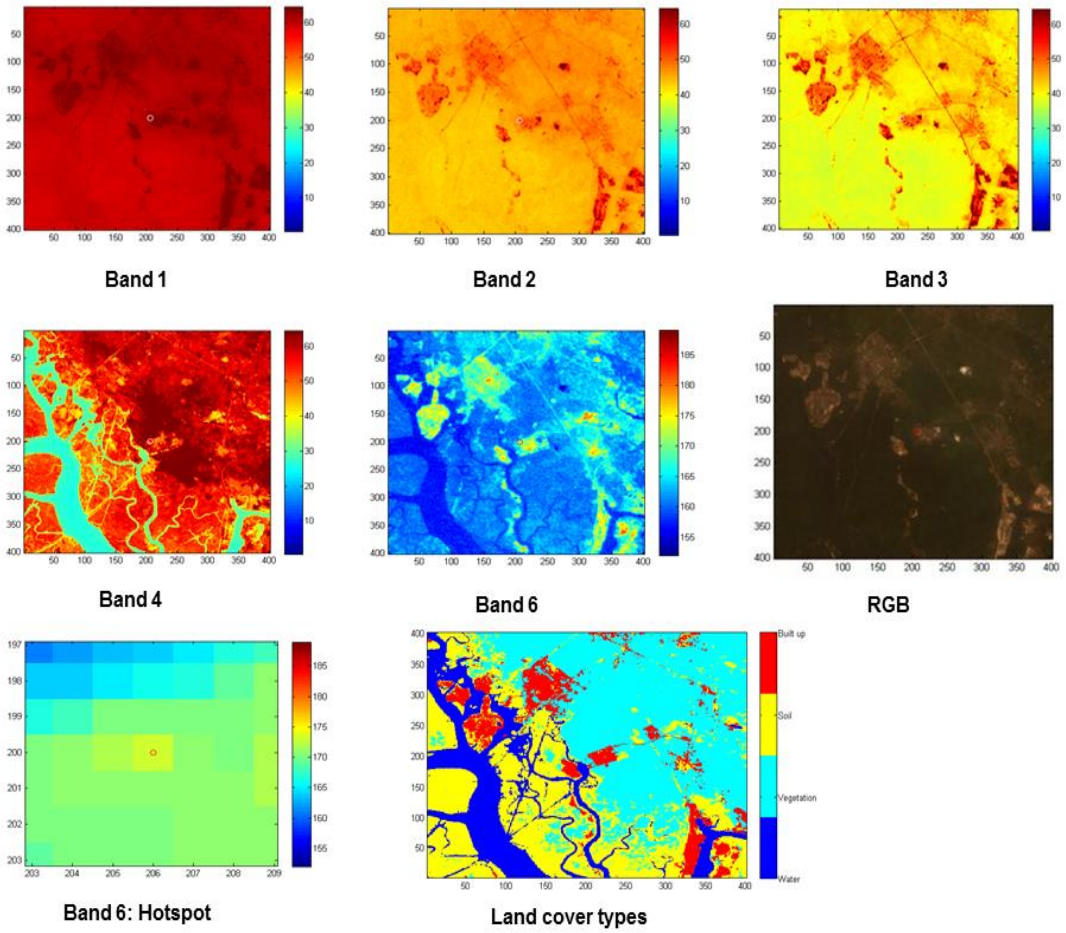

Figure 4-2: Bands 1-4 & 6, RGB, band 6 hotspot pixel and land cover types for Eleme Refinery I (8/1/2003), (X and Y axes: pixel numbers; scale bar: digital number, DN)

4.1.2 Eleme Refinery II Petroleum Company

Eleme Refinery II Petroleum Company is the second refinery site investigated in this study; built in 1988 and commissioned in 1989 (see section 2.3.3) in Eleme town. It is about 2.2 by 1.3 km in size with a flare stack of about 65 m height. There were 41 cloud-free Landsat images for this site. This site was visited from July to September 2012 in order to carry out fieldwork to help validate the satellite data; the description of the site and fieldwork activities are discussed in sections 3.7.1, 3.7.2 and 3.7.4. Figures 4.3-4.4 show the location of the Refinery II within the entire site, the hotspot pixel for the flare stack, towns such as

Abuloma and Ogoni land in Okrika and Eleme Local Government Areas respectively, and the land cover types identified.

A: Eleme Refinery II Petroleum Company, 2000 (Google Earth, 2015)

B: Eleme Refinery II Petroleum Company, 2015 (Google Earth, 2015)

Figure 4-3: Eleme Refinery II Petroleum Company, in 2000 and 2015

4.1.3 Onne Flow Station

Onne Flow Station was built in 2010 and it's the second flaring site visited for the validation of fieldwork activities from July to September 2012. It is about 175 by 130 m in size, within a large fenced compound, with a flare stack (3 pipes connected to a source) being about 3.5 m in height. The number of available Landsat cloud-free images used to study this site was 42. The details of the site and methods used for data gathering during the fieldwork activities are provided in sections 3.7.1, 3.7.2 and 3.7.4. Figure 4.5 A, shows the state of the site in 1984, prior to the building of the flow station, while Figure 4.5 B, shows the position of Onne Flow Station and the considerable development that has taken place particularly to the East and North-East of the site in 2015. Figure

4.6 presents the position of Onne Flow Station, the Landsat data hotspot pixel for the flare stack position on the ground, Onne town in Eleme Local Government Area, Onne Port, Federal Ocean Terminal, West Africa Container Terminal Complex, Onne Oil and Gas Free Zone and different land cover types at the site.

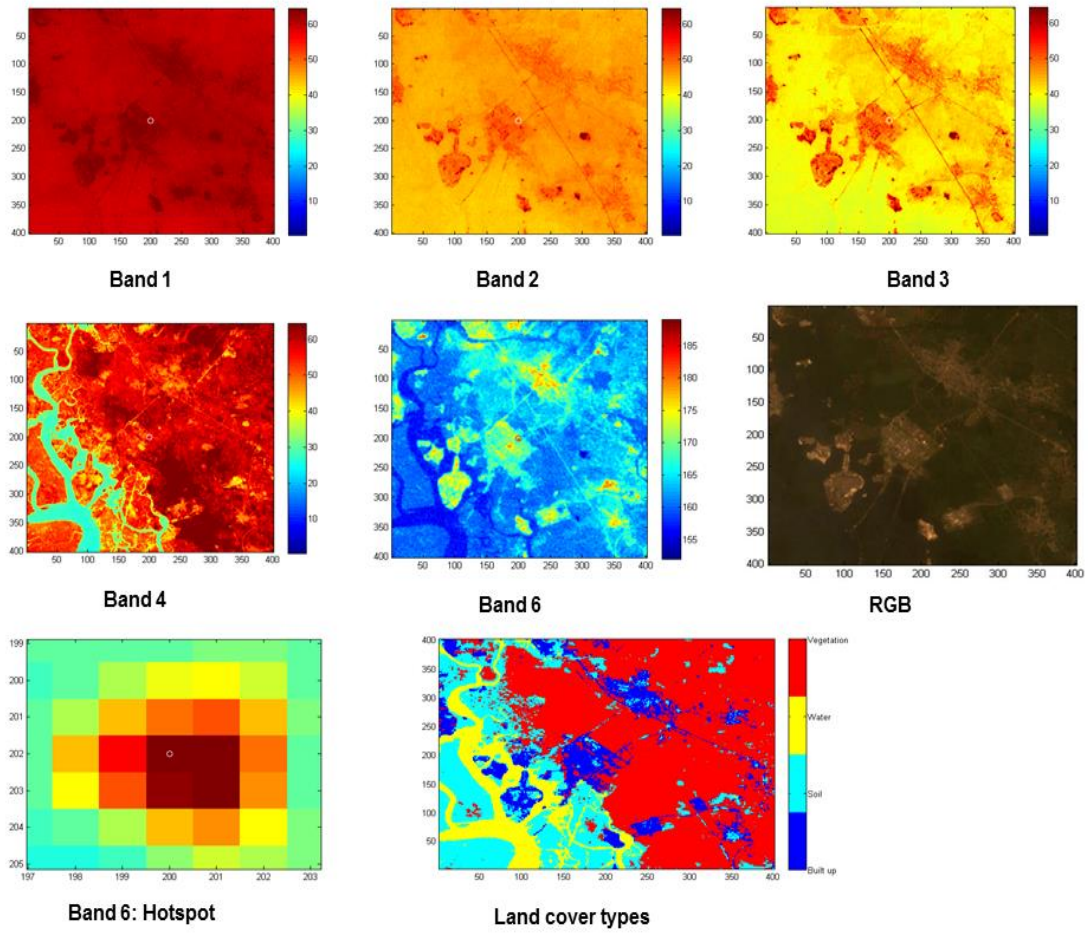

Figure 4-4: Bands 1-4 & 6, RGB, band 6 hotspot pixel and land cover types for Eleme Refinery II (8/1/2003), (X and Y axes: pixel numbers; scale bar: digital number, DN)

A: Onne Flow Station, 1984 (Google Earth, 2015)

B: Onne Flow Station, 2015 (Google Earth, 2015)

Figure 4-5: Onne Flow Station in 1984 and 2015

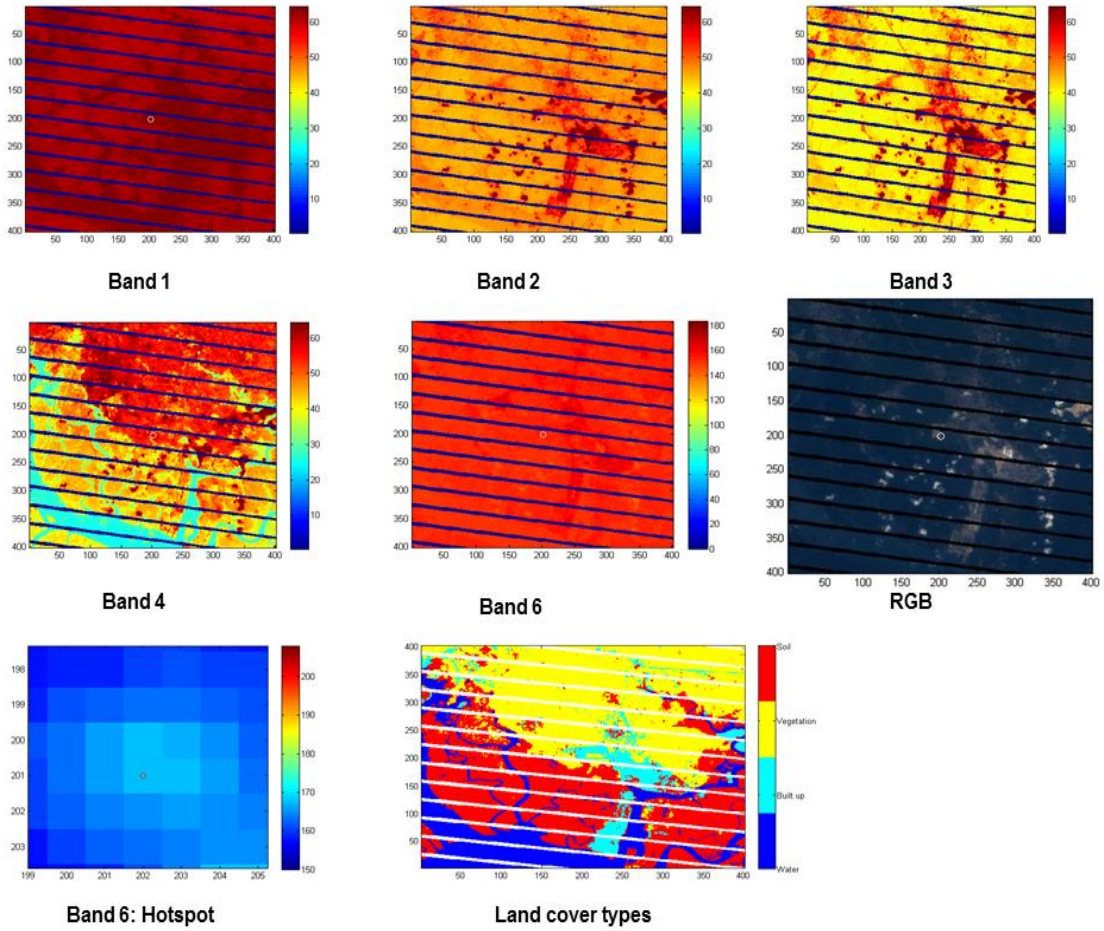

Figure 4-6: Bands 1-4 & 6, RGB, band 6 hotspot pixel and land cover types for Onne (1/1/2012), (X and Y axes: pixel numbers; scale bar: digital number, DN)

4.1.4 Umurolu Flow Station

This is the largest flow station investigated for this study and the information about its build date is not available. It is an inland Flow Station situated at Umurolu town, having five flaring points within an area of approximately 4.2 by 2.4 km and each flare stack is about 60 m high. To the North, it is about 2.5 km from the Port Harcourt-Aba Express road, to the East it is about 400 m away from the Location Road 8, to the south it has a shared boundary with Eleme town while in the West, and it shares boundary with Rumuibekwe town. The number of cloud-free Landsat images used to study this site is 40. Figure 4.7 show the position of the Umurolu Flow Station facility and both natural and artificial features present at the site in 2005 and 2015. Figure 4.8 shows the

position of the facility with the flare stack location marked by a circle, the hotspot pixel for the flare stack, Umurolu and Eleme towns both in Eleme Local Government Area, and details of land cover types.

A: Umurolu Flow Station, 2005 (Google Earth)

B: Umurolu Flow Station, 2015 (Google Earth, 2015)

Figure 4-7: Umurolu Flow Station in 2005 and 2015

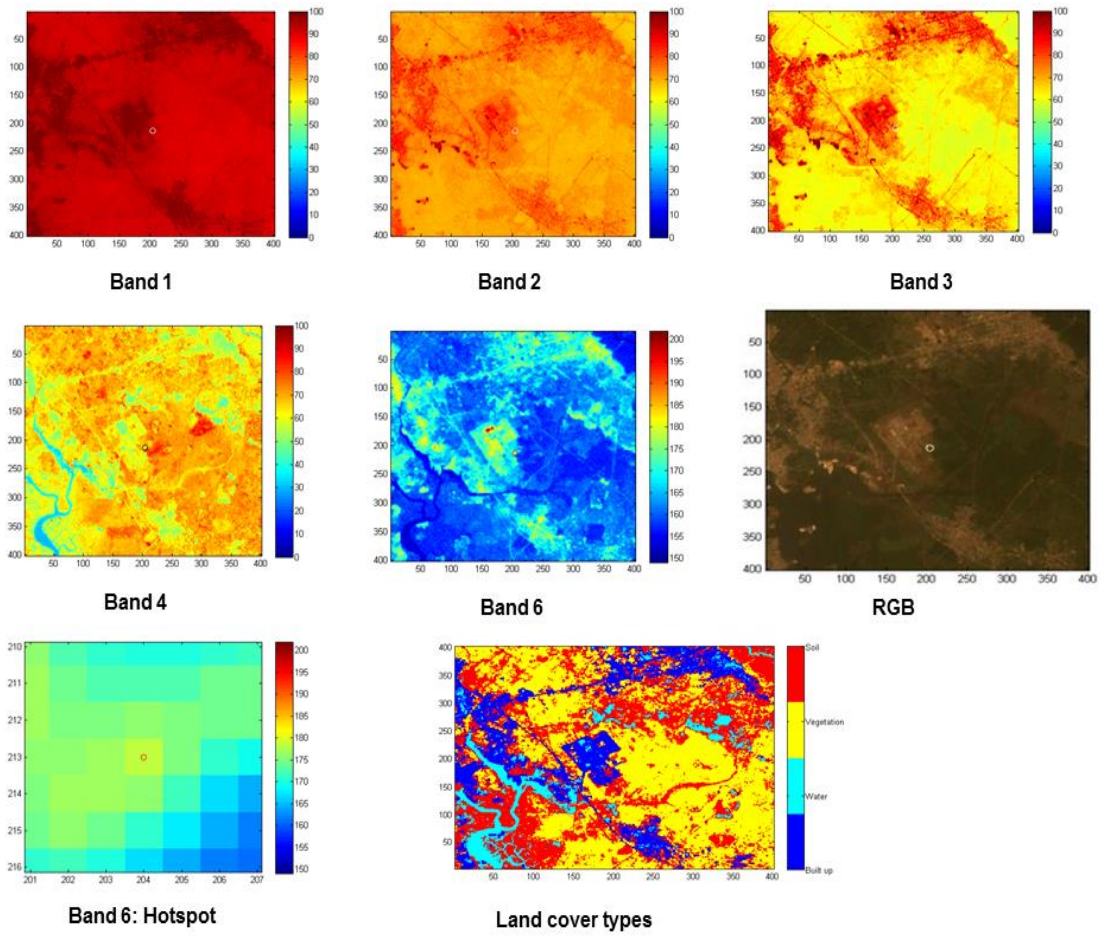

Figure 4-8: Bands 1-4 & 6, RGB, band 6 hotspot pixel and land cover types for Umurolu (17/12/2000), (X and Y axes: pixel numbers; scale bar: digital number, DN)

4.1.5 Bonny Liquefied Natural Gas Plant

Bonny LNG plant is the largest oil and gas facility investigated for this study. It is located at the coastal boundary of Bonny Island and was built in 1989. It shares a fence with a residency in the North-East direction. Also, it is the most difficult and complex site among all the flaring sites that were studied because of the proximity to the Atlantic Ocean, size and variety of structures; about 4.2 by 2.8 km in size. It has five flaring stations with the flare stack height of about 25 m; with two pairs of flaring stations about 100 m and 300 m away from the Atlantic Ocean and the fifth station located at the centre of the facility. The total number of cloud-free Landsat images available to study this site is 33. Figure 4.9 A and B, are images of Bonny LNG in 1984 and 2015 that show considerable

development has taken place. Figure 4.10 show the position of Bonny LNG in relation to the entire site, the hotspot pixel for the flare stack point, Bonny town in Bonny Local Government Area, and land cover types.

A: Bonny LNG, 1984 (Google Earth, 2015)

B: Bonny LNG, 2015 (Google Earth, 2015)

Figure 4-9: Bonny LNG in 1984 and 2015

4.1.6 Alua Flow Station

This is a small inland flow station of about 170 by 90 m in size with a 20 m flare stack height and with unknown build date. It is located at the outskirts of Alua town, and about 2 km from Alua junction on the way to Igrita town. It shares a boundary with the Airport road from Alua town in the North. It is about 2.5 km and 2.6 km distance to the towns to the South-East and West directions respectively. There are 29 cloud-free Landsat images available to study this site. Figure 4.11 from Google Earth present Alua Flow Station and its surroundings in 2002 and 2015. Figure 4.12 show the position of Alua Flow Station within the site, the hotspot pixel for the flare stack point, towns such as Alua, Igrita,

Omuoda, Ozuaha, Igwuruta, Rumuekini and part of Rukpokwu, in Obio-Akpor Local Government Area, and land cover types of the site.

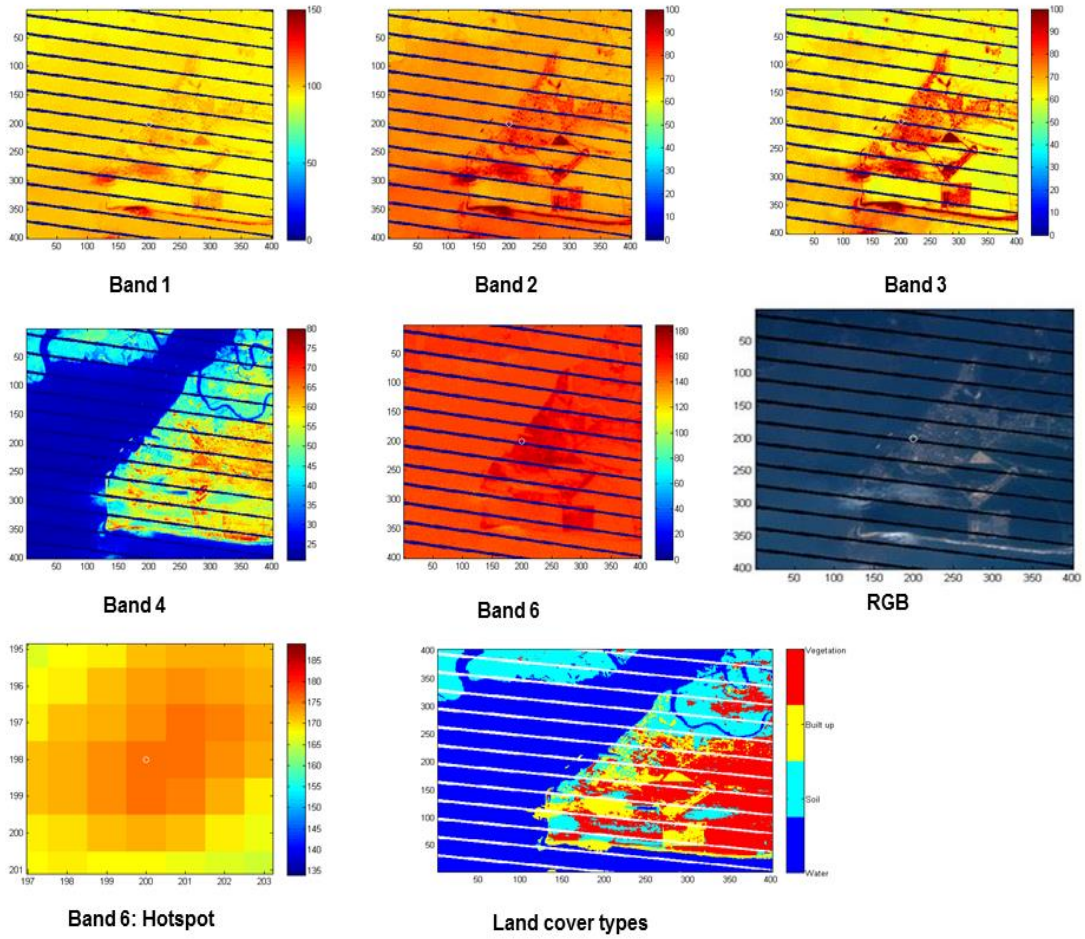

Figure 4-10: Bands 1-4 & 6, RGB, band 6 hotspot pixel and land cover types for Bonny LNG (3/1/2013), (X and Y axes: pixel numbers; scale bar: digital number, DN)

A: Alua Flow Station, 2002 (Google Earth, 2015)

B: Alua Flow Station, 2015 (Google Earth, 2015)

Figure 4-11: Alua Flow Station in 2002 and 2015

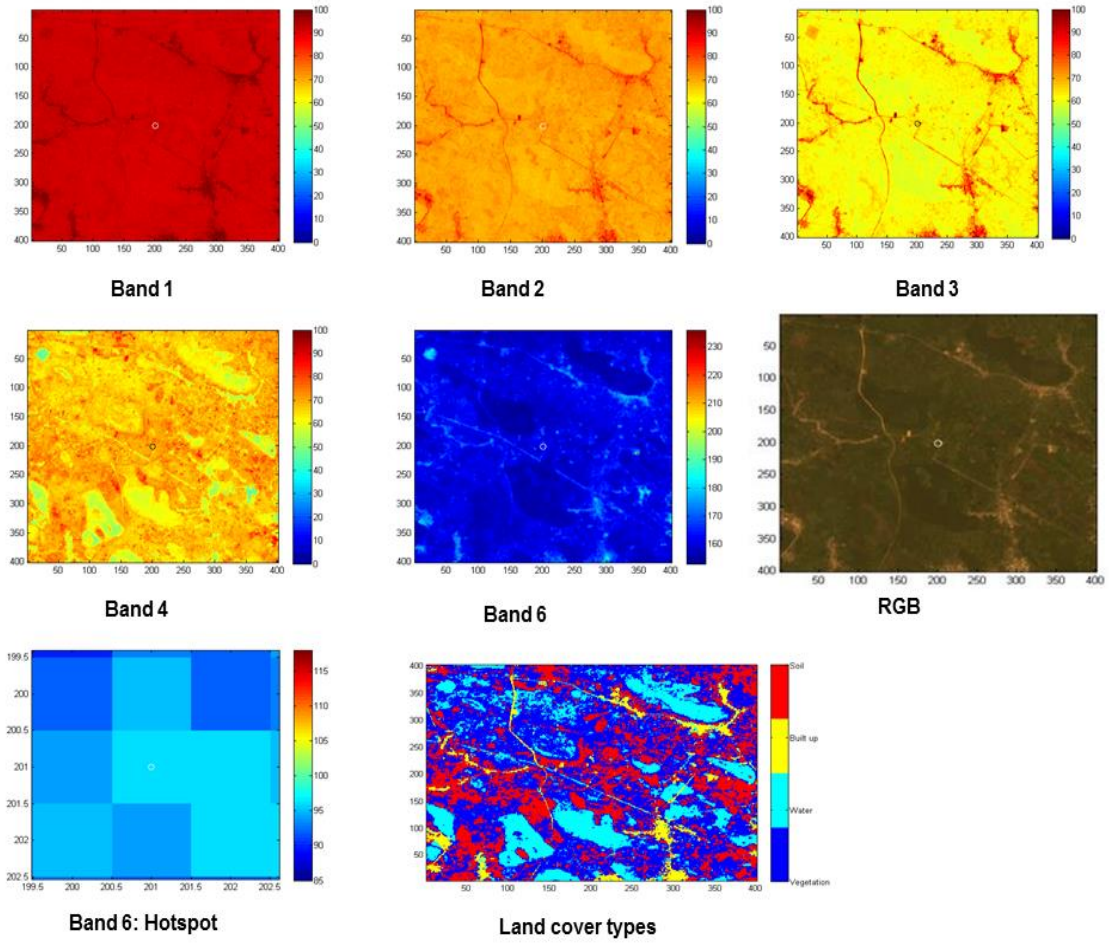

Figure 4-12: Bands 1-4 & 6, RGB, band 6 hotspot pixel and land cover types for Alua (17/12/2000), (X and Y axes: pixel numbers; scale bar: digital number, DN)

4.1.7 Rukpokwu Flow Station

This is another small, inland flow station with dimensions of about 350 by 350 m with unknown flare stack height. It is located on the outskirts of Rukpokwu town and information about the time it was built is not available. To the North it is about 3 km to Igwuruta town, to the East it is about 2 km from Igwuruta-Eliowani Road, to the South is the Rukpokwu town and to the West, it is about 1.8 km from the Rukpokwu-Airport Road. Figure 4.13 present the position of the site in 2002 and 2015, showing that by 2015 development has transformed Rukpokwu site into a fairly human dominated area. There are 40 cloud-free Landsat images available to study this site. Figure 4.14 shows Rukpokwu Flow

Station within the site, the hotspot pixel for the flare stack, towns such as Rukpokwu, Rumuodara, Rumuekini, Igwuruta, Ozuaha, and part of Alua, and land cover types at the site.

A: Rukpokwu Flow Station, 2002 (Google Earth, 2015)

B: Rukpokwu Flow Station, 2015 (Google Earth, 2015)

Figure 4-13: Rukpokwu Flow Station in 2002 and 2015

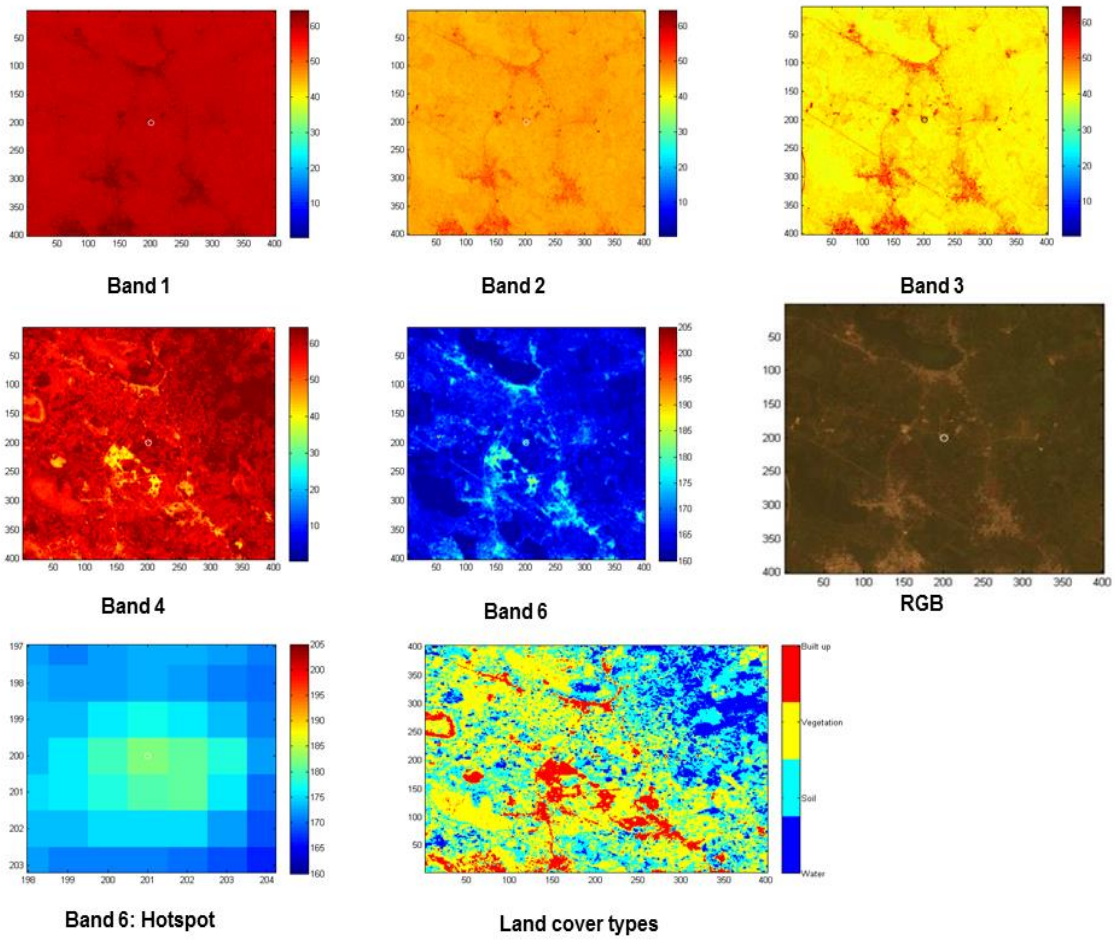

Figure 4-14: Bands 1-4 & 6, RGB, band 6 hotspot pixel and land cover types for Rukpokwu (8/1/2003), (X and Y axes: pixel numbers; scale bar: digital number, DN)

4.1.8 Obigbo Flow Station

Obigbo Flow Station is a medium size flow station of about 650 by 650 m made up of four flaring stacks of about 22 m height. Information about its build date is not available. Figure 4.15 show that development has taken place at the site between 2003 and 2015; the flow station has been surrounded by built up areas hence, it is now located within human habitation. There are up to 28 Landsat cloud-free images available to study Obigbo site. Figure 4.16 presents the position of the flow station, the hotspot pixel for the flare stack, towns within the site such as Obigbo (Obigbo Local Government Area), Igbo-Etche and Rukwangwo (Etche Local Government Area), and land cover types.

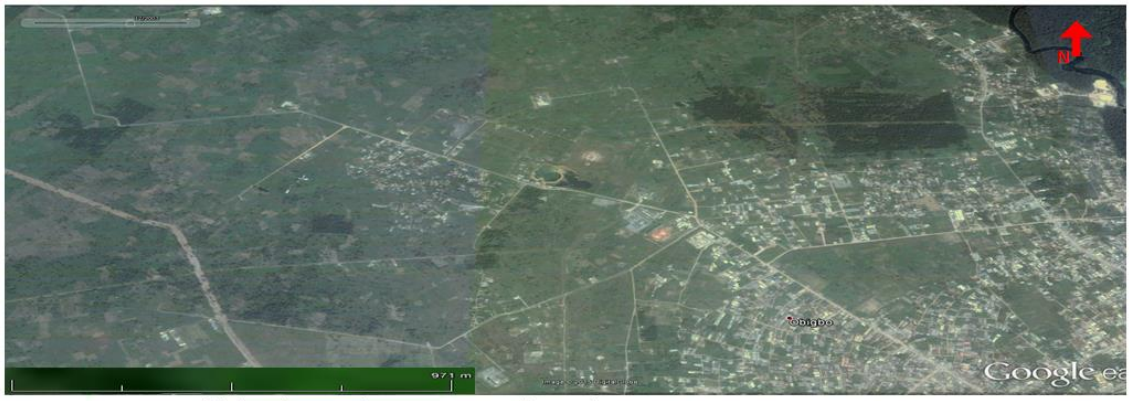

A: Obigbo Flow Station, 2003 (Google Earth, 2015)

B: Obigbo Flow Station, 2015 (Google Earth, 2015)

Figure 4-15: Obigbo Flow Station in 2003 and 2015

4.1.9 Chokocho Flow Station

The dimension of this flow station is about 350 by 120 m and its flare stack height and build date are unknown. It is located about 4.3 km away from Chokocho town; to the East it is about 1.9 km from Igbo-Etche Road and is close to human habitation in both the East (1.7 km) and South-East (1.3 km) directions. Figure 4.17 show Chokocho Flow Station and its surrounding environment in 2003, and the developmental changes that have taken place to 2015. There are only 30 cloud-free Landsat images available for this study site. Figure 4.18 shows the location of the flow station, the hotspot pixel for the flare stack, towns such as Chokocho, Rumuakuru, part of Igwuruta all in Rivers State and Egwi, Okoroagu and Odagba all in Abia State, and land cover types of the site using Landsat data.

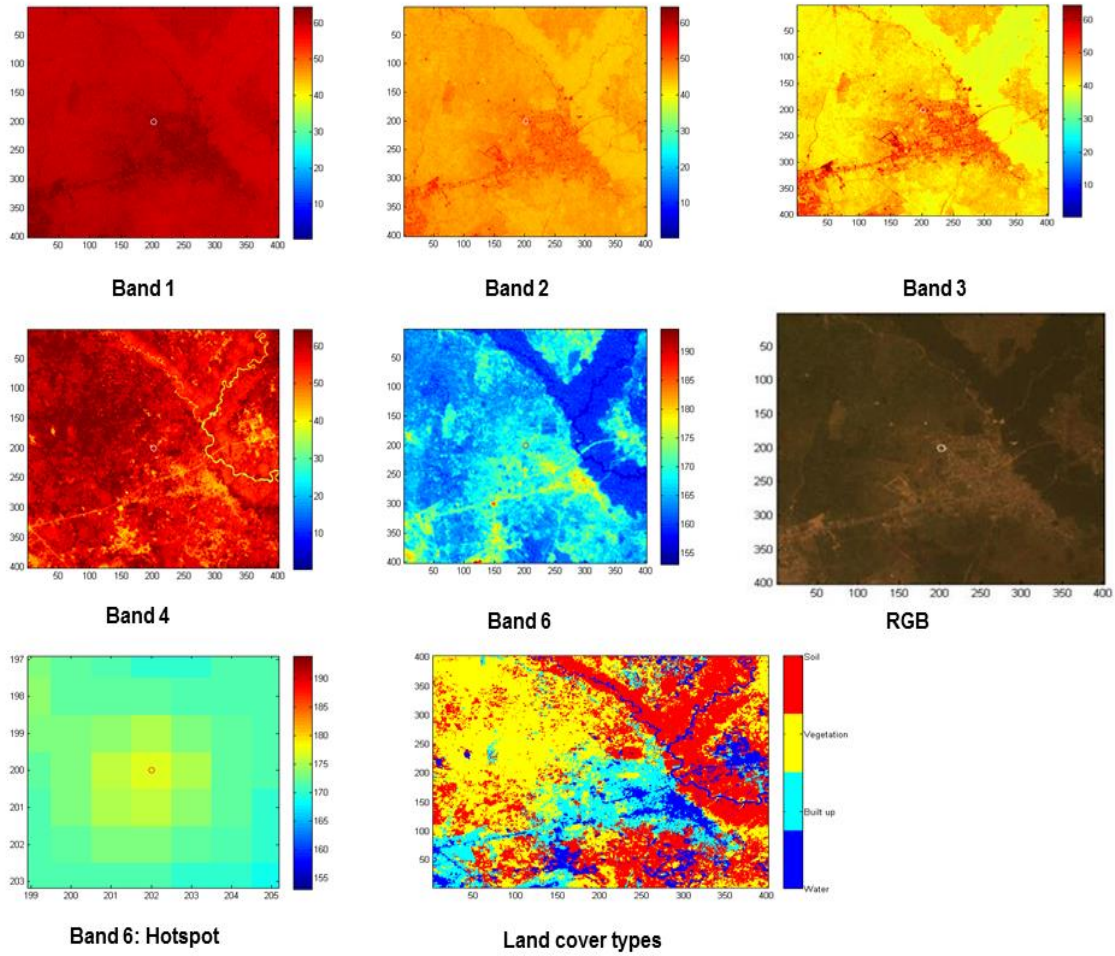

Figure 4-16: Bands 1-4 & 6, RGB, band 6 hotspot pixel and land cover types for Obigbo (8/1/2003), (X and Y axes: pixel numbers; scale bar: digital number, DN)

A: Chokocho Flow Station, 2003 (Google Earth, 2015)

B: Chokocho Flow Station, 2015 (Google Earth, 2015)

Figure 4-17: Chokocho Flow Station in 2003 and 2015

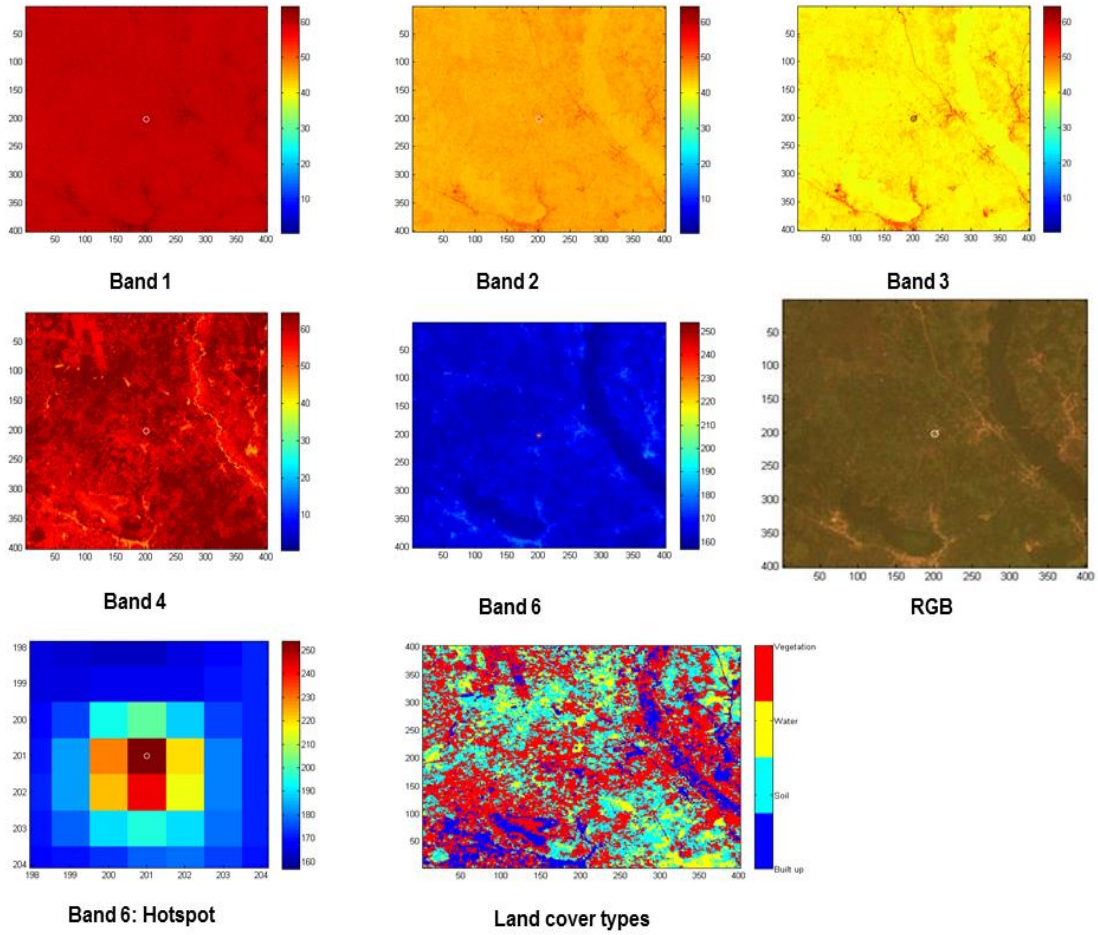

Figure 4-18: Bands 1-4 & 6, RGB, band 6 hotspot pixel and land cover types for Chokocho (8/1/2003), (X and Y axes: pixel numbers; scale bar: digital number, DN)

4.1.10 Umudioga Flow Station

This flow station is the smallest among all the flow stations that were studied; its build date is unknown. It is about 100 by 100 m in size with a flare stack of about 22 m height; and it is not very close to human habitation, being situated about 5 km away from Umudioga town and is about 1.5 km from Ikiri-Airport Road to the East. There are 22 cloud-free Landsat images for this site. Figure 4.19 present the state of this flow station site in 2007 and 2015 respectively. Figure 4.20 shows the location of this Umudioga Flow Station, the hotspot pixel for the flare stack, towns within the boundary of the site such as Umudioga, Egbeda and Erema, and land cover types near the site using with Landsat data.

A: Umudioga Flow Station, 2007 (Google Earth, 2015)

B: Umudioga Flow Station, 2015 (Google Earth, 2015)

Figure 4-19: Umudioga Flow Station in 2007 and 2015

4.1.11 Sara Flow Station

This is another small-sized flow station of about 350 by 250 m with a flare stack height of about 22 m; built in a hostile environment of the coastal town Sara that is situated on the bank of the river Bonny and with unknown build date. The topography at Sara town is swampy and surrounded by several water tributaries, which mean the flow station is far from human habitation. Sara Flow Station receives crude oil from more than ten oil wells for primary treatment and controls. Figure 4.21 show developmental changes between 1984 and 2015 at Sara town and its surroundings. This site was studied using 40 available cloud-free Landsat images. Figure 4.22 shows the location of the flow station with several interconnected pipes linked to oil wells within the boundary area of the site, the hotspot pixel for the flare stack point; Sara town and land cover types at the site.

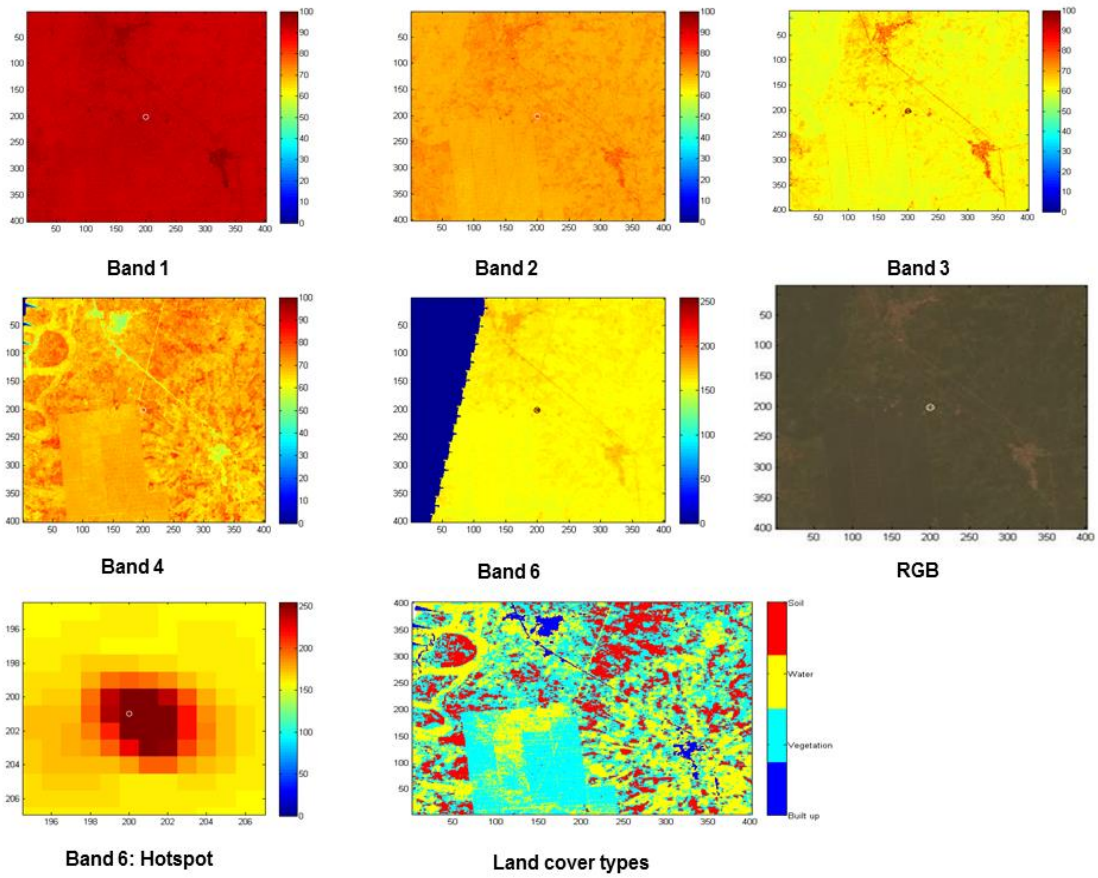

Figure 4-20: Bands 1-4 & 6, RGB, band 6 hotspot pixel and land cover types for Umudioga (17/12/2000), (X and Y axes: pixel numbers; scale bar: digital number, DN)

A: Sara Flow Station, 1984 (Google Earth, 2015)

B: Sara Flow Station, 2015 (Google Earth, 2015)

Figure 4-21: Sara Flow Station in 1984 and 2015

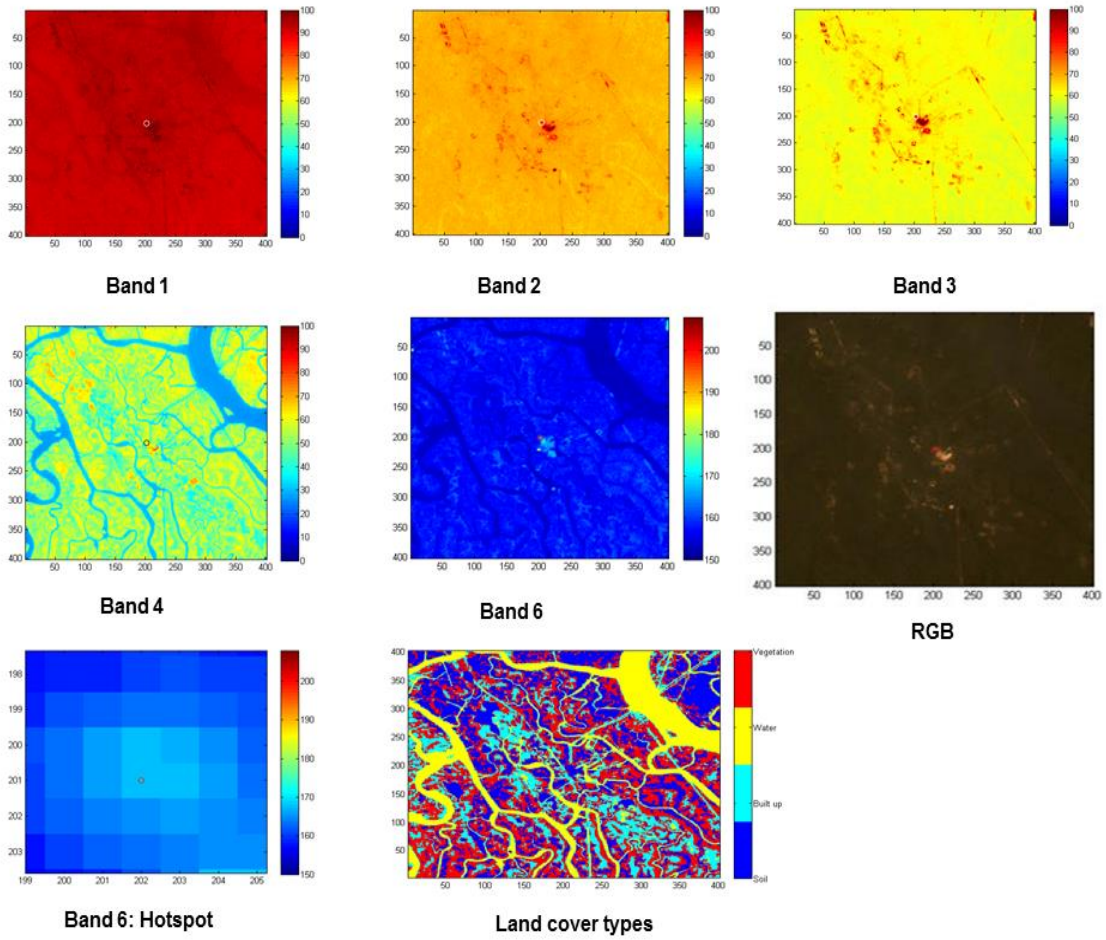

Figure 4-22: Bands 1-4 & 6, RGB, band 6 hotspot pixel and land cover types for Sara (17/12/2000), (X and Y axes: pixel numbers; scale bar: digital number, DN)

4.2 Qualitative analysis of the detection of flare signature

Methods for data analysis described in section 3.6.3 provide information about some of the factors that can affect LST at these flaring sites, including the rate of gas burning, stack height, facility size, vegetation type, vegetation density and time of observation (month) i.e. rainy season or dry season; and those that are available for this study are facility size, stack height and time. The primary method to distinguish the flare stack position was LST. Figure 4.23 presents South-North (direction of prevailing wind in the Niger Delta, see Table 4.3) transect plots of LST at the previously listed flaring sites. For all these facilities, the pixels for the flare stacks were found to have higher LST values than that of the surrounding pixels. In addition, in some cases LST was elevated in adjoining

pixels, suggesting either a warming effect of the flare on surrounding structures or reflecting structures. In a few instances, such as Bonny LNG, some thermal band pixels are also brighter possibly as a result of other facilities such as metal oil storage tanks that absorb heat from both the flare and sun and zero flare at the time of satellite overpass. The author clarified this situation using a combination of images from Google Earth and results from Landsat visible bands (1-4) to ensure that such thermal band pixels were not wrongly interpreted as the flaring source.

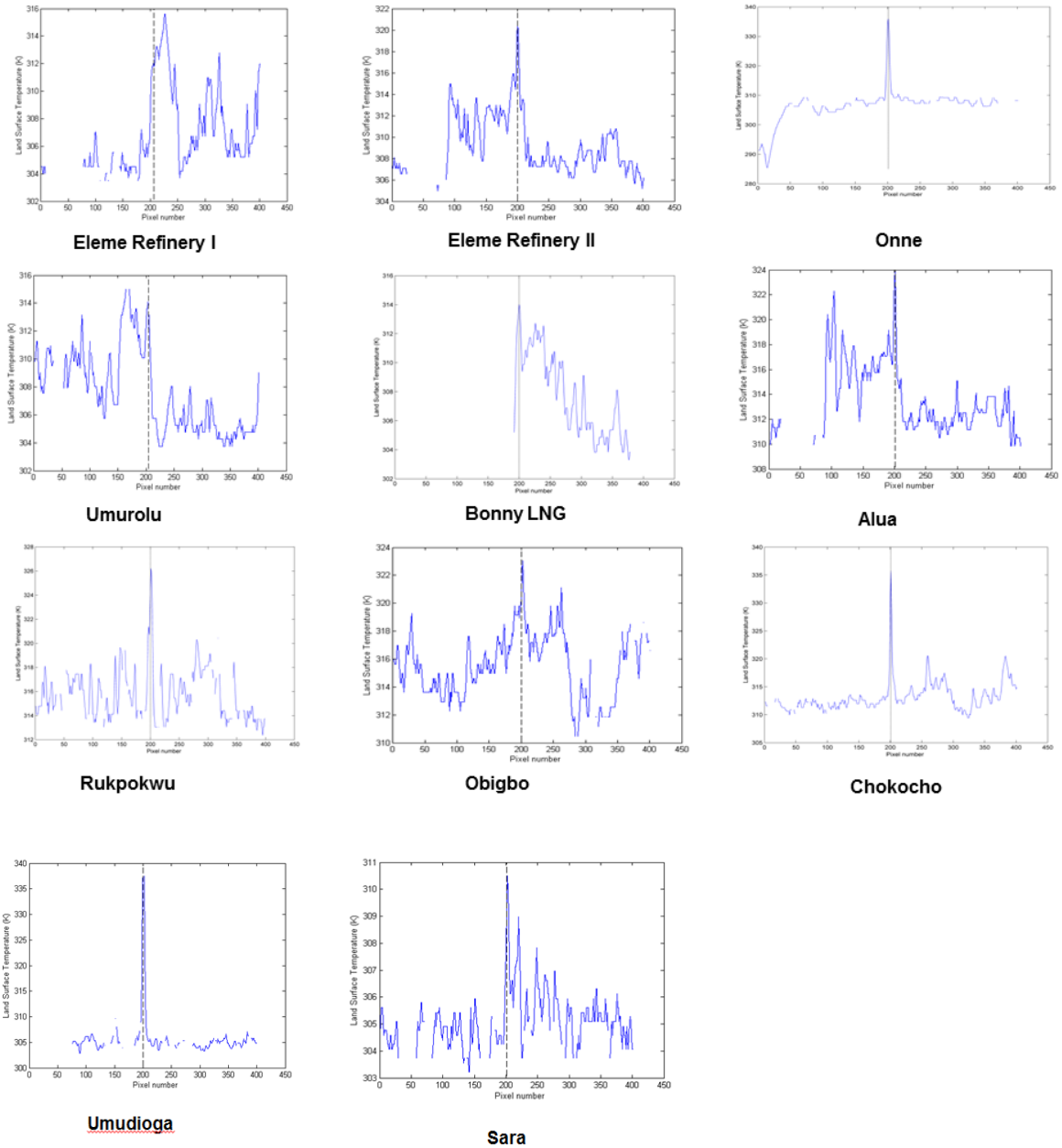

Figure 4-23: Transect plots of Land Surface Temperature of gas flaring Sites. (Dashed line indicates flare location)

Given the variability in station size, site characteristics and LST around the sites, some means of quantifying any potential impact of the flare on LST is needed. This is addressed using a novel approach in section 4.4. The geographical coordinates of the position of the flare stacks in these sites are given in Table 4.2.

Table 4-2: Geographical coordinates of the flare stacks positions

Flaring site	Latitude (θ)	Northing (Y)	Longitude (λ)	Easting (X)
Eleme Refinery I	4.728772	522966	7.118861	291347
Eleme Refinery II	4.762175	526662	7.111025	290487
Onne	4.712321	521140	7.141187	293819
Umurolu	4.829761	534138	7.109251	290311
Bonny LNG	4.424751	489333	7.153231	295073
Alua	4.933330	545636	6.976514	275619
Rukpokwu	4.930209	545277	7.016205	280021
Obigbo	4.892051	541023	7.120232	291549
Chokocho	5.007669	553843	7.019187	280377
Umudioga	5.192664	574400	6.762241	251946
Sara	4.657338	515083	7.059864	284779

4.3 Landsat reflective bands signature and NDVI

Other results acquired, apart from LST, are reflectance values (bands 1-4), land surface cover types derived from the reflectance (as previously explained in section 4.1), and NDVI. In order to acquire information on land cover at each flaring site along the South-North direction of prevailing wind in the Niger Delta, transect plots (through the flare stack pixel) for these results were obtained (Figures 4.24-4.34) with a dashed line indicating the flare location. In addition, the reflective bands were used to inform interpretation of NDVI.

For Eleme Refinery I (Figure 4.24), the reflectance from bands 1 to 3 shows a clear indication of a bright spot at the flare stack pixel with an adjoining pixel having an elevated reflectance while band 4 is different, but shares the same

pattern as NDVI. NDVI value for the flare stack pixel dropped compared to other pixels (not water) along the transect.

For Eleme Refinery II (Figure 4.25), reflective bands 1 to 3 presented similar profiles but the value for the flare stack pixel is high for band 3 compared to bands 1 and 2 while band 4 and NDVI plots have identical patterns.

For Onne Flow Station (Figure 4.26), though the reflective band 1 is slightly noisy, the reflective bands 1 to 3 show an elevated reflectance for the flare stack pixel on ground (and present similar information) while band 4 is similar to NDVI.

For Umurolu Flow Station (Figure 4.27), the reflective band 1 is slightly noisy, reflective bands 1 to 3 plots have identical patterns and band 4 is similar to NDVI. Figures 4.7 and 4.8 previously presented in section 4.1.4 show that Umurolu Flow Station shared boundary with a river in the Southern part of the site. Hence, the Southern part of the plot (higher pixel numbers) presents the water body section.

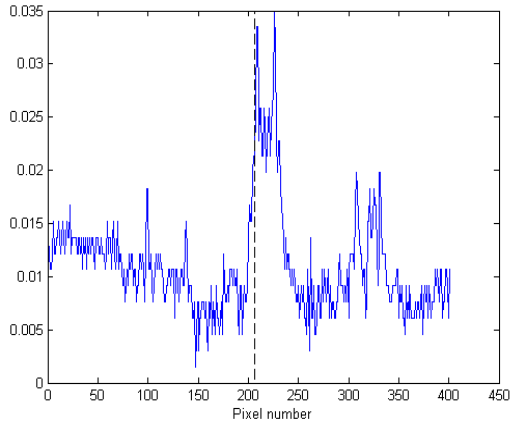

Band 1

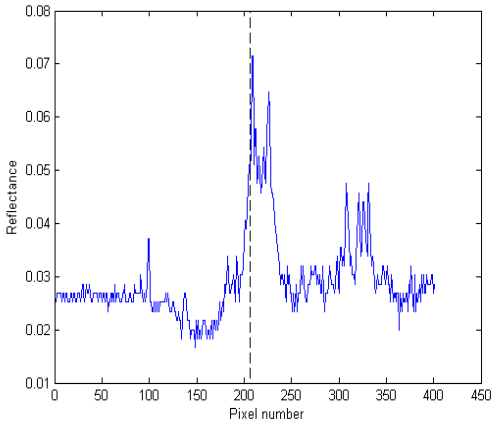

Band 2

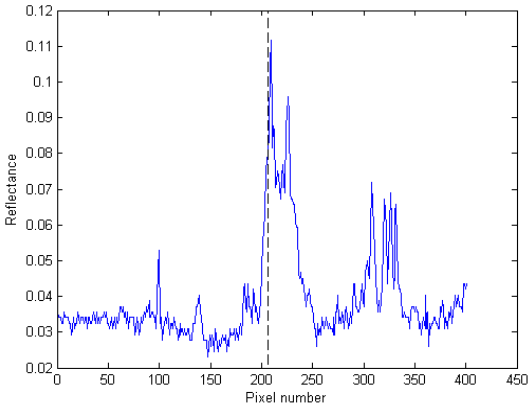

Band 3

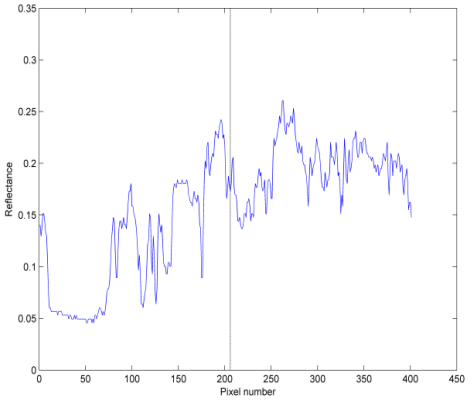

Band 4

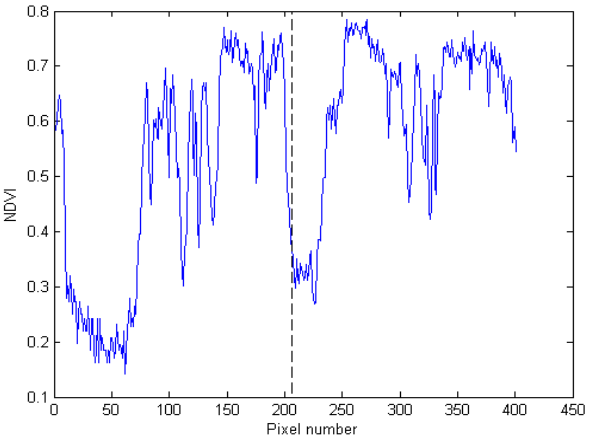

NDVI

Figure 4-24: Reflectance (Bands 1-4) and NDVI for Eleme Refinery I (17/12/2000).

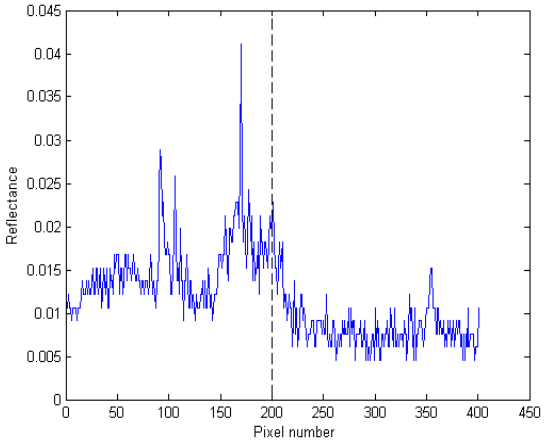

Band 1

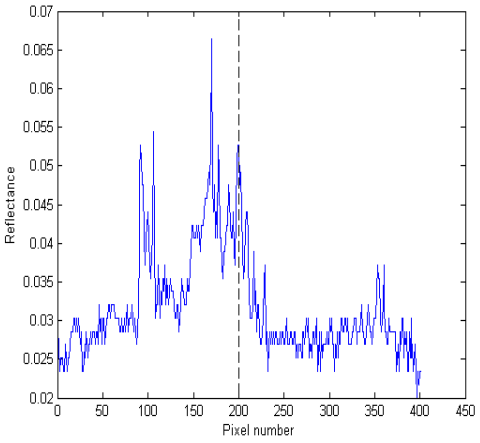

Band 2

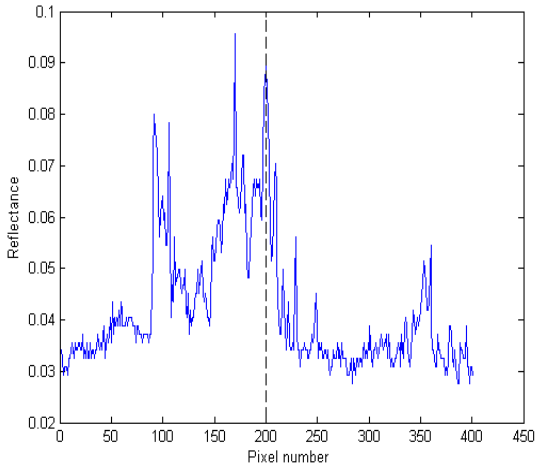

Band 3

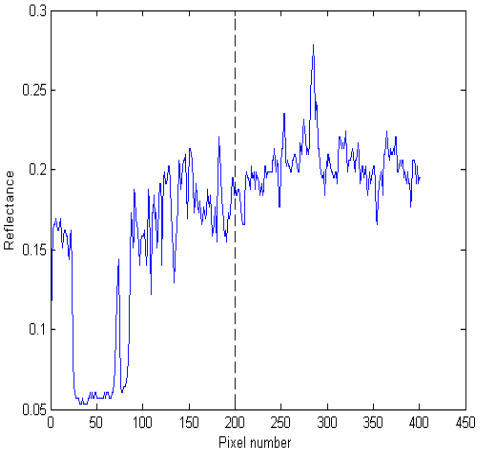

Band 4

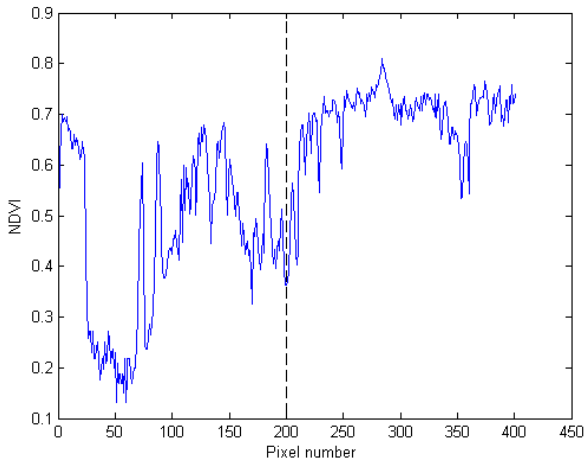

NDVI

Figure 4-25: Reflectance (Bands 1-4), NDVI for Eleme Refinery II (17/12/2000).

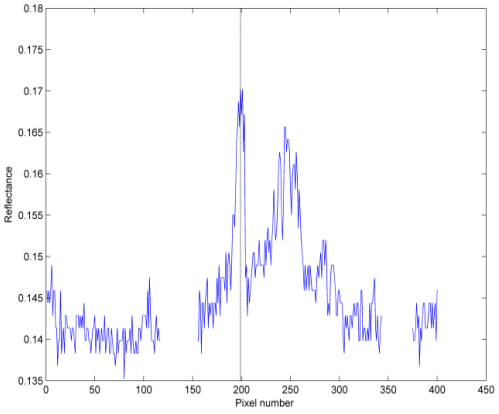

Band 1

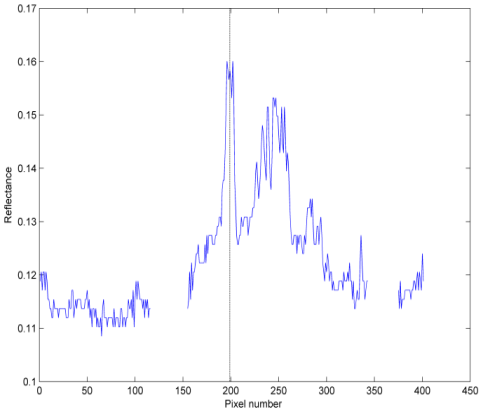

Band 2

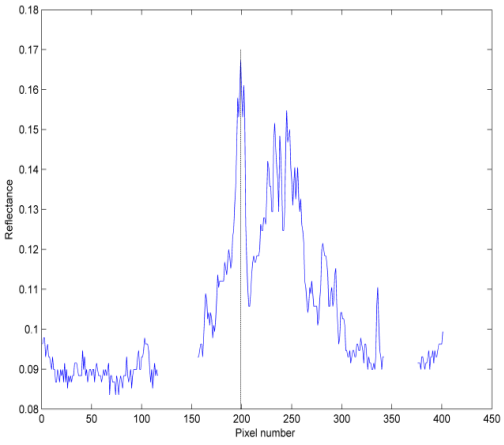

Band 3

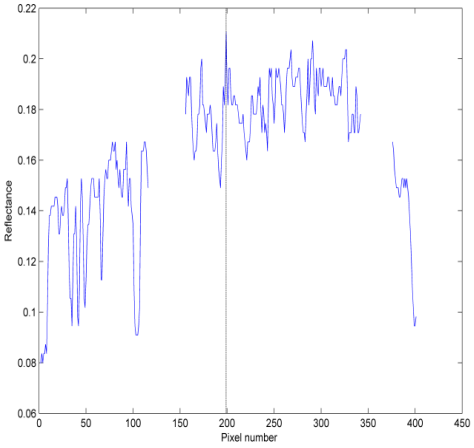

Band 4

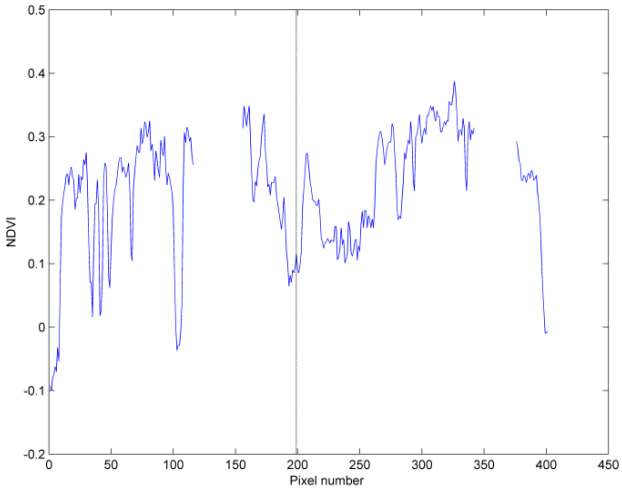

NDVI

Figure 4-26: Reflectance (Bands 1-4) and NDVI for Onne (1/1/2012).

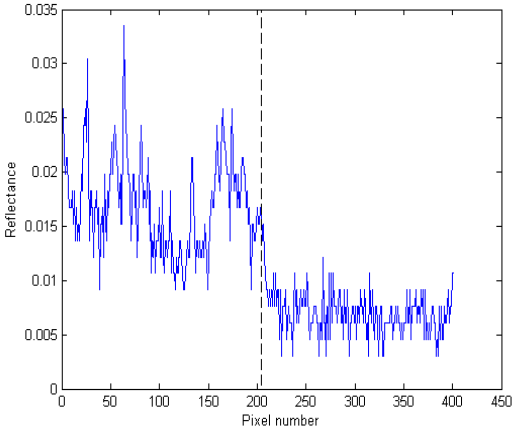

Band 1

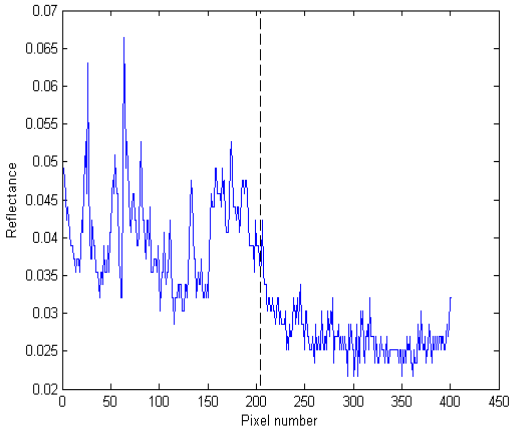

Band 2

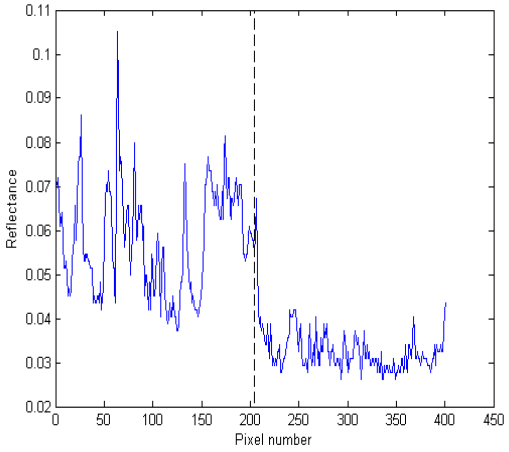

Band 3

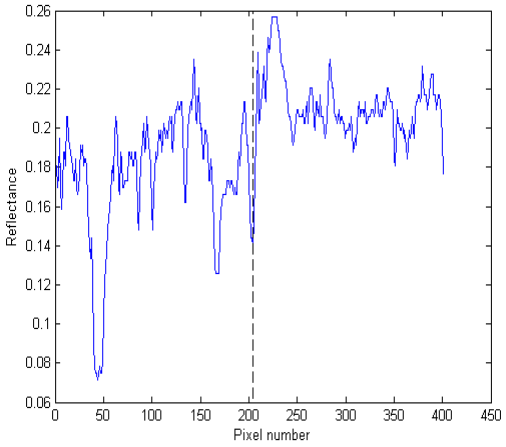

Band 4

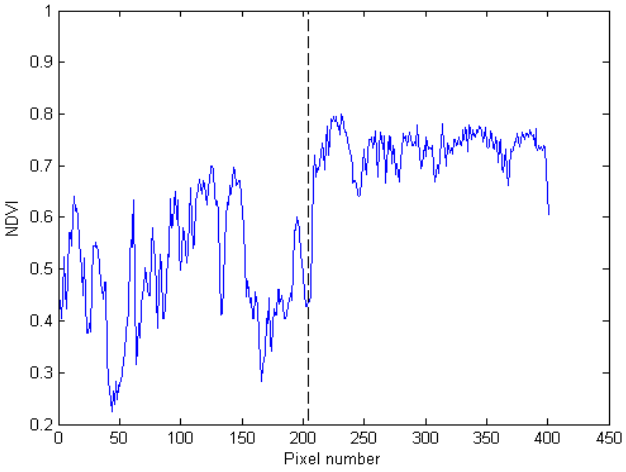

NDVI

Figure 4-27: Reflectance (Bands 1-4) and NDVI for Umurolu (17/12/2000).

For Bonny LNG (Figure 4.28), the plots show that the reflective band 1 is slightly noisy; bands 1 to 3 plots are similar in shape; with an elevated reflectance at the flare stack pixel and some elevated reflectance after the flare stack pixel due to the size of the facility. Band 4 shows a plot that is similar to NDVI. In band 4, the minimum reflectance for the Northern part of the transect (lower pixel numbers) shows that the area is covered with water.

For Alua Flow Station (Figure 4.29), though the reflectance bands 1 to 3 plots are identical in shape with an elevated reflectance at the flare stack pixel, the band 1 plot is slightly noisy, and band 4 does not show any elevated value at the flare stack.

For Rukpokwu Flow Station (Figure 4.30), reflective bands 1 and 2 plots are noisy with an elevated reflectance for the flare stack pixel; bands 1 to 3 have a slightly elevated reflectance for the flare stack pixel and some adjacent pixels where the reflectance values are higher than that of the flare stack. Though band 4 does not have elevated reflectance values for the flare stack, some adjacent pixels show elevated reflectance. Noise is caused by quantisation especially for bands 1 and 2, i.e. the sensor was insufficiently radiometrically sensitive to resolve gradients in the reflected radiation and the format of the data is also limiting in that it is unsigned 8-bit.

For Obigbo site (Figure 4.31), though the reflective band 1 plot is slightly noisy, bands 1 to 3 are plot that are identical in shape showing an elevated reflectance for the flare stack pixel. Also, the band 4 plot is similar to NDVI plot.

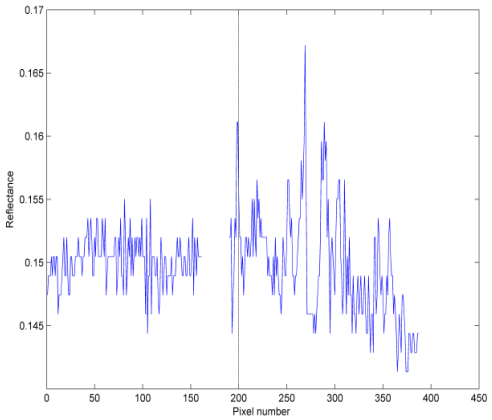

Band 1

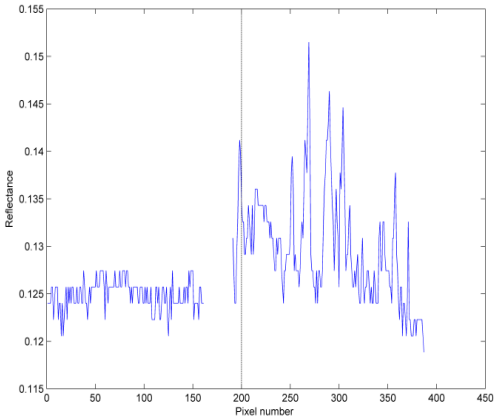

Band 2

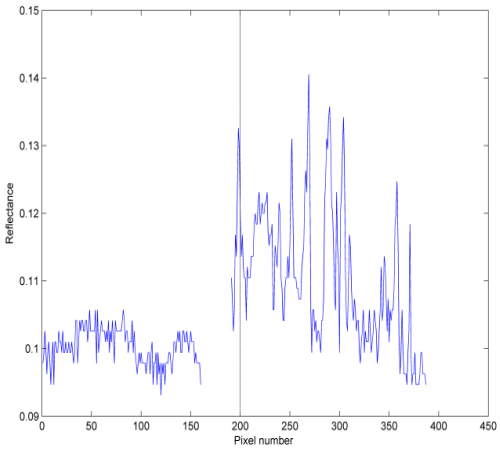

Band 3

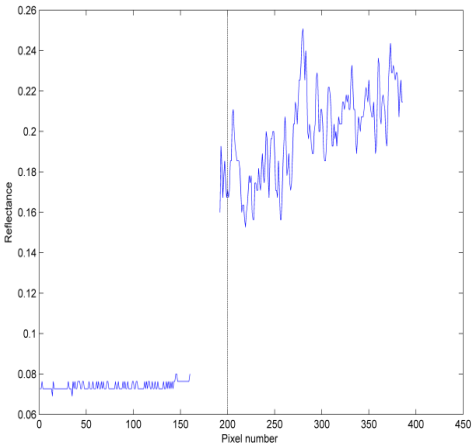

Band 4

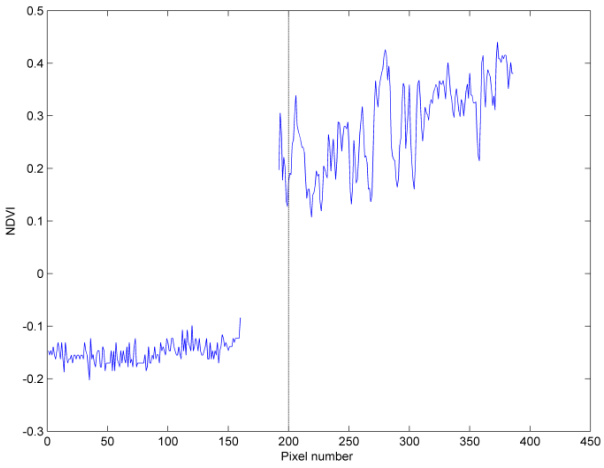

NDVI

Figure 4-28: Reflectance (Bands 1-4) and NDVI for Bonny LNG (3/1/2013).

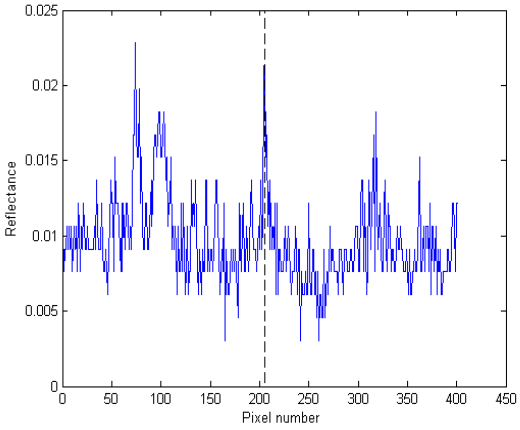

Band 1

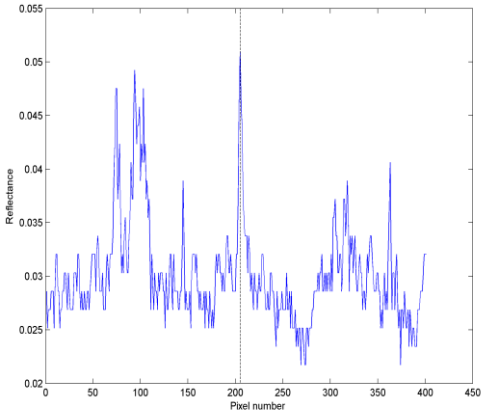

Band 2

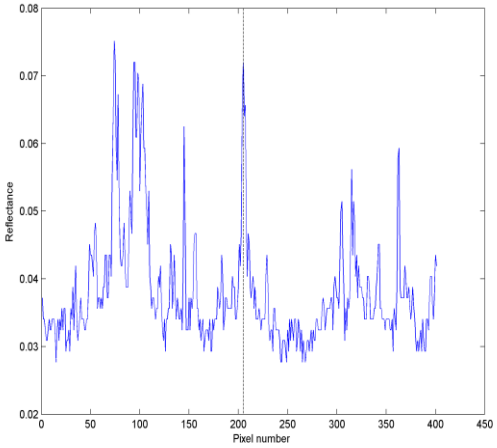

Band 3

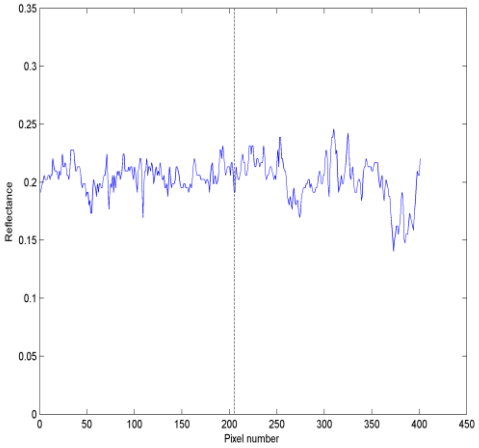

Band 4

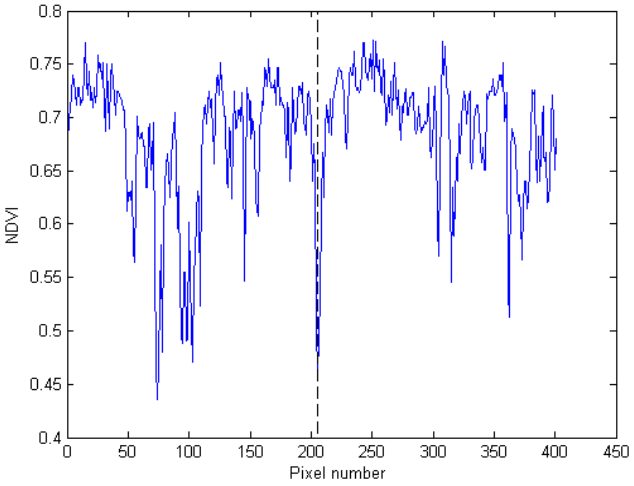

NDVI

Figure 4-29: Reflectance (Bands 1-4) and NDVI for Alua (8/1/2003).

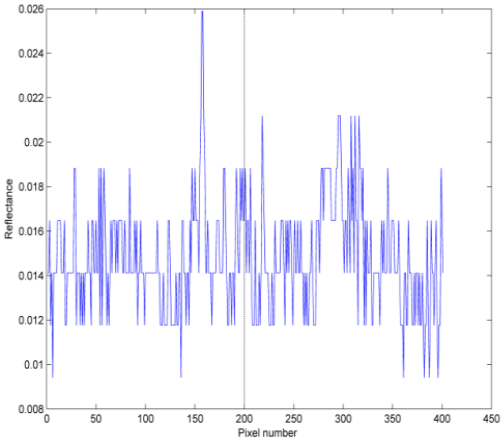

Band 1

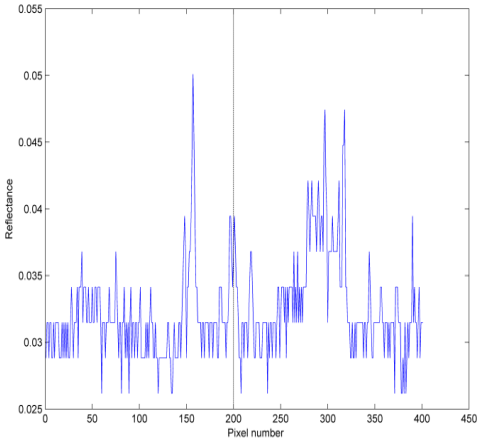

Band 2

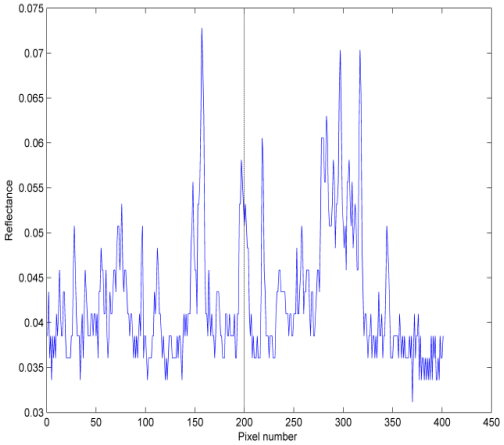

Band 3

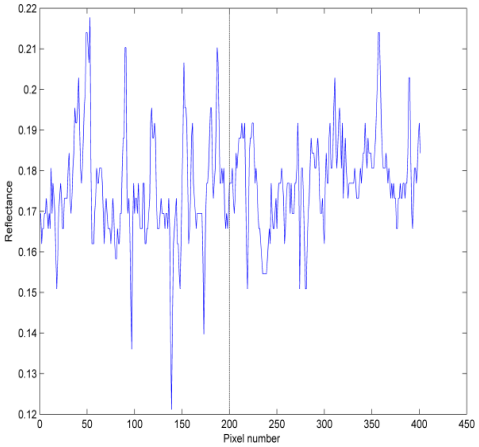

Band 4

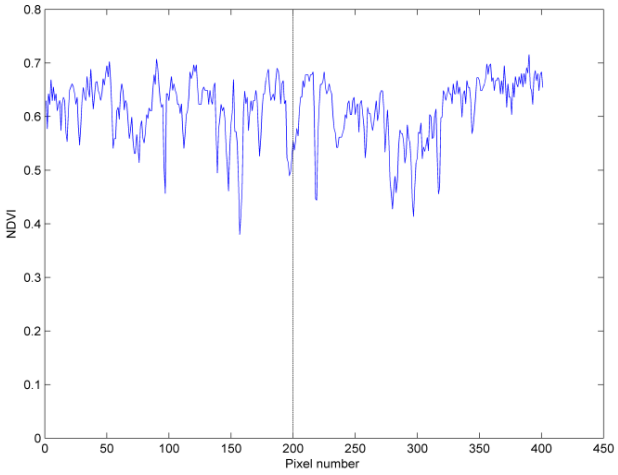

NDVI

Figure 4-30: Reflectance (Bands 1-4) and NDVI for Rukpokwu (8/1/2003).

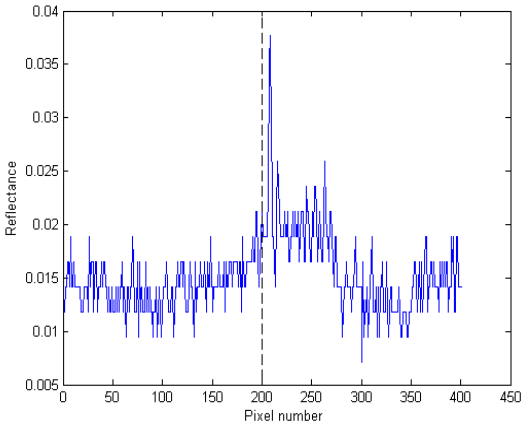

Band 1

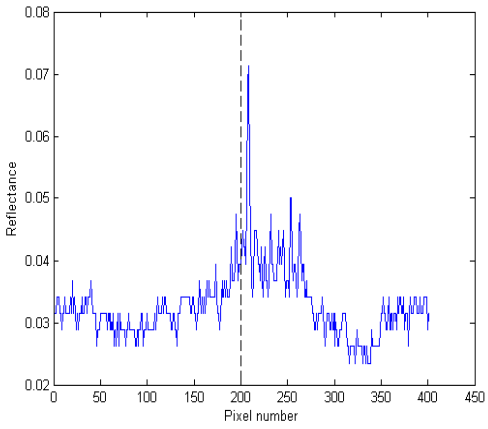

Band 2

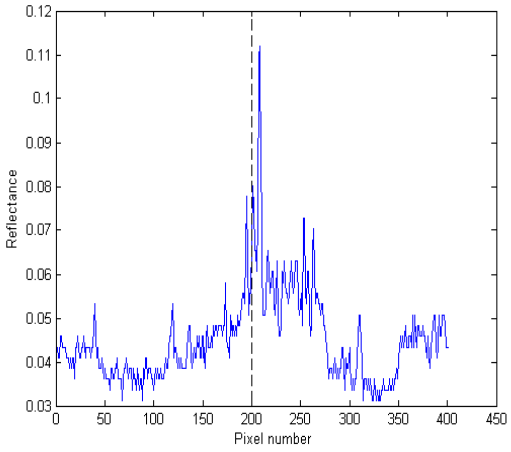

Band 3

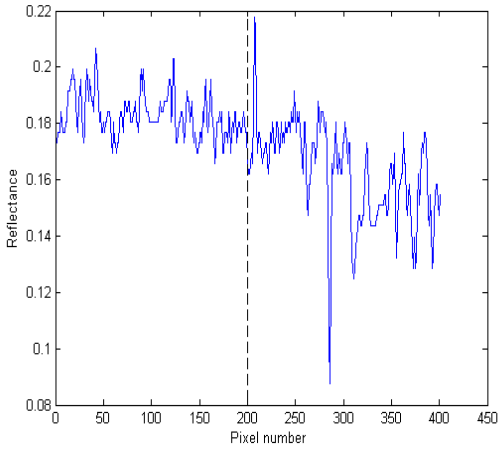

Band 4

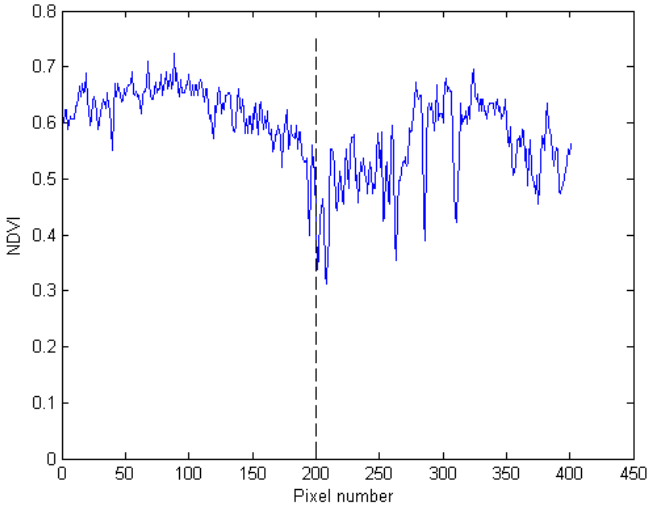

NDVI

Figure 4-31: Reflectance (Bands 1-4) and NDVI for Obigbo (8/1/2003).

For Chokocho site (Figure 4.32), the reflective bands 1 and 2 are noisy; and band 3 has an elevated reflectance for the flare stack pixel that is higher than that of band 1 and 2. Also, the band 4 plot presents identical information to NDVI.

For Umudioga Flow Station (Figure 4.33), the reflective bands 1 to 3 have elevated reflectance for the flare stack pixel, though band 1 is noisy. Band 4 and NDVI plots are similar. Also, there are other few elevated reflectance to both sides of the flare stack for all bands.

For Sara site (Figure 4.34), the reflective band 1 plot is slightly noisy; bands 1 to 3 plots are similar with an elevated reflectance for the flare stack pixel. The reflective band 4 and NDVI plots have identical shapes presenting the same information about the site.

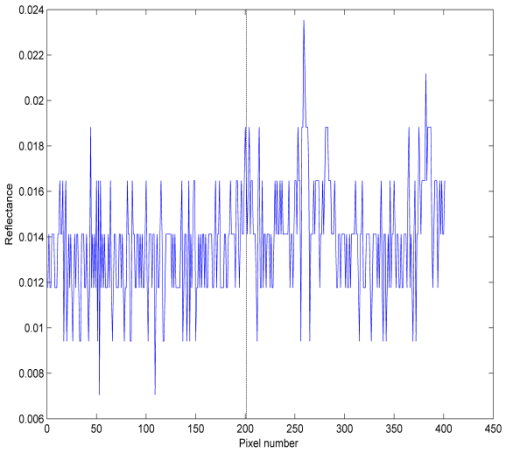

Band 1

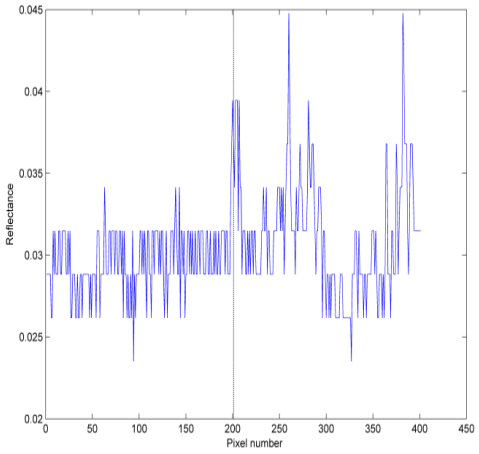

Band 2

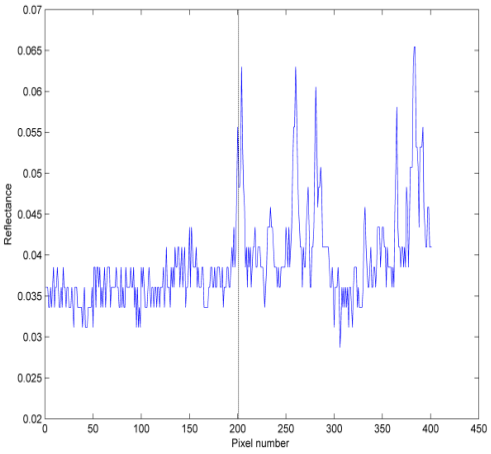

Band 3

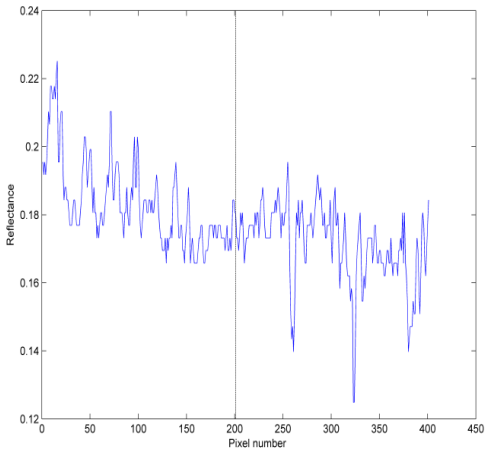

Band 4

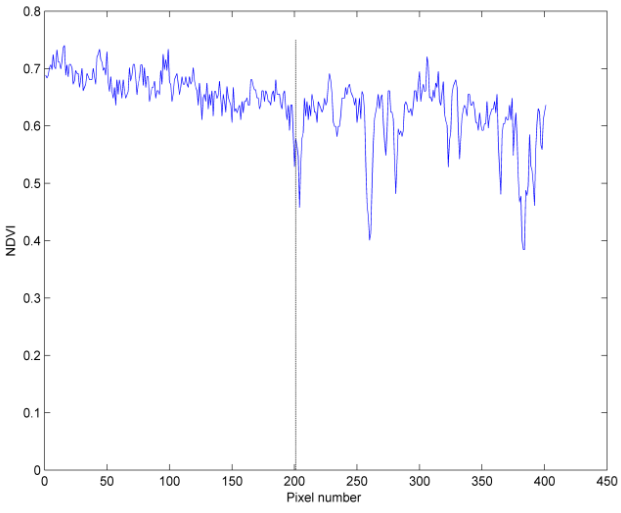

NDVI

Figure 4-32: Reflectance (Bands 1-4) and NDVI for Chokocho (8/1/2003).

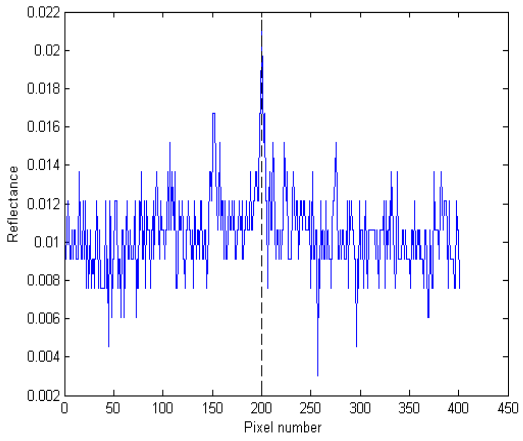

Band 1

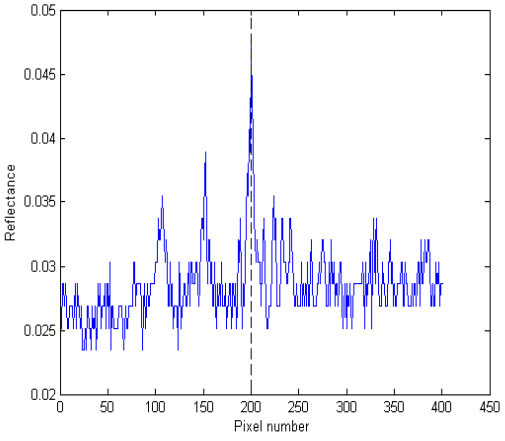

Band 2

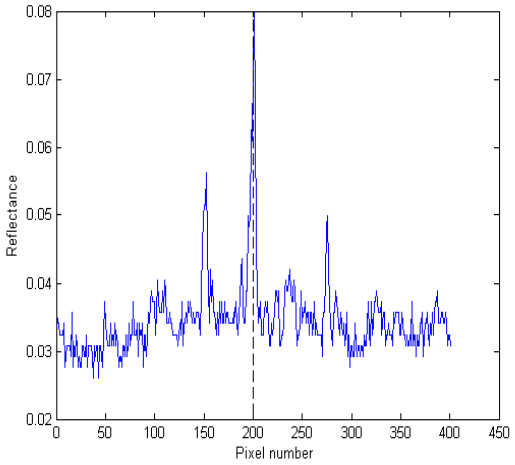

Band 3

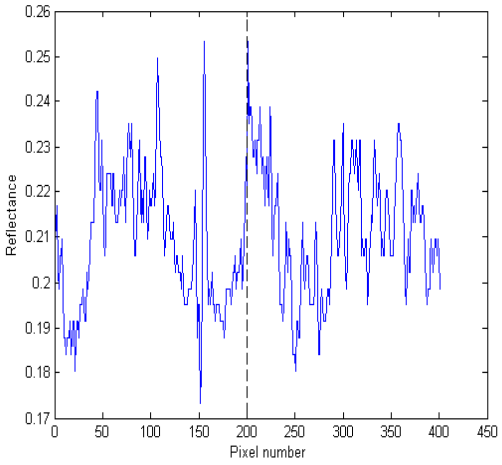

Band 4

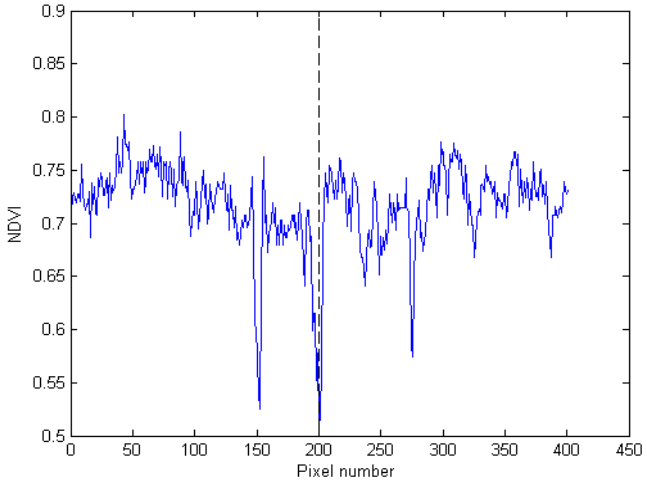

NDVI

Figure 4-33: Reflectance (Bands 1-4) and NDVI for Umudioga (17/12/2000).

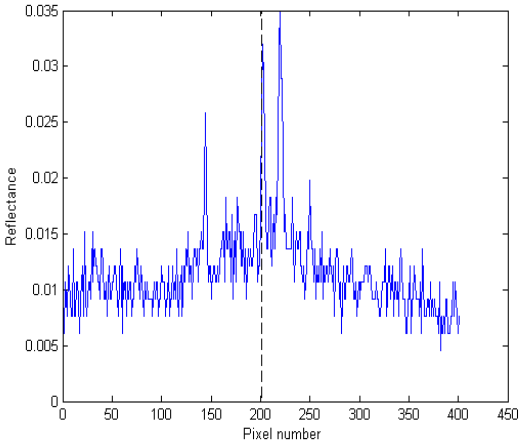

Band 1

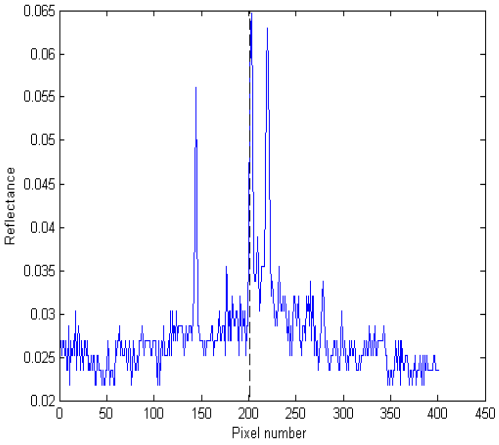

Band 2

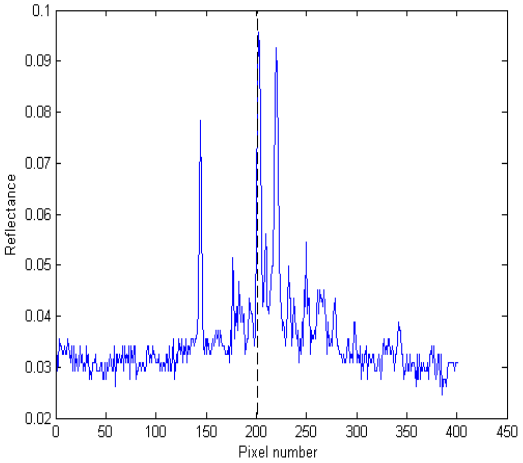

Band 3

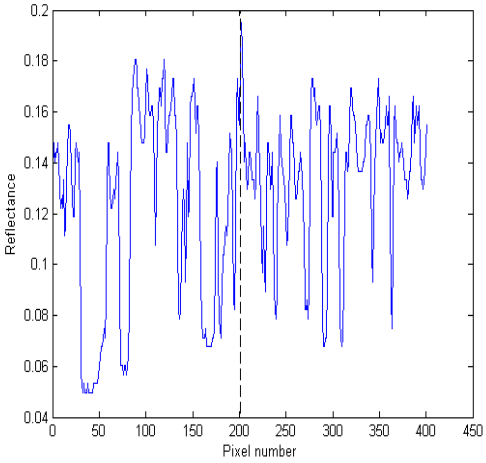

Band 4

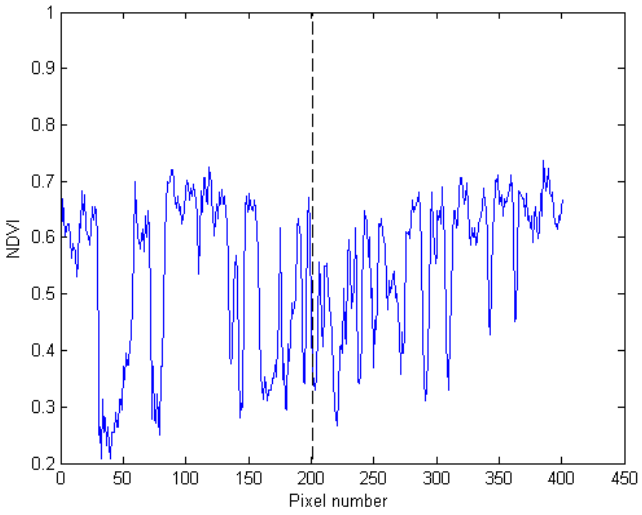

NDVI

Figure 4-34: Reflectance (Bands 1-4) and NDVI for Sara (17/12/2000).

In summary, Figures 4.24-4.34 suggests that the spatial variability in the vegetation indices is sometimes being driven by variability in the Near-Infrared reflectance (vegetation structure or moisture content), for example in Figure 4.26, band 3 ≈ band 4 in magnitude but band 4 is less variable along the transect than band 3, which is mirrored by NDVI; and sometimes by the Red band reflectance (chlorophyll content or vegetation density), for example in Figure 4.34, band 4 is ≫ band 3, NDVI spatial variability mirrors band 4 variability. In general, NDVI value dropped for the flare stack pixel for all the flaring sites investigated. Similar results were obtained for Eleme Refinery I and II, and Sara Flow Station.

4.4 Quantitative analysis of the detection of flare signature

This section details the investigations into the variability in LST with distance from the flare stack, and the characterisation of spatial variability in LST.

4.4.1 Variability in LST with distance from flare

In order to investigate changes in LST with distance from flare, Geospatial Information System (GIS) spatial analysis and four cardinal directional analyses were employed.

4.4.1.1 Spatial analysis of LST through ArcGIS

This analysis helps to fully characterise the 2D shape of each flare plume that enables a better understanding of the similarities and differences between individual plumes. It also helps to determine the best direction of the minimum and maximum LST slope for each site. For the figures, the pseudo-true colour images from the combination of Landsat bands 3, 2 and 1 as red, green and blue

(RGB) were used as the background map for the sites instead of the Google Earth images in order to avoid georeferencing errors that are associated with Google Earth images. In the figures, for the bigger arrow and letter N at the upper corner of the right side shows the direction of the North, the small arrow pointed at the location of the flare within the site and Kelvin (K) in the legend is the International System Unit for temperature. LST was classified into 6 range group with a colour to represent each group. Pure red colour is for highest range of values, followed by light red, light brown, deep orange, light orange and yellow colours respectively. Figures 4.35 A-4.45 A, show the 2D plot for LST for the eleven flaring sites examined with missing data points corresponding to cloud or water, and for Landsat 7 ETM+ also the scan line corrector error. Figures 4.35 B-4.45 B show the 2D plots for LST in 6 different layers while Figures 4.35 C-4.45 C are Figures 4.35 B-4.45 B with additional contours (contour interval of 0.5 K) in order to show the extent and nature of variation in LST within each site. For all the eleven flaring sites investigated, the spatial analysis of LST through ArcGIS shows that the flare sources gives the highest LST, followed by the next adjoining pixels surrounding the flare and continue in that order. Table 4.3 presents the wind direction data at Port-Harcourt, which is used to examine the influence of wind on the flare at the flaring sites. South is the dominant wind origin direction, followed by the West direction with a few instances of South-West, North-West and North-East directions.

Table 4-3: Wind directions in Port Harcourt

Stn	Yr	J	F	M	A	M	J	J	A	S	O	N	D
PH	2000	S	S	S	S	S	S	SW	SW	SW	S	S	NW
PH	2001	NW	S	S	S	S	S	S	SW	W	S	S	NW
PH	2002	NW	S	S	S	S	S	S	SW	SW	S	S	SW
PH	2003	S	S	S	S	S	S	S	S	W	W	S	S
PH	2004	S	N	S	S	S	S	S	W	W	S	S	W
PH	2005	W	W	S	S	S	S	S	W	S	S	S	W
PH	2006	W	SW	S	S	S	S	S	S	SW	S	SW	W
PH	2007	W	W	W	W	W	W	W	W	W	W	W	NE
PH	2008	S	N	S	S	S	S	S	W	W	S	S	W
PH	2009	W	W	S	S	S	S	S	W	S	S	S	W
PH	2010	W	SW	S	S	S	S	S	S	SW	S	SW	W
PH	2011	W	S	S	W	S	S	S	W	W	S	S	W
PH	2012	S	S	S	S	S	S	S	S	W	S	W	S
PH	2013	S	S	S	S	S	S	S	S	W	S	S	W

For Eleme Refinery I (Figures 4.35 A, B and C), six ranges of values of LST presented are 314-317 K plotted in pure red, followed by 312-314 K for light red points, 310-312 K for light brown points, 308-310 K for deep orange points, 306-308 for light orange points and 304-306 K for yellow points. The figure is obtained from a scene that was acquired on 17 December 2000 and the wind direction for that month of the year was North-West. The South direction of the prevailing wind in the Niger Delta show the highest range of values of LST (314-317 K) as indicated by the red points (Figure 4.35 A). This shows that wind that blew from the South towards the North direction has great effects on the flare, causing the impact of the flare to be pronounced in the North direction than that of the North-West direction. The size of the plume (red points) in Figures 4.35 A, B and C is 21 by 23 pixels.

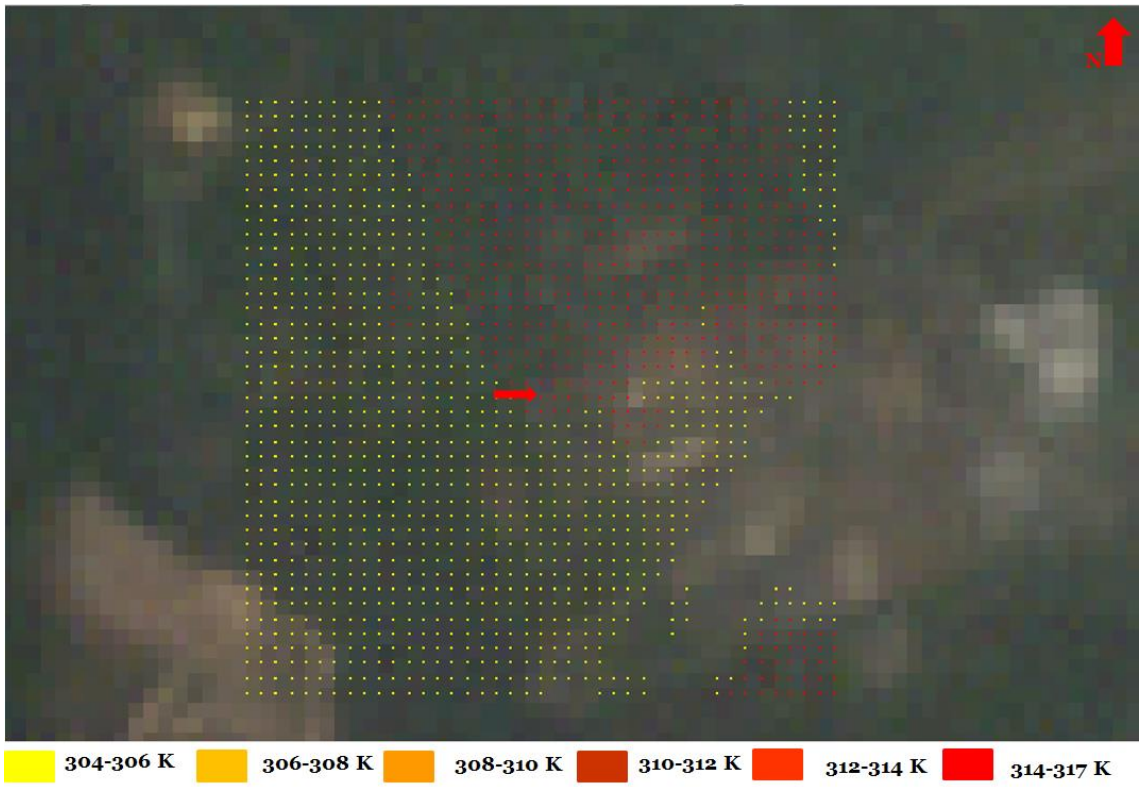

Figure 4.35 A: Eleme Refinery I with LST overlaid

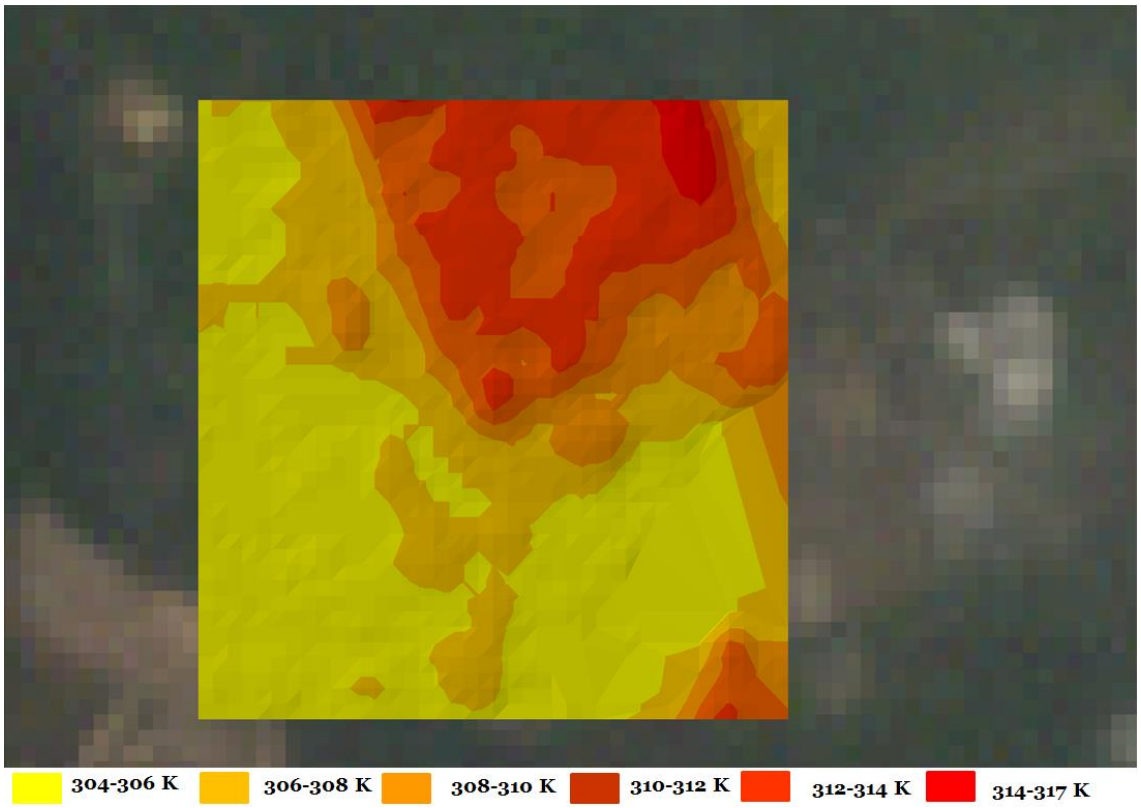

Figure 4.35 B: Eleme Refinery I with LST overlaid showing layers

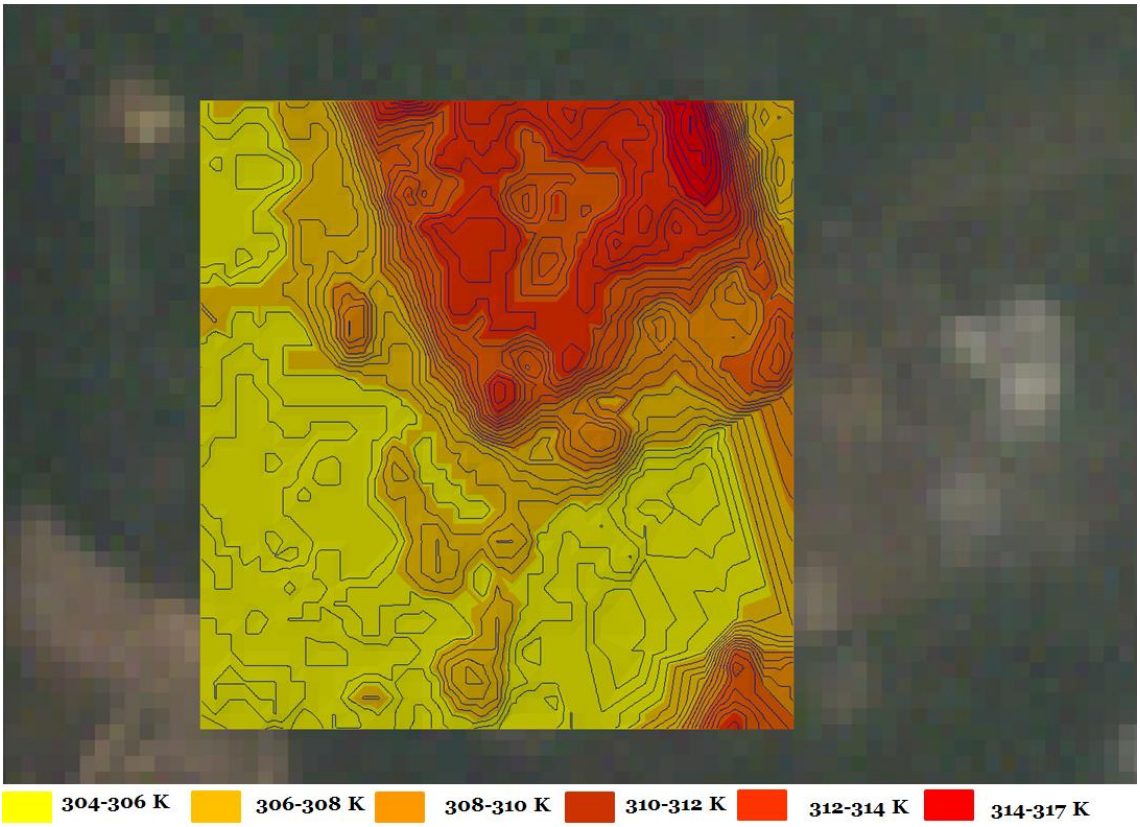

Figure 4.35 C: Eleme Refinery I with LST overlaid showing contours

For Eleme Refinery II (Figures 4.36 A, B and C), six classes of LST values obtained are 316-320 K for pure red points, 312-316 K for light red points, 308-312 K for light brown points, 304-308 K for deep orange points, 300-304 K for light orange points and 296-300 K for yellow points. The plot shows that the flare source has the highest range of values of LST (pure red points) that spread from the centre of the plume downward and toward South-West, West, North-East and East directions. LST recorded in the South-East direction is a mixture of the second (light red points), third (light brown points) and sixth (yellow points) classes of LST with a few of red points (Figure 4.36 A). The North direction comprises of all ranges of LST values and the scene for the figure was acquired on 13 November 2005 with South as the wind direction for the month of the year. The result shows that the influence of the South direction of the prevailing wind does not have significant effect on the flare at the time of

satellite overpass. The size of the plume (red points) in Figures 4.36 A is 11 by 13 pixels.

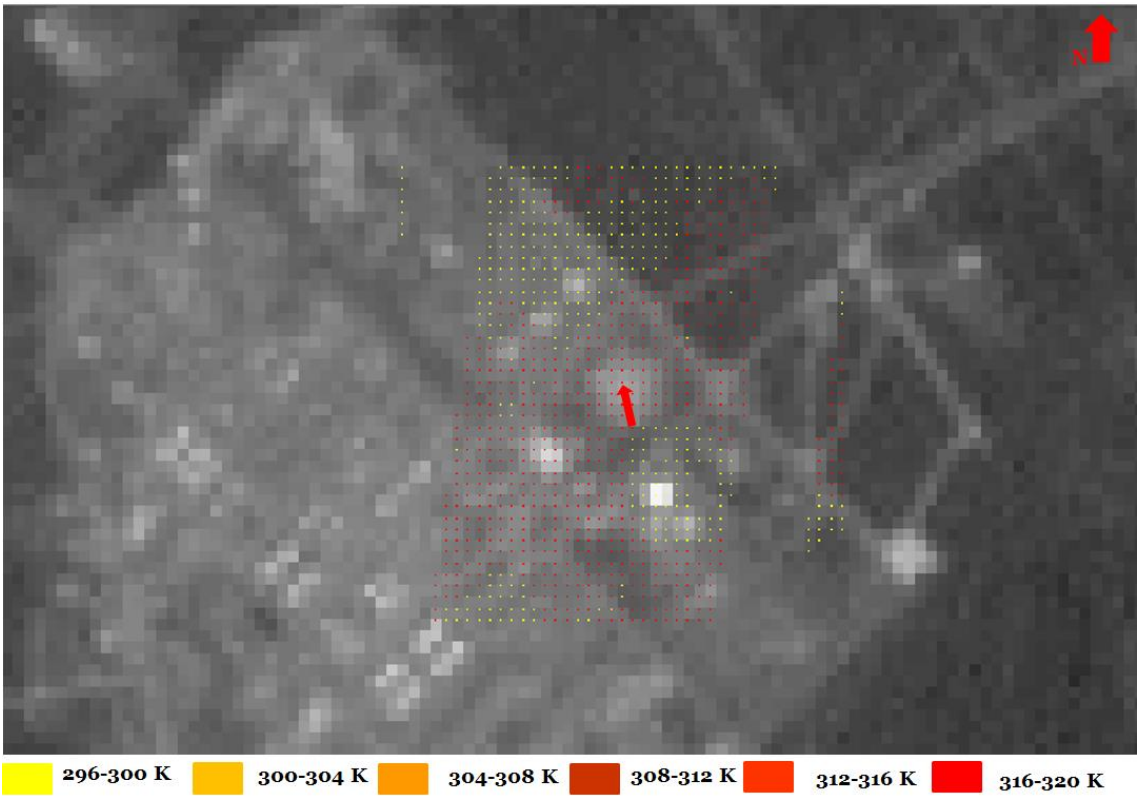

Figure 4.36 A: Eleme Refinery II with LST overlaid

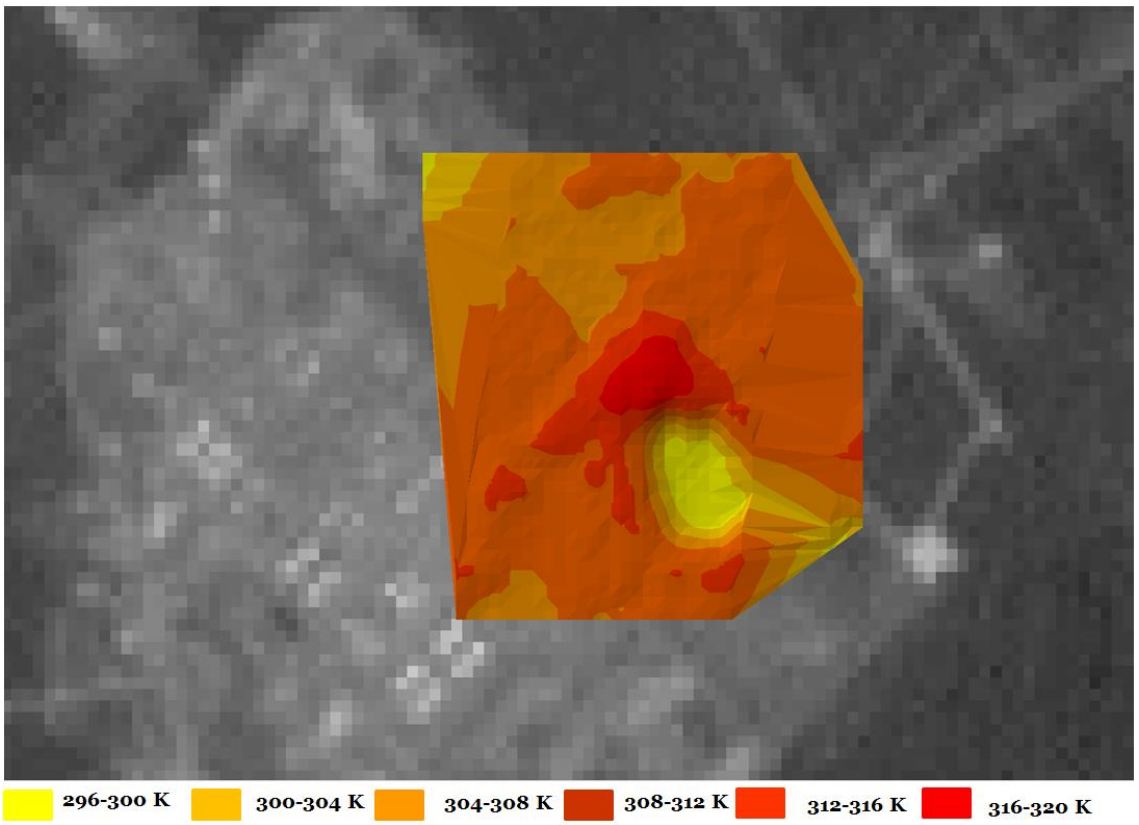

Figure 4.36 B: Eleme Refinery II with LST overlaid showing layers

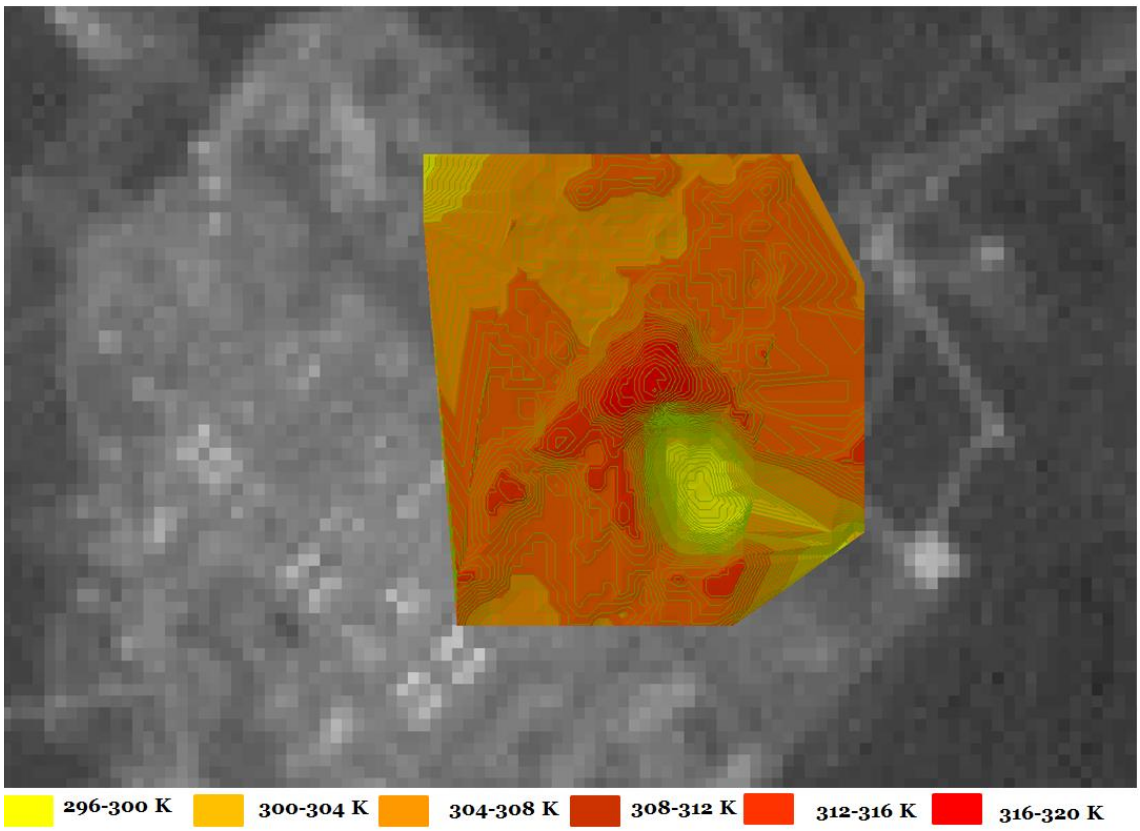

Figure 4.36 C: Eleme Refinery II with LST overlaid showing contours

For Onne Flow Station (Figures 4.37 A, B and C), six classes of LST values acquired are 310-317 K for pure red points, 304-310 K for light red points, 298-304 K for light brown points, 292-298 K for deep orange points, 286-292 K for light orange points and 274-286 K for yellow points. The scene used for production of the figure was acquired on 8 March 2013 and the direction of wind for that month of the year was South. The North, North-West, North-East and West directions of Figures 4.37 A, B and C are dominated by the first three highest ranges of LST values, pure red; light red and light brown points. The result shows that the South direction of the prevailing wind in the Niger Delta has significant effect on the flare which confirms South as the wind direction for the date of the acquisition of the scene that produced Figures 4.37 A, B and C. The wind that blew from the South was strong towards the North, North-West, North-East and West directions. The actual size of the plume is not available

due to missing data points caused by the effect of scan line correction on Landsat 7 ETM+

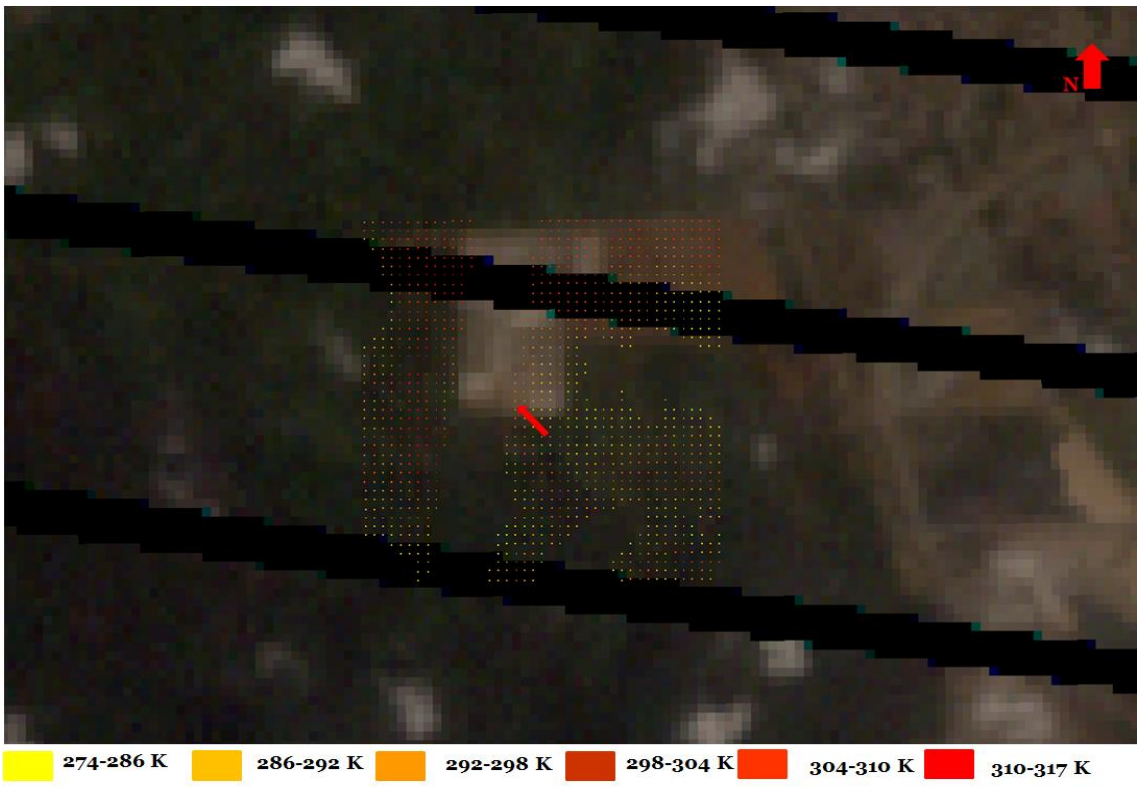

Figure 4.37 A: Onne Flow Station with LST overlaid

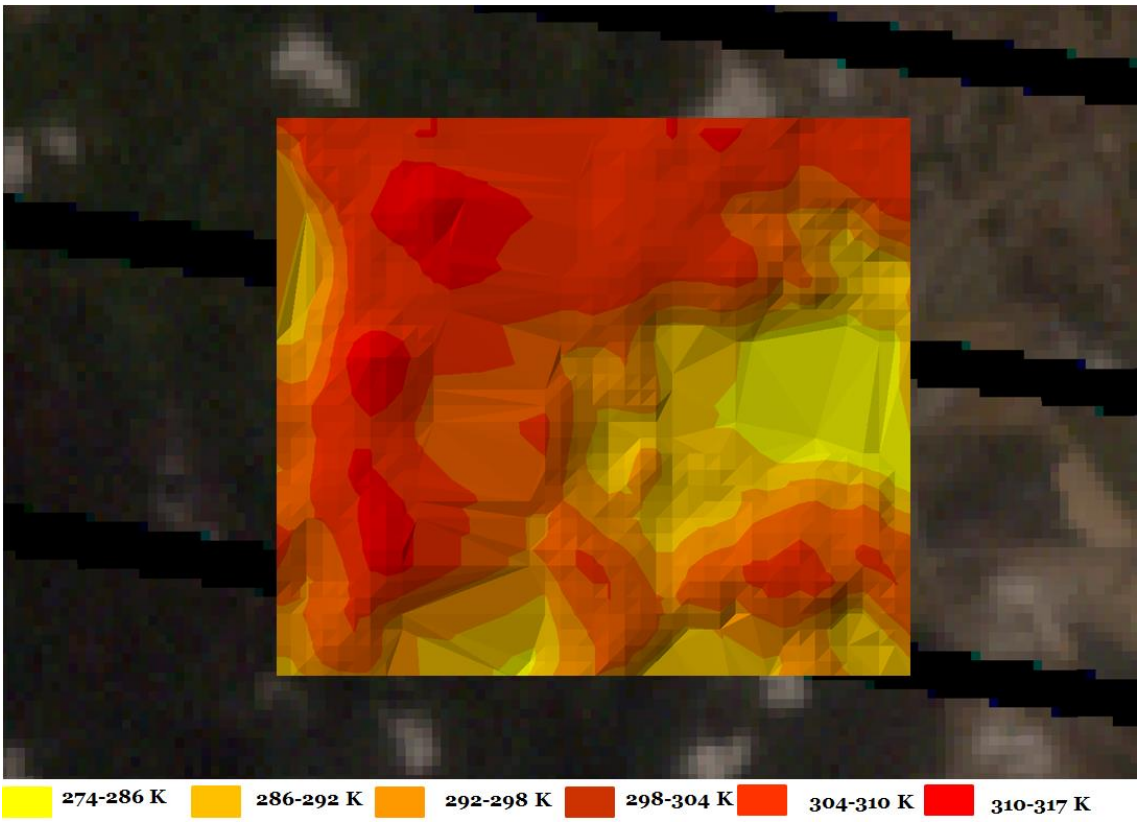

Figure 4.37 B: Onne Flow Station with LST overlaid showing layers

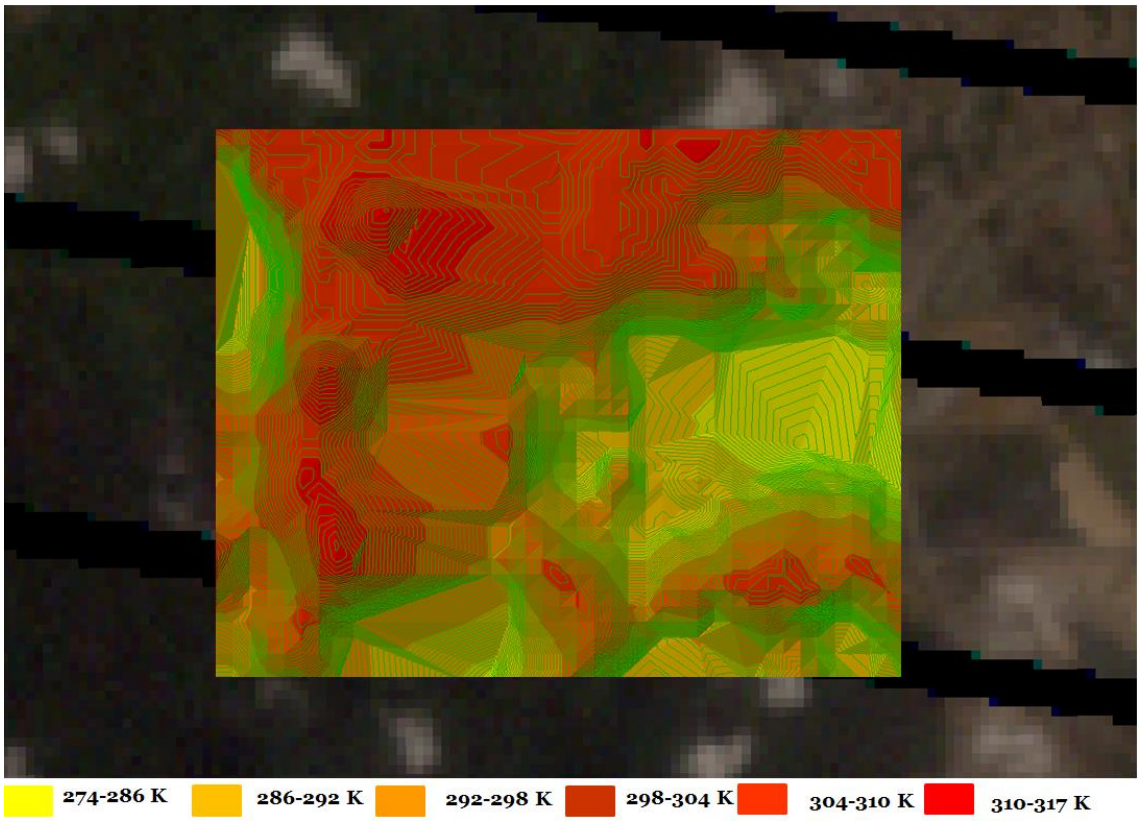

Figure 4.37 C: Onne Flow Station with LST overlaid showing contours

For Umurolu Flow Station (Figures 4.38 A, B and C), 308-318 K (pure red points), 306-308 K (light red points), 304-306 K (light brown points), 301-304 K (deep orange points), 297-301 K (light orange points) and 290-297 K (yellow points) are six ranges of LST values obtained. The scene used for the production of Figures 4.38 A, B and C was acquired on 17 April 2010 with South as the direction of wind for the month of April for that year. The result shows that pure red, light red and light brown points in the South is more than that of the North (Figure 4.38 A). Also, the North-East and East directions are dominated by classes 1 to 3 (Figure 4.38 A). The size of the plume is 19 by 18 pixels. Also, the South direction of prevailing wind for the Niger Delta does not have effect on the flare because South was hotter than the North. The effect of the flare is more pronounced at the North-East and East directions.

Figure 4.38 A: Umurolu Flow Station with LST overlaid

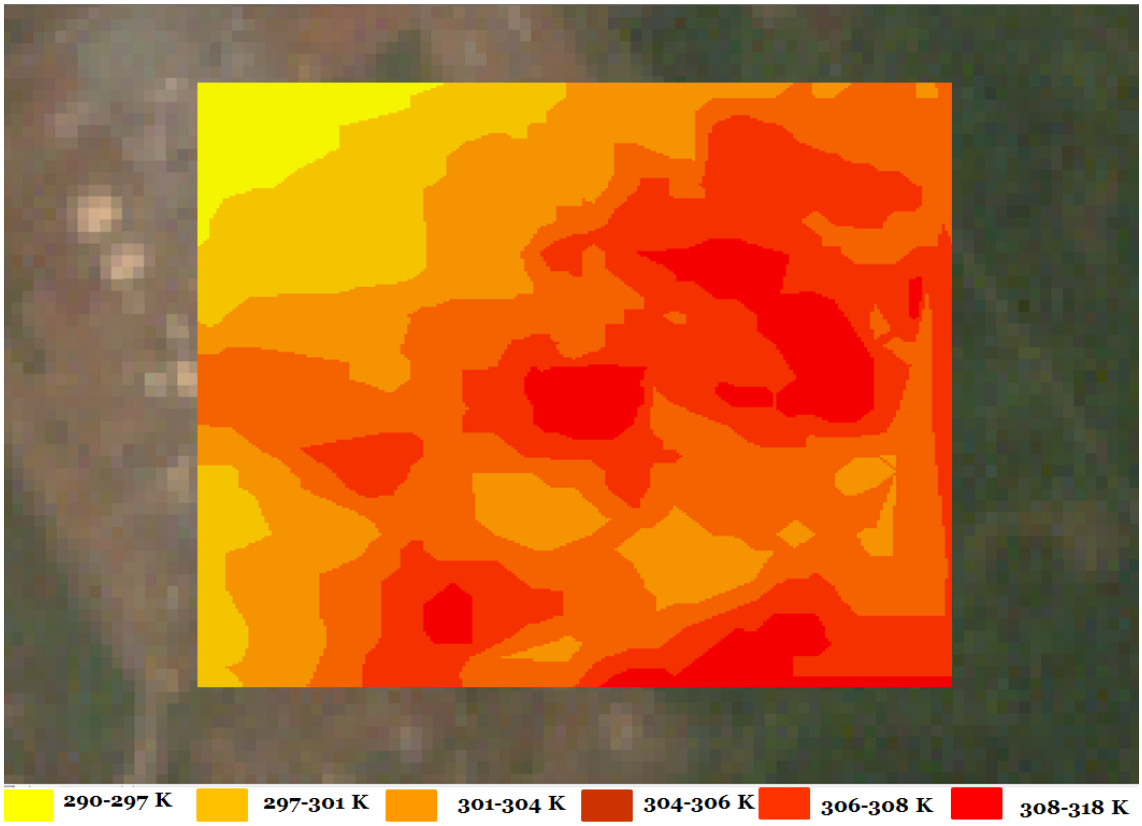

Figure 4.38 B: Umurolu Flow Station with LST overlaid showing layers

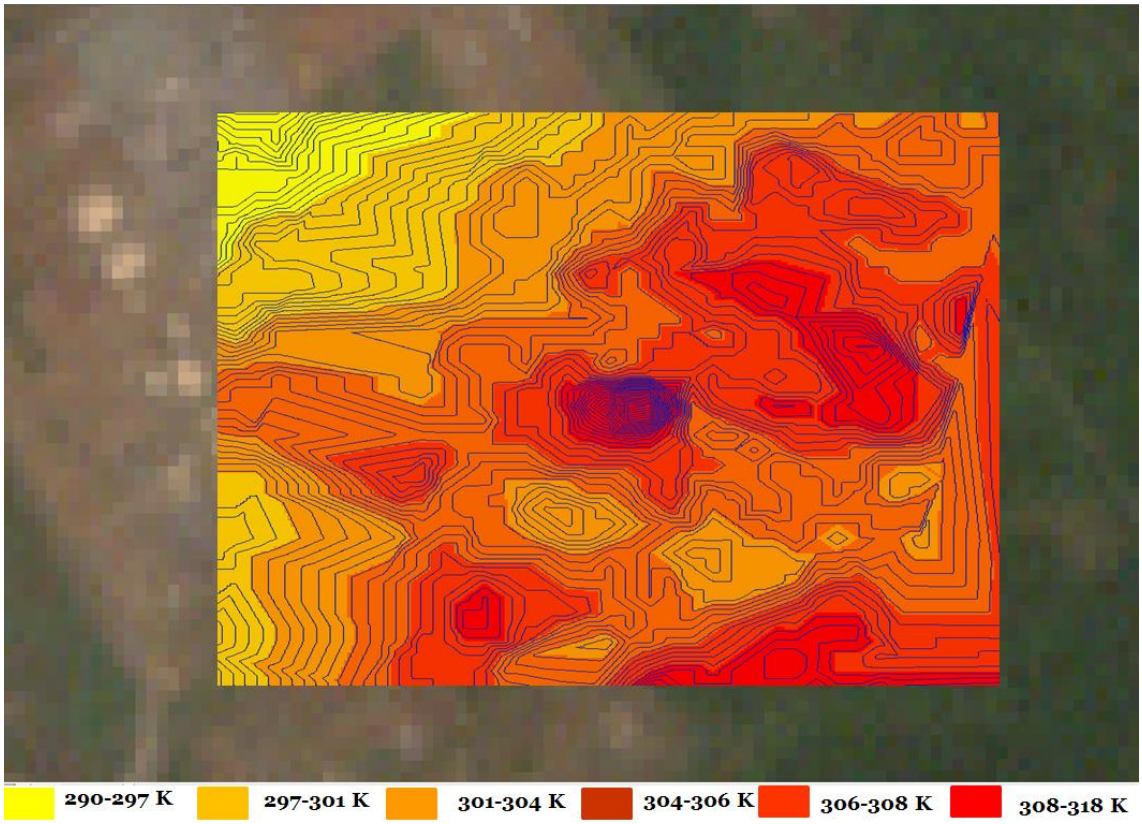

Figure 4.38 C: Umurolu Flow Station with LST overlaid showing contours

Six classes of the range of LST values for Bonny LNG (Figures 4.39 A, B and C) are 332-358 K (pure red points), 320-332 K (light red points), 317-320 K (light brown points) and 313-317 K (deep orange points), 309-313 K (light orange points) and 301-309 K (yellow points). The scene used for the production of Figures 4.39 A, B and C was acquired on 8 January 2003 and the direction of wind for that month of the year in the Niger Delta was South. The North and North-West directions of the Figures 4.39 A, B and C were dominated by the three lowest LST values (Figure 4.39 A). The flare source (centre), East, part of North-East and South-East were dominated by the first three highest LST values (Figure 4.39 A). The problem of missing data points affected the South and West directions of the scene and has much influence on the analysis of the results. The size of the plume for this scene is 16 by 15 pixels. In summary, the impact of the flare is more at those areas surrounding the flare stack and

towards the East direction. This result suggests that the South direction of the prevailing wind in the Niger Delta does not have significant effect on the flare for this particular scene.

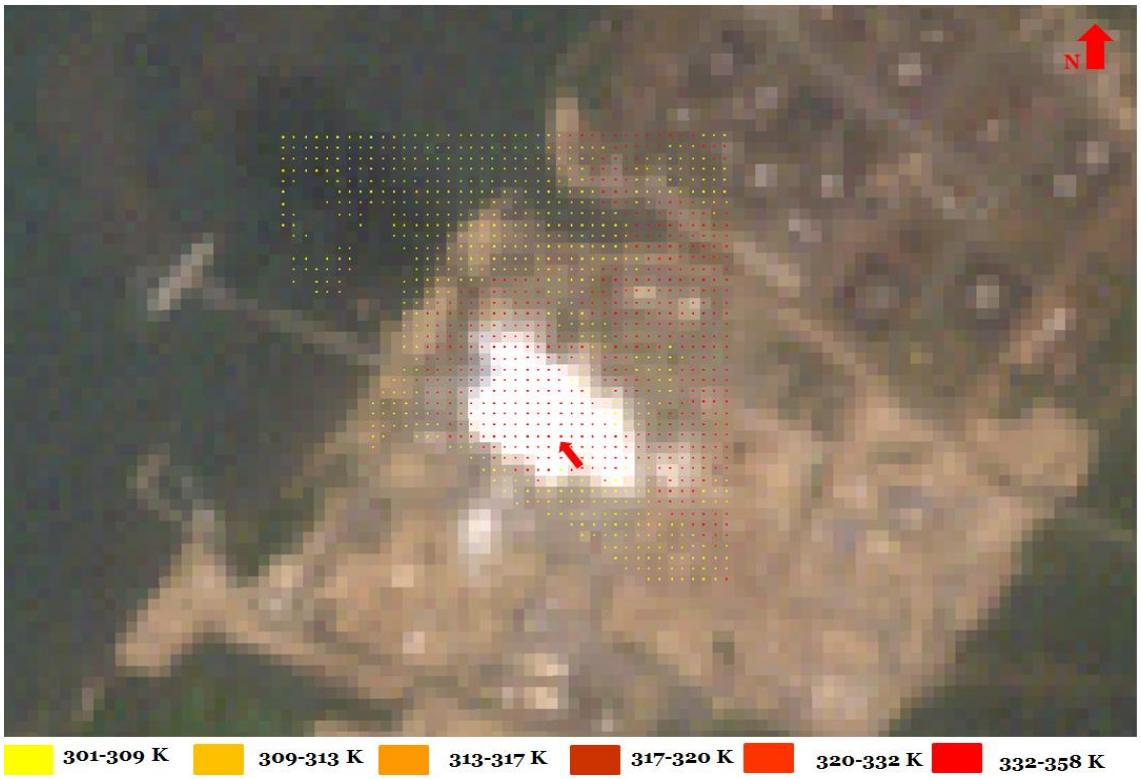

Figure 4.39 A: Bonny LNG Flow Station with LST overlaid

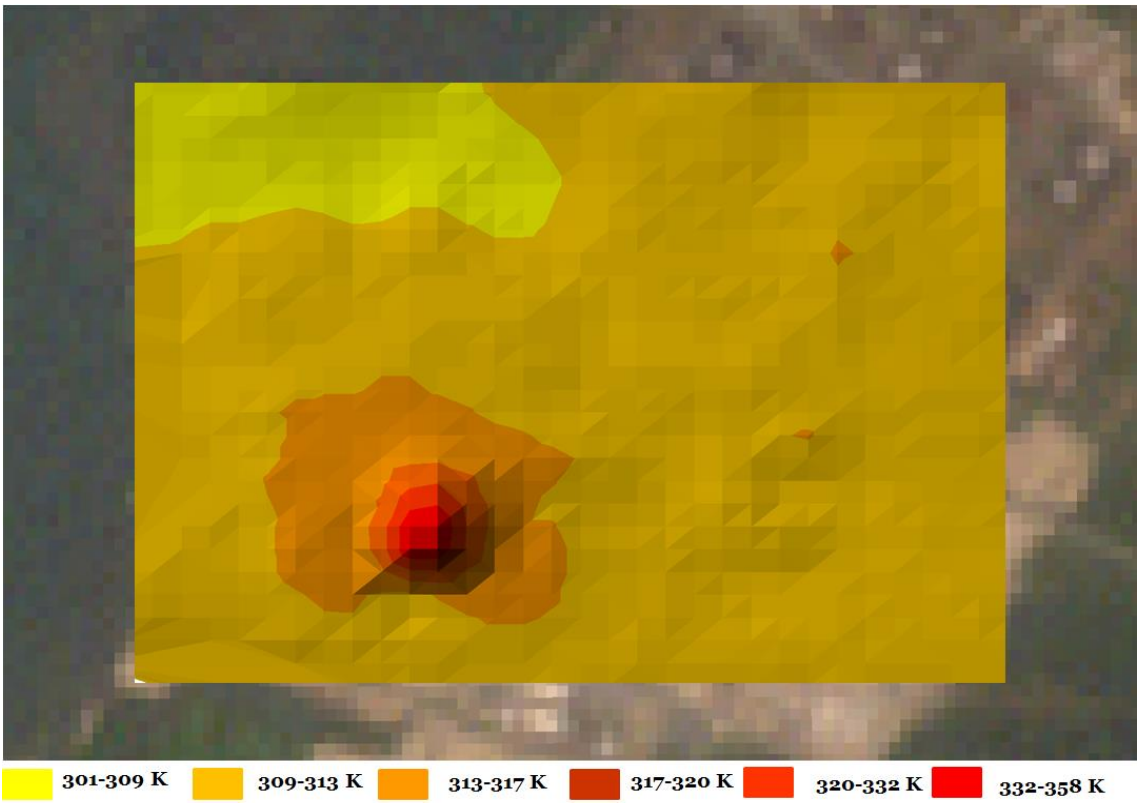

Figure 4.39 B: Bonny LNG Flow Station with LST overlaid showing layers

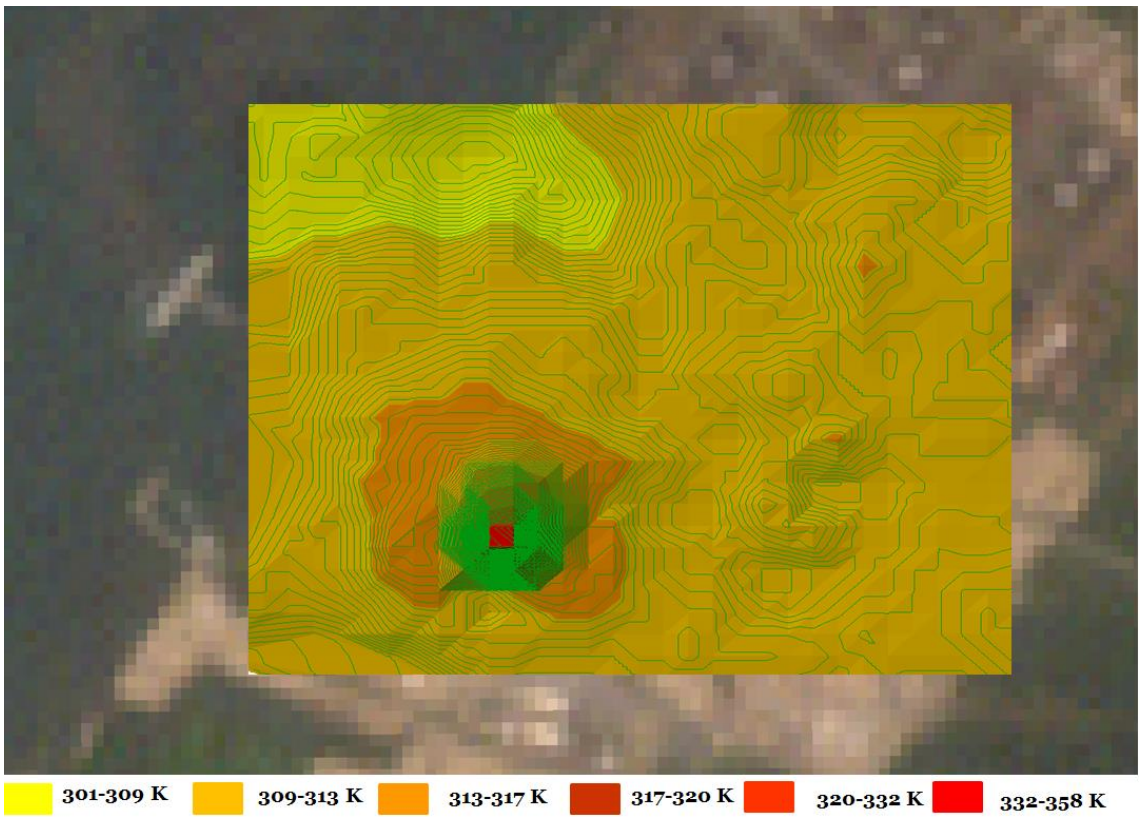

Figure 4.39 C: Bonny LNG Flow Station with LST overlaid showing contours

For Alua Flow Station (Figures 4.40 A, B and C), six classes of LST values obtained are 343-350 K (pure red points), 335-343 K (light red points), 327-335 K (light brown points), 319-327 K (deep orange points), 311-319 K (light orange points) and 304-311 K (yellow points). The scene used for the processing of Figures 4.40 A, B and C was acquired on 19 December 1986. The meteorological data obtained could not cover 1986 and so the wind direction for this date is unknown. The surrounding of the flare stack is dominated by the third higher values of LST, the North-East, East and South-East directions comprises of the first three higher LST values (Figure 4.40 A). Also, the result suggests low burning at the time of satellite overpass for the acquisition of the scene. Also, the South direction of the prevailing wind in the Niger Delta has no or little influence on the results obtained. The dimension of the plume gives 10 by 7 pixels.

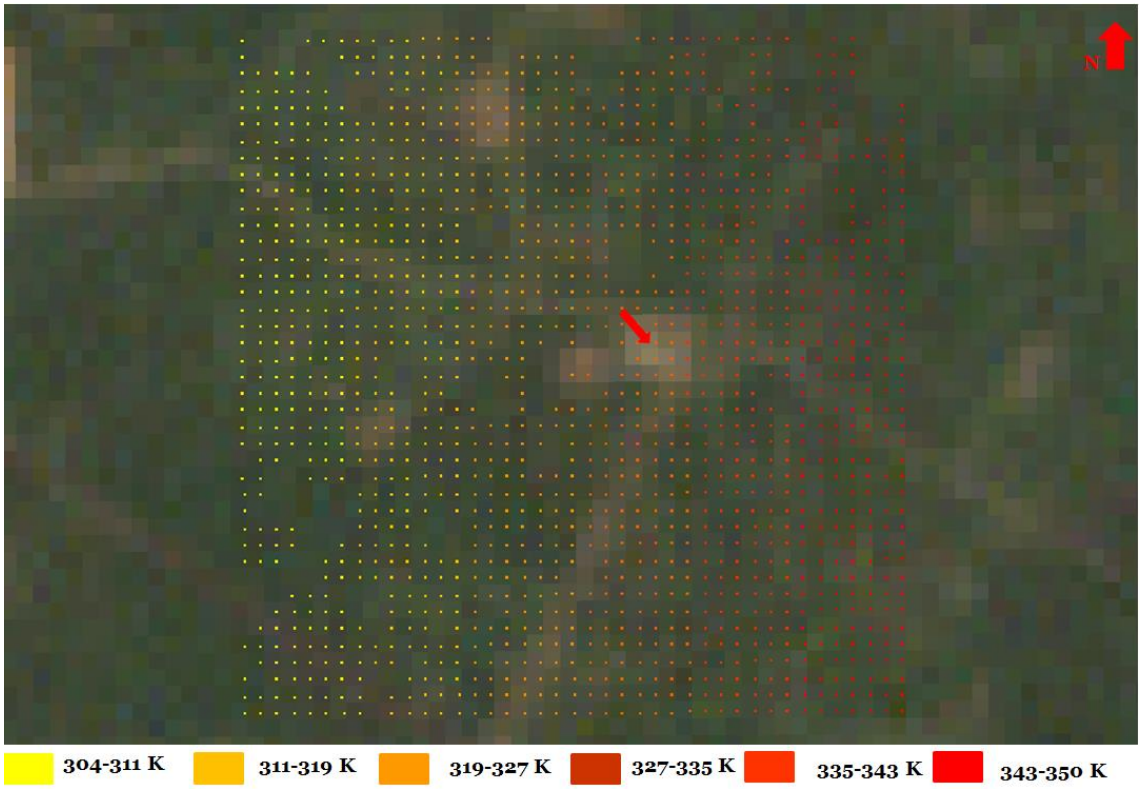

Figure 4.40 A: Alua Flow Station with LST overlaid

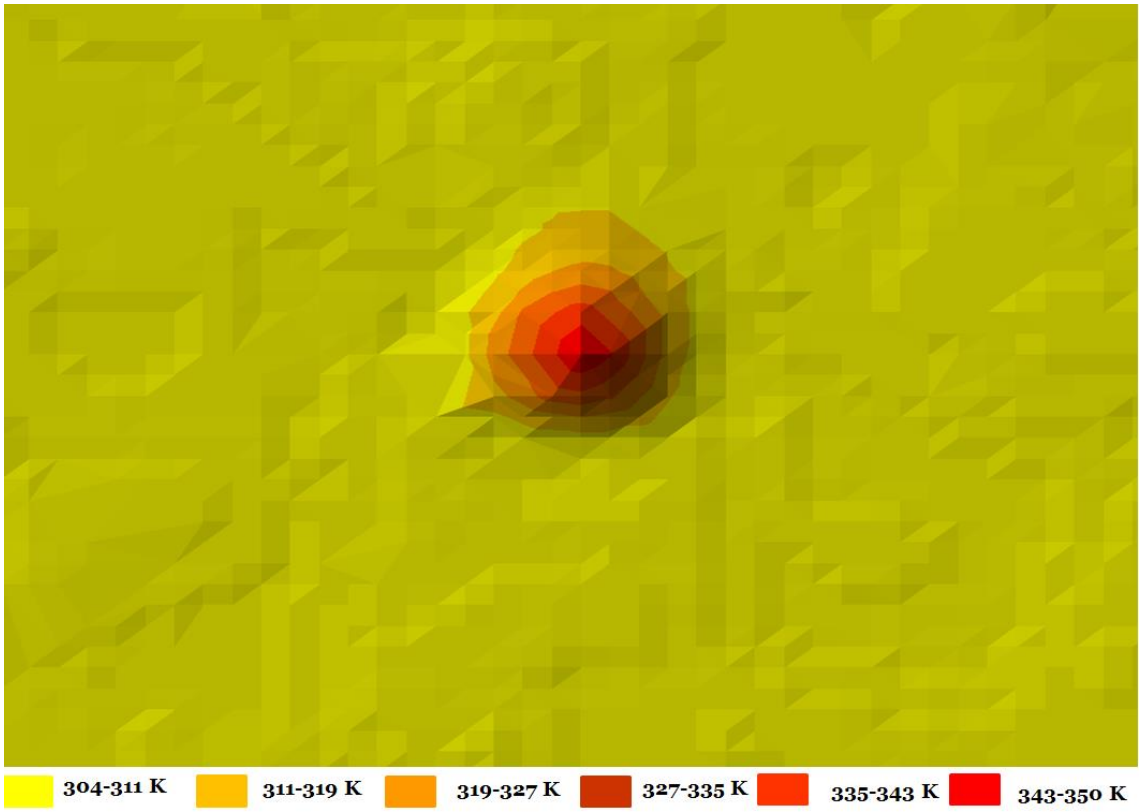

Figure 4.40 B: Alua Flow Station with LST overlaid showing layers

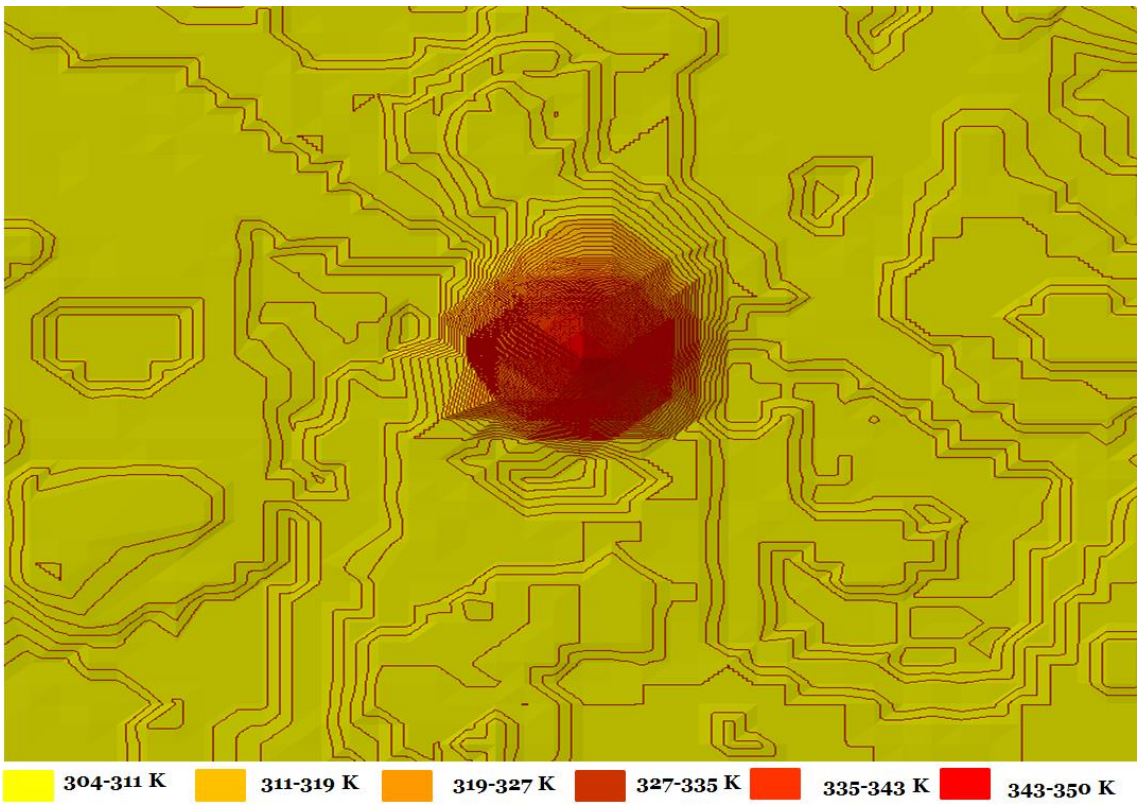

Figure 4.40 C: Alua Flow Station with LST overlaid showing contours

For Rukpokwu Flow Station (Figures 4.41 A, B and C), six classes of LST values recorded are 313-324 K (pure red points), 307-313 K (light red points), 304-307 K (light brown points), 302-304 K (deep orange points), 300-302 K (light orange points) and 298-300 K (yellow points). Figures 4.41 A, B and C were generated from a scene that was acquired on 13 January 2005 and the wind direction for that month of the year was West. In Figures 4.41 A, B and C, the fifth and sixth ranges of LST values dominated the results. The flare source shows the highest values of LST and followed by the surrounding pixels in the order of their closeness. The problem of cloud cover and missing data due to scan line correction error for Landsat 7 ETM+ also affects the analysis of the results. The result shows that the influence of the South direction of the prevailing wind in the Niger Delta could not have strong impact on the flare (Figure 4.41 A). The size of the plume obtained from this scene is 11 by 9 pixels.

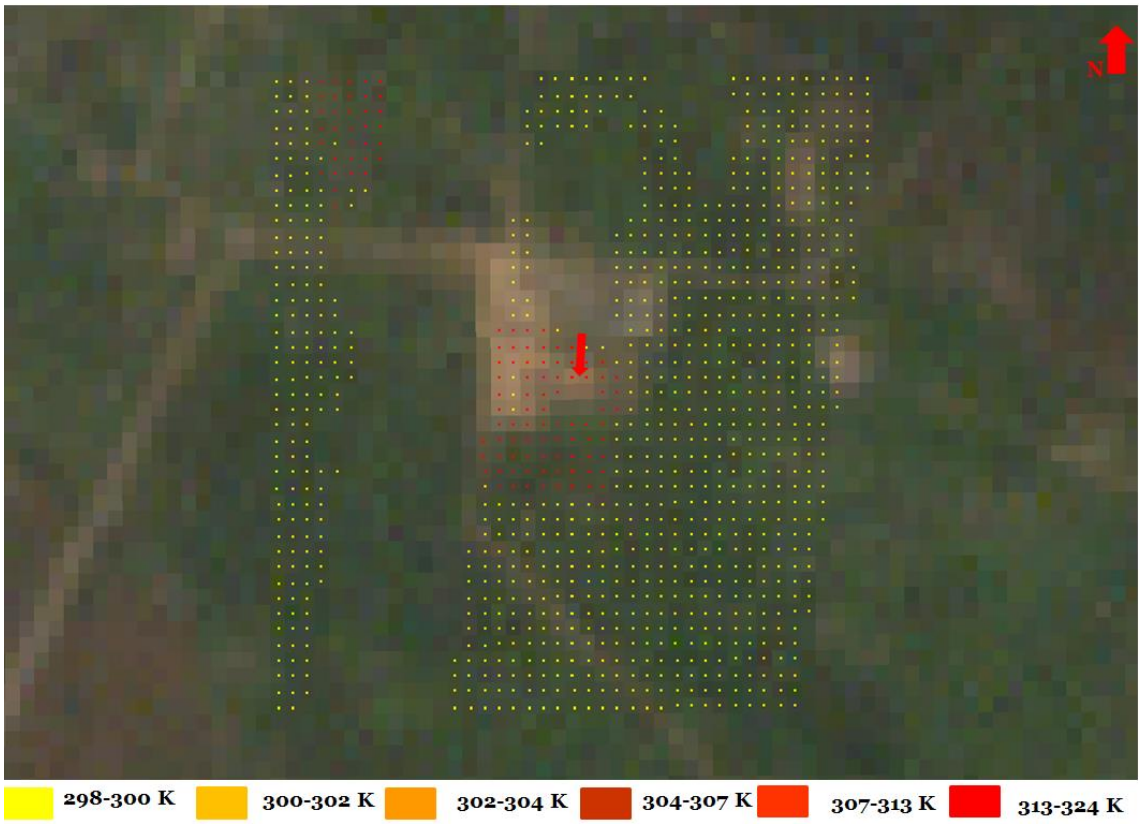

Figure 4.41 A: Rukpokwu Flow Station with LST overlaid

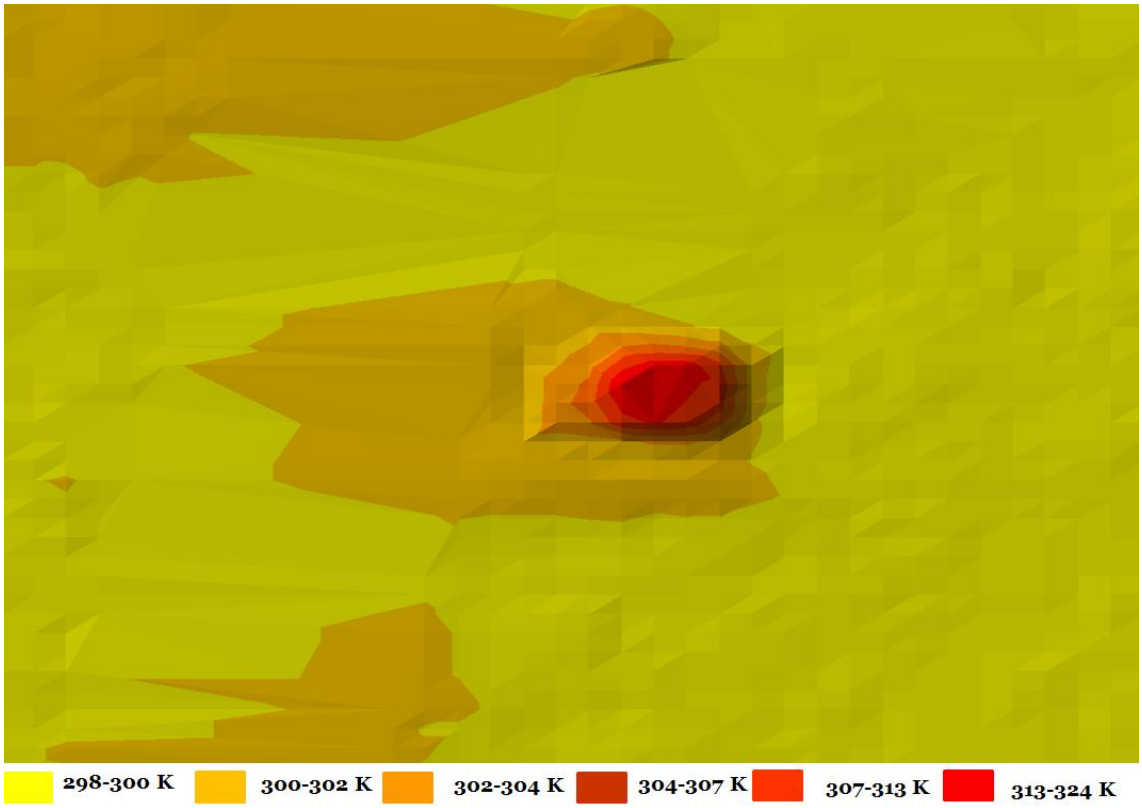

Figure 4.41 B: Rukpokwu Flow Station with LST overlaid showing layers

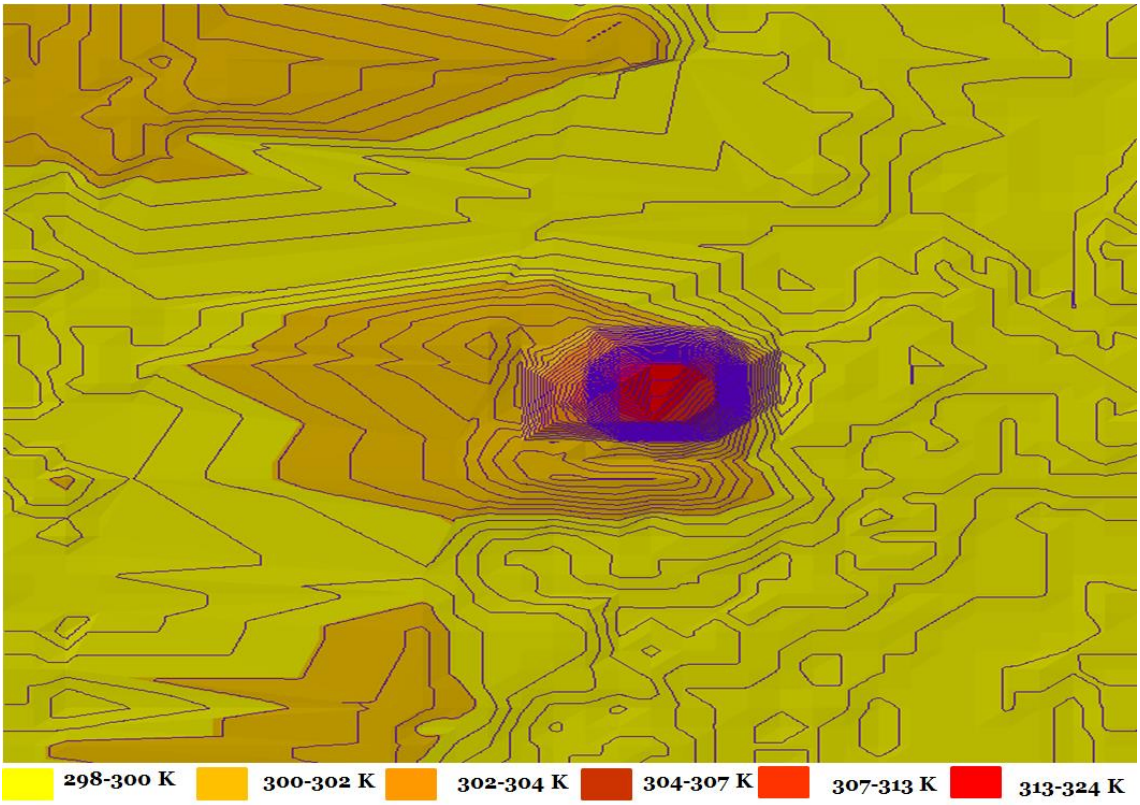

Figure 4.41 C: Rukpokwu Flow Station with LST overlaid showing contours

Six classes of the range of LST values for Obigbo Flow Station (Figures 4.42 A, B and C) are 330-337 K (pure red points), 323-330 K (light red points), 317-323 K (light brown points), 312-317 K (deep orange points), 310-312 K (light orange points) and 307-310 K (yellow points). The acquisition date for the scene used to process Figures 4.42 A, B and C was 22 December 1990 and the meteorological data available is from January 2000 to December 2013. Therefore, the wind direction for the acquisition date of this scene is unknown. Figures 4.42 A, B and C show that the fifth and sixth ranges of LST values dominated the results while the location of the flare stack gives the highest ranges of LST values. The result suggests that the effect of the South prevailing wind direction in the Niger Delta does not have significant influence on the flare at the time of satellite overpass. The flare location and its very immediate surrounding pixels depicted the hottest spot within the site. The size of the plume is 9 by 7 pixels.

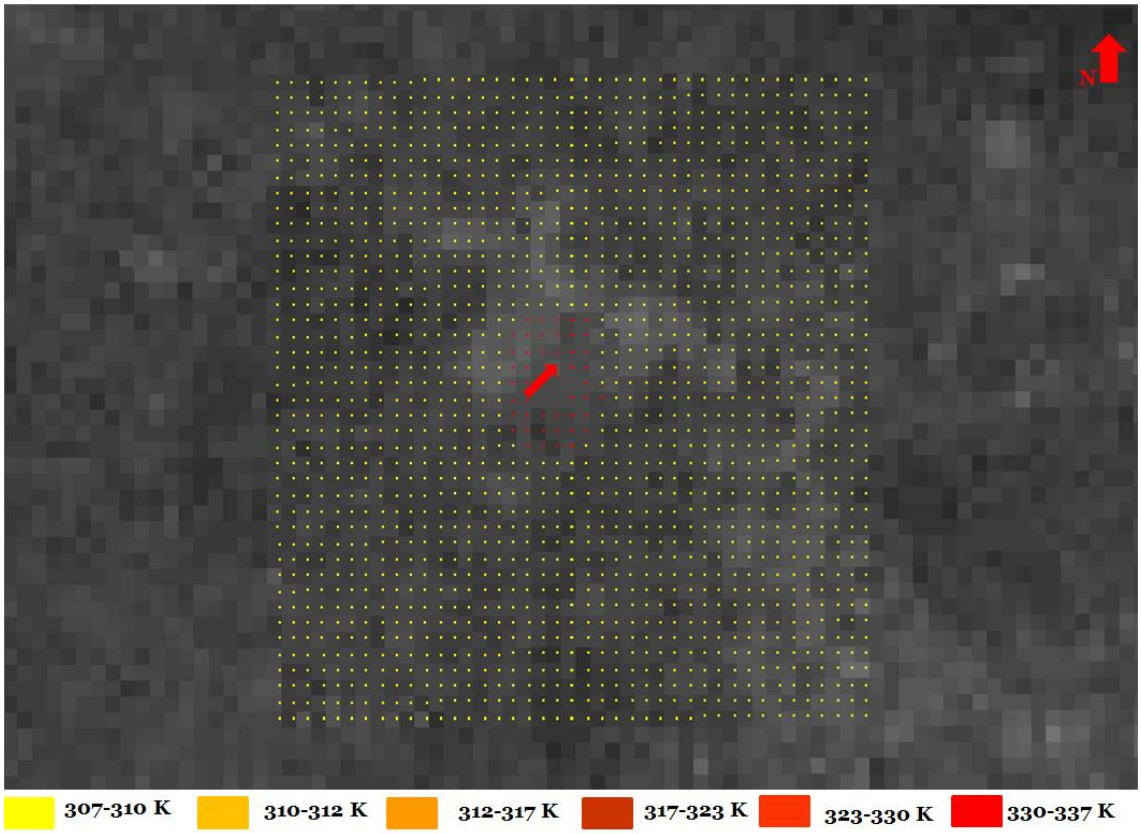

Figure 4.42 A: Obigbo Flow Station with LST overlaid

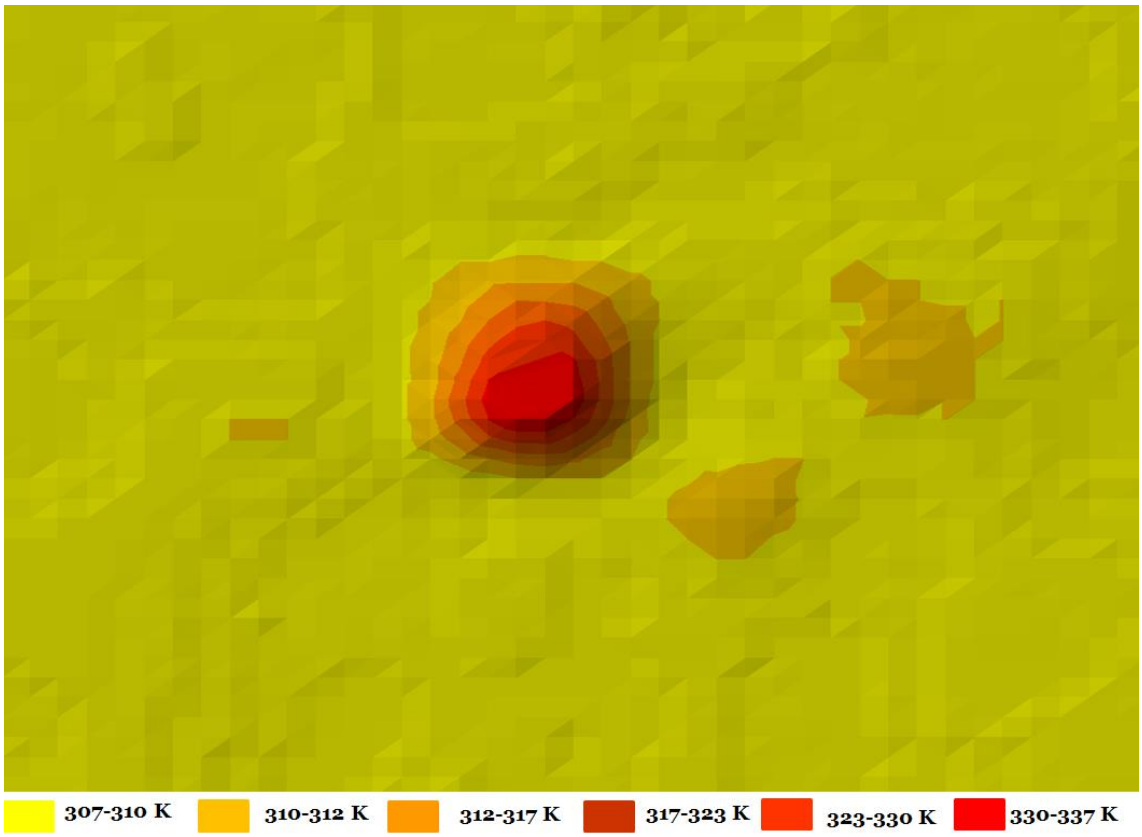

Figure 4.42 B: Obigbo Flow Station with LST overlaid showing layers

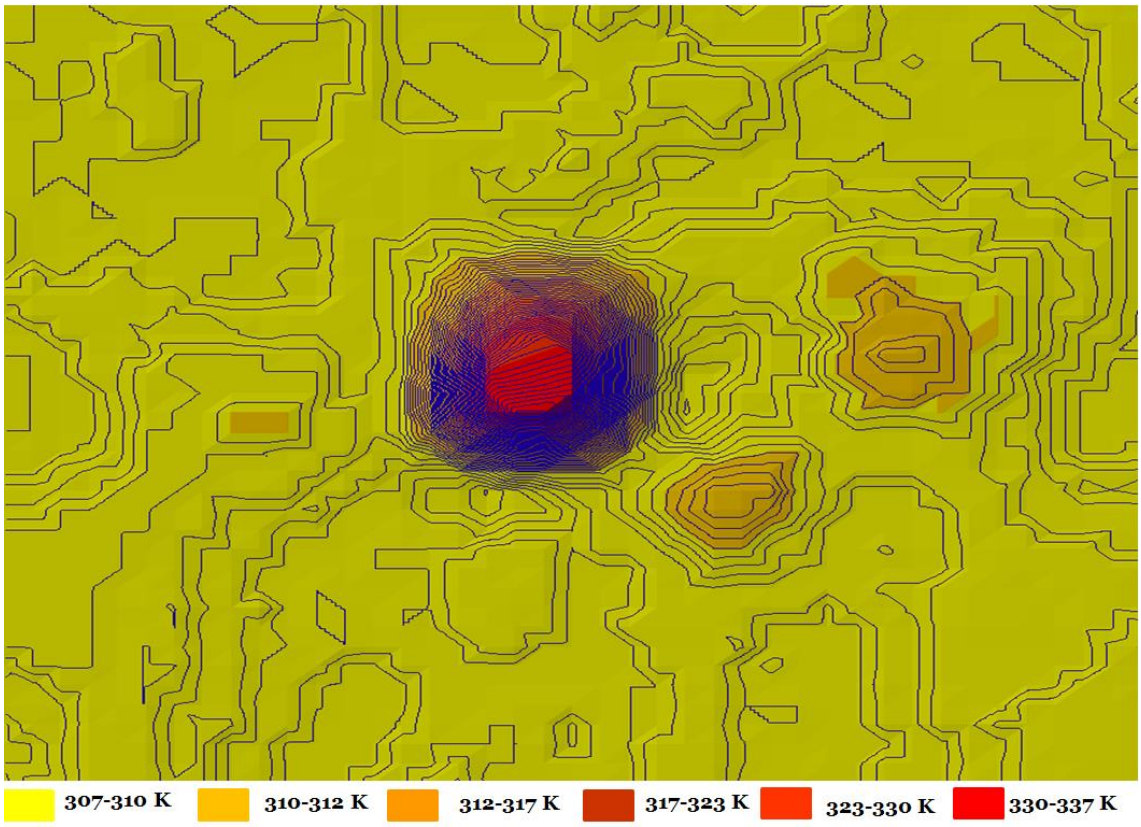

Figure 4.42 C: Obigbo Flow Station with LST overlaid showing contours

For Chokocho Flow Station (Figures 4.43 A, B and C), six classes of the range of LST values are 323-345 K (pure red points), 315-323 K (light red points), 310-315 K (light brown points), 308-310 K (deep orange points), 307-308 K (light orange points) and 305-307 K (yellow points). The wind direction for the acquisition month (21 December 2007) of the scene used for the processing of Figures 4.43 A, B and C was North-East. The result in Figures 4.43 A, B and C shows the extent of the plume from the flare stack; the North direction consists a mixture of LST values for first, second, fifth and sixth classes (Figure 4.43 A); a few locations in the East direction show LST values for the first and second classes (Figure 4.43 A). Also, two LST values for the first class in the South and South-East directions while a single location recorded this LST values in the West direction (Figure 4.43 A). The problem of missing data has greatly influenced the analysis of results for this site. The influence of the North-East

wind direction for the acquisition month of the scene does not have a noticeable impact on the flare because this same North-East direction gives the more values of LST from classes 1 and 2 within the site. However, the effect of the South prevailing wind direction in the Niger Delta is significant causing LST values from the South to be less than that of the North. The size of the plume is 8 by 8 pixels.

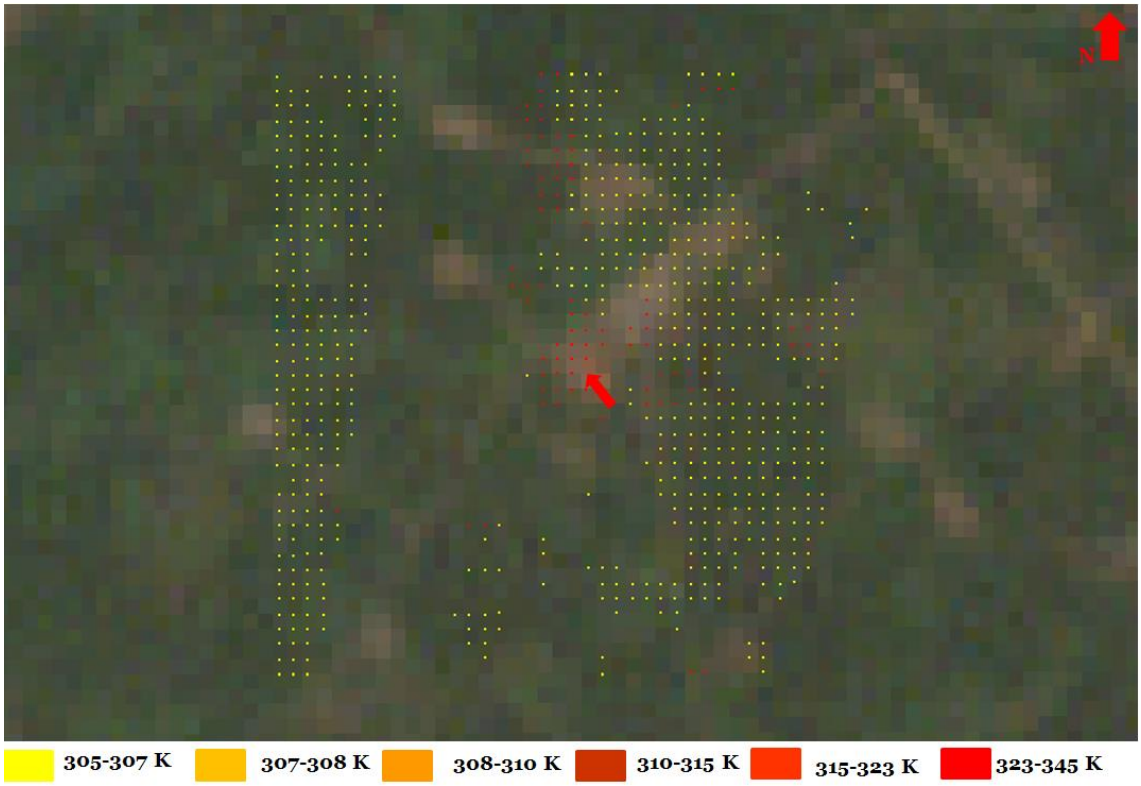

Figure 4.43 A: Chokocho Flow Station with LST overlaid

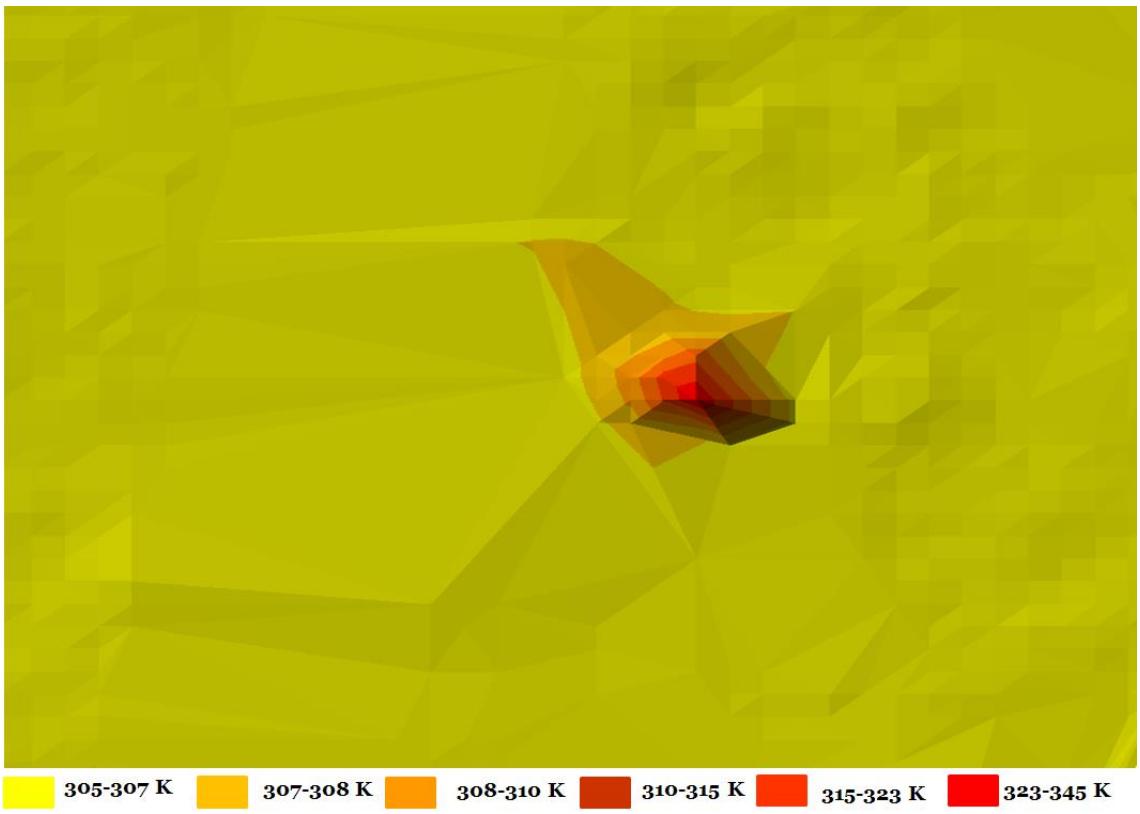

Figure 4.43 B: Chokocho Flow Station with LST overlaid showing layers

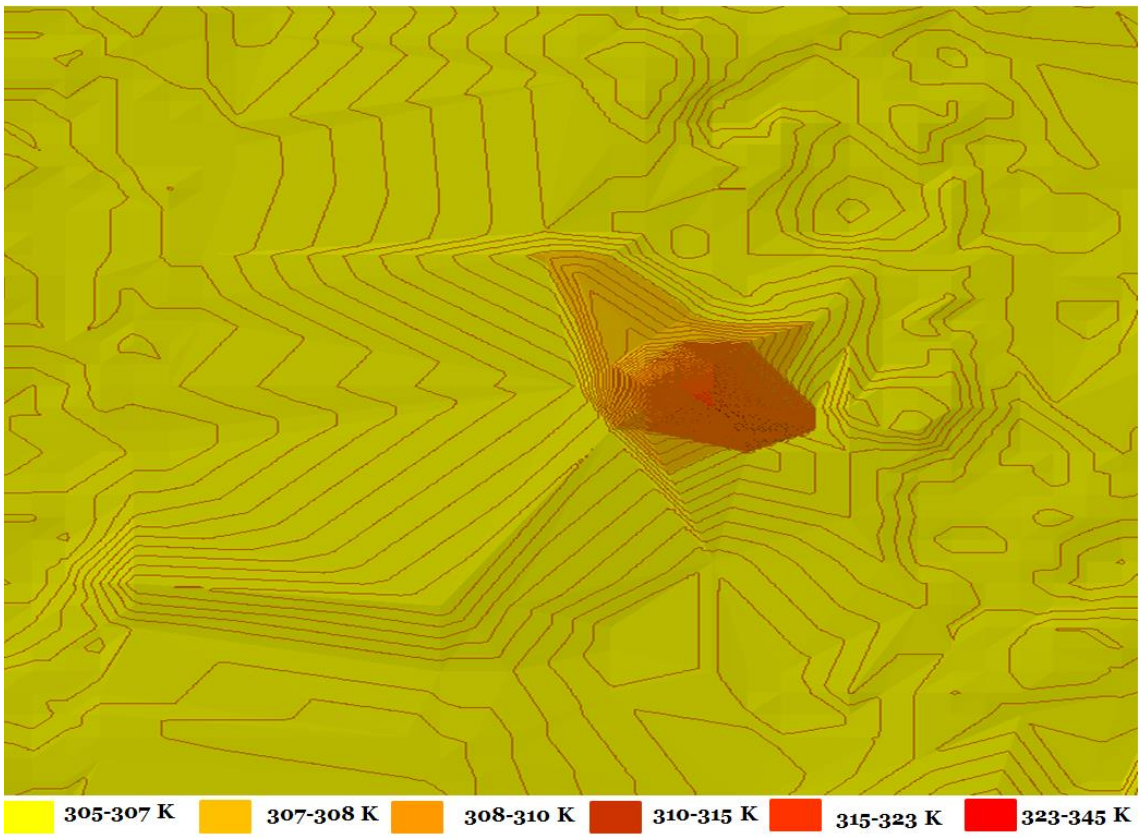

Figure 4.43 C: Chokocho Flow Station with LST overlaid showing contours

Umudioga Flow Station presented six classes of the range of LST values in Figures 4.44 A, B and C as 312-319 K (pure red points), 306-312 K (light red points), 303-306 K (light brown points), 300-303 K (deep orange points), 296-300 K (light orange points) and 290-296 K (yellow points). The result in Figures 4.44 A, B and C shows the extent of the plume from the flare stack and its immediate surrounding pixels gives the highest range of LST values for the scene. The entire result is dominated by LST values from the fourth and fifth classes. Also, there are up to 6 LST values from the third class in the North direction of the scene (Figure 4.44 A). The acquisition date for the scene used to process Figures 4.44 A, B and C was 25 March 1987 that the acquired meteorological data could not cover. The result suggests that the South direction of the prevailing wind for the Niger Delta could not have significant effect on the flare. The dimension of the plume within the site for this scene is 9 by 11 pixels.

Figure 4.44 A: Umudioga Flow Station with LST overlaid

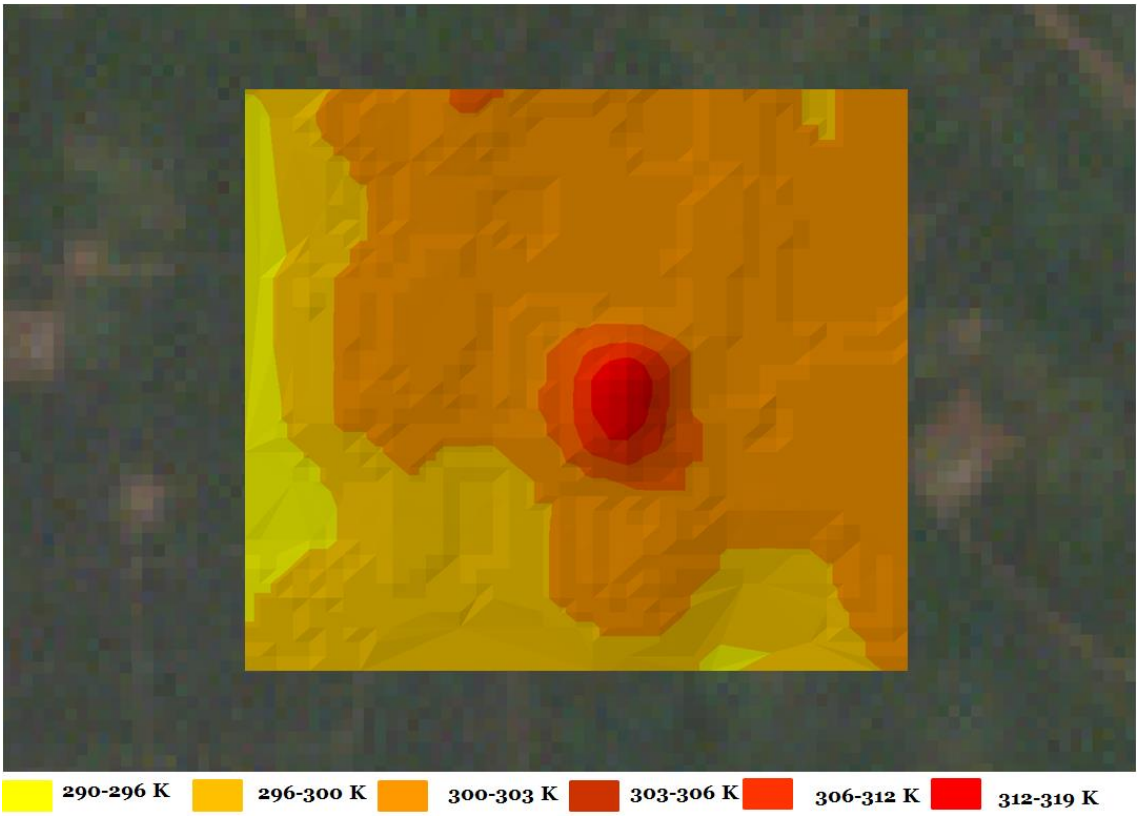

Figure 4.44 B: Umudioga Flow Station with LST overlaid showing layers

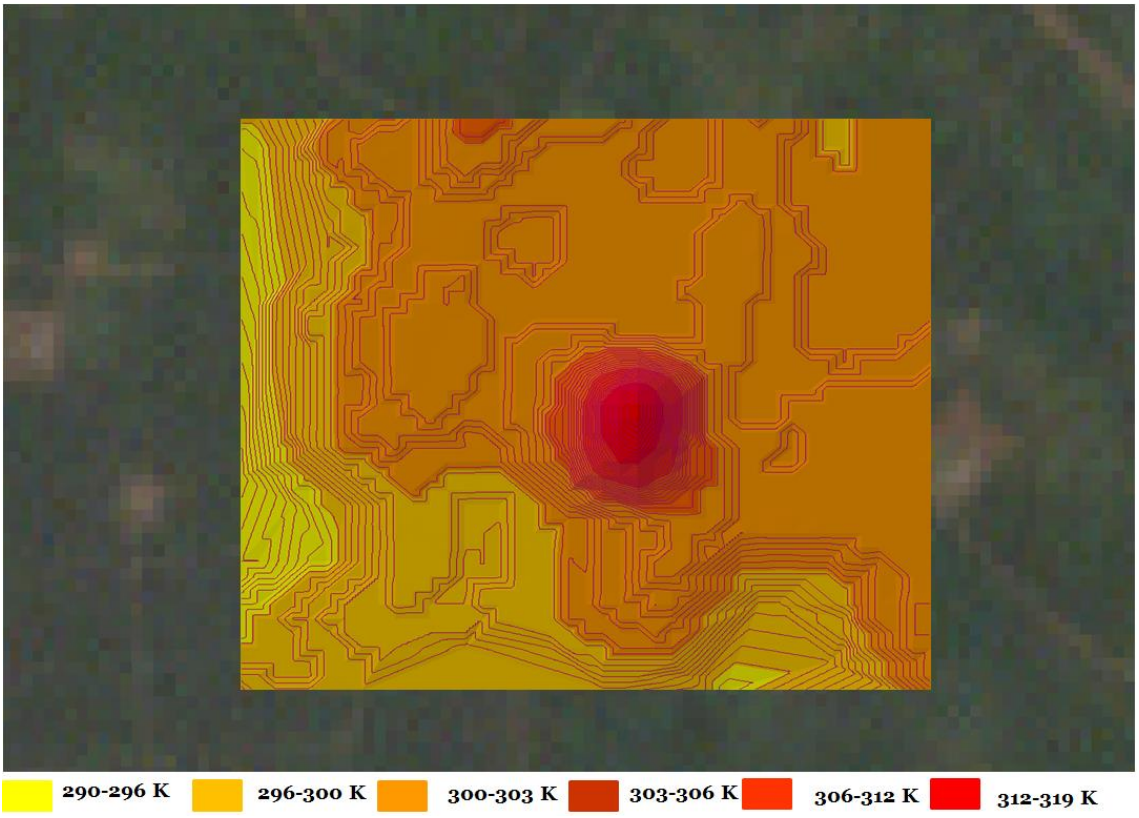

Figure 4.44 C: Umudioga Flow Station with LST overlaid showing contours

Six classes of the range of LST values recorded in Figures 4.45 A, B and C for Sara Flow Station are 321-333 K (pure red points), 313-321 K (light red points), 307-313 K (light brown points), 305-307 K (deep orange points), 302-305 K (for light orange points) and 300-302 K (yellow points). The scene used for the processing of Figures 4.45 A, B and C was acquired on 19 January 2007 and the predominant wind direction for that month of the year 2007 was the West. Throughout the year 2007 the direction of wind in the Niger Delta was the West except North-East for December. The LST values in Figures 4.45 A, B and C shows that both two flares were active at the time of satellite overpass and so their locations and immediate surroundings are the hottest spots (Figure 4.45 A). The LST values were dominated by the fifth and sixth classes. Furthermore, the problem of missing data has affected the analysis of this result. Also, the result suggests that the influence of the West direction of the prevailing wind for the acquisition month of the scene could not impact flares at the time of satellite overpass. The dimension of the plume obtained from this scene for both two flares are 6 by 6 pixels and 4 by 5 pixels.

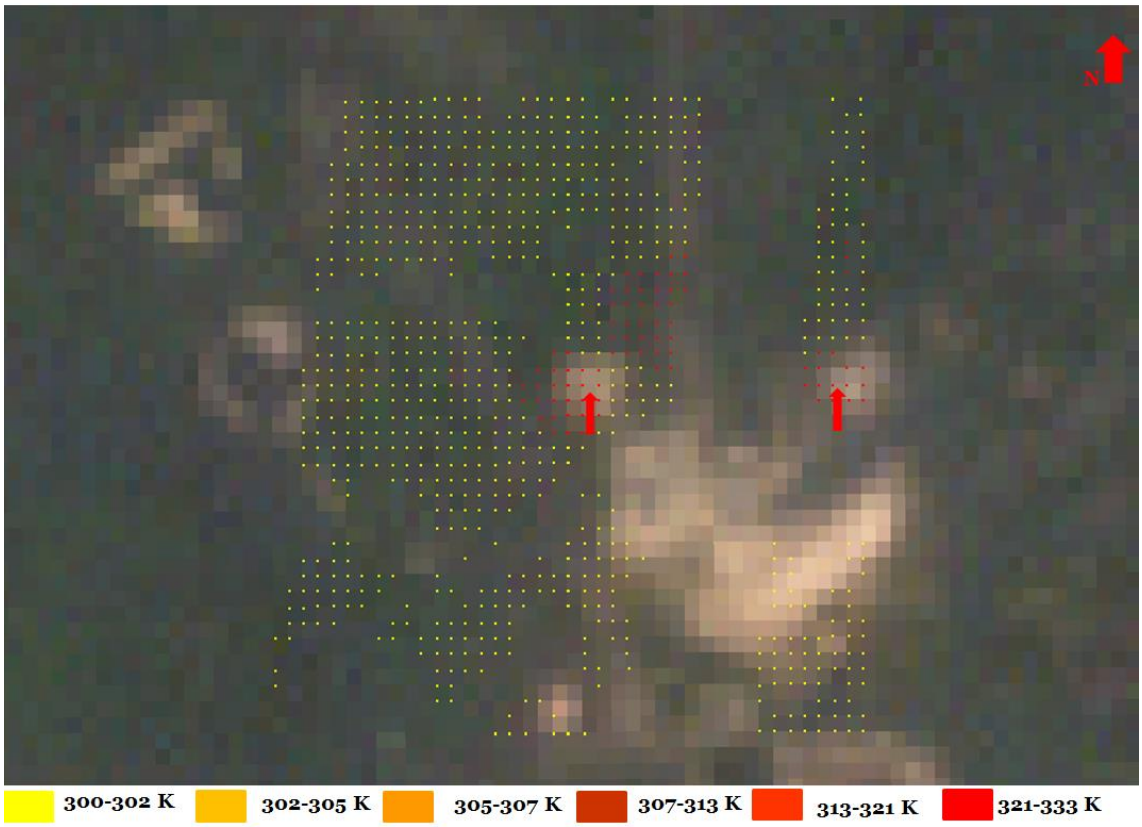

Figure 4.45 A: Sara Flow Station with LST overlaid

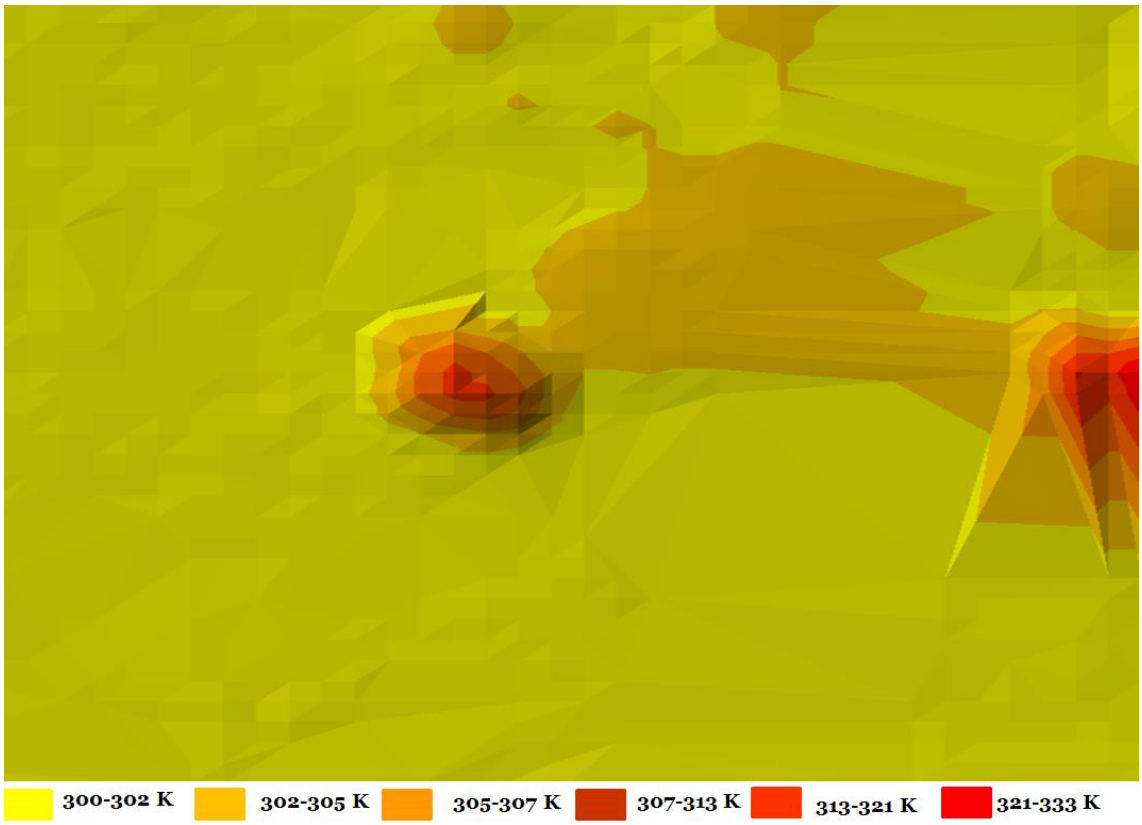

Figure 4.45 B: Sara Flow Station with LST overlaid showing layers

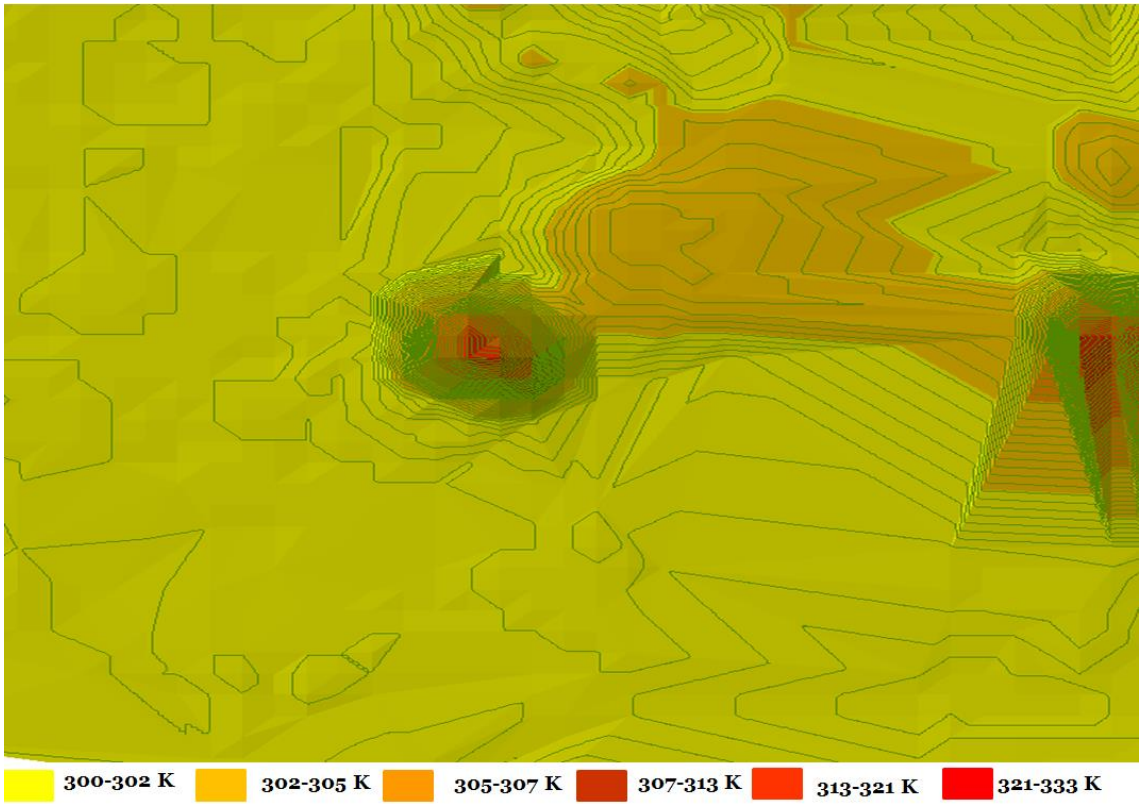

Figure 4.45 C: Sara Flow Station with LST overlaid showing contours

In summary, it is observed that the size and shape of the plume differ from one oil facility to another. For example, the sizes of the plume for the bigger facilities are 21 by 23 pixels for Eleme Refinery I, 11 by 13 pixels for Eleme Refinery II, 19 by 18 pixels for Umurolu and 16 by 15 pixels for Bonny LNG respectively. For the medium and small facilities the sizes of the plume recorded are 10 by 7 pixels for Alua Flow Station, 11 by 9 pixels for Rukpokwu Flow Station, 9 by 7 pixels for Obigbo Flow Station, 8 by 8 pixels for Chokocho Flow Station, 9 by 11 pixels for Umudioga Flow Station and 6 by 6 pixels and 4 by 5 pixels for both flares at Sara Flow Station. These results show that the sizes of the plumes from the bigger oil facilities are larger than those obtained from the medium and small facilities. Therefore, the result suggests that the major factors that determine the size of the plume are the size of facility, volume of burning gas and the rate of its burning at the time of satellite overpass.

4.4.1.2 Four cardinal directional analyses

In order to explore the acquired (LST and NDVI) results, LST gradients along the four cardinal directions (North, East, South and West) were extracted. Four cardinal directions have been applied previously by some researchers and they recorded reliable results, for example, Barnie and Oppenheimer (2015) used four cardinal directions when extracting volcanic high temperature event (HTE) radiance from SEVIRI images and correcting for saturation using Independent Component Analysis (ICA) method. They concluded that the methodology can, in principle, be extended to studies of other kinds of HTEs such as those associated with biomass burning. Also, Vastaranta et al. (2015) worked on measurements of forest sample plots to obtain inventory attributes using four cardinal directions technique for the purpose of evaluation of a Smartphone.

Alhaji (2011) employed four cardinal directions method for the assessment of air toxic near oil and gas drilling site. Furthermore, Aubrecht, et al. (2008) applied four cardinal directions to assess reef location points in order to prevent them from being wrongly located. In this study, for each direction, the pixels adjacent to the flare stack were used as the starting point. LST was then averaged for the four pixels either side of the flare in a given direction, and a nine-pixel average was calculated at successive distances from the flare of up to 14 pixels, or 450 m from the flare i.e. mean LST data in each direction has a dimension of 14 rows and 9 columns. Figure 4.46 is the schematic diagram showing the four cardinal direction plots of the results with the centre marked red colour indicating the pixel for the flare stack and an arrow pointing to the North direction; the distance intervals are 30 m, 60 m and 120 m, which corresponds to the resampled and native resolution of thermal Landsat 7 ETM+ and Landsat 5 TM

pixel size. Mean and standard deviation were computed from the nine pixels at each distance from the stack then LST and NDVI were plotted for each direction against distance from the flare stack.

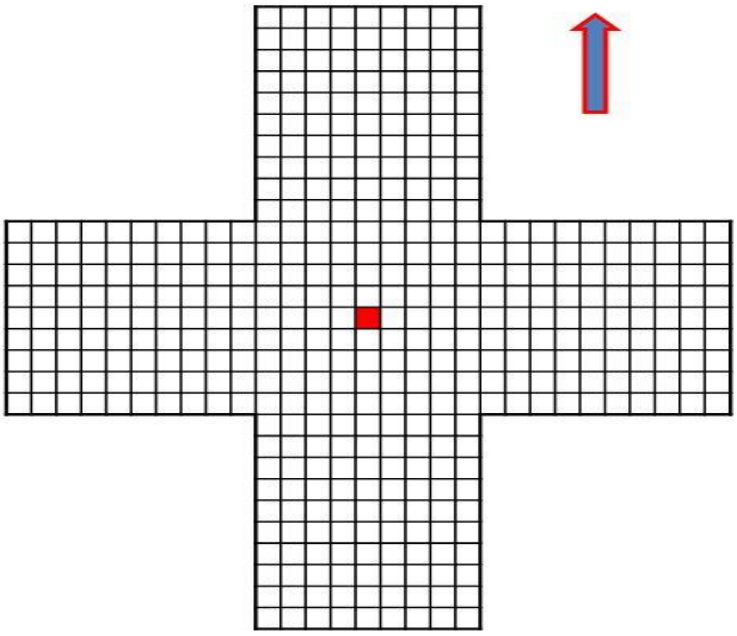

Figure 4-46: A schematic diagram for four cardinal directional plots

The four cardinal directional plots are in the form of a 2 × 2 matrix. The top left represents North, the top right represents East, the lower left represents South, which is the direction of prevailing wind in the Niger Delta and the lower right is for West. Figures 4.47-4.58 show examples of the results for each flare site with missing data points corresponding to cloud or water, and for Landsat 7 also the scan line corrector error. Also, the green points in the Figures 4.47-4.58 show LST obtained at the 60 and 120 m intervals which are the native resolution of thermal Landsat 7 ETM+ and Landsat 5 TM pixel sizes respectively while LST derived for their resampled pixel size interval (30 m) is shown with black point or vertical which is at the middle of two green points.

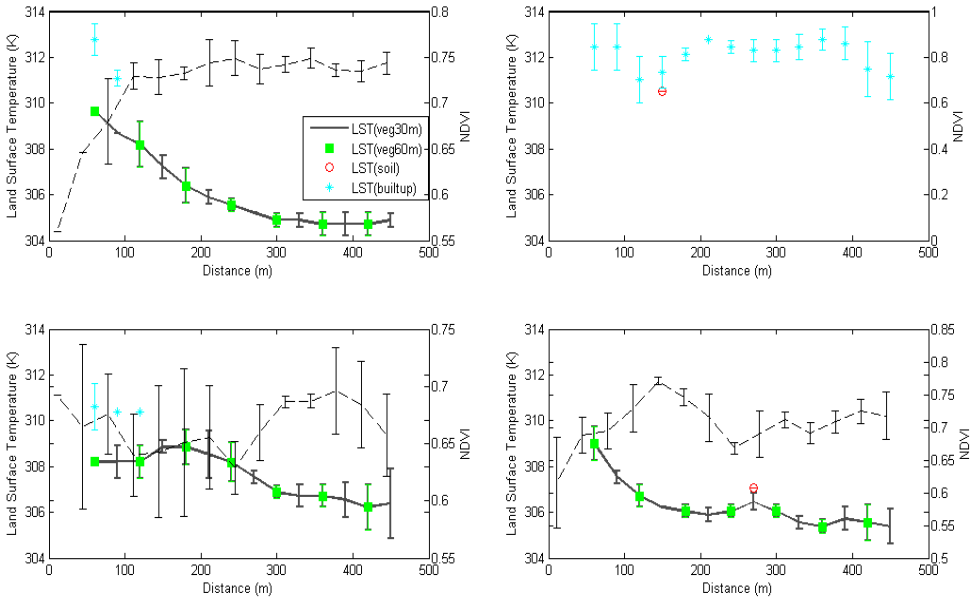

Figure 4-47: Eleme Refinery I (LST and NDVI) (17/12/2000) (Dashed black line: NDVI)

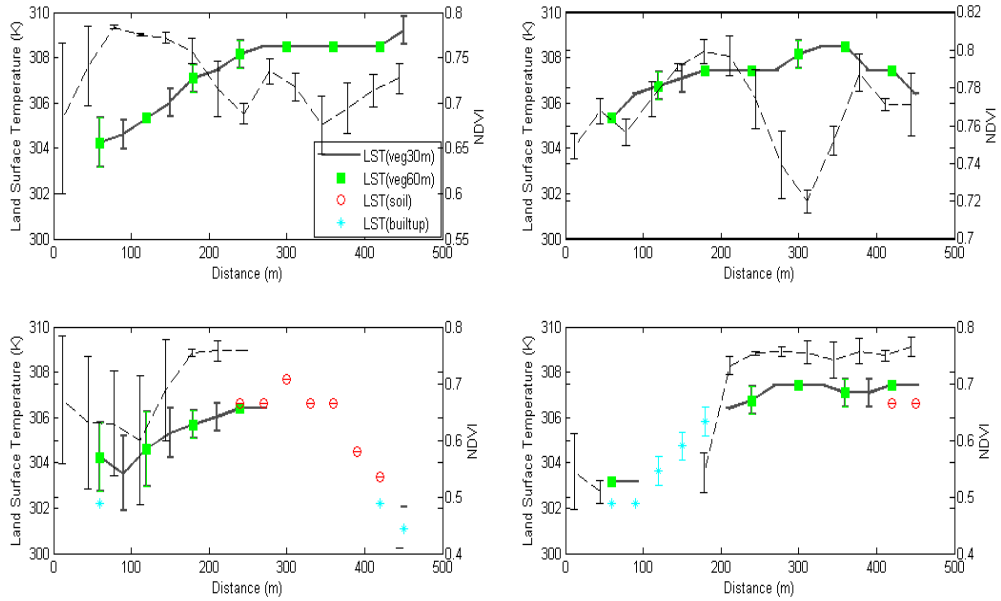

Figure 4-48: Eleme Refinery II (LST and NDVI) (10/10/1984) (Dashed black line: NDVI)

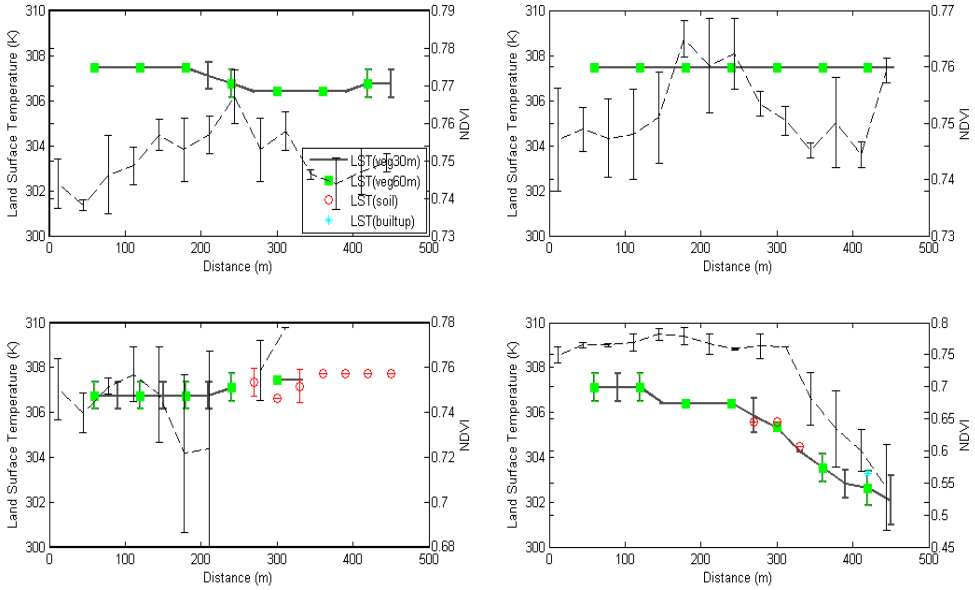

Figure 4-49: Onne Flow Station (LST and NDVI) (10/10/1984) (Dashed black line: NDVI)

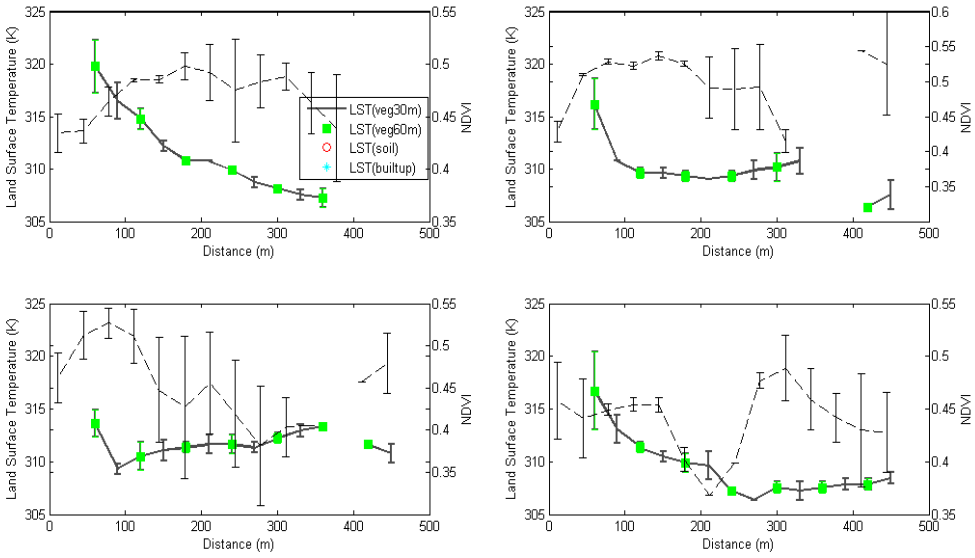

Figure 4-50: Umurolu Flow Station (LST and NDVI) (17/4/2010) (Dashed black line: NDVI)

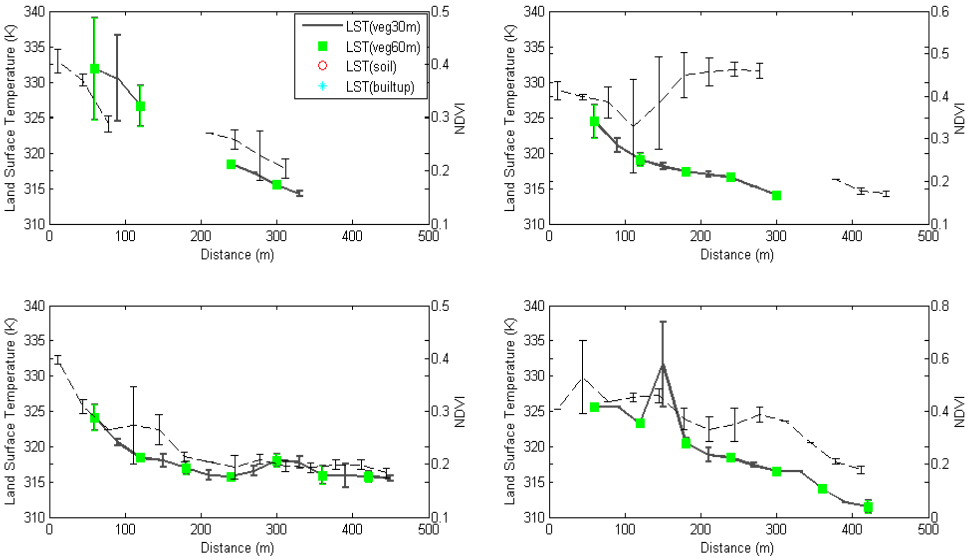

Figure 4-51: Bonny LNG (LST and NDVI) (8/1/2003)
(Dashed black line: NDVI)

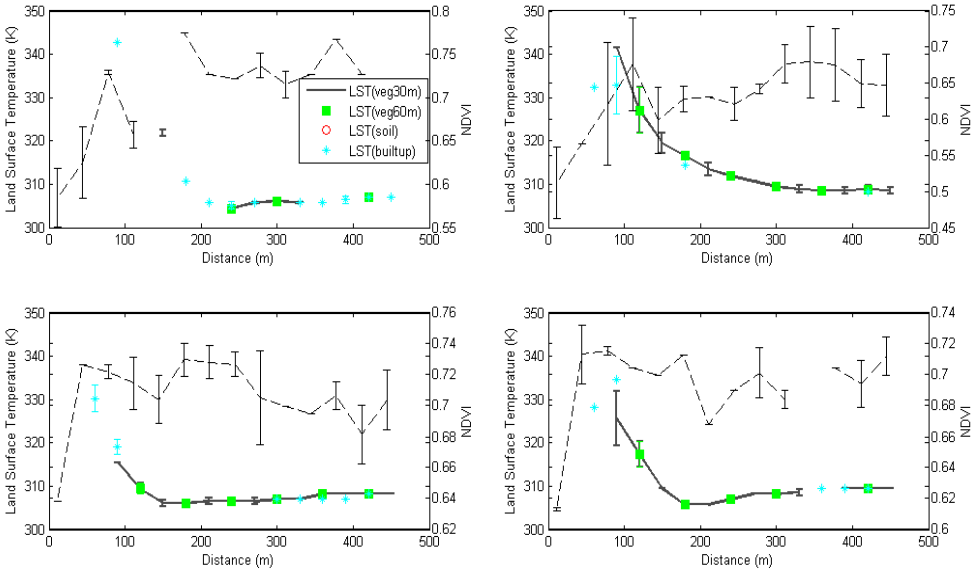

Figure 4-52: Alua Flow Station (LST and NDVI) (19/12/1986)
(Dashed black line: NDVI)

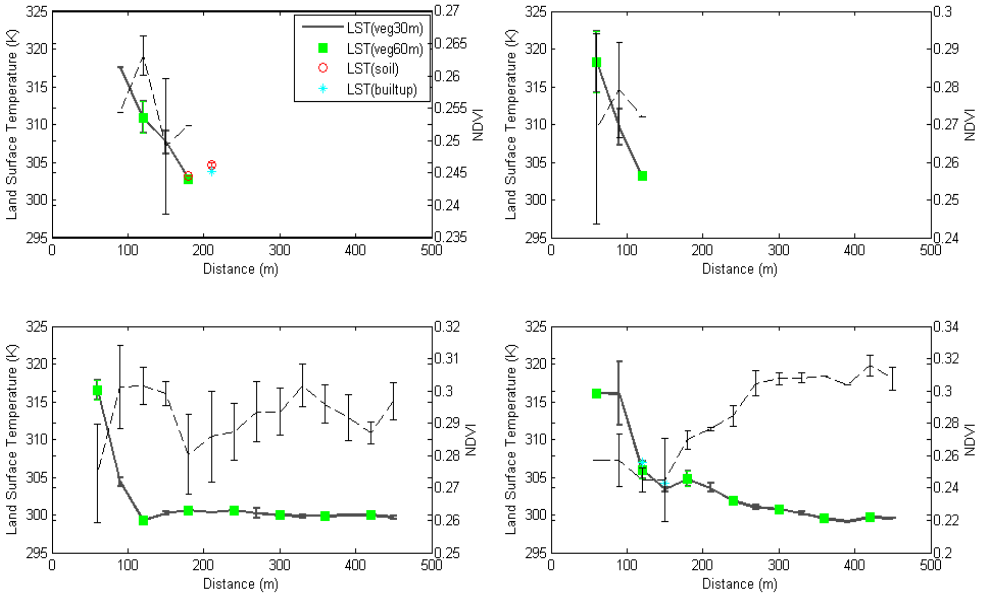

Figure 4-53: Rukpokwu Flow Station (LST and NDVI) (13/1/2005) (Dashed black line: NDVI)

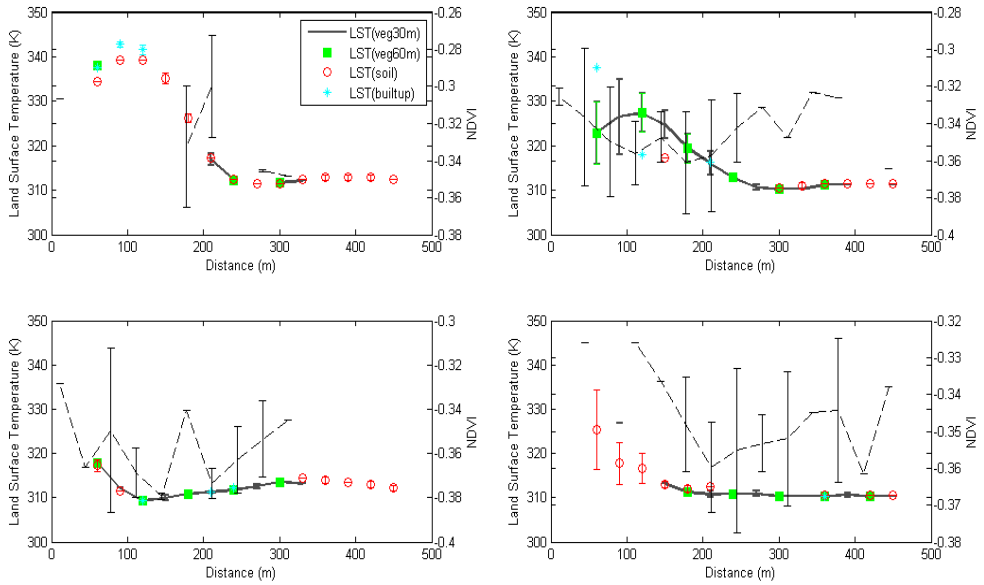

Figure 4-54: Obigbo Flow Station (LST and NDVI) (22/12/1990) (Dashed black line: NDVI)

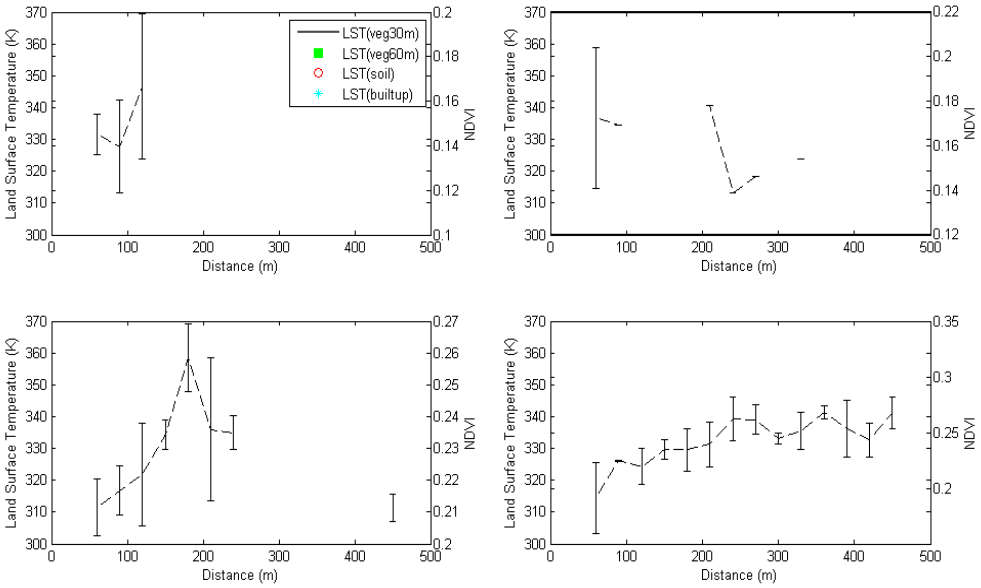

Figure 4-55: Obigbo Flow Station (LST and NDVI) (18/12/2006) (Dashed black line: NDVI)

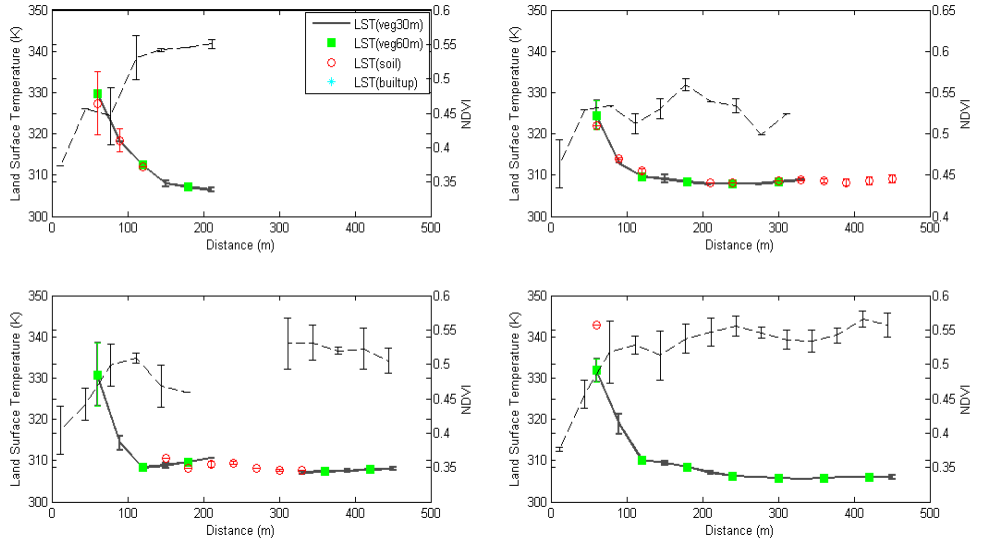

Figure 4-56: Chokocho Flow Station (LST and NDVI) (21/12/2007) (Dashed black line: NDVI)

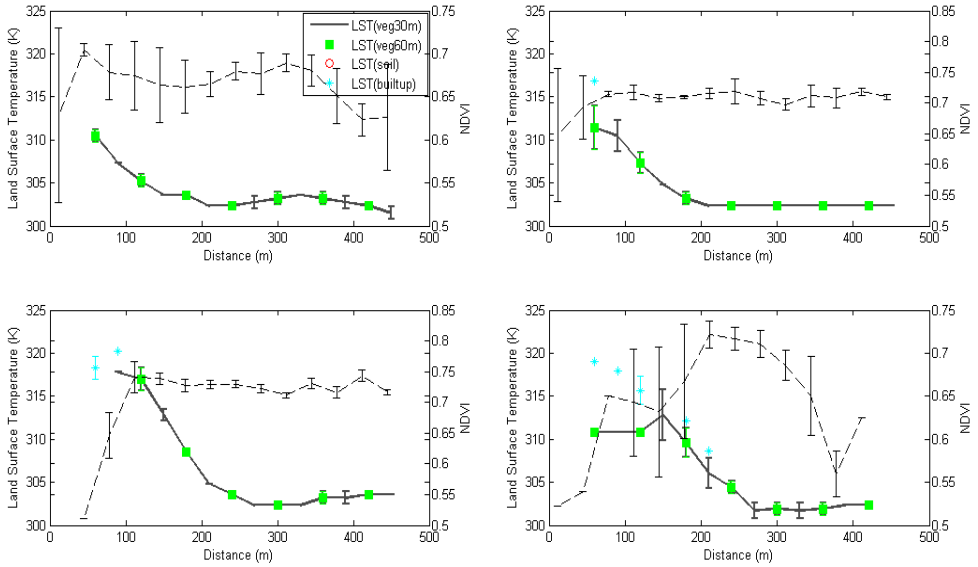

Figure 4-57: Umudioga Flow Station (LST and NDVI) (25/3/1987) (Dashed black line: NDVI)

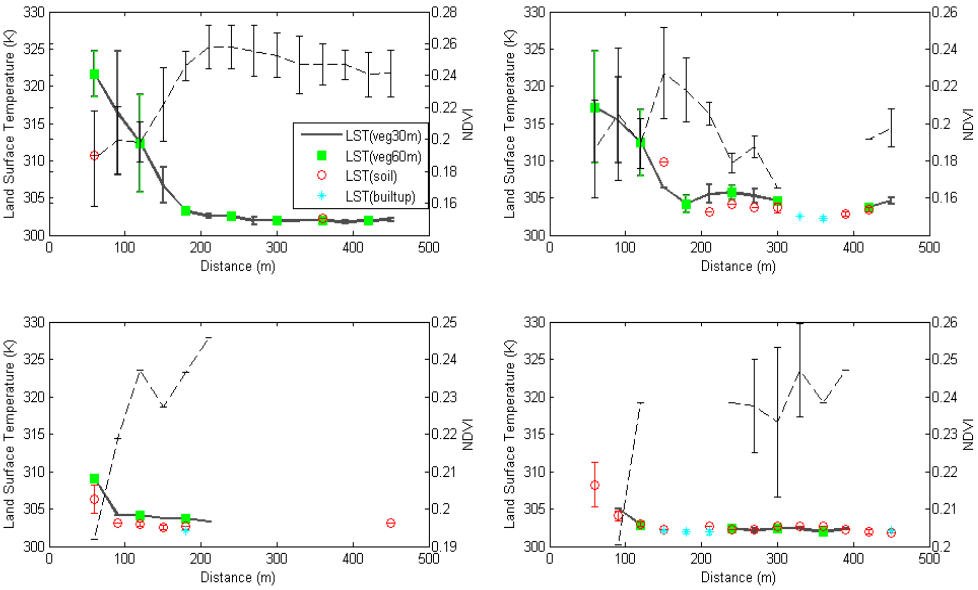

Figure 4-58: Sara Flow Station (LST and NDVI) (19/1/2007) (Dashed black line: NDVI)

These plots help to show the spatial gradients in LST and vegetation health for each land cover type at a given distance in the four different directions. In most cases LST decreases as distance from the flare stack increases. However, depending on the nature of the features that are present, it appears that some absorb more heat from the flare and sun causing a deviation from this pattern.

The value of NDVI for vegetation cover increases as distance increases from the flare stack. However, there are some cases where LST for vegetation cover follows a different spatial pattern. The reason behind this is not investigated in this study (see section 4.4.2).

In the case of Eleme II, Landsat results before and after site development are shown in Figures 4.48 (1984) and 4.59 (2005).The trend in LST changed from an increase of 5 K within 300 m of the flare in the 1984 image to a decrease of at least 5 ^{0}C within 300 m of the flare in the 2005 image. These apparent trends are analysed quantitatively in sections 4.4.2. In addition, it is clear that the spatial variability of LST in Figures 4.48 and 4.59 for Eleme Refinery II site is different. Figure 4.48 was produced from data when the refinery had not been built while data for Figure 4.59 was acquired afterwards; Eleme Refinery II was built in 1988 and commissioned in 1989. Therefore, Figure 4.59 probably shows changes that correspond to the known change in activity at the site; hence the changes in the pattern of LST for vegetated areas from 1984 to 2005 could be attributed to the flaring of gas from the refinery and the changed geographical areas covered by vegetation (see section 4.1, Figures 4.1-4.22).

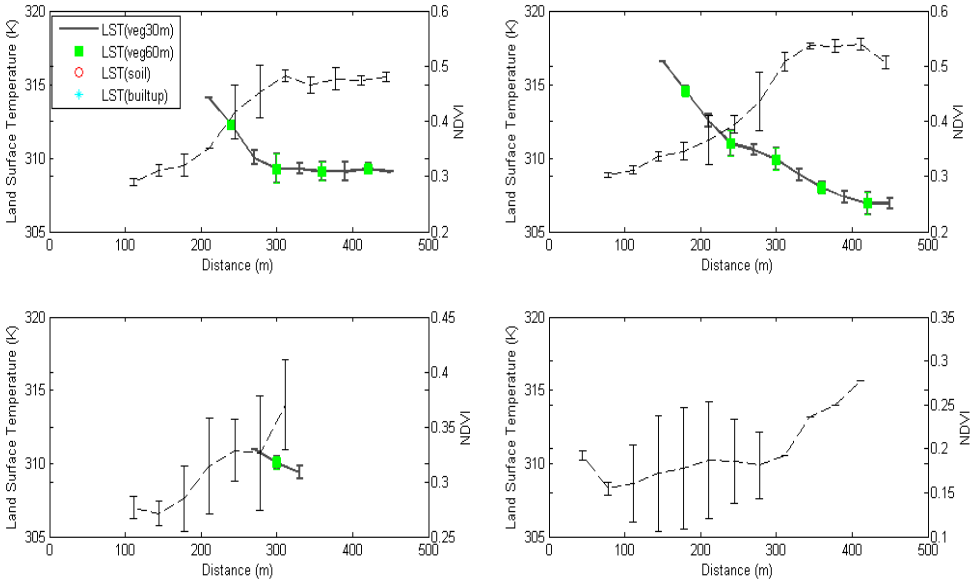

Figure 4-59: Eleme Refinery II (LST and NDVI) (13/11/2005) (Dashed black line: NDVI)

Similarly, Figure 4.49 that was produced from 1984 data (before the construction of Onne Flow Station) and Figure 4.60 generated from 2013 data (after the Onne Flow Station was built in 2010) and so therefore provides another set of scenarios. For the 1984 image, the North direction plot shows a constant temperature from 60-120 m distance from the flare stack while for the 2013 image; there is a constant decrease in LST from 60-150 m distance from the flare stack. Also, for the East direction, the 1984 image shows constant LST values throughout the distance while in the 2013 image, there is a consistent decrease in LST from 60-150 m. Furthermore, for the South direction in 1984, the LST is constant from 60-210 m distance and from there it increases at 240 m and maintains this value to 330 m and at 360 m, the LST increases and this is maintained for the remaining study distance (i.e. to 450 m). For the 2013 image, in the South direction LST decreases consistently from 60-150 m; and at 180 m to 450 m, it maintains a constant value. Therefore, these differences between the two figures could be attributed to the effect of gas flaring. In addition, Figure

4.60 is in agreement with the results of the fieldwork carried out at the Onne flaring site.

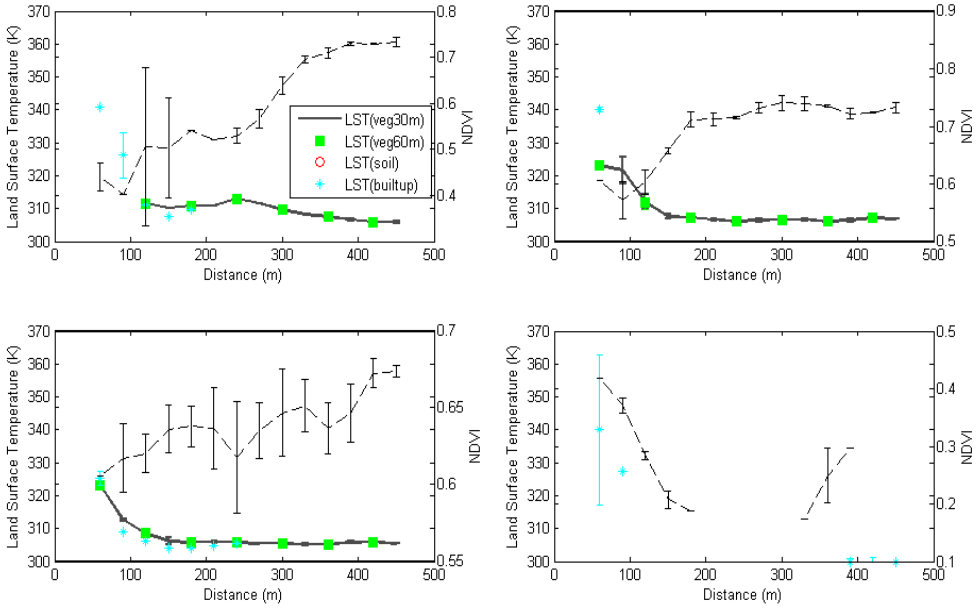

Figure 4-60: Onne Flow Station (LST and NDVI) (8/3/2013) (Dashed black line: NDVI)

In this case, the increase in LST corresponded to a decrease in the NDVI values. The closer pixels to the flare stack have lower values of NDVI, while the further away pixels have high values.

4.4.2 Characterisation of spatial variability in LST

Generally, the trends observed within the figures in section 4.4.1.2 revealed four different types of curves acquired for all sites (Figure 4.61 designated types A, B, C and D). The trend of LST with distance from the flare stack varies between facilities and with time, and is not the same for each land cover type.

Type A: Changes in LST are consistent with the flare being the main local heat source. For instance in Figure 4.61 (A), it is clear that the LST decreases

continuously with distance from the stack up to 300 m. For this type there are 2,503 cases out of 3,001. A case is one direction from one date result.

Type B: This is the same as type A, but a secondary apparent heat source lies within 300 m of flare. In Figure 4.61 (B) at a distance of 180 m from the stack, the LST rose up and from there on the LST decreases with increasing distance from the flare stack. For this type, 151 cases out of 3,001 were identified.

Type C: There is no apparent heat source. Figure 4.61 (C) is a plot with scattered LST points that is specific to the Onne Flow Station. For this type, there are 13 cases out of 3,001 cases.

Type D: Apparent heat source is present but not co-located with the known flare site. Figure 4.61 (D) is the fourth type of plot with 72 out of 3,001 cases. LST increases uniformly as distance increases from the stack till 150 m, and the LST at this point was maintained till 240 m before it decreases uniformly till 360 m and the points from 390 m to 450 m have a constant LST value.

262 curves could not be classified under this system. Only plots classified as Type A were used for further analysis in this study because of the consistent changes in LST mainly caused by the flare.

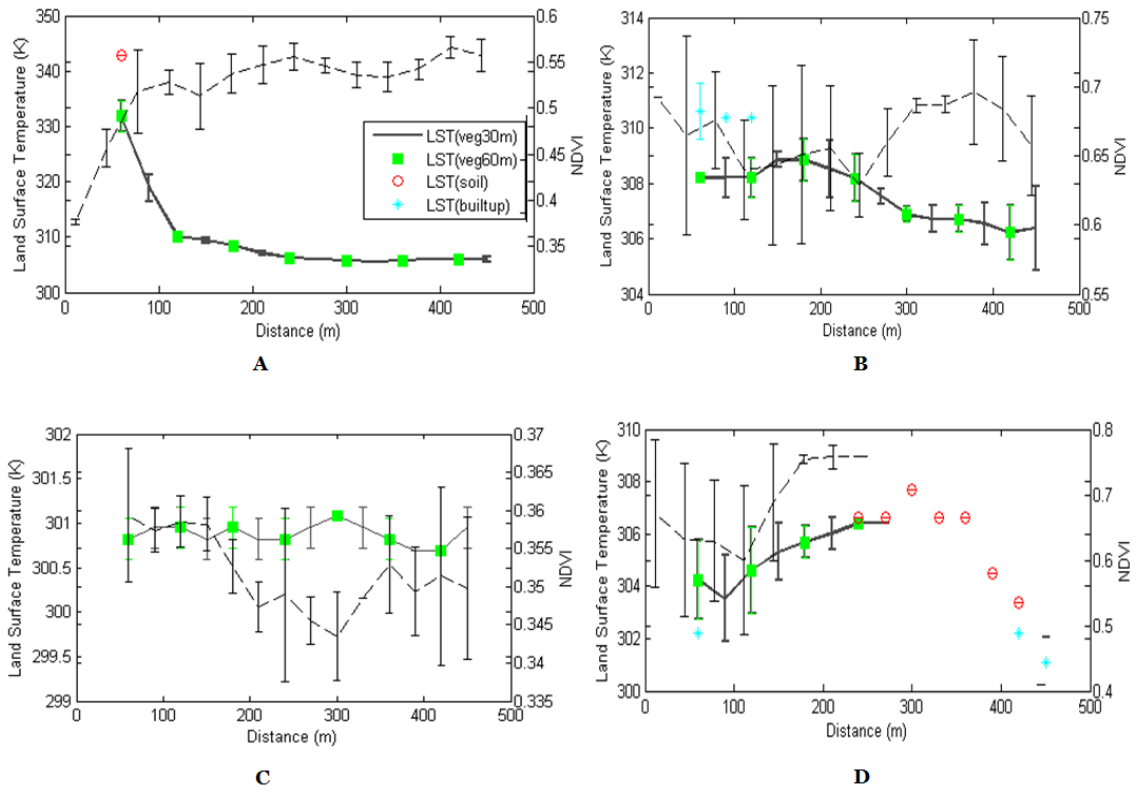

Figure 4-61: Four types of curves acquired for the results (Dashed black line: NDVI)

4.4.3 Significance of LST spatial variability

To facilitate quantitative verification of the heat sources at the flare locations, a new parameter δLST was defined for vegetation. δLST is the difference between the LST for vegetation at 60 m away from the flare stack and the minimum LST for vegetation from between 150 m to 450 m (maximum distance) from the flare stack; 60 m was chosen and used for the pixel after the flare stack to know the LST for vegetation at a near distance from the flare. 150 to 450 m was adopted as a far away distance from the flare and this is supported by Dung et al. (2008) and Isichei and Sandford (1976) that the maximum impact of flare on vegetation is between 100 to 120 m. Figure 4.62 shows the schematic diagram for the definition of δLST. To establish when we can rely on δLST being a true measure of flare impact, an analysis of variance (ANOVA) was carried out to test whether temperatures near and far from the flare were significantly different (with α =

0.01). P-values for all the data in each direction (North, East, South and West), total number of results i.e. the sum of the available Landsat scenes processed for all sites, the number of significant results and the range of δLST are summarised in Table 4.4, with this criterion used to limit the data used for further analysis. Each of the Figures 4.47-4.58 in section 4.4.1.2 is a complete result comprising four cardinal directions (North, East, South and West) from a date scene for each site while a case is referred to as one direction out of four making up a result.

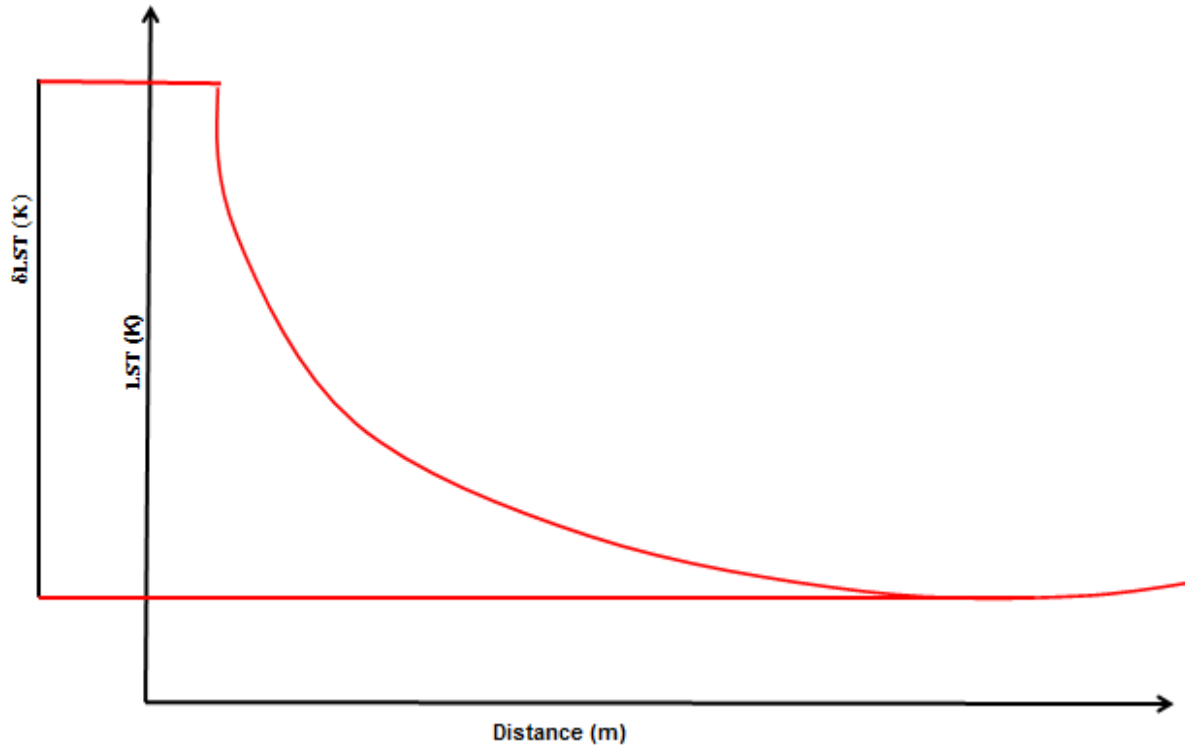

Figure 4-62: Change in LST with distance, and the definition of δLST

Table 4-4: Range of monthly p-values computed from ANOVA analysis

Difference in LST	Range of p-values	No. of significant results	Total No.	Range of δLST (K)
δLST_N	<<0.00001-0.146	286	348	0.6-35.5
δLST_E	<<0.00001-0.127	294	348	0.9-36.7
δLST_S	<<0.00001-0.143	304	348	0.7-28.6
δLST_W	<<0.00001-0.146	253	348	0.7-32.0

4.5 Investigation of potential prevailing wind impact on LST

For this section both linear and non-linear relationships were tested, but non-linear give no better results. Hence, linear regression analysis was used for further analysis to compare δLST in different directions (see section 4.4.3) at the flaring sites. Specifically, it was assumed that a consistent relationship should exist between δLST in pairs of directions at any site where a strong prevailing wind does not influence the impact of the flare on LST values near the flare; i.e. heat from the flare radiates equally in all directions and the resulting heated air mass does not flow in a dominant direction.

4.5.1 Linear regression analysis of $\delta LST_{N, S, E, W}$

Pairwise linear regression analysis was applied to the δLST values in each direction, for all the available images, site by site. The significance level was set a priori to $\alpha = 0.01$ and all relationships with significant impact for each site are shown in bold in Table 4.5. Figures 4.63-4.65 summarise these results.

δLST_{NE} = relationship between δLST_N and δLST_E

δLST_{NS} = relationship between δLST_N and δLST_S

δLST_{NW} = relationship between δLST_N and δLST_W

From Table 4.5, a negative correlation was found for δLST_N compared to δLST_E, and a positive correlation for both the δLST_{NS} and δLST_{NW} directions for Eleme Refinery I. Both Eleme II and Onne were characterised by positive correlations for both the δLST_{NE} and δLST_{NS} directions, and a negative correlation for the δLST_{NW} direction. However, the p-values for both Eleme I and II and Onne showed that no statistically significant relationships between δLST values in different directions existed. Umurolu, Bonny LNG, Alua, Rukpokwu, Chokocho

and Sara were characterised by correlations amongst the four directions and their p-values showed that these were statistically significant. Obigbo and Umudioga had positive correlations with three of the relationships; Obigbo had significant p-values for both δLST_{NE} and $\delta LSTN_W$ while Umudioga only had significant p-values for δLST_{NW}.

Table 4-5: Computed values of Number, r^2 and p-value with α=0.01 from δLST_N, δLST_S, δLST_E, δLST_W for each facility (using linear regression analysis and p-value)

Facility	Number	r^2, p-value (δLST_{NE})	r^2, p-value (δLST_{NS})	r^2, p-value (δLST_{NW})
1 (Eleme I)	19	-0.0001 0.965	0.017 0.594	0.023 0.539
2 (Eleme II)	26	0.0024 0.811	0.019 0.499	-3.611×10^{-4} 0.937
3 (Onne)	42	0.074 0.080	0.046 0.172	-6.241×10^{-3} 0.619
4 (Umurolu)	**40**	**0.538** **7.0×10^{-8}**	**0.206** **0.003**	**0.642** **5.47×10^{-10}**
5 (Bonny)	**33**	**0.501** **4.14×10^{-6}**	**0.377** **1.465×10^{-4}**	**0.584** **2.227×10^{-7}**
6 (Alua)	**29**	**0.898** **6.774×10^{-15}**	**0.753** **1.123×10^{-9}**	**0.662** **8.035×10^{-8}**
7 (Rukpokwu)	**40**	**0.527** **1.138×10^{-7}**	**0.393** **1.516×10^{-5}**	**0.266** **6.657×10^{-4}**
8 (Obigbo)	28	**0.778** **5.70×10^{-10}**	0.2 0.017	**0.272** **0.004**
9 (Chokocho)	**29**	**0.540** **5.587×10^{-6}**	**0.221** **0.010**	**0.805** **4.444×10^{-11}**
10 (Umudioga)	22	0.261 0.015	0.125 0.106	**0.343** **0.004**
11 (Sara)	**40**	**0.707** **1.121×10^{-11}**	**0.196** **0.004**	**0.461** **1.448×10^{-6}**
Total	**348**	**4.325**	**2.553**	**4.051**

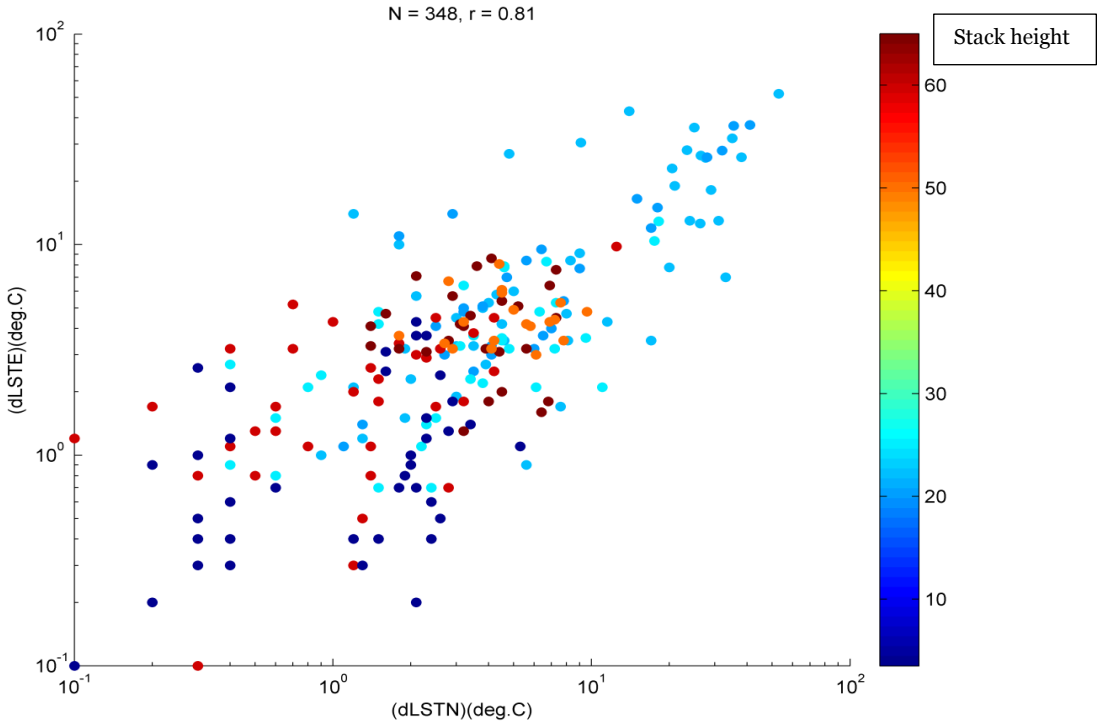

Figure 4-63: δLST_N against δLST_E

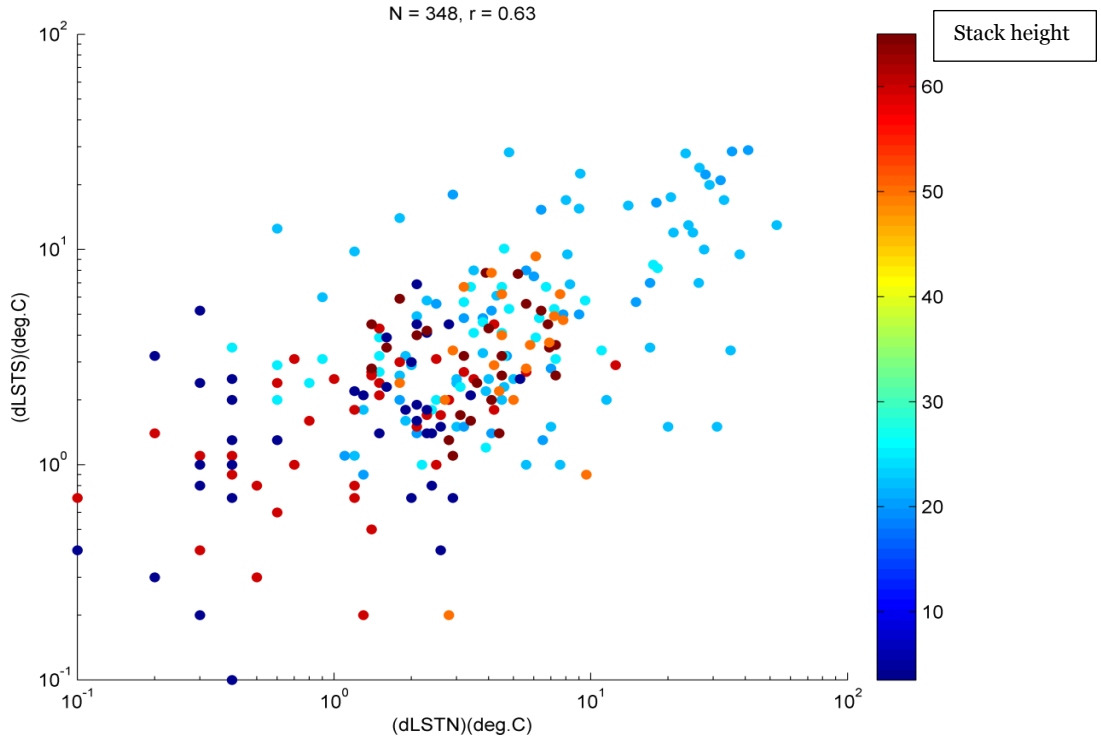

Figure 4-64: δLST_N against δLST_S

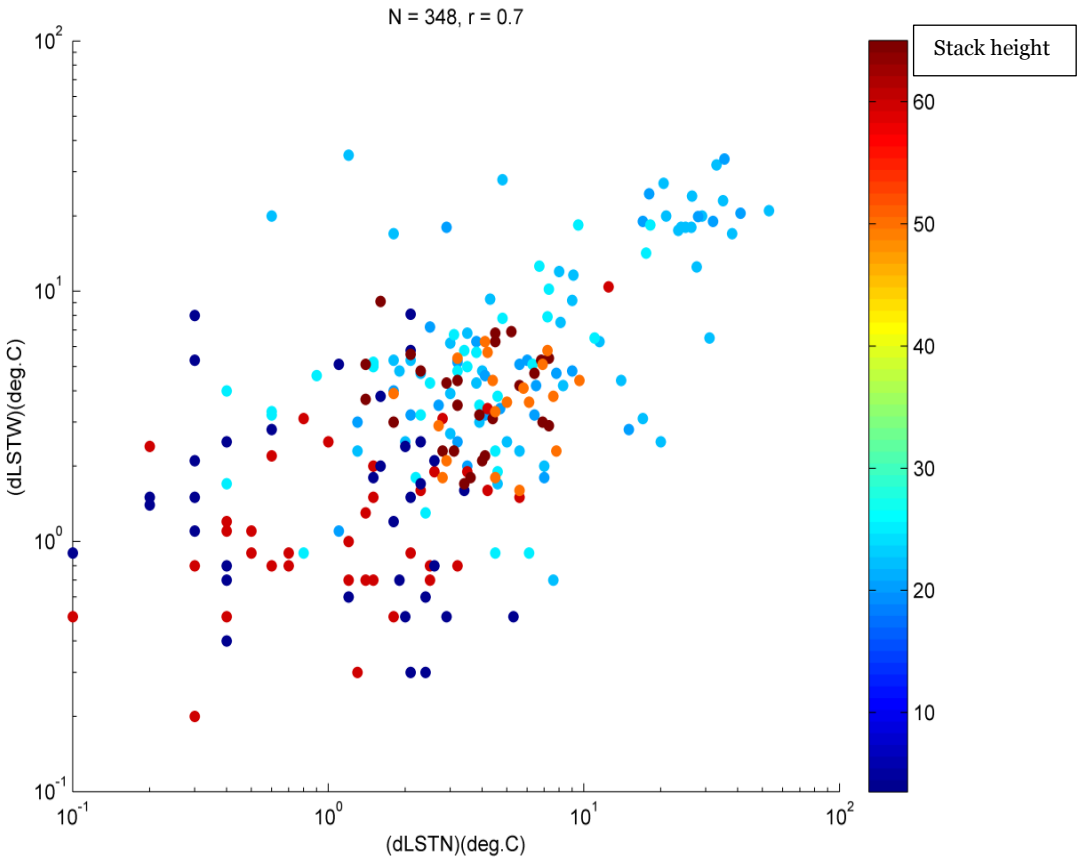

Figure 4-65: δLST_N against δLST_W

Table 4.6 presents another set of correlation coefficients (r^2-value and p-value) for each of the eleven facilities with a condition that any δLST with a p-value (computed from ANOVA, see section 4.4.3) greater than $\alpha = 0.01$ should not be used.

Table 4-6: Computed values of Number, r^2 and p-value for $\alpha = 0.01$ from δLST_N, δLST_E, δLST_S, δLST_W and each facility (using linear regression analysis, p-value computed from ANOVA)

Facility	Number	r^2, p-value (δLST_{NE})	r^2, p-value (δLST_{NS})	r^2, p-value (δLST_{NW})
1 (Eleme I)	18	0.1038 0.6820	0.0196 0.9447	-0.0104 0.9718
2 (Eleme II)	19	0.0433 0.8603	0.2682 0.2980	0.1192 0.6487
3 (Onne)	28	0.2911 0.1580	0.0985 0.6179	-0.0217 0.9197
4 (Umurolu)	**27**	**0.8039** **8.789×10^{-8}**	**0.4740** **0.0100**	**0.8105** **2.9760×10^{-7}**
5 (Bonny)	**19**	**0.7602** **1.5844×10^{-4}**	**0.6349** **0.0026**	**0.7957** **2.7248×10^{-5}**
6 (Alua)	**19**	**0.9616** **5.622×10^{-11}**	**0.9078** **8.0083×10^{-8}**	**0.8143** **7.0484×10^{-6}**
7 (Rukpokwu)	**28**	**0.8086** **1.8165×10^{-7}**	**0.6047** **3.1417×10^{-4}**	**0.4611** **0.00233**
8 (Obigbo)	**19**	**0.8859** **9.2333×10^{-8}**	**0.4742** **0.0346**	**0.4226** **0.00715**
9 (Chokocho)	**22**	**0.7942** **1.0186×10^{-5}**	**0.3795** **0.00815**	**0.9341** **2.6004×10^{-11}**
10 (Umudioga)	**12**	**0.3333** **0.2898**	**0.4879** **0.0552**	**0.6619** **0.0100**
11 (Sara)	**26**	**0.9103** **1.1232×10^{-10}**	**0.3676** **0.00419**	**0.7457** **2.8851×10^{-5}**

4.5.2 Geographical symmetry of LST in relation to the flare

Figure 4.66 is the graphical representation of Table 4.5, and each figure was created based on facilities with statistically significant p-value from any of the three relationships (δLST_{NE}, δLST_{NS}, and δLST_{NW}). In Figure 4.66, three different cases are presented to summarise the spatial geographical shape of δLST around the study sites. For case 1 that is for Obigbo Flow Station only, the p-value for the pairwise linear regression of δLST_N against δLST_E, and for δLST_N

against δLST_W are statistically significant. This shows that the wind from the South may have had an impact on LST in both the North-East and North-West directions.

Case 2 is for Alua, Bonny, Chokocho, Rukpokwu, Umurolu and Sara Flow Stations where there is no evidence for the influence of wind on the flare because δLST is directionally uniform; therefore, the flare δLST footprint is a circle. The p-value obtained is significant for all the three relationships, δLST_{NE}, δLST_{NS} and δLST_{NW}.

For, case 3, which is for Umudioga Flow Station, only δLST_N versus δLST_W is statistically significant. The influence of the wind from the South on the flare was strong; while from the West it was mild suggesting that the influence of the wind might be felt in a North-West direction. See section 4.4.1.1 for the actual values of LST as pixels.

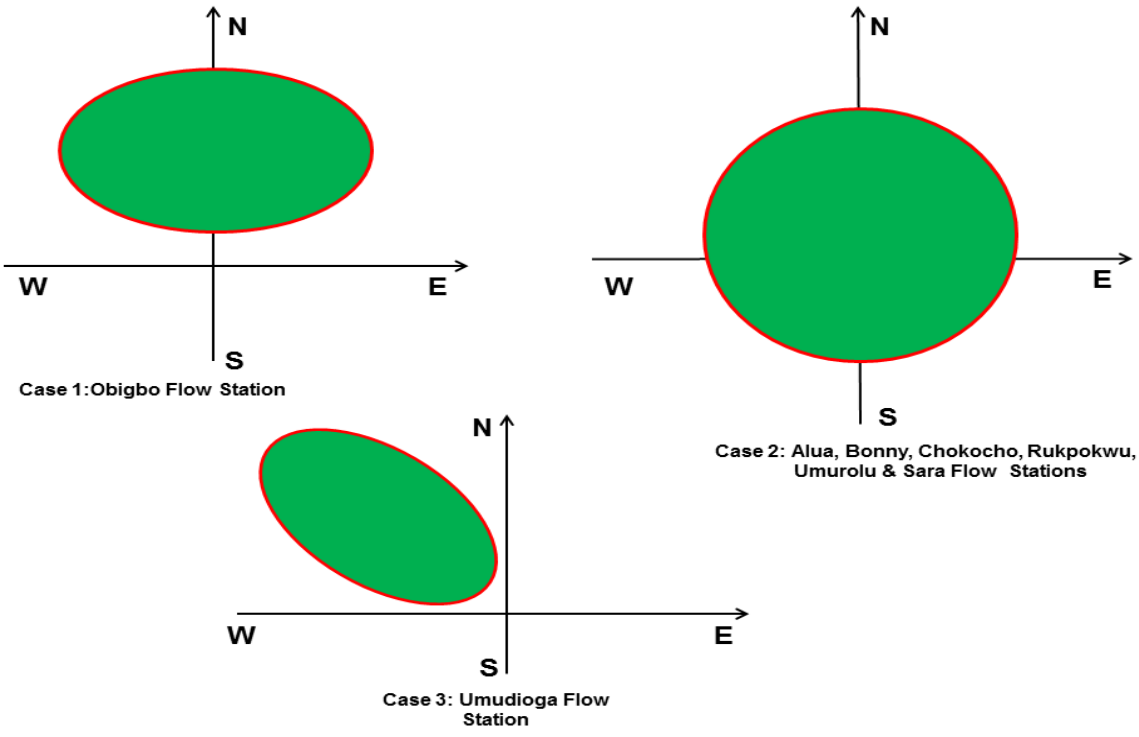

Figure 4-66: Geographical symmetry of LST in relation to the flare

4.6 Evaluation of factors influencing δLST

In this section, parameters that are expected to influence δLST near a flare site were investigated. Available factors include the size of the facility, height of flare stack and time (month, Julian Day and year); both linear and non-linear relationships were tested against the four δLSTs (δLST_N, δLST_E, δLST_S and δLST_W), but non-linear give no better results. Hence, linear relationships were considered for further analysis to assess the impacts on LST. The results obtained from the combination of these factors and relationships are presented in Figures 4.67-4.86 with the colour bar representing height of the flare stack. The graphs are similar; Figures 4.67-4.74 are shown below and the remaining Figures C-1 to C-12 are presented in Appendix C. In order to assess these factors quantitatively, two statistical analyses were used; pairwise linear regression and multiple regression analysis based on the results from the pairwise linear regression.

4.6.1 Pairwise linear regression

Pairwise linear regression analysis was applied to the relationships between the δLST's and available information about parameters that can influence it, with the significance level set a priori to $\alpha = 0.01$ Table 4.7 shows the resulting r-values, p-values and the type of correction that resulted. A second set of correlation coefficients (r-value and p-value) were computed with the same monthly data, but with a condition that any δLST with a p-value (computed from ANOVA, see section 4.4.3) greater than $\alpha = 0.01$ should not be used for the computation. Table C-1, presented in Appendix C, shows the results of the newly computed r-value and p-value for the relationships used. All relationships

with significant impact are shown in bold in Table 4.7 and Table C-1 in Appendix C.

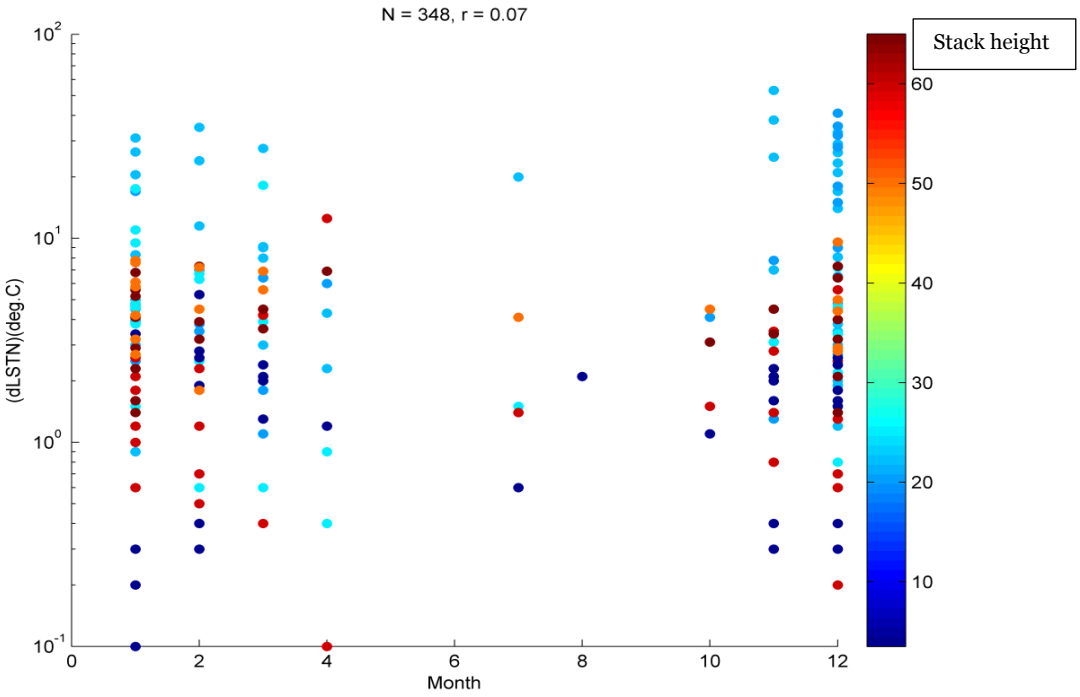

Figure 4-67: Month against δLST_N

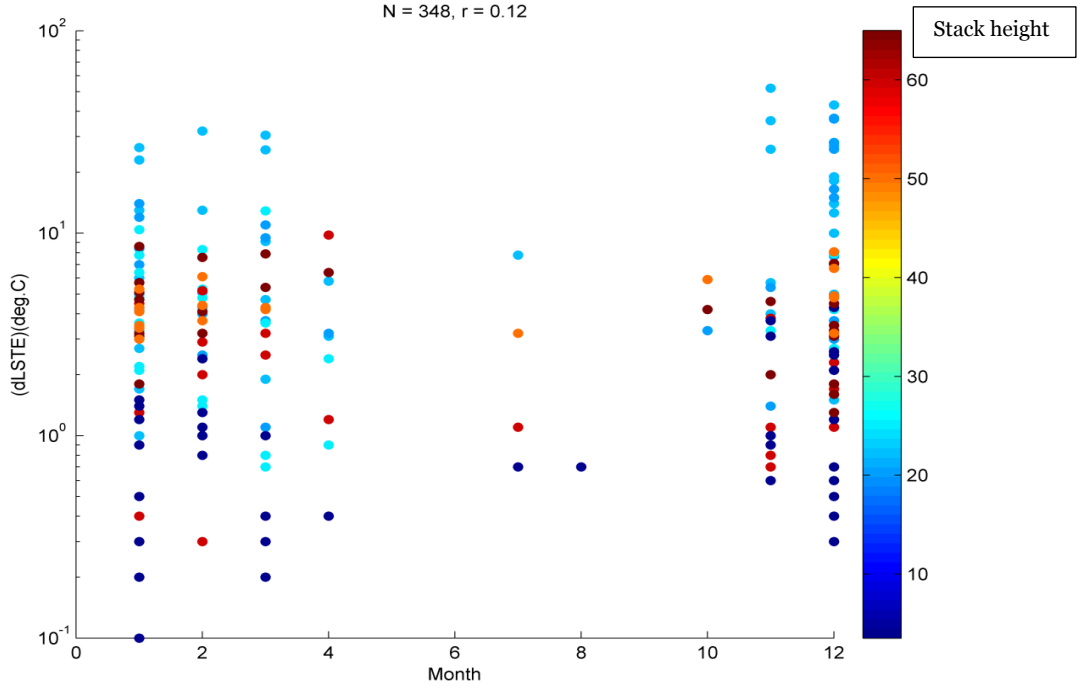

Figure 4-68: Month against δLST_E

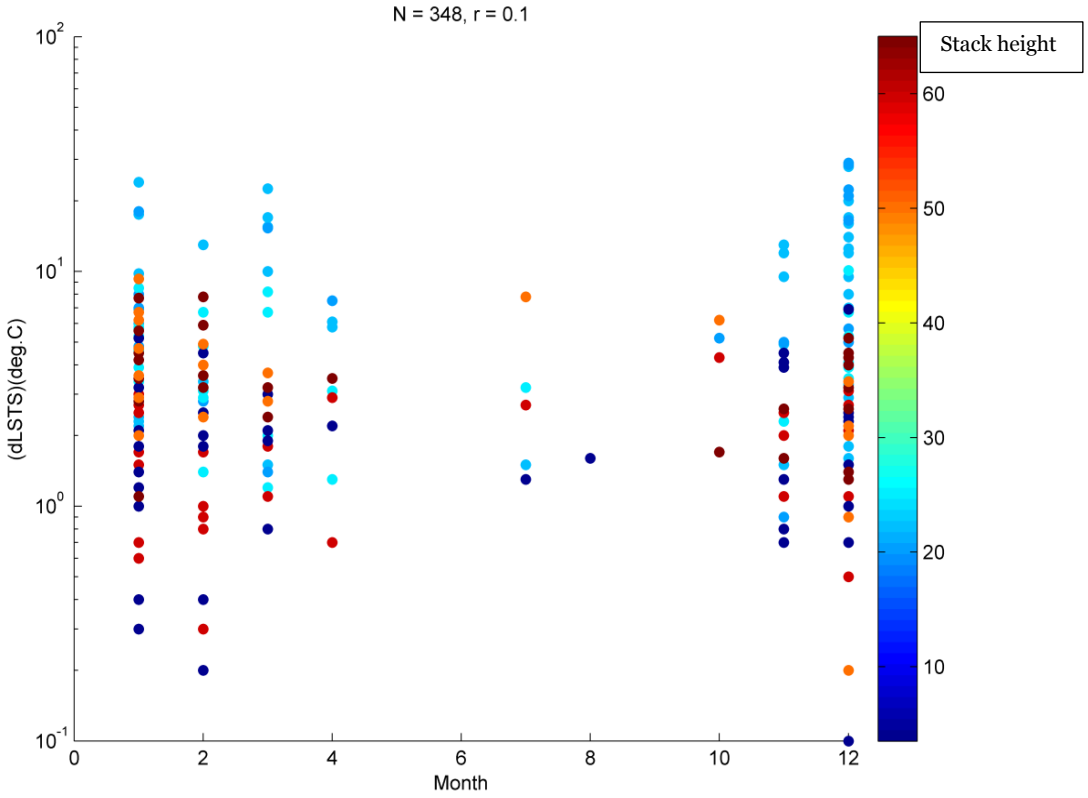

Figure 4-69: Month against δLST_S

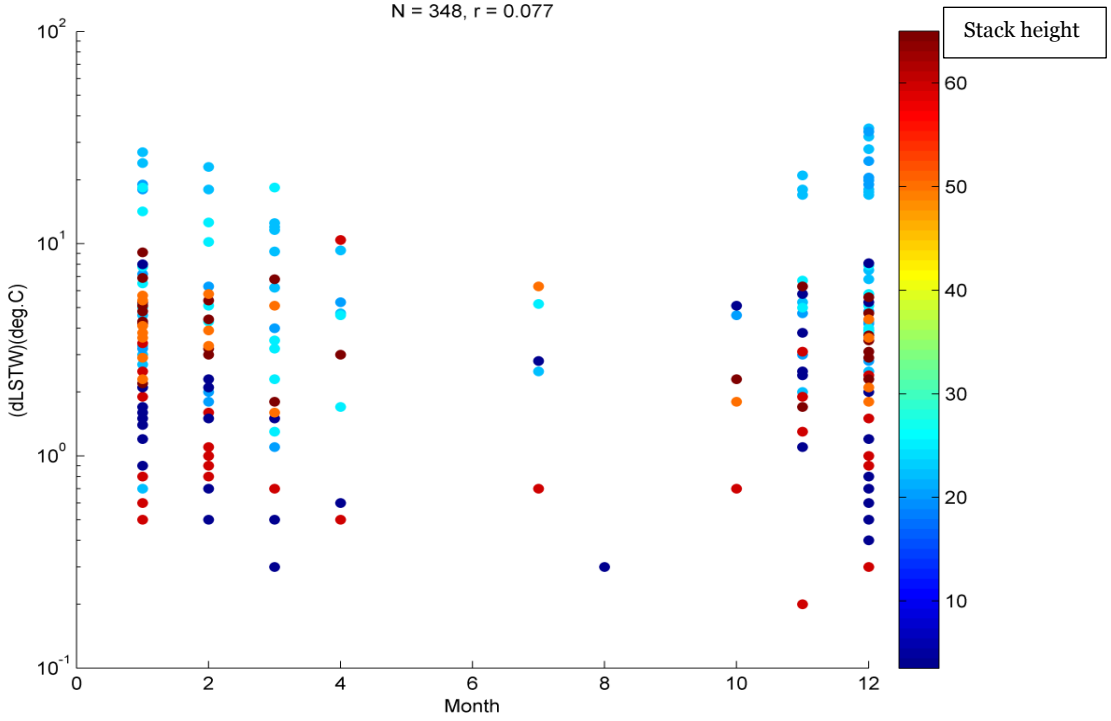

Figure 4-70: Month against δLST_W

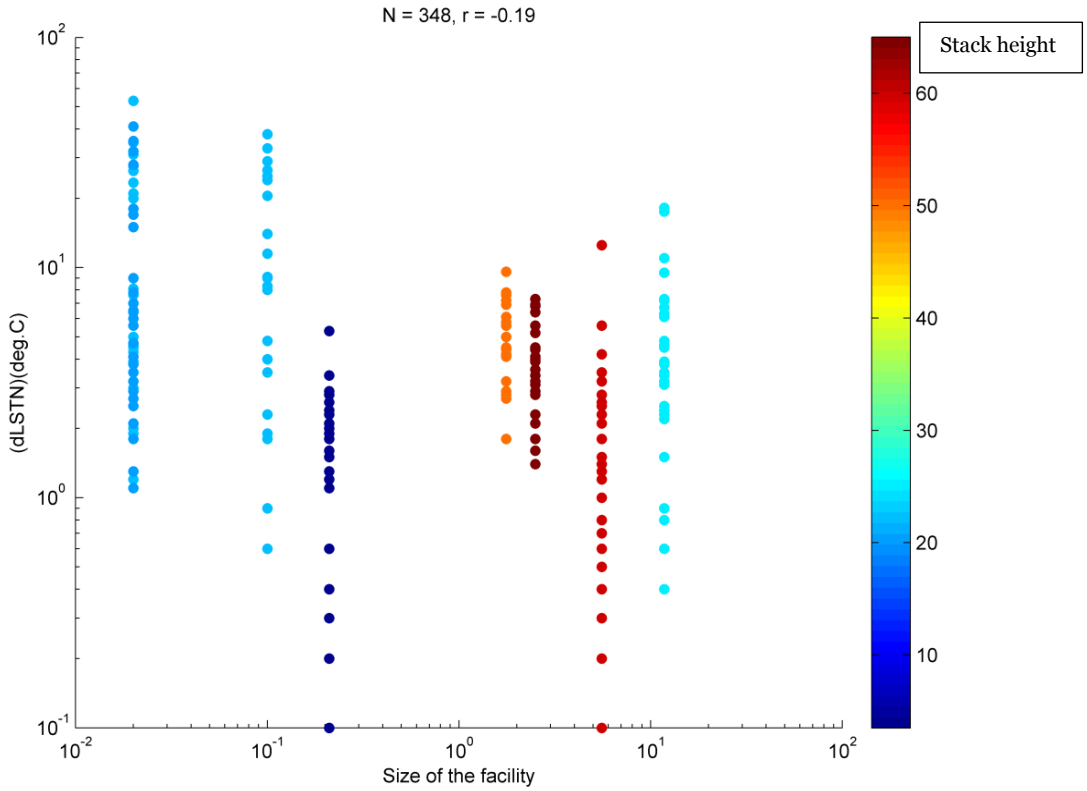

Figure 4-71: Size of the facility against δLST_N

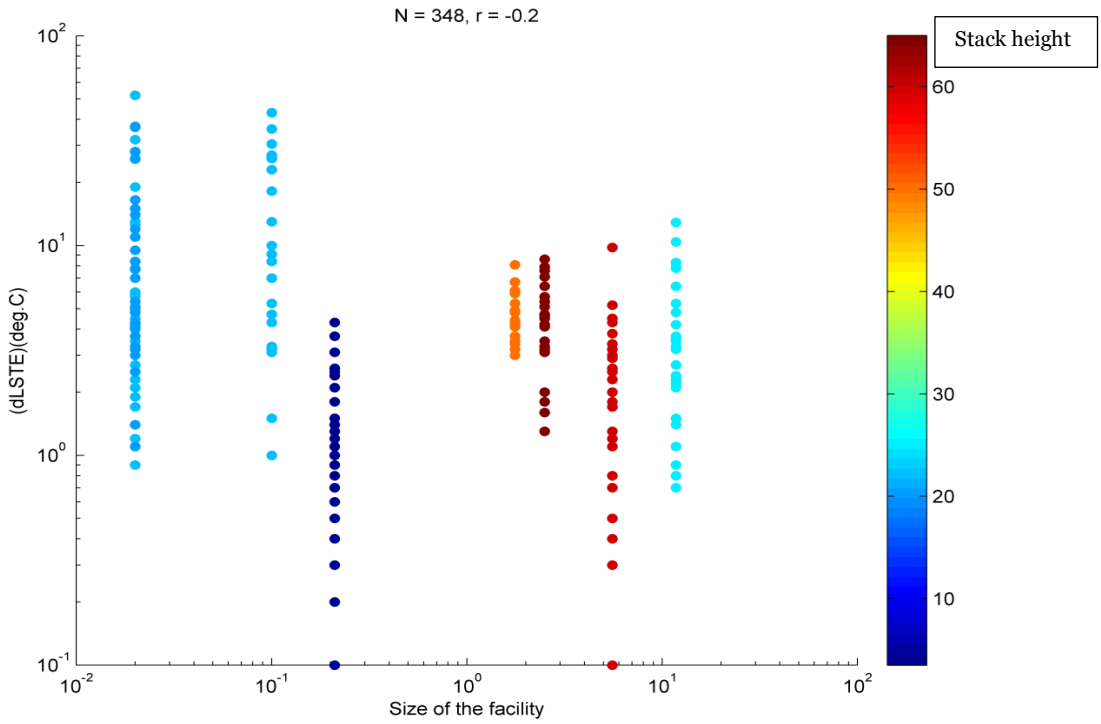

Figure 4-72: Size of the facility against δLST_E

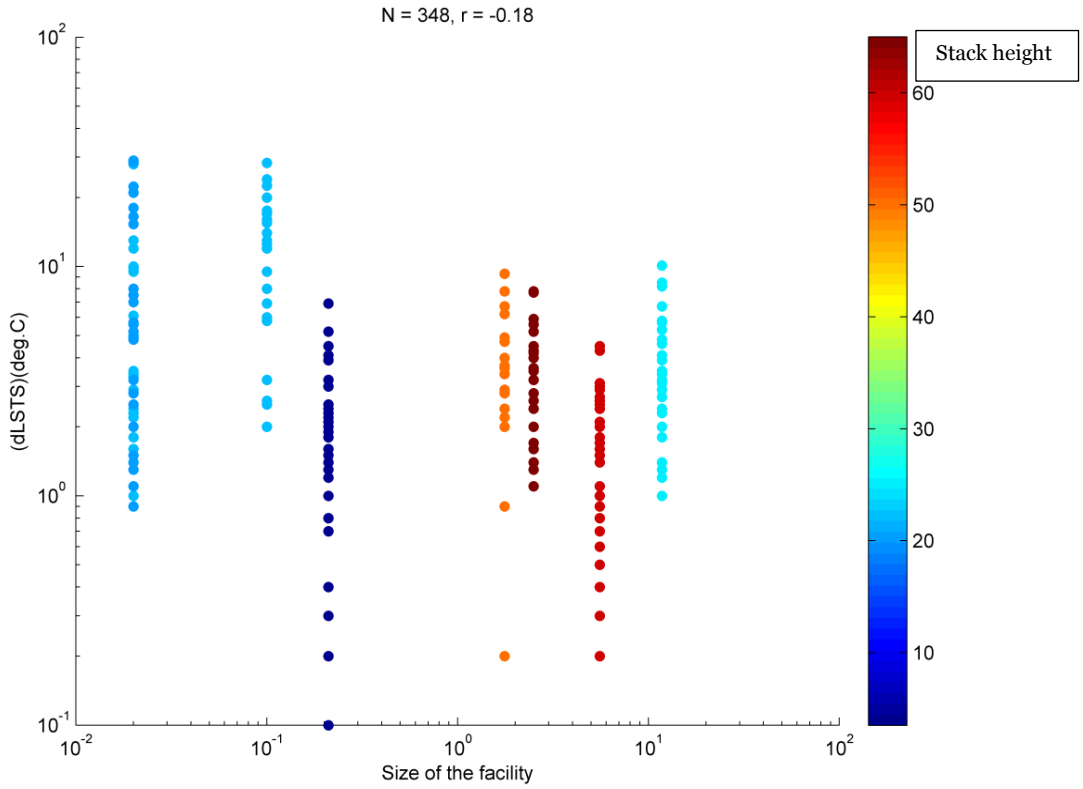

Figure 4-73: Size of the facility against δLST_S

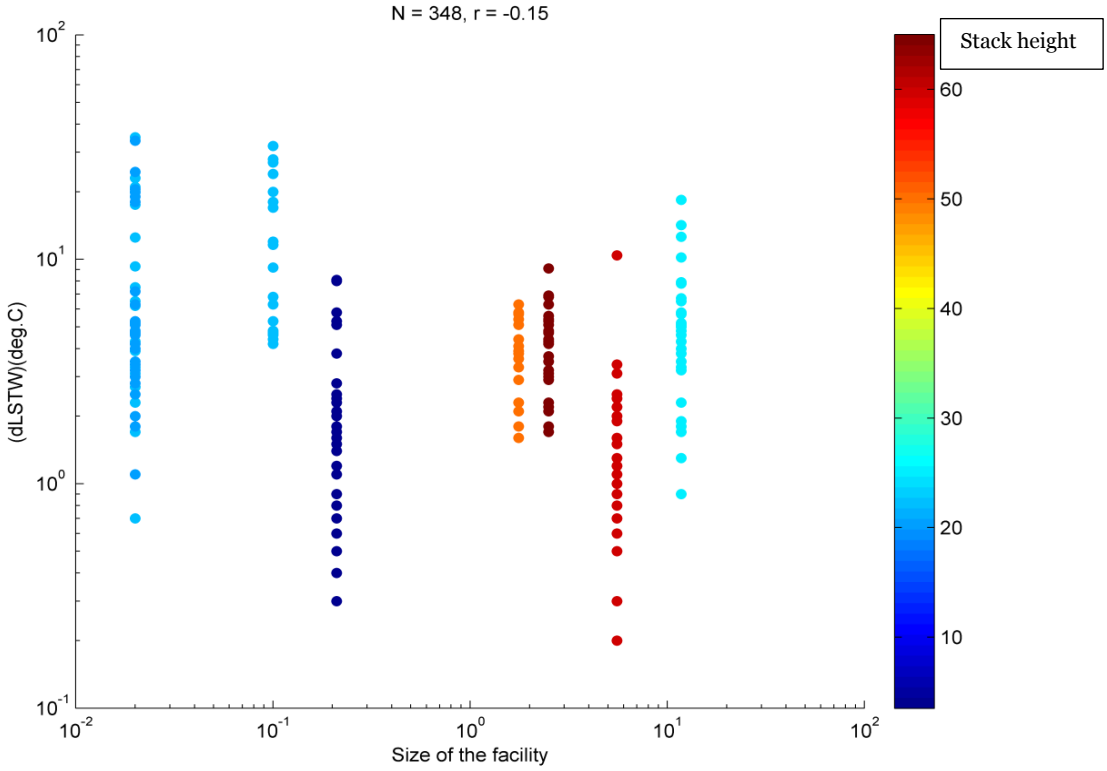

Figure 4-74: Size of the facility against δLST_W

Table 4-7: Correlation coefficient of relationships of factors that impact LST for α=0.01

Relationship	r-value	p-value	Type of correlation
Month v δLST_N	0.07	0.1896	Positive
Month v δLST_E	0.12	0.0250	" "
Month v δLST_S	0.10	0.0605	" "
Month v δLST_W	0.08	0.1504	" "
Size of the facility v δLST_N	-0.19	**3.3903×10^{-4}**	**Negative**
Size of the facility v δLST_E	-0.20	**1.6688×10^{-4}**	" "
Size of the facility v δLST_S	-0.18	**9.9788×10^{-4}**	" "
Size of the facility v δLST_W	-0.15	**0.0039**	" "
Height of stack v δLST_N	-0.12	0.0551	" "
Height of stack v δLST_E	-0.10	0.1309	" "
Height of stack v δLST_S	0.47	0.0279	Positive
Height of stack v δLST_W	-0.16	**0.0124**	**Negative**
Julian Day v δLST_N	0.07	0.2248	Positive
Julian Day v δLST_E	0.12	0.0290	" "
Julian Day v δLST_S	0.10	0.0639	" "
Julian Day v δLST_W	0.07	0.1656	" "
Year v δLST_N	0.003	0.9579	" "
Year v δLST_E	-0.004	0.9470	Negative
Year v δLST_S	-0.0085	0.8750	" "
Year v δLST_W	0.032	0.5515	Positive

In Table 4.7, the relationship between Month and δLST_N, δLST_E, δLST_S and δLST_W show positive correlation and statistically insignificant results. The relationship between the size of facility and each of δLST_N, δLST_E, δLST_S and δLST_W show negative correlation and statistically significant results. The relationship between the height of stack and each of δLST_N, δLST_E and δLST_W show negative correlation while that of δLST_S show positive correlation; and their p-values show that only the relationship between the height of stack and δLST_W give statistically significant result. Also, all the relationship between Julian Day and each of δLST_N, δLST_E, δLST_S and δLST_W show positive correlation and statistically insignificant results. Finally, the relationship between Year and each of δLST_N and δLST_W show positive correlation while the relationship between

Year and δLST_E δLST_S show negative correlation; and all relationships give statistically insignificant results.

The results presented in Table C-1 in Appendix C, is similar to that of Table 4.7 except the relationship between height of stack and δLST_S, and Year and δLST_N that show negative correlation.

4.6.2 Multiple linear regression analysis

The purpose of multiple linear regression analysis is to analyse relationships among multiple variables. The analysis is carried out through the estimation of a relationship $y = f(x_1, x_2,..., x_k)$ and the results serve the following purposes:

- Answer the question of how much y changes with changes in each x (x_1, x_2,...,x_k), and
- Predict the value of y based on the x values.

For this research, x_1 = month, x_2 = size of facility and x_3 = stack height while y_1 = δLST_N and y_2 = δLST_E. x_1, x_2 and x_3 are predictor variables, y_1 and y_2 are response variables and each variable is standardized as shown in equations 4.2-4.4. Generally, the linear model for multiple regressions is:

$$y = bx \quad (4.1)$$

Where b = relative quantitative contribution of each x predictor variable

$$\text{month} = [\text{month} - (\text{meanmonth})] \div \sigma_{\text{month}} \quad (4.2)$$

$$\text{size of facility} = [\text{size of facility} - (\text{meansize of facility})] \div \sigma_{\text{size of facility}} \quad (4.3)$$

$$\text{height of stack} = [\text{height of stack} - (\text{meanheight of stack})] \div \sigma_{\text{height of stack}} \quad (4.4)$$

For this research, equation 4.1 has become the following:

For y_1,

$$\delta LST_N = b_0 + b_1 \times (\text{month})' + b_2 \times (\text{size of facility})' + b_3 \times (\text{height of stack})' \quad (4.5)$$

For y_2,

$$\delta LST_E = b_0 + b_1 \times (\text{month})' + b_2 \times (\text{size of facility})' + b_3 \times (\text{height of stack})' \quad (4.6)$$

Where,

b_0 is a constant.

For equation 4.5, the results obtained are: r-squared value of 0.05, p-value of 0.016 and b values of ~0, 0.09, −0.146 and −0.103. The results for equation 4.6 are: r-squared value of 0.05, p-value of 0.011 and b values of ~0, 0.069, −0.195 and −0.053. Only 5 % of the variability in δLST_N and δLST_E with distance from the stack was explained by these variables (month, size of facility and height of stack) and so is accounted for in the resulting relationship. Other variables that would account for the unexplained variability include factors such as rate of burning gas, volume of burning gas, vegetation density and vegetation types.

4.7 Results of fieldwork

It was revealed from the measurement of air temperature at both sites that the upper reading values for the air temperature are highest and vice-versa. Tables 4.8 and 4.9 show the mean air temperature (K) and relative humidity (%) of the two sets of data observed at both sites. The computed mean and standard deviation for air temperature for Eleme Refinery II and Onne Flow Station (transect lines 1 to 4) are presented in Figures 4.75 to 4.78; and the relative humidity (transect lines 1 to 4) is presented in Figures 4.79 to 4.82. As the observed temperature and relative humidity distributions were similar for all transects, the remaining figures (transect lines 5 to 8) for air temperature and relative humidity for both sites are presented in Appendix C. See Figures C-13 and C-14 for Eleme II air temperature; Figures C-15 and C-16 for Onne Flow Station air temperature; Figures C-17 and C-18 for Eleme II relative humidity;

and Figures C-19 and C-20 for Onne Flow Station relative humidity in Appendix C. The figures show the mean air temperature and relative humidity at 30 m distance away from the flare stack and up to 240 m at 30 m interval.

Table 4-8: Mean Air Temperature of the two sets of fieldwork data for Eleme Refinery II and Onne Flow Station

Eleme II	30 m	60 m	90 m	120 m	150 m	180 m	210 m	240 m
L1	323.8	320.0	318.2	317.3	316.6	316.2	315.4	314.4
L2	323.6	320.0	318.4	317.5	316.7	316.2	314.6	314.0
L3	323.1	319.5	318.4	316.0	316.6	316.2	315.0	313.7
L4	323.9	322.2	317.9	317.4	316.3	316.2	314.8	315.8
L5	322.8	320.3	318.4	317.3	316.5	315.9	315.1	313.9
L6	323.1	320.7	319.1	317.8	317.2	315.9	315.0	314.3
L7	323.8	323.0	318.7	317.3	317.4	317.0	315.1	314.2
L8	323.1	320.8	319.3	318.0	317.2	316.8	315.0	314.3
Onne								
L1	323.3	320.7	319.1	318.4	317.6	316.9	315.6	314.8
L2	322.4	319.8	318.3	317.5	316.9	316.5	315.0	314.5
L3	321.3	319.1	317.7	316.3	315.8	315.2	314.8	314.9
L4	322.5	321.2	318.6	317.6	317.2	316.0	315.0	314.5
L5	321.2	320.0	318.3	317.5	316.6	316.0	314.5	313.9
L6	321.9	320.8	319.0	317.4	316.4	315.8	314.6	313.9
L7	322.4	322.0	319.2	317.8	316.8	316.3	314.5	314.1
L8	322.5	320.8	318.8	317.6	317.0	316.3	314.5	314.0

Table 4-9: Mean Relative Humidity of the two sets of fieldwork data for Eleme Refinery II and Onne Flow Station

Eleme II	30 m	60 m	90 m	120 m	150 m	180 m	210 m	240 m
L1	66.2	68.0	65.5	65.5	63.5	69.5	68.8	67.9
L2	65.1	65.6	65.5	64.8	64.2	70.0	67.2	66.6
L3	68.8	69.3	67.3	66.3	66.9	70.8	73.2	71.8
L4	65.2	65.1	64.4	64.6	65.7	70.9	73.4	69.0
L5	68.0	68.1	66.0	67.0	67.4	78.8	75.8	71.5
L6	70.6	74.3	76.5	75.6	75.6	79.3	77.3	73.2
L7	73.1	71.9	74.1	75.8	72.5	74.9	74.9	71.2
L8	71.9	72.9	73.1	71.1	70.6	73.9	73.6	70.5
Onne								
L1	63.3	63.4	64.4	64.7	63.3	66.9	69.8	69.9
L2	69.9	67.7	68.6	66.1	66.4	69.5	69.3	68.6
L3	65.7	67.9	66.7	64.5	64.3	63.6	62.4	63.3
L4	64.7	65.3	64.1	66.2	69.4	68.3	66.9	69.6
L5	69.7	70.4	70.7	67.9	70.4	67.7	70.4	71.7
L6	68.1	70.3	71.9	71.6	66.4	69.0	71.3	67.7
L7	65.1	68.7	66.9	66.7	67.3	66.8	67.1	66.4
L8	64.7	65.3	68.8	66.8	65.6	68.3	66.3	66.2

The meaning of the abbreviations used in the figure keys are explained below with L1 to L8 representing lines number 1 to 8:

- L1 (Lower 1) = air temperature reading at 1 m above the ground for the first set of data.
- L2 (Lower 2) = air temperature reading at 1 m above the ground for the second set of data.
- M1 (Middle 1) = air temperature reading at 1.5 m above the ground for the first set of data.
- M2 (Middle 2) = air temperature reading at 1.5 m above the ground for the second set of data.
- U1 (Upper 1) = air temperature reading at 2 m above the ground for the first set of data.
- U2 (Upper 2) = air temperature reading at 2 m above the ground for the second set of data.

In Figures 4.79 to 4.82 and Figures C-17 to C-20 in Appendix C, r in the figure key was used to distinguish relative humidity measurements from those for air temperature.

Generally, for Eleme Refinery II, Figures 4.75-4.76, and Figures C-13 and C-14 show that air temperatures from the first fieldwork are lower than that from the second fieldwork; for all the eight transect lines. For Onne Flow Station (Figures 4.77-4.78 and Figures C-15 and C-16), for line 1, the air temperature for L2 and M2 are equal for all the eight points; the air temperature for line 2 recorded for M1 and M2 are equal for all stations, and L2, M2 and U2 have almost the same air temperature for all the eight stations. Also, the air temperature for L2, M2 and U2 are almost equal and M1 and U1 are also equal for line 3. For line 4, L1,

M1 and U1 are equal with a drop from 322 K at 60 m to 318 K at 90 m, and L2, M2 and U2 are all equal too. Furthermore, for line 5, the air temperature for L1, M1 and U1 are the same with an increase from 318 K at 150 m to 319 K at 180 m and dropped to 316 K at 210 m; and then L2, M2 and U2 are also the same. For lines 6, 7 and 8, L1, M1 and U1 are equal as well as L2, M2 and U2 are all equal.

From Figures 4.79-4.82 and Figures C-17 to C-20 for Eleme Refinery and Onne Flow Station, the relative humidity measured showed non uniform trends. For Eleme Refinery the first set of data (L1, M1 and U1) values are all higher than the second set for lines 1 to 4, 7 and 8; for lines 5 and 6, L1 still gives the maximum values for both of them followed by L2 for line 5 and M2 for line 6 that are from the second set of data. Also, for Onne Flow Station, the first set of data is all higher than that of the second set for lines 1 to 3 and 5 to 8 but for line 4, L2 and M2 from the second set of fieldwork data give the maximum values and followed by M1 from the first set of data.

It is interesting to see that generally for both Eleme and Onne sites, the closer the measurements to the gas flare sources for all the projected eight lines, the higher the temperature; and so, the longer the distance the lower the temperature. The case of the relative humidity is different-as the reading varies; at times the closer to the flare source, the lower the relative humidity recorded. In addition, most of the lower height readings of relative humidity give high values and the reverse is the case for the upper height readings values.

The air temperature measured at both sites (see Table 4.8) is higher than air temperature reported for the months of field work observation (August and

September) in the meteorological record (section 3.7.6). The average air temperature reported for the months of August and September from 2000 to 2013 in the meteorological record is 297.8 K and 298.8 K respectively. The relative humidity measured at both sites (see Table 4.9) is lower than relative humidity reported for these months in the meteorological record. The range of relative humidity reported for the months of August and September from 2000 to 2013 in the meteorological record is (84-87) % and (85-89) % respectively.

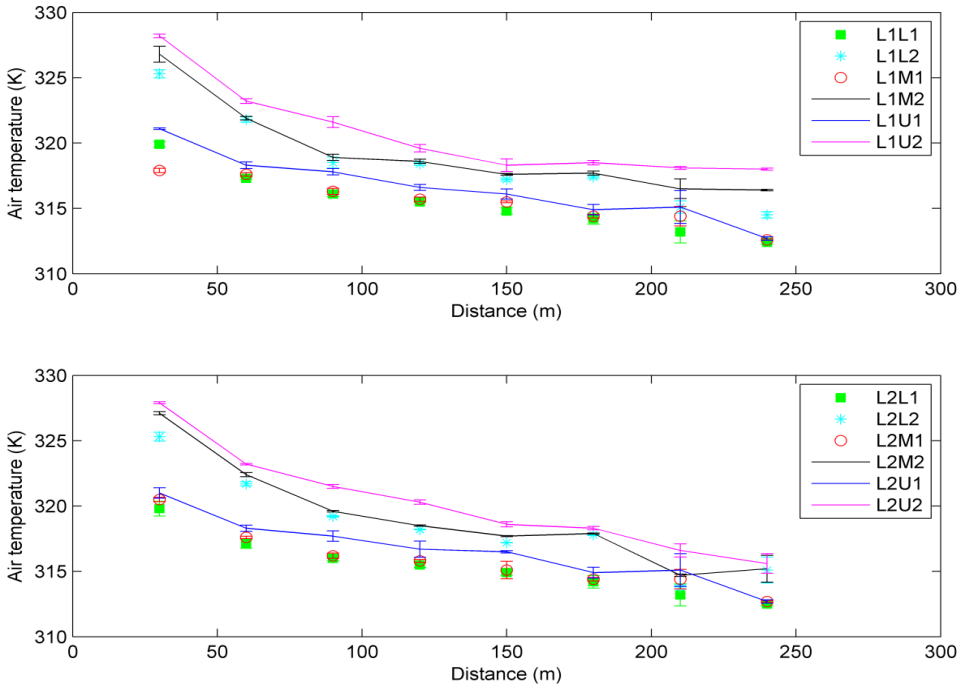

Figure 4-75: Air temperature at Eleme Refinery II gas flaring site (L1 & L2)

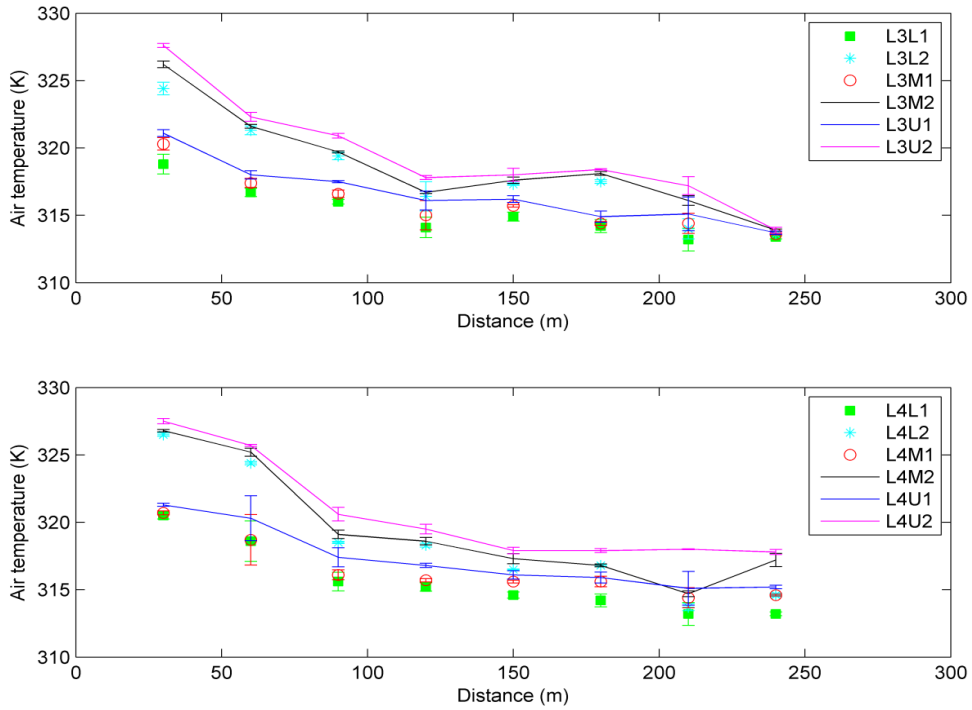

Figure 4-76: Air temperature at Eleme Refinery II gas flaring site (L3 & L4)

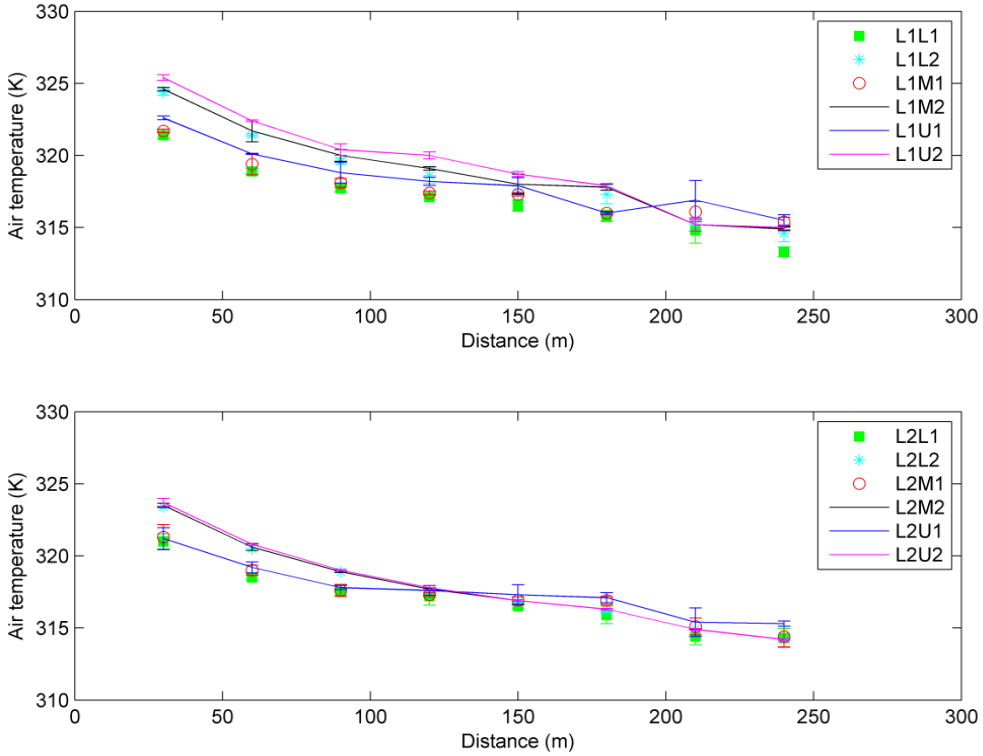

Figure 4-77: Air temperature at Onne Flow Station gas flaring site (L1 & L2)

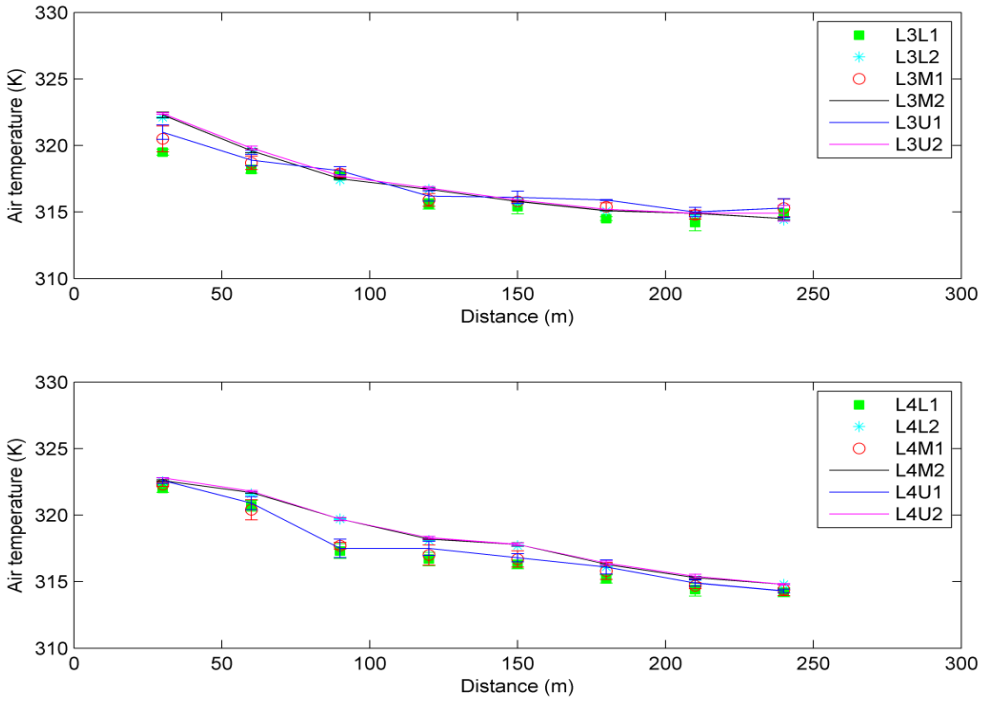

Figure 4-78: Air temperature at Onne Flow Station gas flaring site (L3 & L4)

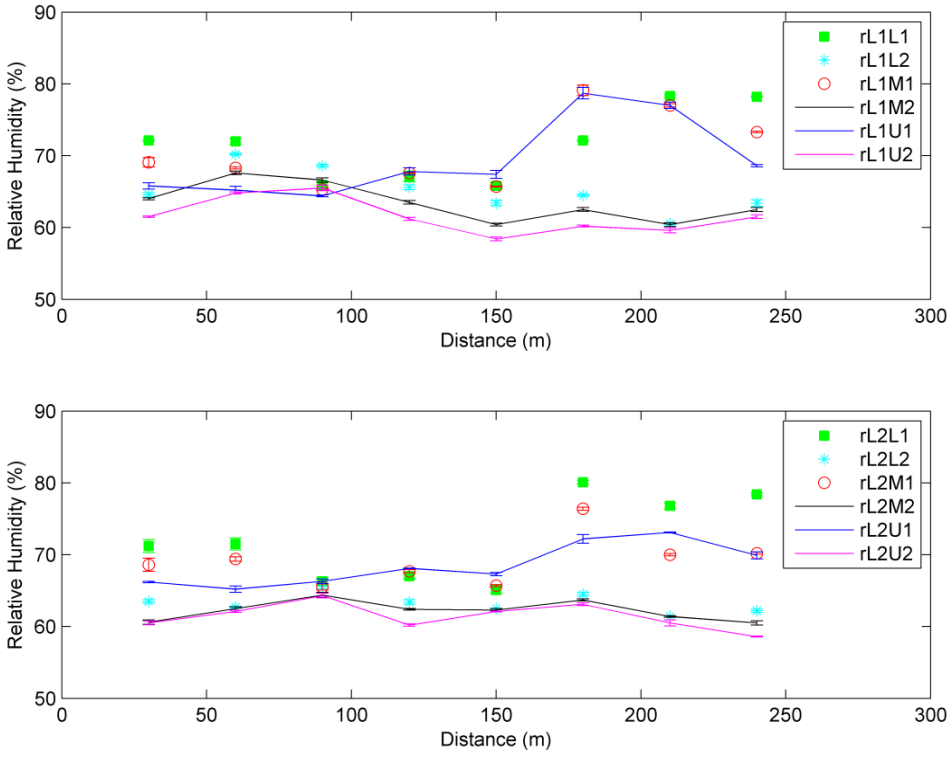

Figure 4-79: Relative humidity at Eleme Refinery II gas flaring site (L1 & L2)

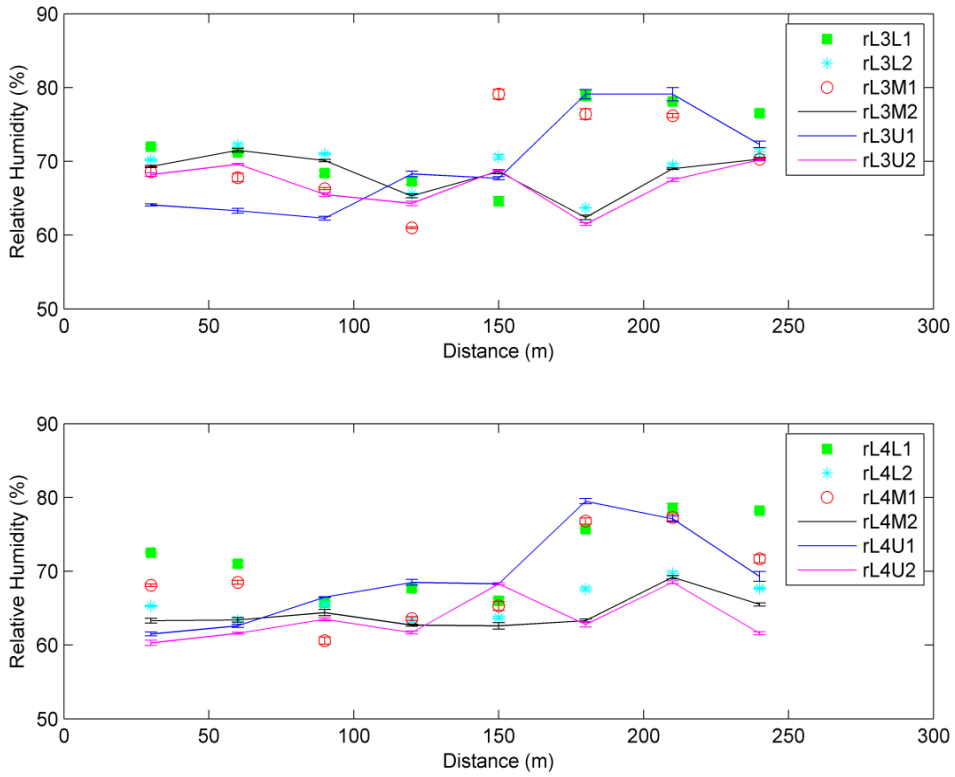

Figure 4-80: Relative humidity at Eleme Refinery II gas flaring site (L3 & L4)

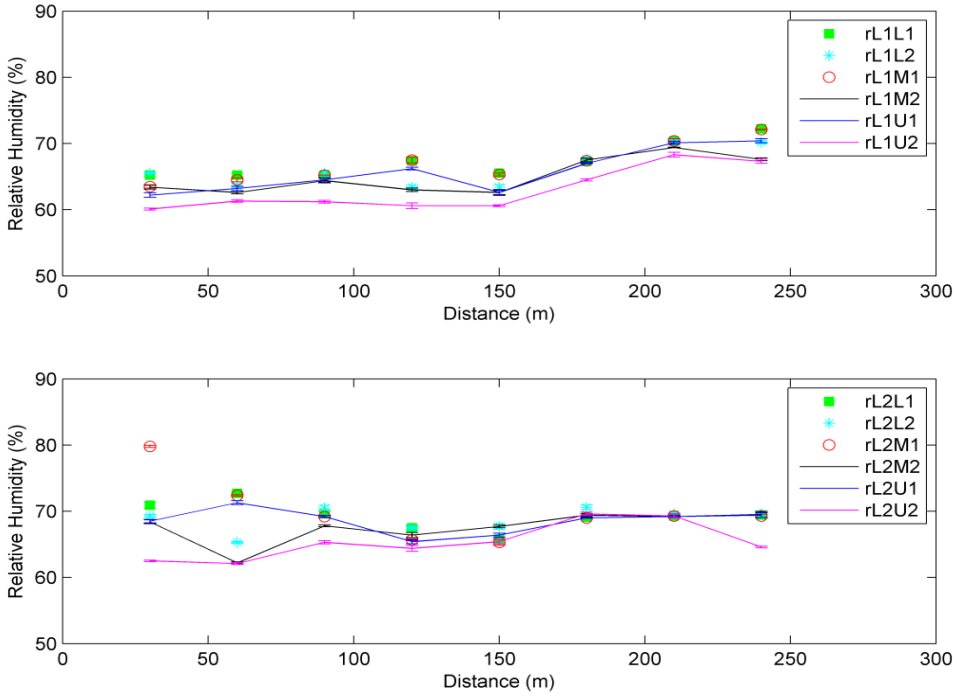

Figure 4-81: Relative humidity at Onne Flow Station gas flaring site (L1 & L2)

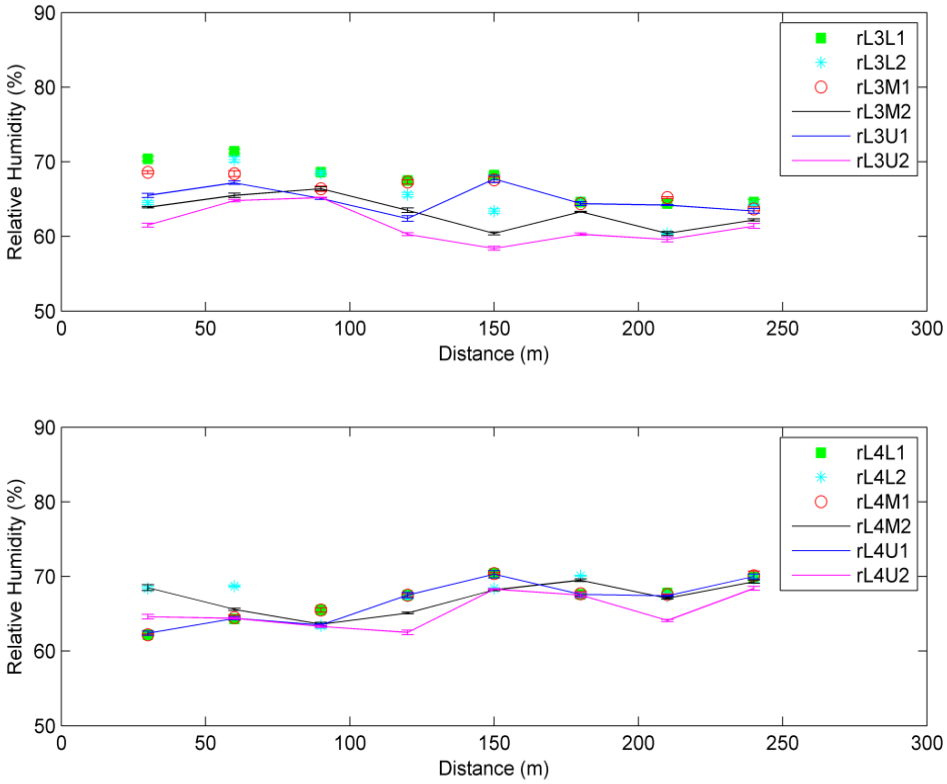

Figure 4-82: Relative humidity at Onne Flow Station gas flaring site (L3 & L4)

4.8 Comparison between field data and Landsat 5 TM and Landsat 7 ETM+ data

In this section, a comparison of spatial variability in ground air temperature measured at Eleme Refinery II and Onne Flow Station with their derived LST from Landsat 5 TM and Landsat 7 ETM+ was carried out. The range of air temperature change (δAT) measured in the field at 30 m away from the flare stack and 240 m at both sites is compared with the range of LST change (δLST) derived from Landsat data using the Type A curve classification data as explained in section 4.4.2. Table 4.10 shows the δAT obtained for Eleme Refinery II and Onne Flow Station for each of the eight lines.

Table 4-10: Range of Air Temperature between 30 m from flare stack and 240 m at Eleme Refinery II and Onne Flow Station

Line No.	Eleme Refinery II (δAT) (K)	Onne Flow Station (δAT) (K)
1	9.1	8.5
2	9.6	7.9
3	9.4	6.4
4	8.1	8.0
5	8.9	7.3
6	8.8	8.0
7	9.6	8.3
8	8.8	8.5
Mean	**9.0**	**7.9**

From Table 4.10 the mean δAT for Eleme Refinery II and Onne Flow Station are 9.0 K and 7.9 K respectively, while their δLST values are 5 K and 4.8 K (image acquired on 13/11/2005) and 20 K and 14.6 K (image acquired on 8/3/2013). The difference between the two δLST values for the two imagery examples can be attributed to factors such as rate and volume of burning gas, human activities such as bush burning for the preparation for planting of crops and the atmospheric conditions at the time of satellite overpass. Of these, only variation in the flare burn parameters can explain the observed elevation of LST close to the flare as described by the δLST parameter.

For Eleme Refinery II, the Landsat derived LST from 1984 to 2013 was plotted together with the air temperature measured in the field for comparison (see Figure 4.83). The results show that the air temperature is higher than most of the calculated Landsat LST values.

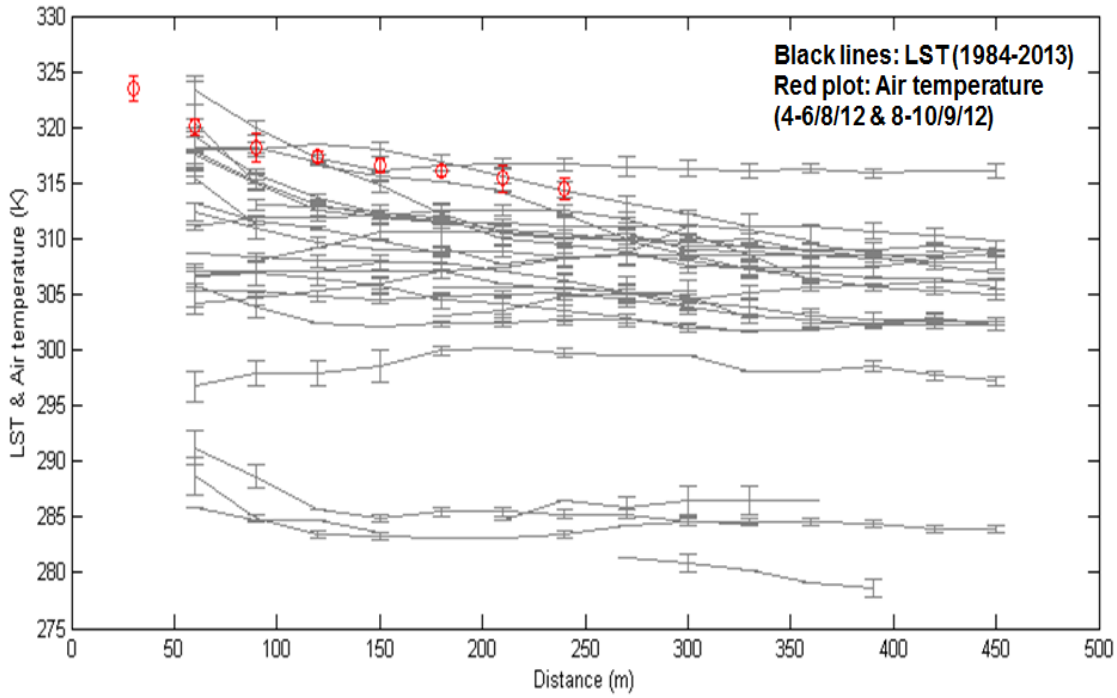

Figure 4-83: Landsat LST and Air temperature at Eleme Refinery II

Similarly, Figure 4.84 shows that the air temperature measured at Onne Flow Station is higher than most of Landsat derived LST values from 1984 to 2013. LST is not exactly the same as air temperature. Satellite-derived LST is influenced by atmospheric effects while air temperature was measured in-situ, i.e. with no need to apply an atmospheric correction. The physical parameters for LST and air temperature are different; radiation from the flare, Sun and land heats the air at a different rate (heat capacities) (see Figure 3.16). Given, the different processes affecting LST and air temperature; and the fact that both measurements are within a few K of each other suggests that the techniques are consistent and the spatial distributions in LST are reliable. The calculated LST and air temperature results for Eleme Refinery II and Onne Flow Station show similar trend.

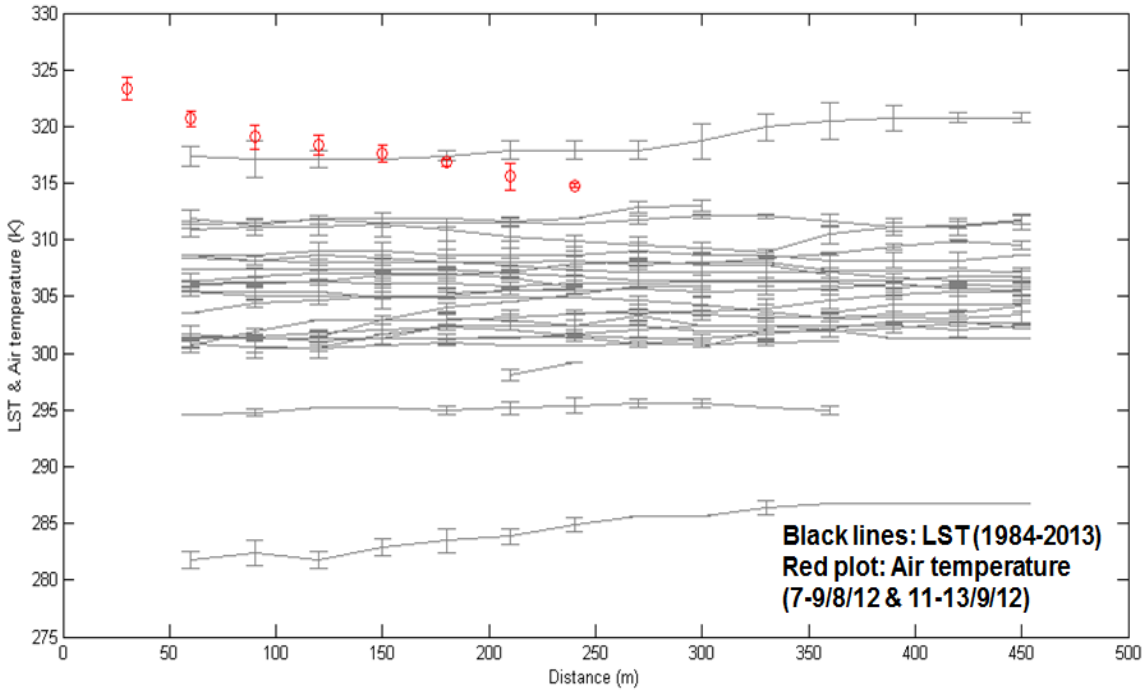

Figure 4-84: Landsat LST and Air temperature at Onne Flow Station

4.9 Summary and conclusions

In this Chapter, some of the factors that are likely to influence LST at these flaring sites were assessed. Firstly, it is interesting to note that both Umurolu and Bonny LNG, the two largest facilities with different site topography, have similar results and this could be attributed to their size and the number of flare stacks; Bonny has five flare stacks and Umurolu has four. Secondly, Alua, Rukpokwu, Obigbo and Chokocho are medium and small size inland flow stations. Their results demonstrate that the impact of facility size on LST is statistically significant, which could be as a result of their rate of burning.

Sara Flow Station is located at the coast and receives crude oil from several oil wells (Figures 4.21 and 4.22: Land cover types). Its size could be limited because of the rough terrain, but the magnitude of δLST suggested that it is functioning at a high capacity with high rate of burning gas. Furthermore, both Eleme Refineries show a non-significant impact for the three parameters investigated

(Tables 4.5 and 4.6) despite their size and this could be attributed to the presence of only a single flare stack at each refinery and damage to the facilities; since 1988, damage has reduced their capacities to almost zero. Multiple linear regression results complement this by revealing that the size of the facility may exert a negative influence on the changes in LST; however, the overall percentage of variability explained is low. Therefore, it is suggested that the rate of gas burning and the number of flare stacks within a facility are the two major factors that influence changes in LST at these flaring sites.

In addition, results acquired from the fieldwork have shown the spatial pattern of air temperature and relative humidity at the Eleme Refinery II and Onne Flow Station. The use of eight lines radiating from the flares to cover the area surrounding the flare source allowed spatial patterns in air temperature to be identified (see Figures 3.14-3.15). This datasets were compared to the LST retrieved from Landsat 5 TM and Landsat 7 ETM+ data, and the spatial distributions are in good agreement to within 3.5 K. Comparison of this result to other previous literature on retrieval of LST from Landsat data are in good agreement. For example Coll et al. (2010) worked on validation of Landsat 7 ETM+ thermal band calibration and atmospheric correction with ground based measurements performed in a homogeneous site of rice crops close to Valencia, Spain. The two results presented are when the atmospheric correction was calculated from local-radiosonde profiles and when the atmospheric correction was obtained from ATMCORR Calculator. For the first approach, the differences between the ground and Landsat 7 ETM+ LSTs ranged from −0.6 to 1.4 K while for the second approach, the differences ranged between −1.8 and 1.3 K. In addition, results from Otukei and Blaschke (2012) on the use of Landsat 7

ETM+ low gain and high gain thermal infrared band for assessing the LST in Kampala, Mukono and Jinja Districts in Uganda give a difference of 0.71 K between ground and Landsat 7 ETM+ LSTs. Furthermore, Ifatimehin and Adeyemi (2008) also used Landsat TM data to retrieve LST in Lokoja, Nigeria. They recorded a difference of 9.6 K between LSTs retrieved from Landsat TM and measured in situ temperature at Meteorological station, Lokoja.

The observed air temperature at both sites showed that the closer the measurement to the flaring source, the higher the temperature and vice-versa, but the relative humidity measured at both sites varied in a less consistent manner. Also, the available meteorological data (air temperature) showed that during the period of this fieldwork, the background air temperatures were lower with higher relative humidity because it was the season of highest rainfall in Nigeria. Also, air temperature is not exactly the same as LST and the conversion of air temperature to get LST is beyond the scope of this study.

As seen, there are limitations encountered in this study as a result of the following: Low N (number of Landsat images per each station), scan-line correction error within Landsat 7 data and the unavailability of key factors such as rate of gas burning and volume of gas burning that mean it's not possible to draw firm conclusions about what drives δLST. In addition, section 3.7.5 give details of problems encountered during the fieldwork.

Chapter 5
Evaluation of environmental impact of gas flaring on vegetation health

This Chapter addresses research questions two and three, and objective five. Research question two is - can satellite data be used to detect the impact of gas flaring on vegetation cover and health? Question three is - what is the spatial and temporal variability in satellite detectable flare impact on vegetation cover and health? Objective five is the preliminary evaluation of the environmental impacts of gas flaring related pollution within Nigeria from 1984 to 2013. These research questions and objective are addressed using NDVI and LST as previously developed in Chapter 3. Furthermore, the approaches used to address these research questions and objective are quantitative analysis of NDVI result, qualitative and quantitative analysis of a change in vegetation health potentially related to flare pollution at a given time, quantitative analysis of the relationship between the spatial gradient in LST and the spatial gradient in NDVI, quantitative analysis of the influence of environmental factors on vegetation health, and quantitative analysis of vegetation health change from 1984 to 2013.

The description of the data analysis adopted methodology for this Chapter is provided in section 5.1. Also, the quantitative analysis of a change in vegetation health at a given time by plotting NDVI versus distance, and change in NDVI (δNDVI) is explained in section 5.2 while section 5.3 examines the relationship between the spatial gradient in LST and the spatial gradient in NDVI around

flare sites using pairwise linear regression analysis. The influence of environmental factors on vegetation cover and health is examined using both linear regression and multiple linear regression analysis in section 5.4. Section 5.5 explains the use of time series analysis within 240 m of a flare and spatio-temporal regression analysis over a larger domain to evaluate change in vegetation health from 1984 to 2013. A summary is given in section 5.6 and conclusions in section 5.7.

5.1 Methodology for data analysis

This section presents the questions that are answered, data used and types of statistical analysis carried out to achieve the aim of the study; Table 5.1 shows the methodological details adopted for the data analysis.

Table 5-1: Methodology for data analysis for objective number five

Section	Questions/topic	Data	Analysis
5.2	How do we parameterise a change in vegetation health potentially related to flare pollution at a given time?	NDVI	Qualitative: Plot NDVI versus distance from flare, Quantitative: Define new parameter δNDVI in N, E, S and W directions.
5.3	Is there a significant relationship between the spatial gradient in LST and the spatial gradient in NDVI around flare sites?	δ LST and δ NDVI, both directionally resolved i.e. N, E, S, and W direction.	Quantitative: Linear regression
5.4	How does vegetation health change with environmental factors?	δ NDVI, Environmental factors: size of facility, flare stack height, year, month and day	Quantitative: Pairwise linear regression analysis and multiple linear regression analysis.
5.5	How has vegetation health changed over a 12 km × 12 km area around each flare, from 1984 to 2013?	NDVI time-series	Qualitative: Time-series plot at 4 distances (60, 90, 120 and 240) m from each flare Quantitative: Spatially resolved linear regression of NDVI against time for 400 × 400 pixel Landsat subscenes.

5.2 Quantitative analysis of a change in vegetation health potentially related to flare pollution at a given time

NDVI was calculated for the available Landsat record from 1984 to 2013, with the NDVI ranges indicating healthy and unhealthy vegetation as discussed in section 3.5.1.1. The two analyses used to evaluate a change in vegetation health at the flaring sites are the plot of NDVI versus distance from the flare, and the derivation of a measure of change in NDVI (δNDVI) with distance from the flare, calculated from the difference in NDVI obtained by choosing firstly the maximum NDVI value from a far distance between 150 m and 450 m, and secondly the NDVI value at a distance of 60 m from the flare, in four cardinal directions.

5.2.1 The plot of NDVI versus distance

In section 4.4.1.2 the results from LST and NDVI for four cardinal directions at each site were plotted together (see Figures 4.47-4.58); the results showed four different types of curve as discussed in section 4.4.2 and shown in Figure 4.61. The Type A curve was adopted for this study because it shows that changes in LST are consistent with the flare being the main local heat source i.e. the shorter the distance to the flare, the higher the LST and the lower the NDVI. Therefore, the plot showed that the vegetation cover around the flare stack is being affected by the flare causing the vegetation cover to become sparse with less photosynthetic activity (Carlson and Ripley, 1997; Goward et al., 1985; Gallo et al., 1985) because of the lower NDVI values, and as distance increases away from the flare the NDVI values increases indicating increases in green vegetation (Weiss et al., 2004). The range of distances used for plotting Figures 4.47-4.58 was 60 to 450 m. Table 5.2 shows examples of the NDVI values at 60 m and 450 m distance from the flare for all flaring sites. The values suggest that

gas flaring activities in these sites influence the vegetation cover and health around the flare negatively; higher NDVI further away.

Table 5-2: Examples of NDVI values at 60 m and 450 m distance from the flare with Type A curve

Flaring site	NDVI (60 m)	NDVI (450 m)	δNDVI	Date	Figure
Eleme Refinery I	0.55	0.74	0.19	17/12/2000	4.36
Eleme Refinery II	0.30 at 120 m	0.52	0.22	13/11/2005	4.48
Onne	0.42	0.75	0.33	8/3/2013	4.49
Umurolu	0.42	0.48	0.06	17/4/2010	4.39
Bonny LNG	0.40	0.48 at 300 m	0.08	8/1/2003	4.40
Alua	0.55	0.76	0.21	19/12/1986	4.41
Rukpokwu	0.26	0.32	0.06	13/1/2005	4.42
Obigbo	0.19	0.24	0.05	18/12/2006	4.44 B
Chokocho	0.38	0.56	0.18	21/12/2007	4.45
Umudioga	0.51	0.71	0.20	25/3/1987	4.46
Sara	0.18	0.24	0.06	19/1/2007	4.47

For the full Landsat dataset analysed, Type A curves in NDVI were obtained in 2503 out of 3001 cases, suggesting that the flare had a measurable impact on vegetation close by in 83 % of cases observed.

5.2.2 Change in NDVI (δNDVI)

Change in NDVI (δNDVI) is the difference between NDVI values at a distance far away and near to the flare i.e. the difference between maximum NDVI value obtained between 150 m and 450 m (far distance) and 60 m (near distance) from the flare (see section 4.4.3). Figure 5.1 is the schematic diagram of the change in NDVI for the Type A curves. δNDVI was computed for all the four cardinal directions, hence, $\delta\,NDVI_N$, $\delta\,NDVI_E$, $\delta\,NDVI_S$ and $\delta\,NDVI_W$ were obtained; showing what has happened to the vegetation cover and health in the four directions.

Figure 5-1: Change in NDVI with distance, and the definition of δNDVI

Table 5.3 presents the three relationships ($\delta NDVI_N$ versus $\delta NDVI_E$, $\delta NDVI_N$ versus $\delta NDVI_S$, and $\delta NDVI_N$ versus $\delta NDVI_W$) adopted as their r-values, p-values and the type of correlation obtained. All results show positive correlations, but only $\delta NDVI_N$ versus $\delta NDVI_W$ has a significant result at 99 % confidence level (p-values = 0.0016) whilst the other two are not significant.

Table 5-3: Correlation coefficient of three relationships of δNDVI with α = 0.01

Relationship	(r-values)	p-values	Type of correlation
$\delta NDVI_N$ v $\delta NDVI_E$	0.0879	0.1018	Positive
$\delta NDVI_N$ v $\delta NDVI_S$	0.1056	0.0490	" "
$\delta NDVI_N$ v $\delta NDVI_W$	0.1689	**0.0016**	" "

Figures 5.2-5.4 are the plots for these three relationships; the total number of data points used for the plotting of each figure (N) is 348. The colour of the stack height helped to identify data that belonged to each oil facility, for example the stack height for Eleme Refinery I is 50 m and that of Eleme

Refinery II is 65 m (see sections 4.1.1 to 4.1.11), hence, all deep red and brown points in these figures are from these two refineries.

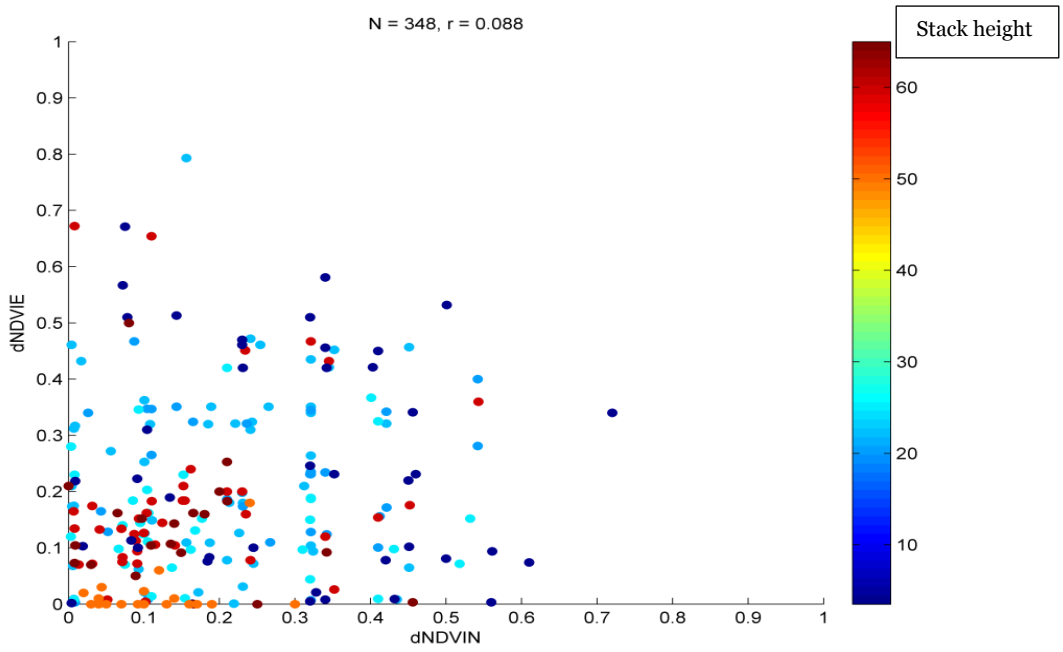

Figure 5-2: $\delta NDVI_N$ against $\delta NDVI_E$

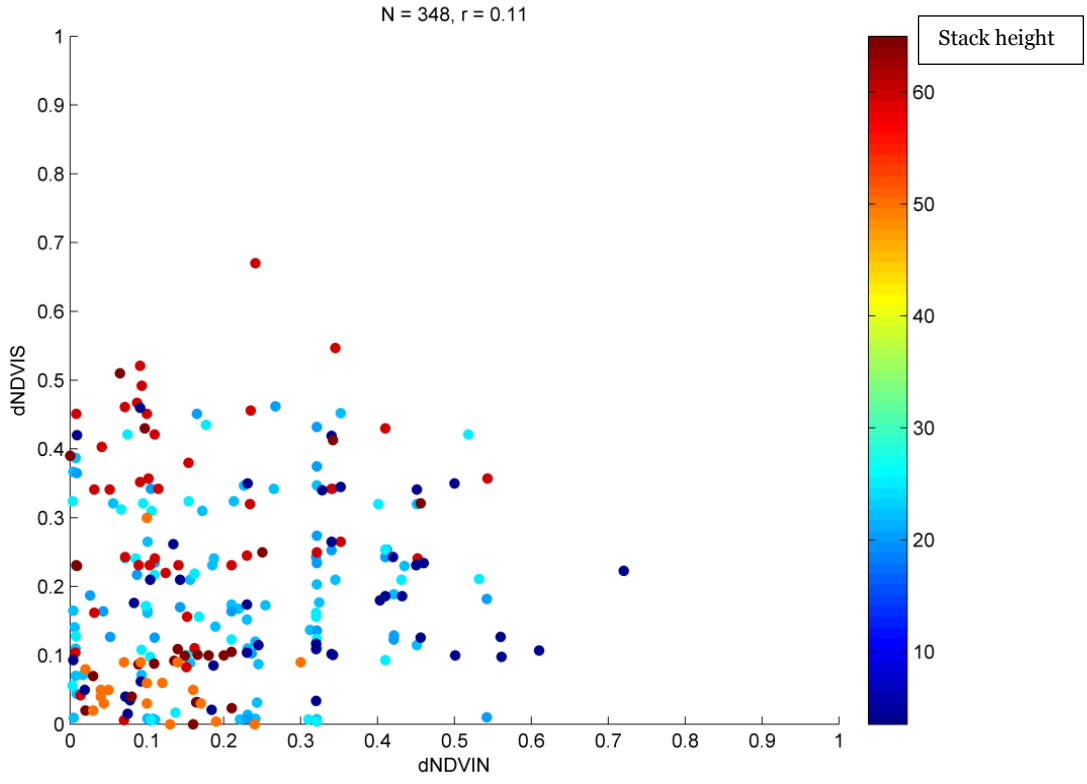

Figure 5-3: $\delta NDVI_N$ against $\delta NDVI_S$

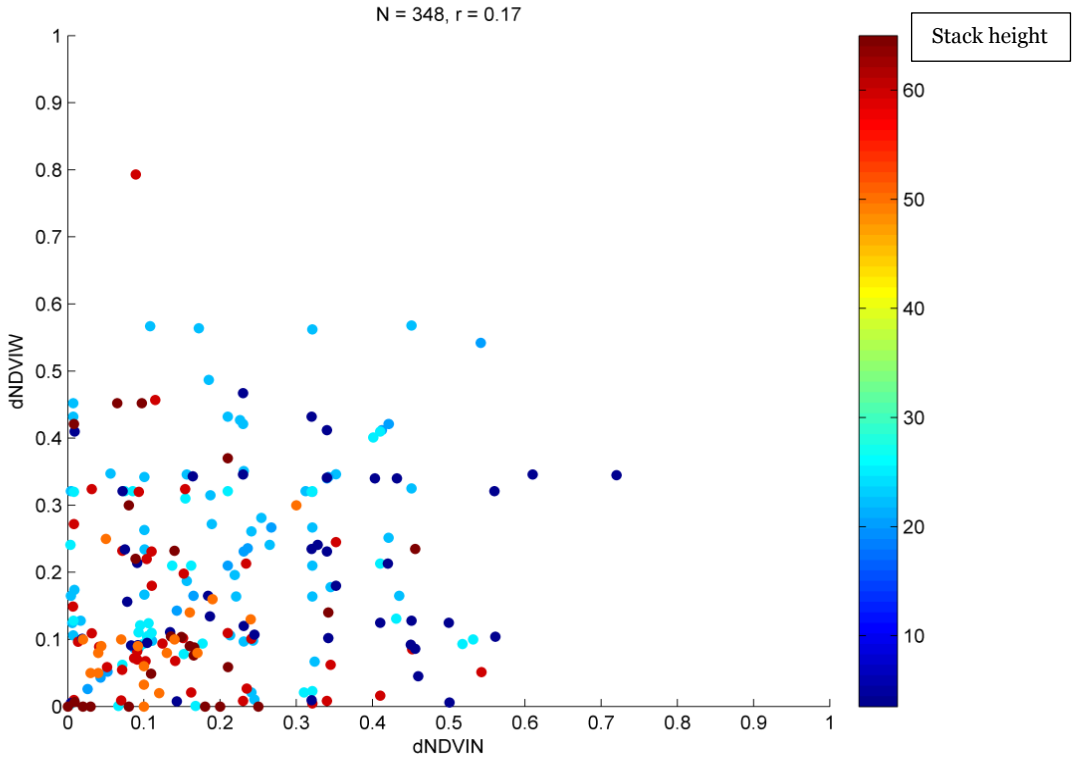

Figure 5-4: $\delta NDVI_N$ against $\delta NDVI_W$

5.3 Relationship between the spatial gradient in LST and the spatial gradient in NDVI around the flare sites

Some researchers have employed linear regression analysis to investigate the relationship between LST and NDVI in the past. For example, Sandholt et al. (2002) adopted linear analysis to carry out the empirical parameterisation of the relationship between LST and NDVI to derive a simplified land surface dryness index. Linear regression analysis was used by Kawabata et al. (2001) to examine the correlations between the seasonal and annual NDVIs for 9 years and land air temperature for the purpose of global monitoring of interannual changes in vegetation activities. Also, Karnieli et al. (2010) used both multiple and single linear regression analysis for drought assessment. In addition, linear regression analysis of LST and NDVI was investigated by Chuvieco et al. (2004) for the estimation of live fuel moisture content in the forest fire danger rating.

Non-linear analysis has been used by other researchers, for example, Cleland et al. (2007) employed change point analysis (Spark and Tryjanowski, 2005) and Bayesian techniques (Doze and Menzel, 2004) to study shifting plant phenology in response to global change. Potter and Brooks (1998) applied both linear and non-linear multiple regression statistical analysis to study global aanalysis of empirical relations between annual climate and seasonality of NDVI. For this study, both linear and non-linear relationships were tested but non-linear give no better results. Hence, linear regression analyses were used for further analysis to examine the relationships between the spatial gradient in LST and the spatial gradient in NDVI around the flare sites.

5.3.1 Linear regression analysis

To find whether there is a significant relationship between the spatial gradient in LST and the spatial gradient in NDVI around the flare, for the eleven flaring sites used for this study, both δLST and δNDVI were calculated. Pairwise linear regression analysis was carried out for the relationships between $\delta LST_{N, E, S, W}$ and $\delta NDVI_{N, E, S, W}$ when δLST and / or δNDVI were not zero. Table 5.4 presents the resulting r-values and p-values. N is the total number for each δLST's and δNDVI's data, r-values shows a positive correlation that exists between each of them and p-values show statistically insignificant results with apriori $\alpha = 0.01$.

Table 5-4: Number, r-values and p-values for δLST against δNDVI

Relationship	Number	r-values	p-values
δLST_N v $\delta NDVI_N$	214	0.0023	0.9732
δLST_E v $\delta NDVI_E$	233	0.0850	0.1972
δLST_S v $\delta NDVI_S$	249	0.0320	0.1984
δLST_W v $\delta NDVI_W$	244	0.1000	0.1147

Furthermore, the same pairwise linear regression analysis was carried out for each of the eleven facilities using the same δLST $_{N, E, S, W}$ and δNDVI $_{N, E, S, W}$ when both are greater than zero. The relationship is investigated without zero values for both δLST and δNDVI to remove the effects of uncertainties. When δLST is equal to zero it means that LST at both near and far away distance (see section 4.4.3) are equal; suggesting the availability of other heat sources at a far away distance or no burning on the stack at the time of satellite overpass. Similarly, when δNDVI is equal to zero, it means that NDVI at both near and far away distance (see section 5.2.2) are equal, suggesting an uncertain condition. The results obtained are presented in Table 5.5.

Figures 5.5-5.8 show the plots of the relationships between δLST and δNDVI, i.e. δLST_N versus $\delta NDVI_N$, δLST_E versus $\delta NDVI_E$, δLST_S versus $\delta NDVI_S$ and δLST_W versus $\delta NDVI_W$. The scale bar is an arbitrary chosen number for the identification of the eleven facilities investigated; for example, 1 represents Eleme Refinery I and 11 is for Sara Flow Station (see sections 4.1.1 to 4.1.11).

Table 5-5: δLST against δNDVI (when both > 0)

Facility	Number r-value p-value (N)	Number r-value p-value (E)	Number r-value p-value (S)	Number r-value p-value (W)
1 (Eleme I)	15 0.5558 0.0315	14 -0.2173 0.4556	15 -0.2033 0.4674	13 -0.0755 0.8062
2 (Eleme II)	17 0.1610 0.5371	19 -0.0333 0.8923	17 0.3306 0.1950	17 0.6002 0.0109
3 (Onne)	23 -0.1647 0.4525	27 0.1462 0.4667	27 0.1505 0.4538	31 -0.3244 0.0750
4 (Umurolu)	22 -0.0601 0.7905	29 -0.1102 0.5693	28 -0.2354 0.2294	27 0.0263 0.8966
5 (Bonny)	15 0.1231 0.6620	24 0.1111 0.6053	20 -0.1183 0.6194	23 0.2291 0.2930
6 (Alua)	20 0.2058 0.3841	17 -0.1022 0.6963	20 0.0184 0.9385	18 0.1788 0.4778
7 (Rukpokwu)	30 -0.1844 0.3294	26 -0.2732 0.1769	31 0.4153 0.0202	30 -0.0055 0.9771
8 (Obigbo)	24 -0.0798 0.7108	18 0.1881 0.4548	20 -0.2020 0.3932	18 -0.3932 0.1065
9 (Chokocho)	21 -0.2001 0.3844	20 0.2849 0.2849	22 0.1844 0.4114	20 0.2941 0.2081
10 (Umudioga)	12 -0.0471 0.8845	14 -0.1469 0.3294	16 0.4619 0.0717	18 -0.0122 0.9616
11 (Sara)	15 -0.0913 0.7461	25 0.1954 0.3494	31 -0.0278 0.8821	29 -0.0786 0.6854

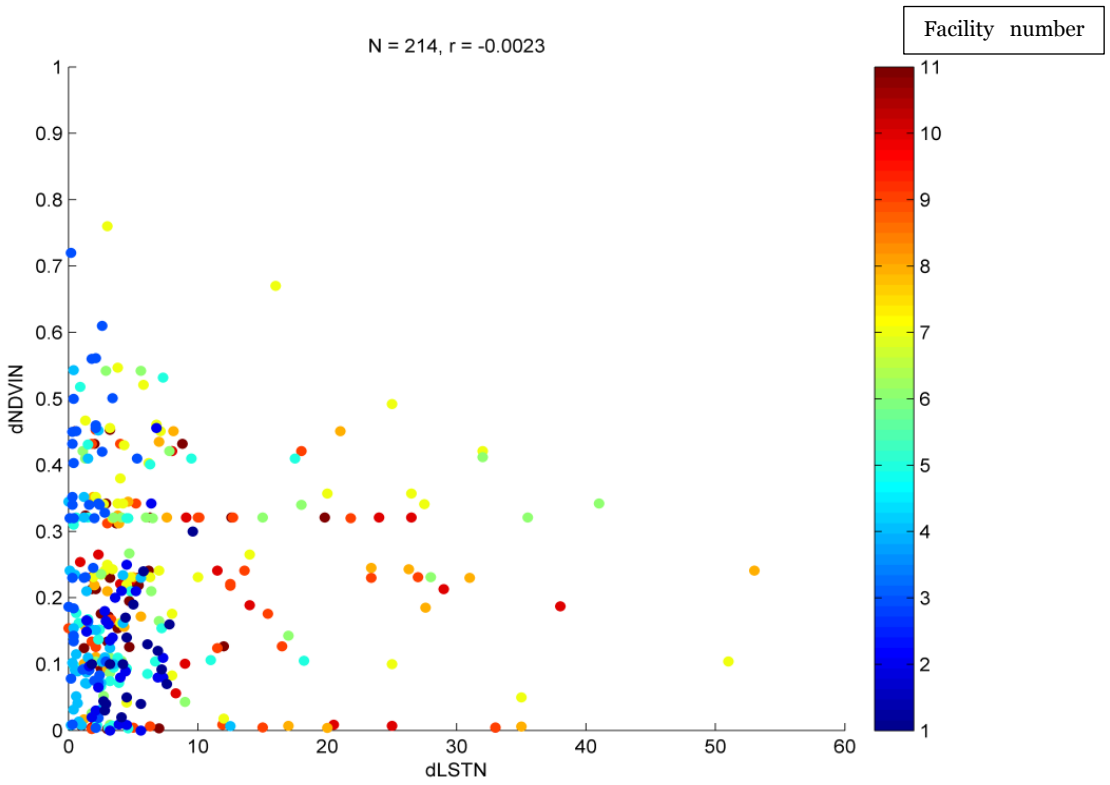

Figure 5-5: δLST_N against $\delta NDVI_N$

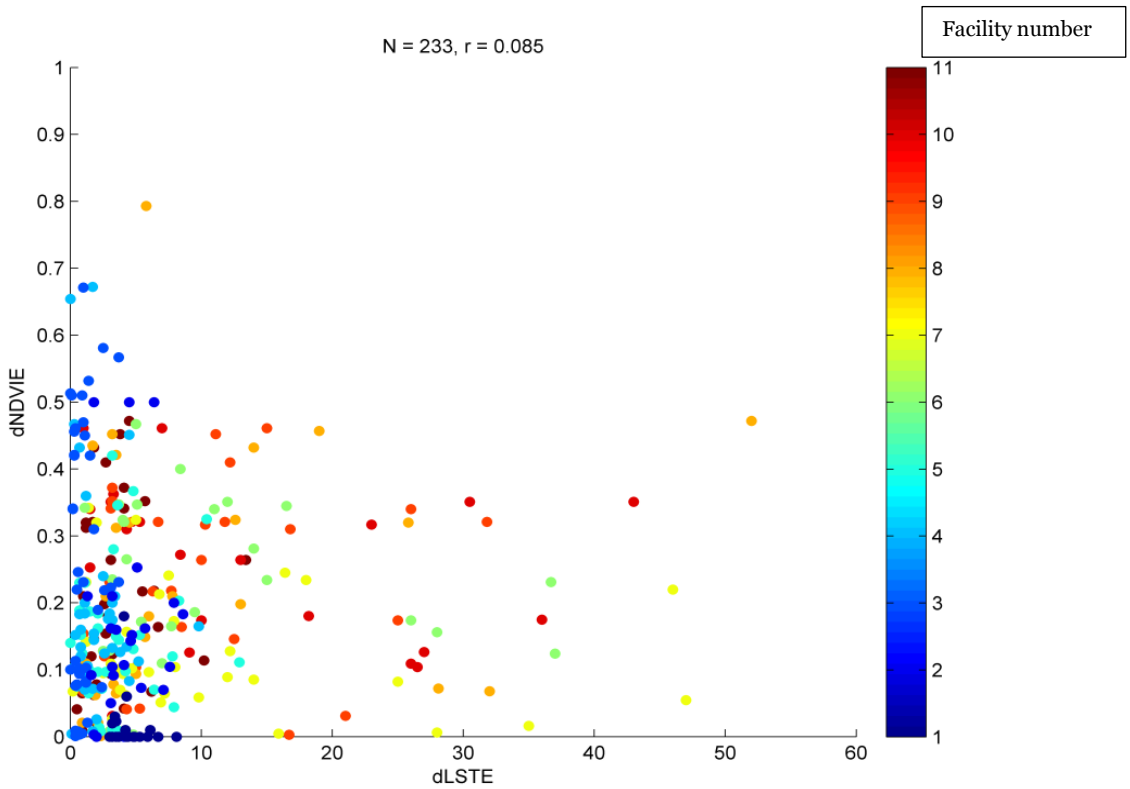

Figure 5-6: δLST_E against $\delta NDVI_E$

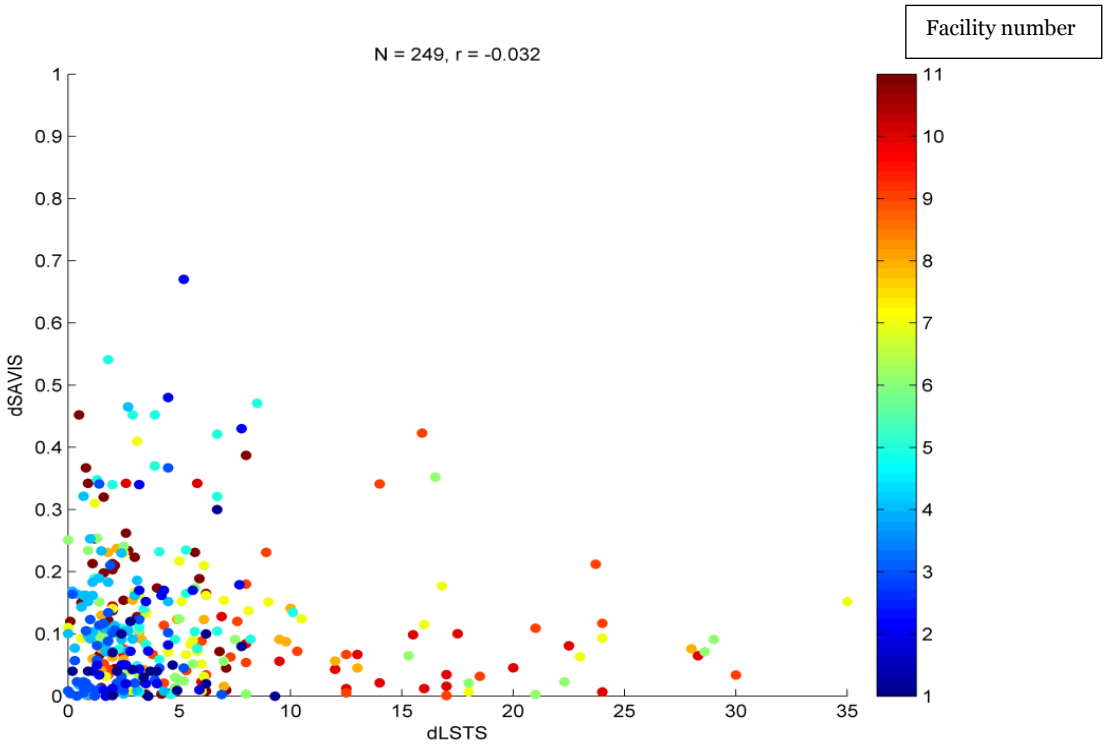

Figure 5-7: δLSTs against δNDVIs

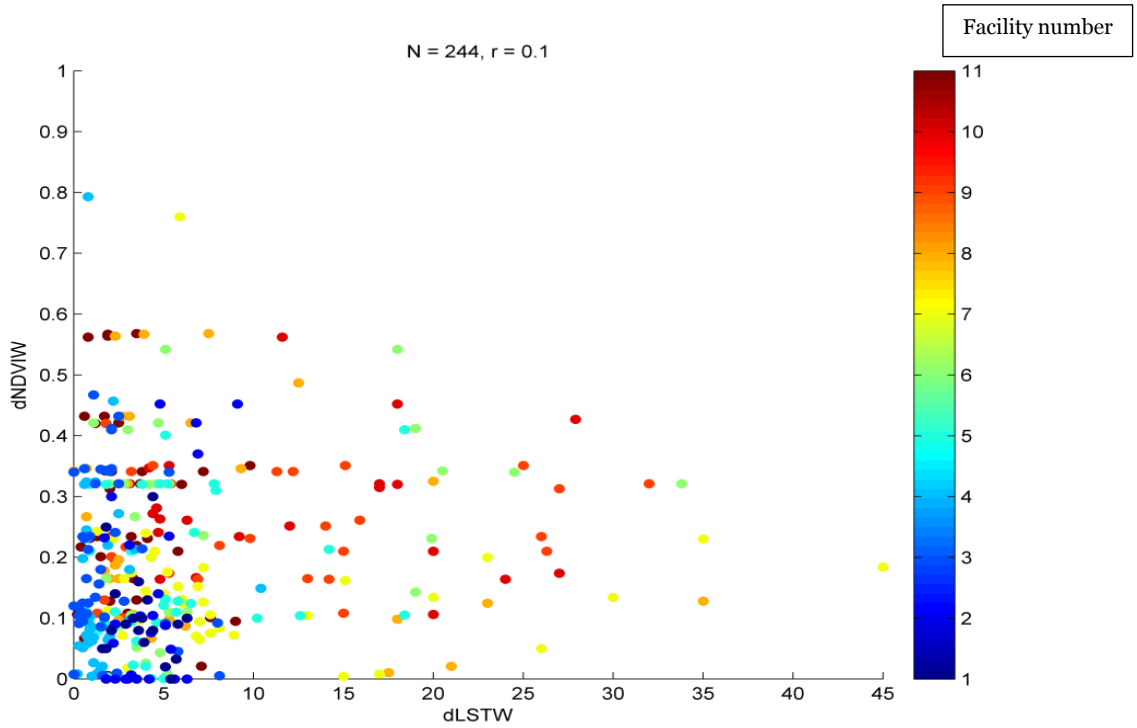

Figure 5-8: δLST_W against $\delta NDVI_W$

From the relationships shown in Table 5.4 and Table 5.5, Eleme Refinery I and II, Bonny LNG and Alua Flow Station have a positive correlation (r-values) and

insignificant results (p-values) in the North direction while Onne, Umurolu, Rukpokwu, Obigbo, Chokocho, Umudioga and Sara flow stations show a negative correlation (r-values) and insignificant results (p-values) in the North direction. In the East direction, Eleme Refinery I and II, Umurolu, Alua and Umudioga have a negative correlation (r-values) and insignificant results (p-values); and Bonny LNG, Onne, Obigbo, Chokocho and Sara Flow Stations have a positive correlation (r-values) and insignificant results (p-values). Also, in the South direction Eleme Refinery I, Bonny LNG, and Umurolu, Obigbo and Sara Flow Stations give a negative correlation (r-values) and insignificant results (p-values) while Eleme Refinery II, Onne, Alua, Rukpokwu, Chokocho and Umudioga Flow Stations have a positive correlation (r-values) and insignificant results (p-values). Finally, in the West direction, Eleme Refinery I, Onne, Rukpokwu, Obigbo, Umudioga and Sara Flow Stations show negative correlation (r-values) and insignificant results (p-values) while Eleme Refinery II, Bonny LNG, Umurolu, Alua and Chokocho show positive correlation (r-values) and insignificant results (p-values).

Furthermore, only the correlation coefficient for Eleme I in the North direction (0.5558) and Eleme II in the West direction (0.6002) show that there is linear interdependence of the two variables, δLST and δNDVI. The correlation coefficient results for the remaining nine facilities show non linear interdependence of these two variables for all directions. In the absence of significant correlations, no conclusions can be drawn about the effect of prevailing wind direction on any relationship between δLST and δNDVI.

5.4 Influence of environmental factors on vegetation cover and health

The list of environmental factors that influence vegetation cover and health at these flaring sites were listed in section 3.6.3. The factors available for study (i.e. size of facility, flare stack height and time i.e. year, month and day) were correlated against δNDVI using both linear and non linear relationships, but non-linear relationship gives no better results. Therefore, pairwise linear regression and multiple linear regression analyses were adopted to assess the relationship of these available factors with vegetation cover and health. The direction of the prevailing wind in the Niger Delta is South as previously stated (see Table 4.3).

5.4.1 Linear regression analysis

The relationships amongst the four δNDVIs ($\delta NDVI_N$, $\delta NDVI_E$, $\delta NDVI_S$ and $\delta NDVI_W$) and the available environmental factors were considered using pairwise linear regression analysis to indicate the relationships that produce significant results (see Table 5.6); significant results are in bold. Figures 5.9-5.12 present the plots of the relationship between size of each facility and $\delta NDVI_N$, $\delta NDVI_E$, $\delta NDVI_S$ and $\delta NDVI_W$. Figures 5.13-5.16 are the plots of the relationship between the height of stack and $\delta NDVI_N$, $\delta NDVI_E$, $\delta NDVI_S$ and $\delta NDVI_W$ respectively. Figures 5.17-5.20 show the relationship between month and $\delta NDVI_N$, $\delta NDVI_E$, $\delta NDVI_S$ and $\delta NDVI_W$. Figures 5.21-5.24 show the relationship between Julian Day and $\delta NDVI_N$, $\delta NDVI_E$, $\delta NDVI_S$ and $\delta NDVI_W$ and finally, Figures 5.25-5.28 show the relationship between year and $\delta NDVI_N$, $\delta NDVI_E$, $\delta NDVI_S$ and $\delta NDVI_W$. The scale bar used is the stack height of each facility.

Table 5-6: Correlation coefficient of relationships of factors that impact NDVI with α = 0.01

Relationship	(r-value)	p-value	Type of correlation
Month v $\delta NDVI_N$	0.0234	0.6636	Positive
Month v $\delta NDVI_E$	-0.0192	0.7208	Negative
Month v $\delta NDVI_S$	0.0661	0.219	Positive
Month v $\delta NDVI_W$	0.0563	0.2946	" "
Size of the facility v $\delta NDVI_N$	-0.1414	**0.008**	Negative
Size of the facility v $\delta NDVI_E$	-0.1017	0.0581	" "
Size of the facility v $\delta NDVI_S$	0.1048	0.0508	Positive
Size of the facility v $\delta NDVI_W$	-0.1589	**0.003**	Negative
Height of stack v $\delta NDVI_N$	-0.3402	$\mathbf{6.9042 \times 10^{-8}}$	" "
Height of stack v $\delta NDVI_E$	-0.2372	$\mathbf{2.1526 \times 10^{-4}}$	" "
Height of stack v $\delta NDVI_S$	0.1167	0.0717	Positive
Height of stack v $\delta NDVI_W$	-0.2621	$\mathbf{4.0952 \times 10^{-5}}$	Negative
Julian Day v $\delta NDVI_N$	0.0173	0.7473	Positive
Julian Day v $\delta NDVI_E$	-0.0196	0.7155	Negative
Julian Day v $\delta NDVI_S$	0.0603	0.2621	Positive
Julian Day v $\delta NDVI_W$	0.0549	0.3072	" "
Year v $\delta NDVI_N$	0.0805	0.134	" "
Year v $\delta NDVI_E$	0.0151	0.7783	" "
Year v $\delta NDVI_S$	0.0112	0.8345	" "
Year v $\delta NDVI_W$	0.1004	0.0613	" "

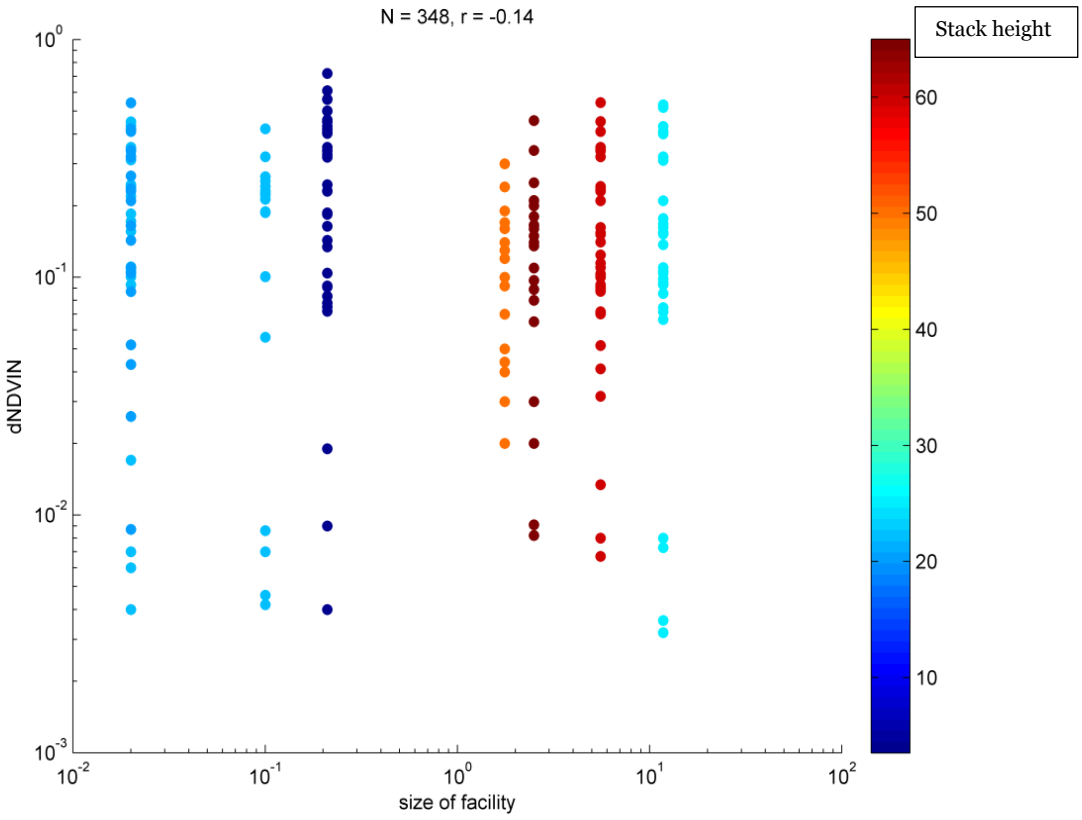

Figure 5-9: Size of facility against $\delta NDVI_N$

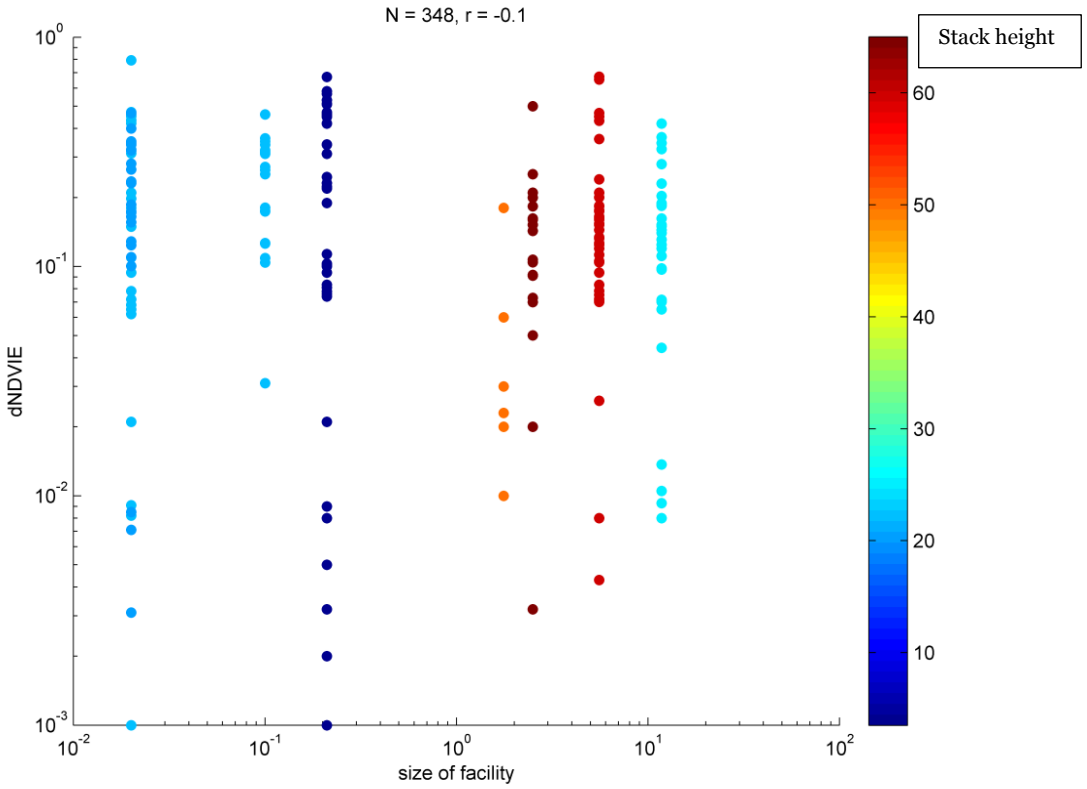

Figure 5-10: Size of facility against $\delta NDVI_E$

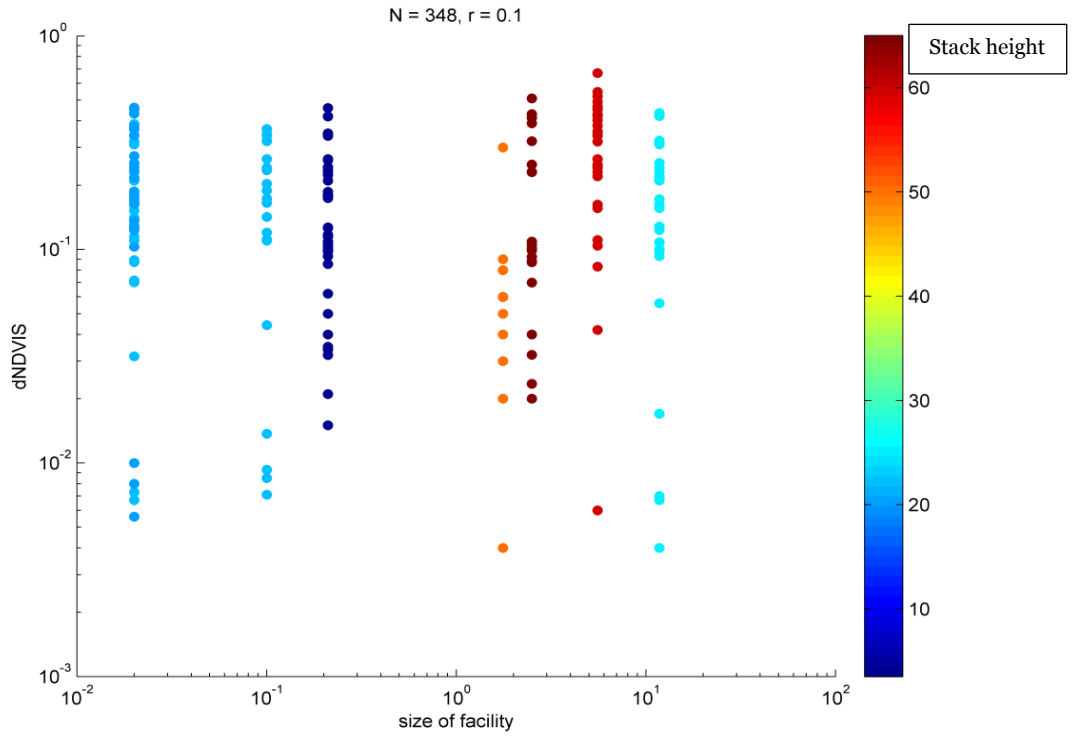

Figure 5-11: Size of facility against $\delta NDVI_S$

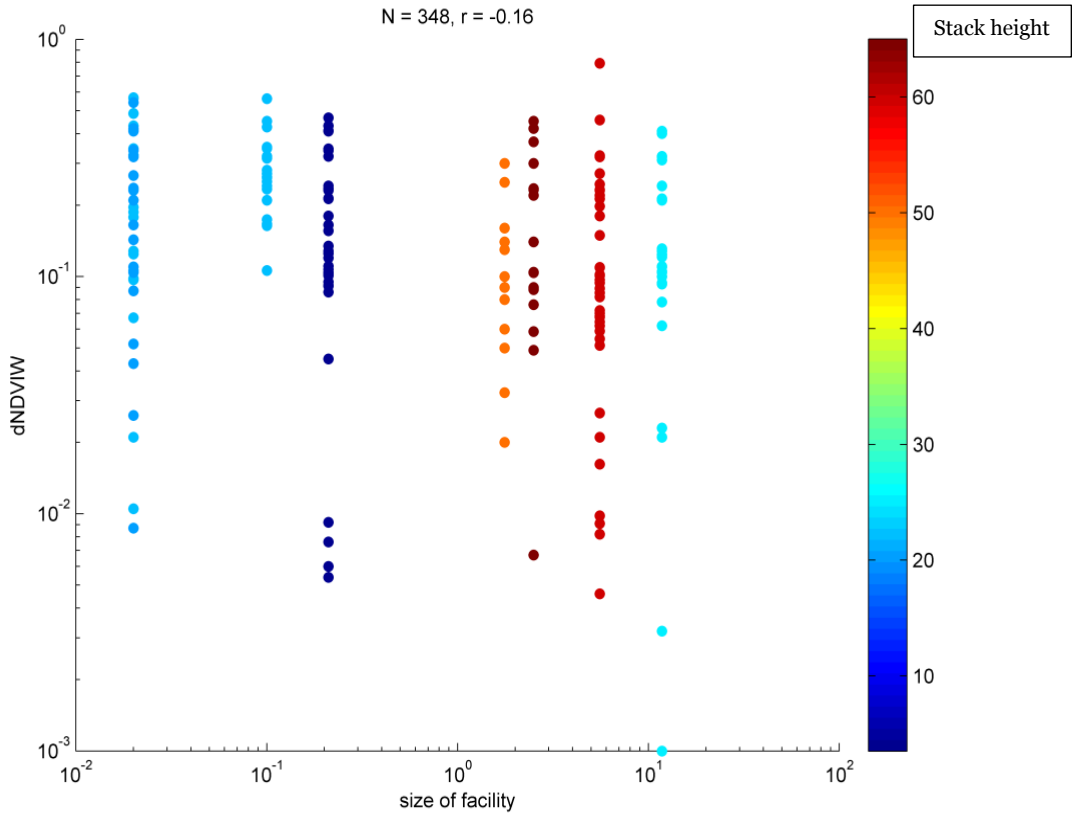

Figure 5-12: Size of facility against δNDVI$_W$

The range in δNDVI values was broad for all facilities, from 0.01 to ~ 0.9. See section 3.5.1.1 for the interpretation of NDVI values to differentiate between healthy and unhealthy vegetation. The statistically significant results are results with the computed p-values less than or equal to the chosen significance level (α = 0.01) while the insignificant results are the opposite. Considering the relationship between the size of facility and δNDVI, both $\delta NDVI_N$ and $\delta NDVI_W$ are significant with negative correlation while $\delta NDVI_E$ and $\delta NDVI_S$ are not significant. Also, for the height of stack and δNDVI relationships, there are significant results for the height of stack versus $\delta NDVI_N$, height of stack versus $\delta NDVI_E$ and height of stack versus $\delta NDVI_W$ but with negative correlations. Only the relationship between height of stack and $\delta NDVI_S$ has a positive correlation, but with an insignificant result because of the direction of the prevailing wind that is South, causing the wind to blow towards the North direction. This is the

reason why the relationship between height of stack versus $\delta NDVI_N$, $\delta NDVI_E$, and $\delta NDVI_W$ gave significant results.

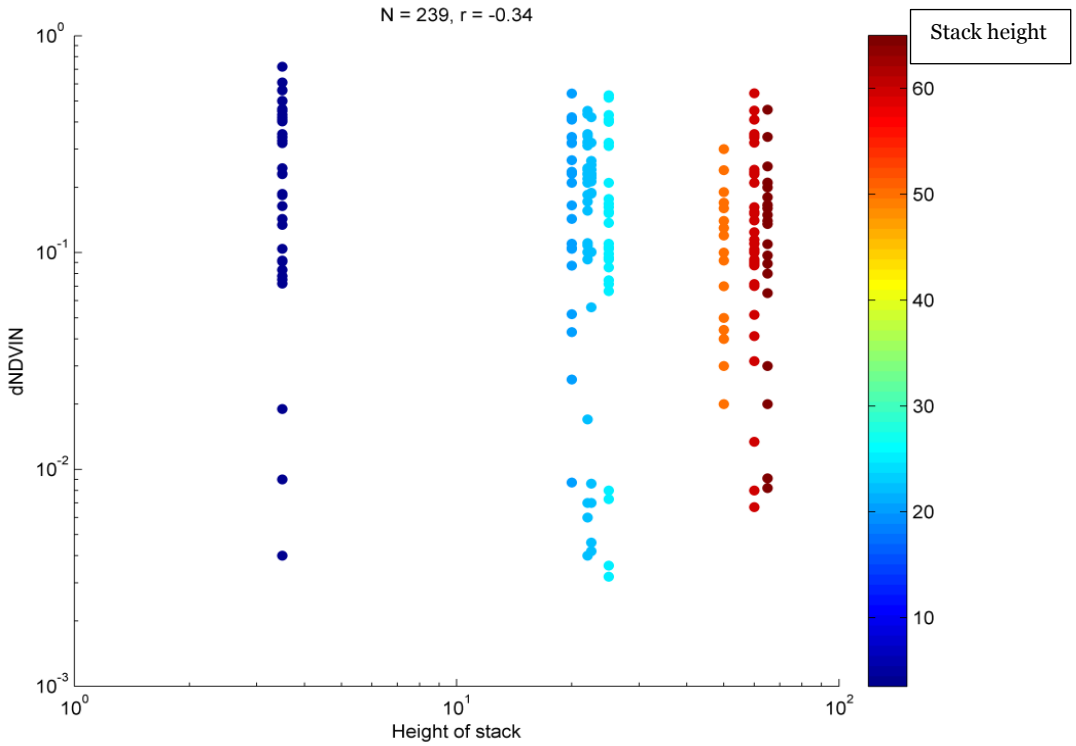

Figure 5-13: Height of stack against $\delta NDVI_N$

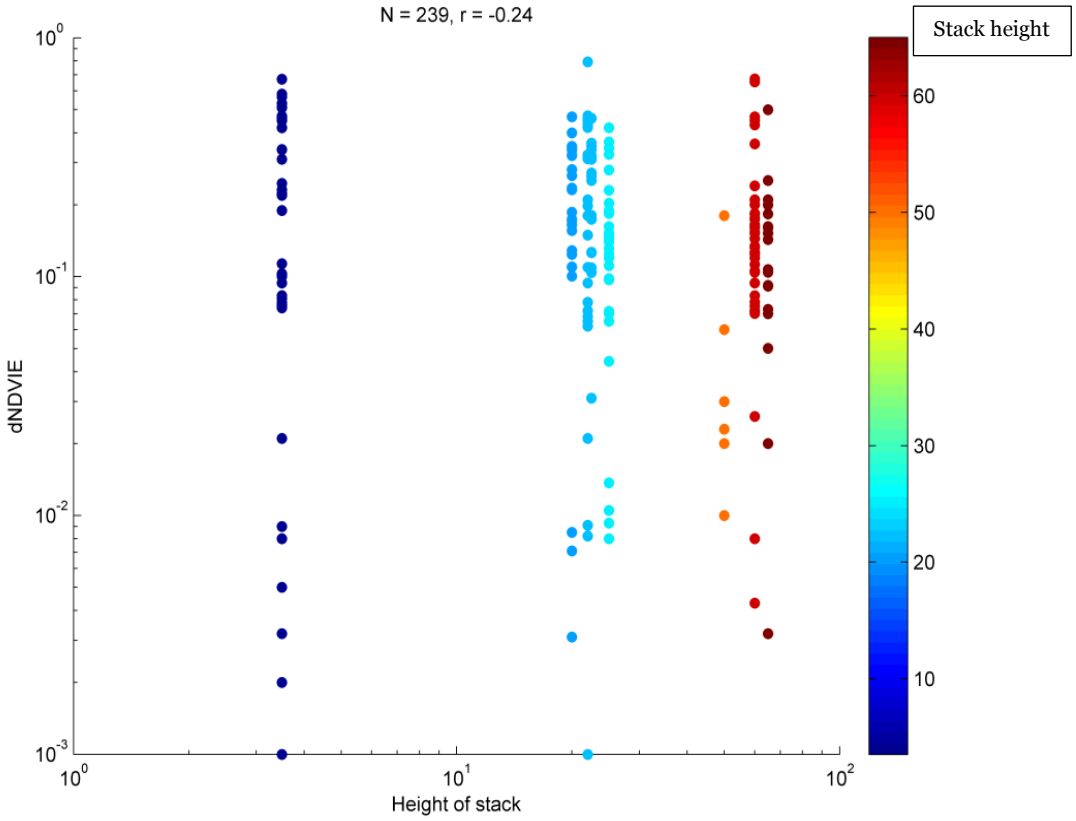

Figure 5-14: Height of stack against $\delta NDVI_E$

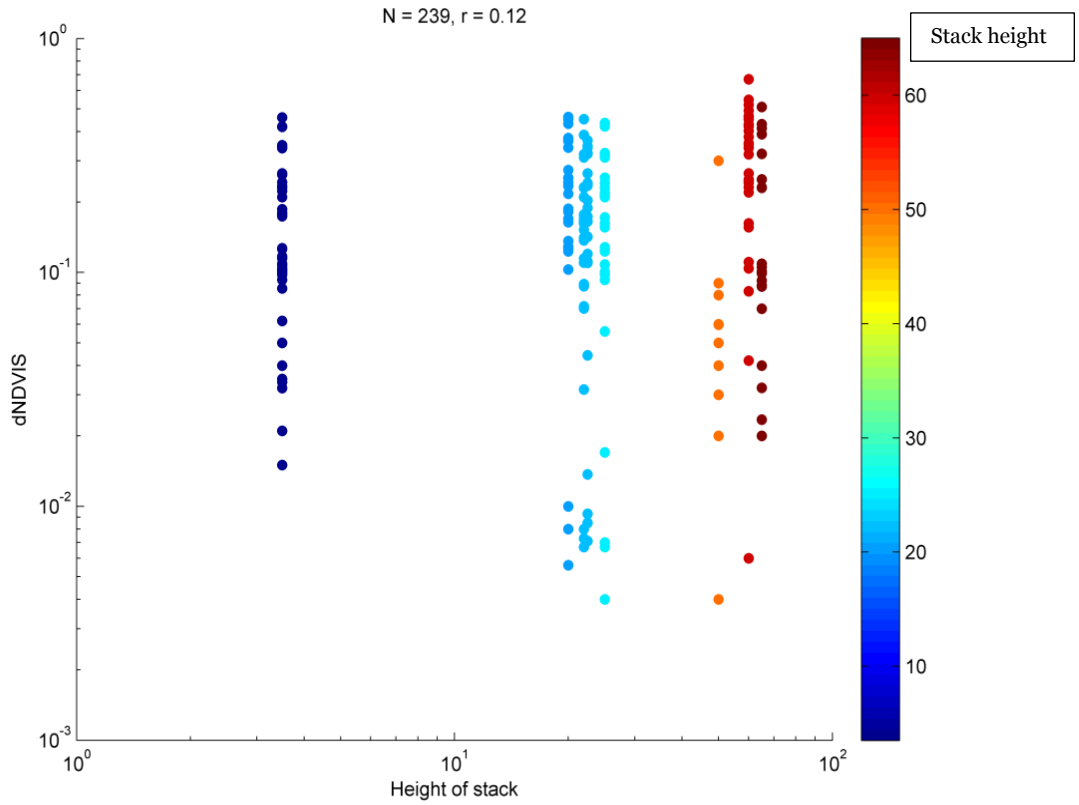

Figure 5-15: Height of stack against δNDVIs

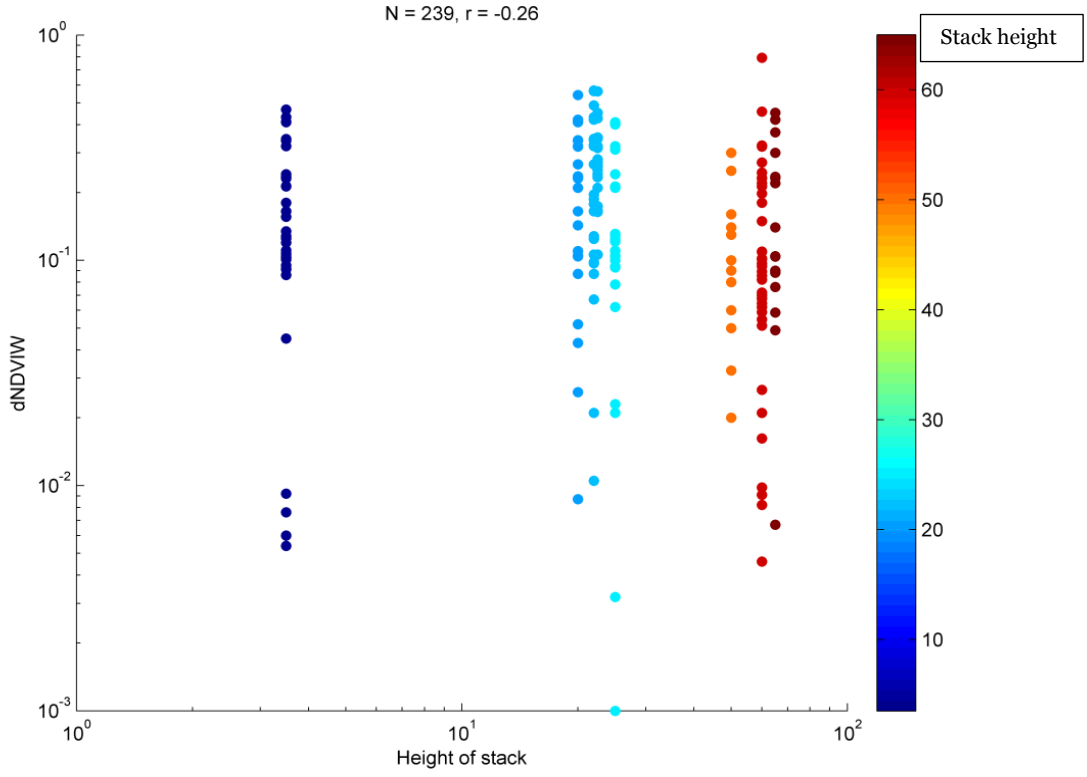

Figure 5-16: Height of stack against δNDVIw

From Table 5.6, the size of the facility versus $\delta NDVI_N$ and $\delta NDVI_W$ (change in NDVI in the North and West directions) indicates a small, but statistically significant impact of flare on NDVI. Similarly, height of stack versus $\delta NDVI_N$, $\delta NDVI_E$ and $\delta NDVI_W$ also revealed a small, but significant impact of flare on NDVI. Furthermore, section 4.5.2 showed that the prevailing wind direction at these sites is from the South which is in agreement with the results that flaring has greater significant impact on NDVI in the North direction; with the wind coming from the South, it will blow towards the opposite direction (North) and force the flare to its direction thereby causing a much greater effect on the vegetation.

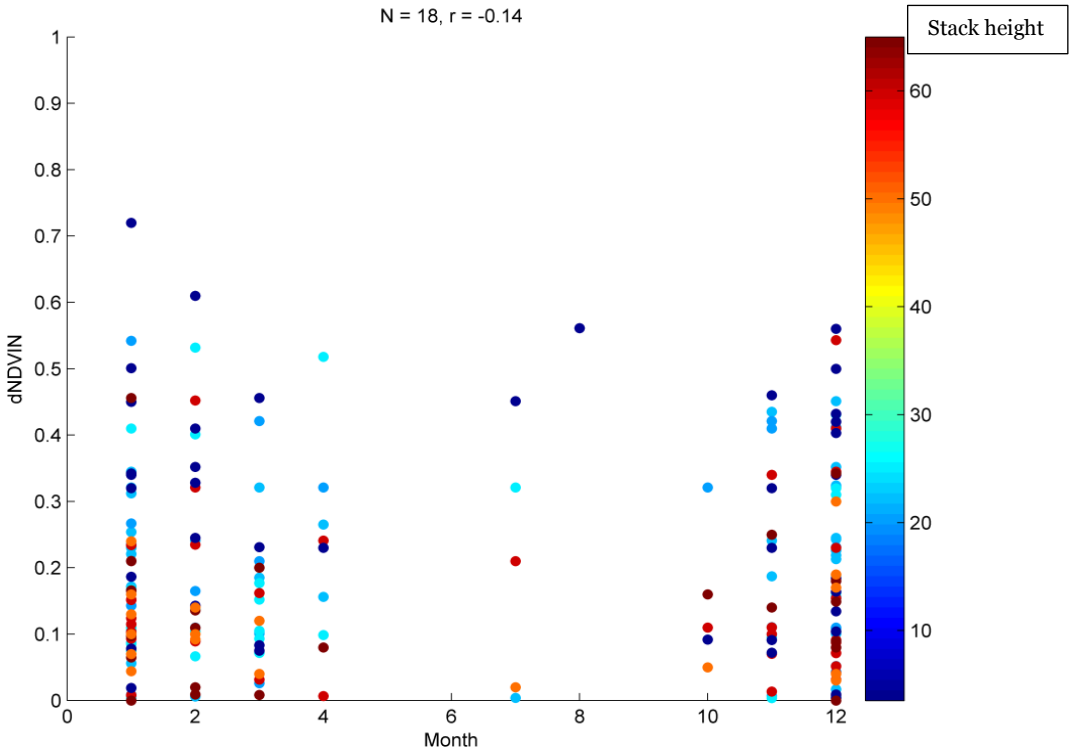

Figure 5-17: Month against $\delta NDVI_N$

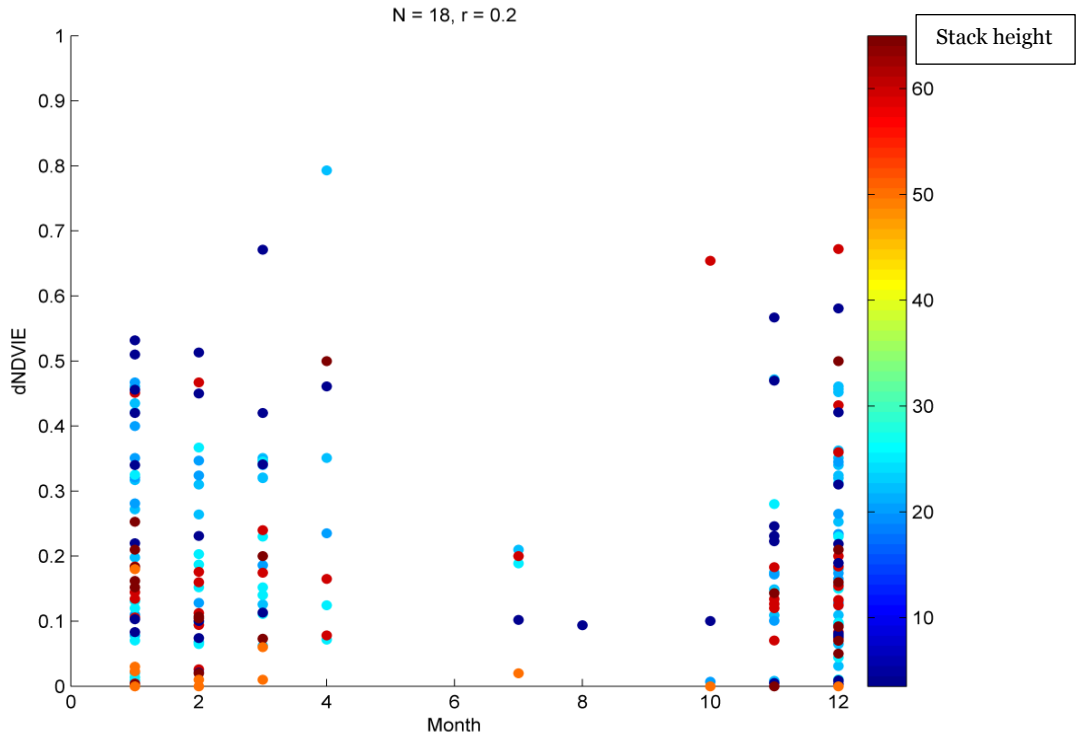

Figure 5-18: Month against $\delta NDVI_E$

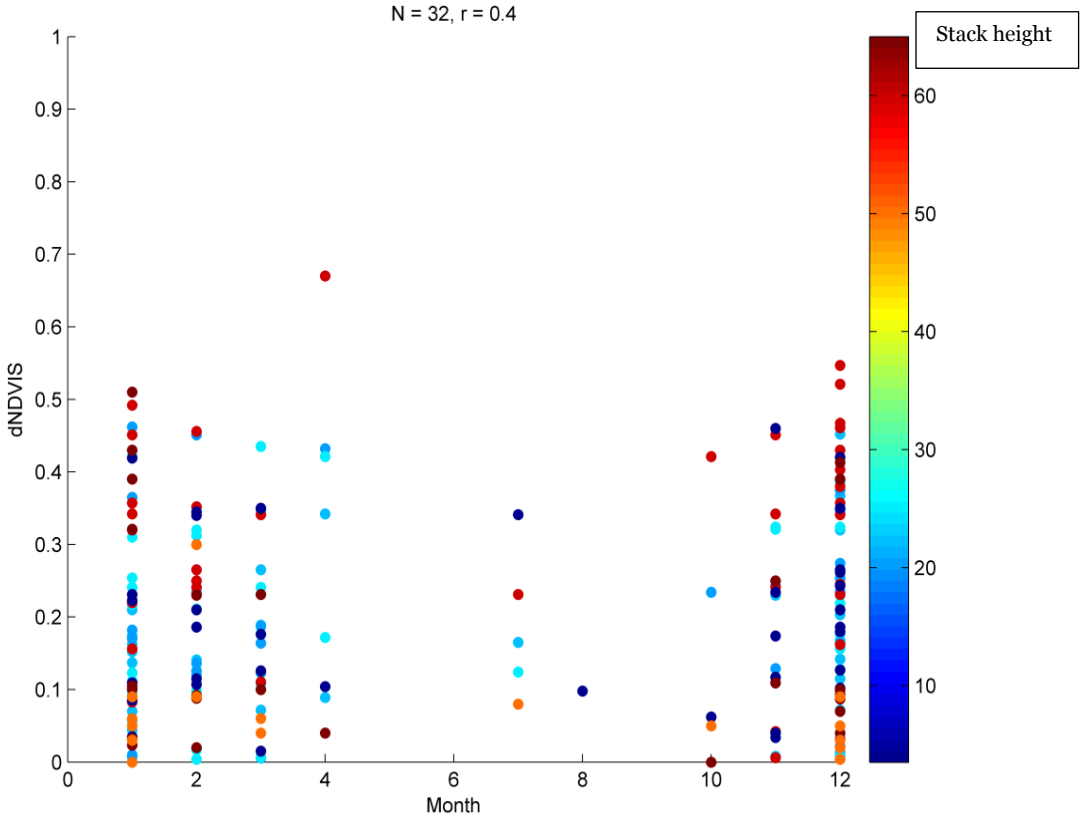

Figure 5-19: Month against $\delta NDVI_S$

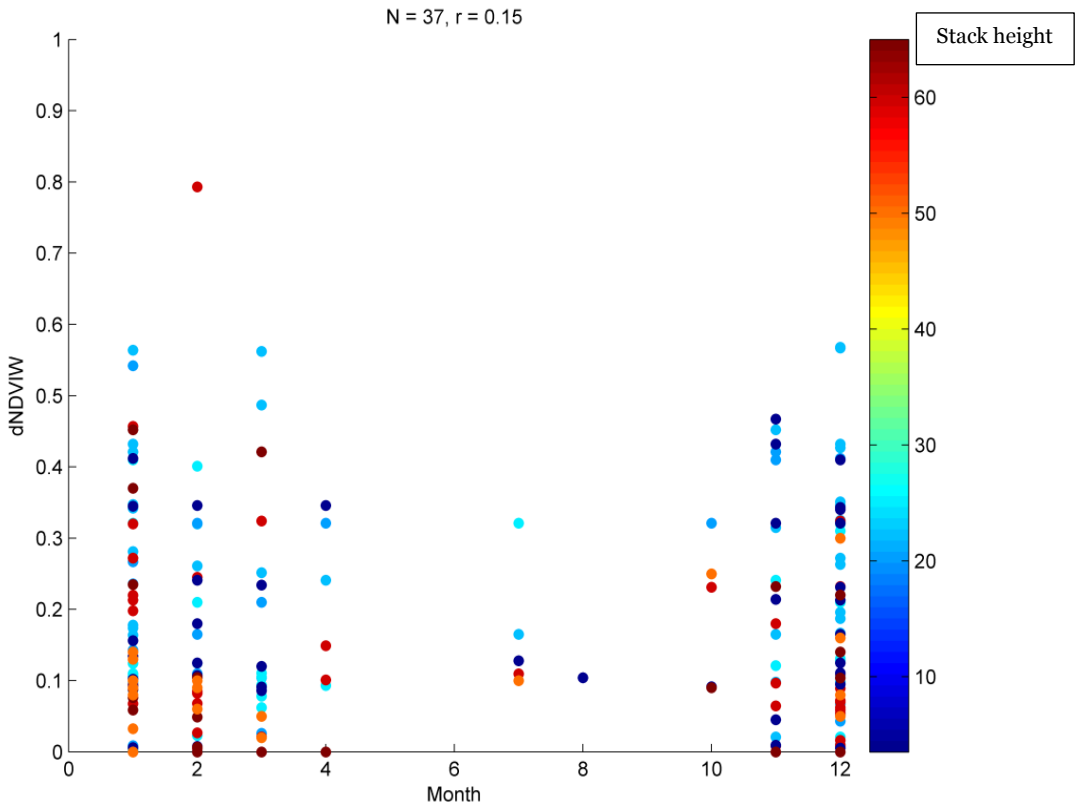

Figure 5-20: Month against δNDVI$_W$

Table 5.6 shows that none of the relationship between month and δNDVI$_{N, E, S, W}$ is statistically significant despite the positive correlation (r-values) for the directions except δNDVI$_E$ that has negative correlation (r-value). It means that all the relationship between month and δNDVI$_{N, E, S, W}$ gave results that are too small to be worth consideration; and there is no linear interdependence of the two variables.

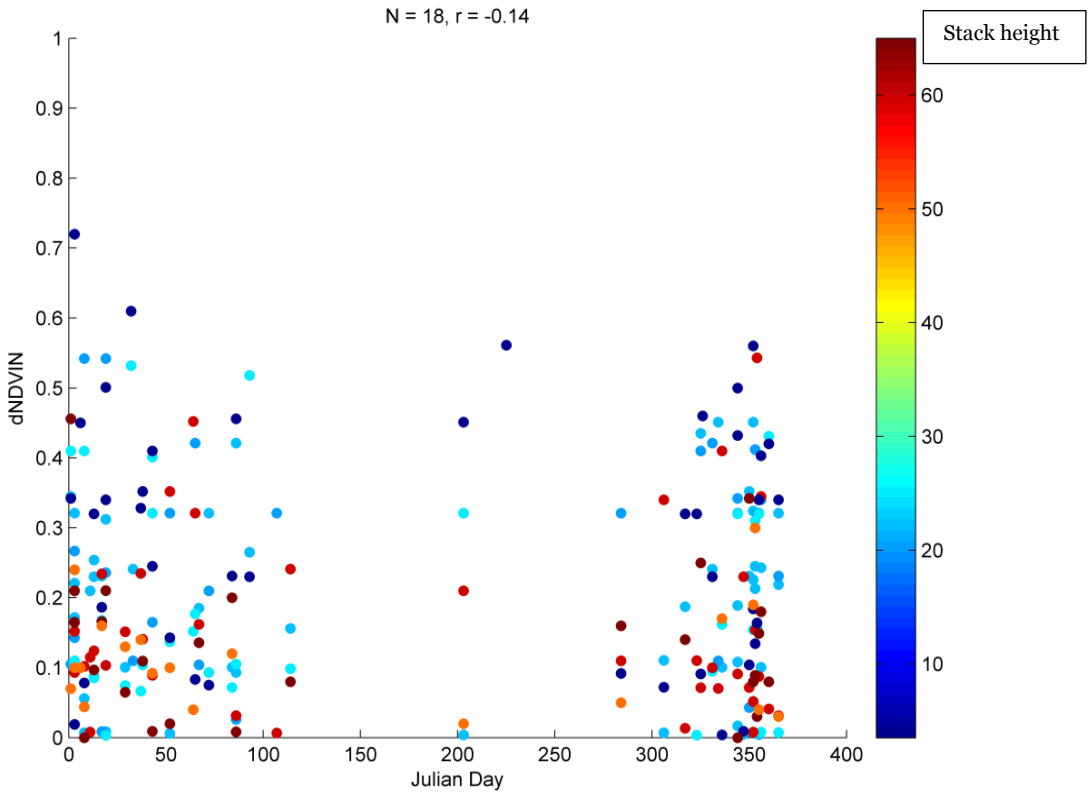

Figure 5-21: Julian Day against $\delta NDVI_N$

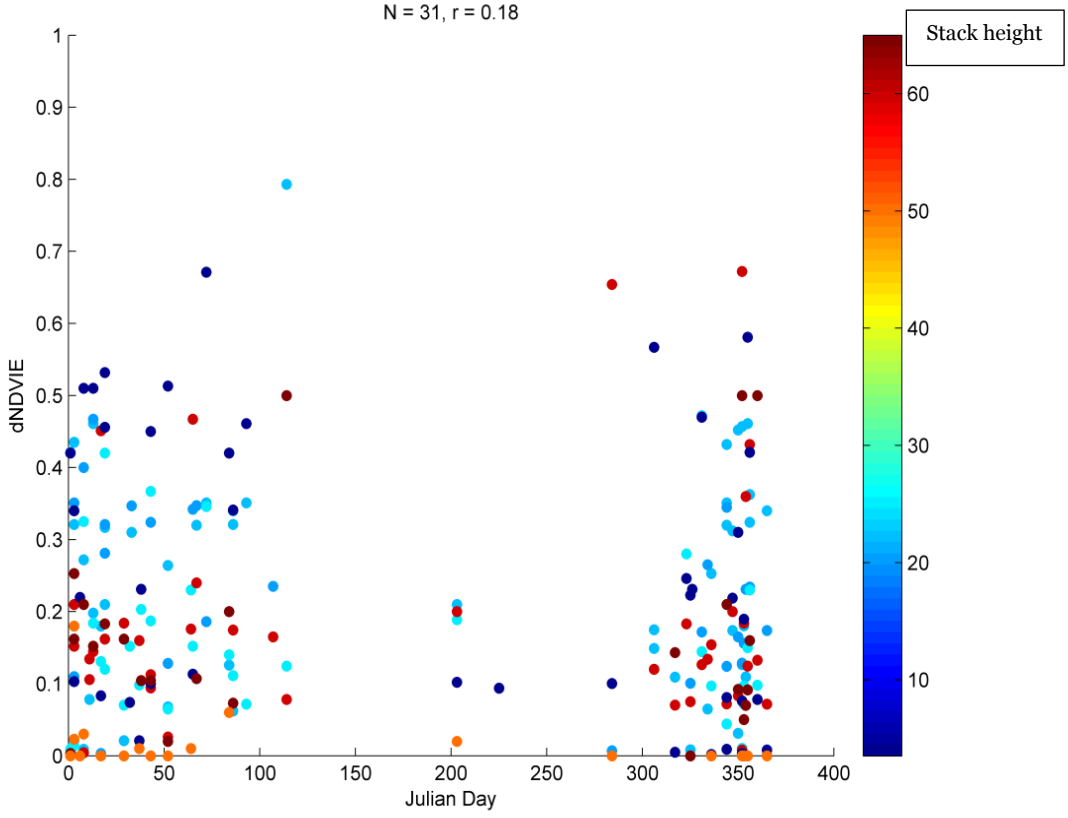

Figure 5-22: Julian Day against $\delta NDVI_E$

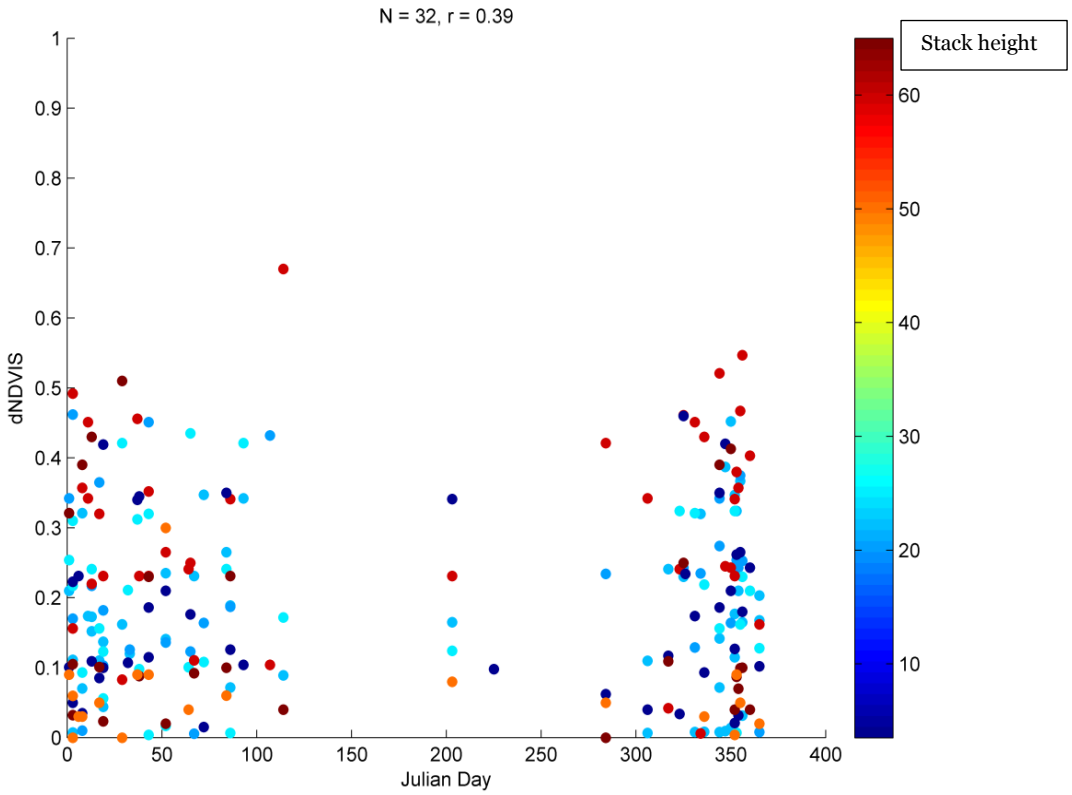

Figure 5-23: Julian Day against δNDVI$_S$

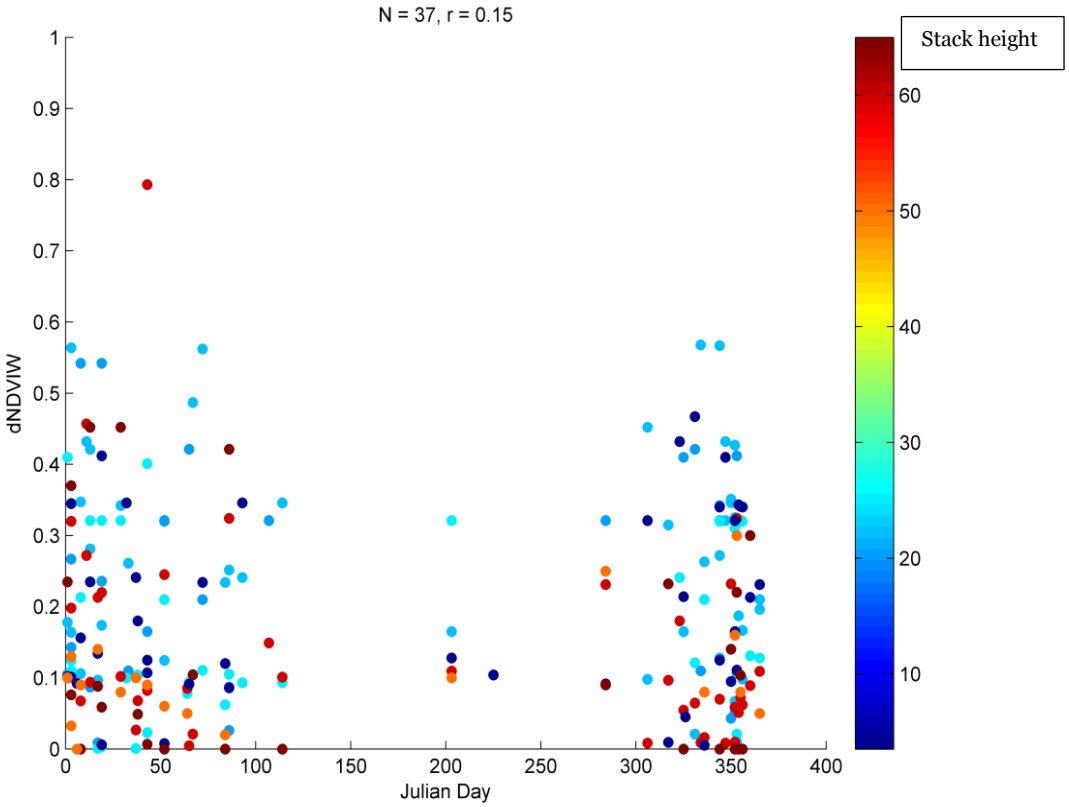

Figure 5-24: Julian Day against δNDVI$_W$

There are no significant results from the relationships between Julian Day and $\delta NDVI_{N, E, S, W}$; and among these relationships only Julian Day with $\delta NDVI_E$ gives negative correlation coefficient (r-value) while others are positive. This means that the relationship between Julian Day and each of the δNDVI four directions gave results that are too small to be worth consideration; and there is no linear relationship of the two variables.

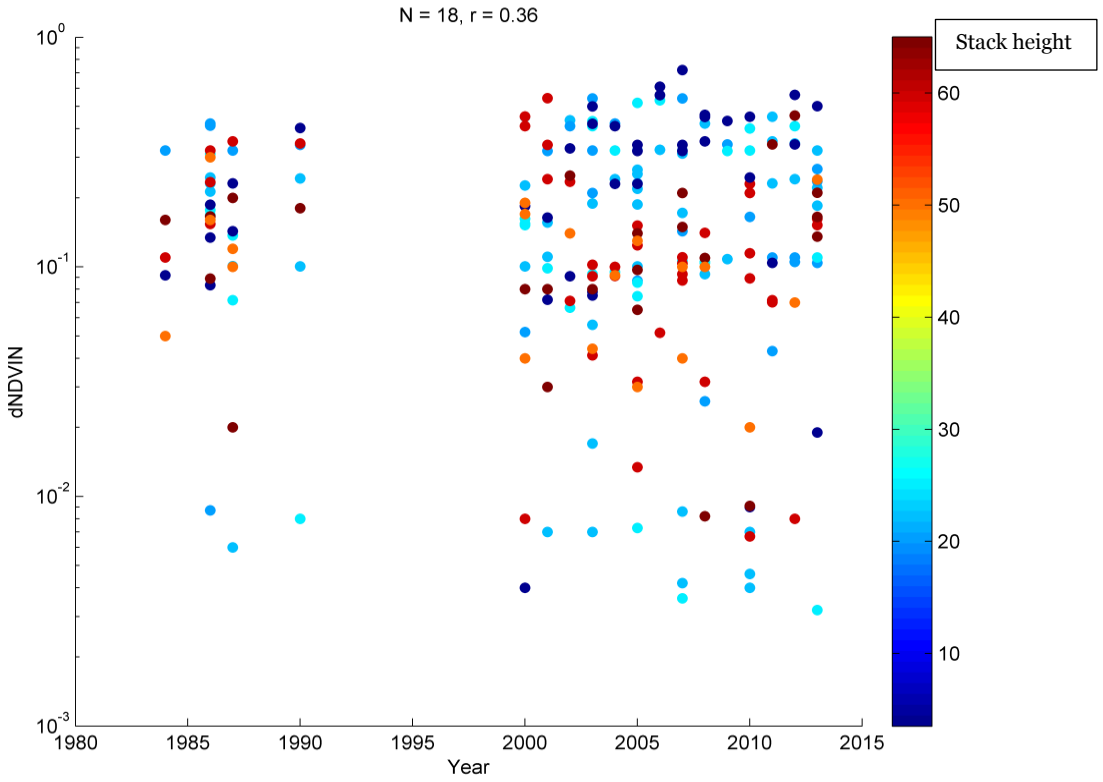

Figure 5-25: Year against $\delta NDVI_N$

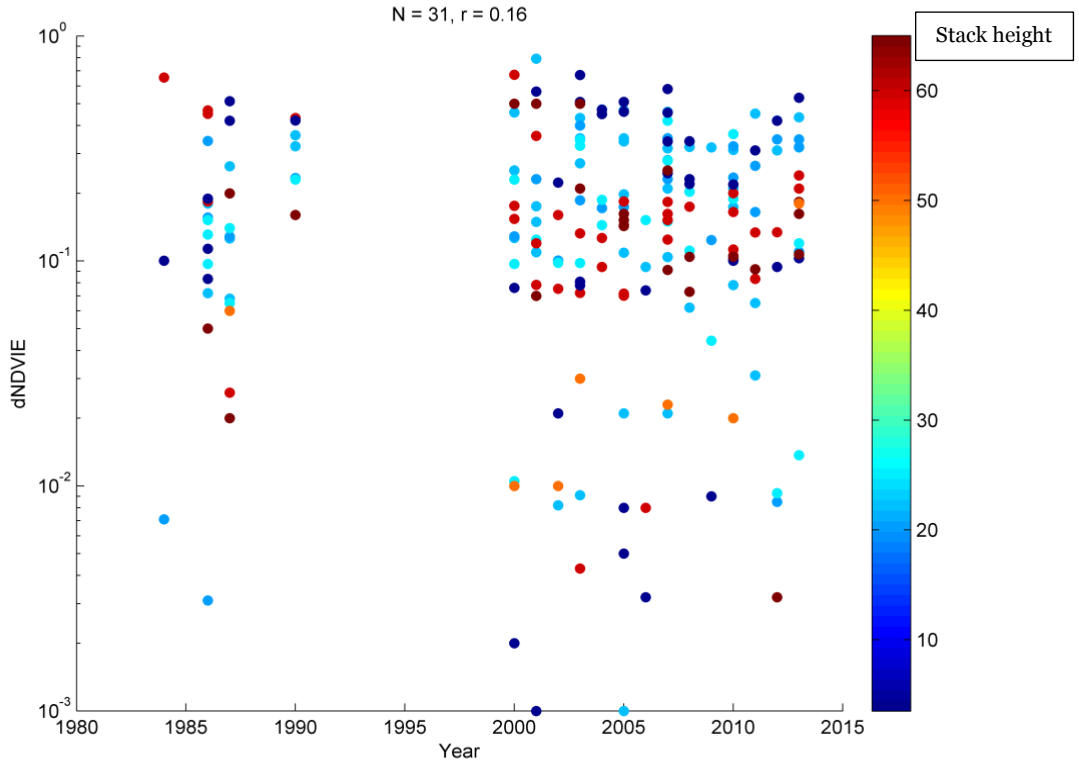

Figure 5-26: Year against $\delta NDVI_E$

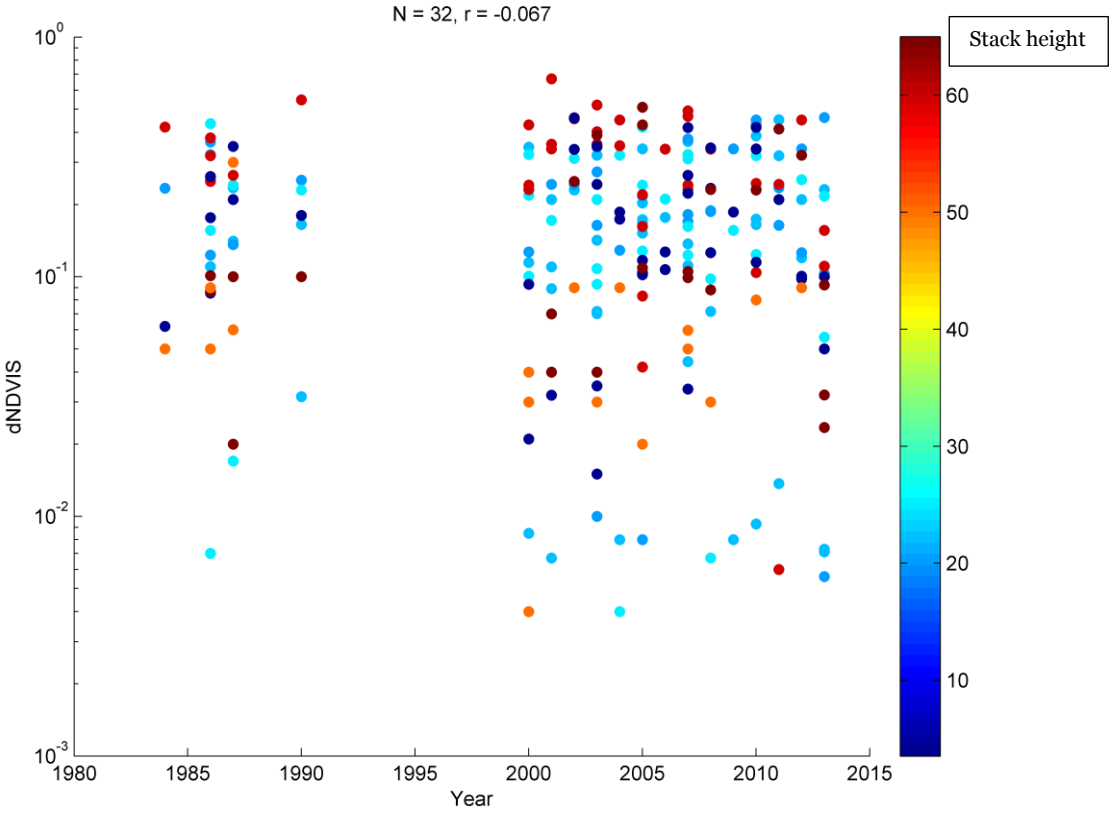

Figure 5-27: Year against $\delta NDVI_S$

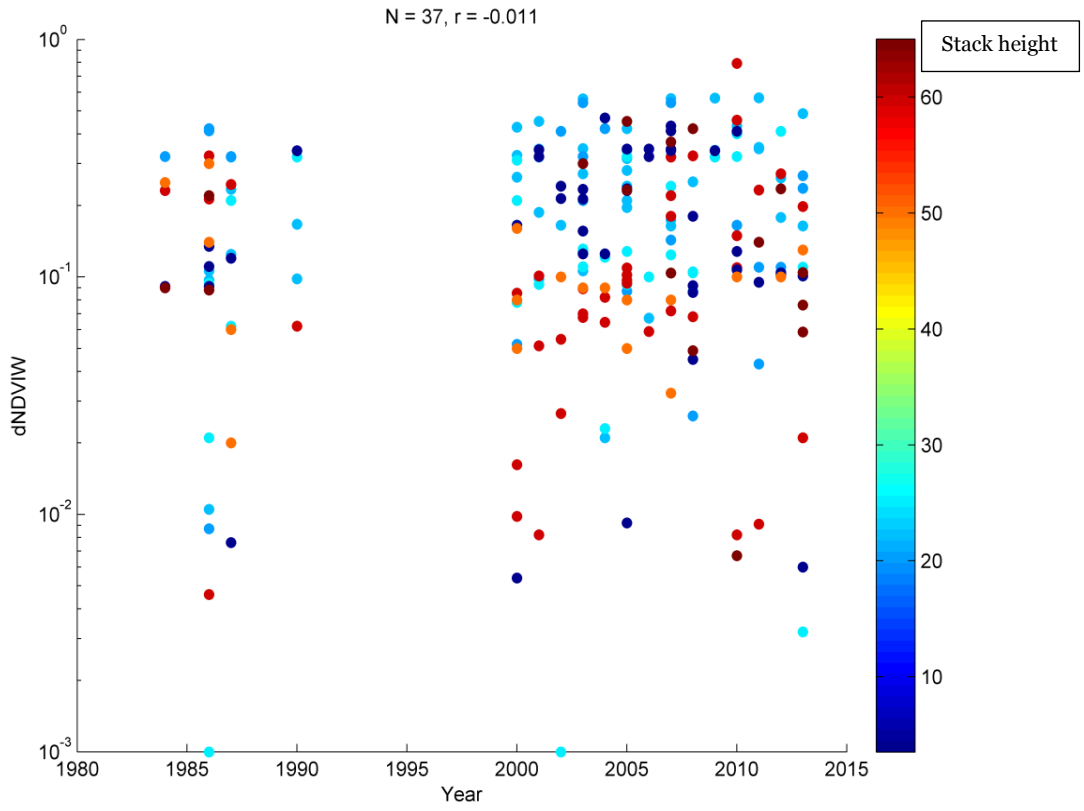

Figure 5-28: Year against δNDVI$_W$

All relationships between the year and δ NDVI$_{N,\ E,\ S,\ W}$ gave statistically insignificant results and positive correlation (r-values), but very small ranging from 0.011 to 0.100. This means that the relationship between the Year and each of the δNDVI four directions gave results that are too small to be worth consideration; and there is no linear relationship of the two variables.

5.4.2 Multiple linear regression analysis

The same principle of multiple linear regression already discussed in Chapter 4, section 4.6.2, was applied to the relationships between δNDVI and the available environmental factors that influence vegetation cover and health (predictive variables: size of facility, height of stack and month). Table 5.7 shows the resulting correlation coefficient, r^2, and p-values.

Table 5-7: Multiple linear regression of environmental and facility characteristics against δNDVI

Response variables	r^2	p-value
$\delta NDVI_N$	0.1161	0.0000
$\delta NDVI_E$	0.0728	0.0016
$\delta NDVI_S$	0.0319	0.0922
$\delta NDVI_W$	0.0321	0.0592

When the predictive variables were applied with $\delta NDVI_N$, $\delta NDVI_E$, $\delta NDVI_S$ and $\delta NDVI_W$ with $\alpha = 0.01$, there are significant results with $\delta NDVI_N$ and $\delta NDVI_E$. Table 4.3 and section 4.5.2 showed that the prevailing wind direction in the Niger Delta is South, which causes a greater influence of the flare towards the North and this could explain these results. However, only 12 % of the variance in $\delta NDVI_N$ is explained by the available data, suggesting that other factors (e.g. rate of burning gas, volume of burning gas and vegetation speciation) play a more significant role.

5.5 Change in vegetation health from 1984 to 2013

Time series analysis and spatio-temporal regression analysis using data from 1984 to 2013 are two statistical analyses employed to evaluate the changes that have occurred in vegetation health within the flaring sites.

5.5.1 Time series analysis

Time series analysis (Huang et al., 2013), with data from 1984 to 2013, was used to assess a change in vegetation cover; the results show yearly changes for all the eleven flaring sites. The changes in the values of NDVI from 1984 to 2013 are presented in Figures 5.29-5.39. The mean NDVI at 60 m, 90 m, 120 m and 240 m distance away from the flare stack were used for the four direction plots for each site, and the results show similar trends for points between 60-120 m with a yearly reduction in the NDVI. For a distance of 240 m, the results for all

stations revealed another trend whereby the changes in NDVI fluctuate throughout the years for all sites. Also, unlike the values from 60-120 m where the highest NDVI values for all sites were recorded for the early years, the NDVI obtained for a distance of 240 m in 2013 is almost the same as that of the early years and even greater for some sites. This shows that for distances from 60-120 m away from the flare, the vegetation cover have become sparse and the photosynthetic actitivity have been reduced to a little at these flaring sites (Carlson and Ripley, 1997; Goward et al., 1985; Gallo et al., 1985). This result is supported by the ground validation activities (previously described) carried out at Eleme Refinery II and Onne Flow Station.

Furthermore, Table 5.8 presents the dates of available data used for the time series analysis, mean annual NDVI range at 60 m, 90 m, 120 m and 240 m away from the flare stack and the time of build for Eleme Refinery I and II, Onne and Bonny LNG as indicated by a red line in the Figures 5.30, 5.31 and 5.33 for Eleme Refinery II, Onne and Bonny LNG respectively. The available data could not cover the time of build for Eleme Refinery I; hence it is not shown in Figure 5.29. For the remaining facilities, their date of build is unknown.

Table 5-8: Mean NDVI range for case studies flaring sites

Facility	Time of build	Dates of available data	Mean NDVI range			
			60 m	90 m	120 m	240 m
Eleme I	1965	1986-2013	N: 0.69-0.20; E: 0.75-0.36 S: 0.80-0.54; W: 0.78-0.23	0.64-0.30; 0.75-0.45 0.77-0.54; 0.75-0.23	0.72-0.49; 0.82-0.55 0.62-0.41; 0.72-0.50	0.62-0.50; 0.86-0.85 0.80-0.77; 0.54-0.48
Eleme II	1988	1984-2013	N: 0.70-0.23; E: 0.74-0.23 S: 0.76-0.21; W: 0.78-0.33	0.74-0.23; 0.76-0.32 0.76-0.34; 0.74-0.23	0.59-0.32; 0.70-0.31 0.64-0.34; 0.62-0.28	0.70-0.60; 0.71-0.65 0.64-0.60; 0.54-0.45
Onne	2010	1984-2013	N: 0.82-0.48; E: 0.79-0.51 S: 0.82-0.48; W: 0.79-0.51	0.83-0.51; 0.81-0.49 0.71-0.39; 0.74-0.44	0.62-0.32; 0.64-0.39 0.59-0.35; 0.70-0.34	0.53-0.45; 0.64-0.62 0.70-0.60; 0.69-0.65
Umurolu	Unknown	1984-2013	N: 0.79-0.15; E: 0.78-0.39 S: 0.88-0.48; W: 0.77-0.48	0.77-0.28; 0.76-0.37 0.78-0.41; 0.76-0.37	0.72-0.46; 0.52-0.29 0.70-0.48; 0.65-0.37	0.58-0.50; 0.56-0.48 0.78-0.75; 0.59-0.50
Bonny	1989	1986-2013	N: 0.68-0.23; E: 0.68-0.23 S: 0.70-0.27; W: 0.68-0.27	0.66-0.23; 0.66-0.23 0.67-0.22; 0.70-0.25	0.51-0.37; 0.65-0.53 0.52-0.38; 0.44-0.32	0.59-0.55; 0.53-0.50 0.52-0.48; 0.53-0.51
Alua	Unknown	1984-2013	N: 0.71-0.25; E: 0.75-0.28 S: 0.80-0.40; W: 0.75-0.28	0.74-0.26; 0.74-0.22 0.72-0.19; 0.84-0.38	0.62-0.30; 0.64-0.35 0.59-0.32; 0.70-0.33	0.53-0.45; 0.64-0.61 0.65-0.60; 0.70-0.69
Rukpokwu	Unknown	1986-2013	N: 0.73-0.25; E: 0.73-0.25 S: 0.67-0.22; W: 0.80-0.39	0.77-0.29; 0.74-0.26 0.75-0.31; 0.74-0.26	0.70-0.44; 0.54-0.16 0.65-0.32; 0.64-0.28	0.79-0.75; 0.81-0.74 0.59-0.48; 0.53-0.51
Obigbo	Unknown	1986-2013	N: 0.61-0.15; E: 0.71-0.25 S: 0.80-0.40; W: 0.73-0.25	0.75-0.31; 0.74-0.26 0.74-0.23; 0.74-0.21	0.65-0.24; 0.44-0.16 0.70-0.33; 0.64-0.36	0.52-0.45; 0.69-0.65 0.67-0.65; 0.84-0.81
Chokocho	Unknown	1986-2013	N: 0.71-0.25; E: 0.81-0.31 S: 0.88-0.40; W: 0.83-0.40	0.74-0.26; 0.74-0.26 0.88-0.35; 0.84-0.31	0.70-0.44; 0.54-0.16 0.65-0.32; 0.64-0.28	0.79-0.75; 0.74-0.73 0.61-0.52; 0.50-0.42
Umudioga	Unknown	1984-2013	N: 0.74-0.40; E: 0.76-0.46 S: 0.78-0.23; W: 0.78-0.18	0.77-0.48; 0.72-0.48 0.78-0.24; 0.75-0.20	0.70-0.48; 0.42-0.16 0.57-0.32; 0.64-0.33	0.78-0.75; 0.69-0.66 0.69-0.61; 0.50-0.42
Sara	Unknown	1986-2013	N: 0.82-0.34; E: 0.71-0.25 S: 0.81-0.34; W: 0.84-0.34	0.88-0.35; 0.74-0.26 0.79-0.31; 0.76-0.21	0.72-0.42; 0.52-0.25 0.70-0.44; 0.65-0.32	0.60-0.50; 0.54-0.48 0.78-0.75; 0.61-0.50

For Eleme Refinery I, in all directions there was a slow and steady decrease in NDVI values at 60 m distance from the flare until 2001 when the rate at which NDVI values fall increased gradually. Also, in the West direction at a distance of 60 m the NDVI value dropped strongly from 0.42 in 2012 to 0.24 in 2013.

For Eleme Refinery II, the plots (Figure 5.30) show that the NDVI values recorded at 60, 90 and 120 m from the flare present the same trend of a decrease on a yearly basis. In the North direction, the NDVI at a distance of 90 m dropped from 0.5 in 2007 to 0.3 in 2008. Also, NDVI values at a distance of 240 m maintained an almost constant value from 1984 to 2000 and from that year there was a gradual increase in NDVI value to 2013.

For Onne (Figure 5.31), in all directions the NDVI values remain almost steady with a little increase from 1984 to 2000, but between 2000 and 2005 there is a fluctuation in the value of NDVI at a distance of 60 and 90 m for all directions. Also, at a distance of 120 m, the NDVI dropped from 0.62 in 2001 to a range of (0.52-0.48) in 2002 and since then, there is a steady decrease in its value. Finally, the plots (Figure 5.31) show that there is a continuous decrease in NDVI values at Onne Flow Station from the time of its build, and this could be attributed to the flaring activity that is on-going there.

For Umurolu flaring site (Figure 5.32), there is a gradual decrease in NDVI values for the four directions. In 2000, NDVI value reduction increases and almost the same in all directions. NDVI values at 240 m from the flare increased gradually from 0.5 m in 1984 to 0.59 m in 2013, with a spike in 2001.

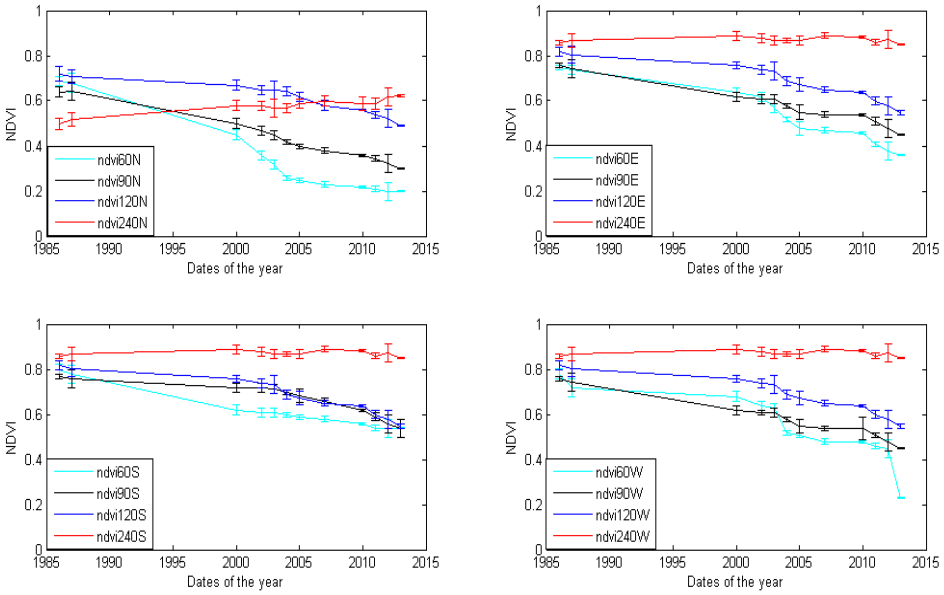

Figure 5-29: Eleme Refinery I, 1986-2013

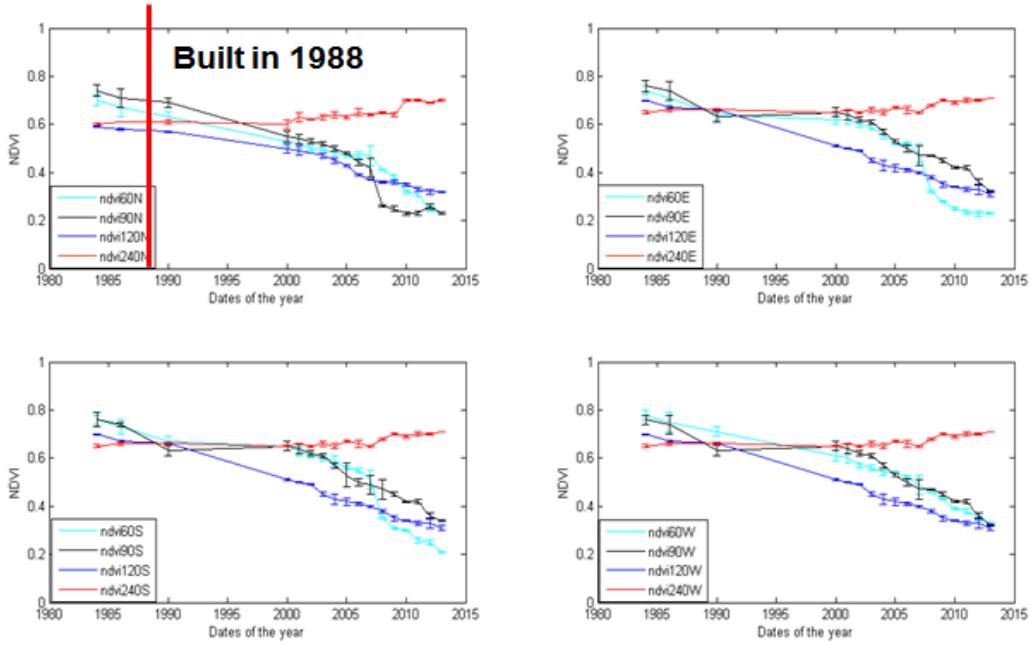

Figure 5-30: Eleme Refinery II, 1984-2013

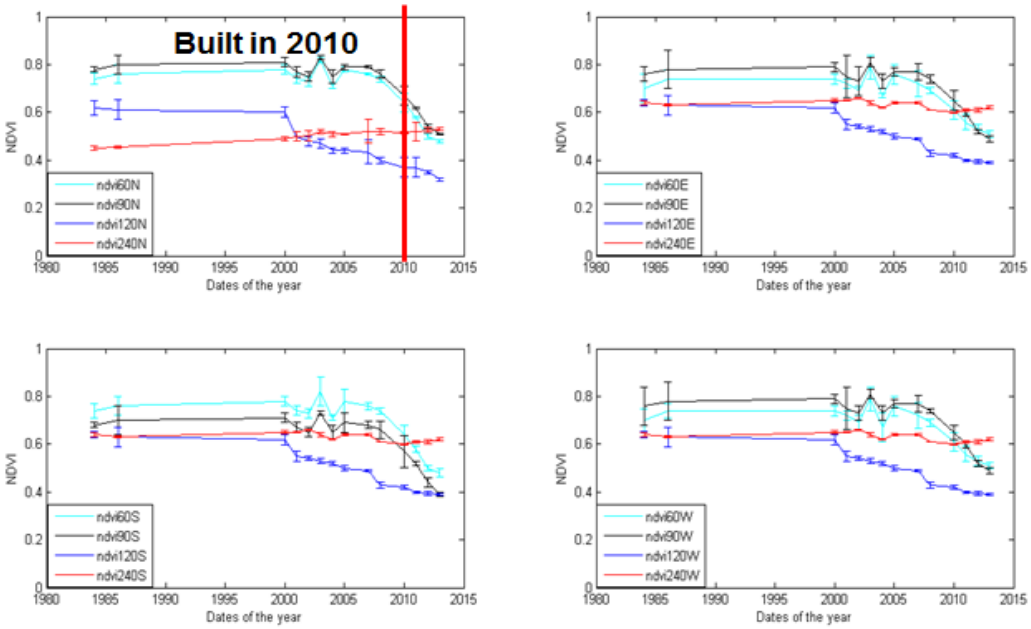

Figure 5-31: Onne Flow Station, 1984-2013

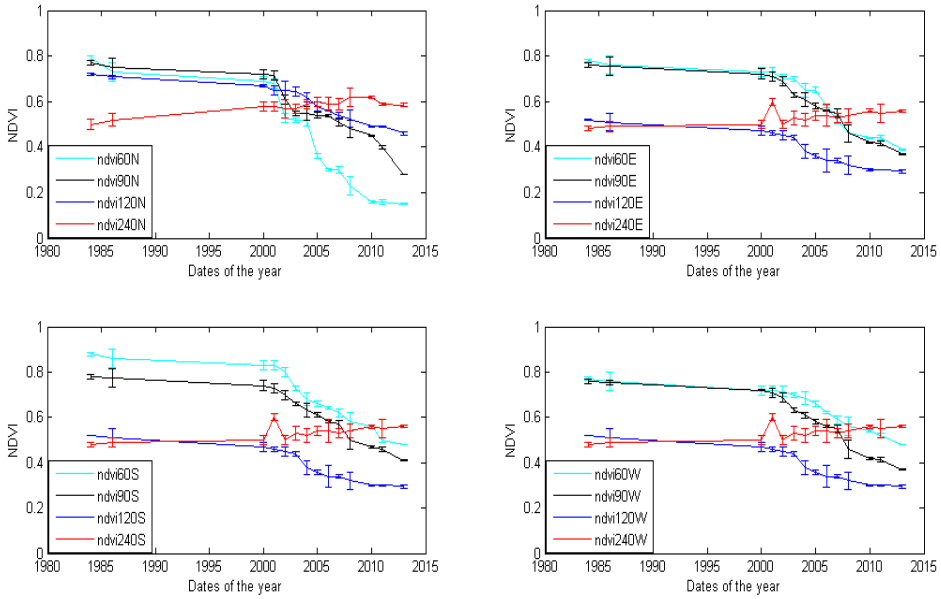

Figure 5-32: Umurolu Flow Station, 1984-2013

For Bonny LNG site, from its build date, there was a slow and steady decrease in the NDVI values in all four directions (Figure 5.33). For the North, at 60 m from the flare, the reduction in NDVI value increase from 2003 to 2013; and at 90 m from the flare, there was a sharp reduction in NDVI up to 2000. Generally, for all directions at 120 m from the flare, NDVI values showed nearly uniform values from 1986 to 2004, and at this point the NDVI began to drop gradually until 2013. Also, for all four directions, at 240 m from the flare, the NDVI value (0.5) was almost constant from 1986 to 2001, after which the NDVI increased to 0.55 from which a gradual increase continued until 2013.

For Alua Flow Station (Figure 5.34), NDVI at a distance of 60, 90 and 120 m from flare decreased slowly every year for all four directions until the year 2000 and, from 2001, the decrease accelerated. At 240 m from the flare, NDVI increased. These trends were similar for East, South and West.

All plots are similar for Rukpokwu Flow Station (Figure 5.35). NDVI at a distance of 60, 90 and 120 m from the flare decreased every year from 1986 to 2013, but for 240 m there is a slow and steady annual increase.

For Obigbo Flow Station (Figure 5.36), all plots are similar and they show that NDVI at a distance of 60, 90, and 120 m from the flare stack decreased every year. At a distance of 240 m, the NDVI recorded shows an almost constant value for all directions.

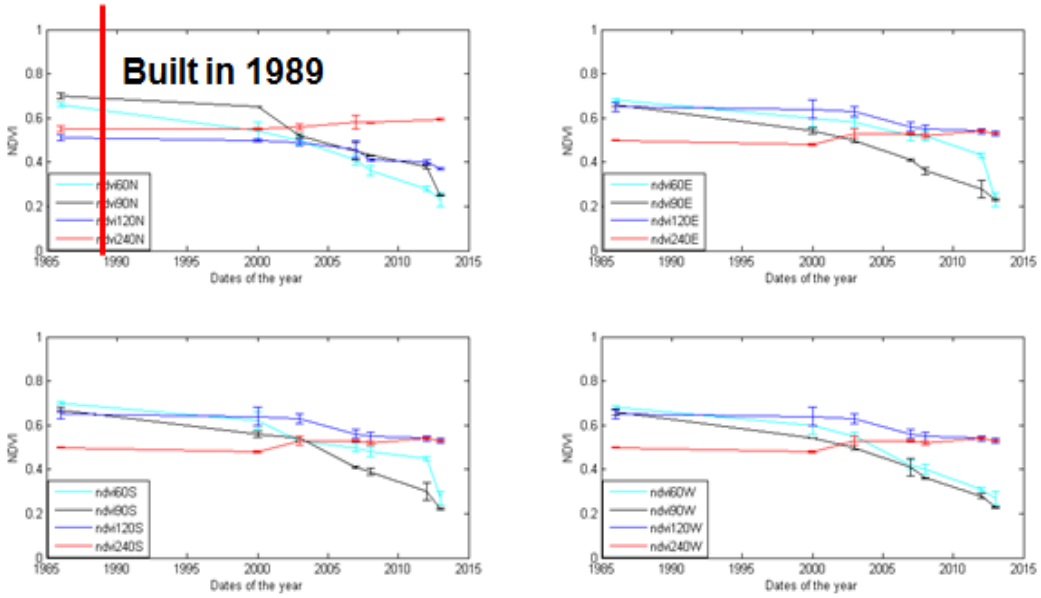

Figure 5-33: Bonny LNG, 1986-2013

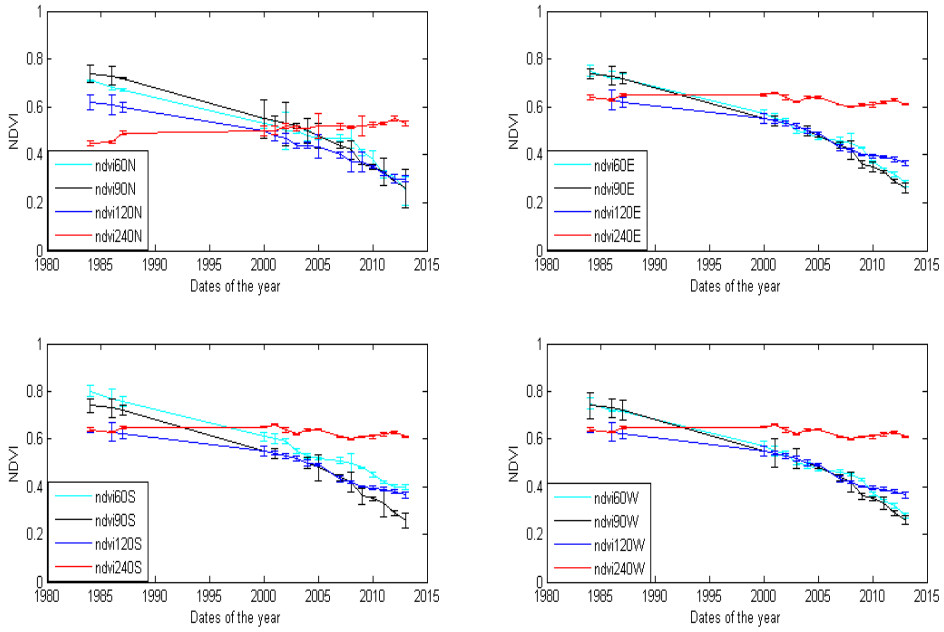

Figure 5-34: Alua Flow Station, 1984-2013

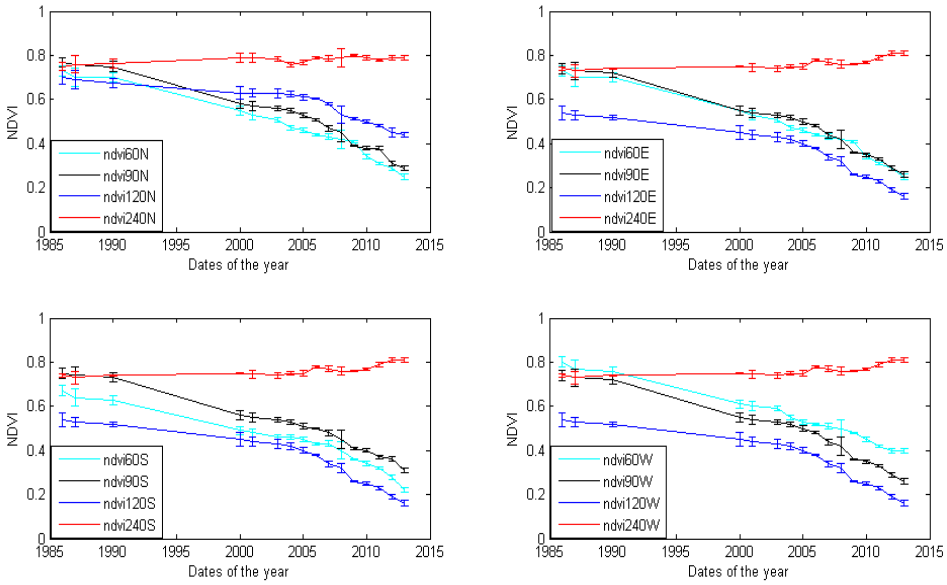

Figure 5-35: Rukpokwu Flow Station, 1986-2013

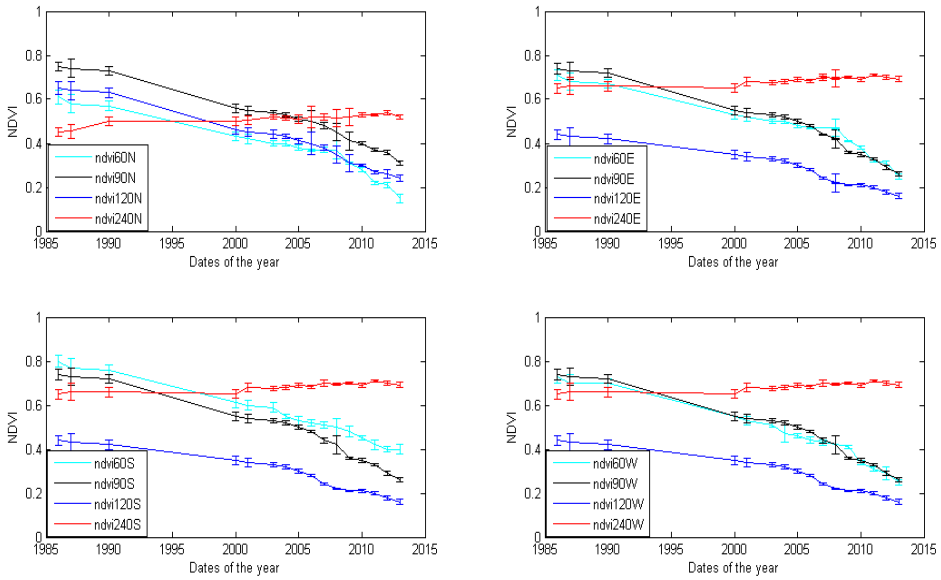

Figure 5-36: Obigbo Flow Station, 1986-2013

The plots for Chokocho (Figure 5.37) are similar to the Obigbo plots.

For Umudioga Flow Station (Figure 5.38), the plots are similar to the Obigbo plots except for the North direction where NDVI dropped from 0.7 to 0.5 in 2004 and the decrease then continues until 2013. The NDVI value at a distance of 60 m from the flare fell from 0.5 in 2010 to 0.3 in 2012.

For Sara Flow Station (Figure 5.39), the plot for the North direction is similar to the Obigbo North plot. For East, South and West directions plots, NDVI recorded at 60, 90 and 120 m distance decreased yearly from 1986 to 2013. NDVI at a distance of 240 m from the flare increased from 0.48 to 0.71 (from 1990 to 2000) and then dropped to 0.58 in 2002, and from there increased steadily until 2013.

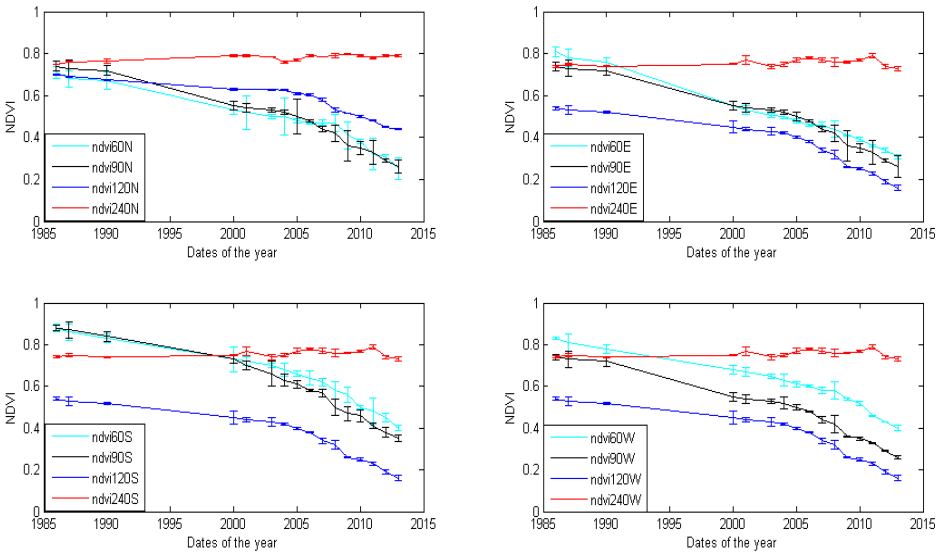

Figure 5-37: Chokocho Flow Station, 1986-2013

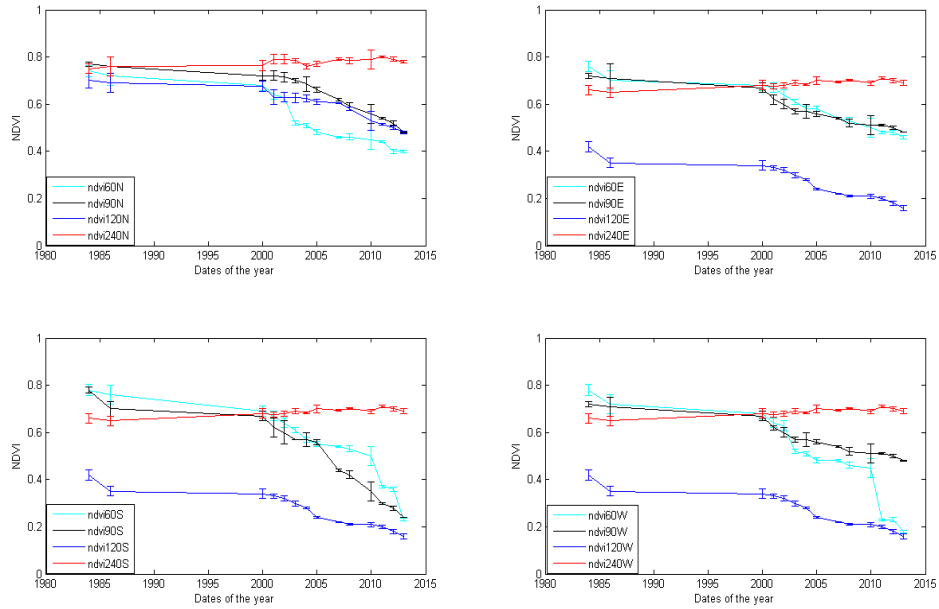

Figure 5-38: Umudioga Flow Station, 1984-2013

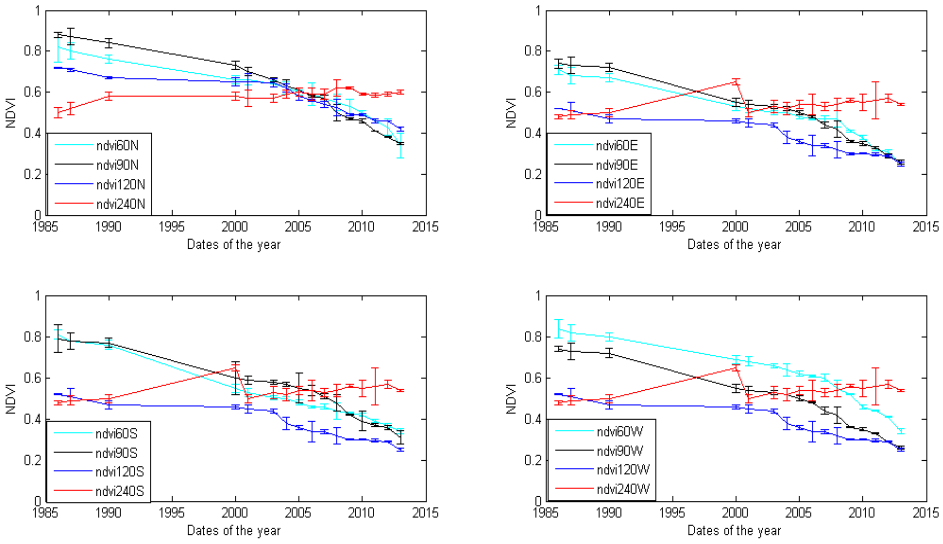

Figure 5-39: Sara Flow Station, 1986-2013

In summary, for all the eleven sites, the NDVI results obtained from time series analysis from 1984 to 2013 show that at 60 m distance from the flare, the lowest values of NDVI were recorded while for the 90 m, 120 and 240m distance from the flare, the NDVI values increases as distance increases. Also, as each year passed away, the NDVI values recorded for all sites decrease except Onne Flow

Station that shows an unstable trend for the years (1984 to 2007) before the flow station was built.

5.5.2 Spatio-temporal analysis

This analysis was used to help assess the spatial and temporal variability in Landsat detectable flare impact on vegetation health and vegetative cover. The spatially-resolved linear regression of NDVI against time from 1984 to 2013 for 12 by 12 km i.e. 400 × 400 pixel areas (see section 3.3.2) around each flare site extracted as Landsat subscenes was carried out for each flaring site. The NDVI results for each pixel in each subscene from 1984 to 2013 were linearly regressed against time to generate three maps for each site; they are the annual change in NDVI (regression slope), regression coefficient, r and p-value for the regression at each pixel. Figure 5.40 is the schematic diagram for the spatio-temporal analysis. Figure 5.41 shows NDVI against time for the spatio-temporal analysis for Eleme Refinery I at a distance of 60 m from the flare in North direction. The mean and standard deviation of NDVI trend values were calculated in each case, firstly taking all positive NDVI trend values, secondly all negative NDVI trend values and followed by all NDVI trend values. Table 5.9 presents the mean and standard deviation for the positive, negative and net slopes of NDVI at each flaring site.

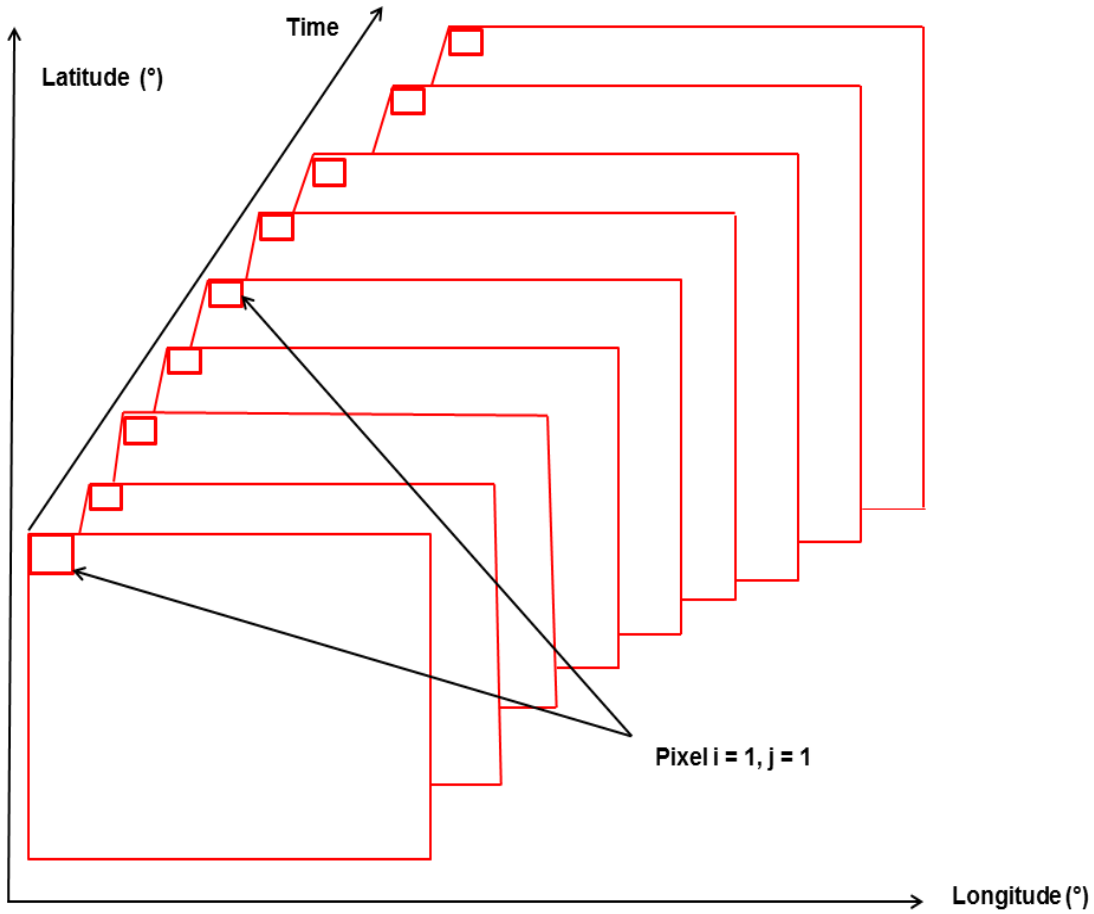

Figure 5-40: Schematic diagram for spatio-temporal analysis

Figures 5.42-5.52 show maps of annual change in NDVI (regression slopes), regression coefficient, r-values and p-values for these flaring sites; the Ps are p-value maps which show where the relationship is statistically significant. The significance level adopted for the analysis is $\alpha > 0.05$. Areas with yellow colour in map slope shows areas of the site where the temporal trend in NDVI is statistically significant. White areas in map P denote areas that are either always cloudy or that are not vegetation.

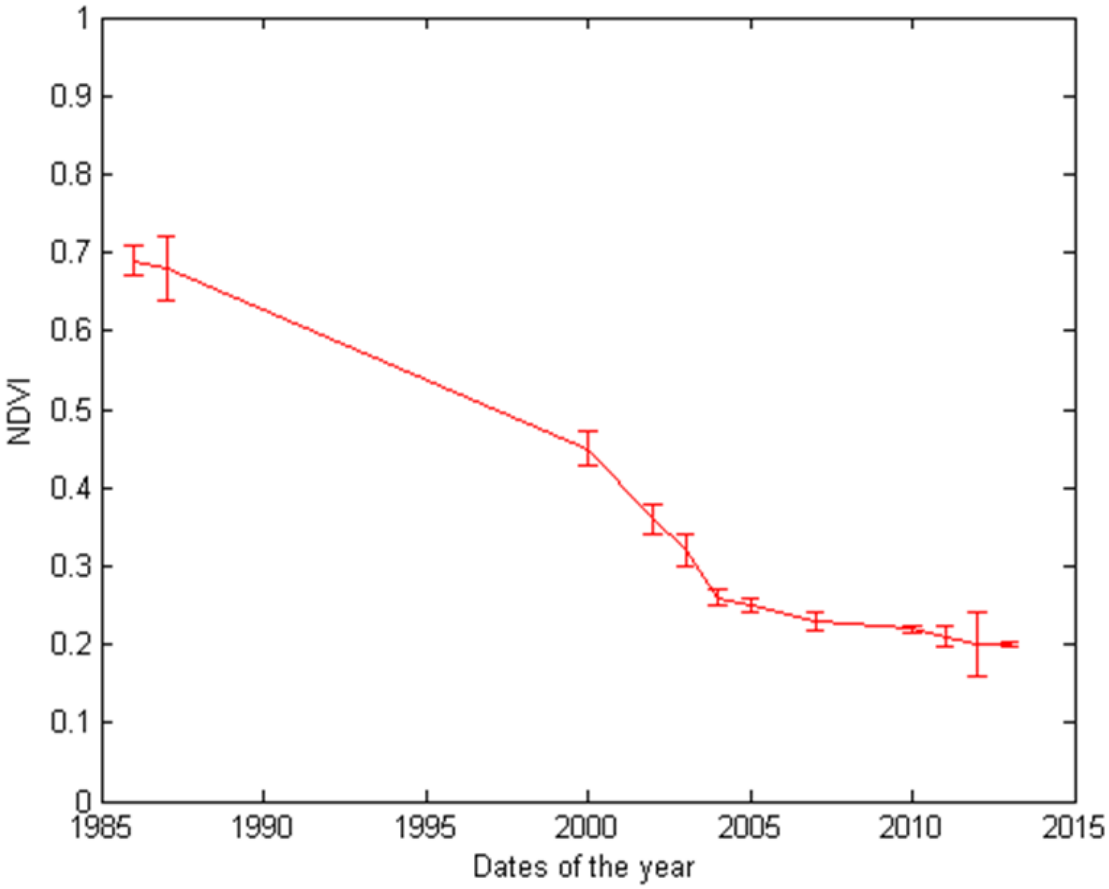

Figure 5-41: NDVI against time for spatio-temporal analysis for Eleme Refinery I at a distance of 60 m from the flare in the North direction

Table 5-9: Mean and standard deviation for positive, negative and net slopes of NDVI for the study sites (Units are change in NDVI per year).

Flaring sites	Mean (pixels with + slope)	SD (pixels with + slope)	Mean (pixels with – slope)	SD (pixels with – slope)	Mean (all)	SD (all)
Eleme I	2.3164×10^{-5}	3.3855×10^{-5}	-2.7076×10^{-5}	3.8550×10^{-4}	1.9166×10^{-5}	2.0689×10^{-4}
Eleme II	2.0741×10^{-5}	3.0926×10^{-5}	-1.7400×10^{-4}	2.5439×10^{-4}	1.5010×10^{-5}	1.3596×10^{-4}
Onne	1.0817×10^{-5}	2.9639×10^{-5}	-2.4278×10^{-5}	1.0757×10^{-4}	2.2849×10^{-6}	7.9515×10^{-5}
Umurolu	5.8684×10^{-5}	3.7938×10^{-5}	-1.6787×10^{-5}	4.2276×10^{-4}	5.8057×10^{-5}	7.4988×10^{-5}
Bonny	2.4228×10^{-5}	3.3757×10^{-5}	-3.0889×10^{-5}	1.8121×10^{-4}	2.1294×10^{-5}	8.2903×10^{-5}
Alua	8.8056×10^{-5}	5.2640×10^{-5}	-2.4815×10^{-4}	0.0011	8.7469×10^{-5}	1.4516×10^{-4}
Rukpokwu	7.6961×10^{-5}	4.1556×10^{-5}	-4.3011×10^{-5}	1.7924×10^{-4}	7.3986×10^{-5}	6.2093×10^{-5}
Obigbo	7.9023×10^{-5}	4.5078×10^{-5}	-3.5435×10^{-4}	7.1281×10^{-4}	7.8273×10^{-5}	1.1192×10^{-4}
Chokocho	1.0546×10^{-4}	3.9183×10^{-5}	-2.1310×10^{-4}	4.3901×10^{-5}	1.0520×10^{-4}	5.0786×10^{-5}
Umudioga	4.8557×10^{-5}	5.8950×10^{-5}	-4.0582×10^{-5}	8.9129×10^{-5}	-3.0408×10^{-5}	1.0120×10^{-4}
Sara	3.3600×10^{-5}	2.4634×10^{-5}	-2.9388×10^{-5}	9.2132×10^{-5}	1.4015×10^{-5}	7.6382×10^{-5}

Eleme Refinery I has some very small locations spread within the site in the North, East, South and North-West directions that show significant temporal trend in NDVI i.e. the locations with yellow colour in Figure 5.42 slope. The range of values for the trend is between -2.71×10^{-5} to 2.32×10^{-5} with a mean of $\pm\ 3.38 \times 10^{-5}$ and the p-value is from 0.05 and above (Figure 5.42 P).

Figure 5.43 shows that for Eleme Refinery II some small few locations spread within the site, pronounced in the North-West, South and South-West has significant temporal trend in NDVI (locations with yellow colour in Figure 5.43 slope). The value of the trend obtained for this site is within -1.740×10^{-4} to 2.074×10^{-5} with a mean of $\pm\ 3.093\ \times 10^{-5}$ and p-value from 0.05 and above (from Figure 5.43 P).

Onne flaring site has some areas of the site that are spatially coherent i.e. the area that's yellow in colour in Figure 5.44 slope. These areas are a small portion in the East direction (close to the boundary), and pronounced in the South-East direction (at the corner edge of the site), and both in the South and West directions before the boundary. The temporal trend in NDVI for these sections is significant. The full range of the trend in NDVI for Onne Station is between -2.428×10^{-5} to 2.9639×10^{-5} with a standard deviation of $\pm\ 7.952 \times 10^{-5}$ and p-value from 0.05 and above (from Figure 5.44 P).

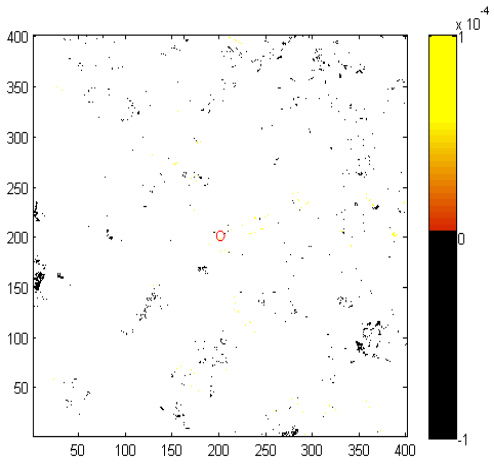

Slope

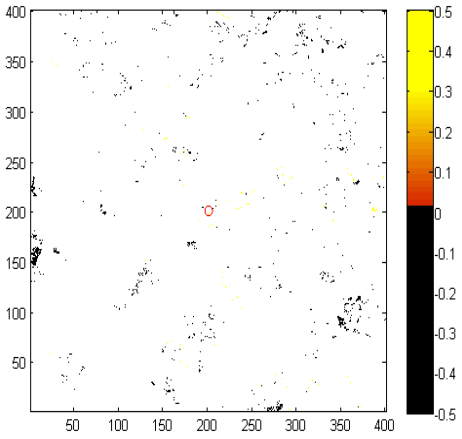

R

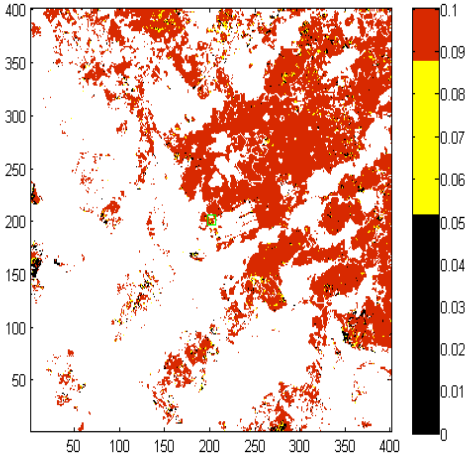

P

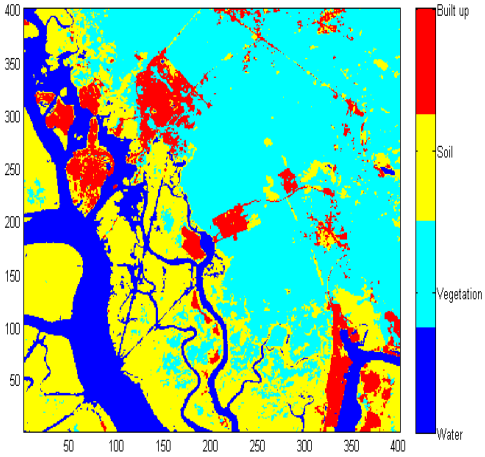

Land cover types

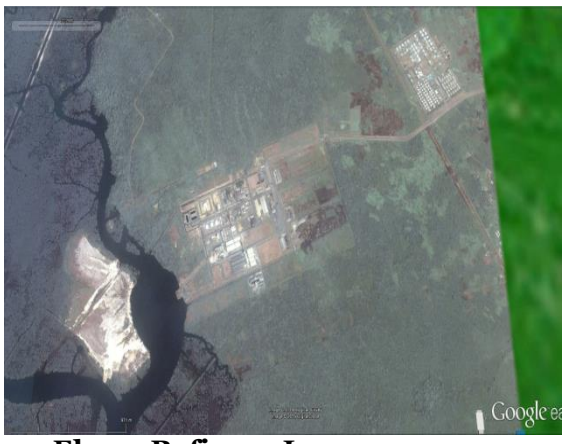

Eleme Refinery I, 2000

Eleme Refinery I, 2015

Figure 5.42: Maps of slope, r-value, p-value and land cover types for Eleme Refinery I flaring site

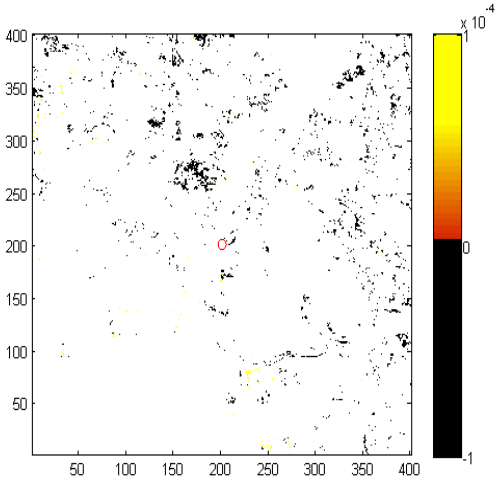

Slope

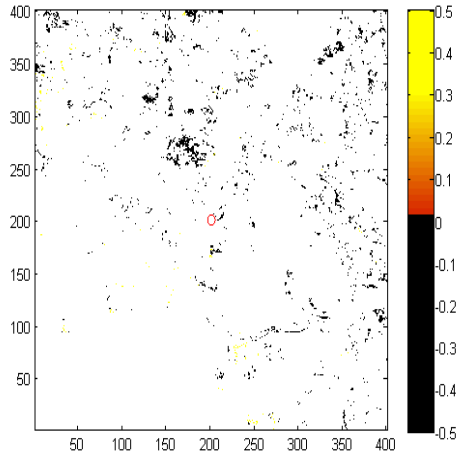

R

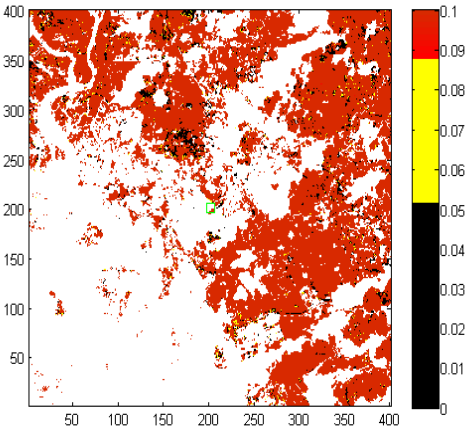

P

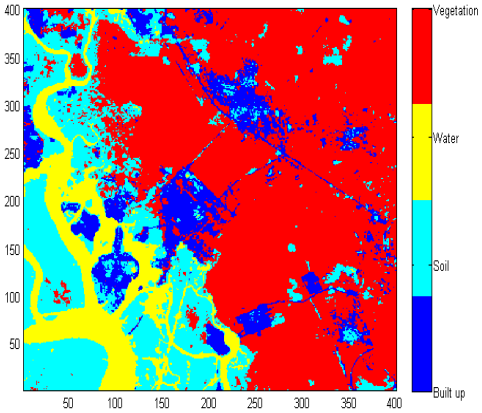

Land cover types

Eleme Refinery II, 2000

Eleme Refinery II, 2015

Figure 5-43: Maps of slope, r-value, p-value and land cover types for Eleme Refinery II flaring site

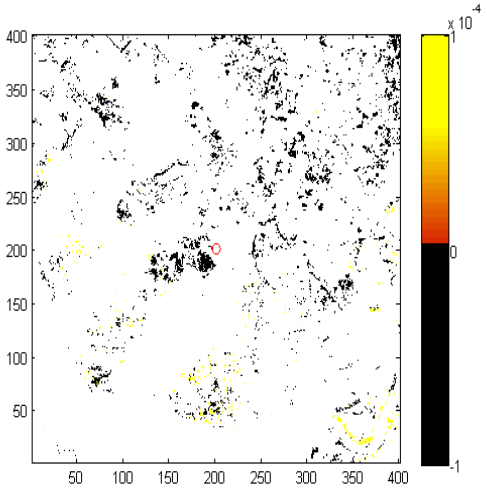

Slope

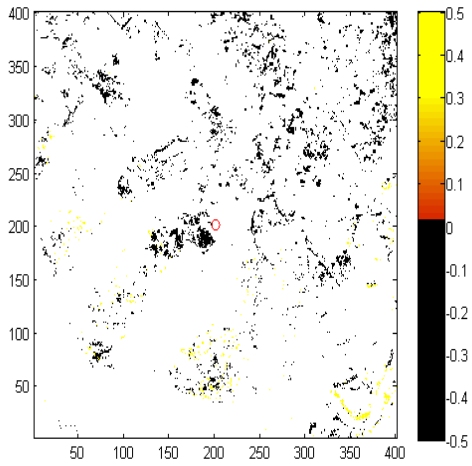

R

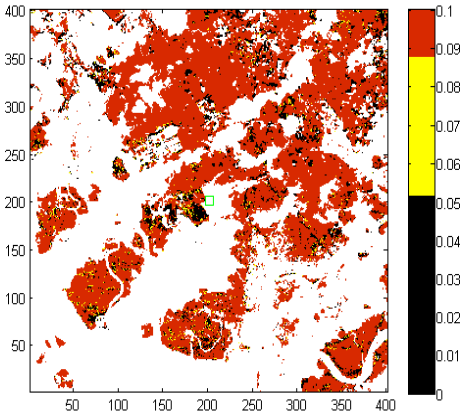

P

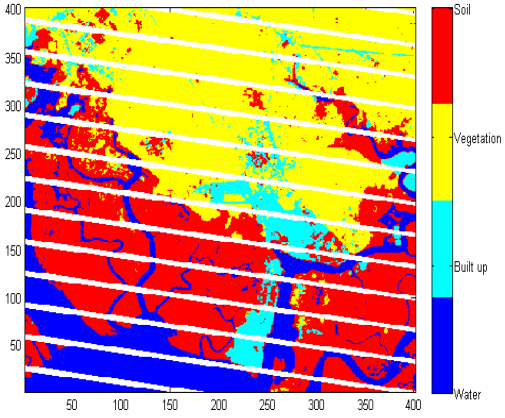

Land cover types

Onne Flow Station, 1984

Onne Flow Station, 2015

Figure 5-44: Maps of slopes, r-value, p-value and land cover type for Onne flaring site

Figure 5.45 slope shows that Umurolu site has sections (portion with yellow colour) within the site that is spatially coherent in NDVI with a trend value ranging from between -1.679×10^{-5} to 5.868×10^{-5} and a standard deviation of $\pm 7.499 \times 10^{-5}$ with the corresponding p-value ranging from 0.05 and above (Figure 5.45 P). This spatially coherent area includes the surrounding boundary of the flow station and an area within the site up to a distance of 90 m from the flare, especially in the East direction. Hence, the result shows that there is a significant positive temporal trend in NDVI within the Umurolu site area.

Figure 5.46 slope shows that some area within the Bonny LNG flaring site in the North, North-East, East, South and South-East directions (area with yellow colour) has significant temporal trends in NDVI. The range of the trend in NDVI for Bonny site is between -3.089×10^{-5} to 2.423×10^{-5} and the p-value recorded is the same as that for the Umurolu site (Figure 5.46 P).

There is a significant temporal trend in NDVI at Alua Flow Station with some locations being spatially coherent (sections with yellow colour) in Figure 5.47 slope, where the trend in NDVI is not equal to zero i.e. slope $\neq 0$ (between -2.482×10^{-4} to 8.806×10^{-5}, with a standard deviation of $\pm 1.452 \times 10^{-4}$) with p-value from 0.05 and above in Figure 5.47 P. Generally, for this site the significant trend in NDVI is shown both around the facility and at a far distance from the facility; especially towards the East, North-East, West and North-West directions.

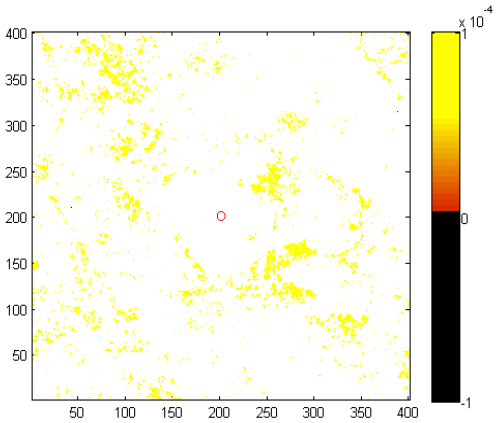

Slope

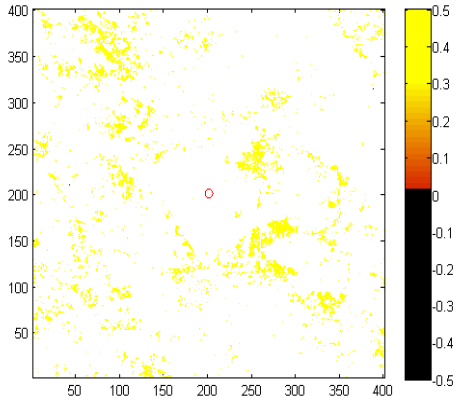

R

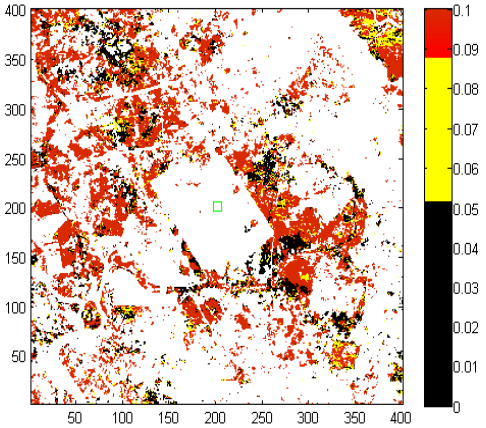

P

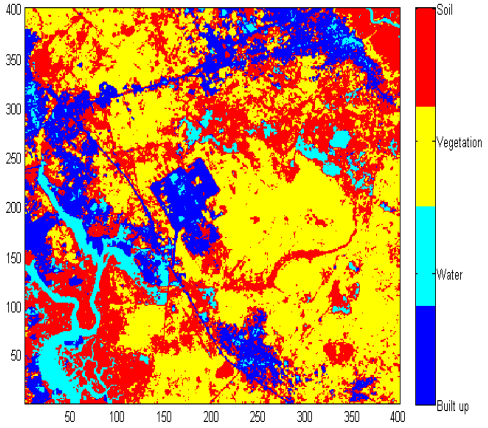

Land cover types

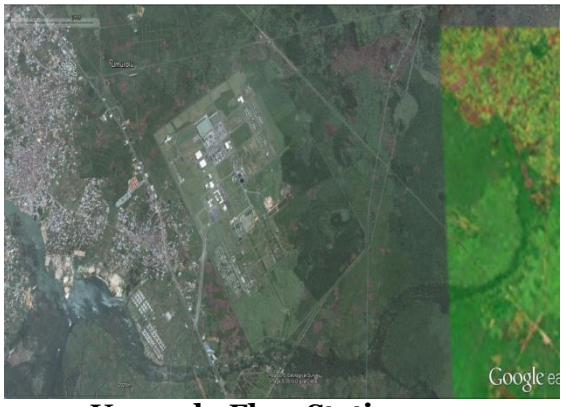

Umurolu Flow Station, 2005

Umurolu Flow Station, 2015

Figure 5-45: Maps of slope, r-value, p-value and land cover types for Umurolu flaring site

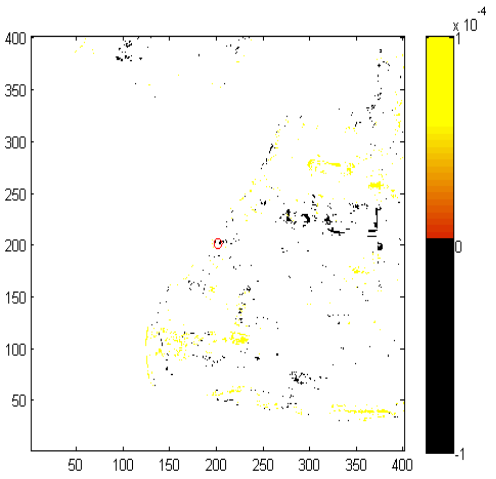

Slope

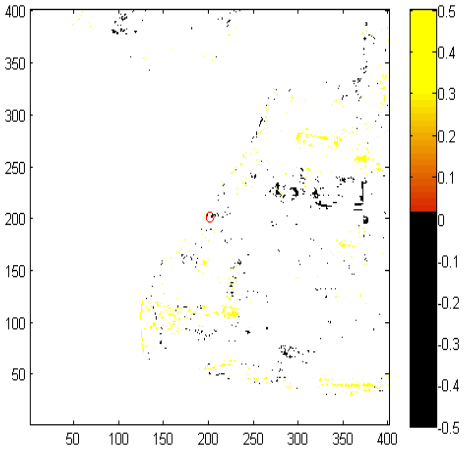

R

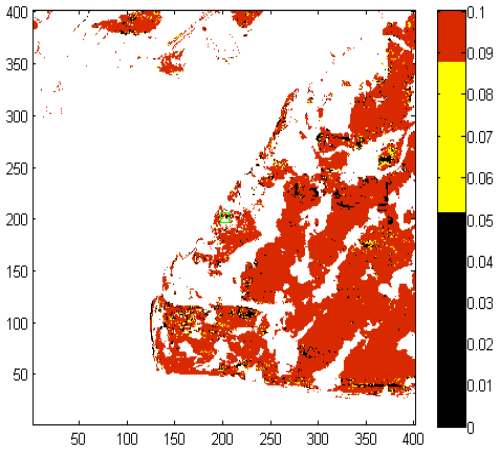

P

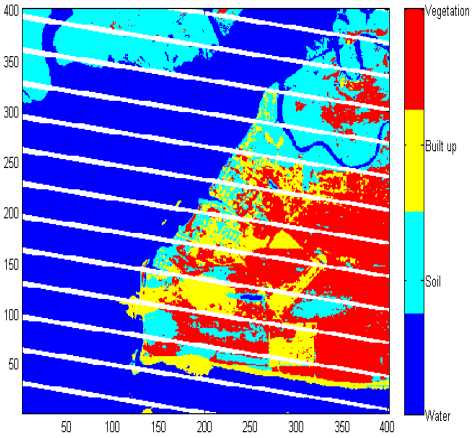

Land cover types

Bonny LNG, 1984

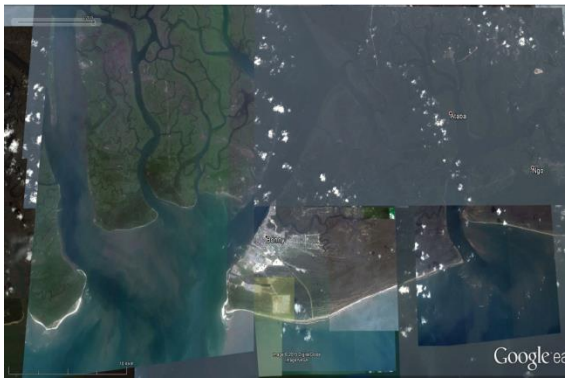

Bonny LNG, 2015

Figure 5-46: Maps of slopes, r-value, p-value and land cover types for Bonny LNG flaring site

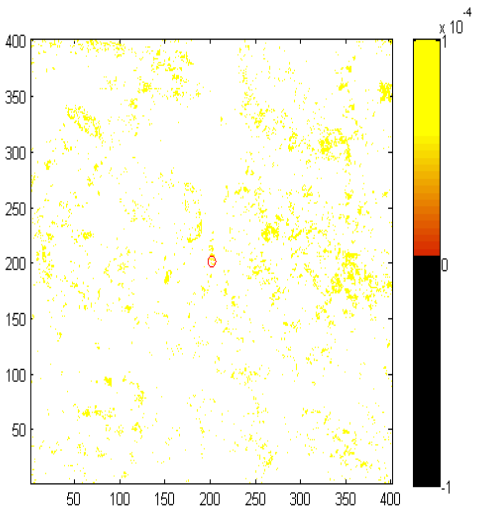

Slope

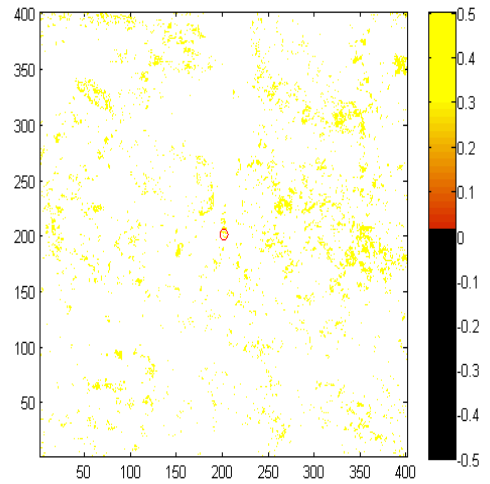

R

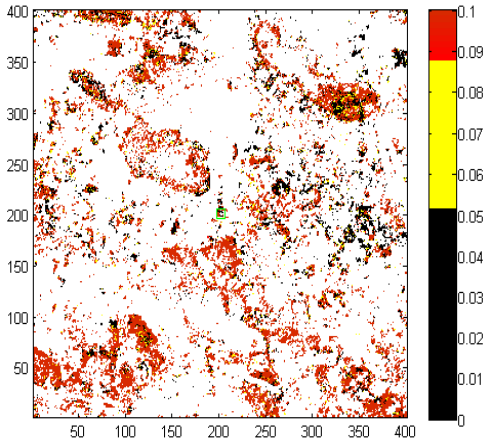

P

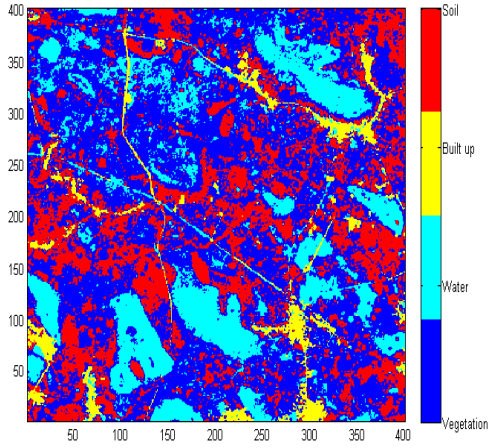

Land cover types

Alua Flow Station, 2002

Alua Flow Station, 2015

Figure 5-47: Maps of slopes, r-value, p-value and land cover types for Alua flaring site

Rukpokwu Flow Station also has areas within the site that are spatially coherent (areas with yellow colour) in Figure 5.48 slope. It has statistically significant temporal trend in NDVI very close to the facility, towards the North, and throughout the site towards the North-West and South-West directions where the changes in NDVI are more pronounced. The full NDVI trend range for the site is between -4.301×10^{-5} to 7.696×10^{-5} with a standard deviation of $\pm 6.209 \times 10^{-5}$ and p-value from 0.05 and above (Figure 5.48 P).

For Obigbo flaring site, Figure 5.49 slope and P show that there is a statistically significant temporal trend in NDVI throughout the site but more pronounced towards the North, North-East, East and South (areas with yellow colour). The range in the NDVI is between -3.544×10^{-4} to 7.902×10^{-5} with a standard deviation of $\pm 1.119 \times 10^{-4}$ and p-value from 0.05 and above (Figure 5.49 P).

Figures 5.50 slope and P show that the Chokocho flaring site has most areas within its site with a significant temporal trend in NDVI, including the surrounding of the flow station except for the top left corner and the lower section of the Southern end of the site. The range in NDVI trend is between -2.131×10^{-4} to 1.055×10^{-5} with a standard deviation of $\pm 5.079 \times 10^{-5}$ and p-value from 0.05 and above (Figure 5.50 P). From Figure 5.50 slope, there is not sufficient data to show that the impact of the flare is the only cause of this trend in NDVI throughout the site; human activities such as bush clearing for planting of crops and for hunting for bush animals, and burning of dumped refuse could be contributing to the result.

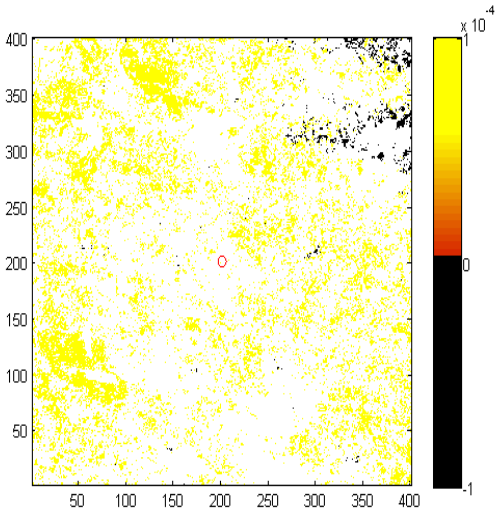

Slope

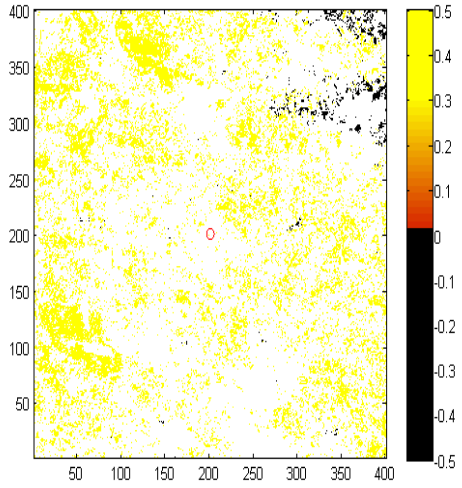

R

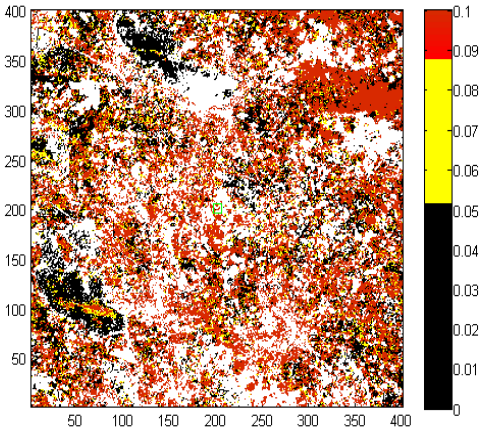

P

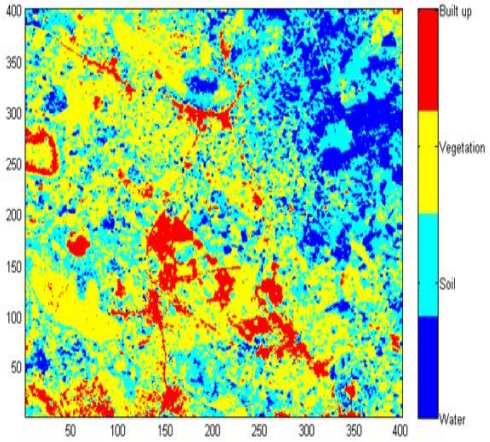

Land cover types

Rukpokwu Flow Station, 2002

Rukpokwu Flow Station, 2015

Figure 5-48: Maps of slopes, r-value, p-value and land cover types for Rukpokwu flaring site

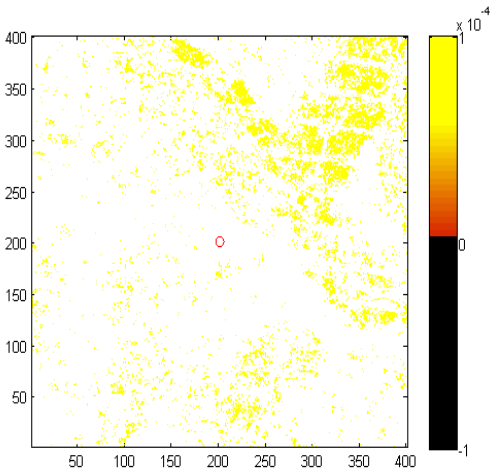

Slope

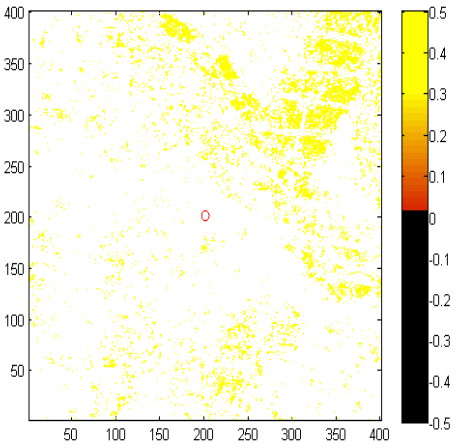

R

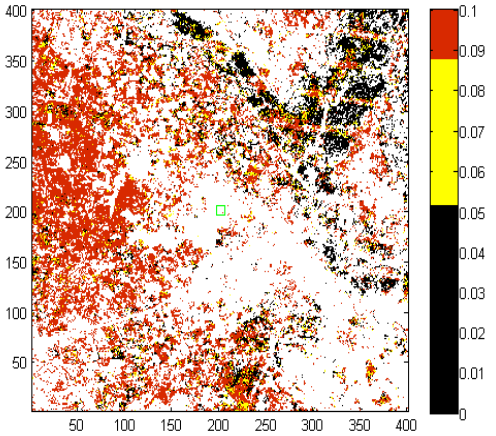

P

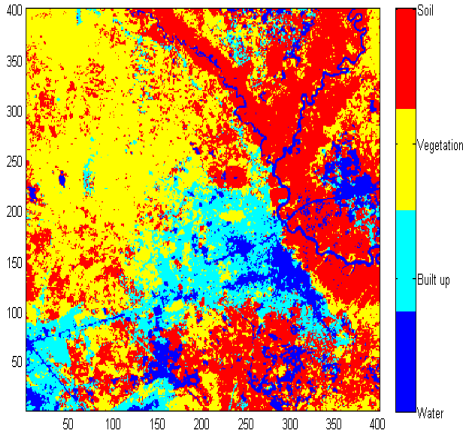

Land cover types

Obigbo Flow Station, 2003

Obigbo Flow Station, 2015

Figure 5-49: Maps of slopes, r-value, p-value and land cover types for Obigbo flaring site

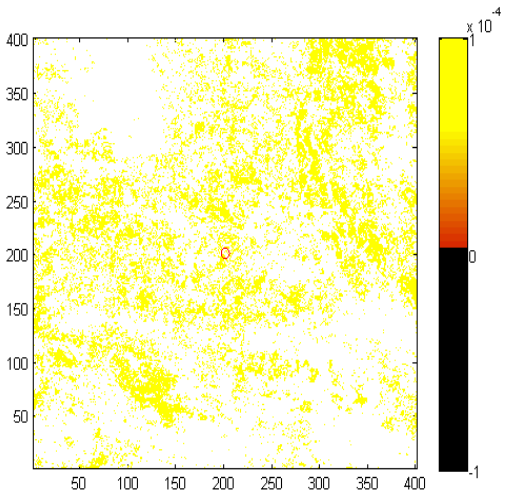

Slope

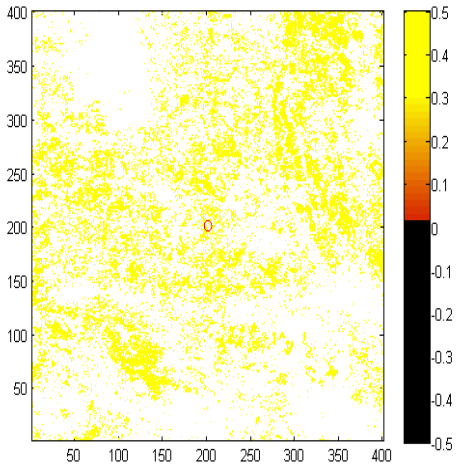

R

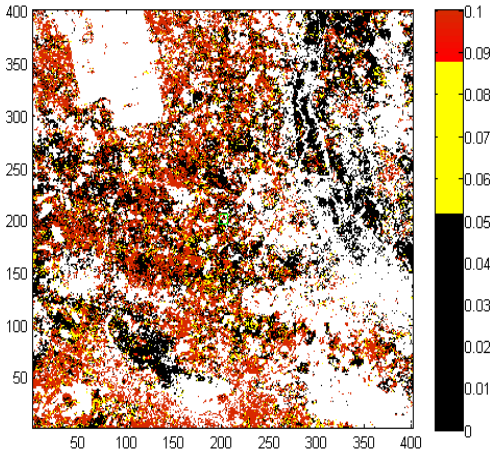

P

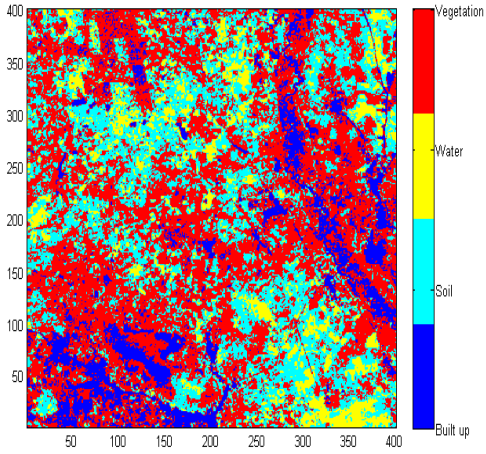

Land cover types

Chokocho Flow Station, 2003

Chokocho Flow Station, 2015

Figure 5-50: Maps of slopes, r-value, p-value and land cover types for Chokocho flaring site

For the Umudioga Flow Station, yellow portion in Figure 5.51 slope shows that the site has a statistically significant temporal trend in NDVI spread within the site except in the North-West direction. The most affected part of the site is towards the West, which is not too far from the flow station; and the top to the North of the site with a partially significant trend shown. The NDVI trend range is between -4.058×10^{-5} to 4.856×10^{-5} with a standard deviation of $\pm 1.012 \times 10^{-4}$ and p-value that shows a significant positive temporal trend in NDVI is from 0.05 and above (Figure 5.51 P).

Figures 5.52 slope and P show that some small areas spread within Sara flaring site have a statistically significant temporal trend in NDVI but less pronounced in the South and South-West directions. This could be attributed to its location at the coastal boundary of River Bonny. The NDVI trend range throughout the site is between -2.939×10^{-5} to 3.360×10^{-5} with a standard deviation 7.638×10^{-5} and p-value from 0.05 and above (Figure 5.52 P).

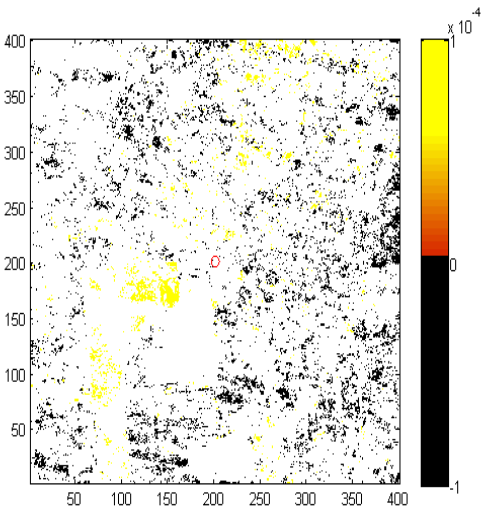

Slope

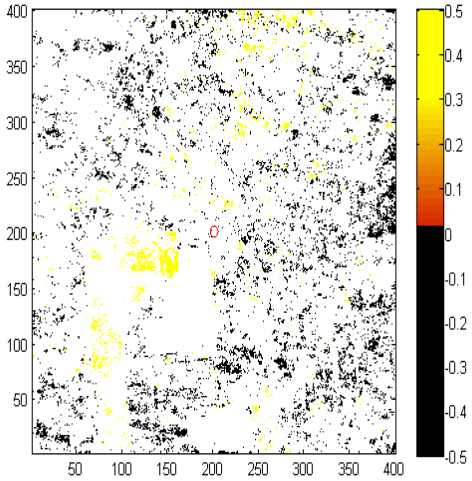

R

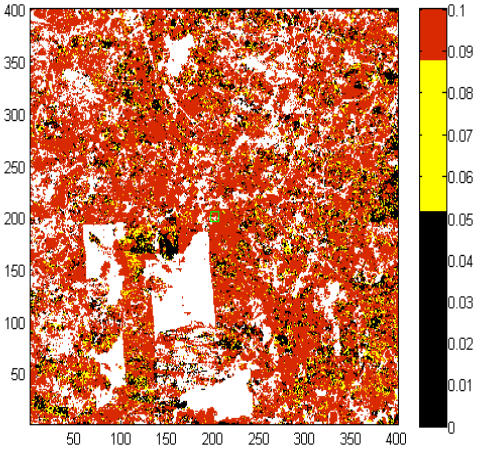

P

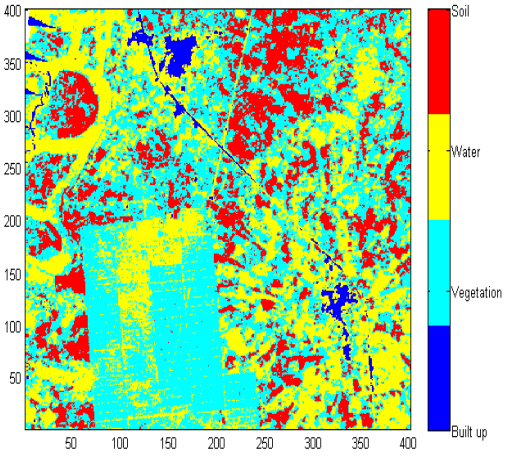

Land cover types

Umudioga Flow Station, 2007

Umudioga Flow Station, 2015

Figure 5-51: Maps of slopes, r-value, p-value and land cover types for Umudioga flaring site

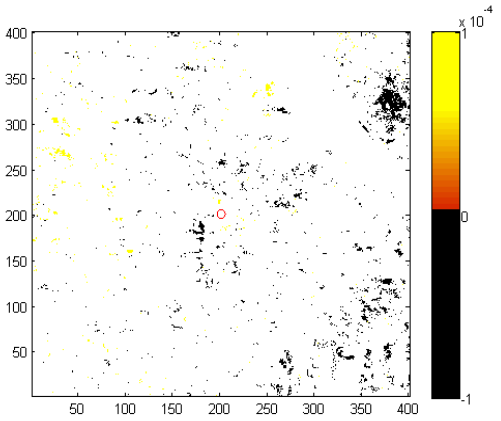

Slope

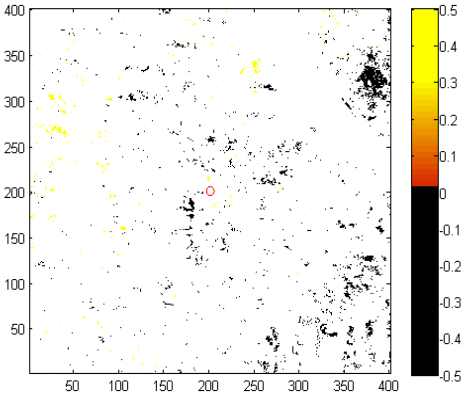

R

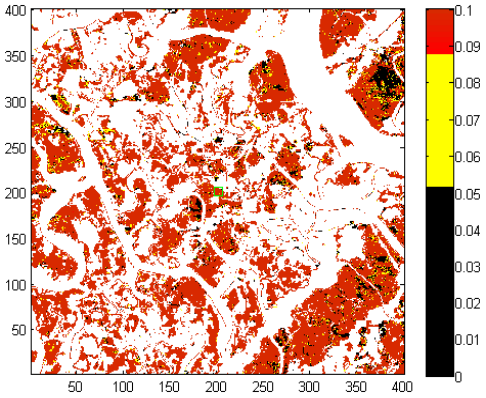

P

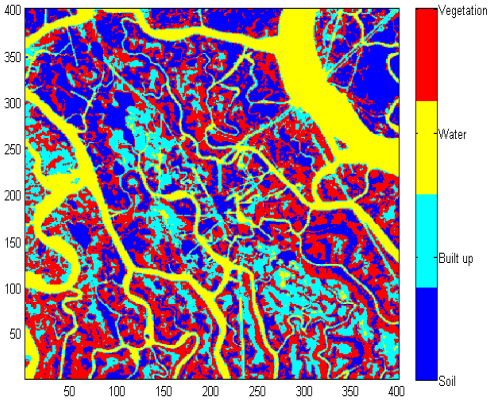

Land cover types

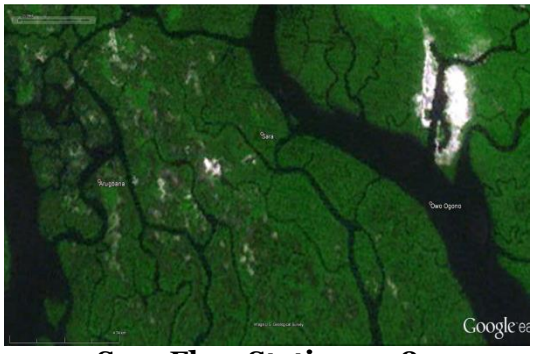

Sara Flow Station, 1984

Sara Flow Station, 1984

Figure 5-52: Maps of slopes, r-value, p-value and land cover types for Sara flaring site

Generally, the spatio-temporal analysis results for each site that all the inland facilities (Umurolu, Alua, Rukpokwu, Obigbo, Chokocho and Umudioga) have significant positive trends in NDVI over a wider area while coastal facilities (such as Eleme I and II, Onne, and Sara) have significant positive trends in NDVI over a narrow area. However, Bonny LNG which is also a coastal facility

shows a positive significant trend in NDVI over a wider area than all other four coastal facilities; and this could be as a result of the five flaring stations located within the facility. The positive significant trend in NDVI shown in the Eastern part of the site could be attributed to the effect of urbanisation.

5.6 Summary of results

It was concluded in Section 4.9 that some small and medium facilities with high rates of burning of flare could impact δLST, and this also impacts δNDVI. A change in NDVI (δNDVI) obtained from this study shows the influence of the flare, demonstrated by the δLST, on the vegetation cover and health around the flare stack. Also, when the influence of environmental factors at these flaring sites was examined, the results show that size of facility with each of $\delta NDVI_N$ (0.008) and $\delta NDVI_W$ (0.003) give significant results; and the relationship between stack height with each of $\delta NDVI_N$ (6.9042×10^{-8}), $\delta NDVI_E$ (2.1526×10^{-4})and $\delta NDVI_W$ (4.0952×10^{-5}) also gives significant results. In addition, time series analysis show that there is a decrease in NDVI values annually within 120 m away from the flare stack, and beyond this point the influence of the flare become minimal.

The spatio-temporal regression analysis shows that the temporal trend of NDVI is specific to each site, and that the impact of the flares on vegetation cover and health does not majorly depend on the size of facility; for example, both Eleme I (-2.71×10^{-5} to 2.32×10^{-5}) and II (-1.740×10^{-4} to 2.074×10^{-5}) give significant results for a narrow area. Umurolu (-1.679×10^{-5} to 5.868×10^{-5}) and Bonny LNG (-3.089×10^{-5} to 2.423×10^{-5}) gave significant results and this could be attributed to the number of flare stacks within them. Also, all medium

and small facilities gave significant results and this could be as a result of the rate and volume of gas burning from them. Though Sara Flow Station gave significant results (-2.939×10^{-5} to 3.360×10^{-5}) over a narrow area, this could be as a result of its location and the topography that is swampy with several tributaries.

Eleme Refineries I and II, Bonny LNG, Umurolu, Obigbo and Chokocho Flow Stations are 6 flare sites amongst others used for this study that are located within 1.5 km of human habitation (see section 4.1). This suggests that the impact of the flare will be affecting people negatively, for example air quality.

One area major of concern for the Landsat data used for this study is that it covers only one season (dry season) out of two seasons within Nigeria (rainy and dry). Therefore, the limitation of these results is that they cannot determine the impact of the flare on the vegetation health and vegetative cover in all seasons. Also, a lack of information on the vegetation types and their photosynthetic rate does not allow an investigation of how each vegetation type responds to the flare. Finally, a lack of data on the rate and volume of the gas burning at each site does not give this study the exact total influence of flare on vegetation cover and health.

5.7 Conclusions

Generally, the NDVI results show a drop from healthy vegetation as the flare stacks are being spatially approached at all sites; and that the vegetation closer to the flare is dead. Also, the effect of the flare is felt up to 120 m away from the stack with an annual reduction in NDVI values over the timescale analysed.

Onne presents an unstable trend from 1984 to 2007; the years before the flow station was built that can be attributed to the vegetation density, vegetation types and their photosynthetic rate as no flare is present.

The spatio-temporal regression analysis shows that each flaring site has its own temporal trend in NDVI from 1984 to 2013. Therefore, it can be concluded that satellite data (Landsat) can be used to detect the impact of gas flaring on vegetation cover and health. However, the spatial and temporal variability in satellite data (Landsat) linked to the detectable flare impact on vegetation cover and health is specific to each flaring site and with their activities, and finally it is dependent on the topography of the site, e.g. Sara Flow Station is built in swampy terrain.

Chapter 6
Discussion

According to the literature (within Chapter 2), Nigeria is the second highest contributing country in the world for gas flaring after Russia: based on the sum of light index values, Russia and Nigeria account for 40 % of global flaring and the top twenty countries account for 85 % (Eseoghene, 2011; Ziskin et al., 2011; Elvidge et al., 2009; Kimberly et al., 2007). With this motivation, a Nigeria-focused methodology was developed that was designed to use multiple satellite based sensors (Landsat 5 TM and Landsat 7 ETM+) to determine the effects of pollution from gas flaring on vegetation health, land and vegetative cover. Validation work in the field was carried out at Eleme Refinery II and Onne Flow Station flaring sites (Chapter 3). The Methods were then implemented to detect and map oil production-linked polluting sources and their surrounding environment (Chapter 4). An evaluation of the environmental impacts of gas flaring related pollution on vegetation health and vegetation cover from 1984 to 2013 within Nigeria was produced (Chapter 5). This Chapter discusses the research methods and the results in Chapters 4 and 5 in the context of the general body of knowledge in flaring and pollution detection by satellite, focussing on the current capabilities of the work and its limitations. Finally, this Chapter will also outline future research.

6.1 Problem of Landsat data used

The scan-line corrector (SLC) for the ETM+ sensor, on board the Landsat 7 satellite that failed permanently on the 31st May 2003, compensates for the forward motion of the satellite. Under this abnormal situation, without an

operating SLC, images have wedge shaped gaps that range from a single pixel in width near the nadir point, to about 12 pixels towards the edges of the scene; the SLC anomaly results in about 22 % of pixels in these images not being scanned. The consequence of the SLC failure (called SLC-off problem) is that it hampers the use of the Landsat 7 ETM+ data (Chen et al., 2012) and so has limited the number of images used for this study.

Another major problem with using Landsat (Landsat 5 TM and Landsat 7 ETM+) data for this study is that the data obtained covers only one season (dry) out of two seasons (rainy and dry) that are available in Nigeria. The available data for the rainy season in the NASA/USGS archive are all cloudy, and so could not be used. AATSR (Spazio, 2015; ESA, 2015a) and MODIS (Spazio, 2015; NASA, 2015d) data were acquired but the problem of 1 km spatial resolution made them inappropriate for use in this study. ASTER (USGS, 2015c; Yamaguchi et al., 1998) data are the most appropriate substitute in terms of technical specification, but the problem of data acquisition for specific request and payment for it prevented its acquisition because the author could not afford it (Tomlinson et al., 2011). Also, the Niger Delta region has a consistent (uniform) topography which has not allowed the comparison of the results at these flaring sites with results in areas with different topographies.

6.2 MATLAB programming tool

Generally, MATLAB code was used for the processing of Landsat 5 TM and Landsat 7 ETM+ data because the author is familiar with it. It was also used for the analysis of the results, which includes quantitative analysis using linear regression and spatio-temporal analysis. The spatio-temporal analysis code

made use of all available data for each site, processed to generate 3 maps that were namely slope (annual change in NDVI), r-values and p-values. These maps were used to evaluate the spatial and temporal variability in the Landsat detectable flare impact on vegetation health and vegetation cover at the flaring sites used for this study.

6.3 Characterisation of land cover types

A combination of WorldView-1 and 2, and Ikonos-2 images obtained from Google Earth and Digital Global, a UK-DMC image, Landsat reflective bands (1-4) and a Landsat pseudo-true colour image (RGB) were used to differentiate land cover types at the flaring sites (see section 4.1). They enabled clear identification of features surrounding oil facilities and other features within the flaring sites. However, to distinguish vegetation types within each site was not possible because of the resolution of the images used; an image of higher spectral and spatial resolution is required (Alvarez, 2009; Andrew et al., 2008; Pengra et al., 2007), and this has in turn limited the differentiation of vegetation types because of a lack of information. For this study, this limitation may affect the estimation of the emissivity values of land cover types at each flaring site (Qin et al., 2011).

6.4 Land cover classification

Results of land cover classification in Chapter 4 show that the cluster analysis method (Hestir et al., 2008) performed well in the classification of land cover types. However, insufficient information was available to discriminate between (Antonarakis et al., 2008) and therefore classify different vegetation types, and this is also explained by Alvarez (2009) in that remotely sensed datasets are

available in different spectral and spatial resolutions and that different resolutions allow for land cover types analysis at small or large scales. Also, Carleer and Wolff (2006) supported this result, that contrast between the vegetation and the non-vegetation is lower. Hence, the number of wavebands used does not resolve differences in vegetation colour and brightness, and so the vegetation types cannot be classified separately. Minor generalization of land cover occurred with small features, such as vegetation types, and linear features during the cluster analysis classification. However, generalization of small features is inevitable since the spatial resolution of Landsat 5 TM and Landsat 7 ETM+ is limited to 30 × 30 m. For a more accurate land cover change assessment a higher spectral and spatial resolution dataset needs to be considered (Alvarez, 2009; Antonarakis et al., 2008).

6.5 Estimation of emissivity value for land cover types

Mallick et al. (2012) derived emissivity by using normalized difference moisture index (NDMI). The emissivity per pixel retrieved directly from Landsat TM data were estimated as narrow band emissivity at the satellite sensor channel in order to minimise the error in the surface temperature estimation (Mallick et al., 2012). The estimated emissivity values over a few land use and land cover classes of Landsat TM were compared with literature values, and the results showed that the satellite derived emissivity values were in the acceptable range (Mallick et al., 2012). For this study, the emissivity values corresponding to different land cover types at the flaring sites in a pixel-by-pixel basis (Peng et al., 2008; Xu et al., 2008) from scene to scene were estimated using a LUT (Table 3.2) compiled from the literature; though there are uncertainties due to the range between minimum and maximum values, the use of a LUT for

estimation of emissivity values of land cover types gives a reliable result than to use the same value of emissivity = 1 for all types of surfaces (Pu et al., 2006) which is supported by Mallick et al. (2012). Land cover type at each flaring site was used to estimate emissivity, which helped to avoid the use of an emissivity value, for example those from ASTER Library, that are not based on the information from the Niger Delta region. However, the accuracy of the LUT method is greatly hindered by the mixed pixel issues and also depends on the precision of the land cover type classification (Qin et al., 2011).

6.6 Computation of Landsat thermal band atmospheric correction parameters: ATMCORR CALCULATOR

The provision of the MODTRAN ATMCORR Calculator by NASA, which generates Landsat thermal (band 6) atmospheric correction parameters for a single point (Coll et al., 2010; Barsi et al., 2005), and the choice of running the calculator over each site of interest helped to overcome the limitation of using a single point for a whole Landsat scene, and also helped to characterize the atmosphere over the whole scene for the Niger Delta (Barsi et al., 2003). Furthermore, the correction for the atmospheric influence on a site by site basis has reduced the uncertainty that would have been introduced if the whole scene were to be corrected using the flaring site at the centre of the scene (see section 3.6.2).

Results from the error analysis for the ATMCORR Calculator in Chapter 3 (Table 3.11) showed that it performed well in the Niger Delta and gave an error in LST as 6.2×10^{-4}-0.0112 K. This result is in agreement with Barsi et al. (2005) who explained that although the ATMCORR Calculator is not expected to

perform quite as well globally, even with the uncertainties in the NCEP model, it is expected that the Calculator should predict atmospheric parameters that allow apparent surface temperatures to be derived within ± 2 K where the surface emissivity is known and the atmosphere is relatively clear. The comparison of the percentage errors obtained for this study with the allowable limit from Barsi et al. (2005) showed that the atmospheric correction parameters (upwelling and downwelling radiance and transmittance) obtained from ATMCORR Calculator for these flaring sites are within this given allowable limit (see Table A-8 in Appendix A).

6.7 LST uncertainties

The results obtained from assessing the variability in emissivity within the computation of LST in Chapter 3 gives an uncertainty range of $\pm$ 4.5 K, which is consistent with Inamdar et al. (2008) who attributed uncertainties to the estimation of an emissivity value from a LUT because the value provided may not completely correspond to the land cover type under investigation. The uncertainties introduced in the estimation of emissivity for vegetation are carried through to the calculation of LST from brightness temperature. This propagation of errors suggested that improved classification of the substrate could reduce uncertainty in LST by up to 4.5 K.

6.8 Results: GIS spatial analysis and four cardinal directional plotting and curve types

GIS analysis enables the presentation of the 2D shape of each flare plume and 6 classes of LST values with their elevation difference using contours for each site. It also helps to determine the best direction of the minimum and maximum LST

slope for each site. Furthermore, GIS analysis helps to know whether the South-North direction of the prevailing winds in the Niger Delta have any significant impact on the flare at the time of satellite overpass. Four cardinal directional plotting allows the presentation of LST and NDVI results in four directions North, East, South and West (see section 4.4.1.2). This is a valuable method that shows the spatial gradients and vegetation health for each land cover type at a given time around the flare sites. This method is also useful in investigating the potential of prevailing wind influence on LST within a site, in the absence of daily or even monthly wind time-series data. The characterisation of spatial variability in LST was undertaken with the type A data, smoothly declining curve, excluding the remaining three curves types which were difficult to interpret in terms of flare stack influence (see section 4.4.2); adopted to avoid the contribution of other local heat sources (apart from the flare) within the site. For this study, the LST derived from both Landsat 5 TM and Landsat 7 ETM+ and the air temperature from the ground validation data at 240 m agreed to within 3.5 K. This is supported by Oseji (2007) who recorded a surface temperature elevation of about 3.7 K within a radius of 270 m at Kwale/Okpai gas flaring site in Delta State of the Niger Delta.

6.9 Comparison of air temperature with Landsat derived LST

Validation of Landsat-derived LST obtained at the flaring sites was not possible because of a lack of in-situ data. The trends of air temperature measured at both Eleme Refinery II and Onne Flow Station showed that the closer to the flare, the higher the air temperature and vice-versa. Results from Dung et al. (2008) are in agreement with this fieldwork acquired results. Dung et al. (2008) reported that the air, soil and leaf temperature measured during fieldwork activities

increased and the relative humidity of the air decreased within 110 m away from the flare for 6 flare sites near Port Harcourt, Rivers State.

The mean air temperature measured at both Eleme Refinery II and Onne Flow Station during the period of fieldwork (Tables 4.8 and 4.10) and the comparison between field data and two Landsat images (13/11/2005 and 8/3/2013) showed that air temperature is higher than LST and that the air temperature has a different spatial distribution from LST. The air temperature was measured directly in the field with no need to consider the atmospheric effects; whilst satellite derived LST is influenced by the state of the atmosphere at the time of satellite overpass. Otukei and Blaschke (2012) found that LST derived from Landsat ETM+ and that from the ground truth data agreed to within 2 K. For this study, the LST derived from both Landsat 5 TM and Landsat 7 ETM+ and the air temperature from the ground validation data agreed to within 3.5 K; and this could be attributed to the difference in the spatial distribution of LST and of the air temperature.

During the fieldwork it was observed, at both sites, that the plume from the flare stacks moved outward. Furthermore, it was clear that during the second visit to both sites the volume of the visible flame was greater than that of the first visit and this was supported by the detection of the higher temperatures being radiated from the flame. Also, the noise coming out from the burning was louder than on the first visit. This could be as a result of the increase in the numbers of barrels of crude oil that were undergoing refining processes at Eleme Refinery II and also the increase in the barrels of crude oil stored at the Onne Flow Station. These field observations are consistent with the finding that

factors other than facility size, stack height and season accounted for the majority of variability in δLST within the site.

6.10 The environmental impact of gas flaring on vegetation health and vegetation cover

Analysis of the NDVI data (Chapter 4) showed that an impact of gas flaring on vegetation health and land cover was detected in the Landsat (Landsat 5 TM and Landsat 7 ETM+) products. In Chapter 5 this result is used to evaluate the impact of pollution from the flare on vegetation health, and vegetation cover and also to assess the spatial and temporal variability of this impact on vegetation. The time series analysis of NDVI results in Chapter 6 showed that the influence of the gas flare on vegetation health and vegetation cover is felt within 120 m of the flare and that the vegetation cover closer to the flare stack is dead (see Figure 2.6 A in section 2.5). The spatio-temporal analysis of NDVI for each flaring site showed decadal trends in satellite detectable NDVI at each flaring site varied and it depended on the features of each site. Therefore, further in-situ data would be required to identify the drivers of change for the large-scale effects; there are some changes at significant distance from any flare that could be attributed to any number of factors that are beyond the scope of this PhD.

The results of the NDVI time series analysis i.e. the impact of flare on vegetation is felt within 120 m from the flare stack is in agreement with the results reported by Isichei and Sandford (1976) that the species composition of the vegetation was affected by the flares up to a distance of 80 to 100m from the stacks and that the total number of species close to the flares decreased. Also, result from

this study is in support of the previous study on gas flaring and its impact on vegetation and crops. For example, Osuji and Avwiri (2005) who reported that flare killed vegetation around the flare stacks; depression in flowering and fruiting (Oluwatimilehin, 1981), retarded growth and productivity (Ologunorisa, 2009) and reduction in the efficiency of vegetation species and density (Nelso, 1997).

However, it is possible that the selection of a single emissivity value affects the LST results because variations in the vegetation cover were not accounted for. Also, there is lack of higher spectral resolution imagery that could have helped to potentially explore whether the NDVI gradient results purely from a change in health related to the higher temperatures or also to change in species composition. These are confounding effects that this study could not address.

6.11 Further research

It's accepted that doctoral research is limited in time and hence scope, so the potential areas of future research are the focus of the sections below.

6.11.1 Conversion of Air temperature to Land Surface Temperature

Air temperature is not exactly the same as land surface temperature. The conversion of air temperature measured at Eleme Refinery II and Onne Flow Station gas flaring sites to get LST will be a useful piece of research to undertake e.g. a sub-pixel scale radiative transfer model. The comparison of this result with the acquired LST from satellite data, such as Landsat data, will help with comparisons of the spatial variability of the impact of flaring at these sites.

6.11.2 NDVI for the Niger Delta and Northern Nigeria

There has not been any research to investigate and compare NDVI from two different geographical climates such as the Niger Delta and Northern region of Nigeria. This type of research would help to evaluate differences in NDVI due to differences in topography and meteorological climate. Also, the availability of data about parameters that influence NDVI at both regions would aid interpretation of the results.

6.11.3 NDVI time series analysis

This analysis could be repeated using the time since each facility was first built as the predictor variable, rather than just the time used for this study. It is not possible to do this for all sites used in this study because the build dates of most of the facilities were not available.

6.11.4 Emissivity retrieval

Land Surface emissivity retrieval over a heterogeneous surface like the Niger Delta is another research area identified that will add more to the knowledge of land cover types and retrieval of LST from satellite data for the Niger Delta region and Nigeria at large. This study should include in-situ vegetation surveys to facilitate a quantitative evaluation of vegetation classes derived from remotely sensed data. Also, to make use of a soft classifier such as Linear Mixture Modeling (LMM) techniques for land cover classification.

6.11.5 Ecosystem, social and economic implications of flaring

It will be beneficial to estimate loss of ecosystem due to the effects of gas flaring and other related oil activities; assessing the social impacts of flaring on people's

health and their standard of living; and then evaluating the economic loss to the Nigerian Government from gas flaring. The integration of an ecosystem approach with a GIS will be useful in conducting this kind of research.

6.11.6 Investigation of Nigerian legislation and policies on flaring with gas flaring volume estimates from satellite data

There has not been enough research on the investigation of Nigerian policies on gas flaring since the exploitation of crude oil and gas began in commercial quantities in 1958. This type of research could be a channel to compare Nigerian policies with that of the developed countries such as Norway, USA, UK, France and Germany and developing countries such as Ghana, Sudan, Equatorial Guinea, The Republic of Congo, Algeria and South Africa. In addition, research on the estimation of gas flaring volumes based on satellite data in Nigeria will spur improved utilization of gas that was simply burnt as waste in previous years (Kimberly et al., 2007).

Chapter 7
Conclusions and recommendations

The aim of this thesis was to create a Nigeria-focused methodology for determining the effects of pollution from burning gas using multiple satellite based sensors. The first objective was the detection and mapping of eleven gas flaring sites with Landsat TM and ETM+ data from 1984 to 2013 (Chapter 4). The results of this mapping indicated that both Landsat TM and ETM+ sensors can detect gas flares with an acceptable accuracy of (0.120 to 1.907 K) for LST. Fieldwork activities at Eleme Refinery II and Onne Flow Station (Chapters 3 and 4), and the evaluation of environmental impacts of gas flaring related pollution on vegetation health within Nigeria from 1984 to 2013 (Chapter 5) were additional objectives used to achieve this aim. The major findings of the thesis can be stated in the context of the research questions presented in Chapter 1, and this Chapter will outline the contribution of this research to knowledge. Finally, the conclusions of the thesis are stated in the context of its aim and objectives.

7.1 How accurately can we detect gas flare from satellite based sensors?

Based on the results from detection and mapping of the eleven gas flaring sites in Chapter 4, Landsat 5 TM and Landsat 7 ETM+ sensors could be used to detect a gas flare in 2,503 cases out of 3,001 available for this study (see section 4.4.2). LST retrieved from both sensors for the flare hotspots are the highest values compared to other locations within the processing sites, which was

clearly shown through the transects plots (see section 4.2) and GIS spatial analysis (see section 4.4.1.1); and then, the closer the distance to the flare, the higher the temperature and vice versa. Also, the LST derived from both Landsat TM and ETM+ sensors (Chapter 4) and the air temperatures obtained from the fieldwork activities agreed to within 3.5 K. Based on these results it can be concluded that satellite based sensors, such as Landsat TM and ETM+, have the ability to detect gas flares in the Niger Delta with (range: 0.120 to 1.907 K) an acceptable accuracy. Landsat 8 OLI/TIR is the best available existing alternative to Landsat TM and ETM+ sensors because it has spatial resolution of 100 m (see section 2.8.1.1) and it is free. One of the potential future sensors designed with the aim of including flare in the detection of fire hotspots is Sentinel-3 SLTSR (see section 2.8.1).

7.2 Can satellite data be used to detect the impact of gas flaring on vegetation health?

NDVI results for the mapping of flaring sites in Chapter 4 answered this question. Landsat 5 TM and Landsat 7 ETM+ data could be used to detect the impact of gas flaring on vegetation health in 2,503 cases out of 3,001 available for this study (see section 4.4.2). NDVI results revealed that the values around the flare are approximately zero; with the closer the location to the flare the lower the NDVI value, and vice versa. Also, the time series analysis of NDVI from 1984 to 2013 in Chapter 5 revealed that the impact of gas flaring is felt within 120 m distance of the flare. Therefore, it can be concluded that satellite data such as Landsat TM and ETM+ data, has the ability to detect the impact of gas flaring on vegetation health and vegetation cover in the Niger Delta.

7.3 What is the spatial and temporal variability in satellite detectable flare impact on vegetation health?

The spatio-temporal regression analysis showed that the temporal trend of NDVI is specific to each site i.e. it varies from site to site depending on several factors that can include the rate and volume of burning gas, number of flare stacks within the oil facility, vegetation type, vegetation density, size of facility, different features and events and topography of the site. Also, the NDVI time series analysis from 1984 to 2013 showed that for all sites investigated, the vegetation cover surrounding the stack (within 120 m distance) experienced a greater influence of the flare and its impact on the vegetation health seems to be consistent at this boundary. Based on the results in Chapter 5, it can be concluded that Landsat satellite data has the ability to detect the extent of the impact of the flare on vegetation health with an acceptable accuracy in NDVI (sd ± 0.004). However, flare impact on vegetation health is specific to each flaring site because of the strong influence of local factors.

7.4 Contribution of this research to knowledge

The stages of methods for the processing of Landsat data (see Figure 3.10), GIS analysis (section 4.4.1.1), presentation of results in four cardinal directions (see section 4.4.1.2) and characterisation of spatial variability in LST in four different types of curves (see section 4.4.2) used in this study will be useful for future users studying land cover types, vegetation indices and retrieval of LST from Landsat 5 TM and Landsat 7 ETM+ data. This kind of research has not been conducted for the Niger Delta at this spatial magnitude before. This study has quantified differences in LST and NDVI within 450 m of flares. In addition, not all factors that influence flare impacts could be considered (see section 3.6.3).

The gas flaring volume and vegetation speciation are the two major missing pieces of information but others might just be as important.

This research demonstrates that only 5 % of the variability in δLST_N and δLST_E, and only 12 % of the variability in $\delta NDVI_N$ with distance from the flare stack is accounted for by the available variables considered in this study. This suggests that other missing factors (e.g. the gas flaring volume and vegetation speciation) play a significant role and potentially account for 95 % and 88 % of the variability in LST and NDVI respectively. In addition, this study has used direction plots to assess the relevance and influence of wind direction on the impact of flares.

The method of projecting eight lines around the flare stack for the measurement of the air temperature, which includes the four cardinal directions, will also be useful to other users in the future. In addition, the method developed for the differentiation of gas flares from other burning fires in this study could serve as a method to build upon for future research relating to flaring.

Furthermore, this research investigated the changes caused by pollution from flares on the vegetation health and land cover over a period of 29 years, and thus the spatial and temporal variability in vegetation health that might be related to pollution from the flare has been identified. The results will serve to inform the Nigerian Government that the problem of flaring and its associated pollution deserves more and urgent attention in order to preserve the lives and livelihood of people and the quality of the environment. The analysis of the spatio-temporal variability of pollution from flares by processing all the

available Landsat data for each site will be useful for users who will be involved in research like this in the future.

7.5 Recommendations

This study discovered that NDVI impact was detected within 120 m distance from the flare and so, the influence of flaring and its associated pollution within 120 m has resulted in damage to vegetation health, and the vegetative cover and these consequences are highlighted in this research. Since it can be confirmed, from the results of this research, that pollution from gas flaring significantly contributes to the loss of vegetation health and rich natural forest surrounding the study sites the following recommendations are made:

- The primary restriction to this study is the lack of sufficient satellite derived and in-situ data. Even, with two satellites owned by the Nigerian Government, satellite data over Nigeria from these satellites could not be accessed. This is as a result of problems with Abuja receiving ground station due to lack of internet facility to operate it, and lack of accessibility to data in Nigeria. In addition, a lack of sufficient meteorological data has also limited the analysis. The Nigerian Government should ensure that these data are available to educational and research institutions that will need them for research in Nigeria. Other alternative satellite data sources in the future are Landsat 8, ASTER, Sentinel-3 and other DMC satellites.

- The lack of direct and open access for the measurement of in-situ data at oil and gas facility sites in the Niger Delta; the lack of data on the history and the time of build of the oil facility i.e. the year of commissioning of gas flaring sites, and data on the volume of gas flare from these sites are further limiting

factors in this study. Therefore, the government should make a provision for the policies that enforce multi-national oil companies to declare information on their oil and gas exploration and exploitation activities to the general public especially to stakeholders and organisations involved in the oil and gas business. There is a possibility for further study in this research in countries with fewer security issues such as Ghana, Cameroon, South Africa and United States of America.

- Furthermore, it is not possible to undertake research like this in Nigeria because of the lack of facilities in the Universities and other research institutions. Therefore, the government should determine and make provision to meet the requirements of a world class educational system by reviewing the curriculum of the Nigerian educational sector and providing adequate funding.

- The provision of an enabling environment and sufficient funding for scientific research on oil and gas related disciplines such as gas flaring and to fully assess it impacts on vegetation, biodiversity and ecosystem, and ensure ways of mitigation, if required.

- The study of water-borne pollution using very high spatial resolution data.

- Staff training, especially for those that are in charge of implementation of policy relating to oil and gas production processes, land economics, and environmental and protection management systems.

- Data archiving and management should be supported as it will encourage dissemination of data to researchers and the general public. The major issues in data management include data availability, integrity of the dataset (quality control), and clear methods for data update, documentation and searching metadata amongst others. Therefore, the Nigerian Government should enforce compulsory data archiving and management for all sectors which should include documentation of the methods for data collection and derivation of these data sets. This will allow the users to be able to take good advantage of it and appreciate the work done. Some examples of good spatial data metadata practices are International Organization for Standardization (ISO), Infrastucture for Spatial Information in Europe (INSPIRE), etc. and the proposals for Africa-wide spatial metadata standards.

References

Abbas, I. I. and Fasona, M. J. (2012). "Remote Sensing and Geographic Information Techniques: Veritable Tools for Land Degradation Assessment". American Journal of Geographic Information System 1(1): 1-6.

Abbaspour, M., Javid, A. H., Moghimi, P. and Keryhan, K. (2006). "Modelling of Thermal Pollution in the Northern Coastal area of the Persian Gulf and its economical and environmental assessment". Water Pollution: Modelling and Management 95(8): 445-453.

Abdulkareem, A. S. (2005). "Evaluation of ground level concentration of pollutant due to gas flaring by computer simulation: A case study of Niger Delta area of Nigeria". Leonardo Electronic Journal of Practices and Technologies 6: 29-42.

Adamu, B., Tansey, K. and Ogutu, B. (2015). “Using vegetation spectral indices to detect oil pollution in the Niger Delta”. Remote Sensing Letters 6(2): 145-154.

African Continental. (2008). “Oil fields, pipelines, oil refineries, oil tanker terminals, gas processing plant and Liquified Natural Gas (LNG) terminal in the Niger Delta”. African Continental. [Online]. Available: http:/www.archive.crossborderinformation.com/Article/NigerDelta+and+offshore+hydrocarbon.aspx?date=20140331 [Accessed 28th April 2015].

Aghalino, S. O. (2009). "Gas flaring, environmental pollution and abatement measures in Nigeria, 1969-2001". Journal of Sustainable Development in Africa 11(4): 219-238.

Ajide, O. M. and Isaac, O. O. (2013). “An Assessment of the Physical Impact of Oil Spillage Using GIS and Remote Sensing Technologies: Empirical Evidence from Jesse Town, Delta State, Nigeria”. British Journal of Arts and Social Sciences ISSN: 2046-9578, Vol.12, No. 2.

Akeredolu, F. (1989). “Atmospheric environment problems in Nigeria-An overview”. Atmospheric Environment 23(4): 783-792

Akhoonadzadeh, M. and Saradjian, M. R. (2008). "Comparison of Land Surface Temperature Mapping Using MODIS and ASTER Images in Semi-Arid Area". The International Archives of the Photogrammetry, Remote Sensing and Spatial Information Science, Beijing 37 (Part B8).

Akubugwo, E. I., Ogbuji, G. C., Chinyere, C. G. and Ugbogu, E. A. (2009). "Physiochemical properties and enzymes activity studies in a refined oil contaminated oil in Isiukwuato, Abia State, Nigeria". Nigerian Society for Experimental Biology 21(2): 79-84.

Alakpodia, I. J. (1989). “Effects of Gas Flaring on the Micro-climate and Adjacent Vegetation in Isoko Area of Bendel State”. An unpublished M.Sc Thesis. Department of Geography, University of Ibadan, Ibadan. [Online].

Available: http://www.intechopen.com/download/pdf/18639. [Accessed 23rd December 2011].

Alcântara, E. H., Stech, J. L., Lorenzzetti, J. A., Bonnet, M. P., Casamitjana, X., Assireu, A. T. and Novo, E. M. D. M. (2010). “Remote sensing of water surface temperature and heat flux over a tropical hydroelectric reservoir”. Remote Sensing of Environment 114: 2651-2665.

Alhaji, H. (2011). “Air Toxic Assessment for Short-term Ambient Air Pilot Study at Private House in Battlement Mesa near oil and gas drilling site”. M.Sc. Thesis submitted to Department of Environmental and Radiological Health Sciences, Colorado State University, Fort Cillins, Colorado, USA. [Online]. Available: digitool.library.colostate.edu [Accessed 17th June 2015]

Allan, A. L. (1997). “Practical Surveying and Computations”. Revised Second Edition, Laxtons, Hartnolls Limited, Bodmin, Cornwall, UK.

Allen, J. R. (1965). "Late quaternary Niger Delta and adjacent areas. Sedimentary environment and lithofacies". Bulletin of American Association Petroleum Geology 49: 547-600.

Alvarez, J. (2009). “Land cover verification along Freeway Corridors, Natomas Basin Area, California, USA”. [Online]. Available: http://www.academic.emporia.edu/aberjame/student/alvarez4/natchange.html [Accessed 26th September 2014].

Alvim, D. S., Gatt, L. V., dos Santos, M. H. and Yamazaki, A. (2011). "Studies of the volatile organic compounds precusors of Ozone in Sao Paulo City". Engenharia Sanitaria E Ambiental 16(2): 189-196.

Amaral, S., Soares, J. V., Alves, D. S., Mello, E. M. K., Almeida, S. A. S., Silva, O. F. and Silveira, A. M. (1997). "Relações entre índice de área foliar (LAI), área basal e índice de vegetação (NDVI) em relação a diferentes estágios de crescimento secundário na Floresta Amazonica em Rondônia". Revista Selper 13: 35-39.

Amici, S., Piscini, A., Wooster, M. and Buongiorno, F. M. (2009). "Use of VIS-SWIR Airborn Hyperspectral Imaging Data for Identification of the Potassium Emission Band in Wildfires". In Proceedings of RSPSoc 2009 Annual Conference, 8-11th September 2009, Leicester, UK (Nottingham:RSPSoc), pp. 678-689.

Amici, S., Wooster, M. J. and Piscini, A. (2011). "Multi-resolution spectral analysis of wildfire potassium emission signatures using laboratory, airborne and spaceborne remote sensing". Remote Sensing of Environment 115(8): 1811-1823.

Aminou, D. M. A. (2002). "MSG Project". ESA Directorate of Earth Observation, ESTEC, Noordwijk, The Netherlands. ESA bulletin 111.

Andreae, M. O. (1991). "Biomass burning: its history, use, and distribution and its impact on environmental quality and global climate". In Global Biomass

Burning, edited by J. S. Levine (Cambridge, Massachusetts: The MIT Press), pp. 3-21.

Andreae, M. O. and Merlet, P. (2001). “Emission of trace gases and aerosols from biomass burning”. Global Biogeochemical Cycles 15: 955-966.

Andrew, M. E. and Ustin, S. L. (2008). “The role of environmental context in mapping invasive plants with hyperspectral image data”. Remote Sensing of Environment 112: 4301-4317.

Anejionu, O. C. D., Blackburn, G. A. and Whyatt, J. D. (2014). “Satellite survey of gas flares: development and application of a Landsat-based technique in the Niger Delta”. International Journal of Remote Sensing 35(5): 1900-1925.

Anejionu, O. C. D., Blackburn, G. A. and Whyatt, J. D. (2015). “Detecting gas flares and estimating flaring volumes at individual flow stations using MODIS data”. Remote Sensing of Environment 158: 81-94.

Aniello, C., Morgan, K., Busbey, A. and Newland, L. (1995). “Mapping micro urban heat islands using Landsat TM and a GIS”. Computers and Geosciences 21: 965-967.

Antonarakis, A. S., Richards, K. S. and Brasington, J. (2008). “Object-based land cover classification using airborne LiDAR”. Remote Sensing of Environment 112(6): 2988-2998.

Aqishev, R. R. and Bajazitov, R. A. (1996). "Spectral-resolvable Remote Sensing and detection of Hydrocarbons based on CW Low-Power Lasers (Proceeding Paper)". International Journal of Optical Inspection and Micromeasurements Christiphe Gorecki Edition: 820-827.

Arino, O. and Melinotte, J. M. (1995). “Fire index atlas. In Earth Observation” Quarterly, 50, edited by T. D. Guyenne, ESA Publications Division, ESA/ESTEC, Keplerplaan 12200 AG, Noordwijk, The Netherlands.

Arino, O., Plummer, S. and Defrenne, D. (2005). “Fire disturbance: the ten years time series of the ATSR World Fire Atlas”. Proceedings MERIS-AATSR Symposium, ESA SP. Frascati, Italy, September 2005.

Arino, O., Casadio, S. and Serpe, D. (2012). "Global night-time fire season timing and fire count trends using the ATSR instrument series". Remote Sensing of Environment 116: 226-238.

Arroyo-Mora, P., Sanchez-Azofeifa, A., Rivard, B. and Calvo, J. C. (2003). “Integrating very high and high resolution imagery for detecting secondary growth in a neo-tropical dry forest ecosystem: a vegetation indices approach”. In: Simpósio Brasileiro de Sensoriamento Remoto, INPE, São Josĕ dos Campos, pp. 2655- 2662.

Aubrecht, C., Elvidge, C. D. and Eakin, C. D. (2008). “Earth Observation Based Assessment of Anthropogenic Stress to Coral Reefs - A Global Analysis”. Geoscience and Remote Sensing Symposium, IGARSS 2008. IEEE International, Vol. 4.

Azibaolanri, N. (1997). ”Vegetation Degradation Around Gas Flares in Southern Nigeria: Study of Flare Sites in Rivers and Bayelsa States”. M.Sc Dissertation. Department of Geography, University of Ibadan, Ibadan. [Online]. Available: http://www.fraw.org.uk/files/extreme/ismail_umukoro_2012.pdf [Accessed 10th January 2012].

Balogun, T. F. (2015). “Utility of Microwave and Optical Remote Sensing in Oil Spill Detection in the Mangrove Region of Nigeria”. Journal of Geoscience and Environment Protection 3: 16-21.

Bannari, A., Morin, D., Bonn, F. and Huete, A. R. (1995). "A review of vegetation indices". Remote sensing reviews 13(1-2): 95-120.

Baret, F. and Guyot, G. (1991). "Potentials and limits of vegetation indices for LAI and APAR assessment". Remote Sensing of Environment 35: 161-173.

Barnes, W. L., Pagano, T. S. and Salomonson, V. V. (1998). “Pre-launch characteristics of Moderate Resolution Imaging Spectroradiometer (MODIS) on EOS-AM1”. IEEE Transactions on Geoscience and Remote Sensing 36: 1088-1100.

Barnie, T. and Oppenheimer, C. (2015). “Extracting High Temperature radiance from satellite images and correcting for saturation using Independent Component Analysis”. Remote Sensing of Environment 158: 56-68.

Barsi, J. A. (2014). Personal communication: “A solution that latitude and longitude with more than one decimal place should not be inputted into the

Calculator". Landsat Project Science Office, Science Systems and Applications, Inc. Greenbelt, United States of America.

Barsi, J. A., Barker, J. L. and Schott, J. R. (2003). "An Atmospheric Correction Parameter Calculator for a Single Thermal Band Earth-Sensing Instrument". IGARSS03, Centre de Congress Pierre Baudis, Toulouse, France, SPIE.

Barsi, J. A., Schott, J. R., Palluconi, F. D., Helder, D. L., Hook, S. J., Markham, B. l., Chander, G. and O'Donnell, E. M. (2003). "Landsat TM and thermal band calibration". Canada Journal of Remote Sensing 29(2): 141-153.

Barsi, J. A., Schott, J. R., Palluconi, F. D. and Hook, S. J. (2005). "Validation of a Web-Based Atmospheric Correction Tool for Single Thermal Band Instruments". Earth Observing Systems X, Proceedings of SPIE Bellingham, WA, 2005.

Basith, A., Matori, A.N., Harahap, I. S. and Talib, J. A. (2010). "Application of land use change detection for identification of land slide risk areas in Pulau Penang using a decade of Landsat 7 ETM+ images". MRSS, PWTC, Malaysia, April 28-29.

Baugh, W. and Groeneveld, A. (2006). "Broadband vegetation index performance evaluated for a low-cover environment". International Journal of Remote Sensing 27(21-22): 4715-4730.

Bawa, K., Rose, J., Ganeshaiah, K. N., Barve, N., Kiran, M. C. and Umashaanker, R. (2002). “Assessing biodiversity from space: an example from the western Ghats, India”. Conservation Ecology 6(7).

Becker, F. and Li, Z. L. (1995). “Surface temperature and emissivity at various scales: definition measurement and related problems”. Remote Sensing Reviews 12: 225-253.

Berk, A., Anderson, G. P., Acharya, P. K., Chetwynd, J. H., Bernstein, L. S., Shettle, E. P., Matthew, M. W. and Adler-Golden, S. M. (1999). “MODTRAN 4 User's Manual”. Air force resource, Laboratory Space Vehicles Directorate, Air Force material command. M. Hanscom AFB. [Online]. Available: ftp://pmodwrc.ch/pub/Vorlesung%20K+S/MOD4_user_guide.pdf. [Accessed January 20th 2013].

Berry, J. (2006). “Quantitative Methods in Education Research. [Online]. Available:
http://www.edu.plymouth.ac.uk/resined/quantitative/quanthme.htm
[Accessed 11th May 2015].

Bhattacharyya, D., Kim, T. and Pal, S. (2010). “A Comparative Study of Wireless Sensor Networks and their Routing Protocols”. Journal of Sensors 10: 10506-10523.

Bonsu, A. and Yankey, A. (2014). “The prospects of SAR onboard a Satellite for monitoring and detection of oil spills in Ghana”. Journal of Applied Thought: A multidisciplinary Approach 3(1).

Boori, M. S., Vozenílek, V., Balzter, H. and Choudhary, K (2015). “Land Surface Temperature with Land Cover Classes in ASTER and Landsat Data”. Journal of Geophysics and Remote Sensing 4(1), http://dx.doi.org/10.4172/2169-0049.1000138.

Brown, D. E. (2013). “Africa’s booming oil and natural gas exploration and production: National security implications for the United States and China”. Strategic Studies Institute and U.S. Army War College Press. [Online]. Available: http://www.StrategicStudiesInstitute.army.mil/ [Accessed April 30th 2015]

Brown, K. (1996). “The Utility of Remote Sensing Technology in Monitoring Carbon Sequestration Agroforestry Projects”. Forest Carbon Monitoring Program. College of Forest Resources, University of Washington, Washington. Pp. 22. [Online]. Available: http://www.amazon.co.uk/technology-monitoring-sequestration-agroforestry-p [Accessed 11th July 2012].

Bruno, A. (2007). “Global Warming is mainly a result of Heat Emissions”. M.Sc Dissertation. Department of Civil and Environmental Engineering. Lulea University of Technology, Lulea, Sweden. [Online]. Available: http:// www.itu.se/cms_fs/1.5035!/summary.pdf [Accessed 15th November 2011].

Brzustowski, T. A. (1976). “Flaring in the energy industry”. Progress in Energy and Combustion Science 2: 129-141.

Campbell, J. B. (1996). “Introduction to Remote Sensing”. The Guilford Press, New York.

Cao, X., Onishi, A., Chen, J. and Imura, H. (2010). “Quantifying the cool island intensity of urban parks using ASTER and IKONOS data”. Landscape and Urban Planning 96: 224-231.

Carleer, A. P. and Wolff, E. (2006). “Urban land cover multi-level region-based classification of VHR data by selecting relevant features”. International Journal of Remote Sensing 27(6): 1035-1051.

Carlson, T. N. and Ripley, D. A. (1997). “On the relation between NDVI, fractional vegetation cover, and leaf area index”. Remote Sensing of the Environment 62(3):241-252.

Carreiras, J., Pereira, J., Pereira, J., 2006. “Estimation of tree canopy cover in evergreen oak woodlands using remote sensing”. Forest Ecology and Management 23(1-3): 45-53.

Casadio, S., Arino, O. and Serpe, D. (2011). "Gas flaring monitoring from space using the ATSR instrument series". Remote Sensing of Environment. Doi: 10.1016/j.rse.2010.11.022.

Caselles, V. and Sobrino, J. A. (1989). “Determination of frosts in orange groves from NOAA-9 AVHRR data”. Remote Sensing of Environment 29: 135-146.

Chaerun, S. K., Asada, R. and Tazaki, K. (2007). "Biodegradation of heavy oil from the Nakhodka oil spill by indigenous microbial consortia". International Journal of Applied Environmental Sciences 2: 19-30.

Chander, G. and Markham, K. (2003). “Revised Landsat-5 TM Radiometric Calibration Procedures and Postcalibration Dynamic Ranges”. IEEE Transactions on Geoscience and Remote Sensing 41(11): 2674-2677.

Chanin, J. I. and Hollaran, A. R. (2009). “Wireless Sensor Network for Monitoring Application”. [Online]. Available: http://www.wpi.edu/Pubs/E-project/Available/E-project-030708-030227/unrestricted/Wireless_Sensor_Network_for_Monitoring_Applications.pdf [Accessed 2nd May 2015]

Chavez, P. S. (1996). “Image-based Atmospheric Corrections-Revisited and Improved”. Photogrammetry Engineering and Remote Sensing 62(9): 1025-1036.

Chen, X., Zhao, H., Li, P. and Yin, Z. (2006). “Remote sensing image-based analysis of the relationship between urban heat island and land use/cover changes”. Remote Sensing of Environment 104: 133-146.

Chen, F., Zhao, X. and Ye, H. (2012). “Making use of the Landsat 7 SLC-off ETM+ image through different recovering approaches”. Postgraduate Conference on Infrastructure and Environment (3rd IPCIE), vol. 2, pp. 557-563. [Online]. Available: http://dx.doi.org/10.5772/48535 [Accessed 26th September 2014].

Cheval, S. and Dumitrescu, A. (2009). “The July urban heat island of Bucharest as derived from MODIS images”. Theoretical and Applied Climatology 96: 145-153.

Cheval, S., Dumitrescu, A. and Bell, A. (2009). “The urban heat island of Bucharest during the extreme high temperatures of July 2007”. Theoretical and Applied Climatology 97: 391-401.

Chuvieco, E., Cocero, D., Riaño, D., Martin, P., Marťinez-Vega., de la Riva, J. and Pérez, F. (2004). “Combining NDVI and surface temperature for the estimation of live fuel moisture content in forest fire danger rating”. Remote Sensing of Environment 92(3, 30): 322-331.

Cleland, E. E., Chuine, I., Menzel, A., Mooney, H. A. and Schwartz, M. D. (2007). “Shifting plant phenology in response to global change”. Trend in Ecology and Evolution 22 (7): 357-365.

Clemente, R., Navarro Cerrillo, R. and Gitas, I. (2009). “Monitoring post-fire regeneration in Mediterranean ecosystems by employing multitemporal satellite imagery”. International Journal of Wildland Fire 18(6): 648-658.

Clerbaux, I. R., Turquety, S. and Coheur, P. (2010). "Infrared Remote Sensing of Atmospheric Composition and Air Quality: Towards operational applications". Geoscience 342: 349-356.

CLO. (2004). Civil Liberty Organization. “Blood Trail”. Lagos, Unilag Press.

Coll, C., Caselles, V., Galve, J., Valor, E., Niclos, R., Sanchez, J. and Rivas, R. (2005). “Ground measurements for the validation of land surface temperatures derived from AATSR and MODIS data”. Remote Sensing of Environment 97: 288-300.

Coll, C., Hook, S. J. and Galve, J. M. (2009). “Land surface temperature from the Advanced Along-Track Scanning Radiometer: validation over inland waters and vegetated surfaces”. IEEE Transactions on Geoscience and Remote Sensing 47: 350-360.

Coll, C., Galve, J. M., Sanchez, J. M. and Caselles, V. (2010). "Validation of Landsat - 7 ETM+ thermal-band calibration and atmospheric correction with ground-based measurement". IEEE Transaction on Geoscience and Remote Sensing 48(1): 547-555.

Collis, J. and Hussey, R. (2003). “Business Research: a practical guide for undergraduate and postgraduate students”. Second Edition. Basingstoke, Open University Press. [Online]. Available: http://www.blackwellpublishing.com/researchproject/reading.asp [Accessed 30th March 2014].

Colwell, R. N., Ed. (1983). “Manual of Remote Sensing”. Microwave and Infrared Satellite Remote Sensors. Virginia, American Society of Photogrammetry, USA.

Coppo, P., Ricciarelli, B., Brandani, F., Delderfield, J., Ferlet, M. and Mutlow, C. (2010). “SLSTR: A high accuracy dual scan temperature radiometer for sea and land surface monitoring from space”. Journal of Modern Optics, 57(18): 1815-1830.

Cracknell, A. P. (1997). “The Advanced Very High Resolution Radiometer”. London: Taylor & Francis.

Cracknell, A. P. (2001). “The exciting and totally unanticipated success of the AVHRR in applications for which it was never intended”. Advances in Space Research 28: 233-240.

Creswell, J. W. (2003). “Research Design: Qualitative, Quantitative and Mixed Method Approaches”. London, Sage. [Online]. Available: http:// www.isites.harvard.edu/.../2003_Creswell_A%20Framework%20for%20Desig [Accessed 14th February 2014].

Csiszar, I., Sullivan, J. (2002). “Recalculated pre-launch saturation temperatures of the AVHRR 3.7 sensors on board the TIROS-N to NOAA-14 satellites”. International Journal of Remote Sensing. 23(24): 5271-5276.

Curran, P. J., Jennifer, L. D. and Henry, L. G. (1992). "Seasonal LAI in slash pine estimated with Landsat TM". Remote Sensing of Environment 39: 3-13.

Davies, D. K., Ilavajhala, S., Wong, M. M. and Justice, C. O. (2009). "Fire Information for Resource Management System: Archiving and Distributing MODIS Active Fire Data". IEEE Transaction on Geoscience and Remote Sensing 47(1): 72-79.

Díaz-Delgado, R., Lloret, F. and Pons, X. (2003). "Influence of fire severity on plant regeneration by means of remote sensing imagery". International Journal of Remote Sensing 24(8): 1751-1763.

Digital Globe. (2014). "Ouickbird image of June 12, 2010 and WorldView-2 image of January 13, 2014 showing Eleme Petroleum Refinery II Company". [Online]. Available: http://browse.digitalglobe.com/imagefinder/public.do [Accessed 15th April 2014].

Digital Muse. (2012). "Map of Africa showing the location of Nigeria". [Online]. Available: http://thedigitalmuse.net/piceenp/map-of-nigeria-africa [Accessed 20th February 2012].

Djepa, V. (2011). "Drought prediction using the Along Track Scanning Radiometer (ATSR2) on board ERS2 satellite". Advances in Space Research 48: 56-60.

Dominguez, A., Kleissl, J., Luvall, J. C and Rickman, D. L. (2011). High resolution urban thermal sharpener (HUTS). Remote Sensing of Environment 115: 1772-1780.

Dose, V. and Menzel, A. (2004). “Bayesian analysis of climate change impacts in phenology”. Global Change Biology 10: 259-272.

Dozier, J. (1981). “A method for satellite identification of surface temperature felds of subpixel resolution”. Remote Sensing of Environment 11: 221-229.

DPR. (1991). Department of Petroleum Resources, Lagos, Nigeria. “Environmental Guidelines and Standards for Oil and Gas Industry in Nigeria”.

Djoundourian, S. S., Nuwayhid, I. A. and Chaaban, F. B. (2007). "Quantification of health impact of air pollution in a developing country". International Journal of Applied Environmental Sciences 2(1): 57-68.

Dublin-Green, C. O., Awosika, L. F. and Folorunsho, R. (1999). “Climate Variability Research Activities in Nigeria”. Nigerian Insitute for Oceanography and Marine Research, Victoria Island, Lagos, Nigeria.

Dung, E. J., Bombom, L. S. and Agusomu, T. D. (2008). "The effects of gas flaring on crops in the Niger Delta, Nigeria". GeoJournal 73: 297-305.

Dupont, M. L., Jahns, S., Marret, F. and Ning, S. (2000). "Vegetation change in equitorial West Africa: Time-slices for the last 150 ka”. Palaeogeography, Palaeoclimatology, Palaeoecology 155: 95-122.

Dwyer, E., Pinnock, S. and Grégiore, J. -M. (2000). “Global spatial and temporal distribution of vegetation fire as determined from satellite observations”. International Journal of Remote Sensing 21: 1289-1302.

Edino, E. O., Nsofor, G. N. and Bombom, S. L. (2010). "Perceptions and attitudes towards gas flaring in the Niger Delta, Nigeria". Environmentalist 30: 67-75.

Edwards, N., Hooper, P., Trapp, G. S. A., Bull, F., Boruff, B. and Giles-Corti, B. (2013). “Development of a Public Open Space Desktop Auditing Tool (POSDAT): A remote sensing approach”. Applied Geography 38: 22-30.

Effiong, J. (2010). "Oil and Gas Industry in Nigeria: The Paradox of the black gold". An International Perspective (Research in Social Problems and Public Policy) 18: 323-349.

Egbogah, E. (2012). NAPE Newsletter. “Nigeria Oil and Gas Industry: Yesterday, Today and Guidelines for Tomorrow”. Inaugural Lecture to mark the opening of a new chapter of National Association of Petroleum Explorationist, NAPE, in Abuja, Nigeria. [Online]. Available: http:// www.nape.org.ng/news/.../23_91f8ab42278fac4695be250a2c403817 [Accessed 17th February 2014].

Ehiorobo, J. O. and Izinyon, O. C. (2011). “Measurement and Documentation for Flood and Erosion Monitoring and Control in the Niger Delta States of

Nigeria". FIG Working Week - Bridging the Gap between Cultures, Morocco, 18th-22 May. [Online]. http: www.fig.net/pub/fig2011/ppt/.../ts07e_ehioro_izinyon_5126_ppt.pdf. [Accessed 10th December 2013].

Eidenshink, J. C. and Faundeen, J. L. (1994). "The 1 km AVHRR globa land data set: First stages in implementation". International Journal of Remote Sensing 15(17): 3443-3462.

Ekpoh, I. J. and Obia, A. E. (2010). "The role of gas flaring in the rapid corrosion of zinc roofs in the Niger Delta Region of Nigeria". Environmentalist 30: 347-352.

Ekwekwe, E. (1981). "The Funiwa-5 Oil Well Blow Out: The Petroleum Industry and Nigerian Environment", NNPC, Lagos: 64-68.

Elvidge, C. D., Ziskin, D., Baugh, K. E., Tuttle, B. T., Ghosh, T., Pack, D. W., Erwin, E. H. and Zhizhin, M. (2009). "A Fifteen Year Record of Global Natural Gas Flaring Derived from Satellite Data". Energies 2(3): 596-622.

Engineering Tool Box. (2013). "Emissivity Coefficients of some common Materials". [Online]. Available: http://www.engineeringtoolbox.com [Accessed 21st October 2013].

ESA. (2015a). European Space Agency. "AATSR Product Handbook", Issue 2.2, Italy. [Online]. Available: http:

www.earth.esa.int/pub/ESA_DOC/.../AATSR/aatsr.ProductHandbook.2_2.pdf [Accessed 24th December 2011].

ESA. (2015b). European Space Agency. "Sentinel Online: User Guides". [Online]. Available: https://earth.esa.int/web/sentinel/user-guides/sentinel-3-slstr/resolutions/radiometric [Accessed 23rd May 2015].

ESA. (2015c). European Space Agency. "Meteosat Second Generation (MSG) Channels: Interpretation guide". [Online]. Available: http://oiswww.eumetsat.org/WEBOPS/msg_interpretation/msg_channels.php [Accessed 13rd June 2015].

ESA. (2015d). European Space Agency. "Sentinel-1 and Sentinel-2: About the launch". [Online]. Available: http://www.esa.int/Our_Activities/Observing_the_Earth/Copernicus/Sentinel-1/About_the_launch [Accessed 12th Setember 2015].

Eseoghene, O. (2011). "Nigeria, Russia still Largest Gas Flaring Nations - Latest Satellite Estimates says". Pinpoint. Lagos, Nigeria.

ESMAP. (2004). "Energy Sector Management Assistance Programme. Nigeria Strategic Gas Plan". ESM Report 279:4. [Online]. Available: http: www.esmap.org/.../FR58200861713_Nigeria_atrategicgasplanfornigeria [Accessed 20th April 2012].

ESRI. (2006). "Environmental Systems Research Institute". [Online]. Available: http://www.web.ornl.gov/sci/casd/etv/esri.htm [Accessed 20th October 2012].

ESRI. (2015). Environmental Systems Research Institute. "Map of Africa showing Nigeria". Adapted from ESRI.

Eva, H. D., Malingreau, J. P., Gregoire, J. M. and Belward, A. S. (1998). "The advance of burnt areas in Central Africa as detected by ERS-1 ATSR-1". International Journal of Remote Sensing 19: 1635-1637.

Evans, M. E., Hall, L., Samuels, P. A., Jackson, L. A., Hanraham, F. E., Hageweiesche, D. P. and Ainodion, M. J. (2002). "Environmental Application of Hyperspectral Remote Sensing: Managing Liability in an Age of Transparency". World Petroleum Congress 17 Rio de Janieiro, Brazil. [Online]. Available: http://www.ellis-geospatial.com/images/World_Petroleum_Conference_Hypers [Accessed 15th July 2012].

Fabiyi, O. (2011). "Change actors' analysis and vegetation loss from remote sensing data in parts of the Niger Delta region". Journal of Ecology and Natural Environment 3(12): 381-391.

Fagbade, S. O. (1981). "An Assessment of the Impact of Oil Production Activities on Fisheries in Port Harcourt, Niger Delta". NDDC, Port Harcourt, River State.

Feldman, M. S. (2010). “Application of Satellite Remote Sensing Data for Regional Air Quality Modelling”. PhD Thesis, The University of Texas, Austin, USA: Pp.157. [Online]. Available: http:// www.nsstc.uah.edu/data/.../Feldman_etal_2010_biogenic_emissions.pdf. [Accessed 2nd August 2012].

Fingas, M. F. and Brown, C. E. (2000). "Oil-Spill Remote Sensing - An Update". Sea Technology: 21-28.

Fletcher, K. (2012). “Sentinel-3: ESA’s Global Land and Ocean Mission for GMES Operational Services (ESA SP-1322/3, October 2012)”. ESA Communications ESTEC, PO Box 299, 2200 AG Noordwijk, the Netherlands, ISBN: 978-92-9221-420-3.

FOE. (2004). Friends of the Earth. “Gas Flaring in Nigeria”. Friends of the Earth Limited, London, UK. [Online]. Available: http:// www.foe.co.uk/sites/default/files/downloads/gasflaringinnigeria.pdf. [Accessed 28th November 2011].

Foody, G. M. (2002). “Status of land cover classification accuracy assessment”. Remote Sensing of Environment 80 (1): 185-201.

Freeborn, P. H., Wooster, M. J., Hao, W. M., Ryan, C. A., Nordgren, B. L., Baker, S. P. and Ichoku, C. (2008). “Relationships between energy release, fuel mass loss, and trace gas and aerosol emissions during laboratory biomass fires”.

Journal of Geophysical Research: Atmospheres, vol. 113, no. D1, pp. D01301-1-D01301-17.

Freitas, S. R. and Cruz, C. B. M. (2003). “Índices de vegetação na caracterização de fragmentos de Mata Atlântica no Estado do RJ. In: XI Simpósio Brasileiro de Sensoriamento Remoto, INPE, São José dos Campos, pp. 2737-2744.

Friedl, M. A., McIver, D. K., Hodges, J. C. F., Zhang, X. Y., Muchoney, D., Strahler, A. H., Woodcock, C. E., Gopal, S., Schneider, A., Cooper, A., Baccini, A., Gao, F. and Schaaf, C. (2002). “Global land cover mapping from MODIS: algorithms and early results”. Remote Sensing of Environment 83: 287-302.

Fuller, D. O. (2000). "Satellite remote sensing of biomass burning with optical and thermal sensors". Progress in Physical Geography 24(4): 543-561.

Gallo, K. P., Daughtry, C. S. T. and Bauer, M. E. (1985). “Spectral estimation of absorbed photosynthetically active radiation in corn canopies”. Remote Sensing of Environment 17: 221-232.

Gallo, K., McNab, A., Karl, T., Brown, J., Hood, J. and Tarpley, J. (1993). “The use of NOAA AVHRR data for assessment of the urban heat-island effect”. Journal of Applied Meteorology 32: 899-908.

Gani, N. D. S. and Abdelsalam, M. G. (2006). “Remote sensing analysis of the Gorge of the Nile, Ethiopia with emphasis on Dejen-Gohatsion region”. Journal of African Earth Sciences 44: 135-150.

Gamon, J. A., Field, C. B., Goulden, M. L., Griffin, K. L., Hartley, A. E., Joel, G., Peñuelas, J. and Valentini, R. (1995). "Relationships between NDVI, canopy structure, and photosynthesis in three californian vegetation types". Ecology Applications 5: 28-41.

Gao, X., Huete, A., Ni, W., Miura, T. (2000). "Optical-biophysical relationships of vegetation spectra without background contamination". Remote Sensing of Environment 74 (3): 609-620.

García, M. J. L. and Caselles, V. (1991). "Mapping Burns and Natural Reforestation Using Thematic Mapper Data". Geocarto International 6 (1): 31-37. doi:10.1080/10106049109354290.

Ge, J. (2010). "MODIS observed impacts of intensive agriculture on surface temperature in the southern Great Plains". International Journal of Climatology 30: 1994-2003.

Gerner, F., Svensson, B. and Djumena, S. (2004). "Gas flaring and venting: A regulatory framework and incentives for gas utilization". Journal of Public Policy for the Private Sector 279, World Bank, Washington, DC.

Ghent, D. (2009). "Intercomparison of Modelled Land-Surface Temperature with Remote Sensing Products over Africa". In Proceedings of RSPSoc 2009, Leicester, UK (Nottingham: RSPSoc).

Giglio, L., Kendall, J. D., and Justice, C. O. (1999). “Evaluation of global fire detection algorithms using simulated AVHRR infrared data”. International Journal of Remote Sensing 20 (10).

Giglio, L., Kendall, J. D. and Tucker, C. J. (2000). “Remote sensing of fires with the TRMM VIRS”. International Journal of Remote Sensing 21: 203-207.

Giglio, L. and Kendall, J. D. (2001). "Application of Dozier retrieval to wildfire characterization - A sensitivity analysis". Remote Sensing of Environment 77(1): 34-49.

Giglio, L., Descloitres, J., Justice, C. O. and Kaufman, Y. J. (2003). "An enhanced contextual fire detection algorithm for MODIS". Remote Sensing of Environment 87: 273-282.

Gillespie, A., Rokugawa, S., Matsunaga, T., Cothern, J. S., Hook, S. and Kahle, A. B. (1998). "A temperature and emissivity separation algorithm for Advanced Spaceborne Thermal Emission and Reflection Radiometer (ASTER) images". IEEE Transactions on Geoscience and Remote Sensing 36 (4): 1113-1126.

Gitelson, A. A., Kaufman, Y. J. and Merzlyak, M. N. (1996). “Use of a Green Channel in Remote Sensing of Global Vegetation from EOS-MODIS.” Remote Sensing of Environment 58 (3): 289-298. Doi: 10.1016/S0034-4257(96)00072-7.

Glenn, E. P., Huete, A. R., Nagler, P. L. and Nelson, S. G. (2008). “Relationship Between Remotely-sensed Vegetation Indices, Canopy Attributes and Plant Physiological Processes: What Vegetation Indices Can and Cannot Tell Us About the Landscape”. Sensors 8: 2136-2160.

Google Earth. (2015). “Image showing Eleme Petroleum Refinery I Company in 2000 and 2015; image showing Eleme Petroleum Refinery II Company in 2000 and 2015; image showing Onne Flow Station in 1984 and 2015; image showing Umurolu Flow Station in 2005 and 2015; image showing Bonny LNG in 1984 and 2015; image showing Alua Flow Station in 2002 and 2015; image showing Rukpokwu Flow Station in 2003 and 2015; image showing Obigbo Flow Station in 2003 and 2015; image showing Chokocho Flow Station in 2002 and 2015; image showing Umudioga Flow Station in 2007 and 2015 and image showing Sara Flow Station in 1984 and 2015”.

Gomez, I. and Martin, M. P. (2011). "Prototyping an artificial neural network for burned area mapping on a regional scale in Mediterranean areas using MODIS images". International Journal of Applied Earth Observation and Geoinformation 13: 741-752.

Gonzalez, R. C. and Woods, R. E. (2008). “Digital Image Processing”. Third Edition. Upper Saddle River, New Jersey, USA, Pearson Prentice Hall.

Google Corporation, N. D. (2006). "Google Earth - a 3D interface to the planet”. [Online]. Available: http://www.earth.google.com/ [Accessed 6th May 2013].

Gould, W. (2000). “Remote sensing of vegetation, plant species richness, and regional biodiversity hotspots”. Ecological Applications 10(6): 1861-1870.

Goward, S. N., Tucker, C. J. and Dye, D. G. (1985). “North American vegetation patterns observed with the NOAA-7 Advanced Very High Resolution Radiometer”. Vegetation 64: 3-14.

Goward, S. N., Xue, Y. and Czajkowski, K. P. (2002). "Evaluating Land Surface moisture conditions from the remotely sensed temperature/vegetation index measurements: An exploration with the simplified simple biosphere model". Remote Sensing of Environment 79: 225-242.

Grutter, M. and Flores, E. (2004). “Air Pollution Monitoring With Two Optical Remote Sensing Techniques in Mexico City”. SPIE, Bellingham, WA.

Guenther, B., Xiong, X., Salomonson, V. V., Barnes, W. L. and Young, J. (2002). “On-orbit performance of the Earth Observing System (EOS) Moderate Resolution Imaging Spectroradiometer (MODIS); first year of data”. Remote Sensing of Environment 83: 16-30.

Hall, D. K., Riggs, G. A., Salomonson, V. V., DiGirolamo, N. E. and Bayr, K. J. (2002). “MODIS snow-cover products”. Remote Sensing of Environment 83: 181-194.

Hamadina, M. K. and Anyawu, D. I. (2012). “A Cursory Review of the Consequences of Human Activities and Land-Use Changes in the Niger Delta”. Research Journal of Environmental and Earth Sciences 4(5): 597-604.

Hammill, K. A. and Bradstock, R. A. (2006). “Remote sensing of fire severity in the Blue Mountains: influence of vegetation type and inferring fire intensity”. International Journal of Wildland Fire 15(2): 213-226 http://dx.doi.org/10.1071/WF05051.

Hanley, M. E. and Fenner, M. (1998). “Pre-germination temperature and the survivorship and onward growth of Mediterranean fire-following plant species”. Acta Oecologica, 19: 181-187.

Hansen, M. C., Sohlberg, R., Dimiceli, C., Carroll, M., DeFries, R. S. and Townshend, J. R. G. (2002). “Towards an operational MODIS continuous field of percent tree cover algorithm: Examples using AVHRR and MODIS data”. Remote Sensing of Environment 83(1-2): 303-319.

Harris, A. R. and Mason, I. M. (1992). “An extension to the split-window technique giving improved atmospheric correction and total water vapour”. International Journal of Remote Sensing, 13, pp. 881-892.

Hartz, D., Prashad, L., Hedquist, B., Golden, J. and Brazel, A. (2006). “Linking satellite images and hand-held infrared thermography to observed neighbourhood climate conditions”. Remote Sensing of Environment 104: 190-200.

Hestir, E. L., Khanna, S., Andrew, M. E., Santos, M. J., Viers, J. H., Greenberg, J. A., Rajapakse, S. S. and Ustin, S. L. (2008). “Identification of invasive vegetation using hyperspectral remote sensing in the California Delta ecosystem”. Remote Sensing of Environment 112: 4034-4047.

Hawbaker, T., Radeloff, V., Syphard, A., Zhu, Z. and Steward, S. (2008). “MODIS active fire data offer new information about global changes”, Remote Sensing of Environment 112 (5): 2656-2664.

Heumann, B. W., Seaquist, J. W., Eklundh, L. and Jösson, P. (2007). “AVHRR derived phenological change in the Sahel and Soudan, Africa, 1982-2005”. Remote Sensing of Environment 108 (4): 385-392.

Hipps, L. E. (1989). "The infrared emissivities of soil and Artemisia tridentate and subsequent temperature corrections in a shrub-steppe ecosystem". Remote Sensing of Environment 27: 337-342.

Hopkins, H. (2006). "Google Earth Growth: What's Behind It?". [Online]. Available: http://weblogs.hitwise.com/heather-hopkins/2006/01/google_earth_growth_whats_the.html [Accessed 14th November 2013].

Howari, F. M. (2004). "Investigation of Hydrocarbon Pollution in the Vicinity of United Arab Emirates Coasts Using Visible and Near Infrared Remote Sensing Data". Coastal Research 20(4): 1089-1095.

Huang, W., Huang, J., Wang, X., Wang, F. and Shi, J. (2013). " Comparability of Red/Near-Infrared Reflectance and NDVI Based on the Spectral Response Function between MODIS and 30 Other Satellite Sensors Using Rice Canopy Spectra". Sensors 13: 16023-16050; doi:10.3390/s131216023.

Huen, I and Sohu, G. (2007). "The Environmental Application of Wireless Sensor Networks". International Journal of Contents 3(4): 1-7.

Huete, A. R. (1988). "A soil-adjusted vegetation index (SAVI)". Remote Sensing of Environment 25: 295-309.

Huete, A. R., Liu, H. Q. and Van Leeuwen, W. J. D. (1997). "The use of vegetation indices in forested regions: issues of linearity and saturation". Proceedings of IGARSS International Geoscience and Remote Sensing Seminar. ESA Publications, Noordwijk, pp. 1966-1968.

Huete, A. R., Didan, K., Miura, T., Rodriguez, E. P., Gao, X.and Ferreira, L. G. (2002). "Overview of the radiometric and biophysical performance of the MODIS vegetation indices". Remote Sensing of Environment 83: 195-213.

Humes, K. S., Kustas, W. P., Moran, M. S., Nichols, W. D. and Weltz, M. A. (1994). "Variability of emissivity and surface temperature over a sparsely vegetated surface". Water resources research 30(5): 1299-1310.

Hung, T., Uchihama, D., Ochi, S. and Yasuoka, Y. (2006). "Assessment with satellite data of the urban heat island effects in Asian mega cities". International Journal of Applied Earth Observation and Geoinformation 8: 34-48.

ICF. (2006). “Nigeria: Guidebook for Carbon Credit Development for Flare Reduction Projects”. June 2006. [Online]. Available: http: www.siteresources.worldbank.org/.../NigeriaGGFRGuidebook_ICF.pdf [Accessed 17th March 2012].

Ifatimehin, O. O. and Adeyemi, S. (2008). “A satellite remote sensing based land surface temperature retrieval from Landsat TM”. Ethiopian Journal of Environmental Studies and Management 1 (3): 63-70.

Imaduddin, O. O. (2008). “Petroleum Exploration, Development and Production processes”. [Online]. Available: http://www.buet.ac.bd/dce/course_material/pdf/petroleum_exploration_development_production_process.pdf [Accessed 12th February 2012].

Imhoff, M., Zhang, P., Wolfe, R. and Bounoua, L. (2010). “Remote sensing of the urban heat island effect across biomes in the continental USA”. Remote Sensing of Environment 114: 504-513.

Inamdar, A. K., French, A., Hook, S., Vanghan, G. and Luckett, W. (2008). “Land surface temperature retrieval at high spatial and temporal resolutions over the south-western United States”. Journal of Geophysical Research: Atmospheres, vol. 113, issue D7 (pp. 1-18).

IPCC. (2007). “Climate Change 2007: The Physical Science Basis. Contribution of Working Group I to the Fourth Assessment Report of the Intergovernmental Panel on Climate Change”, Edited by: Solomon, S., Qin, D. , Manning, M., Chen,

Z., Marquis, M., Averyt, K. B., Tignor, M. and Miller, H. L. Cambridge: Cambridge University Press.

Ishisone, M. (2004). "Gas Flaring in the Niger Delta: the Potential Benefits of its Reduction on the Local Economy and Environment". [Online]. Available: http://nature.berkeley.edu/classes/es196/projects/2004final/Ishone.pdf [Accessed 27th May 2012].

Isichei, A. O. and Sandford, W. W. (1976). "The Effects of Waste Gas Flares on the Surrounding Vegetation of South-Eastern Nigeria". Applied Ecology 13: 177-187.

Istomina, L. G., von Hoyningen-Huene, W., Kokhanovsky, A. A. and Burrows, J. P. (2010). “The detection of cloud-free snow-covered areas using AATSR measurements”. Atmospheric Measurement Techniques 3: 1005-1017.

Ite, A. E., Ibok, U. J., Ite, M. U. and Petters, S. W. (2013). “Map of the Niger Delta States”. American Journal of Environmental Protection 1(4): 78-90.

Ja Eun, J., Su-Jin, K., Dong, W. K., Seung-Kyu, K. and Jong, G. K. (2010). "Proximity of Field Distribution of Polycyclic Aromatic Hydrocarbons to Chemical Equilibra among Air, Water, Soil and Sediment and its Implications to the Coherence Criteria of Environmental Quality Objectives". Environmental Science & Technology 44(21): 8056-8061.

Jacoby, P., Ansley, R. and Trevino, B. (1992). “Technical note: An improved method for measuring temperatures during range fires”. Journal of Range Management 45(2): 216-220.

Jacob, F., Petitcolin, F., Schmugge, T., Vermoté, E., French, A. and Ogawa, K. (2004). “Comparison of land surface emissivity and radiometric temperature derived from MODIS and ASTER sensors”. Remote Sensing of Environment 90: 137-152.

James, G. K., Adegoke, J. O., Saba, E., Nwilo, P. and Akinyede, J. (2007). “Satellite-based assessment of the extent and changes in the mangrove ecosystem of the Niger Delta”. Marine Geodesy 30(3): 249-267.

Jawhar, I., Mohamed, N. and Shuaib, K. (2006). “Framework for Pipeline Infrastructure Monitoring using Wireless Sensor Networks”. [Online]. Available: www.ieeexplore.ieee.org [Accessed 30th April 2015]

Jensen, J. R. (2014). “Remote Sensing of the Environment”: Pearson New International Edition: An Earth Resource Perspective. 2nd Edition. New York: Pearson.

Jha, M. N., Levy, J. and Gao, Y. (2008). "Advances in remote sensing for oil spill disaster management: state-of-the-art sensors technology for oil spill surveillance". Sensor 8: 236-255.

Jiménez-Muñoz, J. C., Sobrino, J. A., El-Kharraz, J., Gómez, M., Romaguera, M. and Sòria, G. (2003). "Synergistic use of DAIS bands to retrieve land surface emissivity and temperature". IGARSS 2003: IEEE International Geoscience and Remote Sensing Symposium, Vols. I-VII, Proceedings: 1062-1064.

Jimenez-Munoz, J. C., Sobrino, J. A., Gillespie, A., Sabol, D. and Gustafson, W. T. (2006). "Improved land surface emissivities over agricultural areas using ASTER NDVI". Remote Sensing of Environment 103: 474-487.

Jin, M., Dickinson, R. E. and Vogelmann, A. M. (1997). "A comparison of CCM2/ BATS skin temperature and surface-air temperature with satellite and surface observations". Climate 10: 1505-1524.

Jin, M. (2004). "Analysis of land skin temperature using AVHRR observations". Bulletin of the American Meteorological Society 85: 587-600.

Jin, M., Dickinson, R., Zhang, D. (2005). "The footprint of urban areas on global climate as characterized by MODIS". Journal of Climate 18: 1551-1565.

Jin, M. and Liang, S. (2006). "An Improved Land Surface Emissivity Parameter for Land Surface Models Using Global Remote Sensing Observations". Journal of Climate 19: 2867-2881.

Joan, M. and Cesar, C. (2009). "Monthly land surface temperature maps over European zone using advanced along track scanning radiometer data for 2007".

Geoscience and Remote Sensing Symposium, IEEE International, IGARSS 2009, 4: 292-295.

Johnson, M. M. (2010). "Participant-based monitoring of indoor and outdoor Nitrogen dioxide, Volatile Organic Compounds, and Polycyclic Aromatic Hydrocarbons among MICA-Air households". Atmospheric Environment 44(38): 4927-4936.

Johnson, M. R. and Kostiuk, L. W. (2000). “Efficiencies of low-momentum jet diffusion flames in crosswinds”. Combustion and Flame 123: 189-200. doi:10.1016/S0010-2180(00)00151-6.

Johnson, M. R. and Kostiuk, L. W. (2002). “A parametric model for the efficiency of a flare in crosswind”. Proceedings of the Combustion Institute 29: 1943-1950. doi:10.1016/S1540-7489(02)80236-X

Johnson, M. R., Kosituk, L. W. and Spangelo, J. L. (2001). "A characterization of solution gas flaring in Alberta". Air Waste Management Association 51(8): 1167-1177.

Johnson, M. R. and Coderre, A. R. (2011). “An analysis of flaring and venting activity in the alberta upstream oil and gas industry”. Journal of Air and Waste Management Association 61: 190-200. doi:10.3155/1047-3289.61.2.190.

Jordan, C. (1969). “Derivation of leaf area index from quality of light on the forest floor”. Ecology 50 (4): 663-666.

Julien, Y., Sobrino, J. A., Mattar, C., Ruescas, A. B., Jimenez-Munoz, J. C., Soria, G., Hidalgo, V., Atitar, M., Franch, B. and Cuenca, J. (2011). "Temporal analysis of Normalized Difference Vegetation Index (NDVI) and Land Cover between 1981 and 2001". International Journal of Remote Sensing 32(7): 2057-2068.

Justice, C. O., Townshend, J. R. G., Holben, B. N. and Tucker, C. J. (1985). "Analysis of the phenology of global vegetation using meteorological satellite data". International Journal of Remote Sensing 6: 1271-1318.

Justice, C. O., Giglio, L., Korontzi, S., Owens, J., Morisette, J., Roy, D. P, Descloitres, J., Alleaume, S., Petitcolin, F., Kaufman, Y. (2002). "The MODIS fire products". Remote Sensing of Environment 83: 244-262.

Kaiser, J. W., Heil, A., Andreae, M. O., Benedetti, A., Chubarova, N., Jones, L., Morcrette, J. -J., Razinger, M., Schultz, M. G., Suttie, M. and van der Werf, G. R. (2012). "Biomass burning emissions estimated with a global fire assimilation system based on observed fire radiative power". Biogeosciences 9: 527-554.

Kalcevic, V. (1980). "Control Device Evaluation Flares and the Use of Emissions as Fuels". Organic Chemical Manufacturing: Combustion Control Devices United State of America (USA), Environmental Protection Agency, Research Triangle Park NC, USA. [Online]. Available: http://www.nepis.epa.gov/Exe/ZyPURL.cgi?Dockey=2000MF11.TXT [Accessed 6th April 2012].

Karnieli, A., Agam, N., Pinker, R. T., Anderson, M., Imhoff, M. L., Gutman, G. G., Panov, N. and Goldberg, A. (2010). “Use of NDVI and Land Surface Temperature for Drought Assessment: Merits and Limitations”. Journal of Climate 23: 618-633, doi: http://dx.doi.org/10.1175/2009JCLI2900.1.

Kaufman, Y. J., Wald, A., Lorraine, L. A., Gao, B. C., Li, R. R. and Flynn, L. (1997). “Remote sensing of aerosol over the continents with the aid of a 2.2 μm channel”. IEEE Transaction. Geoscience and Remote Sensing 35: 1286-1298.

Kaufman, Y. J., Karnieli, A. and Tanre, D. (2000). "Detection of dust over deserts using satellite data in the solar wavelengths". IEEE Transactions on Geoscience and Remote Sensing 38: 525-531.

Kawabata, A., Ichii, K. and Yamaguchi, Y. (2001). “Global monitoring of interannual changes in vegetation activities using NDVI and its relationships to temperature and precipitation”. International Journal of Remote Sensing 22 (7): 1377-1382.

Kenneth, C., Hood, L. M., Wenger, O. P. and Harrison, S. C. (2002). "Hydrocarbon System Analysis of the Northern Gulf of Mexico: Delineation of Hydrocarbon Migration Pathways Using Seeps and Seismic Imaging". American Association of Petroleum Geologist (AAPG) 48(11): 25-40.

Khandewal, S. and Goyal R. (2010). "Analysis of Land Surface Temperature Variation Due to Fire at Oil Terminal, Jaipur, India". Remote Sensing for

Science, Education, and Natural and Cultural Heritage Rainer Reuter (Edition) EARSeL.

Khanna, S., Santos, M. J., Ustin, S. L., Koltunov, A., Kokaly, R. F. and Roberts, D. A. (2013). "Detection of Salt Marsh Vegetation Stress and Recovery after the Deepwater Horizon Oil Spill in Barataria Bay, Gulf of Mexico Using AVIRIS Data." PLoS ONE 8 (11): e78989.

Khlystova, I. G. (2010). "Analysis and Interpretation of Satellite Measurements in the Near-infrared Spectral Region with the focus on Carbon Monoxide". PhD Thesis. Bremen, University of Bremen. [Online]. Available: http://www.elib.suub.uni-bremen.de/edocs/00101099-1.pdf [Accessed 15th December 2012].

Kimberly, E. B., Benjamin, T. T., Ara, T. H., Dee, W. P., Cristina, M. and Edward, H. E. (2007). "A twelve year record of national and global gas flaring volumes estimated using satellite data - Final Report to the World Bank". [Online]. Available: http://www.siteresources.worldbank.org/.../DMSP_flares_20070530_b-sm.pdf [Accessed 1st October 2011].

Klogo, G. S., Gasonoo, A. and Ampomah, K. E. I. (2013). "On the performance of filters for reduction of speckle noise in SAR images off the coast of the Gulf of Guinea". International Journal of Information Technology, Modelling and Computing (IJIMC) 1(4).

Kostianoy, A. G., Lavrova, O. Y. and Solovyov, D. M. (2014). “Oil Pollution in Coastal Waters of Nigeria”. Remote sensing of the African Seas, pp 149-165.

Kremer, R. G. and Running, S. W. (1993). “Community type differentiation using NOAA/AVHRR data within a sagebrush-steppe ecosystem”. Remote Sensing of Environment 46: 311-318.

Kuenzer, C., van Beijma, S., Gessner, U. and Dech, S. (2014). “Land surface dynamics and environmental challenges of the Niger Delta, Africa: Remote sensing-based analyses spanning three decades (1986-2013)”. Applied Geography 53: 354-368.

Kummerow, C., Barnes, W., Kozu, T., Shiue, J., and Simpson, J. (1998). “The tropical rainfall measuring mission (TRMM) sensor package”. Journal of Atmospheric and Oceanic Technology 15: 808-816.

Labed, J. and Stoll, M. P. (1991). "Spatial variability of land surface emissivity in the thermal infrared band: Spectral signature and effective surface temperature". Remote Sensing of Environment 38(1-7).

Langer, M., Westermann, S. and Boike, J. (2010). “Spatial and temporal variations of summer surface temperatures of wet polygonal tundra in Siberia – implications for MODIS LST based permafrost monitoring”. Remote Sensing of Environment 114: 2059-2069.

Lavender, S. J. (2007). “A review of remote sensing in the marine environment”. Institute of Marine Studies, University of Plymouth, Plymouth: 1-20.

Leahey, D. M. and Davies, M. J. E. (1984). “Observations of plume rise from sour gas flares”. Atmospheric Environment 18(5): 917-922.

Leahey, D. M., Preston, K. and Strosher, M. (2001). "Theoretical and observational assessments of flare efficiencies". Journal for Air Waste Management Association 51(12): 1610-1616.

Lee, H. (1993). “An application of NOAA AVHRR thermal data to the study of urban heat islands”. Atmospheric Environment. Part B: Urban Atmosphere 27: 1-13.

Legall, D. (2009). "New Petroleum Industrial Bill for Nigeria. International Bar Association; The Global Voice of the Legal Profession". [Online]. Available: https://www.nassnig.org/nass/legislation.php?id=1182 [Accessed 15th May 2012].

Leifer, I., Roberts, D., Margolis, J. and Kiannaman, F. (2006). "In-situ Sensing of Methane Emissions from Natural Marine Hydrocarbon Seeps: A potential remote sensing technology". Earth and Planetary Science 245: 509-522.

Leifera, I., Luyendykb, B. and Broderickc, K. (2006). "Tracking an oil slick from multiple natural sources, Coal Oil Point, California". Marine and Petroleum Geology 23: 621-630.

Levin, M. and Heimowitz, A. (2012). “Mapping of spatial and temporal patterns of Mediterranean wildfires from MODIS". Remote Sensing of Environment 126(2012): 12-26.

Leprieur, C., Kerr, Y. and Pichon, J. (1996). “Critical assessment of vegetation indices from AVHRR in a semi-arid environment”. International Journal of Remote Sensing 17 (13): 2549-2563.

LFN. (1990). Laws of The Federation of Nigeria. “Nigerian National Petroleum Corporation (NNPC) Act 1973, Cap 320”. [Online]. Available: http:// www.nigeria-law.org/Nigeria%20National%20Petroleum%20Corporati... [Accessed 18th October 2011].

Li, Z. L. and Becker, F. (1993). “Feasibility of land surface temperature and emissivity determination from AVHRR data”. Remote Sensing of Environment 43: 65-85.

Li, J. J., Wang, X. R., Wang, X. J., Ma, W. C. and Zhang, H. (2009). “Remote sensing evaluation of urban heat island and its spatial pattern of the Shanghai metropolitan area, China”. Ecological Complexity 6: 413-420.

Li, L., Ustin, S. L. and Lay, M. (2005). “Application of AVIRIS Data in Detection of Oil-Induced Vegetation Stress and Cover Change at Jornada, New Mexico.” Remote Sensing of Environment 94 (1): 1-16. doi:10.1016/j.rse.2004.08.010.

Liang, S., Fallah-Adl, H., Kalluri, S., JaJa, J., Kaufman, Y. and Townshend, J. (1997). “Development of an operational atmospheric correction algorithm for TM imagery”. Journal of Geophysical Research 102: 17173-17186.

Liang, S., Zhong, B. and Fang, H. (2006). “Improved estimation of aerosol optical depth from MODIS imagery over land surfaces”. Remote Sensing of Environment 104: 416-425.

Liang, S. (2001). "An optimization algorithm for separating land surface temperature and emissivity from multispectral thermal infrared imagery". IEEE Transaction on Geoscience and Remote Sensing 39: 264-274.

Liang, S., Fang, H. and Chen, M. (2001). "Atmospheric Correction of Landsat ETM+ Land Surface Imagery - Part I: Methods". IEEE Transactions on Geoscience and Remote Sensing 39(11): 2490-2498.

Liang, S., Ed. (2004). “Quantitative Remote Sensing of Land Surfaces”, John Wiley and Sons.

Liu, Y., Yamaguchi, Y. and Ke, C. (2007). “Reducing the discrepancy between ASTER and MODIS land surface temperature products”. Sensors 7: 3043-3057.

Liu, R., Wen, J., Wang, X., Wang, L., Tian, H., Zhang, T., Shi, X., Zhang J. and LV, S. (2010). “Actual daily evapotranspiration estimated from MERIS and AATSR data over the Chinese Loess Plateau”. Hydrology and Earth System Sciences 14: 47-58.

Llewellyn-Jones, D. and Remedios, J. (2011). "The Advanced Along Track Scanning Radiometer (AATSR) and its predecessors ATSR-1 and ATSR-2: An introduction to the special issue". Remote Sensing of Environment 116(2012): 1-3.

Loveland, T. R., Reed, B. C., Brown, J. F., Ohlen, D. O., Zhu, Z., Yang, L. and Merchant, J. W. (2000). "Development of a global land cover characteristics database and IGBP DISCover from 1 km AVHRR data". International Journal of Remote Sensing 21: 1303-1330.

Lovett, A. and Turner, J. (2009). "Assessing Soil and Vegetation Characteristics in Breckland, UK using ASTER Thermal Infra-red Imagery". In Proceedings of RSPSoc 2009, Leicester, UK (Nottingham: RSPSoc).

Lowhorn, G. L. (2015). "Qualitative and Quantitative Research: How to Choose the Best Design". [Online]. Available: https://www.google.co.uk/webhp?source=search_app&gfe_rd=cr&ei=C4hQVZWKMOHLowXAlYGgBw&gws_rd=ssl#q=why+choose+quantitative+research+methodology [Accessed 11th May 2015].

Lu, D. and Weng, Q. (2006). "Spectral mixture analysis of ASTER images for examining the relationship between urban thermal features and biophysical descriptors in Indianapolis, Indiana, USA". Remote Sensing of Environment 104: 157-167.

Lyon, J. G., Yuan, D., Lunetta, R. S. and Elvidge, C. D. (1998). “A change detection experiment using vegetation indices”. Photogrammetric Engineering. Remote Sensing 64(2): 143-150.

MacDonald, I. R., Leifer, I., Sassen, R., Stine, P., Mitchell, R. and Guinasso, N. (2002). "Transfer of Hydrocarbons from Natural Seeps to the Water Column and Atmosphere". Geofluids 2(2): 95-107.

Majumdar, D. (2008). "Source apportionment of VOCs at the Petrol Pumps in Kolkata, India; exposure of workers and assessment of associated health risk". Transportation Research 13(8): 524-530.

Malak, D. and Pausas, J. (2006). “Fire regime and post-fire Normalized Difference Vegetation Index changes in the eastern Iberian peninsula. International Journal of Wildland Fire 15 (3): 407-413.

Mallick, J., Singh, C. K., Shashtri, S., Rahman, A. and Mukherjee, S. (2012). “Land surface emissivity retrieval based on moisture index from Landsat TM satellite data over heterogeneous surfaces of Delhi city”. International Journal of Applied Earth Observation and Geoinformation 19: 348-358.

Malumfashi, G. I. (2007). "Phase-out of gas flaring in Nigeria by 2008: The prospect of a multi-win project (Review of the Regulatory, Environmental and Socio-Economic Issues)". Nigeria Gas Flaring Petroleum Training Journal (PTJ) 14(2).

Mao, K., Qin, Z., Shi, J. and Gong, P. (2005). "A practical split-window algorithm for retrieving land surface temperature from MODIS data". International Journal of Remote Sensing 26(15): 3181-3204.

Markham, B. L. and Barker, J. L. (1986). "Landsat MSS and TM post-calibration dynamic ranges, exoatmospheric reflectances and at-satellite temperature". EOSAT Landsat Technical Notes: 3-8.

Masuda, K., Takashima, T. and Takayama, Y. (1988). "Emissivity of Pure and Sea Waters for the Model Sea Surface in the Infrared Window Regions". Remote Sensing of Environment 24:313-329.

Mather, P. M. (2004). "Computer processing of remotely sensed images: An Introduction", 3rd Edition. West Sussex, England, John Willey and Sons.

Maxwell, E. R. (1981). "Biomass measurement from Landsat drought and energy applications". Proceedings of the Second Eastern Regional Remote Sensing Applications Conference, Danvers, Massachusetts, March 9-11.

McCartney, J. K. (1990). "Letter from J. Keith McCartney (John Zink Co., Tulsa, OK) to William M. Vatavuk R. T. P. U.S. Environmental Protection Agency", NC USA. [Online]. Available: http://www.nepis.epa.gov/Exe/ZyPURL.cgi?Dockey=910118Ci.TXT [Accessed 10th January 2012].

McCarville, D., Buenemann, M., Bleiweiss, M. and Barsi, J. A. (2011). "Atmospheric Correction of Landsat Thermal Infrared Data: A Calculator Based on North America Regional Reanalysis (NARR)". ASPRS. Milwaukee, Wisconsin: 12.

McEwen, J. D. N. and Johnson, M. R. (2012). “Black carbon particulate matter emission factors for buoyancy-driven associated gas flares”. Journal of the Air and Waste Management Association 62(3): 307-321.

McMichael, C., Hope, A., Roberts, D. and Anaya, M. (2004). “Post-fire recovery of leaf area index in California chaparral: a remote sensing-chronosequence approach”. International Journal of Remote Sensing 25 (21): 4743-4760.

Mohd, H., Pakhriazad, H. Z. and Shahrin, M. F. (2009). “Evaluating supervised and unsupervised techniques for land cover mapping using remote sensing data”. Malaysian Journal of Society and Space 5(1): 1-10.

Moreno, J., Moreno-Grau, S., Garcia-Sanchez, A., Vergara, N., Moreno-Clavel, J., Pesch, M. and Weidauer, D. (2004). “Measurement of Hydrocarbons in the UV by using a Mobile Multiwavelength-LIDAR”. International Laser RADAR Conference (ILDRD), Matera, Italy.

Morgan, P., Hardy, C. C., Swetnam, T. W., Rollins, M. G. and Long, D. G. (2001). "Mapping fire regimes across time and space: understanding coarse and fine-scale fire patterns”. International Journal of Wild-land Fire 10: 329-342.

Mucahit, C. (2011). "Fundamental pollutants in the European Union (EU) countries and their effects on Turkey". Procedia Social and Behavioural Sciences 19: 467-473.

Myeni, R., Keeling, C., Tucker, C., Asrar, G. and Nemani, R. (1997). “Increased plant growth in the northern high latitudes from 1981-1991”. Nature 386 (6626): 698-702.

Myneni, R. B., Hoffman, S., Knyazikhin, Y., Privette, J. L., Glassy, J., Tian, Y. and Wang, Y. (2002). “Global Products of Vegetation Leaf Area and Fraction Absorbed PAR from Year One of MODIS Data”. Remote Sensing of Environment 83: 214-231. doi:10.1016/S0034-4257(02) 00074-3.

NASA. (2002). National Aeronautics and Space Administration. “Landsat 7 ETM+ Science Data Users Handbook”. [Online]. Available: http://www.landsathandbook.gsfc.nasa.gov/data_prod/prog_sect11_3.html [Accessed 23rd January 2012].

NASA. (2006). National Aeronautics and Space Administration. "World Wind”. [Online]. Available: http://www.worldwindcentral.com/wiki/NASA_World_Wind_Download [Accessed 20th October 2012].

NASA. (2011). National Aeronautics and Space Administration. “The Landsat program”. [Online]. Available: http://www.landsat.gsfc.nasa.gov/about/landsat1.html [Accessed 19th December 2011].

NASA. (2015a). National Aeronautics and Space Administration. “Landsat Science”. [Online]. Available: http://landsat.gsfc.nasa.gov/?p=3180 [Accessed 1st May 2015]

NASA. (2015b). National Aeronautics and Space Administration. “NASA, USGS Begin Work on Landsat 9 to Continue Land Imaging Legacy”. [Online]. Available: http://www.nasa.gov/press/2015/april/nasa-usgs-begin-work-on-landsat-9-to-continue-land-imaging-legacy [Accessed 10th June 2015]

NASA. (2015c). National Aeronautics and Space Administration. “VIRS-Precipitation Measurement Missions”. [Online]. Available: pmm.nasa.gov/trmm/vir [Accessed 8th June 2015]

NASA. (2015d). National Aeronautics and Space Administration. “MODIS design”. [Online]. Available: http://modis.gsfc.nasa.gov/about/design.php [Accessed 6th June 2015]

NASA. (2015e). National Aeronautics and Space Administration. “GOES Project Science”. [Online]. Available: http://goes.gsfc.nasa.gov/ [Accessed 26th July 2015]

NASRDA. (2005). National Space Research and Development Agency, Nigeria. “Gas flaring sites in the Niger Delta, Nigeria”.

NBS. (2006). National Bureau of Statistics. “The Nigerian Statistical Fact Sheet on Economic and Social Development”. Abuja, Nigeria: 1-101. [Online]. Available: http://www.nigerianstat.gov.ng/ [Accessed 28th June 2013].

NDDC. (2004). Niger Delta Development Commission. “NDDC at a Glance”. Port Harcourt, River State. [Online]. Available: http://www.e-ir.info/2010/12/05/the-politics-of-oil-in-the-niger-delta/ [Accessed 11th August 2011].

NDRDMP. (2006). “Niger Delta Regional Development Master-plan”. Facilitated by the Niger Delta Development Commission (NDDC) in partnership with the Niger Delta Nine States’ Governments, LGAs, Oil Companies, Civil Society Organizations and Communities in the Niger Delta.

Nduka, J. K. C., Orisakwe, O. E., Ezenweke, L. O., Ezenwa, T. E., Chendo, M. N. and Ezeabasili, N. G. (2008). "Acid rain phenomenon in the Niger Delta region of Nigeria: Economic, biodiversity, and public health concern”. The Scientific World Journal 8: 811-818.

Nelson, A. (1997). “Vegetation degradation around gas fires in south-eastern Nigeria: A study of flare sites in Rivers and Bayelsa States. Unpublished M.Sc. Thesis, Dept. of Geography, University of Ibadan, Ibadan.

Neteler, M. (2005). “Time series processing of MODIS satellite data for landscape epidemiological applications”. International Journal of Geoinformatics 1: 133-138.

Neville, C. (2007). “Introduction to research and research methods”. School of Management, Bradford University, UK: 1-46. [Online]. Available:

http://www.brad.ac.uk/management/.../management/.../introduction-to-Research [Accessed 19th April 2014].

Nichol, J. E., Fung, W. Y., Lam, K. S. and Wong, M. S. (2009). "Urban heat island diagnosis using ASTER satellite images and in situ air temperature". Atmospheric Research 94: 76-284.

Nieto, H., Sandholt, I., Aguado, I., Chuvieco, E. and Stisen, S. (2011). "Air temperature estimation with MSG-SEVIRI data: calibration and validation of the TVX algorithm for the Iberian Peninsula". Remote Sensing of Environment 115: 107-116.

NNPC. (1997). Nigerian National Petroleum Corporation. "Annual Statistical Bulletin". Corporate Planning and Development Division (CPDD). January-December 1997. [Online]. Available: http://www.nnpcgroup.com/.../1997%20Annual%20Statistical%20Bulletin%20 [Accessed 4th January 2012].

NNPC. (2006). Nigerian National Petroleum Corporation. "Annual Report". [Online]. Available: http://www.nnpcgroup.com/.../OilandGasStatistics/AnnualStatisticsBulletin/Mo [Accessed 2nd September 2012].

NNPC. (2009). Nigerian National Petroleum Corporation. "Annual Statistical Bulletin". Corporate Planning and Development Division (CPDD). January-December 2009. [Online]. Available:

http://www.nnpcgroup.com/.../1997%20Annual%20Statistical%20Bulletin%20 [Accessed 4th June 2012].

NNPC. (2012). Nigerian National Petroleum Corporation. "NNPC Business". Energy. Abuja. [Online]. Available: http://www.nnpcgroup.com/ [Accessed 24th October 2012].

NOAA. (2011). National Oceanic and Atmospheric Administration. "Global Gas Flaring Reduction - Estimated Flared Volumes from Satellite Data". USA. [Online]. Available: http://web.worldbank.org [Accessed 14th June 2012].

NOAA. (2011b). "The GOES-15 Science Test: Imager and Sounder Radiance and Product Validations". NOAA Technical Report NESDIS 141. U.S. Department of commerce, National Oceanic and Atmospheric Administration, National Environmental Satellite, Data, and Information Service. [Online]. Available: www.learningace.com/.../noaa_technical_report_141_goes-15_science_test [Accessed 9th June 2015]

NOAA. (2015). National Oceanic and Atmospheric Administration. "Geophysical Data". National Geophysical Data Centre. [Online]. Available: http://maps.ngdc.noaa.gov/viewers/wcs-client/ [Accessed 14th June 2014].

NOAA. (2015). National Oceanic and Atmospheric Administration. "Advanced Very High Resolution Radiometer (AVHRR): Overview". [Online]. Available: https://www.ngdc.noaa.gov/ecosys/cdroms/AVHRR97_d1/avhrr.htm [Accessed 15th June 2014].

Noyes, E., Good, S., Corlet, G., Kong, X., Remedios, J. and LLewellyn-Jones, D. (2006). “AASTR LST Product Validation 2nd Working Meeting on MERIS and (A)ATSR Calibration and Geophysical Validation (MAVT-2006)”. ESA, ESRIN, Frascati, Italy.

Nwankwo, C. O. and Ogagarue, D. O. (2011). "Effects of gas flaring on surface and groundwaters in Delta State, Nigeria". Geology and Mining Research 3(5): 131-136.

Nwankwo, C. O. and Ogagarue, D. O. (2012). "An Investigation of Temperature Variation at Soil Depths in Parts of Southern Nigeria”. American Journal of Environmental Engineering 2(5): 142-147.

Nwanya, S. C. (2011). "Climate change and energy implications of gas flaring for Nigeria”. International Journal of Low Carbon Technologies :1-7.

Nweke, F. H. and Ogbu, N. H. (2015). “Wireless Sensor Networks based Pipeline Vandalisation and oil spillage monitoring and detection: Main benefits for Nigeria oil and gas sectors”. The SIJ Transactions on Computer Science Engineering and its Applications (CSEA) 3(1).

Obioh, I. B., Oluwole, A. F. and Akeredolu, F. A. (1994). "Non-CO_2 gaseous emissions from upstream oil and gas operations in Nigeria”. Environmental Monitoring and Assessment 31: 67-72.

Odjugo, P. A. and Osemwenkhae, E. J. (2009). "Natural gas flaring affects microclimate and reduces maize (Zea mays) yield". International Journal of Agriculture and Biology 11(4): 408-412.

Odu, C. T. I. (1981). "Degradation and Weathering of Crude Oil under Tropical Conditions". The Petroleum Industry and the Nigerian Environment. NNPC. Lagos, NNPC**:** 143-153.

Odukoya, O. A. (2006). "Oil and sustainable development in Nigeria: A case study of the Niger Delta". Human Ecology 20(4): 249-258.

Ofomata, G. E. K. (1997). "The oil industry and the Nigerian environment". Environmental review 1 (1): 8-20.

Okon, S. M. (2006). "The Influence of Oil Exploration and Exploitation on the Coastal Environment of the Niger Delta Area of Nigeria". Bachelor of Science (B.Sc.) Degree Project Report. Department of Geoinformatics & Surveying, University of Uyo, Uyo, Akwa Ibom, State, Nigeria. Pp 1-153.

Ologunorisa, T. E. (2001). "A review of the effects of gas flaring on the Niger Delta environment". International Journal of Sustainable Development & World Ecology 8 (3): 249-255, DOI: 10.1080/13504500109470082

Olukoju, A. (1996). "Nigeria's Coastal Zone: Environmental Problems, Responses and suggested Remedies". International Journal of Maritime History. [Online]. Available: https://

www.unilag.edu.ng/staffdirectorydetails.php?username=3640&id [Accessed 20th July 2013].

Olusola, J. A. and Okoroigwe, I. N. (2010). "Evaluation Findings for Exploration and Exploitation Activities and Its Effects on Biodiversity using GIS, Remote Sensing and GPS Technology: A case Study of Nigerian Niger-Delta Coastal Environment with Particular Reference to Rivers State". [Online]. Available: https://sites.google.com/a/aag.org/mycoe-servir/the-team/nigeria [Accessed 30th August 2013].

Oluwatimilehin, J. O. (1981). "The ecological impact of the oil industry in the Niger Delta area of Nigeria". Unpublished M.Sc. Thesis, University of Ife (Now Obafemi Awolowo, University) Ile-Ife, Nigeria.

Omodanisi, E. O., Salami, A. T. and Eludoyin, A. O. (2010). "Protecting Oil pipeline Corridor and Associated Disasters in Nigeria: the Geoinformation Challenge". Process & Plant Engineering 28(2).

Omodanisi, E. O. (2013). "Resultant Land Use and Land Cover Change from Oil Spillage using Remote Sensing and GIS". Research Journal of Applied Sciences, Engineering and Technology 6(11): 2032-2040.

Omo-Irabor, O. O. and Oduyemi, K. (2012). "A Hybrid Classification Approach for the Systematic Analysis of Land Cover Changes in the Niger Delta Region". [Online]. Available: http://www.scribd.com/.../A-Hybrid-Image-Classification-Approach-for-the-Sy [Accessed 15th May 2012].

Omokaro, O. (2009). "Oil and gas extraction in the Niger Delta Region of Nigeria: The social and environmental challenges". Freiberg, Online Geology 24: 13-20.

Onojeghuo, A. O. and Blackburn, G. A. (2011). "Forest transition in an ecologically important region: Patterns and causes for landscape dynamics in the Niger Delta". Ecological Indicators 11: 1437-1446.

Onosode, G. O. (2003). "Environmental Issues and challenges of the Niger Delta (Perspectives from the Niger Delta Environmental Survey Process)". Lagos, Lilybank Property and Trust Limited.

Oseji, O. J. (2007). "Thermal gradient in the vicinity of Kwale/Okpai gas plant, Delta state, Nigeria: Preliminary observations". Environmentalist 27: 311-314.

Osuji, L. C. and Avwiri, G. O. (2005). "Flared Gases and Other Pollutants Associated with Air Quality in Industrial Areas of Nigeria: An Overview". Chemistry and Biodiversity 2.

Ottle, C. and Vidal-Madjar, D. (1992). "Estimation of land surface temperature with NOAA-9 data". Remote Sensing of Environment 40: 27-41.

Otukei, J. R. and Blaschke, T. (2012). "You Know The Temperature at the Weather Station But Do You Know It Anywhere Else? Assessing Land Surface Temperature Using Landsat ETM+ Data". In Proceedings of The first Conference on Advances in Geomatics Research. [Online]. Available:

http://www.cedat.mak.ac.ug/wp-content/themes/CEDAT-Theme/Publications/You%20Know%20The%20Temperature%20at%20the%20Weather%20Station%20But%20Do%20You%20Know%20It%20Anywhere%20Else_Assessing%20Land%20S.pdf [Accessed 17th February 2014].

Park, P. K., Erod, J. A. and Kester, D. R. (1991). "Applications of Satellite Remote Sensing to Marine Pollution Studies". Chemistry and Ecology 5(1 & 2): 57-73.

Paugam, R., Wooster, M. J. and Roberts, G. (2013). "Use of Handheld Thermal Imager Data for Airborne Mapping of Fire Radiative Power and Energy and Flame Front Rate of Spread". IEEE Transactions on Geoscience and Remote Sensing 51(6).

Paul, M. D., Libe, W., Benjamin, H. and Burton, H. J. (2004). "Coastal Pollution Hazards in Southern California observed by SAR Imagery: Storm-water plumes, waste-water plumes and natural hydrocarbon seeps". Marine Pollution Bulletin 49: 1013-1024.

Pearson, L. and Miller, L. (1972). "Remote mapping of standing crop biomass for estimation of the productivity of the short-grass prairie, Pawnee National Grasslands, Colorado". Proceedings of the 8th International Symposium on Remote Sensing of the Environment, Michigan, 2-6 October, pp. 1357-1381.

PEFS. (2005). Programme on Ethnic and Federal Studies (PEFS). "Constitutional reforms dialogues: The South-South Agenda for Constitutional reform. Ibadan, Nigeria". [Online]. Available:

https://openlibrary.org/.../Programme_on_Ethnic_and_Federal_Studies_(PEFS),_University_of_Ibadan [Accessed 20th December 2011].

Pena, S. and Abdelsalam, M. (2006). "Orbital remote sensing for geological mapping in Southern Tunisia: Implication of oil and gas exploration". Journal of African Earth Sciences 44(2): 203-219.

Peng, D. Q., Chen, Y. H., Li, J., Zhou, J. and Ma, W. (2008). "Research on urban surface emissivity based on unmixing pixel". The International Archives of the Photogrammetry, Remote Sensing and Spatial Information Sciences, vol. XXXVII, Beijing, Part B6b.

Peñuelas, J., Filella, I., Biel, C., Serrano, L. and Savé, R. (1993). "The reflectance at the 950-970 nm region as an indicator of plant water status." International Journal of Remote Sensing 14 (10): 1887-1905, doi:10.1080/01431169308954010.

Peters, A. J. and Eve, M. D. (1995). "Satellite monitoring of desert plant community response to moisture availability". Environmental Monitoring and Assessment 37: 273-287.

Philip, S. (2007). "Active Fire Detection Using Remote Sensing Based Polar-Orbiting and Geostationary observations: An approach towards near real-time fire monitoring". Master of Science (M.Sc.) Dissertation. The Netherlands, International Institute for Geo-information Science and Earth Observation,

Enschede, The Netherlands. [Online]. Available: http://www.gem-msc.org/Academic%20Output/Susan%20Philip.pdf [Accessed 1st March 2012].

Pinker, R. T., Sun, D., Hung, M. P., Li, C. and Basara, J. B. (2009). "Evaluation of satellite estimates of land surface temperature from GOES over the United States". Journal of Applied Meteorology and Climatology 48: 167-180.

Pongrácz, R., Bartholy, J. and Dezso, Z. (2006). "Remotely sensed thermal information applied to urban climate analysis". Advances in Space Research 37: 2191-2196.

Pongrácz, R., Bartholy, J. and Dezso, Z. (2010). "Application of remotely sensed thermal information to urban climatology of Central European cities". Physics and Chemistry of the Earth 35: 95-99.

Popp, T. (1995). "Correcting atmospheric masking to retrieve the spectral albedo of land surface from satellite measurements". International Journal of Remote Sensing 16: 3483-3508.

Potter, C. S. and Brooks, V. (1998). "Global analysis of empirical relations between annual climate and seasonality of NDVI." International Journal of Remote Sensing 19 (15): 2921-2948.

Pouteau, R., Rambal, S., Ratte, J., Gogé, F., Joffre, R. and Winkel, T. (2010). "Downscaling MODIS-derived maps using GIS and boosted regression trees: the

case of frost occurrence over the arid Andean highlands of Bolivia". Remote Sensing of Environment 115: 117-129.

Prata, A. J. (1994). "Land surface temperatures derived from the advanced very high resolution radiometer and the along-track scanning radiometer 2. Experimental results and validation of AVHRR algorithms". Journal of Geophysical Research 99: 13025-13058.

Prata, A. (2002). "Land Surface Temperature Measurement from Space: AATSR Algorithm Theoretical Basis Document. Contract Report to ESA". CSIRO Atmospheric Research: Aspendale: 1-34.

Pressler, R. R. and Walker, D. B. (1999). "Integrating Deep Tow and Conventional 3D Seismic For Deepwater Seafloor Imaging". Offshore 59(7): 98-99.

Price, J. C. (1977). "Thermal Inertial Mapping: A New View of the Earth". Geophysical Research 82: 2582-2590.

Prince, S. D., Goetz, S. J. and Goward, S .N. (1995). "Monitoring primary productivity from earth observing satellites". Water, Air, and Soil Pollution 82: 509-522.

Prins, E. M. and Menzel, W. P. (1994). "Trends in South American biomass burning detected with the GOES VAS from 1983-1991". Journal of Geophysical Research 99: 16719-16735.

PTT. (2008). "Flaring and venting philosophy". [Online]. Available: http:// www. Scribd.com/doc/108536828/Flaring-and-Venting-Philosophy [Accessed 12th February 2013].

Pu, R., Gong, P., Michishita, R. and Sasagawa, T. (2006). "Assessment of multiresolution and multi-sensor data for urban surface temperature retrieval". Remote Sensing of Environment 104: 211-225.

Purevdorj, T., Tateishi, R., Ishiyama, T. and Honda, Y. (1998). "Relationships between percent vegetation cover and vegetation indices". International Journal of Remote Sensing 19(18): 3519-3535.

Pyne, S. J., Andrews, P. L. and Laven, R. D. (1996). "Introduction to Wildland Fire". New York: Wiley.

Qi, J., Chehbounidi, A., Huete, A., Kerr, Y. and Sorooshian, S. (1994). "A modified soil adjusted vegetation index". Remote Sensing of Environment 48 (2): 119-126.

Qin, Z., Olmo, G. D. and Karnieli, A. (2001). "Derivation of split window algorithm and its sensitivity analysis for retrieving land surface temperature from NOAA-advanced very high resolution radiometer data". Geophysical Research : 22655-22 670.

Qin, Q., Zhang, N., Nan, P. and Chai, L. (2011). "Geothermal area detection using Landsat ETM+ thermal infrared data and its mechanistic analysis: A case

study in Tengchong, China". International Journal of Applied Earth Observation and GeoInformation 13: 552-559.

Quaye-Ballard, J. A., An, R., Andam-Akorful, S. A. and Quaye-Ballard, N. L. (2013). "Role of Geoinformatics for Ghana oil and gas industry". International Journal on Recent and Innovation Trends in Computing and Communication 1(6): 539-546.

Reed, B., Brown, J., VanderZee, D., Loveland, T., Merchant, J. and Ohlen, D. (1994). "Measuring phenological variability from satellite imagery". Journal of Vegetation Science 5 (5): 703-714.

Retalis, A., Paronis, D., Lagouvardos, K. and Kotroni, V. (2010). "The heat wave of June 2007 in Athens, Greece – part 1: study of satellite derived land surface temperature". Atmospheric Research 98: 458-467.

Richardson, A. and Wiegand, L. (1997). "Distinguishing vegetation from soil background information". Photogrammetric Engineering and Remote Sensing 43 (12): 1541-1552.

Richter, A. (2005). "Satellite observations of the atmosphere and the ocean surface: A lecture presented at Heraeus-summer school on physics of the environment". Institute of Environmental Physics, University of Bremen, Bremen: 1-25. [Online]. Available: http://www.iup.uni-heidelberg.de/institut/stuium/lehre/Heraeus/material.html [Accessed 30th September 2012].

Rigo G, Parlow E and Oesch, D. (2006). “Validation of satellite observed thermal emission with in-situ measurements over an urban surface”. Remote Sensing of Environment 104: 201-210.

Ripple, W. J. (1985). “Landsat Thematic Mapper bands for characterising fescue grass vegetation”. International Journal of Remote Sensing 6: 1373-1384.

Roberts, A., Sherwood, R. L. and Coburn, C. (2000). "Low Cost Integrated Airborne Multispectral Remote Sensing”. International Archives of Photogrammetry and Remote Sensing XXXIII(B2).

Roberts, J. J., Best, B. D., Dunn, D. C., Treml, E. A. and Halpin, P. N. (2010). “Marine geospatial ecology tools: an integrated framework for ecological geoprocessing with ArcGIS, Python, R, MATLAB, and C++”. Environmental Modelling and Software 25: 1197-1207.

Robinson, I. S., Ed. (1995). “Satellite Oceanography: An Introduction to Oceanographers & Remote Sensing Scientist”. Baffins Lane, Chichester, West Sussex PO19, IUD, England, John Wiley & Sons. Ltd.

Robinson, I. S., Ed. (2004). “Ocean from space. The principles and methods of satellite oceanography”. Chichester, UK, Praxis publishing limited.

Rondeaux, G., Steven, M. and Baret, M. (1996). “Optimization of soil-adjusted vegetation indices”. Remote Sensing of Environment 55 (2): 95-107.

Rossner, P. (2011). "Expression of XRCC5 in Peripheral Blood Lymphocytes is regulated in subjects from a heavily polluted region in the Czech Republic". Mutation Research-Fundamental and Molecular Mechanism of Mutagenesis 713(1-2): 76-82.

Rouse, J. W., Haas, R. H., Schell, J. A., Deering, D. W. and Harlan J. C. (1974). "Monitoring the Vernal Advancement of Retrogradiation (greenwave effect) of Natural Vegetation". 1st Edition, College Station: Texas A and M University, USA. P. 371.

Roy, D. P., Frost, P., Justice, C. O., Landmann, T., Le Roux, J., Gumbo, K., Makungwa, S., Dunham, K., Du Toit, R., Mhwandagara, K., Zacarias, A., Tacheba, B., Dube, O., Pereira, J., Mushove, P., Morisette, J., Vannan, S. and Davies, D. (2005). "The Southern Africa Fire Network (SAFNet) regional burned area product validation protocol". International Journal of Remote Sensing 26:4265-4292.

Sabins, F. F., Ed. (1978). "Remote Sensing Principles and Interpretation". San Francisco, Freeman and Company.

Sader, S. A., Waide, R. B., Lawrence, W. T. and Joyce, A. T. (1989). "Tropical forest biomass and successional age class relationships to a vegetation index derived from Landsat TM data". Remote Sensing of Environment 28: 143-156.

Sader, S. A., Stone, T. A. and Joyce, A. T. (1990). "Remote sensing of tropical forests: An overview of research and applications using non-photographic sensors". Photogrammetric Engineering and Remote Sensing 56: 1343-1351.

Sáez, A. (2010). "Industrial application of natural gas". [Online]. Available: http://www.intechopen.com/books/natural-gas/industrial-applications-of-natural-gas [Accessed 1st March 2013].

Saleska, S. R., Didan, K., Huete, A. R. and da Rocha, H. R. (2007). "Amazon Forests Green-Up during 2005 Drought". Science 318 (5850): 612. doi:10.1126/science.1146663.

Salomonson, V. V., Barnes, W. L., Maymon, P. W., Montgomery, H. E. and Ostrow, H. (1989). "MODIS: advanced facility instrument for studies of the earth as a system". IEEE Transactions on Geoscience and Remote Sensing 27: 145-153.

Sandau, R., Brieß, K. and Derrico, M. (2010). "Small satellites for global coverage: potential and limits". ISPRS Journal of Photogrammetry and Remote Sensing 65: 492-504.

Sandholt, I., Rasmussen, K. and Andersen, J. (2002). "A simple interpretation of the surface temperature/vegetation index space for assessment of surface moisture status". Remote Sensing of Environment 79(2-3): 213-224.

Santer, R., Carrere, V., Dubuisson, P. and Roger, J. C. (1999). "Atmospheric correction over land for MERIS". International Journal of Remote Sensing 20: 1819-1840.

Şatır, O. and Berberoğlu, S. (2012). "Land Use/Cover Classification Techniques Using Optical Remotely Sensed Data in Landscape Planning", Landscape

Planning, Dr. Murat Ozyavuz (Ed.), ISBN: 978-953-51-0654-8, InTech. [Online]. Available: http://www.intechopen.com/books/landscape-planning/land-use-cover-classificationtechniques-using-optical-remotely-sensed-data-in-landscape-plannin [Accessed 15th May 2015]

Schaaf, C. B., Gao, F., Strahler, A. H., Lucht, W., Li, X., Tsang, T., Strugnell, N. C., Zhang, X., Jin, Y., Muller, P., Lewis, P., Barnsley, M., Hobson, P., Disney, M., Roberts, G., Dunderdale, M., Doll, C., d'Entremont, R. P., Hu, B., Liang, S., Privette, J. L. and Roy, D. (2002). "First operational BRDF, albedo nadir reflectance products from MODIS". Remote Sensing of Environment 83: 135-148.

Schifter, I. (2005). "Air emission assessment from offshore oil activities in Sonda de Campeche, Mexico". Environmental Monitoring and Assessment 109(1-3): 135-145.

Schmidt, H. and Karnieli, A. (2001). "Sensitivity of vegetation indices to substrate brightness in hyper-arid environment: the Maktesh Ramon Crater (Israel) case study". International Journal of Remote Sensing 22 (17): 3503-3520.

Schmetz, J., Pili, P., Tjemkes, S., Just, D., Kerkmann, J., Rota, S. and Ratier, A. (2002). "Supplement to an introduction to meteosat second generation (MSG)". Bulletin of the American Meteorological Society 83(7): 977-992.

Schmit, T. J., Prins, E. M., Schreiner, A. J. and Gurka, J. J. (2002). "Introducing the GOES-M Imager". National Weather Association Digest 25: 2-10.

Schneider, S. and McGinnis, Jr., D. (1977). “Spectral differences between VHRR and VISSR data and their impact of environmental studies”. In Proceedings of American Society of Photogrammetry, 43 Meeting, 27 February to 5 March 1977. Washington, DC.

Schneising, O. (2008). “Analysis and Interpretation of satellite measurements in the near-infrared spectral region: Atmospheric carbon dioxide and methane”. PhD Thesis. University of Bremen, Bremen. [Online]. Available: http://www.iup.uni-bremen.de/sciamachy/NIR.../schnneising_diss_druck.pdf [Accessed 28th December 2011].

Seinfeld, J. H. (2004). "Air pollution". American Insitute of Chemical Engineers 50: 1096-1108.

Sen, D. C. (1988). "Process design for offshore oil and gas production in Cold Ocean environment”. The Canadian Journal of Chemical Engineering 66(5): 864-869.

Serpetti, N., Heath, M., Armstrong, E. and Witte, U. (2011). "Blending single beam RoxAnn and multi-beam swathe QTC hydro-acoustic discrimination techniques for the Stonehaven area, Scotland, UK”. Sea Research 65(4): 442-455.

Sherrie A. Peňa, S. A. and Abdelsalam, M. G. (2006). “Orbital remote sensing for geological mapping in southern Tunisia: Implication for oil and gas exploration”. Journal of African Earth Sciences 44: 203-219.

Shimabukuro, Y. E., Novo, E. M. and Ponzoni, F. J. (1998). “Índice de vegetação e modelo linear de mistura espectral no monitoramento da região do Pantanal”. Pesquisa Agropecuária Brasileira 33: 1729-1737.

Shore, D. (1990). Letter from David Shore (Flare gas Corp. Spring Valley, NY) to William M. Vatavuk. R. T. P. U.S. Environmental Protection Agency, NC. USA. [Online]. Available: http:// www.epa.gov/ttncatc1/dir1/cs3-2ch1.pdf [Accessed 6th December 2012].

Shore, D. (1996). "Making the flare safe”. Journal of Loss Prevention in the Process Indusrties 9(6).

Short, K. C. and A. J. Stauble (1967). "Outline of the geology of Niger Delta”. Bulletin of American Association of Petroleum Geology 51: 761-776.

S.I.C. (2015). Satellite Imaging Corporation. “ASTER Satellite Sensor”. [Online]. Available: http://www.satimagingcorp.com/satellite-sensors/other-satellite-sensors/aster/ [Accessed 22nd July 2015].

Silberberg, M. (2004). The Molecular Nature of Matter and Change. New York, Mc Graw-Hill.

Simpson, J., Kummerow, C., Tao, W. K. and Adler, R. F. (1996). “On the tropical rainfall measuring mission (TRMM)”. Meteorology and Atmospheric Physics, 60: 19-36.

Singh, A. (1987). “Spectral separability of tropical forest cover classes”. International Journal of Remote Sensing 8: 971-979.

Slonecker, E. T. and Fisher, G. B. (2011). “An Evaluation of Traditional and Emerging Remote Sensing Technologies for the Detection of Fugitive Contamination at selected Superfund Waste Sites”. U. S. G. Survey. Reston, Virginia. Open-File Report**:** 2011-1050. [Online]. Available: http:// www.pubs.usgs.gov/of/2011/1050 [Accessed 2nd January 2012].

Smith, K., Loughlin, S., Vye, C. and Ager, G. (2009). “The Application of Thermal Remote Sensing for the Enhanced Mapping and Monitoring of Volcanic Terrain”. In Proceedings of RSPSoc 2009 Annual Conference, 8-11th September 2009, Leicester, UK (Nottingham: RSPSoc).

Snyder, W. C., Wan, Z., Zhang, Y. and Feng, Y. Z. (1998). “Classification-based emissivity for land surface temperature measurement from space”. International Journal of Remote Sensing 19: 2753-2774.

Sobrino, J. A., Li, Z. -L. and Stoll, M. P. (1993). “Impact of the atmospheric transmittance and total water vapor content in the algorithms for estimating satellite sea temperature”. IEEE Transactions on Geoscience and Remote Sensing, 31, pp. 946-952.

Sobrino, J. A., Jiménez-Muñoz, J. C., Labed-Nachbrand, J. and Nelly, F. (2002). "Surface emissivity retrieval from Digital Airborne Imaging Spectrometer data”.

Journal of Geophysical Research 107(D23), 4729, doi: 10.1029/2002JD002197, 2002.

Sobrino, J. (2004). “Land surface temperature retrieval from MSG1-SEVIRI data”. Remote Sensing of Environment 92: 247-254.

Social Action. (2009). “Nigeria: Gas flares still a burning issue in the Niger Delta”. [Online]. Available: http:// www.irinnews.org/.../nigeria-gas-flares-still-a-burning-issue-in-the-niger [Accessed 2nd May 2015].

Song, C. and Woodcock, C. E. (2003). “Monitoring Forest Succession with Multitemporal Landsat Images: Factors of Uncertainty”. IEEE Transactions on Geoscience and Remote Sensing 41(11): 2557-2567.

Sonibare, J. A. and Akeredolu, F. A. (2004). "A theoretical prediction of non-methane gaseous emissions from natural gas combustion”. Energy Policy 32: 1653-1665.

Sonibare, J. A. and Akeredolu, F. A. (2006). "Natural gas domestic market development for total elimination of routine flares in Nigeria’s upstream petroleum operations”. Energy Policy 34(743-753).

Sòria G, Sobrino J. 2007. ENVISAT/AATSR derived land surface temperature over a heterogeneous region. Remote Sensing of Environment 111: 409-422.

Sousa, C. L. and Ponzoni, F. J. (1998). “Avaliaçáo de Índices de vegetação e de bandas TM/Landsat para estimativa de volume de madeira em floresta implantada de Pinus spp”. In: IX Simpósio Brasileiro de Sensoriamento Remoto, INPE/SELPER, São José dos Campos, p. 11.

Spanner, M. A., Pierce, L. L., Running, S. W. and Peterson, D. L. (1990). “The seasonality of AVHRR data of temperate coniferous forests: relationships with leaf area index”. Remote Sensing of Environment 33: 97-112.

Sparks, T. H. and Tryjanowski, P. (2005). “The detection of climate impacts: Some methodological considerations”. International Journal of Climatology 25: 271-277.

Spazio, S. (2015). “The Earth Observation Handbook” - Special Edition for Rio+20. ESA Publication.

SPDC. (2002). Shell Petroleum Development Company. Shell Annual Report. [Online]. Available: http://www.iufro.org/science/special/spdc/iufro-spdc-archive/archive-of-iufro-spdcannual-reports/annual-report-2002/es/. [Accessed 25th September 2013].

Sperling, S., Wooster, M. and Malamud, B. (2009). “An Investigation of the Performance Characteristics of MODIS Fire Radiative Power (FRP) Measurements and their use in determining the effects of Regional Anthropogenic and Natural Drivers of Fire”. In Proceedings of RSPSoc 2009 Annual Conference, 8th-11th September 2009, Leicester, UK (Nottingham: RSPSoc).

Stathopoulou, M. and Cartalis, C. (2007). "Daytime urban heat island from Landsat ETM+ and Corine land cover data: An application to major cities in Greece". Solar Energy 81: 358-368.

Stathopoulou, M. and Cartalis, C. (2009). "Downscaling AVHRR land surface temperatures for improved surface urban heat island intensity estimation". Remote Sensing of Environment 113: 2592-2605.

Stephens, S. L., Weise, D. R., Fry, D. L., Keiffer, R. J., Dawson, J., Koo, E., Potts, J. and Pagni, P. J. (2008). "Measuring the rate of spread of chaparral prescribed fires in Northern California". Fire Ecology, vol. 4, no. 1, pp. 74-86.

Stone, D. K., Lynch, S. K., Pandullo, R. F., Evans, L. B. and Vatavuk, W. M. (2000). "Flares". USA, Office of Air Quality Planning and Standards, US Environmental Protection Agency, Research Triangle Park, NC 27711 USA: 44. [Online]. Available: http://www.epa.gov/ttncatc1/dir1/cs3-2ch1.pdf [Accessed 15th October 2011].

Streutker, D. (2003). "Satellite-measured growth of the urban heat island of Houston, Texas". Remote Sensing of Environment 85: 282-289.

Sun, D. (2003). "Estimation of land surface temperature from a Geostationary Operational Environmental Satellite (GOES-8)". Journal of Geophysical Research 108: 1-15.

Sun, D., Pinker, R. and Basara, J. (2004). “Land surface temperature estimation from the next generation of geostationary operational environmental satellites: GOES M-Q”. Journal of Applied Meteorology 43: 363-372.

Sun, D., Pinker, R. T. and Kafatos, M. (2006). “Diurnal temperature range over the United States: a satellite view”. Geophysical Research Letters 33: 1-4.

Sundt, R. C., Pampanin, D. M., Grung, M., Baršiene, J. and Ruus, A. (2011). "PAH Body Burden and Biomarker Responses in Mussels (Mytilus edulis) exposed to Produced Water from a North Sea Oil Field: Laboratory and Field Assessments”. Marine Pollution Bulletin 62(7): 1498-1505.

Taylor, B. T., Fernando, P., Bauman, A. E., Williamson, A., Craig, J. C. and Redman, S. (2011). “Measuring the Quality of Public Open Space Using Google Earth”. American Journal of Preventive Medicine 40(2): 276-277.

Teillet, P. M. and Fedosejevs, G. (1995). "On the dark target approach to atmospheric correction of remotely sensed data". Canada Journal of Remote Sensing 21: 374-387.

Teillet, P. M., Staenz, K. and Williams, D. (1997). “Effects of Spectral, Spatial, and Radiometric Characteristics on Remote Sensing Vegetation Indices of Forested Regions.” Remote Sensing of Environment 61(1): 139-149, doi:10.1016/S0034-4257(96)00248-9.

Thurmond, A. K., Abdelsalam, M. G. and Thurmond, J. B. (2006). "Optical-radar-DEM remote sensing data integration for geological mapping in the Afar Depression, Ethiopia". Journal of African Earth Sciences 44: 119-134.

Tomlinson, C. J., Chapman, L., Thornes, J. E. and Baker, C. (2011). "Review Remote sensing land surface temperature for meteorology and climatology: a review". Meteorological Application 18: 296-306.

Tortilla-Soup. (2012). "Landforms of the Niger Delta". [Online]. Available : http://tortilla-soup.blogspot.c[Accessed March 2012].o.uk/2012/11/usa-africa-dialogue-series-point.html

Townshend, J. R. G. and Justice, C. O. (1986). "Analysis of the dynamics of African vegetation using the normalized difference vegetation index". International Journal of Remote Sensing 7: 1435-1446.

Trigo, I. F., Monteiro, I. T., Olesen, F. and Kabsch, E. (2008). "An assessment of remotely sensed land surface temperature". Journal of Geophysical Research 113: 1-12.

Tucker, C. J. (1977). "Atmospheric nature of grass canopy spectral reflectance". Applied Optics 16: 1151-1156.

Tucker, C. (1979). "Red and photographic infrared linear combinations for monitoring vegetation". Remote Sensing of Environment 8: 127-150.

Tucker, C. J., Townsend, J. R. G. and Goff, T. E. (1985). “African land-cover classification using satellite data”. Science 227: 369-375.

Twomey, S. (1974). “Pollution and the planetary albedo”. Atmospheric Environment (1967) 8(12): 1251-1256.

Twomey, S., Piepgrass, M. and Wolfe, T. L. (1984). “An assessment of the impact of pollution on global cloud albedo”. Tellus, 36 B, 356-366.

Twumasi, Y. A. and Merem, E. C. (2006). "GIS and Remote Sensing Applications in the Assessment of Change within a Coastal Environment in the Niger Delta Region of Nigeria”. International Journal of Environmental Research and Public Health 3(1): 98-106.

Uchegbulam, O. and Ayolabi, E. A. (2013). “Satellite image analysis using remote sensing data in parts of Western Niger Delta, Nigeria”. Journal of Emerging Trends in Engineering and Applied Sciences (JETEAS) 4(4): 612-617.

Ud, D., Al, D. A. and Literathy, P. (2008). "Evidence of Hydrocarbon Contamination from the Burgan Oil Field Kuwait: Interpretations from Thermal Remote Sensing Data”. Environmental Management 86(4): 605-619.

Ugochukwu, C. N. C. (2008). “Sustainable Environmental Management in the Niger Delta Region of Nigeria: Effects of Hydrocarbon Pollution on Local Economy”. PhD Thesis. Faculty of Environmental Sciences and Process Engineering, Brandenburg University of Technology Cottbus, Germany. [Online]. Available:

http://www.opus.kobv.de/btu/volltexte/.../Collins_Ugochukwu_PhD_Dissertation.pdf [Accessed 29th June 2014].

Ugochukwu, C. N. C and Ertel, J. (2008). "Negative impacts of oil exploration on biodiversity management in the Niger Delta area of Nigeria". Impact Assessment and Project Appraisal 26 (2): 139-147

UK-DMC (SLIM 6-22). (2011). "Image of January 18, 2011 for the Niger Delta".

Ukegbu, D. and Okeke, A .O. (1987). "Flaring of associated gas in oil and gas industry: Impact on growth, productivity and yield of selected farm crops". Petroleum Industry and the Nigerian Environment, Proceedings of 1987 Seminar, NNPC, Lagos.

Umamaheshwaran, R., Bijker, W. and Stein, A. (2007). "Image mining for modeling of forest fires from meteosat images". IEEE Transactions on Geoscience and Remote Sensing 45: 246-253.

Underwood, E., Ustin, S. and DiPietro, D. (2003). "Mapping nonnative plants using hyperspectral imagery". Remote Sensing of Environment 86: 150-161.

UNEP. (2009). United Nations Environment Programme. "Gas flaring at Eleme Refinery II, Eleme, Rivers State". [Online]. Available: http://www.unep.org. [Accessed 10th January 2012].

UNEP. (2011). United Nations Environment Programme. "Environmental Assessment of Ogoniland". Nairobi, Kenya: pp 1-248. [Online]. Available:

http://www.unep.org/disasterandconflicts/CountryOperations/Nigeria/EnvironmentalAssessmentofOgonilandreport/tabid/54419/Default.aspx [Accessed 5th October 2011].

U.S.A. (2005). "Nigeria Country Analysis Brief". Energy Information and Administration, United State of America. [Online]. Available: https://www.google.co.uk/webhp?source=search_app&gfe_rd=cr&ei=8xg0U6-gHMHR8gf794CgCA#q=nigeria+country+analysis+brief+2005 [Accessed 20th July 2012].

U.S.A. (2010). "Nigeria country analysis briefs". Energy Information and Administration, United State of America. [Online]. Available: https://mulrickillion.wordpress.com/2010/07/24/nigeria-country-analysis-brief-released-july-2010/ [Accessed 16th July 2013].

USGS. (2011). United States Geological Survey. U.S. Department of the Interior. [Online]. Available: http://eros.usgs.gov/#/Find_Data/Products_and_Data_Available/ETM. [Accessed 19th June 2011].

USGS. (2015a). United States Geological Survey. "Technical Announcement: USGS Completes Decommissioning of Landsat 5". U.S. Department of the Interior, U.S. Geological Survey Office of Communications and Publishing 12201 Sunrise Valley Dr, MS 119 Reston, VA 20192 [Online]. Available: http://www.usgs.gov/newsroom/article.asp?ID=3626&from=rss#.VUOFdI7F98F [Accessed 1st May 2015]

USGS. (2015b). United States Geological Survey. “Moderate Resolution Imaging Spectroradiometer (MODIS)”. [Online]. Available: https://lta.cr.usgs.gov/MODIS [Accessed 21st May 2015]

USGS. (2015c). United States Geological Survey. “ASTER Overview”. [Online]. Available: https://lpdaac.usgs.gov/dataset_discovery/aster [Accessed 28th June 2015]

Usman, S. (2007). “Nigeria: Scorching the natural resource curse”. THIS DAY Newspaper, Nigeria, 14th October. [Online]. Available: http//www.allafrica.com/stories/200710151464.html [Accessed 5th January 2012].

Utomwen, D. (2011). “Doubt Still Over Gas Flaring”. The NEWS Magazine. Abuja, Nigeria, The NEWS.

Valor, E. and Caselles, V. (1996). "Mapping land surface emissivity from NDVI: Application to European, African, and South American areas”. Remote Sensing of Environment 57(3): 167-184.

van de Griend, A. A., Owe, M., Groen, M. and Stoll, M. P. (1991). "Measurement and spatial variation of thermal infrared surface emissivity in a savanna environment”. Water Resources Research 27: 371-379.

Van de Griend, A. A. and Owe, M. (1993). “On the relationship between thermal emissivity and the normalized difference vegetation index for natural surfaces”. International Journal of Remote Sensing 14: 1119-1131.

Van Der Meer, F., Van Dijk, P., Kroonenberg, S., Hong, Y. and Lang, H. (2000). “Hyperspectral Hydrocarbon Microseepage Detection and Monitoring: Potentials and Limitations.” In Proceedings of the Second EARsel Workshop on Imaging Spectroscopy. Enschede, Muster: EARSeL. [Online]. Available: http://www.earsel.org/workshops/imaging-spectroscopy-2000/index.html [Accessed 30th April 2013].

Van der Werff, H. M. A., Noomen, M. F., Van der Mejide, M. and Van der Meer, F. D. (2007). "Use of Hyperspectral Remote Sensing to detect hazardous gas leakage from pipelines”. New Developments and Challenges in Remote Sensing Z. Bochenek (edition), Millpress, Rotterdam.

Vastaranta, M., Latorre, E. G., Luoma, V., Saarinen, N., Holopainen, M. and Hyyppä, J. (2015). ”Evaluation of a Smartphone App for Forest Sample Plot Measurements”. Forest 6(4): 1179-1194.

Vázquez, D. P., Reyes, F. J. O. and Arboledas, L. A. (1997). “A comparative study of algorithms for estimating land surface temperature from AVHRR data”. Remote Sensing of Environment 62: 215-222.

Vega, M. B., Craig, M. and Lindo, G. A. (2011). "Ground truthing of remotely identified fortifications on the Central Coasts of Peru”. Archaeological Science 38(7): 1680-1689.

Veraverbeke. S., Gitas, I., Katagis, T., Polychronaki, A., Somers, B. and Goossens, R. (2012). “Assessing post-fire vegetation recovery using red–near infrared vegetation indices: Accounting for background and vegetation variability”. ISPRS Journal of Photogrammetry and Remote Sensing 68: 28-39.

Vermote, E. F., El Saleous, N. Z. and Justice, C. O. (2002). “Atmospheric correction of MODIS data in the visible to middle infrared: first results”. Remote Sensing of Environment 83: 97-111.

Vesanto, J., Himberg, J., Alhoniemi, E. and Parhankangas, J. (2000). “Self-Organizing Map in Matlab: the SOM Toolbox”. SOM Toolbox team, Laboratory of Computer and Information Science, Helsinki University of Technology, P.O.Box 5400, FIN-02015 HUT, Finland. [Online]. Available: http://www.cis.hut.fi/projects/somtoolbox/ [Accessed 6th May 2013].

Vila, G. and Barbosa, P. (2010). “Post-fire vegetation regrowth detection in the Deiva Marina region (Liguria-Italy) using Landsat TM and ETM+ data”. Ecological Modelling 221 (1): 75-84.

Villasenor, R. (2003). "An air quality emission inventory of offshore operations for the exploration and production of petroleum by the Mexican Oil Industry”. Atmospheric Environment 37(26).

Wan, Z. and Dozier, J. (1996). “A generalized split-window algorithm for retrieving land surface temperature measurement from space”. IEEE Transactions on Geoscience and Remote Sensing 34: 892-905.

Wan, Z. and Li, Z. (1997). "A physics-based algorithm for retrieving land-surface emissivity and temperature from EOS/ MODIS data". IEEE Transaction on Geoscience and Remote Sensing 35 (4): 980-996.

Wan, Z. (2002). "Validation of the land-surface temperature products retrieved from Terra Moderate Resolution Imaging Spectroradiometer data". Remote Sensing of Environment 83: 163-180.

Wan, Z., Zhang, Y., Zhang, Q. and Li, Z. (2004). "Quality assessment and validation of the MODIS global land surface temperature". International Journal of Remote Sensing 25: 261-274.

Wan, Z. (2008). "New refinements and validation of the MODIS land-surface temperature/emissivity products". Remote Sensing of Environment 112: 59-74.

Wang, K. and Liang, S. (2009). "Evaluation of ASTER and MODIS land surface temperature and emissivity products using long-term surface long wave radiation observations at SURFRAD sites". Remote Sensing of Environment 113: 1556-1565.

WDC. (2015). "Visible and Infrared Scanner". [online]. Available: https://wdc.dlr.de/sensors/virs/ [Accessed 8th June 2015].

Weiss, J. L., Gutzler, D. S., Allred Coonrod, J. E. and Dahm, C. N. (2004). "Long-term vegetation monitoring with NDVI in a diverse semi-arid setting, central New Mexico, USA". Journal of Arid Environments 58 (2004) 248-271.

Wendisch, M., Pilewskie, P., Jäkel, E., Schmidt, S., Pommier, J., Howard, S., Jonsson, H. H., Guan, H., Schröder, M. and Mayer, B. (2004). “Airborne measurements of areal spectral surface albedo over different sea and land surfaces”. Journal of Geophysical Research 109: D08203, doi:10.1029/2003JD004392.

Weng, Q. (2003). “Fractal analysis of satellite-detected urban heat island effect”. Photogrammetric Engineering and Remote Sensing 69: 555-566.

Weng, Q., Lu, D. and Schubring, J. (2004). “Estimation of land surface temperature-vegetation abundance relationship for urban heat island studies”. Remote Sensing of Environment 89: 467-483.

Wilks, D. S. (2006). On “Field Significance” and the False Discovery Rate. Applied Meteorology and Climatology 45: 1181-1189.

Williams, C. A., Hanan, N. P., Neff, J. C., Scholes, R. J., Berry, J. A., Denning, A. S. and Baker, D. F. (2007). "Africa and the global carbon cycle”. Carbon Balance and Management 2(3).

Williams, D. (2012). "NDVI: What It Is? And What Does It Measure?". [Online]. Available: http://www.kars.ku.edu/media/uploads/work/griffith_jeq.pdf [Accessed 6th May 2012].

Winter, F., Wartha, C and Hofbauer, H. (1999). "NO and NO_2 formation during the combustion of wood, straw, malt waste, and peat". Bioresource Technology 70: 39-49.

Wolf, A. F. (2012). "Using WorldView-2 Vis-NIR Multispectral Imagery to Support Land Mapping and Feature Extraction Using Normalizes Difference Index Ratios". Proceedings of SPIE 8390, Algorithms and Technologies for Multispectral, Hyperspectral, and Ultraspectral imagery XVIII, 83900N, Baltimore, Maryland, USA.

Wolfe, R. E., Nishihama, M., Fleig, A. J., Kuyper, J. A., Roy, D. P., Storey, J. C. and Patt, F. S. (2002). "Achieving sub-pixel geolocation accuracy in support of MODIS Land Science". Remote Sensing of Environment 83: 31-49.

Wooster, M. J., Roberts, G., Perry, G. L. W. and Kaufman, Y. J. (2005) "Retrieval of biomass combustion rates and totals from fire radiative power observations: FRP derivation and calibration relationships between biomass consumption and fire radiative energy release". Journal of Geophysical Research: Atmospheres, vol. 110, no. D24, pp. D24311-1-D24311-24.

Wooster, M. J., Xu, W. and Nightingale, T. (2012). "Sentinel-3 SLSTR active fire detection and FRP product: pre-launch algorithm development and performance evaluation using MODIS and ASTER datasets". Remote Sensing of Environment 120: 236-254.

World Bank. (2002). “Report on Consultations with Stakeholders. World Bank–GGFR Report 1 Global Gas Flaring Reduction Public-Private Partnership”. Washington, D. C. [Online]. Available: http://www.documents.worldbank.org/curated/en/2004/01/5005873/report-consultations-stakeholders [Accessed 24th June 2011].

World Bank. (2003). “Kyoto Mechanism For Flaring Reduction. World Bank Group Report 2. Global Gas Flaring Reduction Public-Private Partnership”. Washington, D. C. [Online]. Available: http://www.siteresources.worldbank.org/INTGGFR/Resources/gfrmethodologyno6revised.pdf [Accessed 6th July 2011].

World Bank. (2004). “Strategic Gas Plan for Nigeria, Joint UNDP/World Bank Energy Sector Management Assistance Programme (ESMAP) (February 2004)”. [Online]. Available: http://www.esmap.org/sites/esmap.org/filesFR58200861713_Nigeria_strategicgasplanfornigeria.pdf [Accessed 24th August 2012].

World Bank. (2011). "Nigeria: Associated Gas Usage”. Global Gas Flaring Reduction Public-Private Partnership. [Online]. Available: http://web.worldbank.org/WBSITE/EXTERNAL/TOPICS/EXTOGMC/EXTGGFR/0,,menuPK:578075~pagePK:64168427~piPK:64168435~theSitePK:578069,00.html [Accessed 21th November 2011].

Xian, G. and Crane, M. (2006). “An analysis of urban thermal characteristics and associated land cover in Tampa Bay and Las Vegas using Landsat satellite data”. Remote Sensing of Environment 104: 147-156.

Xiaoxa, H., Zhnhai, Z. and Hongga, L. (2010). “Remote Sensing Applications for Petroleum Resources Exploration in Offshore Basins of China”. Geoscience and Remote Sensing Symposium (IGARSS), IEEE International, Honolulu, HI.

Xu, W., Wooster, M. J. and Grimmond, C. S. B. (2008). “Modelling of urban sensible heat flux at multiple scales: a demonstration using airborne hyperspectral imagery of Shanghai and a temperature-emissivity separation approach”. Remote Sensing of Environment 112: 3493-3510.

Xu, W., Wooster, M. J., Roberts, G. and Freeborn, P. (2010). "New GOES imager algorithms for cloud and active fire detection and fire radiative power assessment across North, South and Central America”. Remote Sensing of Environment 114(9): 1876-1895.

Yamaguchi, Y., Kahle, A. B., Tsu, H., Kawakami, T. and Pniel, M. (1998). “Overview of advanced spaceborne thermal emission and reflection radiometer (ASTER)”. IEEE Transactions on Geoscience and Remote Sensing 36: 1062–1071.

Yoder, B. J., and Waring, R. H. (1994). “The Normalized Difference Vegetation Index of Small Douglas-Fir Canopies with Varying Chlorophyll Concentrations.”

Remote Sensing of Environment 49 (1): 81-91, doi:10.1016/0034-4257(94)90061-2.

Yoon, S., Ye, W., Heidemann, J., Littlefield, B. and Shahabi, C. (2011). “SWATS: Wireless Sensor Networks for Steamflood and Waterflood Pipeline Monitoring”. IEEE Network: The Magazine of Global Internetworking 25(1): 50-56.

Zarco-Tejada, P. J., Berjón, A., López-Lozano, R., Miller, J. R., Martín, P., Cachorro, V., González, M. R. and De Frutos, A. (2005). “Assessing Vineyard Condition with Hyperspectral Indices: Leaf and Canopy Reflectance Simulation in a Row-Structured Discontinuous Canopy.” Remote Sensing of Environment 99 (3): 271-287. doi:10.1016/j.rse.2005.09.002.

Zhang, Z. M., He, G. J., Xiao, R. B., Wang, W. and Zhiyun, O. (2006). "Land Surface Temperature Retrieval of Beijing city using MODIS and TM Data”. 2006 IEEE International Geoscience and Remote Sensing Symposium, Vols. 1-8: 1094-1096.

Zekai, S. (2004). "Solar energy in progress and future research trends”. Progress in Energy and Combustion Science 30(4): 367-416.

Zhan, X., Sohlberg, R. A., Townshend, J. R. G., DiMiceli, C., Carroll, M. L., Eastman, J. C., Hansen, M. C and DeFries, R. S. (2002). “Detection of land cover changes using MODIS 250 m data”. Remote Sensing of Environment 83: 336-350.

Zhu, T. G. L. D. (2006). “Thermal Remote Sensing”. Publishing House of Electronics Industry, Beijing, China.

Zhukov, B., Lorenz, E., Oertel, D., Wooster, M. and Roberts, G. (2005). “Experience of detection and quantitative characterisation of fires during the experimental small satellite mission BIRD”. DLR Forschungsbericht 2005-04, DLR Optical Informations Systems, Rutherfordstr. 2, 2489 Berlin, Germany.

Ziskin, D., Elvidge, C. D., Baugh, K. E., Ghosh, T. and Sharolyn, A. (2011). “Gas Flare Brightness - Land or Offshore”. G. F. R. Partnership. Colorado, USA, NOAA. [Online]. Available: http://www.ngdc.noaa.gov/eog/interest/flare_docs/NGDC_annual_report_onshore_offshore_20110209.pdf [Accessed 10th July 2011].

A ppendices

Appendix A

Data used

Data on gas produced and amount of gas flared by petroleum companies in Nigeria; sensors and their technical characteristics; Landsat 5TM and Landsat 7 ETM+ solar irradiance; Earth-Sun distance for Landsat 5 TM and Landsat 7 ETM+; List of Landsat 5 TM and Landsat 7 ETM+ used for this study; atmospheric correction parameters from ATMCORR Calculator; and air temperature and relative humidity measured at Eleme Refinery II Petroleum Company gas flaring site, (1st set of fieldwork data).

Table A-1: Gas production versus flare (mscf) by petroleum companies in Nigeria for 2001–2010 (NNPC, 2012)

Company	2001	2002	2003	2004	2005	2006	2007	2008	2009	2010
Joint Venture										
SHELL										
Gas produced	593,567,893	527,922,606	703,097,857	740,302,238	671,326,319	735,315,476	763,905,871	800,689,383	455,894,266	777,170,431
Gas flared	321,866,427	212,456,424	262,661,338	275,248,361	216,876,732	163,405,866	96,967,320	97,879,670	77,819,939	103,477,380
% of gas flared	**54.22**	**40.24**	**37.36**	**37.18**	**32.31**	**22.22**	**12.69**	**12.22**	**17.07**	**13.31**
MOBIL										
Gas produced	431,631,620	378,350,669	320,757,623	392,065,111	446,743,226	491,110,702	464,537,142	427,115,491	427,919,671	479,251,266
Gas flared	135,229,930	123,981,525	181,228,300	174,859,914	179,534,640	201,026,922	183,528,046	130,586,764	122,567,197	122,745,744
% of gas flared	**31.33**	**32.77**	**56.50**	**44.60**	**40.19**	**40.93**	**39.51**	**30.57**	**28.64**	**25.61**
CHEVRON										
Gas produced	216,161,767	197,133,906	207,250,100	209,897,271	238,352,653	235,249,063	191,186,784	243,040,550	166,573,783	194,327,349
Gas flared	148,239,311	102,960,919	128,284,853	125,087,325	136,523,011	192,602,299	162,780,356	142,625,580	112,931,552	118,309,010
% of gas flared	**68.58**	**52.23**	**61.90**	**59.59**	**57.28**	**81.87**	**85.14**	**58.68**	**67.80**	**60.88**
TOTAL E & P										
Gas produced	111,953,117	122,444,099	138,676,284	209,208,860	207,893,532	218,968,851	289,817,162	320,372,686	302,772,348	277,253,720
Gas flared	42,134,124	44,002,030	49,644,800	47,752,399	29,840,233	64,224,402	33,842,081	35,758,806	26,825,119	30,475,467
% of gas flared	**37.64**	**35.94**	**35.80**	**22.83**	**14.35**	**29.33**	**11.68**	**11.16**	**8.86**	**10.99**
NAOC										
Gas produced	410,631,099	375,748,053	381,206,202	433,997,252	429,003,689	423,716,209	320,927,714	293,668,636	272,334,581	441,864,139
Gas flared	216,151,951	212,203,266	156,210,687	178,670,250	161,837,476	109,926,431	108,696,157	96,353,534	71,103,491	102,888,514
% of gas flared	**52.64**	**56.47**	**40.98**	**41.17**	**37.72**	**25.94**	**33.87**	**32.81**	**26.11**	**23.29**
PAN-OCEAN										
Gas produced	23,319,037	22,156,600	20,184,097	27,265,601	27,067,500	3,944,139	0	21,752,432	207,473	8,082,809
Gas flared	22,212,576	20,997,851	19,222,841	25,967,694	25,779,438	3,756,324	0	21,211,546	201,909	6,796,633
% of gas flared	**95.26**	**94.77**	**95.24**	**95.24**	**95.24**	**95.24**	**0**	**97.51**	**97.32**	**84.09**

TEXACO										
Gas produced	33,390,760	20,215,464	15,938,409	13,721,063	7,366,467	5,941,278	2,479,303	4,803,727	7,085,828	7,683,657
Gas flared	33,210,246	20,084,262	15,796,986	13,605,041	7,251,079	5,828,277	2,421,926	4,746,874	6,999,689	7,553,166
% of gas flared	**99.46**	**99.35**	**99.11**	**99.15**	**98.43**	**98.10**	**97.69**	**98.82**	**98.78**	**98.30**
JVC SUB-TOTAL										
Gas produced	1,820,657,293	1,643,971,397	1,787,110,572	2,026,457,396	2,027,753,386	2,114,245,717	2,032,853,975	2,111,442,905	1,632,787,949	2,185,633,371
	919,044,565	736,686,277	813,049,805	841,190,984	757,642,609	740,770,521	588,235,886	529,162,773	418,448,895	492,245,933
Gas flared	**50.48**	**44.81**	**45.50**	**41.51**	**37.36**	**35.04**	**28.94**	**25.06**	**25.63**	**22.52**
% of gas flared										
Production Sharing										
ADDAX										
Gas produced	N/A	N/A	40,723,887	38,036,721	46,481,560	54,580,697	68,093,192	83,876,751	72,678,580	84,989,027
Gas flared	N/A	N/A	32,261,507	28,204,432	36,112,453	46,268,969	58,549,342	73,028,019	58,614,336	64,920,466
% of gas flared	**0.00**	**0.00**	**79.22**	**74.15**	**77.69**	**84.77**	**85.98**	**87.07**	**80.65**	**76.39**
ESSO										
Gas produced	N/A	N/A	N/A	N/A	N/A	N/A	28,310,625.7	75,260,665.6	110,648,124	104,990,025
Gas flared	N/A	N/A	N/A	N/A	N/A	N/A	2,070,035,90	3,865,012	11,537,589.9	7,379,772
% of gas flared	**0.00**	**0.00**	**0.00**	**0.00**	**0.00**	**0.00**	**7.31**	**5.14**	**10.43**	**7.03**
PSC SUB-TOTAL										
Gas produced	N/A	N/A	40,723,887	38,036,721	46,481,560	54,580,697	96,403,818	159,137,417	183,326,704	189,979,052
Gas flared	N/A	N/A	32,261,507	28,204,432	36,112,453	46,268,969	60,619,378	76,893,031	70,151,926	72,300,238
% of gas flared	**0.00**	**0.00**	**79.22**	**74.15**	**77.69**	**84.77**	**62.88**	**48.32**	**38.27**	**38.06**
Service contract										
AENR										
Gas produced	N/A	N/A	N/A	N/A	N/A	N/A	N/A	7,249,199	9,948,654	6,713,476

Gas flared	N/A	N/A	N/A	N/A	N/A	N/A	N/A	7,208,919	9,891,084	6,531,333
% of gas flared	**0.00**	**0.00**	**0.00**	**0.00**	**0.00**	**0.00**	**0.00**	**99.44**	**99.42**	**97.29**
Service Contract sub-total										
Gas produced	N/A	N/A	N/A	N/A	N/A	N/A	N/A	7,249,199	9,948,654	6,713,476
Gas flared	N/A	N/A	N/A	N/A	N/A	N/A	N/A	7,208,919	9,891,084	6,531,333
% of gas flared	**0.00**	**0.00**	**0.00**	**0.00**	**0.00**	**0.00**	**0.00**	**99.44**	**99.42**	**97.29**
Sole risk/ Independent										
Gas produced	2,264,818	7,620,091	2,468,310	17,789,072	19,393,913	13,605,669	11,016,913	4,610,874	11,215,000	10,513,000
Gas flared	1,861,106	7,421,759	2,303,370	16,675,139	18,577,715	12,958,880	10,513,171	4,354,153	10,860,000	10,490,849
% of gas flared	**82.17**	**97.40**	**93.32**	**93.74**	**95.79**	**95.25**	**95.43**	**94.43**	**96.83**	**99.79**
Grand Total										
Gas produced	1,822,922,111	1,651,591,488	1,830,302,769	2,082,283,189	2,093,628,859	2,182,432,084	2,140,274,706	2,282,440,395	1,837,278,307	2,392,838,898
Gas flared	920,905,671	744,108,036	847,614,682	886,070,555	812,332,777	799,998,369	659,368,435	617,618,876	509,351,905	581,568,354
% of gas flared	**50.52**	**45.05**	**46.31**	**42.55**	**38.80**	**36.66**	**30.81**	**27.06**	**27.72**	**24.30**

Table A-2: Sensors and their technical characteristics (Bond, 2015)

Sensors	Missions	Agency	Type	Status	Wavelength/frequency	Applications
ABI	GOES-R, GOES-S, GOES-T, GOES-U	NOAA	Imaging multi-spectral radiometers (Vis/IR)	Being developed	16 bands in VIS, NIR and IR ranging from 0.47 µm to 13.3 µm VIS (~0.40 µm - ~0.75 µm) NIR (~0.75 µm - ~1.3 µm) SWIR (~1.3 µm - ~3.0 µm) MWIR (~3.0 µm - ~6.0 µm) TIR (~6.0 µm - ~15.0 µm) Resolution summary: 0.5 km in 0.64 µm band; 2.0 km in long wave IR and in the 1.378 µm band; 1.0 km in all others. [Best Resolution: 500 m]	Detects clouds, cloud properties, water vapour, land and sea surface temperatures, dust, aerosols, volcanic ash, fires, total ozone, snow and ice cover, and vegetation index.
Advanced IKFS-2	Advanced DCS, Advanced GGAK-M, Advanced IKFS-2, Advanced KMSS, Advanced MSU-MR, Advanced MTVZA, Advanced Radiomet, Advanced SAR, Advanced Scatterometer, TGSP	ROSHYDROMET (ROSKOSMOS)	Atmospheric temperature and humidity sounders	Planned	3.7-15.5 µm, more than 8000 spectral channels MWIR (~3.0 µm - ~6.0 µm) TIR (~6.0 µm - ~15.0 µm) Resolution Summary: 35-100 km. [Best Resolution: 35 m] Swath Summary: 1000/2000 km [Max Swath: 2000 km] Accuracy Summary: 0.5 K	Atmospheric temperature/humidity profiles, data on cloud parameters, water vapour and ozone columns amounts and surface temperature.
Advanced KMSS	Meteor-MP N1, Meteor-MP N2, Meteor-MP N3,	ROSHYDROMET (ROSKOSMOS	Imaging multi-spectral radiometers (Vis/IR)	Planned	0.4-0.9 µm, 6 channels VIS (~0.4 µm - ~0.75 µm) NIR (~0.75 µm - ~1.3 µm)	Multispectral images of land and sea surfaces and ice cover.

					Resolution Summary: 60-100 m. [Best Resolution: 60 m] Swath Summary 900 km. [Maximum Swathe: 900 km]	
Advanced MTVZA	Meteor-MP N1, Meteor-MP N2, Meteor-MP N3,	ROSHYDROMET (ROSKOSMOS	Imaging multi-spectral radiometers (Passive microwave)	Planned	10.6-183.3 GHZ, 26 channels MW (~1.0 µm - ~100 µm) Resolution Summary : 12-75 km Swath Summary : 2600 km Accuracy Summary : 0.4-2.0 k, depending on spectral band	Atmospheric temperature and humidity profiles, precipitation, sea-level wind speed, snow/ice coverage.
AEISS	KOMPSAT-3	KARI (ASTRIUM)	High resolution optical imagers	Operational	Panchromatic VIS: 0.50-0.90 µm, VIS: 0.45-0.52 µm, 0.52-0.60 µm, 0.63-0.69 µm, NIR: 0.76-0.90 µm VIS (~0.40 µm - ~0.75 µm) NIR (~0.75 µm - ~1.3 µm) Resolution Summary: Pan: 0.8 m; VIR: 4 m. [Best Resolution: 0.8 m] Swath Summary: 15 km. [Max Swath: 15 km]	High resolution imager for land applications of cartography and disaster monitoring.
AIRS	Aqua-Aqua (formerly EOS PM-1)	NASA	Atmospheric temperature and humidity sounders	Operational	VIS-TIR: 0.4-1.7 µm, 3.4-15.4 µm, Has approximately 2382 bands from VIS to TIR VIS (~0.40 µm - ~0.75 µm)	High spectral resolution measurement of temperature and

					NIR (~0.75 µm - ~1. 3 µm) MWIR (~3.0 µm - ~6.0 µm) TIR (~6.0 µm - ~15.0 µm) Resolution Summary: 1.1 degree (13 × 13 km at nadir) Swath Summary: ± 48.95 degrees Accuracy Summary: Humidity: 20 %, Temperature: 1 K	humidity profiles in the atmosphere. Long-wave Earth surface emissivity. Cloud diagonistics. Trace gas profiles. Surface temperatures.
ALISS III	RESOURCESAT-3	ISRO	Imaging multi-spectral radiometers (Vis/IR)	Planned	3 bands in VNIR and 1 band in SWIR VIS (~0.40 µm - ~0.75 µm) NIR (~0.75 µm - ~1. 3 µm) SWIR (~1.3 µm - ~3.0 µm) Resolution Summary: 23.5, 10 m. [Best Resolution: 10 m] Swath Summary: 700 km. [Maximum Swath: 700 km]	For crops and vegetation dynamics, natural resources census, disaster management and large scale mapping themes.
ATMS	Suomi NPP, NPOESS-1, JPSS-1, JPSS-2, NPOESS-3, NPOESS-5	NASA (NOAA)	Atmospheric temperature and humidity sounders	Operational	Microwave: 22 bands, 23-184 GHz MW (~1.0 µm - ~100 µm) Resolution Summary: 5.2-1.1 degree Swath Summary: 2300 km Accuracy Summary: 0.75-3.60 K	Collects microwave radiance data that when combined with the CrlS data will permit calculation of atmospheric temperature and water vapour profiles.
AWiFS	RESOURCESAT-1, RESOURCESAT-2, AWiFSSAT, RESOURCESAT-2A,	ISRO	Imaging multi-spectral radiometers (VIS/IR)	Operational	VIS: 0.52-0.59 µm and 0.62-0.68 µm, NIR: 0.77-0.86 µm, SWIR: 1.55-1.7 µm VIS (~0.4 µm - ~0.75 µm) NIR (~0.75 µm - ~1.3 µm) SWIR (~1.3 µm - ~3.0 µm)	Vegetation and crop monitoring, resource assessment (regional scale), forest mapping, land cover/land use mapping and change detection.
C-Band SAR	Sentinel-1 A,	ESA	Imaging	Operation	C-band: 5.405 GHz; HH, VV, W,	Marine core services,

	Sentinel-1 B, Sentinel-1 C		microwave radars	al	HH+HV; Incidence angle: 20-45 MW (~1.0 cm - ~100 cm) C-Band (8-4 GHz) Resolution Summary: Strip mode: 9 m; Interferometric wide swath mode: 20 m, extra swath mode: 50 m, wave mode: 50 m. [Best Resolution: 9 m] Swath Summary: Strip mode: 80 km; Interferometric wide swath mode: 250 km, extra-wide swath mode: 400 km, Wave mode: sampled images [Maximum Swath: 400 km] Accuracy Summary: NESZ: -22 Db; PTAR; -25 d B; DTAR: -22 Db; Radiometric accuracy 1 Db (3sigma); Radiometric stability: 0.5 Db (3 sigma)	land monitoring and emergency services. Monitoring sea ice zones and arctic environment. Surveillance of marine environment, monitoring land surface motion risks, mapping of land surfaces (forest, water and soil, agriculture), mapping in support of humanitarian aid in crisis situations.
CCD (HJ)	HJ-1 A, HJ-1 B	CAST	High resolution optical imagers	Operation al	0.43-0.9 μm (4 bands) VIS (~0.4 μm - ~0.75 μm) NIR (~0.75 μm - ~1.3 μm) Resolution Summary: 30 m [Best Resolution: 30 m] Swath Summary: 360 km (per set), 720 km (two sets) [Maximum Swath: 720 km]	Multi-spectral measurements of Earth surface for natural environment and disaster applications.
CCD (ZY-02C and ZY-3)	ZY-02C, ZY-3	CRESDA	Imaging multi-spectral radiometers (Vis/IR)	Operation al	0.5-0.8 μm VIS (~0.4 μm - ~0.75 μm) Resolution Summary: 2.36 m (ZY-02C HR), 2.1 m (ZY-3) Swath Summary: 52 km (ZY-3, 54 KM (ZY-02C)	Earth resource, environmental monitoring, land use
CCD camera	INSAT-2E, INSAT-3A	ISRO	Imaging multi-spectral	Operation al	VIS : 0.62-0.68 μm; NIR: 0.77-0.86 μm; SWIR: 1.55-1.69 μm	Cloud and vegetation monitoring

			radiometers (Vis/IR)		VIS (~0.4 µm - ~0.75 µm) NIR (~0.75 µm - ~1.3 µm) SWIR (~1.3 µm - ~3.0 µm)	
CIRC	ALOS-2	JAXA	Other	Operational	TIR: 8-12 µm TIR (~6.0 µm - ~15.0 µm) Accuracy Summary: 0.2 K @ 300K Resolution Summary: 200 m [Best Resolution: 200 m] Swath Summary: 0.2 km [Maximum Swath: 128 km]	Active fire detection. Land surface temperature.
COSI	KOMPSAT-5	KARI (TAS-i)	Imaging microwave radars	Operational	Microwave: MW (~1.0 cm- ~100 cm) ; X-Band (12.5-8 GHz) Resolution Summary: High: 1 m; Swath Summary: 100 km [Maximum Swath: 100 km]	SAR for land applications of cartography and disaster monitoring.
CrIS	Suomi NPP, NPOESS-1, JPSS-1, JPSS-2, NPOESS-3, NPOESS-5,	NOAA	Atmospheric temperature and humidity sounders	Operational	MWIR-TIR: 3.92-4.4 µm, 5.7-8.62 µm, 9.1-14.7 µm, 1300 spectral channels NIR (~0.75 - ~1.3 µm) MWIR (~3.0 - ~6.0 µm) TIR (~6.0 - ~15.0 µm) Resolution Summary : IFOV 14 km diameter, 1 km vertical layer resolution Swath Summary: 2200 km Accuracy Summary: Temperature profiles: to 0.9 K; Moisture profiles: 20-35 %, Pressure profiles: 1 %	Daily measurements of vertical atmospheric distribution of temperature, moisture and pressure
CSG SAR	CSG-1, CSG-2	ASI (MoD Italy)	Imaging microwave radars	Approved	Microwave: X-band (9.6 GHz) single-, dual- and qua-polarization. MW (~1.0 - ~100 cm) X-Band (12.5-8 GHz) Resolution Summary: [range × azimuth]; Spotlight: 0.8 × 0.8 m (Single pol) 1 × 1 m (Single/Dual pol),	All-weather images of ocean, land and ice for monitoring of land surface processes, ice, environmental monitoring, risk management,

					Stripmap: 3 × 3 m (Single/Dual/Quad pol), ScanSAR: 4 × 20 or 6 × 40 m (Single/Dual pol). [Best Resolution: 0.8 m] Swath Summary: Dual polarisation modes: Spotlight: 10 km; Stripmap: 40 km; ScanSAR: 100 or 200 km. Quad polarisation modes: 15 km. [Maximum Swath: 200 km]	environmental resources, maritime management, Earth topographic mapping.
DCS (SABIA_MAR)	SAC-E/SABIA_MAR-A, SAC-E/SABIA_MAR-B,	CONAE	Data collection	Proposed	Not available.	Environmental and meteorological data collection from ground platforms (UHF 401.62 MHz uplink // S-band downlink).
DCS (SAC-D)	SAC-D/Aquarius	CONAE	Data collection	Operational	Not available.	Environmental and meteorological data collection from ground platforms (UHF 401.55 MHz uplink).
ECOSTRESS	ECOSTRESS-on-ISS	NASA	Imaging multi-spectral radiometers (VIS/IR)	Being developed	TIR (~6.0 μm - ~15.0 μm)	This project will use a high-resolution thermal infrared radiometer to measure plant evapotranspiration, the loss of water from growing leaves and evaporation from the soil.
Event Imaging Spectrometer from GEO (GeoCape)	GEO-CAPE	NASA	High resolution optical imagers	Proposed	UV/VIS (310-481 nm) and the VIS/NIR (500-900 nm) VIS (~0.40 μm - ~0.75 μm) Resolution Summary: 250 m spatial resolution, 20-50 nm (MODIS-like) spectral bands. [Best Resolution: 250	Predictions of impacts from oil spills, fires, water pollution from sewage and other sources, fertilizer runoff, and other

					nm]. Swath Summary: 300 km swath width coastal regions at targets of opportunity.	environmental threats. Detection and tracking of waterborne hazardous materials. Monitoring and improvement of coastal health.
GEDI	GEDI-on-ISS	NASA	Lidars	Being developed	Not available.	This project will use a laser-based system to study a range of climates, including the observation of the forest canopy structure over the tropics, and the tundra in high northern latitudes.
GeoSTAR	PATH	NASA	Imaging multi-spectral radiometers (Passive microwave)	Proposed	50-57 GHz, 165-183 GHz, and possibly 118-125 GHz. MW (~1.0 cm - ~100 cm) Resolution Summary: Temporal resolution is 15 to 30 minutes; 25-50 km nadir Swath Summary: Temporal resolution is 15 to 30 minutes; 25-50 km nadir. Accuracy Summary: < .5 K (brightness temperature).	High frequency, all-weather temperature and humidity soundings for weather forecasting and SST.
Geoton-L1(2)	Resurs-P N1, Resurs-P N2, Resurs-P N3,	ROSKOSMOS	High resolution optical imagers	Operational	0.58-0.8 μm; 0.45-0.52 μm; 0.52-0.60 μm; 0.61-0.68 μm; 0.72-0.80 μm; 0.80-0.90 μm. VIS (~0.40 μm - ~0.75 μm) NIR (~0.75 μm - ~1.3 μm) Resolution Summary: 1 m; 3 m [Best Resolution: 1m].	Multi-spectral images of land surface and oceans.

					Swath Summary: [Maximum Swath: 950 km]	
GERB	Meteosat-8, Meteosat-9, Meteosat-10, Meteosat-11	EUMETSAT (ESA) (RAL)	Earth radiation budget radiometers	Operational	SW: 0.32-4.0 µm; LW: 4.0-30 µm (by subtraction) UV (~0.01 µm - ~0.40 µm) VIS (~0.40 µm - ~0.75 µm) NIR (~0.75 µm - ~1.3 µm) SWIR (~1.3 µm - ~3.0 µm) MWIR (~3.0 µm - ~6.0 µm) TIR (~6.0 µm - ~15.0 µm) FIR (~15.0 µm - ~0.1 cm)	Measures long and short wave radiation emitted and reflected from the Earth's surface, clouds and top of atmosphere. Full Earth disk, all channels in 5 minutes.
GOCI	COMS	KARI (ASTRIUM) KORDI	Ocean colour instruments	Operational	VIS-NIR: 0.40-0.88 µm (8 channels) VIS (~0.40 µm - ~0.75 µm) NIR (~0.75 µm - ~1.3 µm) Resolution Summary : 236 × 500 m.[Best Resolution : 236 m] Swath Summary: 1440 km [Maximum Swath: 1440 km]	Ocean colour information, coastal zone monitoring, land resources monitoring.
GPSRO (Oersted)	Ørsted (Oersted)	NASA	Atmospheric temperature and humidity sounders	Operational	Not available	Measurements of atmospheric temperature, pressure and water vapour content.
GPSRO (Terra-SAR)	Terra-SAR-X	NASA	Atmospheric temperature and humidity sounders	Operational	Not available	Measurements of atmospheric temperature, pressure and water vapour content.
GSA (1)	Resurs-P N1, Resurs-P N2, Resurs-P N3	ROSKOSMOS	Other	Operational	0.4-1.1 µm , 96 spectral bands VIS (~0.40 µm - ~0.75 µm) NIR (~0.75 µm - ~1.3 µm) Resolution Summary; [Best Resolution: 30 m]	Land surface monitoring.

					Swath Summary: [Maximum Swath; 950 km]	
GSA (2)	Obzor-O N1, Obzor-O N2	ROSKOSMOS	Other	Prototype	0.4-1.1 µm VIS (~0.40 µm - ~0.75 µm) NIR (~0.75 µm - ~1.3 µm) Resolution Summary; [Best Resolution: 30 m] Swath Summary: [Maximum Swath; 22 km]	Land surface monitoring.
HDWL (3D Winds)	3D Winds	NASA	Lidars	Proposed	2.051 µm and 0.355 µm UV (~0.01 µm - ~0.40 µm) SWIR (~1.3 µm - ~3.0 µm) Resolution Summary: 300 km along track horizontal resolution Swath Summary: View 45 degrees of nadir at four azimuth angles: 45, 135, 225, 315 deg. Accuracy Summary; 2-3 m/s LOS wind accuracy projected into horizontal from all effects including sampling error.	Tropospheric winds for weather forecasting and pollution transport.
HIRDLS	Aqua-Aqua, Aura-Aura	NASA (UKSA)	Atmospheric chemistry	Operational	TIR; 612-17.76 µm (21 channels) TIR (~6.0 µm - ~0.40 µm) FIR (~15.0 µm - ~0.1 cm) Resolution Summary: Vertical: 1 km; Horizontal 10 km Accuracy Summary: Trace gas: 10 %;	Measures atmospheric temperature, concentrations of ozone, water vapour, methane, NO_x, N_2, CFCs and other minor

					Temperature; 1K; Ozone: 10 %	species, aerosol concentration, location of polar stratospheric clouds and cloud tops. Currently not collecting data on Aqua.
HiRI	Pleiades 1A, Pleiades 1B	CNES	High resolution optical imagers	Operational	4 bands + PAN: Near IR (0.77-0.91 µm)); Red (0.61-0.71 µm); Green (0.50-0.60 µm); Blue (0.44-0.54 µm); Pan (0.47-0.84 µm) VIS (~0.40 µm - ~0.75 µm) NIR (~0.75 µm - ~1.3 µm) Resolution Summary: 0.70 m [Best Resolution: 0.70 m] Swath Summary: 20 km swath at nadir. Agile platform ± off-track [Best Swath: 20 km]	Cartography, land use, risk, agriculture and forestry, civil planning and mapping, digital terrain models, defence.
HIRS/3	NOAA-15, NOAA-16, NOAA-17,	NOAA	Atmospheric temperature and humidity sounders	Operational	VIS-TIR: 0.69-14.95 µm (20 channels) VIS (~0.40 µm - ~0.75 µm) NIR (~0.75 µm - ~1.3 µm) SWIR (~1.3 µm - ~3.0 µm) MWIR (~3.0 µm - ~6.0 µm) TIR (~6.0 µm - ~15.0 µm) FIR (~15.0 µm - ~0.1 cm) Resolution Summary: 20.3 km Swath Summary: 2240 km	Atmospheric temperature profiles and data on cloud parameters, humidity soundings, water vapour, total ozone content, and surface temperatures.
HIRS/4	NOAA-18, Metop-A, NOAA-19, Metop-B	NOAA	Atmospheric temperature and humidity sounders	Operational	VIS-TIR: 0.69-14.95 (20 channels) VIS (~0.40 µm - ~0.75 µm) NIR (~0.75 µm - ~1.3 µm) SWIR (~1.3 µm - ~3.0 µm)	Atmospheric temperature profiles and data on cloud parameters, humidity

					MWIR (~3.0 µm - ~6.0 µm) TIR (~6.0 µm - ~15.0 µm) Resolution Summary: 20.3 km Swath Summary: 2240 km	soundings, water vapour, total ozone content, and surface temperatures. Same as HIRS/3, with 10 km IFOV.
HRMX	CARTOSAT-2C, CARTOSAT-2E	ISRO	Imaging multi-spectral radiometers (VIS/IR)	Proposed	4 bands MX in VIS and NIR VIS (~0.40 µm - ~0.75 µm) NIR (~0.75 µm - ~1.3 µm) Resolution Summary: 0.65 m / 2 m [Best Resolution: 0.65 m] Swath Summary: 10 km [Max Swath: 10 km]	For crops and vegetation dynamics, natural resources census, disaster management and large scale mapping of themes.
HRMX-TIR	GISAT	ISRO	Imaging multi-spectral radiometers (VIS/IR)	Proposed	MX (3 Bands TIR) TIR (~6.0 µm - ~15.0 µm) Resolution Summary: 1.5 km [Best Resolution: 1500 m]	Continuous monitoring of the earth and natural resources applications in hyperspectral thermal bands.
HRMX-VNIR	GISAT	ISRO	Imaging multi-spectral radiometers (VIS/IR)	Proposed	MX (4 Bands VNIR) VIS (~0.40 µm - ~0.75 µm) NIR (~0.75 µm - ~1.3 µm) Resolution Summary: 50 m [Best Resolution: 50 m]	Continuous monitoring of the earth and natural resources applications in Visible and VNIR bands.
HSC (SAC-D/Aquarius)	SAC-D/Aquarius	CONAE	Imaging multi-spectral radiometers (VIS/IR)	Operational	PAN (VIR-NIR) : 450-900 nm VIS (~0.40 µm - ~0.75 µm) NIR (~0.75 µm - ~1.3 µm) Resolution Summary : 200-300 m [Best Resolution : 200 m] Swath Summary : 1600 km [Best Swath : 1600 km]	High Sensitivity Camera (HSC) measures top of atmosphere radiance in the VIS spectral range measured by a high sensitivity sensor detects: urban lights, electric storms, polar

						regions, snow cover, forest fires, sea surveillance.
HIS	EnMAP	DLR	Hyperspectral imagers and imaging multi-spectral radiometers (VIS/IR)	Approved	420-2450 nm VIS (~0.40 µm - ~0.75 µm) NIR (~0.75 µm - ~1.3 µm) SWIR (~1.3 µm - ~3.0 µm) Resolution Summary: GSD 30 m [Best Resolution: 30 m] Swath Summary: 30 km [Maximum Swath: 30 km] Radiometric: < 5 %	Detailed monitoring and characterization of rock and soil targets, vegetation, inland and coastal waters on a global scale.
HIS (HJ-1A)	HJ-1A	CAST	Imaging multi-spectral radiometers (VIS/IR)	Operational	0.45-0.95 µm (128 bands) VIS (~0.40 µm - ~0.75 µm) NIR (~0.75 µm - ~1.3 µm) Resolution Summary : 100 m [Best Resolution : 100 m] Swath Summary: 50 km [Maximum Swath: 50 km]	Hyperspectral measurements for environment and disaster management operations.
HYC	PRISMA	ASI	Hyperspectral imagers and imaging multi-spectral radiometers (VIS/IR)	Approved	VNIR: 400-1010nm; SWIR: 920-2500 nm VIS (~0.40 µm - ~0.75 µm) NIR (~0.75 µm - ~1.3 µm) SWIR (~1.3 µm - ~3.0 µm) Resolution Summary : 30 m [Best Resolution : 30 m] Swath Summary: 30 km [Maximum Swath: 30 km] Accuracy Summary: Spectral resolution: 10 nm	Hyperspectral data for complex land ecosystem studies.

Hyperion	NMP EO-1	NASA	Hyperspectral imagers and imaging multi-spectral radiometers (VIS/IR)	Operational	VIS-NIR: 400-1000 nm; NIR-SWIR: 900-2500; 10 nm spectral resolution for 220 bands VIS (~0.40 µm - ~0.75 µm) NIR (~0.75 µm - ~1.3 µm) SWIR (~1.3 µm - ~3.0 µm) Resolution Summary : 30 m [Best Resolution : 30 m] Swath Summary: 185 km [Maximum Swath: 185 km] Accuracy Summary: SNR @ 10 % reflected target; vis: 10-40; swir: 10-20.	Hyperspectral imaging of land surfaces.
HYSI (Cartosat-3)	CARTOSAT-1A, CARTOSAT-1B, CARTOSAT-1C,	ISRO	High resolution optical imagers	Being developed	VNR: 0.40-0.9 (50 bands); SWIR: 0.9-2.4 µm (150 bands) NIR (~0.75 µm - ~1.3 µm) SWIR (~1.3 µm - ~3.0 µm) Resolution Summary 12 m Swath Summary: 15 km [Maximum Swath: 15 km]	High resolution images for study agriculture, geology and water resources for generation of spectral library, geological mapping, water quality assessment, precision agriculture, discrimination of vegetation types, coastal studies, oil and mineral exploration etc.
IASI-NG	EPS-SG-a-EUMETSAT Polar System	CNES (EUMETSAT)	Atmospheric temperature and humidity sounders	Proposed	MWIR-TIR: 645-2760 cm-1 or 3.4-15.5 µm (16921 channels) MWIR (~3.0 µm - ~6.0 µm) TIR (~6.0 µm - ~15.0 µm) Resolution Summary: Vertical: 1-30	Measures tropospheric moisture and temperature, column integrated contents of ozone, carbon

					km; Horizontal: 25 km Swath Summary: 2052 km Accuracy Summary: TBC	monoxide, methane, dinitrogen oxide and other minor gases which affect tropospheric chemistry. Also, measures sea and land surface temperature.
IK-radiometer (1)	Obzor-O N1, Obzor-O N2	ROSKOSMOS	Imaging multi-spectral radiometers	Proposed	MWIR (~3.0 µm - ~6.0 µm) TIR (~6.0 µm - ~15.0 µm)	Parameters of clouds, snow, ice and land cover, vegetation, surface temperature, fire detection.
IRS	CBERS-3, CBERS-4,	CAST (INPE)	Imaging multi-spectral radiometers (VIS/IR)	Operational	0.5-0.9 ; 1.55-1.75 ; 2.08-2.35 ; 10.4-12.5 VIS (~0.4.µm - ~0.75 µm) NIR (~0.75 µm - ~1.3 µm) SWIR (~1.3 µm - ~3.0 µm) TIR (~6.0 µm - ~15.0 µm) Resolution Summary: PAN, SWIR: 40 m; TIR: 80 m [Best Resolution: 40 m] Swath Summary: 120 km [Maximum Swath : 120 km]	Earth resources, environmental monitoring, land use.
IRS	MTG-S1 (Meteosat), MTG-S1 (Sounding), MTG-S2 (Meteosat), MTG-S2 (Sounding)	EUMETSAT (ESA)	Atmospheric temperature and humidity sounders	Being developed	LWIR: 700-1210 cm^-1; MWIR: 1600-2175 cm^-1 MWIR (~3.0 µm - ~6.0 µm) TIR (~6.0 µm - ~15.0 µm) Resolution Summary: Horizontal: 4 km at SSP; Vertical: 1 km [Best Resolution: 4000 m] Swath Summary: 640 × 640 km	Measurements of vertically resolved clear sky atmospheric motion vectors, temperature and water vapour profiles.

					dwells, step and stare, moving alternately E-W and W-E moving up S-N one dwell step at the end of each row of dwells. Each disc is divided in 4 areas of Local Area Coverage (LAC). Accuracy Summary: Clear sky AMVs: 2 m/s; temperature profile: 1K; water vapour profile: 5 %	
Laser altimeter (LIST)	LIST	NASA	Lidars	Proposed	Planned: 1030 µm FIR (~15.0 µm - ~0.1 cm)	New technology laser system that performs spatial mapping of Earth's surface from an orbital platform.
L-band Radiometer (SMAP)	SMAP	NASA	Imaging multi-spectral radiometers (passive microwave)	Being developed	L-band (1.4 GHz) L-band (2-1 GHz) Resolution Summary: 40 km spatial resolution; 3 days temporal resolution. Swath Summary: 40 degrees constant incidence angle across the 1000 km swath [Maximum Swath: 1000 km] Accuracy Summary: 1.3 K accuracy brightness temperature	High-accuracy measurements of brightness temperatures for global estimates of surface soil moisture for climate modelling and weather prediction.
LISS-IV	RESOURCESAT-1, RESOURCESAT-2, RESOURCESAT-2A,	ISRO	High resolution optical imagers	Operational	VIS: 0.52-0.59 µm, 0.62-0.68 µm; NIR: 0.77-0.86 µm VIS (~0.4.µm - ~0.75 µm) NIR (~0.75 µm - ~1.3 µm) Resolution Summary : 5.8 m [Best Resolution : 5.8 m] Swath Summary: 70 km [Maximum Swath: 70 km]	Vegetation monitoring, improved crop discrimination, crop yield, disaster monitoring and rapid assessment of natural resources.
LOTUSat 1 SAR	LOTUSat 1	VAST	Imaging microwave radars	Proposed	X-band SAR X-Band (12.5-8 GHz)	The LOTUSSat 1 SAR instrument is designed for land cover measurements and

						applications.
MERSI	FY-3A, FY-3B, FY-3C	NRSCC, (CAST), (NSMC-CMA)	Imaging multi-spectral radiometers (VIS/IR)	Operational	25 channels from 0.47-12.0 µm VIS (~0.4.µm - ~0.75 µm) NIR (~0.75 µm - ~1.3 µm) Resolution Summary : 250 m for broadband channels, 1 km for narrowband channels [Best Resolution: 250 m] Swath Summary: 2800 km [Maximum Swath: 2800 km Accuracy Summary: 0.25-1.0 km	Measurement of vegetation indexes and ocean colour.
MERSI-2	FY-3D, FY-3E, FY-3F, FY-3G	NRSCC (CAST), (NSMC-CMA), (CNSA)	Imaging multi-spectral radiometers (VIS/IR)	Approved	Not available	Measurement of vegetation indexes and ocean colour.
MIRS	Sich-2	NSAU	Imaging multi-spectral radiometers (VIS/IR)	Operational	NIR : 1.55-1.7 µm SWIR : (~1.3 µm - ~3.0 µm) Resolution Summary: 41.4 m [Best Resolution: 41:4 m] Swath Summary: 55.3 km pointable ± 35 ° from nadir [Maximum Swath: 55 km Accuracy Summary: 8 bits	Scanner images of land surface in middle infra-red range.
MS (GIS TDA)	THEOS	GISTDA	Imaging multi-spectral radiometers (VIS/IR)	Operational	0.45-0.52 µm, 0.53-0.60 µm, 0.62-0.69 µm, 0.77-0.90 µm VIS (~0.4.µm - ~0.75 µm) NIR (~0.75 µm - ~1.3 µm) Resolution Summary: 15 m [Best Resolution: 15 m] Swath Summary: 90 km [Maximum Swath: 90 km	THEOS MS consists of 4 spectral bands (R,G,B, NIR) with resolution 15 m and swath width at 90 km. The applications which are suitable for this instrument such as cartography, land use,

					Accuracy Summary: GSD for MS =15 m± 10 %; MTF for MS > 0.12 in each band.	land cover change management, agricultural and natural resources management, etc.
MSI (EarthCARE)	EarthCARE	ESA	Imaging multi-spectral radiometers (VIS/IR)	Approved	VIS-NIR : Band 1 : VIS, 670nm ; Band 2 : NIR, 865 nm ; Band 3 : SWIR-1, 1.67 µm; Band 4 : SWIR-2, 2.21 µm; Thermal infrared : Band 5 : 8.8 µm; Band 6 : 10.8 µm; Band 7 : 12.0 µm VIS (~0.4.µm - ~0.75 µm) SWIR (~1.3 µm - ~3.0 µm) TIR (~6.0 µm - ~15.0 µm)	Observation of cloud properties and aerosol (aerosol to be confirmed)
MSI (Sentinel-2)	Sentinel-2 A, Sentinel-2 B, Sentinel-2 C	ESA (EC)	High resolution optical imagers	Being developed	13 bands in the VNIR-SWIR VIS (~0.4.µm - ~0.75 µm) SWIR (~1.3 µm - ~3.0 µm) Resolution Summary: 10 m [Best Resolution: 10 m] Swath Summary: 290 km [Maximum Swath: 290 km Accuracy Summary: Absolute radiometric accuracy for Level 1C data: 3-5 %.	Optical high spatial resolution imagery over land and coastal areas for GMES operational services.
Multi-spectral thermal infrared imager (HyspIRI)	HyspIRI	NASA	Imaging multi-spectral radiometers (VIS/IR)	Proposed	3-5 µm, 7.5-12 µm MWIR (~3.0 µm - ~6.0 µm) TIR (~6.0 µm - ~15.0 µm) Resolution Summary: 60 m at nadir; 1 week revisit time [Best Resolution: 60 m] Swath Summary: 600 km [Maximum Swath: 600 km	Ecosystem focussed mission with measurements of surface and cloud imaging with high spatial resolution, stereoscopic observation of local

					Accuracy Summary: 0.1 K, < .01 μm.	topography, cloud heights, volcanic plumes, and generation of local surface digital elevation maps, surface temperature and emissivity.
MVIRS	FY-3F, FY-3G	NRSCC, (CAST), (CNSA)	Imaging multi-spectral radiometers (VIS/IR)	Approved	VIS-TIR : 0.47-12.5 (20 channels) VIS (~0.40 μm - ~0.75 μm) SWIR (~1.3 μm - ~3.0 μm) MWIR (~3.0 μm - ~6.0 μm) TIR (~6.0 μm - ~15.0 μm)	Measures surface temperature and cloud and ice cover. Used for snow and flood monitoring and surface temperature.
MWTS-2	FY-3C, FY-3D, FY-3E, FY-3F, FY-3G	CAST, (NSMC-CMA), (CNSA)	Atmospheric temperature and humidity sounders	Operational	Not available	Temperature sounding in nearly all weather conditions.
MWS	EPS-SG-a, EPS-SG-b	EUMETSAT, (ESA)	Atmospheric temperature and humidity sounders	Proposed	25 channels from 23.8 to 229 GHz MW (~1.0 cm - ~100 cm) Resolution Summary: Footprint size: 17-80 km (Threshold)	All-weather night-day temperature sounding.
NigeriaSat Medium Resolution	NigeriaSat-X	NASRDA	Imaging multi-spectral radiometers (VIS/IR)	Operational	NIR : ~0.75 μm - ~1.3 μm, VIS : ~0.40 μm - ~0.75 μm VIS (~0.40 μm - ~0.75 μm) NIR (~0.75 μm - ~1.3 μm) Resolution Summary: 22 m multispectral (red, green and NIR) [Best Resolution: 22 m] Swath Summary: 600 km × 600 km [Maximum Swath: 600 km Accuracy Summary: 150-300 m.	High resolution images for monitoring of land surface and coastal processes and for agricultural, geological and hydrological applications.

NigeriaSat Medium and High Resolution	NigeriaSat-2	NASRDA	High resolution imagers	Operational	NIR : ~0.75 µm - ~1.3 µm, VIS : ~0.40 µm - ~0.75 µm VIS (~0.40 µm - ~0.75 µm) NIR (~0.75 µm - ~1.3 µm) Resolution Summary: 2.5 PAN, 5 m multispectral (red, blue, green and NIR), 32 m multispectral (red, green, NIR) [Best Resolution: 2.5 m] Swath Summary: 20 km × 20 km, 300 km × 300 km, [Maximum Swath: 300 km] Accuracy Summary: 35-45 m.	High resolution images for monitoring of land surface and coastal processes and for agricultural, geological and hydrological applications.
NIRST	SAC-D/Aquarius	CONAE (CSA)	Imaging multi-spectral radiometers (VIS/IR)	Operational	Band 1 : 3.4-4.2 ; Band 2 : 10.4-11.3 ; Band 3 : 11.4-12.3 MWIR (~3.0 µm - ~6.0 µm) TIR (~6.0 µm - ~15.0 µm) Resolution Summary: Space resolution: 450 m (at nadir) [Best Resolution: 450 m] Swath Summary: Instant: 182 km; Extended: 1000 km [Maximum Swath: 1000 km]	NIRST (two linear microbolometric arrays, respectively sensitive to the TIR bands). It measures the characteristics of high temperature events on land (fires & volcanoes) and sea surface temperatures on selected targets.
OLCI	Sentinel-3 A, Sentinel-3 B, Sentinel-3 C	ESA (EC)	Imaging multi-spectral radiometers (VIS/IR)	Approved	21 bands in VNIR/SWIR VIS (~0.40 µm - ~0.75 µm) NIR (~0.75 µm - ~1.3 µm) Resolution Summary: 300 m [Best Resolution: 300 m] Swath Summary: 1270 km, across-track tilt 12.2 degrees to the West	Marine and land services

					[Maximum Swath: 1270 km] Accuracy Summary: 2 % absolute, 0.1 % relative	
OLI	Landsat 8	USGS (NASA)	Imaging multi-spectral radiometers (VIS/IR)	Operational	VIS-SWIR : 9 bands : 0.43-2.3 µm VIS (~0.40 µm - ~0.75 µm) NIR (~0.75 µm - ~1.3 µm) SWIR (~1.3 µm - ~3.0 µm) Resolution Summary: Pan: 15 m; VIS-SWIR: 30 m [Best Resolution: 15 m] Swath Summary: 185 km, [Maximum Swath: 185 km] Accuracy Summary: Absolute geodetic accuracy of 65 m; relative geodetic accuracy of 25 m (excluding terrain effects); geometric accuracy of 12 m or better.	Measures surface radiance and emittance, land cover state and change (e.g. vegetation type). Used as multi-purpose imagery for land applications.
OLS	DMSP F-8, DMSP F-9, DMSP F-10, DMSP F-11, DMSP F-12, DMSP F-13, DMSP F-14, DMSP F-15, DMSP F-16, DMSP F-17, DMSP F-18, DMSP F-19, DMSP F-29	NOAA, DoD (USA)	Imaging multi-spectral radiometers (VIS/IR)	Operational	VIS-NIR: 0.4-1.1 µm; TIR : 10.0-13.4 µm, and 0.47-0.95 µm VIS (~0.40 µm - ~0.75 µm) NIR (~0.75 µm - ~1.3 µm) TIR (~6.0 µm - ~15.0 µm) Resolution Summary: 0.56 km (fine), 5.4 km (stereo products) [Best Resolution: 560 m] Swath Summary: 3000 km,	Day and night cloud cover imagery
PAN (CartoSat-3)	CARTOSAT-3	ISRO	High resolution optical imagers	Being developed	Panchromatic VIS : 0.5-0.75 µm VIS (~0.40 µm - ~0.75 µm)	High resolution images for study of

					Resolution Summary : 0.3 m [Best Resolution: 0.3 m] Swath Summary: 15 km [Maximum Swath: 15 km]	topography, urban areas, development of DTM, run-off models etc. Urban sprawl, forest cover/timber volume, land use change.
PAN (ZY-02C)	ZY-02C	CRESDA	High resolution optical imagers	Operational	0.5-0.59 µm, 0.63-0.69 µm, 0.77-0.89 µm, 0.51-0.85 µm VIS (~0.40 µm - ~0.75 µm) Resolution Summary : 5 m panchromatic and 10 m multispectral [Best Resolution: 5 m] Swath Summary: 60 km [Maximum Swath: 60 km]	Earth resources, environmental monitoring, land use.
PAN+MS (RGB+NIR)	Ingenio	CDTI (ESA)	High resolution optical imagers	Being developed	VIS+NIR band: 520-670 nm, 410-480 nm, 610-670 nm, 790-880 nm VIS (~0.40 µm - ~0.75 µm) NIR (~0.75 µm - ~1.3 µm) Resolution Summary : PAN: 2.5 m; MS: 10 m [Best Resolution: 2.5 m] Swath Summary: Swath will move between 55 and 60 km depending on latitude. [Maximum Swath: 60 km] Accuracy Summary: SNR: 100 in PAN and 120 in MS. The geo-location accuracy of level 1c PAN data product shall be better than or equal to 2.5 m RMS 2D in nadir view.	High resolution multi-spectral land optical images for applications in cartography, land use, urban management, water management, agriculture and environmental monitoring, risk management and security.
P-Band SAR	BIOMASS	ESA	Imaging microwave	Being developed	P-band: 435 MHz; four polarization channels-HH, HV,VH, and VV-	Forest biomass monitoring

			radars		together with height measurements from polarimetric interferometry; incidence angles ranging from 23 to 31 degrees Resolution Summary: Strip mode: 9 m, interferometric wide swath mode: 20 m, extra-wide swath mode: 50 m, wave mode: 50 m [Best Resolution: 9 m] Swath Summary: Strip mode: 80 km, interferometric wide swath mode: 250 km, extra-wide swath mode: 400 m, wave mode: sampled images [Best Resolution: 400 km] Accuracy Summary: NESZ: -22 dB; PTAR: -25 dB; DTAR: -22dB; Radiometric accuracy 1 dB (3 sigma); Radiometric stability: 0.5 dB (3 sigma)	
RASAT VIS Multispectral	RASAT	TUBITAK	Imaging multi-spectral radiometers (VIS/IR)	Operational	Band 1 : 0.42-0.55 μm, Band 2 : 0.55-0.63 μm, Band 3 : 0.58-0.73 μm VIS (~0.40 μm - ~0.75 μm) Resolution Summary : 15 m [Best Resolution : 15 m] Swath Summary: 30 km [Maximum Swath: 30 km]	High resolution images for monitoring of land surface and coastal processes and for agricultural, geological and hydrological applications.
SAR-L	SAOCOM 1A, SAOCOM 1B, SAOCOM 2A, SAOCOM 2B	CONAE	Imaging microwave radars	Being developed	L-band (1.275 GHz) MW (~1.0 cm - ~100 cm) L-band (2-1 GHz) Resolution Summary: 10 × 10 m-100 × 100 m [Best Resolution: 10 m] Swath Summary: 20-350 km	Land, ocean, emergencies, soil moisture, interferometry, others.

					[Maximum Swath: 350 km] Accuracy Summary: 0.5 dB	
SGLI	GCOM-C, GCOM-C2, GCOM-C3	JAXA	Imaging multi-spectral radiometers (VIS/IR) and Ocean colour instruments	Approved	VIS-NIR : 0.38-0.865 µm; SW : 1.05-2.21 µm; TIR : 10.8-12.0 µm UV (~0.01 µm - ~0.40 µm) VIS (~0.40 µm - ~0.75 µm) NIR (~0.75 µm - ~1.3 µm) SWIR (~1.3 µm - ~3.0 µm) TIR (~6.0 µm - ~15.0 µm) Resolution Summary : SGLI-VNR : 250 m, 1000m ; SGLI-IRS : 250 m, 500 m, 1000 m [Best Resolution : 250 m] Swath Summary: SGLI-VNR : 1150 km; SGLI-IRS : 1400 km [Maximum Swath: 1400 km]	Medium resolution multi-spectral imaging of land, ocean and atmosphere. SGLI-VNR is an optical sensor capable of multi-channel nadir observation at wavelengths from near-UV to NIR and forward or backward polarization observation at red and near infrared wavelengths (Push-broom scanning). SGLI-IRS is an optical sensor capable of multi-channel nadir observation at wavelengths from SWIR to TIR wavelengths (Cross-track scanning).
SLIM-6-22	UK-DMC2	UKSA	High resolution optical imagers	Operational	VIS : 0.63-0.69 µm, 0.52-0.61 µm; NIR: 0.77-0.90 µm VIS (~0.40 µm - ~0.75 µm) NIR (~0.75 µm - ~1.3 µm) Resolution Summary : 22 m [Best Resolution : 22 m] Swath Summary: Two imaging banks	Visible and NIR imagery in support of disaster management – part of the Disaster Management Constellation.

					each with a 330 km swath. The two swaths overlap by 11 km, providing a total swath up to 638 km [Maximum Swath: 638 km] Accuracy Summary: S/N: 150: 1 @ target albedo of 0.1	
SLSTR	Sentinel-3 A, Sentinel-3 B, Sentinel-3 C	ESA (EC)	Imaging multi-spectral radiometers (VIS/IR)	Approved	9 bands in VNIR/SWIR/TIR VIS (~0.40 µm - ~0.75 µm) NIR (~0.75 µm - ~1.3 µm) SWIR (~1.3 µm - ~3.0 µm) TIR (~6.0 µm - ~15.0 µm) Resolution Summary : 500 m (VNIR/SWIR), 1 km (TIR) [Best Resolution : 500 m] Swath Summary: 1675 km (near-nadir view), 750 km (backward view) [Maximum Swath: 1675 km] Accuracy Summary: 0.2 K absolute, 80 Mk relative.	Marine and land services.
TIRS	Landsat 8	USGS (NASA)	Imaging multi-spectral radiometers (VIS/IR)	Operational	TIR : 10.5 µm and 12 µm TIR (~6.0 µm - ~15.0 µm) Resolution Summary: 100 m [Best Resolution: 100m] Swath Summary: 185 km [Maximum Swath: 185 km]	Measures surface radiance and emittance, lands cover state and change (e.g. vegetation type). Used as multipurpose imagery
UVAS	Ingenio	CTDI	Atmospheric chemistry	Being developed	UV/VIS 290-490 nm UV (~0.01 µm - ~0.40 µm) VIS (~0.40 µm - ~0.75 µm) NIR (~0.75 µm - ~1.3 µm)	High spatial resolution observations of air quality and climate gases such as ozone

					Resolution Summary : 20 km nominal, 10 km [Best Resolution : 10000 m] [Maximum Swath: 250 km] Accuracy Summary: Trace gas profile: 10-40 %	(O3), nitrogen dioxide (NO2), sulphur dioxide (SO2), formaldehyde (HCHO) glyoxal (CHO-CHO), and aerosols over selected zones of interest (urban and industrialized areas, major motorways, and special events like forest fires, volcano eruption and sand storms). Also, measurements of halogenated compounds will be performed, including bromine monoxide (BrO) and iodine monoxide (IO).
UVN	MTG-S1-Meteosat, MTG-S1 (Sounding), MTG-S2-Meteosat, MTG-S2 (Sounding)	EUMETSAT (ESA)	Atmospheric chemistry	Approved	UV-1: 290-308 nm; UV-2: 308-400 nm; VIS: 400-500 nm; NIR: 750-775 nm UV (~0.01 µm - ~0.40 µm) VIS (~0.40 µm - ~0.75 µm) NIR (~0.75 µm - ~1.3 µm) Resolution Summary : < 5 km at SSP, possibly relaxed to 50 km for wavelengths < 308 nm Swath Summary: FOVE E-W: 30 °W-45 ° E @ 40 °N; N-S: 30 °N-65 ° N Accuracy Summary: H2CO: 50 %; NO2: 50 %; O3: 10 %; SO2: 50 %	Measurements of atmospheric trace gases, mainly O3, NO2, SO2, H2CO. The product list is not yet approved, the accuracy summary column lists the breakthroughs user requirements.

Vegetation	PROBA-V	ESA	Imaging multi-spectral radiometers (VIS/IR)	Operational	Equivalent spectral bands to Spot Vegetation : VNIR : Blue (438-486 nm), Red (615-696 nm), Near IR (772-914 nm), SWIR (1564-1634) VIS (~0.40 µm - ~0.75 µm) NIR (~0.75 µm - ~1.3 µm) SWIR (~1.3 µm - ~3.0 µm) Resolution Summary: 100 m resolution at Nadir, 350 m on full field of view [Best Resolution: 100 m] Swath Summary: 102 ° field of view with 2250 km wide swath [Maximum Swath: 2250 km]	Global coverage every two days for uses including climate impact assessments, surface water resource management, agricultural monitoring, and food security estimates.
VHR PAN Camera and MS Camera	OPSIS	ASI	High resolution optical imagers	Proposed	PAN = 450-900 nm; BLUE = 450-520 nm; GREEN = 520-600 nm; RED = 630-690 nm; NIR = 760-900 nm VIS (~0.40 µm - ~0.75 µm) NIR (~0.75 µm - ~1.3 µm) SWIR (~1.3 µm - ~3.0 µm) Resolution Summary: PAN = 0.5 m; MS = 2 m [Best Resolution: 0.5 m] Swath Summary: 10 km × 10 km [Maximum Swath: 10 km]	Land use, risk, agriculture and forestry, topographic and cartography, vegetation and agriculture, natural resources, security, cultural heritage.
VIIRS	DWSS, Suomi NPP, NPOESS-1, NPOESS-2, JPSS-1, NPOESS-5, NPOESS-3, NPOESS-6, NPOESS-4, JPSS-2	NASA	Imaging multi-spectral radiometers (VIS/IR) and Ocean colour instruments	Operational	VIS-TIR: 0.4-12.5 µm (22 channels) VIS (~0.40 µm - ~0.75 µm) NIR (~0.75 µm - ~1.3 µm) SWIR (~1.3 µm - ~3.0 µm) MWIR (~3.0 µm - ~6.0 µm) TIR (~6.0 µm - ~15.0 µm) Resolution Summary: 400 m-1.6 km [Best Resolution: 400 m]	Global observations of land, ocean, and atmosphere parameters, cloud/weather imagery, sea-surface temperature, ocean colour, land surface

					Swath Summary: 3000 km [Maximum Swath: 3000 km] Accuracy Summary: SST: 0.35 K	vegetation indices.
VNREDSat 1 HS	VNREDSat 1b	VAST	Hyperspectral imagers	Proposed	Hyperspectral NIR NIR (~0.75 µm - ~1.3 µm)	The VNREDSat 1b hyperspectral instrument is designed for land cover measurements and applications.
VNREDSat 1 MS	VNREDSat 1	VAST (ASTRIUM)	Imaging multi-spectral radiometers (VIS/IR)	Operational	There are 4 bands of multispectral, visible and panchromatic VIS (~0.40 µm - ~0.75 µm) Resolution Summary : MS bands : 10 m ; panchromatic : 2.5 m [Best Resolution: 2.5 m] Swath Summary: 17.5 km	The VNREDSat 1 multispectral instrument is designed for land cover measurements and applications.
VSC	VENUS	CNES (ISA)	Imaging multi-spectral radiometers (VIS/IR)	Being developed	420 nm centre wavelength (width : 40 nm) ; 443 nm(40) ; 490 nm (40) ; 555 nm (40) ; 620 nm (40) ; 667 nm (30) ; 702 nm (24) ; 742 nm (16) ; 782 nm (16) ; 865 nm (40) ; 910 nm (20) VIS (~0.40 µm - ~0.75 µm) NIR (~0.75 µm - ~1.3 µm) Resolution Summary : 5.3 spatial resolution with 27 km swath [Best Resolution: 5.3 m] Swath Summary: 27 km [Maximum Swath: 27 km]	High resolution super-spectral images (12 spectral bands) for vegetation and land cover applications.
WFI-2 (Amazonia)	AMAZONIA-1	INPE	Imaging multi-spectral radiometers	Approved	VIS : 0.45-0.50 µm, 0.52-0.57 µm, 0.63-0.69 µm, NIR : 0.76-0.90 µm VIS (~0.40 µm - ~0.75 µm)	Used for fire detection measurement, coastal and vegetation

			(VIS/IR)		NIR (~0.75 µm - ~1.3 µm) Resolution Summary : VIS-NIR: 60 m [Best Resolution: 60 m] Swath Summary: 740 km [Maximum Swath: 740 km]	monitoring, land cover use mapping. WFI-2 (Amazonia-1) is the same instrument as WFI-2 (CBERS), however due to differences in orbital latitude, they have different spatial resolutions.
WFI-2 (CBERS)	CBERS-3, CBERS-4	INPE (CAST)	Imaging multi-spectral radiometers (VIS/IR)	Operational	0.45-0.52 µm, 0.52-0.59 µm, 0.63-0.69 µm ; 0.77-0.89 µm VIS (~0.40 µm - ~0.75 µm) NIR (~0.75 µm - ~1.3 µm) Resolution Summary : 64 n Nadir [Best Resolution: 64 m] Swath Summary: 866 km [Maximum Swath: 866 km]	Earth resources, environmental monitoring, land use. WFI-2 (Amazonia-1) is the same instrument as WFI-2 (CBERS), however due to differences in orbital latitude, they have different spatial resolutions.
X-Band SAR	TerraSAR-X, TanDEM-X	DLR	Imaging microwave radars	Operational	9.65 GHz, 300 MHz bandwidth, all 4 polarisation modes MW (~1.0 cm - ~100 cm) X–Band (~12.5-8 GHz)	High resolution images for monitoring of land surface and coastal processes and for agricultural, geological and hydrological applications.

Table A-3: Landsat 5 TM Solar Irradiances	
Bands	**($Wm^{-2}\mu m^{-1}$)**
1	1957
2	1826
3	1554
4	1036
5	215.0
7	80.67

Source: Chander and Markham (2003)

Table A-4: Landsat 7 ETM+ Solar Irradiances (Generated using the Thuillier solar spectrum)	
Bands	**($Wm^{-2}\mu m^{-1}$)**
1	1997
2	1812
3	1533
4	1039
5	230.8
7	84.90
8	1362

Source: NASA (2002)

Table A-5: Earth-Sun Distance in Astronomical Units for Landsat 5 TM

DOY	Distance	DOY	Distance	DOY	Distance
1	0.9832	121	1.0076	242	1.0092
15	0.9836	135	1.0109	258	1.0057
32	0.9853	152	1.014	274	1.0011
46	0.9878	166	1.0158	288	0.9972
60	0.9909	182	1.0167	305	0.9925
74	0.9945	196	1.0165	319	0.9892
91	0.9993	213	1.0149	335	0.986
106	1.0033	227	1.0128	349	0.9843
DOY-Day of Year (Julian Day)				365	0.9833

Source: Chander and Markham (2003)

Table A-6: Earth-Sun Distance in Astronomical Units for Landsat 7 ETM+

DOY	Distance	DOY	Distance	DOY	Distance
1	0.98331	121	1.00756	242	1.00969
15	0.98365	135	1.01087	258	1.00566
32	0.98536	152	1.01403	274	1.00119
46	0.98774	166	1.01577	288	0.99718
60	0.99084	182	1.01667	305	0.99253
74	0.99446	196	1.01646	319	0.98916
91	0.99926	213	1.01497	335	0.98608
106	1.00353	227	1.01281	349	0.98426
DOY-Day of Year (Julian Day)				365	0.98333

Source: NASA (2002)

Table A-7: List of Landsat 5 TM and Landsat 7 ETM+ used for the study

Scene Identity No.	Date	UTC Time	Path/ row	Processing level
LT51880571984284XXX01	10-10-1984	09:15	188/057	L1T
LT51880571984348AAA07	14-12-1984	09:14	188/057	L1T
LT51880571985046AAA03	15-02-1985	09:14	188/057	L1T
LT51880571986017AAA04	17-01-1986	09:12	188/057	L1T
LT51880571986065XXX01	06-03-1986	09:11	188/057	L1T
LT51880571986353XXX10	19-12-1986	09:04	188/057	L1T
LT51880571987004XXX04	04-01-1987	09:04	188/057	L1T
LT51880571987052XXX01	21-02-1987	09:06	188/057	L1T
LT51880571987084XXX02	25-03-1987	09:07	188/057	L1T
LT51880571990356XXX03	22-12-1990	09:10	188/057	L1T
LT51880571991007XXX03	07-01-1991	09:09	188/057	L1T
LE71880571999317EDC00	13-11-1999	09:38	188/057	L1T
LE71880571999333AGS00	29-11-1999	09:37	188/057	L1T
LE71880572000064SGS00	04-03-2000	09:37	188/057	L1T
LE71880572000112EDC00	21-04-2000	09:37	188/057	L1T
LE71880572000336AGS00	01-12-2000	09:35	188/057	L1T
LE71880572000352EDC00	17-12-2000	09:35	188/057	L1T
LE71880572001114EDC00	24-04-2001	09:35	188/057	L1T

LE71880572001306SGS00	02-11-2001	09:33	188/057	L1T
LE71880572001354SGS00	20-12-2001	09:33	188/057	L1T
LE71880572002037SGS00	06-02-2002	09:34	188/057	L1T
LE71880572002325SGS00	21-11-2002	09:33	188/057	L1T
LE71880572003008SGS00	08-01-2003	09:33	188/057	L1T
LE71880572003072SGS00	13-03-2003	09:33	188/057	L1T
LE71880572003344EDC01	10-12-2003	09:33	188/057	L1T
LE71880572003360EDC01	26-12-2003	09:34	188/057	L1T
LE71880572004043ASN01	12-02-2004	09:34	188/057	L1T
LE71880572004331ASN00	26-11-2004	09:34	188/057	L1T
LE71880572005013ASN00	13-01-2005	09:34	188/057	L1T
LE71880572005029ASN00	29-01-2005	09:34	188/057	L1T
LE71880572005093ASN00	03-04-2005	09:34	188/057	L1T
LE71880572005317EDC00	13-11-2005	09:34	188/057	L1T
LE71880572005365ASN00	31-12-2005	09:34	188/057	L1T
LE71880572006016ASN00	16-01-2006	09:35	188/057	L1T
LE71880572006032ASN00	01-02-2006	09:35	188/057	L1T
LE71880572006352ASN00	18-12-2006	09:35	188/057	L1T
LE71880572007003ASN00	03-01-2007	09:35	188/057	L1T
LE71880572007019ASN00	19-01-2007	09:35	188/057	L1T
LE71880572007035ASN00	04-02-2007	09:35	188/057	L1T
LE71880572007323ASN00	19-11-2007	09:35	188/057	L1T
LE71880572007355ASN00	21-12-2007	09:35	188/057	L1T
LE71880572008006ASN00	06-01-2008	09:35	188/057	L1T
LE71880572008038ASN00	07-02-2008	09:35	188/057	L1T
LE71880572008086ASN00	26-03-2008	09:35	188/057	L1T
LE71880572008326ASN00	21-11-2008	09:34	188/057	L1T
LE71880572009344ASN00	10-12-2009	09:36	188/057	L1T
LE71880572010011ASN00	11-01-2010	09:36	188/057	L1T
LE71880572010043ASN00	12-02-2010	09:37	188/057	L1T
LE71880572010107ASN00	17-04-2010	09:37	188/057	L1T
LE71880572010203ASN00	22-07-2010	09:37	188/057	L1T
LE71880572010347ASN00	13-12-2010	09:38	188/057	L1T
LE71880572011334ASN00	30-11-2011	09:38	188/057	L1T

LE71880572011350ASN00	16-12-2011	09:39	188/057	L1T
LE71880572012001ASN00	01-01-2012	09:39	188/057	L1T
LE71880572012017ASN00	17-01-2012	09:39	188/057	L1T
LE71880572012033ASN00	02-02-2012	09:39	188/057	L1T
LE71880572012225ASN00	12-08-2012	09:40	188/057	L1T
LE71880572013003ASN00	03-01-2013	09:41	188/057	L1T
LE71880572013019ASN00	19-01-2013	09:41	188/057	L1T
LE71880572013067ASN00	08-03-2013	09:41	188/057	L1T

Table A-8: Atmospheric correction parameters from ATMCORR Calculator

Station	**Latitude** (θ)	**Longitude** (λ)	**L↑ ($Wm^{-2}sr^{-1}\mu m^{-1}$)**	**L↓ ($Wm^{-2}sr^{-1}\mu m^{-1}$)**	***τ***
March 4, 2000					
Eleme I	4.728	7.119	3.48	5.31	0.59
Eleme II	4.762	7.111	3.43	5.26	0.59
Onne	4.712	7.141	3.50	5.34	0.58
Bonny LNG	4.421	7.163	3.90	5.81	0.54
MODTRAN grid centre	5.008	7.019	3.29	5.08	0.61
December 1, 2000					
Eleme I	4.728	7.119	4.54	6.57	0.42
Eleme II	4.762	7.111	4.54	6.58	0.42
Onne	4.712	7.141	4.53	6.57	0.42
Bonny LNG	4.421	7.163	4.50	6.54	0.42
MODTRAN grid centre	5.008	7.019	4.55	6.60	0.42
February 6, 2002					
Eleme I	4.728	7.119	4.60	6.69	0.43
Eleme II	4.762	7.111	4.59	6.68	0.43
Onne	4.712	7.141	4.61	6.69	0.43
Bonny LNG	4.421	7.163	4.72	6.78	0.41

MODTRAN grid centre	5.008	7.019	4.29	6.32	0.46
November 21, 2002					
Eleme I	4.728	7.119	4.77	6.79	0.40
Eleme II	4.762	7.111	4.77	6.79	0.40
Onne	4.712	7.141	4.77	6.79	0.40
Bonny LNG	4.421	7.163	4.79	6.82	0.39
MODTRAN grid centre	5.008	7.019	4.64	6.70	0.42
February 12, 2004					
Eleme I	4.728	7.119	4.68	6.73	0.42
Eleme II	4.762	7.111	4.68	6.73	0.42
Onne	4.712	7.141	4.69	6.74	0.41
Bonny LNG	4.421	7.163	4.78	6.82	0.40
MODTRAN grid centre	5.008	7.019	4.87	6.91	0.35
November 26, 2004					
Eleme I	4.728	7.119	5.09	7.18	0.33
Eleme II	4.762	7.111	5.09	7.18	0.33
Onne	4.712	7.141	5.09	7.18	0.33
Bonny LNG	4.421	7.163	5.07	7.14	0.34
January 16, 2006					
Eleme I	4.728	7.119	4.44	6.52	0.43
Eleme II	4.762	7.111	4.44	6.51	0.43
Onne	4.712	7.141	4.45	6.52	0.43
Bonny LNG	4.421	7.163	4.56	6.63	0.42
MODTRAN grid centre	5.008	7.019	4.09	6.06	0.47
December 18, 2006					
Eleme I	4.728	7.119	3.88	5.80	0.52
Eleme II	4.762	7.111	3.85	5.76	0.53
Onne	4.712	7.141	3.90	5.83	0.52
Bonny LNG	4.421	7.163	4.18	6.14	0.48

MODTRAN grid centre	5.008	7.019	3.71	5.60	0.55
January 6, 2008					
Eleme I	4.728	7.119	4.96	7.11	0.34
Eleme II	4.762	7.111	4.96	7.11	0.34
Onne	4.712	7.141	4.95	7.11	0.34
Bonny LNG	4.421	7.163	4.93	7.06	0.35
MODTRAN grid centre	5.008	7.019	4.96	7.12	0.34
November 21, 2008					
Eleme I	4.728	7.119	4.93	6.94	0.38
Eleme II	4.762	7.111	4.92	6.93	0.39
Onne	4.712	7.141	4.93	6.95	0.38
Bonny LNG	4.421	7.163	4.99	6.98	0.37
MODTRAN grid centre	5.008	7.019	4.90	6.93	0.39
February 12, 2010					
Eleme I	4.728	7.119	5.34	7.42	0.32
Eleme II	4.762	7.111	5.34	7.43	0.32
Onne	4.712	7.141	5.33	7.42	0.32
Bonny LNG	4.421	7.163	5.30	7.36	0.33
MODTRAN grid centre	5.008	7.019	5.06	7.14	0.35
December 13, 2010					
Eleme I	4.728	7.119	4.01	5.99	0.50
Eleme II	4.762	7.111	3.98	5.95	0.50
Onne	4.712	7.141	4.03	6.02	0.50
Bonny LNG	4.421	7.163	4.27	6.29	0.46
MODTRAN grid centre	5.008	7.019	3.28	5.07	0.58
January 17, 2012					
Eleme I	4.728	7.119	3.16	4.92	0.62
Eleme II	4.762	7.111	3.14	4.90	0.62
Onne	4.712	7.141	3.17	4.94	0.62

Bonny LNG	4.421	7.163	3.31	5.08	0.60
MODTRAN grid centre	5.008	7.019	2.36	3.76	0.70
August 12, 2012					
Eleme I	4.728	7.119	4.25	6.24	0.45
Eleme II	4.762	7.111	4.25	6.25	0.45
Onne	4.712	7.141	4.24	6.23	0.45
Bonny LNG	4.421	7.163	4.17	6.07	0.45
MODTRAN grid centre	5.008	7.019	4.28	6.31	0.45

Table A-9: Air temperature and relative humidity at Eleme Refinery II Petroleum Company gas flaring site, (1st set of fieldwork data)

Date	Distance (m)	Time (min.)	Air temperature (K)	Relative Humidity (%)
04/08/2012	Line 1			
L	30 m	9.00	319.48	72.0
M		9.01	320.15	68.5
U		9.02	321.09	65.3
L	30 m	9.07	319.71	72.2
M		9.08	319.93	69.1
U		9.09	321.04	66.0
L	30 m	9.14	319.87	69.4
M		9.15	320.26	69.8
U		9.16	321.15	62.3
L	60 m	9.21	317.37	72.1
M		9.22	317.53	68.4
U		9.23	318.54	65.2
L	60 m	9.28	317.21	70.4
M		9.29	317.71	66.3
U		9.30	318.04	65.8
L	60 m	9.35	317.32	71.6
M		9.36	317.43	68.3
U		9.37	318.37	64.7
L	90 m	9.42	315.82	65.9
M		9.43	315.98	66.0
U		9.44	317.87	66.3

L	90 m	9.49	316.21	65.4
M		9.50	316.43	65.4
U		9.51	317.93	64.5
L	90 m	9.56	316.15	66.2
M		9.57	316.37	62.3
U		9.58	317.48	64.5
L	120 m	10.03	315.54	67.9
M		10.04	315.87	67.7
U		10.05	316.82	68.3
L	120 m	10.10	315.43	66.5
M		10.11	315.54	65.8
U		10.12	316.37	67.3
L	120 m	10.17	315.54	64.8
M		10.18	315.76	64.9
U		10.19	316.48	65.1
L	150 m	10.24	315.09	65.7
M		10.25	315.59	65.8
U		10.26	316.54	67.5
L	150 m	10.31	314.65	65.5
M		10.32	315.48	63.2
U		10.33	315.76	58.4
L	150 m	10.38	314.76	66.3
M		10.39	315.43	64.7
U		10.40	316.09	61.5
L	180 m	10.45	316.09	80.3
M		10.46	316.20	79.5
U		10.47	316.59	79.4
L	180 m	10.52	316.59	79.8
M		10.53	316.42	79.6
U		10.54	317.32	79.6
L	180 m	10.59	315.76	80.0
M		11.00	316.48	78.3
U		11.01	316.65	78.4
L	210 m	11.06	312.21	76.2
M		11.07	315.09	77.3
U		11.08	316.48	77.5
L	210 m	11.13	313.76	78.1
M		11.14	314.43	76.9
U		11.15	314.65	76.7

L	210 m	11.20	313.59	74.5
M		11.21	313.59	70.8
U		11.22	314.09	71.2
L	240 m	11.27	315.48	73.1
M		11.28	315.54	73.2
U		11.29	316.76	68.5
L	240 m	11.34	315.54	78.3
M		11.35	315.65	70.4
U		11.36	316.76	65.8
L	240 m	11.41	315.26	70.2
M		11.42	315.65	70.2
U		11.43	316.54	68.5

Appendix B

MATLAB programming code for data processing and data analysis.

A: Data processing

1. Reflectance

```
clear all;
% Three folders for data used are: 1 = L5_folder310513;
% 2 = L7_folder010613_SLCON; 3 = L7_folder020613_SLCOFF;
datadir = 'C:\PhD\landsat\data\matlab_june_13\L7_folder010613_SLCON'
cd(datadir);
d1 = dir(datadir);
vegetationemissivity = 0.97;
soilemissivity = 0.96;
builtupemissivity = 0.964;
% Read in XL radiometric calibration file
% Fill in ALL gaps in XL file with Nan
%  Save  XL  file  as  plain  ascii  text  i.e  to  change  file  from  Excel  to
text
[StnNo,  Stnlon,  Stnlat]  =  textread('Flare_stations_PhD.txt',  '%d  %f
%f', 'headerlines',1);
[sceneName, Aa, Bb, Cc, Dd, Ee, Ff, Gg, Hh, Ii, Jj, Kk, Ll, Mm, Nn,
Oo,...
Pp, Qq, Rr, Ss, Tt, Uu, Vv, dark_Stnlat, dark_Stnlon, Aaa, Bbb, Ccc,
Ddd,...
Eee, Fff, Ggg, Hhh, Iii, Jjj, Kkk, Lll, Mmm, Nnn, Ooo, Ppp, Qqq, Rrr,
Sss, ...
Ttt, Uuu, Vvv, Www, Xxx, Yyy, Zzz, Aaaa, Bbbb, Cccc, Dddd, Eeee, Ffff,
...
Gggg, Hhhh, Iiii, Jjjj, Kkkk, Llll, Mmmm, Nnnn, Oooo, Pppp, Qqqq, ...
Rrrr,          Ssss,          Tttt,          Uuuu,          Vvvv]          =
textread('Radcorr1234aa_MAY162014.txt', '%s %f %f %f %f%f %f %f %f %f
%f %f %f %f %f %f %f %f %f %f %f %f %f %f %f %f %f %f %f %f %f %f %f
%f %f %f %f %f %f %f %f %f %f %f %f %f %f %f %f %f %f %f %f %f %f %f
%f  %f  %f  %f  %f  %f  %f  %f  %f  %f  %f  %f  %f  %f  %f  %f
%f','headerlines',1,'emptyvalue',NaN);
% For each SceneName, convert specific characters into numerical path,
% row, year, day.
sceneName = char(sceneName);
% or Size(sceneName)= 21 * 60 then sceneName = char(sceneName);
for iStn = 1:11; % the total number of flare stations studied
     thisStnlon = Stnlon(iStn);
     thisStnlat = Stnlat(iStn);
 for i = 1:60;
 scenePath(i) = str2num(sceneName(i,4:6));
 sceneRow(i) = str2num(sceneName(i,7:9));
 sceneYear(i) = str2num(sceneName(i,10:13));
 sceneDay(i) = str2num(sceneName(i,14:16));
 end
% plot(scenePath,'x')
% plot(sceneYear,'x')
% plot(sceneDay,'x')
% bar(hist(sceneDay,20))
% bar(hist(sceneDay,12))
 for ifile = 1:720; % for ifile = 3: length(d1), % the first two files
are the MATLAB invisible files
     thisfile = d1(ifile).name
```

```
     test = strfind(thisfile,'B1.TIF'); % to count from the begining
of the scene name to the location of B
     if isempty(test); % if is empty the result is '1' but if not the
result is '0'
         ;
     else
        thispath = str2num(thisfile(4:6));
        thisrow = str2num(thisfile(7:9));
        thisyear = str2num(thisfile(10:13));
        thisday = str2num(thisfile(14:16));
        namestem = thisfile(1:22);
        band2fileb = [namestem 'B2.TIF']
        band3fileb = [namestem 'B3.TIF']
        band4fileb = [namestem 'B4.TIF']
        band6fileb = [namestem 'B6.TIF']
        mtl_filename = [namestem 'MTL.txt']

% To read landsat data files
band1=imread(thisfile);
band2=imread(band2fileb);
band3=imread(band3fileb);
band4=imread(band4fileb);
band6=imread(band6fileb);

% Reading .mtl files:
% 1. To figure out what the MTL file name will be, and create a
filename variable for it,
%    as I did for the different band .tif files:
mtl_filename = [namestem 'MTL.txt']; % you just have to adapt your
existing code for this.

% 2. In a similar approach to the one I took for reading netcdf files,
I need to
%    make a file handle - this is a variable that I use to store the
memory location
%    of the MTL file as I open and read through it:
fid_mtl = fopen(mtl_filename);

% 3a.  To explore the MTL file, I start by reading one line at a time
and allowing
%    matlab to display it on-screen (by omitting the ';'):
fgets(fid_mtl)

% used this fgets command repeatedly to see the line-by-line file
contents.

% 3b. Rewind the file pointer now, so it goes back to the beginning of
the file:
frewind(fid_mtl);

% 3c. Write a loop to automatically go through each line of the file.
Instead of printing
% the line to the screen, I assigned it to a new variable called
'line_mtl', and I
% also searched for the first of the important parameters within each
line:
linecounter = 0; % this is a safety catch - to limit the number of
lines parsed
     % just in case the formal 'end of file' function (feof())
doesn't work.
```

```
while (~feof(fid_mtl)   & linecounter < 200)   % instead of using 'for
i=1; i<200; i++), here
     % just start a loop and keep it going *while* the conditions in
the parentheses test true.
     % this process is repeated from while to the linecounter to
process for each x & y
clear thisline;
thisline = fgets(fid_mtl)    % leave off the ';' to see the line on
screen as well.
linecounter = linecounter+1;
% test whether this line contains a specific parameter that I am
looking for:
got_ul_easting = strfind(thisline,'CORNER_UL_PROJECTION_X_PRODUCT'); %
this is line 32 in the mtl file
if ~isempty(got_ul_easting)   % if I've found the parameter we want:
    ul_easting                                                    =
str2num(thisline(length('CORNER_UL_PROJECTION_X_PRODUCT')+3          +
got_ul_easting                                                       :
length('CORNER_UL_PROJECTION_X_PRODUCT')+got_ul_easting +13))
end
got_ul_northing = strfind(thisline,'CORNER_UL_PROJECTION_Y_PRODUCT');
if ~isempty(got_ul_northing)   % if I've found the parameter we want:
   ul_northing                                                    =
str2num(thisline(length('CORNER_UL_PROJECTION_Y_PRODUCT')+3
+got_ul_northing      :      length('CORNER_UL_PROJECTION_Y_PRODUCT')+
got_ul_northing+13))
end
got_ur_easting = strfind(thisline,'CORNER_UR_PROJECTION_X_PRODUCT');
if ~isempty(got_ur_easting)   % if I've found the parameter we want:
   ur_easting                                                     =
str2num(thisline(length('CORNER_UR_PROJECTION_X_PRODUCT')+3
+got_ur_easting       :      length('CORNER_UR_PROJECTION_X_PRODUCT')+
got_ur_easting  +13));
end
got_ur_northing = strfind(thisline,'CORNER_UR_PROJECTION_Y_PRODUCT');
if ~isempty(got_ur_northing)   % if I've found the parameter we want:
   ur_northing                                                    =
str2num(thisline(length('CORNER_UR_PROJECTION_Y_PRODUCT')+3
+got_ur_northing:            length('CORNER_UR_PROJECTION_Y_PRODUCT')+
got_ur_northing +13))
end
got_ll_easting = strfind(thisline,'CORNER_LL_PROJECTION_X_PRODUCT');
if ~isempty(got_ll_easting)   % if I've found the parameter we want:
   ll_easting                                                     =
str2num(thisline(length('CORNER_LL_PROJECTION_X_PRODUCT')+3
+got_ll_easting:             length('CORNER_LL_PROJECTION_X_PRODUCT')+
got_ll_easting +13))
end
got_ll_northing = strfind(thisline,'CORNER_LL_PROJECTION_Y_PRODUCT');
if ~isempty(got_ll_northing)   % if I've found the parameter we want:
   ll_northing                                                    =
str2num(thisline(length('CORNER_LL_PROJECTION_Y_PRODUCT')+3
+got_ll_northing      :      length('CORNER_LL_PROJECTION_Y_PRODUCT')+
got_ll_northing +13))
end
got_lr_easting = strfind(thisline,'CORNER_LR_PROJECTION_X_PRODUCT');
if ~isempty(got_lr_easting)   % if I've found the parameter we want:
   lr_easting                                                     =
str2num(thisline(length('CORNER_LR_PROJECTION_X_PRODUCT')+3
+got_lr_easting:             length('CORNER_LR_PROJECTION_X_PRODUCT')+
got_lr_easting+ 13))
end
got_lr_northing = strfind(thisline,'CORNER_LR_PROJECTION_Y_PRODUCT');
```

```
if ~isempty(got_lr_northing)   % if I've found the parameter we want:
   lr_northing                                                    =
str2num(thisline(length('CORNER_LR_PROJECTION_Y_PRODUCT')+3
+got_lr_northing:             length('CORNER_LR_PROJECTION_Y_PRODUCT')+
got_lr_northing +13))
end
got_Xaxis_pixelno = strfind(thisline,'REFLECTIVE_SAMPLES');
if  ~isempty(got_Xaxis_pixelno)     % if I've found the parameter we
want:
   Xaxis_pixelno    =    str2num(thisline(length('REFLECTIVE_SAMPLES')+3
+got_Xaxis_pixelno:  length('REFLECTIVE_SAMPLES')+  got_Xaxis_pixelno  +
7))
end
end
fclose(fid_mtl);

% Choice of dimension of area around flare station for investigation
a_pixel = (ur_easting - ul_easting) / Xaxis_pixelno;
diff_easting = (thisStnlon - ul_easting);
diff_northing = (ul_northing - thisStnlat);
pixels_easting = diff_easting / a_pixel; i.e No of pixels
pixels_northing = diff_northing / a_pixel; i.e No of pixels
tflarepixels_easting = (ceil(pixels_easting) - 200);
tflarepixels_northing = (ceil(pixels_northing) - 200);
lflarepixels_easting = (ceil(tflarepixels_easting) + 400);
lflarepixels_northing = (ceil(tflarepixels_northing) + 400);

B1F =
band1(tflarepixels_northing:lflarepixels_northing,tflarepixels_easting
:lflarepixels_easting);
B2F =
band2(tflarepixels_northing:lflarepixels_northing,tflarepixels_easting
:lflarepixels_easting);
B3F =
band3(tflarepixels_northing:lflarepixels_northing,tflarepixels_easting
:lflarepixels_easting);
B4F =
band4(tflarepixels_northing:lflarepixels_northing,tflarepixels_easting
:lflarepixels_easting);
B6F =
band6(tflarepixels_northing:lflarepixels_northing,tflarepixels_easting
:lflarepixels_easting);

B1F = double(B1F);
B2F = double(B2F);
B3F = double(B3F);
B4F = double(B4F);
B6F = double(B6F);

figure(105);clf;
imagesc(B6F);
colorbar;
caxis([0 100]);
hold on
plot(201,201,'ow');


% To remove zero values or bad values
ibad = find(B1F(:) <=1 | B1F(:)>= 254);
B1F(ibad) = nan; clear ibad;
ibad = find(B2F(:) <=1 | B2F(:)>= 254);
B2F(ibad) = nan; clear ibad;
```

```
ibad = find(B3F(:) <=1 | B3F(:)>= 254);
B3F(ibad) = nan; clear ibad;
ibad = find(B4F(:) <=1 | B4F(:)>= 254);
B4F(ibad) = nan; clear ibad;
ibad = find(B6F(:) <=1 | B6F(:)>= 254);
B6F(ibad) = nan; clear ibad;
% Dark pixel method of Atmospheric Correction for the Landsat
reflective bands
a_pixel = (ur_easting - ul_easting) / Xaxis_pixelno;
darkdiff_easting = (dark_Stnlon - ul_easting);
darkdiff_northing = (ul_northing - dark_Stnlat);
darkpixels_easting = darkdiff_easting / a_pixel;
darkpixels_northing = darkdiff_northing / a_pixel;
darktflarepixels_easting = (ceil(darkpixels_easting) - 30);
darktflarepixels_northing = (ceil(darkpixels_northing) - 30);
darklflarepixels_easting = (ceil(darktflarepixels_easting) + 60);
darklflarepixels_northing = (ceil(darktflarepixels_northing) + 60);

B1F_dark                                                              =
band1(darktflarepixels_northing:darklflarepixels_northing,darktflarepi
xels_easting:darklflarepixels_easting);
B2F_dark                                                              =
band2(darktflarepixels_northing:darklflarepixels_northing,darktflarepi
xels_easting:darklflarepixels_easting);
B3F_dark                                                              =
band3(darktflarepixels_northing:darklflarepixels_northing,darktflarepi
xels_easting:darklflarepixels_easting);
B4F_dark                                                              =
band4(darktflarepixels_northing:darklflarepixels_northing,darktflarepi
xels_easting:darklflarepixels_easting);

B1F_dark = double(B1F_dark);
B2F_dark = double(B2F_dark);
B3F_dark = double(B3F_dark);
B4F_dark = double(B4F_dark);

% This command help to channel the reading of both scene and
radiometric calibration files
thisline = find(sceneRow == thisrow & scenePath == thispath &...
    sceneYear == thisyear & sceneDay == thisday);

% Radiometric calibrations for multispectral bands 1, 2, 3 and 4:
LMIN_B1 = Aa(thisline); LMAX_B1 = Bb(thisline);
QCALMIN_B1 = Cc(thisline); QCALMAX_B1 = Dd(thisline);

LMIN_B2 = Ee(thisline); LMAX_B2 = Ff(thisline);
QCALMIN_B2 = Gg(thisline); QCALMAX_B2 = Hh(thisline);

LMIN_B3 = Ii(thisline); LMAX_B3 = Jj(thisline);
QCALMIN_B3 = Kk(thisline); QCALMAX_B3 = Ll(thisline);

LMIN_B4 = Mm(thisline); LMAX_B4 = Nn(thisline);
QCALMIN_B4 = Oo(thisline); QCALMAX_B4 = Pp(thisline);

LMIN_B6 = Qq(thisline); LMAX_B6 = Rr(thisline);
QCALMIN_B6 = Ss(thisline); QCALMAX_B6 = Tt(thisline);

% Convert digital numbers DN back to top-of-atmosphere radiances Lt
% for all Landsat bands.
%    L = [ (LMAX - LMIN) / (QCALMAX - QCALMIN)) ] * (DN - QCALMIN) +
LMIN;
```

```
L_B1 = ( (LMAX_B1 - LMIN_B1) / (QCALMAX_B1 - QCALMIN_B1) ) *...
(B1F - QCALMIN_B1) + LMIN_B1;
L_B2 = ( (LMAX_B2 - LMIN_B2) / (QCALMAX_B2 - QCALMIN_B2) ) *...
(B2F - QCALMIN_B2) + LMIN_B2;

L_B3 = ( (LMAX_B3 - LMIN_B3) / (QCALMAX_B3 - QCALMIN_B3) ) *...
(B3F - QCALMIN_B3) + LMIN_B3;

L_B4 = ( (LMAX_B4 - LMIN_B4) / (QCALMAX_B4 - QCALMIN_B4) ) *...
(B4F - QCALMIN_B4) + LMIN_B4;

L_B6 = ( (LMAX_B6 - LMIN_B6) / (QCALMAX_B6 - QCALMIN_B6) ) *...
(B6F - QCALMIN_B6) + LMIN_B6;

% Computation of at sensor radiance for dark pixels
darkL_B1 = ( (LMAX_B1 - LMIN_B1) / (QCALMAX_B1 - QCALMIN_B1) ) *...
(B1F_dark - QCALMIN_B1) + LMIN_B1;
darkL_B2 = ( (LMAX_B2 - LMIN_B2) / (QCALMAX_B2 - QCALMIN_B2) ) *...
(B2F_dark - QCALMIN_B2) + LMIN_B2;
darkL_B3 = ( (LMAX_B3 - LMIN_B3) / (QCALMAX_B3 - QCALMIN_B3) ) *...
(B3F_dark - QCALMIN_B3) + LMIN_B3;
darkL_B4 = ( (LMAX_B4 - LMIN_B4) / (QCALMAX_B4 - QCALMIN_B4) ) *...
(B4F_dark - QCALMIN_B4) + LMIN_B4;

% Apply a simple sun angle correction to calculate reflectance Rt at
% the flaring sites from the top-of-atmosphere radiance
% Rti = (pi * Lti * d2) / (Eoi * T0 * T1 * cos(thetaSZ))
% where i indicates a band number;
% d2 = Earth-Sun distance in astonomical units
% Eoi = mean solar irradiance at top of atmosphere - look it up
% in Table 11.4;
% T0 = T1: assuming no atmospheric absorption!
% thetaSZ = sun zenith at the time of the overpass - it is in metadata
file
d2 = Vv(thisline);
Eo_b1= 1997 %1997; % for landsat 7 ETM+, for landsat 5TM = 1957;
Eo_b2= 1812 %1812; % for landsat 7 ETM+, for landsat 5TM = 1826;
Eo_b3= 1533 %1533; % for landsat 7 ETM+, for landsat 5TM = 1554;
Eo_b4= 1039 %1039; % for landsat 7 ETM+, for landsat 5TM = 1036;
T0=1.0; % check atmospheric tranmittance for band 3, band 4
T1=1.0; % Are they the same for band 3, band 4? Are they valid?
thetaSZ = Uu(thisline); % in metadata file
thetaSZrad = (thetaSZ/180)*pi;

Rt1 = (pi * L_B1 * d2) / (Eo_b1 * T0 * T1 * cos(thetaSZrad));
Rt2 = (pi * L_B2 * d2) / (Eo_b2 * T0 * T1 * cos(thetaSZrad));
Rt3 = (pi * L_B3 * d2) / (Eo_b3 * T0 * T1 * cos(thetaSZrad));
Rt4 = (pi * L_B4 * d2) / (Eo_b4 * T0 * T1 * cos(thetaSZrad));

% Application of atmospheric correction to reflective bands 1-4
% Computation of dark pixel reflectance for bands 1-4
Rt1e = (pi * darkL_B1 * d2) / (Eo_b1 * T0 * T1 * cos(thetaSZrad));
Rt2e = (pi * darkL_B2 * d2) / (Eo_b1 * T0 * T1 * cos(thetaSZrad));
Rt3e = (pi * darkL_B3 * d2) / (Eo_b1 * T0 * T1 * cos(thetaSZrad));
Rt4e = (pi * darkL_B4 * d2) / (Eo_b1 * T0 * T1 * cos(thetaSZrad));

error1e = min(Rt1e(:))
error2e = min(Rt2e(:))
error3e = min(Rt3e(:))
error4e = min(Rt4e(:))
% True reflectance for bands 1 to 4
R1 = (Rt1 - error1e);
```

```
R2 = (Rt2 - error2e);
R3 = (Rt3 - error3e);
R4 = (Rt4 - error4e);

% To make a 'pseudo'-true-colour image (RGB:
clear tmp;
tmp(1,:) = R1(200,:);
tmp(2,:) = R2(200,:);
tmp(3,:) = R3(200,:);
tmp(4,:) = R4(200,:);

clear tmp;
tmp(:,:,1) = R3; % play with R4, R3, R2
tmp(:,:,2) = R2;
tmp(:,:,3) = R1;
tmp2 = (tmp - min(tmp(:)))/(max(tmp(:)) - min(tmp(:)));
figure(4 );clf;
imagesc(tmp2);
colorbar; caxis([0 0.3])
hold on
% plot(206,200,'or');
plot(201,201,'ow')
% set(gca, 'xlim',[170 260],'ylim',[160 250])
%   newfilenameB   =['c:\PhD\results\RGBimagesc_'   num2str(iStn)   '_'
namestem '.png']
% print('-f1','-dpng','-r300','newfilenameB.png');
```

2. Cluster processing (1)

```
% kmeans for unsupervised and supervised land cover classifications
% The toolbox I need for kmeans clustering in Matlab is 'Statistics
Toolbox'. To look at the clusters and decide how many classes I need,
I will do something like:
% R6 = [BT5/max(BT5(:))]*0.5946; % Note that 0.5946 is the highest
value in R4

X1 = [R1(:)   R2(:)   R3(:)   R4(:)];
size(160801*4) % check you've created a N x 4 matrix. If not, you'll
need to adjust the line above, e.g. using [R1(:) ; R2(:);  etc.

% IDX = kmeans(X1, 4); % for 4 clusters.

isub   =   find(~isnan(R1(:))   &   ~isnan(R2(:))   &   ~isnan(R3(:))
&~isnan(R4(:)));
IDXsub = kmeans(X1(isub,:), 4);
IDXall = ones(size(R1)) * nan;
IDXall(isub) = IDXsub;
IDX2 = reshape(IDXall, size(R1));
figure(40); clf;
pcolor(flipud(IDX2)); shading flat;
colormap(jet(4));
colorbar('ytick',[1:1:5],'yticklabel',{'Class   1','Class   2','Class
3','Class 4'});
hold on
plot(206,200,'ow');
```

3. Masking of cloud

```
% To identify cloud and mask it from the data
tmp = input('Enter class number for cloud 1','s');
cloud1 = str2num(tmp);
tmp = input('Enter class number for cloud 2','s');
cloud2 = str2num(tmp);
```

```
cloud1 = 0; % when it was remove, there was a comment that marrtix
dimension is not agree
cloud2 = 0; % when it was remove, there was a comment that marrtix
dimension is not agree
R1mask=R1; R1mask((IDXall == cloud1)|(IDXall == cloud2)) = nan;
R2mask=R2; R2mask((IDXall == cloud1)|(IDXall == cloud2)) = nan;
R3mask=R3; R3mask((IDXall == cloud1)|(IDXall == cloud2)) = nan;
R4mask=R4; R4mask((IDXall == cloud1)|(IDXall == cloud2)) = nan;
% BTmask=BT_stn1; BTmask((IDXall == cloud1)|(IDXall == cloud2)) = nan;
% BT1mask=BT1; BT1((IDXall == cloud1)|(IDXall == cloud2)) = nan;
% BT2mask=BT2; BT2((IDXall == cloud1)|(IDXall == cloud2)) = nan;
% BT3mask=BT3; BT3((IDXall == cloud1)|(IDXall == cloud2)) = nan;
% BT4mask=BT4; BT4((IDXall == cloud1)|(IDXall == cloud2)) = nan;
% LSTmask=LST; LSTmask((IDXall == cloud1)|(IDXall == cloud2)) = nan;
% ndvimask=ndvi; ndvimask((IDXall == cloud1)|(IDXall == cloud2)) =
nan;
```

4. Calculation of NDVI

```
% calculate Normalised Differential Vegetation Index (NDVI)
ndvi = (R4 - R3) ./ (R4 + R3);
```

5. Cluster processing (II) & land cover classifications

```
X2 = [R1mask(:)   R2mask(:)   R3mask(:)   R4mask(:)];
clear IDXsub; clear IDXall;
isub = find(~isnan(R1mask(:)) & ~isnan(R2mask(:)) & ~isnan(R3mask(:))
&~isnan(R4mask(:)));
IDXsub = kmeans(X2(isub,:), 4);
IDXall = ones(size(R1)) * nan;
IDXall(isub) = IDXsub;
IDX3 = reshape(IDXall, size(R1));

% To look at the classes as a map:
figure(6); clf;
pcolor(flipud(IDX3)); shading flat;
colormap(jet(4));
colorbar('ytick',[1:1:5],'yticklabel',{'class   1','class   2','class
3','class 4'}); % this makes it easy to interpret classes.
hold on
plot(206,200,'or');
% To look at the centroid and range of each band and each cluster:
class1(1,:) = R1(IDX3 == 1); % this picks out all the band 1
reflectance data     % for pixels classified as class 1;
class1(2,:) = R2(IDX3 == 1);  % same for band 2, class 1;
class1(3,:) = R3(IDX3 == 1);  % same for band 3, class 1;
class1(4,:) = R4(IDX3 == 1);  % same for band 4, class 1;

class1_mean = mean(class1'); % this gives a 1x4 vector made
% up of [mean band 1 for class 1, mean band 2 for class 1, mean band 3
for class 1, mean band 4 for class 1]. i.e., the class 1
% centroid reflectance 'spectrum'.

class1_std = std(class1'); % ditto for standard deviation - this
should also be a 1x4. if these aren't 1x4 then use e.g. class1_std =
std(class1');


class2(1,:) = R1(IDX3 == 2);   % this picks out all the band 2
reflectance data for pixels classified as class 2;
class2(2,:) = R2(IDX3 == 2);  % same for band 2, class 2;
```

```
class2(3,:) = R3(IDX3 == 2);  % same for band 3, class 2;
class2(4,:) = R4(IDX3 == 2);  % same for band 4, class 2;

class2_mean = mean(class2');
class2_std = std(class2');

class3(1,:) = R1(IDX3 == 3);   % this picks out all the band 3
reflectance data for pixels classified as class 3;
class3(2,:) = R2(IDX3 == 3);  % same for band 2, class 3;
class3(3,:) = R3(IDX3 == 3);  % same for band 3, class 3;
class3(4,:) = R4(IDX3 == 3);  % same for band 4, class 3;

class3_mean = mean(class3');
class3_std = std(class3');

class4(1,:) = R1(IDX3 == 4);   % this picks out all the band 4
reflectance data for pixels classified as class 1;
class4(2,:) = R2(IDX3 == 4);  % same for band 2, class 4;
class4(3,:) = R3(IDX3 == 4);  % same for band 3, class 4;
class4(4,:) = R4(IDX3 == 4);  % same for band 4, class 4;

class4_mean = mean(class4');
class4_std = std(class4');

% And compare the 'spectra' for the 4 classes:
figure(7); clf;
errorbar([485, 560, 660, 830], class1_mean, class1_std, 'k+'); % plots
class 1 spectrum against landsat 5 central
hold on          % band wavelengths using a black 'plus' symbol with 1
standard deviation as the error bar;
errorbar([485, 560, 660, 830], class2_mean, class2_std, 'gs');
errorbar([485, 560, 660, 830], class3_mean, class3_std, 'c*');
errorbar([485, 560, 660, 830], class4_mean, class4_std, 'ro');
legend ('class 1 = water', 'class 2 = cloud locations', 'class 3 =
vegetation', 'class 4 = soil')
title('elemeerrorbar2000064-cloud')
print('-f114','-dpng','-r300','elemeerrorbar2000064-cloud.png')


% To give each land cover classification as vegetation; water; soil;
built up
vegetationclass = input('Enter class for vegetation','s');
vegetation = str2num(vegetationclass);
waterclass = input('Enter class for water','s');
water = str2num(waterclass);
soilclass = input('Enter class for soil','s');
soil = str2num(soilclass);
builtupclass = input('Enter class for builtup','s');
builtup = str2num(builtupclass);

emissivity = IDX3 * nan;
emissivity(IDX3 == vegetation) = vegetationemissivity;
emissivity(IDX3 == soil) = soilemissivity;
emissivity(IDX3 == builtup) = builtupemissivity;
```

6. Error analysis of the estimated emissivity value used

```
% To carry out error analysis on the emisivity of vegetation, soil and
built-up land cover
 emissivityuppererror(IDX3 == vegetationclass) =
vegetationemisserror1;
```

```
 emissivitylowererror(IDX3 == vegetationclass) =
vegetationemisserror2;

 emissivityuppererror(IDX3 == soilclass) = soilemisserror1;
 emissivitylowererror(IDX3 == soilclass) = soilemisserror2;

 emissivityuppererror(IDX3 == builtupclass) = builtupemisserror1;
 emissivitylowererror(IDX3 == builtupclass) = builtupemisserror2;
```

7. Brightness Temperature

```
% computation of Brightness Temperature (BT)and Land Surface
Temperature (LST)to read thermal atmospheric correction parameters
(upwelling radiance, downwelling radiance and transmittance) from the
file.
Stn1uwr = Aaa(thisline); Stn1dwr = Bbb(thisline); Stn1tr =
Ccc(thisline);
Stn2uwr = Ddd(thisline); Stn2dwr = Eee(thisline); Stn2tr =
Fff(thisline);
Stn3uwr = Ggg(thisline); Stn3dwr = Hhh(thisline); Stn3tr =
Iii(thisline);
Stn4uwr = Jjj(thisline); Stn4dwr = Kkk(thisline); Stn4tr =
Lll(thisline);
Stn5uwr = Mmm(thisline); Stn5dwr = Nnn(thisline); Stn5tr =
Ooo(thisline);
Stn6uwr = Ppp(thisline); Stn6dwr = Qqq(thisline); Stn6tr =
Rrr(thisline);
Stn7uwr = Sss(thisline); Stn7dwr = Ttt(thisline); Stn7tr =
Uuu(thisline);
Stn8uwr = Vvv(thisline); Stn8dwr = Www(thisline); Stn8tr =
Xxx(thisline);
Stn9uwr = Yyy(thisline); Stn9dwr = Zzz(thisline); Stn9tr =
Aaaa(thisline);
Stn10uwr = Bbbb(thisline); Stn10dwr = Cccc(thisline); Stn10tr =
Dddd(thisline);
Stn11uwr = Eeee(thisline); Stn11dwr = Ffff(thisline); Stn11tr =
Gggg(thisline);
Stn12uwr = Hhhh(thisline); Stn12dwr = Iiii(thisline); Stn12tr =
Jjjj(thisline);
Stn13uwr = Kkkk(thisline); Stn13dwr = Llll(thisline); Stn13tr =
Mmmm(thisline);
Stn14uwr = Nnnn(thisline); Stn14dwr = Oooo(thisline); Stn14tr =
Pppp(thisline);
Stn15uwr = Qqqq(thisline); Stn15dwr = Rrrr(thisline); Stn15tr =
Ssss(thisline);
Stn16uwr = Tttt(thisline); Stn16dwr = Uuuu(thisline); Stn16tr =
Vvvv(thisline);

% computation of Brightness Temperature (BT) proper
BT_stn1 = ((L_B6 - Stn1uwr)./(emissivity * Stn1tr)) -...
(((1 - emissivity)./(emissivity))* Stn1dwr);

BT_stn2 = ((L_B6 - Stn2uwr)./(emissivity * Stn2tr)) -...
(((1 - emissivity)./(emissivity))* Stn2dwr);

BT_stn3 = ((L_B6 - Stn3uwr)./(emissivity * Stn3tr)) -...
(((1 - emissivity)./(emissivity))* Stn3dwr);

BT_stn4 = ((L_B6 - Stn4uwr)./(emissivity * Stn4tr)) -...
(((1 - emissivity)./(emissivity))* Stn4dwr);
```

```
BT_stn5 = ((L_B6 - Stn5uwr)./(emissivity * Stn5tr)) -...
(((1 - emissivity)./(emissivity))* Stn5dwr);

BT_stn6 = ((L_B6 - Stn6uwr)./(emissivity * Stn6tr)) -...
(((1 - emissivity)./(emissivity))* Stn6dwr);

BT_stn7 = ((L_B6 - Stn7uwr)./(emissivity * Stn7tr)) -...
(((1 - emissivity)./(emissivity))* Stn7dwr);

BT_stn8 = ((L_B6 - Stn8uwr)./(emissivity * Stn8tr)) -...
(((1 - emissivity)./(emissivity))* Stn8dwr);

BT_stn9 = ((L_B6 - Stn9uwr)./(emissivity * Stn9tr)) -...
(((1 - emissivity)./(emissivity))* Stn9dwr);

BT_stn10 = ((L_B6 - Stn10uwr)./(emissivity * Stn10tr)) -...
(((1 - emissivity)./(emissivity))* Stn10dwr);

BT_stn11 = ((L_B6 - Stn11uwr)./(emissivity * Stn11tr)) -...
(((1 - emissivity)./(emissivity))* Stn11dwr);

BT_stn12 = ((L_B6 - Stn12uwr)./(emissivity * Stn12tr)) -...
(((1 - emissivity)./(emissivity))* Stn12dwr);

BT_stn13 = ((L_B6 - Stn13uwr)./(emissivity * Stn13tr)) -...
(((1 - emissivity)./(emissivity))* Stn13dwr);
BT_stn14 = ((L_B6 - Stn14uwr)./(emissivity * Stn14tr)) -...
(((1 - emissivity)./(emissivity))* Stn14dwr);

BT_stn15 = ((L_B6 - Stn15uwr)./(emissivity * Stn15tr)) -...
(((1 - emissivity)./(emissivity))* Stn15dwr);

BT_stn16 = ((L_B6 - Stn16uwr)./(emissivity * Stn16tr)) -...
(((1 - emissivity)./(emissivity))* Stn16dwr);

% error analysis for Brightness Temperature (BT)i.e. when the range of
% emissivity is considered. uprad, downrad and transmittance depends
% on the station number considered.
% for maximum emissivity value
BT_Uppererror   =   ((L_B6   -   uprad_central)./(emissivityUppererror   *
trans_central)) -...
(((1          -          emissivityUppererror)./(emissivityUppererror))*
dwnrad_central);

% for minimum emissivity value
BT_Lowererror   =   ((L_B6   -   uprad_central)./(emissivityLowererror   *
trans_central)) -...
(((1          -          emissivityLowererror)./(emissivityLowererror))*
dwnrad_central);

BT1 = (((L_B6+1) - uprad_central))./((mod_emissivity * trans_central))
-...
(((1 - mod_emissivity)./(mod_emissivity))* dwnrad_central);

BT2    =    (L_B6    -    (uprad_central+diff_uprad))./((mod_emissivity    *
trans_central)) -...
(((1 - mod_emissivity)./(mod_emissivity))* dwnrad_central);

BT3 = ((L_B6 - uprad_central)./(mod_emissivity * trans_central)) -...
```

```
(((1                -                mod_emissivity)./(mod_emissivity))*
(dwnrad_central+diff_dwnrad));

BT4      =      ((L_B6      -      uprad_central)./(mod_emissivity      *
(trans_central+diff_trans))) -...
(((1 - mod_emissivity)./(mod_emissivity))* dwnrad_central);

BT5  =  ((L_B6  -  uprad_central)./((mod_emissivity+diff_emissivity)  *
trans_central)) -...
(((1 - mod_emissivity)./(mod_emissivity))* dwnrad_central);
```

8. Land Surface Temperature

```
% computation of Land Surface Temperature
% the pertubation analysis for Land Surface Temperature (LST)
K1 = 666.09 % for ETM+ image 666.09; for TM image 607.76;
K2 = 1282.71 % "   "     "   1282.71;  "       "   1260.56;
LST = K2./log(K1./BT_stn5 + 1);

% the mask BT, LST, ndvi and savi for the concentric computations
BTmask=BT_stn5; BTmask((IDXall == cloud1)|(IDXall == cloud2)) = nan;
LST_mask=LST; LST_mask((IDXall == cloud1)|(IDXall == cloud2)) = nan;
ndvi_mask=ndvi;  ndvi_mask((IDXall  ==  cloud1)|(IDXall  ==  cloud2))  =
nan;
savi_mask=savi;  savi_mask((IDXall  ==  cloud1)|(IDXall  ==  cloud2))  =
nan;
% comparison of LST with distance away from the flare source
(concentric plot), j = row and i = column. Dont forget to interchange
row and column used
% for the transect
Distance = [0:30:240];
j1 = 201;
i1 = 202;
LST_flaresource_mask = LST_mask(j1,i1);
meanLST_mask(1) = LST_flaresource_mask;
stdLST_mask(1) = nan;

LST_30m_mask  =  [LST_mask(j1-1,i1-1:i1+1),  LST_mask(j1+1,i1-1:i1+1),
LST_mask(j1,i1-1), LST_mask(j1,i1+1)];
meanLST_mask(2) = nanmean(LST_30m_mask);
stdLST_mask(2) = nanstd(LST_30m_mask);

LST_60m_mask    =    [LST_mask(j1-2,i1-2:i1+2),    LST_mask(j1-1,i1-2),
LST_mask(j1-1,i1+2),LST_mask(j1,i1-2),LST_mask(j1,i1+2),
LST_mask(j1+1,i1-2),LST_mask(j1+1,i1+2),LST_mask(j1+2,i1-2:i1+2)];
meanLST_mask(3) = nanmean(LST_60m_mask);
stdLST_mask(3) = nanstd(LST_60m_mask);

LST_90m_mask    =    [LST_mask(j1-3,i1-3:i1+3),    LST_mask(j1-2,i1-3),
LST_mask(j1-2,i1+3),LST_mask(j1-1,i1-3),LST_mask(j1-
1,i1+3),LST_mask(j1,i1-3), LST_mask(j1,i1+3)...
   LST_mask(j1+1,i1-3),LST_mask(j1+1,i1+3),LST_mask(j1+2,i1-
3),LST_mask(j1+2,i1+3),LST_mask(j1+3,i1-3:i1+3)];
meanLST_mask(4) = nanmean(LST_90m_mask);
stdLST_mask(4) = nanstd(LST_90m_mask);

LST_120m_mask    =    [LST_mask(j1-4,i1-4:i1+4),    LST_mask(j1-3,i1-4),
LST_mask(j1-3,i1+4),LST_mask(j1-2,i1-4),LST_mask(j1-
2,i1+4),LST_mask(j1-1,i1-4),        LST_mask(j1-1,i1+4),LST_mask(j1,i1-
4),LST_mask(j1,i1+4)...
```

```
    LST_mask(j1+1,i1-4),LST_mask(j1+1,i1+4),LST_mask(j1+2,i1-
4),LST_mask(j1+2,i1+4),LST_mask(j1+3,i1-
4),LST_mask(j1+3,i1+4),LST_mask(j1+4,i1-4:i1+4)];
meanLST_mask(5) = nanmean(LST_120m_mask);
stdLST_mask(5) = nanstd(LST_120m_mask);

LST_150m_mask    =    [LST_mask(j1-5,i1-5:i1+5),    LST_mask(j1-4,i1-5),
LST_mask(j1-4,i1+5),LST_mask(j1-3,i1-5),LST_mask(j1-
3,i1+5),LST_mask(j1-2,i1-5),   LST_mask(j1-2,i1+5),LST_mask(j1-1,i1-5),
LST_mask(j1-1,i1+5),LST_mask(j1,i1-5),LST_mask(j1,i1+5)...
    LST_mask(j1+1,i1-5),LST_mask(j1+1,i1+5),LST_mask(j1+2,i1-
5),LST_mask(j1+2,i1+5),LST_mask(j1+3,i1-
5),LST_mask(j1+3,i1+5),LST_mask(j1+4,i1-5),
LST_mask(j1+4,i1+5),LST_mask(j1+5,i1-5:i1+5)];
meanLST_mask(6) = nanmean(LST_150m_mask);
stdLST_mask(6) = nanstd(LST_150m_mask);

LST_180m_mask    =    [LST_mask(j1-6,i1-6:i1+6),    LST_mask(j1-5,i1-6),
LST_mask(j1-5,i1+6),LST_mask(j1-4,i1-6),LST_mask(j1-
4,i1+6),LST_mask(j1-3,i1-6),   LST_mask(j1-3,i1+6),LST_mask(j1-2,i1-6),
LST_mask(j1-2,i1+6),LST_mask(j1-1,i1-6),                  LST_mask(j1-
1,i1+6),LST_mask(j1,i1-6),LST_mask(j1,i1+6)...
    LST_mask(j1+1,i1-6),LST_mask(j1+1,i1+6),LST_mask(j1+2,i1-
6),LST_mask(j1+2,i1+6),LST_mask(j1+3,i1-
6),LST_mask(j1+3,i1+6),LST(j1+4,i1-6),
LST_mask(j1+4,i1+6),LST_mask(j1+5,i1-6),LST_mask(j1+5,i1+6),
LST_mask(j1+6,i1-6:i1+6)];
meanLST_mask(7) = nanmean(LST_180m_mask);
stdLST_mask(7) = nanstd(LST_180m_mask);

LST_210m_mask    =    [LST_mask(j1-7,i1-7:i1+7),    LST_mask(j1-6,i1-7),
LST_mask(j1-6,i1+7),LST_mask(j1-5,i1-7),LST_mask(j1-5,i1+7),LST(j1-
4,i1-7),     LST_mask(j1-4,i1+7),LST_mask(j1-3,i1-7),     LST_mask(j1-
3,i1+7),LST_mask(j1-2,i1-7),   LST_mask(j1-2,i1+7),LST_mask(j1-1,i1-7),
LST_mask(j1-1,i1+7), LST_mask(j1,i1-7)...
    LST_mask(j1,i1+7),LST_mask(j1+1,i1-
7),LST_mask(j1+1,i1+7),LST_mask(j1+2,i1-
7),LST_mask(j1+2,i1+7),LST_mask(j1+3,i1-
7),LST_mask(j1+3,i1+7),LST_mask(j1+4,i1-7),
LST_mask(j1+4,i1+7),LST_mask(j1+5,i1-7),LST_mask(j1+5,i1+7),
LST_mask(j1+6,i1-7),LST_mask(j1+6,i1+7),LST_mask(j1+7,i1-7:i1+7)];
meanLST_mask(8) = nanmean(LST_210m_mask);
stdLST_mask(8) = nanstd(LST_210m_mask);

LST_240m_mask    =    [LST_mask(j1-8,i1-8:i1+8),    LST_mask(j1-7,i1-8),
LST_mask(j1-7,i1+8),LST_mask(j1-6,i1-8),LST(j1-6,i1+8),LST_mask(j1-
5,i1-8),     LST_mask(j1-5,i1+8),LST_mask(j1-4,i1-8),     LST_mask(j1-
4,i1+8),LST_mask(j1-3,i1-8),   LST_mask(j1-3,i1+8),LST_mask(j1-2,i1-8),
LST_mask(j1-2,i1+8),LST_mask(j1-1,i1-8),          LST_mask(j1-1,i1+8),
LST_mask(j1,i1-8)...
    LST_mask(j1,i1+8),LST_mask(j1+1,i1-
8),LST_mask(j1+1,i1+8),LST_mask(j1+2,i1-
8),LST_mask(j1+2,i1+8),LST_mask(j1+3,i1-
8),LST_mask(j1+3,i1+8),LST_mask(j1+4,i1-8),
LST_mask(j1+4,i1+8),LST_mask(j1+5,i1-8),LST_mask(j1+5,i1+8),
LST_mask(j1+6,i1-8),LST_mask(j1+6,i1+8),LST_mask(j1+7,i1-
8),LST_mask(j1+7,i1+8), LST_mask(j1+8,i1-8:i1+8)];
meanLST_mask(9) = nanmean(LST_240m_mask);
stdLST_mask(9) = nanstd(LST_240m_mask);

% To plot error bar for LST parameter and save the results as picture
figure(508); clf;
```

```
errorbar(Distance, meanLST_mask, stdLST_mask, 'c*');
hold on;
xlabel('Distance (m)');
ylabel('Land Surface Temperature (K)');
print('-f508','-dpng','-r300','Eleme1_2003008LST.png');
```

10. Profile/ transect plotting

```
% for 100 stands for the pixel no for eleme for example while
% counting from the x axis while 167 is the dimension of y axis
figure(216);clf;
xval = [1:401];
yval = xval; % yval = double(yval);
yval(1,1:401) = LST_mask(200,1:401);
% for i = 1:401
% xval(i)=i;
% end
plot(xval,yval);
xlabel('Pixel number');
ylabel('Land Surface Temperature (K)');
% ylabel('SAVI');
 ylabel('Reflectance');
% ylabel('Wm^-2sr^-1') % It help to label the unit for Brightness
Temperature during plotting
hold on;
% That is i am plotting vertically
plot([201 201],[308 322],'k--')
print('-f201','-dpng','-r600','Eleme_I_2000352R4.png')

% plot([202 202],[min(yval)-5 max(yval)+5],'k--') % this help to plot
a vertical line through the flare source
% set(gca,'ylim',[-1 1]);% this is apply to ndvi & savi
print('-f20','-dpng','-r600','Sara_FL_2000352LST_transect.png')

% To print results data for a specific transect line out to a text
file:
newfilename = '';
newfilename    =['c:\PhD\results\transectdata_'    num2str(iStn)    '_'
namestem '.txt']
clear tmp;
tmp(1,:) = R1mask(1:401);
tmp(2,:) = R2mask(1:401);
tmp(3,:) = R3mask(1:401);
tmp(4,:) = R4mask(1:401);
tmp(5,:) = ndvimask(1:401);
tmp(6,:) = savimask(1:401);
tmp(7,:) = BTmask(1:401);
tmp(8,:) = LSTmask(1:401);
% tmp(9,:) = meanLST(161,:);
% tmp(10,:) = stdLST(1,401);
fid2 = fopen(newfilename, 'w');
fprintf(fid2, '%f \n', tmp);
fclose(fid2)
clear tmp;

% To save parameters (results) listed below through a directory in the
MATLAB environment
outname = ['C:\PhD\landsat\data\matlab_june_13' thisfile(1:23) '_Stn_'
num2str(iStn) '.mat'];
save(outname,'thisStnlon',                                    'thisStnlat',
'R1mask','R2mask','R3mask',...
    'R4mask','ndvi_mask','savi_mask','BTmask','LST_mask','IDX3',...
```

```
    'vegetation','water','soil','builtup');

end
 end
```

11 Generation of X and Y coordinates for the computed LST_mask

```
% to generate X and Y coordinates for each pixel in order to plot LST
in ArcGIS. 41 by 41 pixels were selected and used for this analysis.
clear thisX;
clear thisY;
% outputfile = ['C:\Users\bomorakinyo\External_Examiners_corrections\'
thisfile(1:23) '_Stn_' num2str(iStn) '.txt'];
outputfile =
['C:\Users\bomorakinyo\External_Examiners_corrections_01072015\'
thisfile(1:23) '_Stn_' num2str(iStn) '.txt'];
fid = fopen(outputfile,'w');
for i = 1:size(LST_mask,1)
    % thisX = ((i-1)*30 ) +  ll_easting;
    ll_eastingA = 284149;
    ll_northingA = 514453;
     thisX = ((i-1)*30 ) +  ll_eastingA;
    for j = 1:size(LST_mask,2)
        thisY = ((j-1)*30) + ll_northingA;
        clear thisline;
        thisline = [num2str(thisX) ' ' num2str(thisY) ' '
num2str(LST_mask(i,j))];
        fprintf(fid,'%s \n',thisline);
    end
end
fclose(fid);
```

B. Data analysis

1. Land surface Temperature and NDVI

```
% Three folders for data used are: 1 = L5_folder310513;
% 2 = L7_folder010613_SLCON; 3 = L7_folder020613_SLCOFF;
% datadir = C:\PhD\landsat\data\matlab_june_13\L7_folder020613_SLCOFF'
datadir = 'C:\PhD\landsat\data'; % the directory of the results files
cd(datadir);
d1 = dir(datadir);
for ifile = 1:487;
    thisfile = d1(ifile).name
    load(d1(ifile).name);
LST_veg = LST_mask;
LST_soil = LST_mask;
LST_builtup = LST_mask;
LST_water = LST_mask;

% to mask (remove) the unwanted classes out of the data
LST_veg((IDX3 == water)|(IDX3 == soil)| (IDX3 == builtup)) = nan;
LST_soil((IDX3 == water)|(IDX3 == vegetation)| (IDX3 == builtup)) =
nan;
LST_builtup((IDX3 == water)|(IDX3 == soil)| (IDX3 == vegetation)) =
nan;
LST_water((IDX3 == soil)|(IDX3 == vegetation)|(IDX3 == builtup)) =
nan;

j1 = 202; % row
i1 = 201; % column
```

```
clear Distance;
Distance = 60:30:450;

% computation of mean LST for vegetation in the Northern direction.
LSTveg60N    =    [LST_veg(j1-1,i1-1),LST_veg(j1-1,    i1),    LST_veg(j1-
1,i1+1)];
meanLSTvegN(1) = nanmean(LSTveg60N);
stdLSTvegN(1) = nanstd(LSTveg60N);

LSTveg90N = [LST_veg(j1-2,i1-1),LST_veg(j1-2,i1),LST_veg(j1-2,i1+1)];
meanLSTvegN(2) = nanmean(LSTveg90N);
stdLSTvegN(2) = nanstd(LSTveg90N);

LSTveg120N = [LST_veg(j1-3,i1-1),LST_veg(j1-3,i1),LST_veg(j1-3,i1+1)];
meanLSTvegN(3) = nanmean(LSTveg120N);
stdLSTvegN(3) = nanstd(LSTveg120N);

LSTveg150N = [LST_veg(j1-4,i1-1),LST_veg(j1-4,i1),LST_veg(j1-4,i1+1)];
meanLSTvegN(4) = nanmean(LSTveg150N);
stdLSTvegN(4) = nanstd(LSTveg150N);

LSTveg180N = [LST_veg(j1-5,i1-1),LST_veg(j1-5,i1),LST_veg(j1-5,i1+1)];
meanLSTvegN(5) = nanmean(LSTveg180N);
stdLSTvegN(5) = nanstd(LSTveg180N);

LSTveg210N = [LST_veg(j1-6,i1-1),LST_veg(j1-6,i1),LST_veg(j1-6,i1+1)];
meanLSTvegN(6) = nanmean(LSTveg210N);
stdLSTvegN(6) = nanstd(LSTveg210N);

LSTveg240N = [LST_veg(j1-7,i1-1),LST_veg(j1-7,i1),LST_veg(j1-7,i1+1)];
meanLSTvegN(7) = nanmean(LSTveg240N);
stdLSTvegN(7) = nanstd(LSTveg240N);

LSTveg270N = [LST_veg(j1-8,i1-1),LST_veg(j1-8,i1),LST_veg(j1-8,i1+1)];
meanLSTvegN(8) = nanmean(LSTveg270N);
stdLSTvegN(8) = nanstd(LSTveg270N);

LSTveg300N = [LST_veg(j1-9,i1-1),LST_veg(j1-9,i1),LST_veg(j1-9,i1+1)];
meanLSTvegN(9) = nanmean(LSTveg300N);
stdLSTvegN(9) = nanstd(LSTveg300N);

LSTveg330N     =     [LST_veg(j1-10,i1-1),LST_veg(j1-10,i1),LST_veg(j1-
10,i1+1)];
meanLSTvegN(10) = nanmean(LSTveg330N);
stdLSTvegN(10) = nanstd(LSTveg330N);

LSTveg360N=          [LST_veg(j1-11,i1-1),LST_veg(j1-11,i1),LST_veg(j1-
11,i1+1)];
meanLSTvegN(11) = nanmean(LSTveg360N);
stdLSTvegN(11) = nanstd(LSTveg360N);
LSTveg390N     =     [LST_veg(j1-12,i1-1),LST_veg(j1-12,i1),LST_veg(j1-
12,i1+1)];
meanLSTvegN(12) = nanmean(LSTveg390N);
stdLSTvegN(12) = nanstd(LSTveg390N);

LSTveg420N     =     [LST_veg(j1-13,i1-1),LST_veg(j1-13,i1),LST_veg(j1-
13,i1+1)];
meanLSTvegN(13) = nanmean(LSTveg420N);
stdLSTvegN(13) = nanstd(LSTveg420N);
```

```
LSTveg450N     =     [LST_veg(j1-14,i1-1),LST_veg(j1-14,i1),LST_veg(j1-
14,i1+1)];
meanLSTvegN(14) = nanmean(LSTveg450N);
stdLSTvegN(14) = nanstd(LSTveg450N);


% computation of mean LST for vegetation in the Eastern direction
LSTveg60E = [LST_veg(j1-1,i1+1),LST_veg(j1,i1+1), LST_veg(j1+1,i1+1)];
meanLSTvegE(1) = nanmean(LSTveg60E);
stdLSTvegE(1) = nanstd(LSTveg60E);

LSTveg90E = [LST_veg(j1-1,i1+2),LST_veg(j1,i1+2),LST_veg(j1+1,i1+2)];
meanLSTvegE(2) = nanmean(LSTveg90E);
stdLSTvegE(2) = nanstd(LSTveg90E);

LSTveg120E = [LST_veg(j1-1,i1+3),LST_veg(j1,i1+3),LST_veg(j1+1,i1+3)];
meanLSTvegE(3) = nanmean(LSTveg120E);
stdLSTvegE(3) = nanstd(LSTveg120E);

LSTveg150E = [LST_veg(j1-1,i1+4),LST_veg(j1,i1+4),LST_veg(j1+1,i1+4)];
meanLSTvegE(4) = nanmean(LSTveg150E);
stdLSTvegE(4) = nanstd(LSTveg150E);

LSTveg180E = [LST_veg(j1-1,i1+5),LST_veg(j1,i1+5),LST_veg(j1+1,i1+5)];
meanLSTvegE(5) = nanmean(LSTveg180E);
stdLSTvegE(5) = nanstd(LSTveg180E);

LSTveg210E = [LST_veg(j1-1,i1+6),LST_veg(j1,i1+6),LST_veg(j1+1,i1+6)];
meanLSTvegE(6) = nanmean(LSTveg210E);
stdLSTvegE(6) = nanstd(LSTveg210E);

LSTveg240E = [LST_veg(j1-1,i1+7),LST_veg(j1,i1+7),LST_veg(j1+1,i1+7)];
meanLSTvegE(7) = nanmean(LSTveg240E);
stdLSTvegE(7) = nanstd(LSTveg240E);

LSTveg270E = [LST_veg(j1-1,i1+8),LST_veg(j1,i1+8),LST_veg(j1+1,i1+8)];
meanLSTvegE(8) = nanmean(LSTveg270E);
stdLSTvegE(8) = nanstd(LSTveg270E);

LSTveg300E = [LST_veg(j1-1,i1+9),LST_veg(j1,i1+9),LST_veg(j1+1,i1+9)];
meanLSTvegE(9) = nanmean(LSTveg300E);
stdLSTvegE(9) = nanstd(LSTveg300E);

LSTveg330E = [LST_veg(j1-
1,i1+10),LST_veg(j1,i1+10),LST_veg(j1+1,i1+10)];
meanLSTvegE(10) = nanmean(LSTveg330E);
stdLSTvegE(10) = nanstd(LSTveg330E);

LSTveg360E = [LST_veg(j1-
1,i1+11),LST_veg(j1,i1+11),LST_veg(j1+1,i1+11)];
meanLSTvegE(11) = nanmean(LSTveg360E);
stdLSTvegE(11) = nanstd(LSTveg360E);

LSTveg390E = [LST_veg(j1-
1,i1+12),LST_veg(j1,i1+12),LST_veg(j1+1,i1+12)];
meanLSTvegE(12) = nanmean(LSTveg390E);
stdLSTvegE(12) = nanstd(LSTveg390E);
```

```
LSTveg420E = [LST_veg(j1-
1,i1+13),LST_veg(j1,i1+13),LST_veg(j1+1,i1+13)];
meanLSTvegE(13) = nanmean(LSTveg420E);
stdLSTvegE(13) = nanstd(LSTveg420E);

LSTveg450E = [LST_veg(j1-
1,i1+14),LST_veg(j1,i1+14),LST_veg(j1+1,i1+14)];
meanLSTvegE(14) = nanmean(LSTveg450E);
stdLSTvegE(14) = nanstd(LSTveg450E);


% computation of mean LST for vegetation in the Southern direction
LSTveg60S = [LST_veg(j1+1,i1-1),LST_veg(j1+1, i1),
LST_veg(j1+1,i1+1)];
meanLSTvegS(1) = nanmean(LSTveg60S);
stdLSTvegS(1) = nanstd(LSTveg60S);

LSTveg90S = [LST_veg(j1+2,i1-1),LST_veg(j1+2,i1),LST_veg(j1+2,i1+1)];
meanLSTvegS(2) = nanmean(LSTveg90S);
stdLSTvegS(2) = nanstd(LSTveg90S);

LSTveg120S = [LST_veg(j1+3,i1-1),LST_veg(j1+3,
i1),LST_veg(j1+3,i1+1)];
meanLSTvegS(3) = nanmean(LSTveg120S);
stdLSTvegS(3) = nanstd(LSTveg120S);

LSTveg150S = [LST_veg(j1+4,i1-1),LST_veg(j1+4,i1),LST_veg(j1+4,i1+1)];
meanLSTvegS(4) = nanmean(LSTveg150S);
stdLSTvegS(4) = nanstd(LSTveg150S);

LSTveg180S = [LST_veg(j1+5,i1-1),LST_veg(j1+5,i1),LST_veg(j1+5,i1+1)];
meanLSTvegS(5) = nanmean(LSTveg180S);
stdLSTvegS(5) = nanstd(LSTveg180S);

LSTveg210S = [LST_veg(j1+6,i1-1),LST_veg(j1+6,i1),LST_veg(j1+6,i1+1)];
meanLSTvegS(6) = nanmean(LSTveg210S);
stdLSTvegS(6) = nanstd(LSTveg210S);

LSTveg240S = [LST_veg(j1+7,i1-1),LST_veg(j1+7,i1),LST_veg(j1+7,i1+1)];
meanLSTvegS(7) = nanmean(LSTveg240S);
stdLSTvegS(7) = nanstd(LSTveg240S);

LSTveg270S = [LST_veg(j1+8,i1-1),LST_veg(j1+8,i1),LST_veg(j1+8,i1+1)];
meanLSTvegS(8) = nanmean(LSTveg270S);
stdLSTvegS(8) = nanstd(LSTveg270S);

LSTveg300S = [LST_veg(j1+9,i1-1),LST_veg(j1+9,i1),LST_veg(j1+9,i1+1)];
meanLSTvegS(9) = nanmean(LSTveg300S);
stdLSTvegS(9) = nanstd(LSTveg300S);

LSTveg330S = [LST_veg(j1+10,i1-
1),LST_veg(j1+10,i1),LST_veg(j1+10,i1+1)];
meanLSTvegS(10) = nanmean(LSTveg330S);
stdLSTvegS(10) = nanstd(LSTveg330S);

LSTveg360S = [LST_veg(j1+11,i1-
1),LST_veg(j1+11,i1),LST_veg(j1+11,i1+1)];
meanLSTvegS(11) = nanmean(LSTveg360S);
stdLSTvegS(11) = nanstd(LSTveg360S);
```

```
LSTveg390S = [LST_veg(j1+12,i1-
1),LST_veg(j1+12,i1),LST_veg(j1+12,i1+1)];
meanLSTvegS(12) = nanmean(LSTveg390S);
stdLSTvegS(12) = nanstd(LSTveg390S);

LSTveg420S = [LST_veg(j1+13,i1-
1),LST_veg(j1+13,i1),LST_veg(j1+13,i1+1)];
meanLSTvegS(13) = nanmean(LSTveg420S);
stdLSTvegS(13) = nanstd(LSTveg420S);

LSTveg450S = [LST_veg(j1+14,i1-
1),LST_veg(j1+14,i1),LST_veg(j1+14,i1+1)];
meanLSTvegS(14) = nanmean(LSTveg450S);
stdLSTvegS(14) = nanstd(LSTveg450S);


% computation of mean LST for vegetation in the Western direction
LSTveg60W = [LST_veg(j1+1,i1-1),LST_veg(j1,i1-1),LST_veg(j1-1,i1-1)];
meanLSTvegW(1) = nanmean(LSTveg60W);
stdLSTvegW(1) = nanstd(LSTveg60W);

LSTveg90W = [LST_veg(j1+1,i1-2),LST_veg(j1,i1-2),LST_veg(j1-1,i1-2)];
meanLSTvegW(2) = nanmean(LSTveg90W);
stdLSTvegW(2) = nanstd(LSTveg90W);

LSTveg120W = [LST_veg(j1+1,i1-3),LST_veg(j1,i1-3),LST_veg(j1-1,i1-3)];
meanLSTvegW(3) = nanmean(LSTveg120W);
stdLSTvegW(3) = nanstd(LSTveg120W);

LSTveg150W = [LST_veg(j1+1,i1-4),LST_veg(j1,i1-4),LST_veg(j1-1,i1-4)];
meanLSTvegW(4) = nanmean(LSTveg150W);
stdLSTvegW(4) = nanstd(LSTveg150W);

LSTveg180W = [LST_veg(j1+1,i1-5),LST_veg(j1,i1-5),LST_veg(j1-1,i1-5)];
meanLSTvegW(5) = nanmean(LSTveg180W);
stdLSTvegW(5) = nanstd(LSTveg180W);

LSTveg210W = [LST_veg(j1+1,i1-6),LST_veg(j1,i1-6),LST_veg(j1-1,i1-6)];
meanLSTvegW(6) = nanmean(LSTveg210W);
stdLSTvegW(6) = nanstd(LSTveg210W);

LSTveg240W = [LST_veg(j1+1,i1-7),LST_veg(j1,i1-7),LST_veg(j1-1,i1-7)];
meanLSTvegW(7) = nanmean(LSTveg240W);
stdLSTvegW(7) = nanstd(LSTveg240W);

LSTveg270W = [LST_veg(j1+1,i1-8),LST_veg(j1,i1-8),LST_veg(j1-1,i1-8)];
meanLSTvegW(8) = nanmean(LSTveg270W);
stdLSTvegW(8) = nanstd(LSTveg270W);
LSTveg300W = [LST_veg(j1+1,i1-9),LST_veg(j1,i1-9),LST_veg(j1-1,i1-9)];
meanLSTvegW(9) = nanmean(LSTveg300W);
stdLSTvegW(9) = nanstd(LSTveg300W);

LSTveg330W  =  [LST_veg(j1+1,i1-10),LST_veg(j1,i1-10),LST_veg(j1-1,i1-
10)];
meanLSTvegW(10) = nanmean(LSTveg330W);
stdLSTvegW(10) = nanstd(LSTveg330W);

LSTveg360W  =  [LST_veg(j1+1,i1-11),LST_veg(j1,i1-11),LST_veg(j1-1,i1-
11)];
meanLSTvegW(11) = nanmean(LSTveg360W);
stdLSTvegW(11) = nanstd(LSTveg360W);
```

```
LSTveg390W   =   [LST_veg(j1+1,i1-12),LST_veg(j1,i1-12),LST_veg(j1-1,i1-
12)];
meanLSTvegW(12) = nanmean(LSTveg390W);
stdLSTvegW(12) = nanstd(LSTveg390W);

LSTveg420W   =   [LST_veg(j1+1,i1-13),LST_veg(j1,i1-13),LST_veg(j1-1,i1-
13)];
meanLSTvegW(13) = nanmean(LSTveg420W);
stdLSTvegW(13) = nanstd(LSTveg420W);

LSTveg450W   =   [LST_veg(j1+1,i1-14),LST_veg(j1,i1-14),LST_veg(j1-1,i1-
14)];
meanLSTvegW(14) = nanmean(LSTveg450W);
stdLSTvegW(14) = nanstd(LSTveg450W);



% computation of vegetation index: NDVI
% NDVI for vegetation i.e to mask water, soil and built up classes to
% remain only vegetation
ndvi_veg = ndvi_mask;
ndvi_veg((IDX3 == water)|(IDX3 == soil)| (IDX3 == builtup)) = nan;

% computation of mean ndvi for vegetation in the Northern direction
ndviveg60N   =   [ndvi_veg(j1-1,i1-1),ndvi_veg(j1-1,   i1),   ndvi_veg(j1-
1,i1+1)];
meanndvivegN(1) = nanmean(ndviveg60N);
stdndvivegN(1) = nanstd(ndviveg60N);

ndviveg90N     =     [ndvi_veg(j1-2,i1-1),ndvi_veg(j1-2,i1),ndvi_veg(j1-
2,i1+1)];
meanndvivegN(2) = nanmean(ndviveg90N);
stdndvivegN(2) = nanstd(ndviveg90N);

ndviveg120N    =    [ndvi_veg(j1-3,i1-1),ndvi_veg(j1-3,i1),ndvi_veg(j1-
3,i1+1)];
meanndvivegN(3) = nanmean(ndviveg120N);
stdndvivegN(3) = nanstd(ndviveg120N);

ndviveg150N    =    [ndvi_veg(j1-4,i1-1),ndvi_veg(j1-4,i1),ndvi_veg(j1-
4,i1+1)];
meanndvivegN(4) = nanmean(ndviveg150N);
stdndvivegN(4) = nanstd(ndviveg150N);

ndviveg180N    =    [ndvi_veg(j1-5,i1-1),ndvi_veg(j1-5,i1),ndvi_veg(j1-
5,i1+1)];
meanndvivegN(5) = nanmean(ndviveg180N);
stdndvivegN(5) = nanstd(ndviveg180N);

ndviveg210N    =    [ndvi_veg(j1-6,i1-1),ndvi_veg(j1-6,i1),ndvi_veg(j1-
6,i1+1)];
meanndvivegN(6) = nanmean(ndviveg210N);
stdndvivegN(6) = nanstd(ndviveg210N);

ndviveg240N    =    [ndvi_veg(j1-7,i1-1),ndvi_veg(j1-7,i1),ndvi_veg(j1-
7,i1+1)];
meanndvivegN(7) = nanmean(ndviveg240N);
stdndvivegN(7) = nanstd(ndviveg240N);
```

```
ndviveg270N    =    [ndvi_veg(j1-8,i1-1),ndvi_veg(j1-8,i1),ndvi_veg(j1-
8,i1+1)];
meanndvivegN(8) = nanmean(ndviveg270N);
stdndvivegN(8) = nanstd(ndviveg270N);

ndviveg300N    =    [ndvi_veg(j1-9,i1-1),ndvi_veg(j1-9,i1),ndvi_veg(j1-
9,i1+1)];
meanndvivegN(9) = nanmean(ndviveg300N);
stdndvivegN(9) = nanstd(ndviveg300N);

ndviveg330N   =   [ndvi_veg(j1-10,i1-1),ndvi_veg(j1-10,i1),ndvi_veg(j1-
10,i1+1)];
meanndvivegN(10) = nanmean(ndviveg330N);
stdndvivegN(10) = nanstd(ndviveg330N);

ndviveg360N   =   [ndvi_veg(j1-11,i1-1),ndvi_veg(j1-11,i1),ndvi_veg(j1-
11,i1+1)];
meanndvivegN(11) = nanmean(ndviveg360N);
stdndvivegN(11) = nanstd(ndviveg360N);

ndviveg390N   =   [ndvi_veg(j1-12,i1-1),ndvi_veg(j1-12,i1),ndvi_veg(j1-
12,i1+1)];
meanndvivegN(12) = nanmean(ndviveg390N);
stdndvivegN(12) = nanstd(ndviveg390N);

ndviveg420N   =   [ndvi_veg(j1-13,i1-1),ndvi_veg(j1-13,i1),ndvi_veg(j1-
13,i1+1)];
meanndvivegN(13) = nanmean(ndviveg420N);
stdndvivegN(13) = nanstd(ndviveg420N);

ndviveg450N   =   [ndvi_veg(j1-14,i1-1),ndvi_veg(j1-14,i1),ndvi_veg(j1-
14,i1+1)];
meanndvivegN(14) = nanmean(ndviveg450N)
stdndvivegN(14) = nanstd(ndviveg450N);

% computation of mean ndvi for vegetation in the Eastern direction
ndviveg60E       =       [ndvi_veg(j1-1,i1+1),ndvi_veg(j1,       i1+1),
ndvi_veg(j1+1,i1+1)];
meanndvivegE(1) = nanmean(ndviveg60E);
stdndvivegE(1) = nanstd(ndviveg60E);

ndviveg90E                          =                          [ndvi_veg(j1-
1,i1+2),ndvi_veg(j1,i1+2),ndvi_veg(j1+1,i1+2)];
meanndvivegE(2) = nanmean(ndviveg90E);
stdndvivegE(2) = nanstd(ndviveg90E);
ndviveg120E                         =                          [ndvi_veg(j1-
1,i1+3),ndvi_veg(j1,i1+3),ndvi_veg(j1+1,i1+3)];
meanndvivegE(3) = nanmean(ndviveg120E);
stdndvivegE(3) = nanstd(ndviveg120E);
ndviveg150E                         =                          [ndvi_veg(j1-
1,i1+4),ndvi_veg(j1,i1+4),ndvi_veg(j1+1,i1+4)];
meanndvivegE(4) = nanmean(ndviveg150E);
stdndvivegE(4) = nanstd(ndviveg150E);
ndviveg180E                         =                          [ndvi_veg(j1-
1,i1+5),ndvi_veg(j1,i1+5),ndvi_veg(j1+1,i1+5)];
meanndvivegE(5) = nanmean(ndviveg180E);
stdndvivegE(5) = nanstd(ndviveg180E);

ndviveg210E                         =                          [ndvi_veg(j1-
1,i1+6),ndvi_veg(j1,i1+6),ndvi_veg(j1+1,i1+6)];
meanndvivegE(6) = nanmean(ndviveg210E);
```

```
stdndvivegE(6) = nanstd(ndviveg210E);

ndviveg240E                          =                          [ndvi_veg(j1-
1,i1+7),ndvi_veg(j1,i1+7),ndvi_veg(j1+1,i1+7)];
meanndvivegE(7) = nanmean(ndviveg240E);
stdndvivegE(7) = nanstd(ndviveg240E);
ndviveg270E                          =                          [ndvi_veg(j1-
1,i1+8),ndvi_veg(j1,i1+8),ndvi_veg(j1+1,i1+8)];
meanndvivegE(8) = nanmean(ndviveg270E);
stdndvivegE(8) = nanstd(ndviveg270E);

ndviveg300E                          =                          [ndvi_veg(j1-
1,i1+9),ndvi_veg(j1,i1+9),ndvi_veg(j1+1,i1+9)];
meanndvivegE(9) = nanmean(ndviveg300E);
stdndvivegE(9) = nanstd(ndviveg300E);

ndviveg330E                          =                          [ndvi_veg(j1-
1,i1+10),ndvi_veg(j1,i1+10),ndvi_veg(j1+1,i1+10)];
meanndvivegE(10) = nanmean(ndviveg330E);
stdndvivegE(10) = nanstd(ndviveg330E);

ndviveg360E                          =                          [ndvi_veg(j1-
1,i1+11),ndvi_veg(j1,i1+11),ndvi_veg(j1+1,i1+11)];
meanndvivegE(11) = nanmean(ndviveg360E);
stdndvivegE(11) = nanstd(ndviveg360E);

ndviveg390E                          =                          [ndvi_veg(j1-
1,i1+12),ndvi_veg(j1,i1+12),ndvi_veg(j1+1,i1+12)];
meanndvivegE(12) = nanmean(ndviveg390E);
stdndvivegE(12) = nanstd(ndviveg390E);

ndviveg420E                          =                          [ndvi_veg(j1-
1,i1+13),ndvi_veg(j1,i1+13),ndvi_veg(j1+1,i1+13)];
meanndvivegE(13) = nanmean(ndviveg420E);
stdndvivegE(13) = nanstd(ndviveg420E);

ndviveg450E                          =                          [ndvi_veg(j1-
1,i1+14),ndvi_veg(j1,i1+14),ndvi_veg(j1+1,i1+14)];
meanndvivegE(14) = nanmean(ndviveg450E)
stdndvivegE(14) = nanstd(ndviveg450E);

% computation of mean ndvi for vegetation in the Southern direction
ndviveg60S = [ndvi_veg(j1+1,i1-1),ndvi_veg(j1+1, i1),
ndvi_veg(j1+1,i1+1)];
meanndvivegS(1) = nanmean(ndviveg60S);
stdndvivegS(1) = nanstd(ndviveg60S);

ndviveg90S = [ndvi_veg(j1+2,i1-
1),ndvi_veg(j1+2,i1),ndvi_veg(j1+2,i1+1)];
meanndvivegS(2) = nanmean(ndviveg90S);
stdndvivegS(2) = nanstd(ndviveg90S);

ndviveg120S = [ndvi_veg(j1+3,i1-1),ndvi_veg(j1+3,
i1),ndvi_veg(j1+3,i1+1)];
meanndvivegS(3) = nanmean(ndviveg120S);
stdndvivegS(3) = nanstd(ndviveg120S);
ndviveg150S = [ndvi_veg(j1+4,i1-
1),ndvi_veg(j1+4,i1),ndvi_veg(j1+4,i1+1)];
meanndvivegS(4) = nanmean(ndviveg150S);
stdndvivegS(4) = nanstd(ndviveg150S);
```

```
ndviveg180S = [ndvi_veg(j1+5,i1-
1),ndvi_veg(j1+5,i1),ndvi_veg(j1+5,i1+1)];
meanndvivegS(5) = nanmean(ndviveg180S);
stdndvivegS(5) = nanstd(ndviveg180S);

ndviveg210S = [ndvi_veg(j1+6,i1-
1),ndvi_veg(j1+6,i1),ndvi_veg(j1+6,i1+1)];
meanndvivegS(6) = nanmean(ndviveg210S);
stdndvivegS(6) = nanstd(ndviveg210S);

ndviveg240S = [ndvi_veg(j1+7,i1-
1),ndvi_veg(j1+7,i1),ndvi_veg(j1+7,i1+1)];
meanndvivegS(7) = nanmean(ndviveg240S);
stdndvivegS(7) = nanstd(ndviveg240S);

ndviveg270S = [ndvi_veg(j1+8,i1-
1),ndvi_veg(j1+8,i1),ndvi_veg(j1+8,i1+1)];
meanndvivegS(8) = nanmean(ndviveg270S);
stdndvivegS(8) = nanstd(ndviveg270S);

ndviveg300S = [ndvi_veg(j1+9,i1-
1),ndvi_veg(j1+9,i1),ndvi_veg(j1+9,i1+1)];
meanndvivegS(9) = nanmean(ndviveg300S);
stdndvivegS(9) = nanstd(ndviveg300S);

ndviveg330S = [ndvi_veg(j1+10,i1-
1),ndvi_veg(j1+10,i1),ndvi_veg(j1+10,i1+1)];
meanndvivegS(10) = nanmean(ndviveg330S);
stdndvivegS(10) = nanstd(ndviveg330S);

ndviveg360S = [ndvi_veg(j1+11,i1-
1),ndvi_veg(j1+11,i1),ndvi_veg(j1+11,i1+1)];
meanndvivegS(11) = nanmean(ndviveg360S);
stdndvivegS(11) = nanstd(ndviveg360S);

ndviveg390S = [ndvi_veg(j1+12,i1-
1),ndvi_veg(j1+12,i1),ndvi_veg(j1+12,i1+1)];
meanndvivegS(12) = nanmean(ndviveg390S);
stdndvivegS(12) = nanstd(ndviveg390S);

ndviveg420S = [ndvi_veg(j1+13,i1-
1),ndvi_veg(j1+13,i1),ndvi_veg(j1+13,i1+1)];
meanndvivegS(13) = nanmean(ndviveg420S);
stdndvivegS(13) = nanstd(ndviveg420S);

ndviveg450S = [ndvi_veg(j1+14,i1-
1),ndvi_veg(j1+14,i1),ndvi_veg(j1+14,i1+1)];
meanndvivegS(14) = nanmean(ndviveg450S)
stdndvivegS(14) = nanstd(ndviveg450S);

% computation of mean ndvi for vegetation in the Western direction
ndviveg60W  =  [ndvi_veg(j1+1,i1-1),ndvi_veg(j1,i1-1),ndvi_veg(j1-1,i1-
1)];
meanndvivegW(1) = nanmean(ndviveg60W);
stdndvivegW(1) = nanstd(ndviveg60W);

ndviveg90W  =  [ndvi_veg(j1+1,i1-2),ndvi_veg(j1,i1-2),ndvi_veg(j1-1,i1-
2)];
meanndvivegW(2) = nanmean(ndviveg90W);
stdndvivegW(2) = nanstd(ndviveg90W);
```

```
ndviveg120W = [ndvi_veg(j1+1,i1-3),ndvi_veg(j1,i1-3),ndvi_veg(j1-1,i1-
3)];
meanndvivegW(3) = nanmean(ndviveg120W);
stdndvivegW(3) = nanstd(ndviveg120W);

ndviveg150W = [ndvi_veg(j1+1,i1-4),ndvi_veg(j1,i1-4),ndvi_veg(j1-1,i1-
4)];
meanndvivegW(4) = nanmean(ndviveg150W);
stdndvivegW(4) = nanstd(ndviveg150W);

ndviveg180W = [ndvi_veg(j1+1,i1-5),ndvi_veg(j1,i1-5),ndvi_veg(j1-1,i1-
5)];
meanndvivegW(5) = nanmean(ndviveg180W);
stdndvivegW(5) = nanstd(ndviveg180W);

ndviveg210W = [ndvi_veg(j1+1,i1-6),ndvi_veg(j1,i1-6),ndvi_veg(j1-1,i1-
6)];
meanndvivegW(6) = nanmean(ndviveg210W);
stdndvivegW(6) = nanstd(ndviveg210W);

ndviveg240W = [ndvi_veg(j1+1,i1-7),ndvi_veg(j1,i1-7),ndvi_veg(j1-1,i1-
7)];
meanndvivegW(7) = nanmean(ndviveg240W);
stdndvivegW(7) = nanstd(ndviveg240W);

ndviveg270W = [ndvi_veg(j1+1,i1-8),ndvi_veg(j1,i1-8),ndvi_veg(j1-1,i1-
8)];
meanndvivegW(8) = nanmean(ndviveg270W);
stdndvivegW(8) = nanstd(ndviveg270W);

ndviveg300W = [ndvi_veg(j1+1,i1-9),ndvi_veg(j1,i1-9),ndvi_veg(j1-1,i1-
9)];
meanndvivegW(9) = nanmean(ndviveg300W);
stdndvivegW(9) = nanstd(ndviveg300W);

ndviveg330W   =   [ndvi_veg(j1+1,i1-10),ndvi_veg(j1,i1-10),ndvi_veg(j1-
1,i1-10)];
meanndvivegW(10) = nanmean(ndviveg330W);
stdndvivegW(10) = nanstd(ndviveg330W);

ndviveg360W   =   [ndvi_veg(j1+1,i1-11),ndvi_veg(j1,i1-11),ndvi_veg(j1-
1,i1-11)];
meanndvivegW(11) = nanmean(ndviveg360W);
stdndvivegW(11) = nanstd(ndviveg360W);

ndviveg390W   =   [ndvi_veg(j1+1,i1-12),ndvi_veg(j1,i1-12),ndvi_veg(j1-
1,i1-12)];
meanndvivegW(12) = nanmean(ndviveg390W);
stdndvivegW(12) = nanstd(ndviveg390W);

ndviveg420W = [ndvi_veg(j1+1,i1-13),ndvi_veg(j1,i1-13),ndvi_veg(j1-
1,i1-13)];
meanndvivegW(13) = nanmean(ndviveg420W);
stdndvivegW(13) = nanstd(ndviveg420W);

ndviveg450W = [ndvi_veg(j1+1,i1-14),ndvi_veg(j1,i1-14),ndvi_veg(j1-
1,i1-14)];
meanndvivegW(14) = nanmean(ndviveg450W)
stdndvivegW(14) = nanstd(ndviveg450W);

figure(20); clf;
```

```
% to plot all four directions (N, E, S, W) on a MATLAB page
% to plot North direction: LST and NDVI
subplot(2,2,1); % to plot first row and first column
errorbar(Distance, meanLSTvegN, stdLSTvegN, 'color', [0.3 0.3 0.3]);
 hold on
errorbar(Distance(1:2:end), meanLSTvegN(1:2:end), stdLSTvegN(1:2:end),
'gs', 'markerfacecolor', 'g');
errorbar(Distance, meanLSTsoilN, stdLSTsoilN, 'ro');
errorbar(Distance, meanLSTbuiltupN, stdLSTbuiltupN, 'c*');

h1a = gca;
set(gca, 'xlim',[0 500], 'ylim',[300 370]);
xlabel('Distance (m)');
ylabel('Land Surface Temperature (K)');
legend({'LST(veg)', 'LST(soil)', 'LST(builtup)'})

h1b = axes('position', get(h1a, 'position'));
errorbar(Distance, meanndvivegN, stdndvivegN, 'k--');
set(h1b,'yaxislocation', 'right');
set(h1b, 'xtick', [ ])
set(h1b, 'color', 'none')
ylabel('NDVI');

% to plot East direction: LST and NDVI
subplot(2,2,2); % to plot first row and second column
errorbar(Distance, meanLSTvegE, stdLSTvegE, 'color', [0.3 0.3 0.3]);
 hold on
errorbar(Distance(1:2:end), meanLSTvegE(1:2:end), stdLSTvegE(1:2:end),
'gs', 'markerfacecolor', 'g');
errorbar(Distance,        meanLSTvegE,        stdLSTvegE,        'gs',
'markerfacecolor','g');
errorbar(Distance, meanLSTsoilE, stdLSTsoilE, 'ro');
errorbar(Distance, meanLSTbuiltupE, stdLSTbuiltupE, 'c*');

h2a = gca;
set(gca, 'xlim',[0 500], 'ylim',[300 370]);
xlabel('Distance (m)');
ylabel('Land Surface Temperature (K)');

h2b = axes('position', get(h2a, 'position'));
errorbar(Distance, meanndvivegE, stdndvivegE, 'k--');
set(h2b,'yaxislocation', 'right');
set(h2b, 'xtick', [ ])
set(h2b, 'color', 'none')
ylabel('NDVI’);



% to plot South direction: LST and NDVI
subplot(2,2,3); % to plot second row and first column
errorbar(Distance, meanLSTvegS, stdLSTvegS, 'color', [0.3 0.3 0.3]);
 hold on
errorbar(Distance(1:2:end), meanLSTvegS(1:2:end), stdLSTvegS(1:2:end),
'gs', 'markerfacecolor', 'g');
errorbar(Distance, meanLSTsoilS, stdLSTsoilS, 'ro');
errorbar(Distance, meanLSTbuiltupS, stdLSTbuiltupS, 'c*');

h3a = gca;
set(gca, 'xlim',[0 500], 'ylim',[300 370]);
xlabel('Distance (m)');
ylabel('Land Surface Temperature (K)');

h3b = axes('position', get(h3a, 'position'));
errorbar(Distance, meanndvivegS, stdndvivegS, 'k--');
```

```
set(h3b,'yaxislocation', 'right');
set(h3b, 'xtick', [ ])
set(h3b, 'color', 'none')
ylabel('NDVI');


% to plot West direction: LST and NDVI
subplot(2,2,4); % to plot second row and second column
errorbar(Distance, meanLSTvegW, stdLSTvegW, 'color', [0.3 0.3 0.3]);
 hold on
errorbar(Distance(1:2:end), meanLSTvegW(1:2:end), stdLSTvegW(1:2:end),
'gs', 'markerfacecolor', 'g');
errorbar(Distance, meanLSTsoilW, stdLSTsoilW, 'ro');
errorbar(Distance, meanLSTbuiltupW, stdLSTbuiltupW, 'c*');

h4a = gca;
set(gca, 'xlim',[0 500], 'ylim',[300 370]);
xlabel('Distance (m)');
ylabel('Land Surface Temperature (K)');

h4b = axes('position', get(h4a, 'position'));
errorbar(Distance, meanndvivegW, stdndvivegW, 'k--');
set(h4b,'yaxislocation', 'right');
set(h4b, 'xtick', [ ])
set(h4b, 'color', 'none')
ylabel('NDVI');


% to save the plotted graphs in a directory with the image
identification
updated1_outname_results                                                =
['C:\PhD\landsat\data\analysis_results_updated\'
thisfile(1:length(thisfile)-4) '.png'];
print('-f20','-dpng','-r600',updated1_outname_results);
```

2. Differences in Land Surface Temperature and NDVI

```
% Computation of LST difference for the vegetation at 60 m from the
stack & the lowest LST value from 150 m away from the flare to 450 m
meanLSTvegN(1) = nanmean(LSTveg60N);
meanLSTvegE(1) = nanmean(LSTveg60E);
meanLSTvegS(1) = nanmean(LSTveg60S);
meanLSTvegW(1) = nanmean(LSTveg60W);
a = min(meanLSTvegN(5:end));
b = min(meanLSTvegE(5:end));
c = min(meanLSTvegS(5:end));
d = min(meanLSTvegW(5:end));
diff_LSTVvN = (meanLSTvegN(1) - a)
diff_LSTVvE = (meanLSTvegE(1) - b)
diff_LSTVvS = (meanLSTvegS(1) - c)
diff_LSTVvW = (meanLSTvegW(1) - d)

% Computation of NDVI difference between 450 m & 60 m for vegetation
meanndvivegN(1) = nanmean(ndviveg60N);
meanndvivegE(1) = nanmean(ndviveg60E);
meanndvivegS(1) = nanmean(ndviveg60S);
meanndvivegW(1) = nanmean(ndviveg60W);
a = max(meanndvivegN(5:end))
b = max(meanndvivegE(5:end))
c = max(meanndvivegS(5:end))
d = max(meanndvivegW(5:end))
diff_ndviVvN = (a - meanndvivegN(1))
```

```
diff_ndviVvE = (b - meanndvivegE(1))
diff_ndviVvS = (c - meanndvivegS(1))
diff_ndviVvW = (d - meanndvivegW(1))
```

3. Regression analysis (ANOVA) for LST and NDVI

```
% for North direction
a = min(meanLSTvegN(5:end));
imin = find(meanLSTvegN(5:end)== a);
myDistance = [60:30:450];
XanovaLSTN(1:3,1) =eval(['LSTveg' num2str(myDistance(imin)) 'N']);
XanovaLSTN(4:6,1) = LSTveg60N
Group = [1,1,1,2,2,2]';
PdLSTN = anova1(XanovaLSTN, Group);

% for East direction
b = min(meanLSTvegE(5:end));
imin = find(meanLSTvegE(5:end)== b);
myDistance = [60:30:450];
XanovaLSTE(1:3,1) =eval(['LSTveg' num2str(myDistance(imin)) 'E']);
XanovaLSTE(4:6,1) = LSTveg60E
Group = [1,1,1,2,2,2]';
PdLSTE = anova1(XanovaLSTE, Group);

% for South direction
c = min(meanLSTvegS(5:end));
imin = find(meanLSTvegS(5:end)== c);
myDistance = [60:30:450];
XanovaLSTS(1:3,1) =eval(['LSTveg' num2str(myDistance(imin)) 'S']);
XanovaLSTS(4:6,1) = LSTveg60S
Group = [1,1,1,2,2,2]';
PdLSTS = anova1(XanovaLSTS, Group);

% for West direction
d = min(meanLSTvegW(5:end));
imin = find(meanLSTvegW(5:end)== d);
myDistance = [60:30:450];
XanovaLSTW(1:3,1) =eval(['LSTveg' num2str(myDistance(imin)) 'W']);
XanovaLSTW(4:6,1) = LSTveg60W
Group = [1,1,1,2,2,2]';
PdLSTW = anova1(XanovaLSTW, Group);
```

4. Regression analysis for LST and NDVI using ANOVA results (p-values)

```
% computation of N, r-value & p-value & scatter plot of dLST for all
facilities
clear;
% flt if facility = 1;
% yr is year = 2;
% jd is julian day = 3;
% mm is month = 4;
% sht is stack height = 5;
% sz is size = 6;
% ct is curve type = 7;
% dLSTn is north direction plot = 8;
% dLSTe is east direction plot = 9;
% dLSTs is south direction plot = 10;
% dLSTw is west direction plot = 11;
% PN is the p-value from anova, north direction = 12;
% PE is the p-value from anova, east direction = 13;
```

```
% PS is the p-value from anova, south direction = 14;
% PW is the p-value from anova, west direction = 15;
% dNDVIN for north = 16;
% dNDVIE for east = 17;
% dNDVIS for south = 18;
% dNDVIW for west = 19;
% PNNDVI is the p-value from anova, north direction = 20;
% PENDVI is the p-value from anova, east direction = 21;
% PSNDVI is the p-value from anova, south direction = 22;
% PWNDVI is the p-value from anova, west direction = 23;
% dSAVIN for north = 24;
% dSAVIE for east = 25;
% dSAVIS for south = 26;
% dSAVIW for west = 27;
% PNSAVIN is the p-value from anova, north direction = 28;
% PSAVIE is the p-value from anova, east direction = 29;
% PSAVIS is the p-value from anova, south direction = 30;
% PSAVIW is the p-value from anova, west direction = 31;

data = load ('dLST_dNDVI_dSAVI_Veg_11A.txt');
iok = find(~isnan(data(:,8))> 0 & ~isnan(data(:,27))> 0 & data(:,15)
<= 0.01 & data(:,31) <= 0.01 & data(:,1)==11);
N = length(iok);
[r1,P1] = corr(data(iok,8),data(iok,27));
figure(103);clf;
scatter(data(:,8),data(:,27) ,30,data(:,1),'filled');
colorbar;
set(gca,'xscale','log');
set(gca,'yscale','log');
% set(gca, 'xlim',[0 1]);
% set(gca, 'ylim',[0 1]);
title([ 'N = ' num2str(N) ', r = ' num2str(r,2)]);
xlabel('dLSTN');
ylabel('dNDVIW');

set(gca,'xtick',[1:1:11],'xticklabel',{'El1','El2','Onn','Umu','Bon','
Alu','Ruk','Obi','Cho','Umd','Sar'});
print('-f103','-dpng','-r600', 'dLSTN_dNDVIW');
```

5. Multiple linear regression analysis

```
data = load ('dLST_Veg_Advance_11_anova_A.txt');
% Multiple regression analysis
% to create a new matrix of 'predictor variables' - chosen from the
factors that impact LST i.e. with significant correlation against
dLSTn; they are size of facility, height of stack.
% (Focus on one of the dLST directions to begin with). The response
variable is then dLSTn. So loading the big Excel file of results, then
normalise the chosen predictor variables using the mean and standard
deviation of each variable, e.g.:
x1 = ( data(:,4) - nanmean(data(:,4)) ) / nanstd(data(:,4)); % where 4
is the column for month.
x2 = ( data(:,5) - nanmean(data(:,5)) ) / nanstd(data(:,5)); % where 6
is the column for facility size.
x3 = ( data(:,6) - nanmean(data(:,6)) ) / nanstd(data(:,6)); % where 5
is the column for month stack height.

iok = find(data(:,15) <= 0.01  & ~isnan(data(:,4)) & ~isnan(data(:,5))
& ~isnan(data(:,6)) & ~isnan(data(:,23)));
clear x1; clear x2; clear x3;
x1 = (data(iok,4) - nanmean(data(iok,4)) ) / nanstd(data(iok,4));
x2 = (data(iok,5) - nanmean(data(iok,5)) ) / nanstd(data(iok,5));
x3 = ( data(iok,6) - nanmean(data(iok,6)) ) / nanstd(data(iok,6));
```

```
clear X;
X = [ones(length(iok),1) x1 x2 x3];
size(X);
y = (data(iok,23) - nanmean(data(iok,23))) / nanstd(data(iok,23));
size(iok);
[b, bint, r, rint, stats] = regress(y, X);
```

6. Conversion from Julian day to month and day

```
% JNS 7 2014 formal function for converting julian day into month+day
of
% month for a given year (leap / not leap year)
 function [month,day] = jd2monthday(jd, year);
% define days per month:
leapmonths = [31,29,31,30,31,30,31,31,30,31,30,31];
months = [31,28,31,30,31,30,31,31,30,31,30,31];
% years divisible by 4 are leap years:
lp = mod(year,4);
switch lp
    case 0
        dpm = leapmonths;
    otherwise
        dpm = months;
end

daydiff = jd - cumsum(dpm);

% catch days in January:
if jd < 32
    month = 1;
    day = jd;
elseif jd > sum(dpm(1:11))
    month = 12;
    day = jd - sum(dpm(1:11));
else
    imonth = find(daydiff <= 0);
    month = imonth(1);
    day = jd - sum(dpm(1:imonth(1)-1));
end
 end
```

7. Spatio-temporal regression analysis

```
datadir = 'C:\PhD\landsat\data'; % the directory of the results files
cd(datadir);
d1 = dir(datadir);
c = 0;
for ifile = 3:length(d1); % stop at 307 for the processing of NDVI &
SAVI
    thisfile = d1(ifile).name
    if strfind(thisfile, 'Stn_12.')
        c = c + 1;
        load(d1(ifile).name,        'ndvi_mask',        'IDX3','water',
'vegetation', 'builtup', 'soil') ;
        ndvi(:,:,c) = ndvi_mask;
        IDX(:,:,c) = IDX3;
        years(c)= str2num(thisfile(24:27));
        jdays(c)= str2num(thisfile(28:30));
        allwater(c) = water;
        allvegetation(c) = vegetation;
        allbuiltup(c) = builtup;
        allsoil(c) = soil;
```

```
    end
end
% conversion to julian days
for i = 1:c
    [months(i),days(i)] =jd2monthday(jdays(i), years(i));
    thistime(i,1) = datenum(years(i), months(i), days(i));
end

% initialise output variables:
slopes = ones(401,401) * nan;
pvalues = ones(401,401) * nan;
rvalues = ones(401,401) * nan;

for i = 1:size(ndvi, 1)

    for j = 1 : size(ndvi, 2)
        thisline =squeeze(ndvi(i,j,:));
        thisidx = squeeze(IDX(i,j,:));
        for ik = 1: length(thisidx)
            if thisidx(ik) == allvegetation(ik)
                match(ik) =1;
            else
                match(ik) = 0;
            end
        end

        iok = find(~isnan(thisline)& match(:) == 1);
        if ~isempty(iok)
             if length(iok) > 2

                tmp = polyfit(thistime(iok),thisline(iok),1);
                slopes(i,j) = tmp(1);
                intercepts(i,j) = tmp(2);

                [tmp1, tmp2] = corr(thistime(iok),thisline(iok));
                rvalues(i,j) = tmp1;
                pvalues(i,j) = tmp2;
                n(i,j) = length(iok);

             end
        end
    end
end
ibad = find(IDX3(:) == water | IDX3(:) == soil | IDX3(:) == builtup);
slopes(ibad) = nan;
rvalues(ibad) = nan;
pvalues(ibad) = nan;
n(ibad) = nan;

Nbad = length(ibad);
% by hand - only do this when you edit the colormap
% mycmap = get(gcf,'Colormap');
% save('redwhiteblue','mycmap');

load('redwhiteblue','mycmap');

ibad = find(pvalues(:)>0.05);
slopes(ibad) = nan;
rvalues(ibad) = nan;

figure(150);clf;
```

```
subplot(1,3,1);
pcolor(flipud(slopes)* 365);shading flat;
h = gca;set(h,'position',[0.05 0.1 0.25 0.8]);
set(gcf,'Colormap',mycmap)
c1= colorbar;
set(c1,'position',[0.31 0.3 0.01 0.4]);
caxis([-1 1]);
hold on
plot(201,201,'ks')

subplot(1,3,2);
pcolor(flipud(rvalues));shading flat;
h1 = gca;set(h1,'position',[0.37 0.1 0.25 0.8]);
c2= colorbar;
set(c2,'position',[0.63 0.3 0.01 0.4]);
caxis([-1 1]);
hold on
plot(201,201,'ks')

subplot(1,3,3);
pcolor(flipud(pvalues));shading flat;
h2 = gca;set(h2,'position',[0.69 0.1 0.25 0.8]);
c3= colorbar;
set(c3,'position',[0.95 0.3 0.01 0.4]);
caxis([0 0.1]);
hold on
plot(201,201,'gs')

% to plot only slopes and rvalues
figure(151);clf;
subplot(1,2,1);
pcolor(flipud(slopes)* 365);shading flat;
% h = gca;set(h,'position',[0.05 0.1 0.25 0.8]);
set(gcf,'Colormap',mycmap)
c1= colorbar;
set(c1,'position',[0.48 0.3 0.01 0.4]);
caxis([-1 1]);
hold on
plot(201,201,'ks')

subplot(1,2,2);
pcolor(flipud(rvalues));shading flat;
% h1 = gca;set(h1,'position',[0.37 0.1 0.25 0.8]);
c2= colorbar;
set(c2,'position',[0.92 0.3 0.01 0.4]);
caxis([-1 1]);
hold on
plot(201,201,'ks')

print('-f150','-r600','-dpng', 'spatial_regression_Stn_1.png')
```

Appendix C

Results and published posters

A. Results

1. Environmental factors that influence change in LST at gas flaring sites.

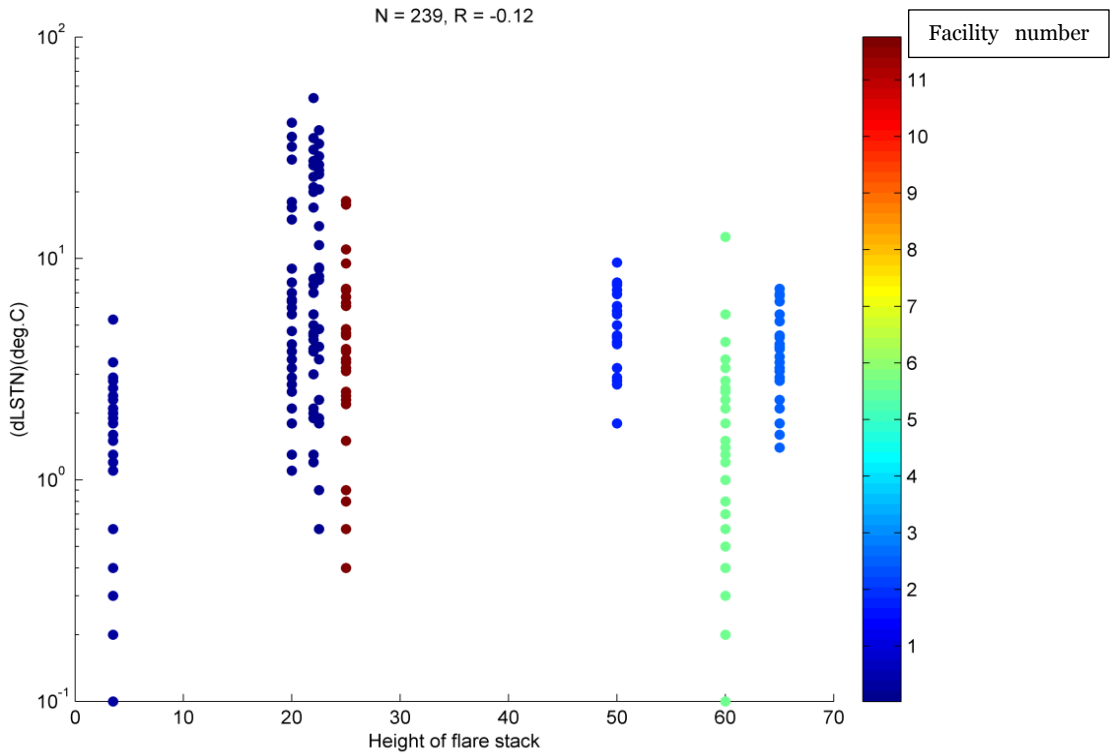

Figure C-1: Height of flare stack against δLST_N

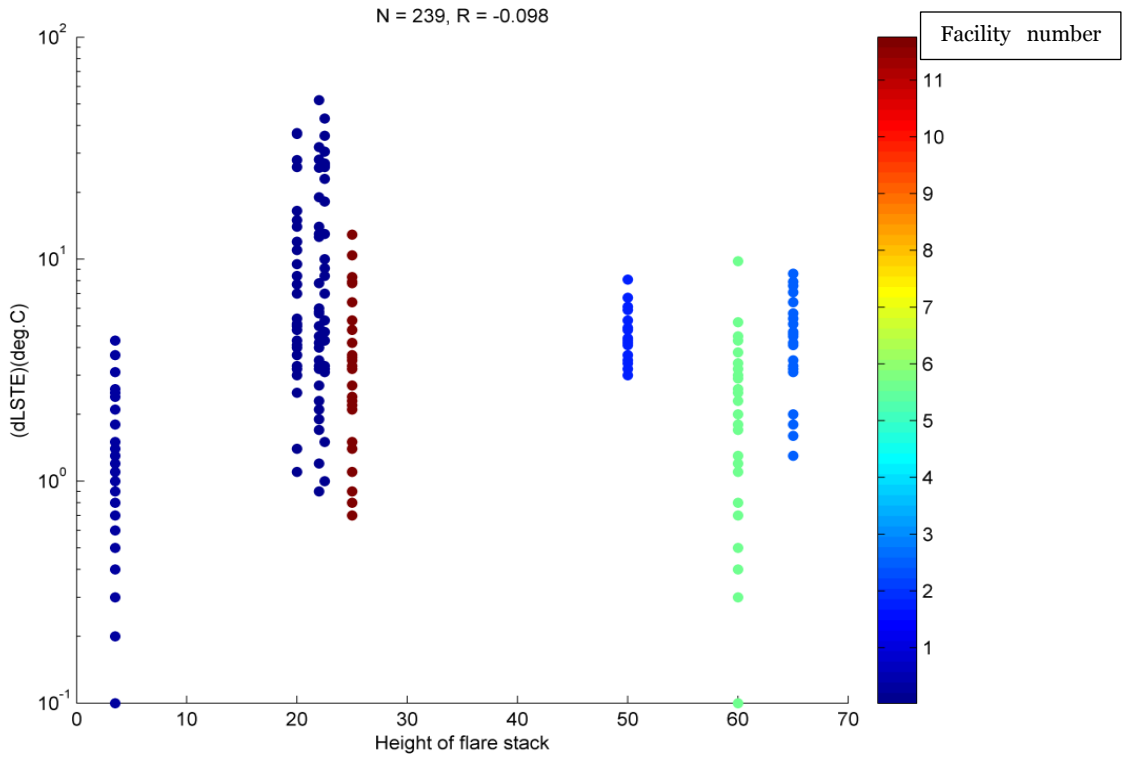

Figure C-2: Height of flare stack against δLST_E

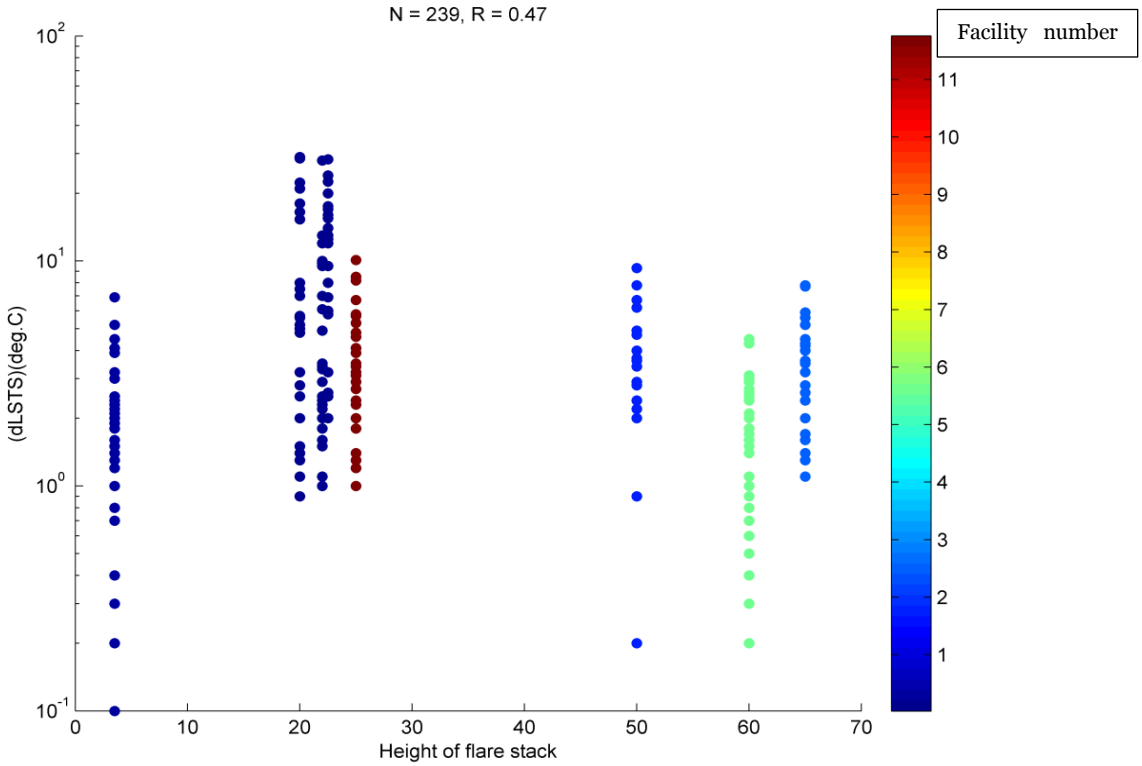

Figure C-3: Height of flare stack against δLST_S

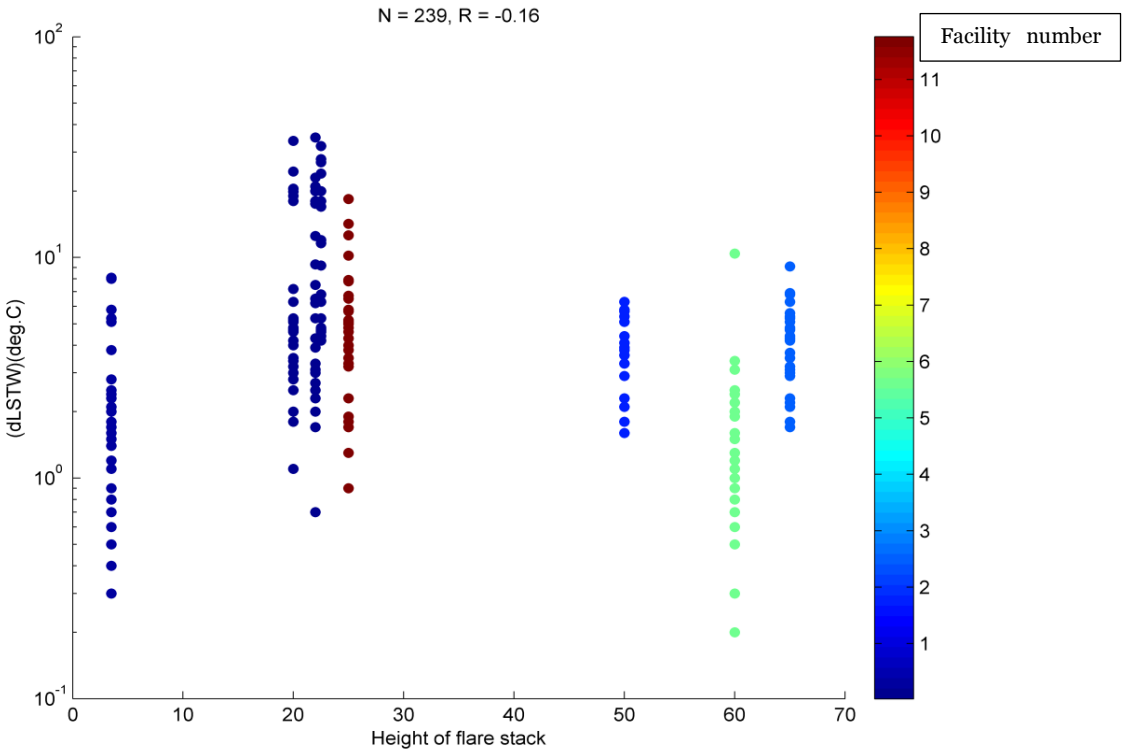

Figure C-4: Height of flare stack against δLST_W

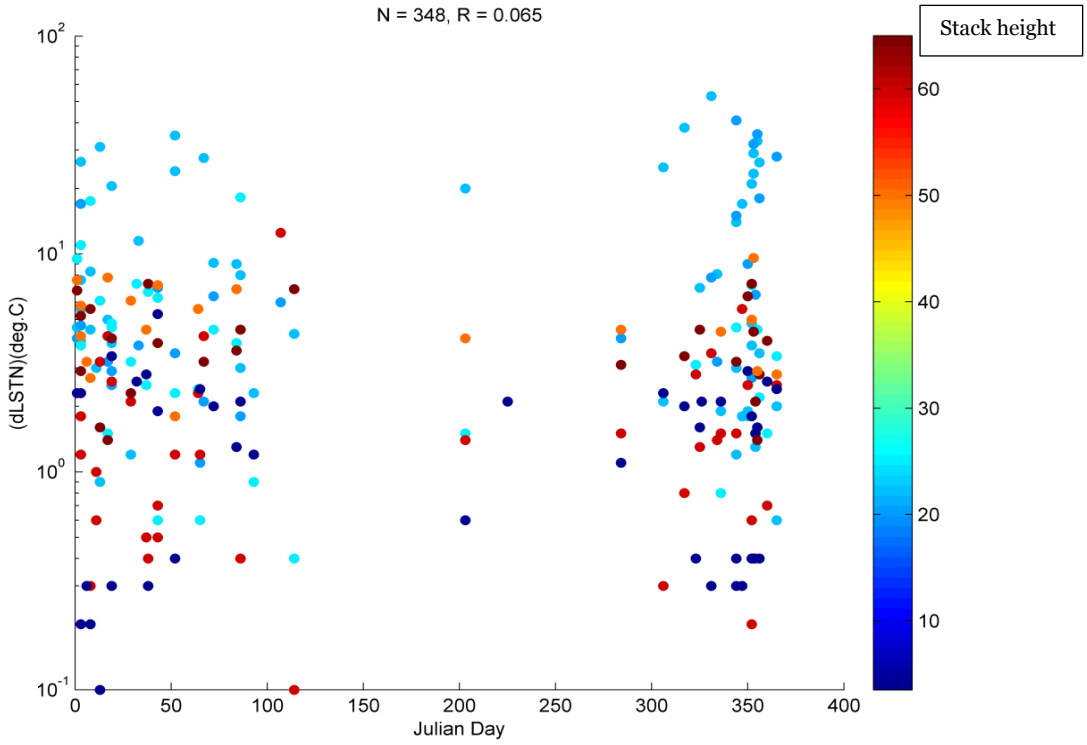

Figure C-5: Julian Day against δLST_N

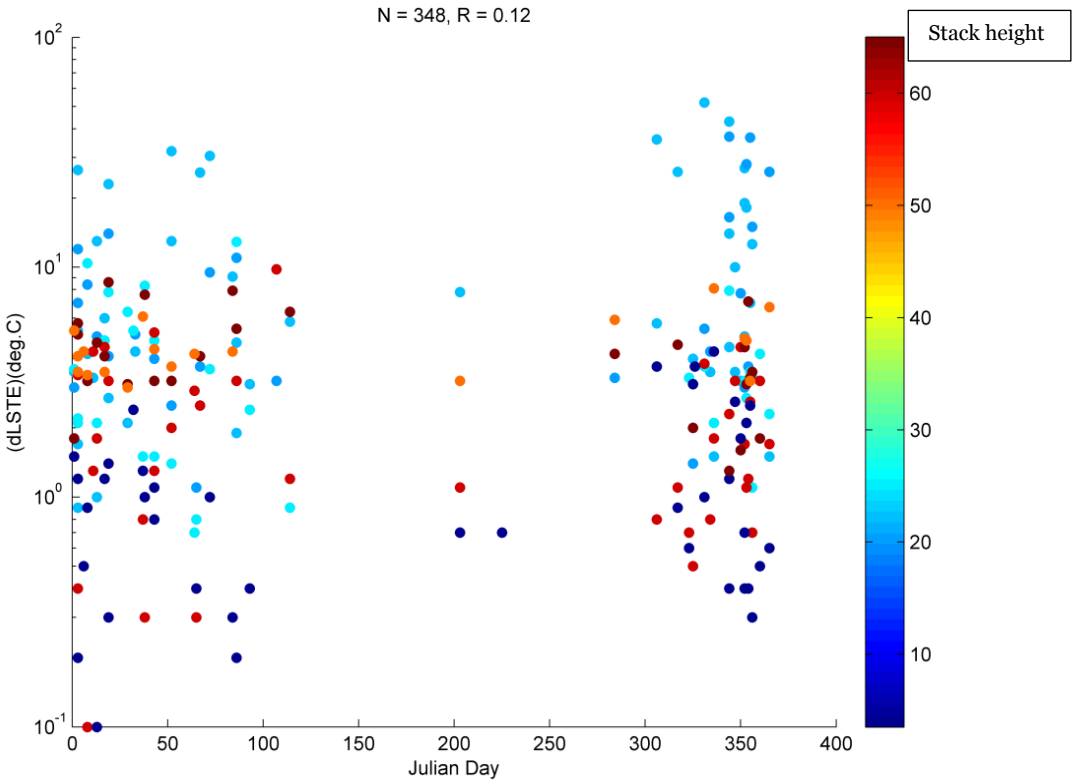

Figure C-6: Julian Day against δLST_E

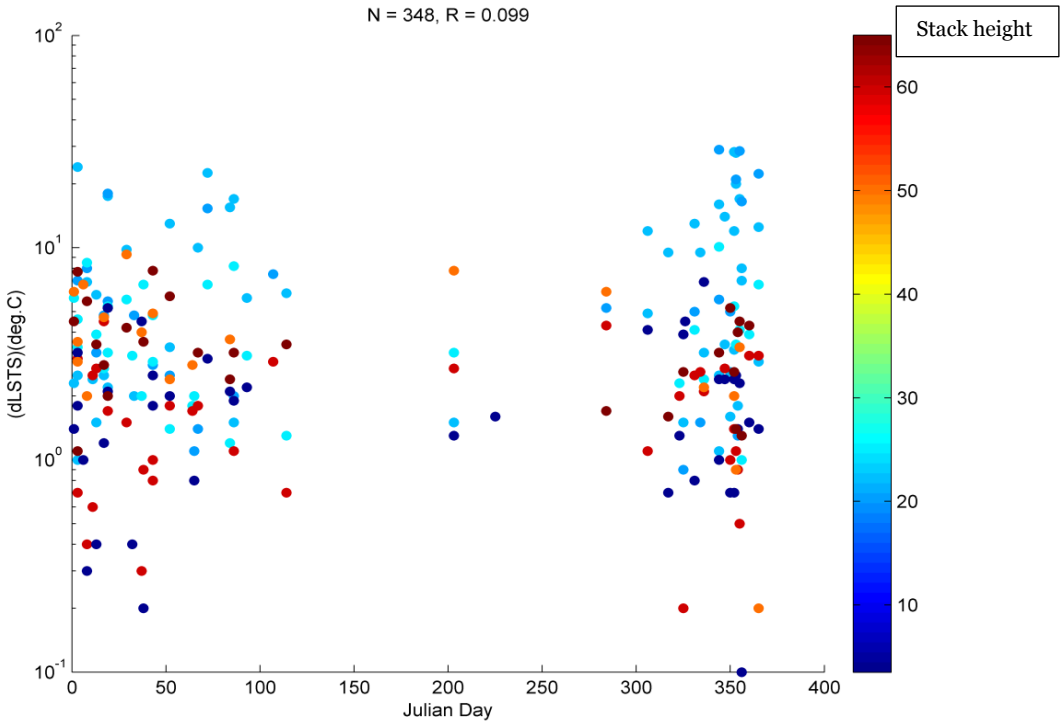

Figure C-7: Julian Day against δLST_S

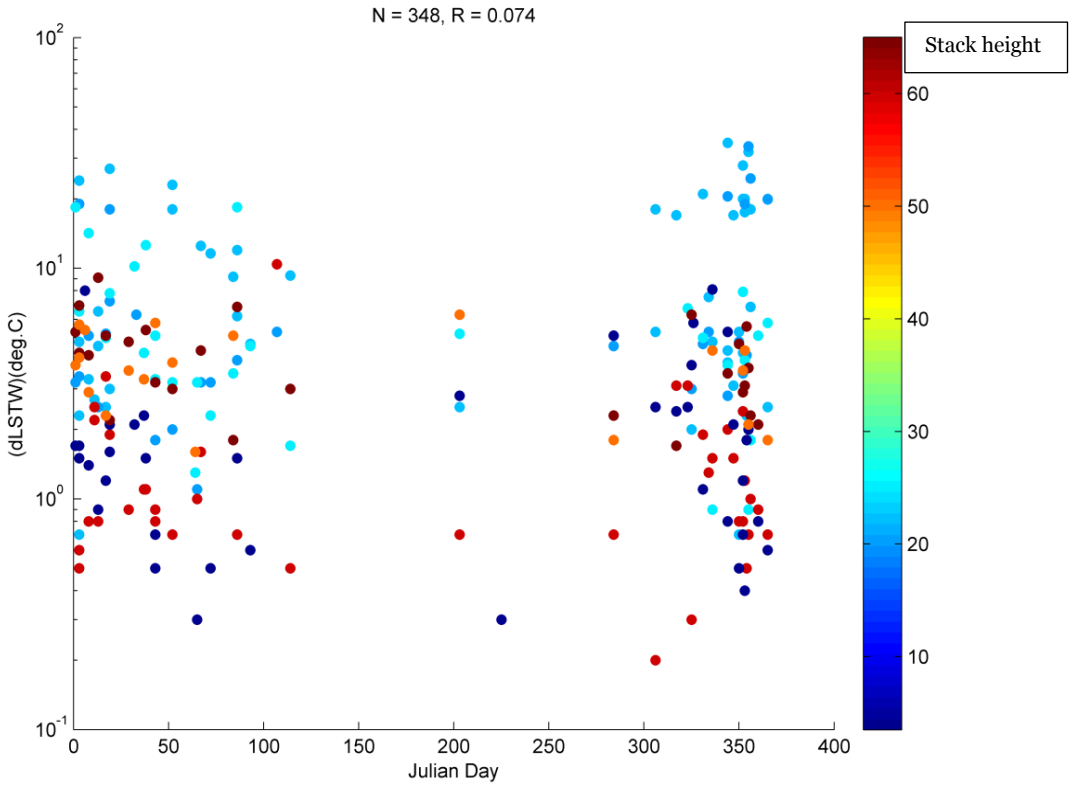

Figure C-8: Julian Day against δLST_W

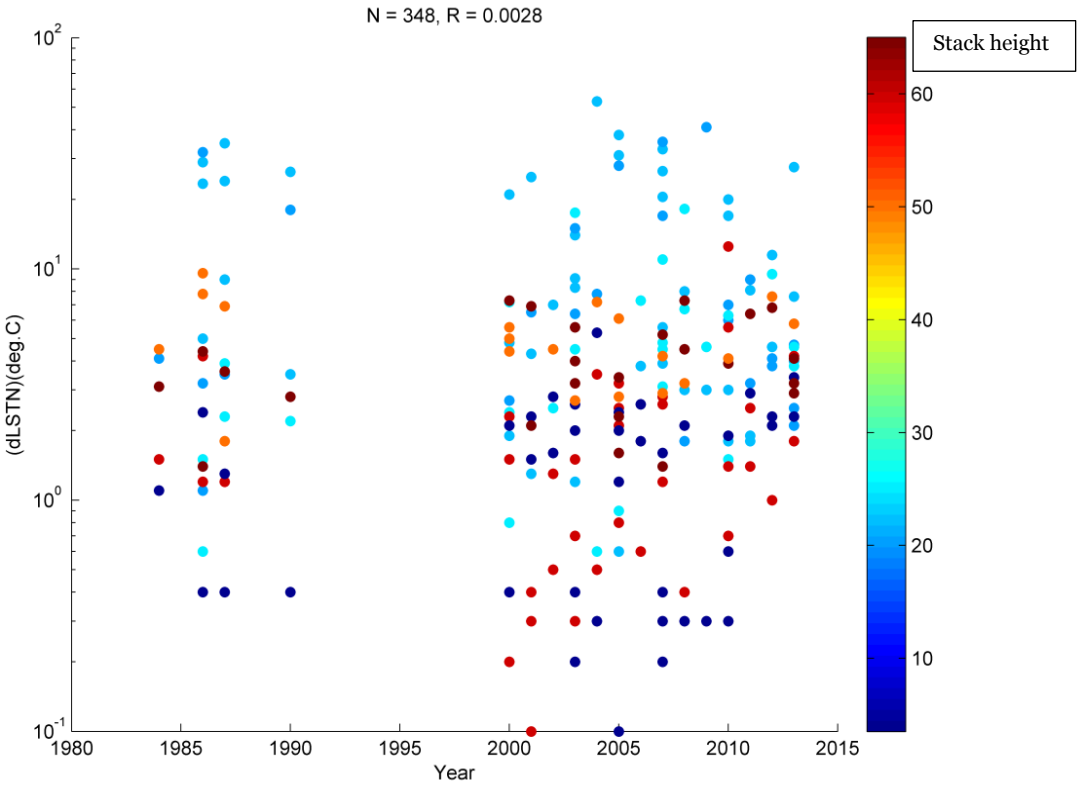

Figure C-9: Year against δLST_N

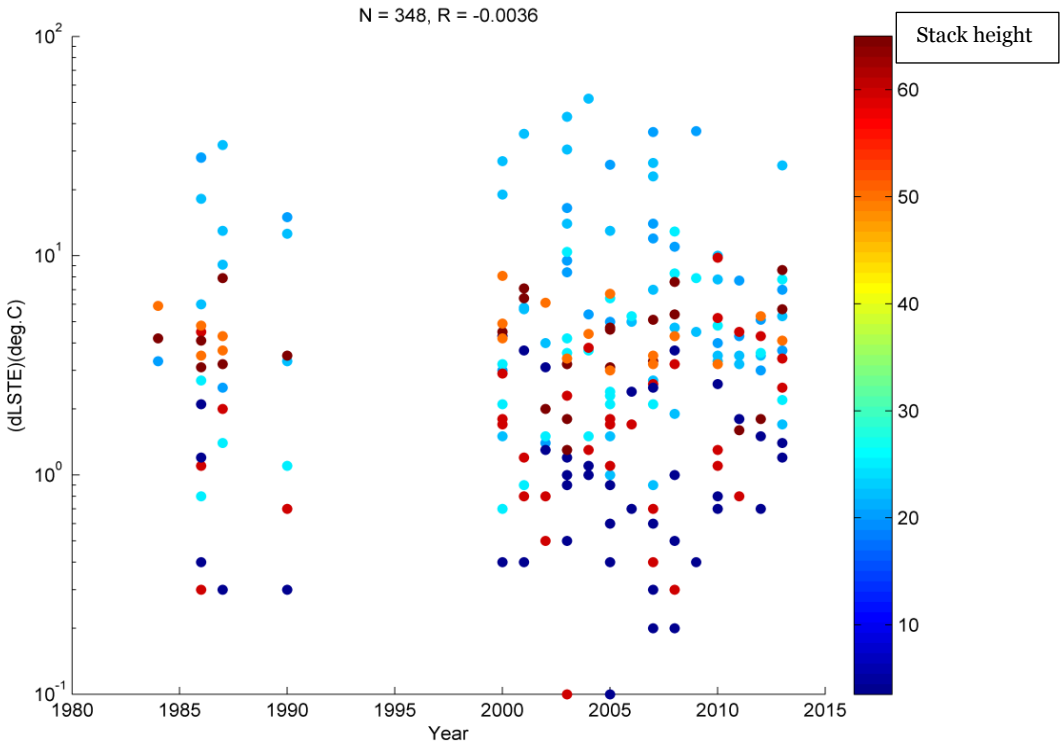

Figure C-10: Year against δLST_E

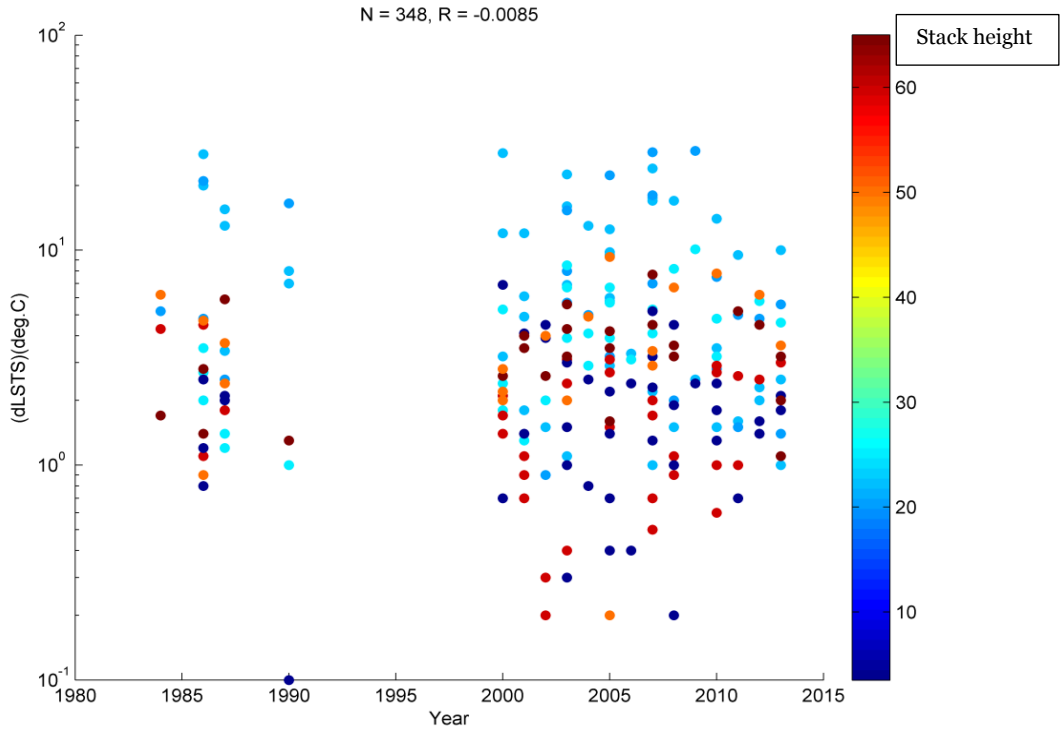

Figure C-11: Year against δLST_S

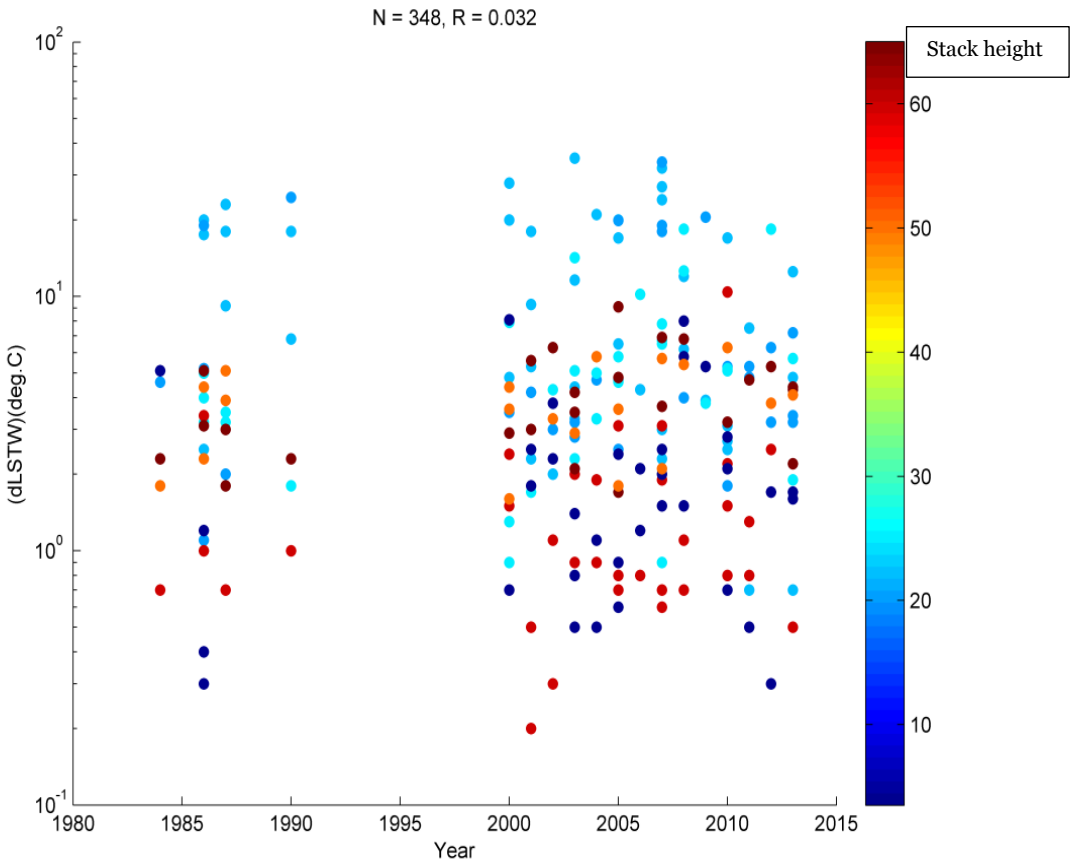

Figure C-12: Year against δLST_W

Table C-1: Correlation coefficient of relationship of factors that influence LST using linear regression analysis

Relationship	r-value	p-value	Type of correlation
Month v δLST_N	0.1047	0.0781	Positive
Month v δLST_E	0.1123	0.0548	" "
Month v δLST_S	0.1148	0.0466	" "
Month v δLST_W	0.0749	0.2133	" "
Size of the facility v δLST_N	-0.1823	**0.002**	**Negative**
Size of the facility v δLST_E	-0.2019	**5.0776×10^{-4}**	" "
Size of the facility v δLST_S	-0.1712	**0.0029**	" "
Size of the facility v δLST_W	-0.1398	**0.0197**	" "
Height of stack v δLST_N	-0.1523	0.0345	" "
Height of stack v δLST_E	-0.1030	0.1415	" "
Height of stack v δLST_S	-0.1264	0.0739	" "
Height of stack v δLST_W	-0.1692	**0.0193**	" "
Julian Day v δLST_N	0.1013	0.0883	Positive
Julian Day v δLST_E	0.1097	0.0608	" "
Julian Day v δLST_S	0.1132	0.0497	" "
Julian Day v δLST_W	0.0701	0.2440	" "
Year v δLST_N	-0.0273	0.6468	Negative
Year v δLST_E	-0.0054	0.9269	" "
Year v δLST_S	-0.0287	0.6195	" "
Year v δLST_W	0.0426	0.4789	Positive

2. Fieldwork results: Air temperature and relative humidity at Eleme Refinery II and Onne Flow Station.

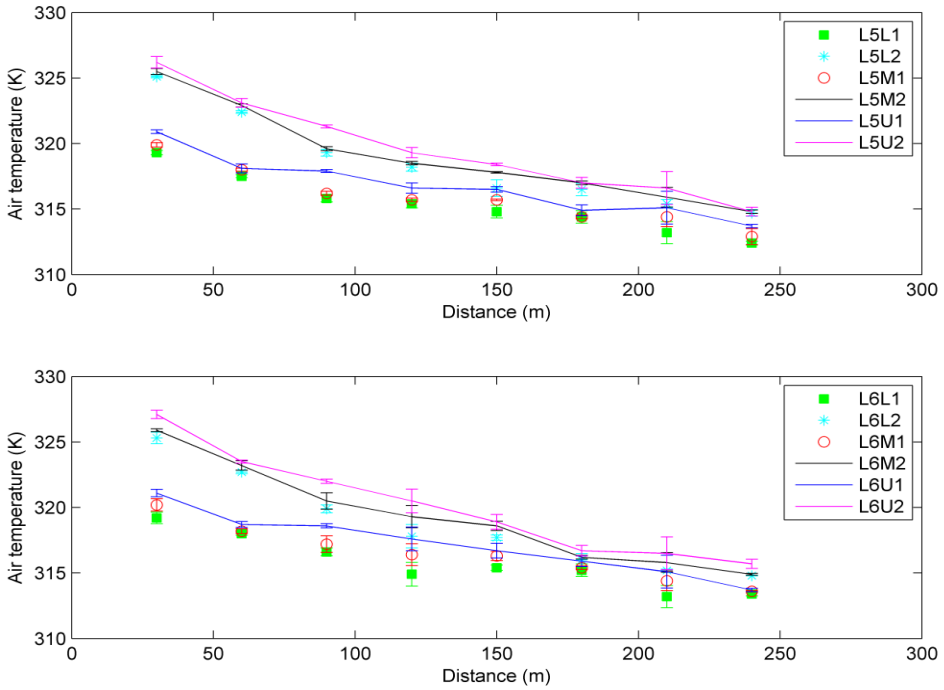

Figure C-13: Air temperature at Eleme Refinery II gas flaring site (L5 & L6)

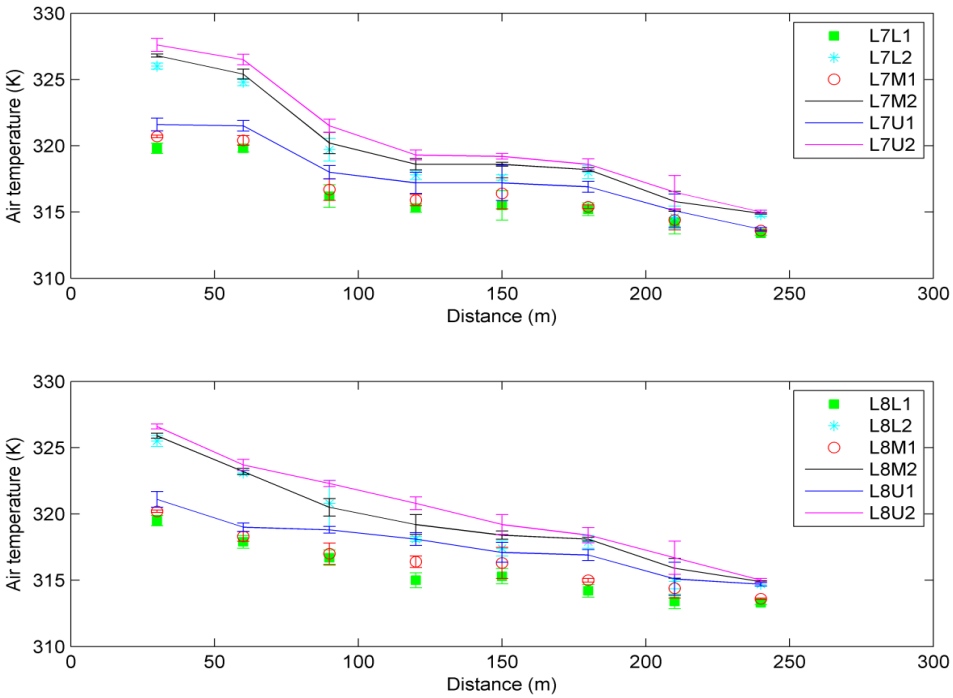

Figure C-14: Air temperature at Eleme Refinery II gas flaring site (L7 & L8)

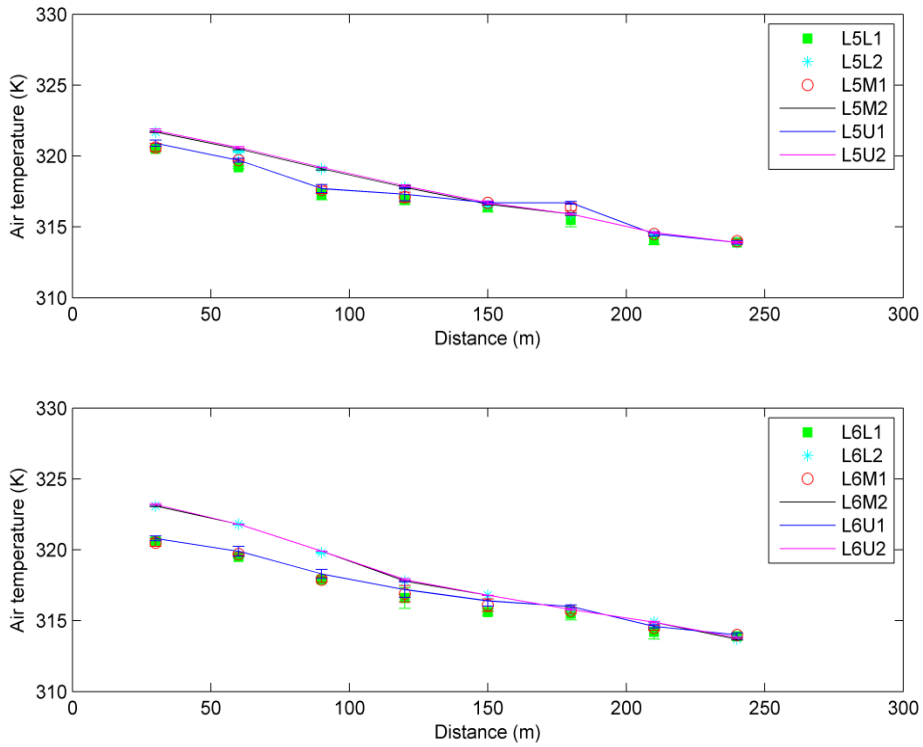

Figure C-15: Air temperature at Onne Flow Station gas flaring site (L5 & L6)

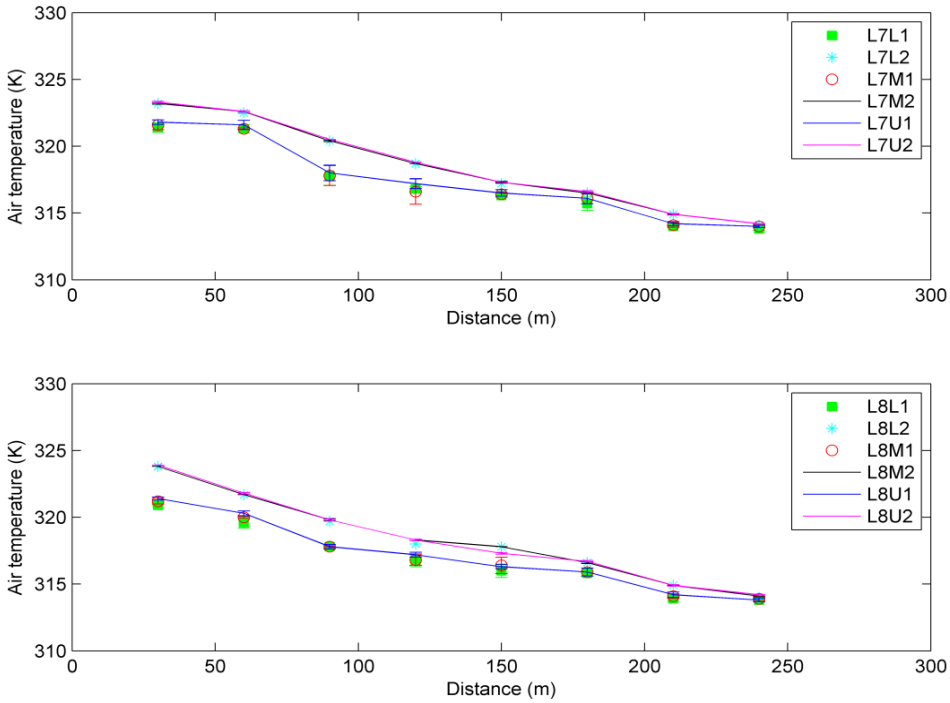

Figure C-16: Air temperature at Onne Flow Station gas flaring site (L7 & L8)

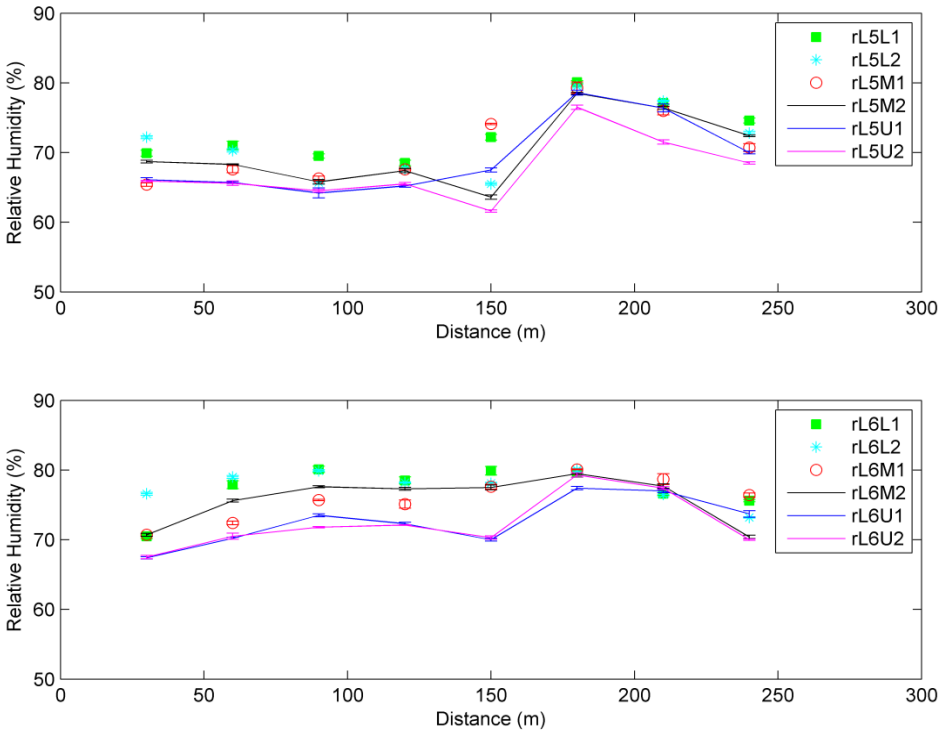

Figure C-17: Relative humidity at Eleme Refinery II gas flaring site (L5 & L6)

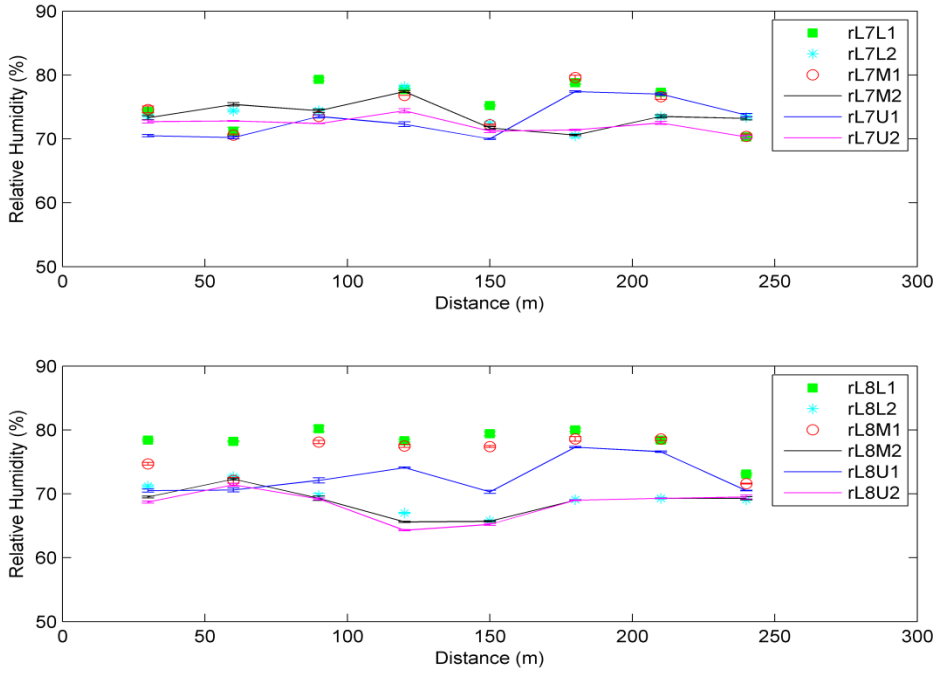

Figure C-18: Relative humidity at Eleme Refinery II gas flaring site (L7 & L8)

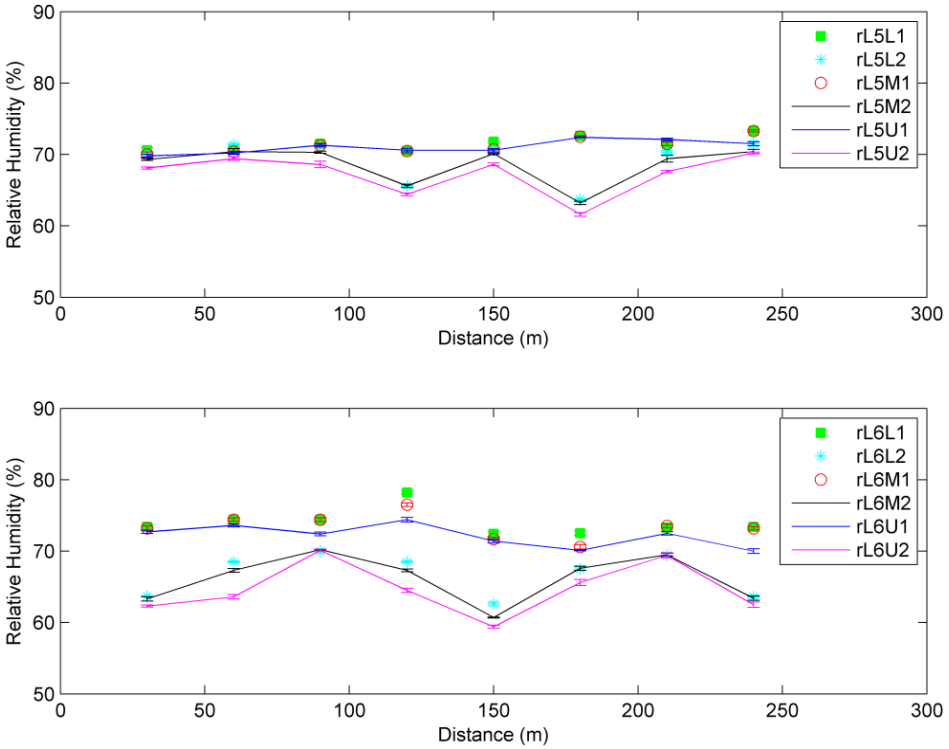

Figure C-19: Relative humidity at Onne Flow Station gas flaring site (L5 & L6)

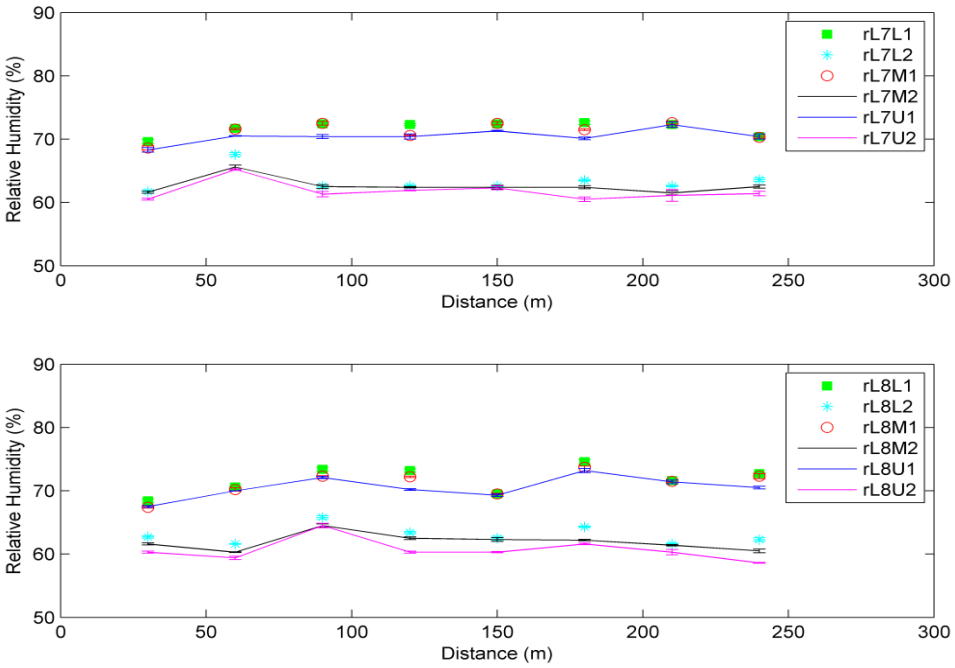

Figure C-20: Relative humidity at Onne Flow Station gas flaring site (L7 & L8)

3. Published posters

FLARING AND POLLUTION DETECTION IN THE NIGER DELTA USING REMOTE SENSING

Barnabas Morakinyo[a], Victor Abbott[a] and Samantha Lavender[b]
(a) School of Marine Science & Engineering, University of Plymouth, Plymouth, UK;
(b) ARGANS Ltd, Tamar Science Park, Plymouth, UK
barnabas.morakinyo@plymouth.ac.uk

INTRODUCTION

The Niger Delta is a region of oil exploration in Nigeria that has experienced extensive environmental degradation. Nigeria has a long history of petroleum exploration but the gas flaring associated with it is recognised as contributing to environmental, social and economic problems in the Niger Delta area and beyond. Nigeria is rated second in the world on gas flaring after Russia.

Nigeria in West Africa (Google Maps)

AIMS OF THE STUDY

This PhD aims to examine gas flaring sites both on land and off-shore, determining pollution resulting from flaring and its impact on the environment and human population.

Top: Flaring at sea
Middle: Flaring on land
Bottom: Degradation of a land environment
Images via Google

Gas flaring sites off the Niger Delta;
http://www.pambazuka.org/images/articles/455/455pics/nigeria_flares.jpg

METHODOLOGY

Remote sensing is seen as an available, cost-effective and appropriate technology for the study (2). An active fire detection and characterisation algorithm for land and ocean hotspots developed for the SLSTR sensor on-board the future GMES Sentinel-3 satellite by King's College London (Martin Wooster) will be used. The appropriate sensors for the research are MODIS, ATSR-2, TM, ETM+, SAR and NigeriaSat Medium Resolution.

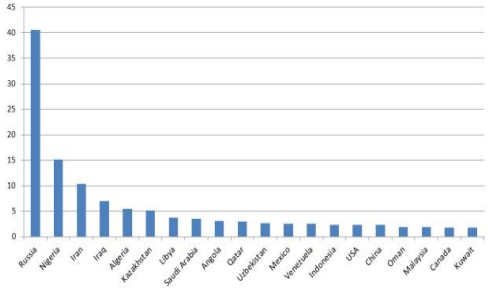

2008 top 20 flaring countries

REFERENCES AND ACKNOWLEDGEMENTS

(1) Elvidge CD, Baugh KE, Ghosh T, Anderson S, Ziskin D, 2009, A Fifteen Year Record of Global Natural Gas Flaring Derived from Satellite Data. Journal of Energies 2009, 2, 595-622
(2) Susan P, 2007, Active Fire Detection using Remote Sensing Based Polar-Orbiting and Geostationary Observations: An approach towards near real-time fire monitoring. M.Sc. Thesis. International Institute for Geo-information Science and Earth Observation, Enschede, The Netherlands

Retrieval of Land Surface Temperature from Landsat 7 ETM+ Data: A case study of gas flaring sites in Nigeria

Barnabas Morakinyo[a,b,c], Victor Abbott[a], Samantha Lavender[c] and Jill Schwarz[a]
(a) School of Marine Science & Engineering, University of Plymouth, Plymouth, UK;
(b) ARGANS Ltd, Plymouth Science Park, Plymouth, UK;
(c) Pixalytics Ltd, Plymouth Science Park, Plymouth, UK
barnabas.morakinyo@plymouth.ac.uk

Introduction

Nigeria is second only to Russia for the volume of gas flared. Poor governmental regulatory policies have been mostly unsuccessful in phasing it out. Studies have revealed that the decrease of leaf chlorophyll content and the retarded growth of crops in the area of gas flares are caused by the gas flaring.
The availability of high spatial resolution satellite data such as Landsat 7 ETM+ has made possible the detection of oil-related flaring and its impact on the surrounding vegetation.

Aims

1. To present methods used for the processing of Landsat 7 ETM+ data to obtain LST at Eleme Petroleum Refinery II Company, East-West Road Flow Station and Bonny Liquefied Natural Gas Plant gas flaring sites.
2. To compare results from the satellite data with ground truthing.

Study area locations

Figure 2-4 show the locations of Eleme Petroleum Refinery II Company, East-West Road Flow Station and Bonny Liquefied Natural Gas Plant (LNG) in Rivers State of the Niger Delta.

Methods

Landsat 7 ETM+ data were used to derive land surface temperature as well as land surface cover using Matlab version R2013a (Figure 1) around known gas flaring sites (Figures 2 to 7). Spatial gradients in relation to flare stacks were investigated (Figures 8 to 16).

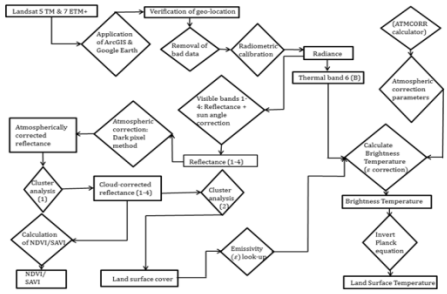

Fig. 1: Schematic diagram of methods of processing Landsat 7 ETM+ data

Fig. 2: Eleme Petroleum Refinery II Company

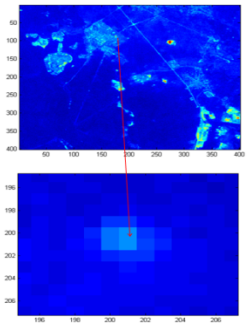

Fig. 3: East-West Road Flow Station

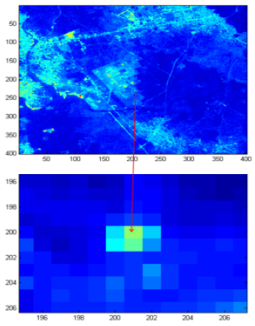

Fig. 4: Bonny Liquefied Natural Gas Plant (LNG)

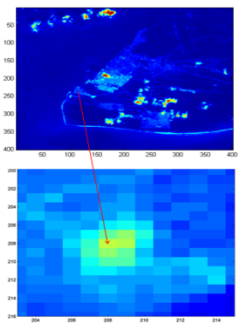

Fig. 5: Hot pixels for flare source at Eleme Refinery II Company

Fig. 6: Hot pixels for flare source at East-West Road Flow Station

Fig. 7: Hot pixels for flare source at Bonny plant LNG Plant

Satellite results: Landsat 7 ETM+

1. Figures 8-10 give details of land cover surface types at Eleme Petroleum Refinery II Company, East-West Road Flow Station and Bonny Liquefied Natural Gas Plant gas flaring sites.
2. In figure 10 the white pixels are for bad data that were removed. Also, for this image, the double-classification for cloud detection has not eliminated the cloud edges and confuses them with 'built-up' areas.
3. Figures 11-13 show that LST falls with increasing distance from the three flare sources studied.
4. Also, figures 14-16 show that Air Temperature falls with increasing distance from the flare stack at Eleme Petroleum Refinery II Company during fieldwork activities.

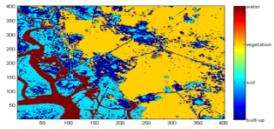

Fig. 8: Eleme Refinery II land cover surface type

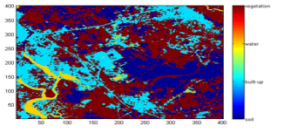

Fig. 9: East-West Road Flow Station land cover surface type

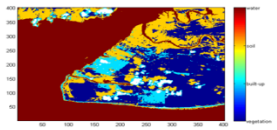

Fig. 10: Bonny LNG land cover surface type

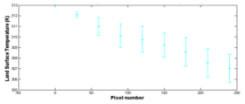

Fig. 11: LST at Eleme Refinery II

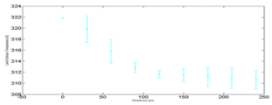

Fig.12: LST at East-West Road Flow Station

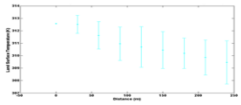

Fig. 13: Bonny LNG LST

Fieldwork results: Air temperature

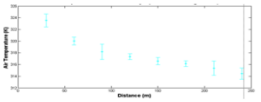

Fig. 14: Eleme (Line 1)

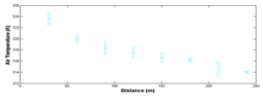

Fig. 15: Eleme (Line 2)

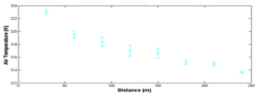

Fig. 16: Eleme (Line 3)

Conclusion: Flares were detected using Landsat-derived LST. The limitation of my method of double-classification for cloud detection is shown in figure 10 where the cloud edges was not eliminated and confuses them with 'built-up' areas. Work on using NDVI and SAVI to evaluate flare impacts on vegetation cover and health is ongoing.

References: 1. Barsi, J. A., Barker, J. L and Schott, J. R. (2003). An Atmospheric Correction Parameter Calculator for a Single Thermal Band Earth-Sensing Instrument. IGARSS03, Centre de Congress Pierre Baudis, Toulouse, France. SPIE. 2. Onosode, G. O. (2003). Environmental Issues and challenges of the Niger Delta (Perspectives from the Niger Delta Environmental Survey Process). Lagos, Lilybank Property and Trust Limited.

Acknowledgements: Landsat 7 ETM+ data were used courtesy of NASA/USGS and obtained using Glovis/Earth Explorer. Also, MODTRAN data were used courtesy of NCEP.

Appendix D

Communications relating to the field visits in the Niger Delta

A. Letter of application for the approval by Federal Ministry of Petroleum Resources (Department of Petroleum Resources), Lagos, Nigeria for research near gas flaring sites (see Letter A).

B. Letter of application for the approval by Eleme Petrochemical Refineries for research near gas flaring sites.

C. Letter of application for the approval by Shell Petroleum Development Company for research near gas flaring sites.

D. Letter of introduction from Federal Ministry of Petroleum Resources (Department of Petroleum Resources), Lagos, Nigeria to the Managing Director, Eleme Petrochemical Refineries for assistance to carry out fieldwork activities near Eleme Petrochemical Refineries gas flaring sites.

E. Letter of introduction from Federal Ministry of Petroleum Resources (Department of Petroleum Resources), Lagos, Nigeria to the Managing Director, Shell Petroleum Development Company for assistance to carry out fieldwork activities near Shell Petroleum Development Company gas flaring sites.

F. Letter from Federal Ministry of Petroleum Resources (Department of Petroleum Resources), Lagos, Nigeria to Plymouth University stating actions taken to ensure that Eleme Petrochemical Refineries and Shell Petroleum Development Company grant access to their gas flaring sites.

CONNECT WITH PLYMOUTH UNIVERSITY

The Director,
Department of Petroleum Resources,
7, Kofo Abayomi Street,
Victoria Island,
Lagos State,
Nigeria

25 May 2012

Dear Sir,

APPLICATION FOR THE APPROVAL BY THE DEPARTMENT OF PETROLEUM RESOURCES FOR RESEARCH NEAR GAS FLARING SITES

I hereby apply for the approval to use Eleme Refineries and Shell Petroleum Company flaring sites for research work.

Mr Barnabas Morakinyo is undertaking doctoral studies with me here in Plymouth, UK. He has studied the usefulness of satellite-based Remote Sensing in the detection of gas flaring sites. Following eighteen months of theoretical and computer-based investigations, he needs to undertake field work as a form of 'ground truthing', i.e. to enable him to correlate measurements at and near gas flares with the satellite-derived imagery.

The ground truthing will involve physical inspection of the sites and the taking of some field measurements, such as ground level temperatures near to and at a distance from the flare stack.

Such measurements will include:

- Mapping of relevant features such as vegetation, farmland and open land around the flaring sources and those within the selected 2-3 km control;
- Measurement of air temperature and humidity at different intervals from the flaring sources e.g. 30 m, 60 m, 90 m and 120 m;
- Taking pictures of the flaring sources and the local environment.

My thanks for your anticipated cooperation.

Yours sincerely,

V Abbott

Dr Victor Abbott, CMarSci, FIMarEST

School of Marine Science & Engineering
University of Plymouth
Drake Circus
Plymouth
Devon
PL4 8AA

School of Marine Science and Engineering
Plymouth University
Drake Circus Plymouth
Devon PL4 8AA United Kingdom

T +44 (0) 1752 586 100
F +44 (0) 1752 586 101
E connectMSE@plymouth.ac.uk
W www.plymouth.ac.uk

Professor M Neil James
DSc (Eng) D Tech (Honoris Causa) PhD
BSc (Eng) CEng FIM
Head of School, Associate Dean - Research

Letter A: Letter of application for the approval by the Department of Petroleum Resources for research near gas flaring sites

CONNECT WITH PLYMOUTH UNIVERSITY

The Director,
Eleme Petrochemical Refineries
Alesa, Eleme
Port-Harcourt
River State
Nigeria

15 June 2012

Dear Sir,

APPLICATION FOR THE APPROVAL BY ELEME PETROCHEMICAL REFINERIES FOR RESEARCH NEAR GAS FLARING SITES

Mr Barnabas Morakinyo is undertaking doctoral studies with me here in Plymouth, UK. He has studied the usefulness of satellite-based Remote Sensing in the detection of gas flaring sites. Following eighteen months of theoretical and computer-based investigations, he needs to undertake field work as a form of 'ground truthing', i.e. to enable him to correlate measurements at and near gas flares with the satellite-derived imagery.

The ground truthing will involve physical inspection of the sites and the taking of some field measurements, such as ground level temperatures near to and at a distance from the flare stack.

Such measurements will include:

- Mapping of relevant features such as vegetation, farmland and open land around the flaring sources and those within the selected 2-3 km control;
- Measurement of air temperature and humidity at different intervals from the flaring sources e.g. 30 m, 60 m, 90 m and 120 m;
- Taking pictures of the flaring sources and the local environment.

My thanks for your anticipated cooperation.

Yours sincerely,

Dr Victor Abbott, CMarSci, FIMarEST

School of Marine Science & Engineering
University of Plymouth
Drake Circus
Plymouth
Devon
PL4 8AA

School of Marine Science and Engineering
Plymouth University
Drake Circus Plymouth
Devon PL4 8AA United Kingdom

T +44 (0) 1752 586 100
F +44 (0) 1752 586 101
E connectMSE@plymouth.ac.uk
W www.plymouth.ac.uk

Professor M Neil James
DSc (Eng) D Tech (Honoris Causa) PhD
BSc (Eng) CEng FIM
Head of School, Associate Dean - Research

Letter B: Letter of application for the approval by Eleme Petrochemical Refineries for research near gas flaring sites

CONNECT WITH PLYMOUTH UNIVERSITY

The Shell Petroleum Development Company of Nigeria Ltd,
PO Box 263
Shell Industrial Area
Rumuobiakani
Port Harcourt
River State
Nigeria

15 June 2012

Dear Sir,

APPLICATION FOR THE APPROVAL BY SHELL PETROLEUM COMPANY FOR RESEARCH NEAR GAS FLARING SITES

Mr Barnabas Morakinyo is undertaking doctoral studies with me here in Plymouth, UK. He has studied the usefulness of satellite-based Remote Sensing in the detection of gas flaring sites. Following eighteen months of theoretical and computer-based investigations, he needs to undertake field work as a form of 'ground truthing', i.e. to enable him to correlate measurements at and near gas flares with the satellite-derived imagery.

The ground truthing will involve physical inspection of the sites and the taking of some field measurements, such as ground level temperatures near to and at a distance from the flare stack.

Such measurements will include:

- Mapping of relevant features such as vegetation, farmland and open land around the flaring sources and those within the selected 2-3 km control;
- Measurement of air temperature and humidity at different intervals from the flaring sources e.g. 30 m, 60 m, 90 m and 120 m;
- Taking pictures of the flaring sources and the local environment.

My thanks for your anticipated cooperation.

Yours sincerely,

Dr Victor Abbott, CMarSci, FIMarEST

School of Marine Science & Engineering
University of Plymouth
Drake Circus
Plymouth
Devon
PL4 8AA

School of Marine Science and Engineering
Plymouth University
Drake Circus Plymouth
Devon PL4 8AA United Kingdom

T +44 (0) 1752 586 100
F +44 (0) 1752 586 101
E connectMSE@plymouth.ac.uk
W www.plymouth.ac.uk

Professor M Neil James
DSc (Eng) D Tech (Honoris Causa) PhD
BSc (Eng) CEng FIM
Head of School, Associate Dean - Research

Letter C: Letter of application for the approval by Shell Petroleum Development Company for research near gas flaring sites

MINISTRY OF PETROLEUM RESOURCES

DEPARTMENT OF PETROLEUM RESOURCES

7, KOFO ABAYOMI STREET, VICTORIA ISLAND, LAGOS

P.M.B. No: 12650
Telephone: 2790000
Website: www.dprnigeria.com

Ref. No: PI.EXPL/3804/REQ/V.5/321
Date: July 25, 2012

The Managing Director,
Eleme Petrochemicals Complex,
East-West road,
Eleme, Port Harcourt,
Rivers State.

Dear Sir,

REQUEST FOR RESEARCH MATERIALS

Barnabas O. Morakinyo is a doctorate student of the School of Marine Science and Engineering, University of Plymouth, Devon, United Kingdom.

His head of department has requested the Department's assistance to obtain research materials for his research project titled **"Flaring and Pollution Detection in the Niger Delta Using Remote Sensing".**

We hereby solicit your assistance to provide him access to your company's facilities to enable him gather the requisite data to successfully execute his project.

The student has been advised to treat such data as confidential and make copies of the project available to both the **Department of Petroleum Resources** and **your company** on completion of the project.

Yours faithfully,

Z.M. Aji
For: Director, Petroleum Resources

Letter D: Letter of request for research materials from Ministry of Petroleum Resources (Department of Petroleum Resources) to the Managing Director Eleme Petrochemical Refineries

MINISTRY OF PETROLEUM RESOURCES

DEPARTMENT OF PETROLEUM RESOURCES

7, KOFO ABAYOMI STREET, VICTORIA ISLAND, LAGOS

12650

P.M.B. No: 2790000

Telephone:

Website: www.dpr.gov.ng

PI.EXPL/3804/REQ/V.5/320

Ref. No:

July 25, 2012

Date:

The Managing Director,
The Shell Petroleum Development Company,
Freeman House,
21/22 Marina,
Lagos.

Dear Sir,

REQUEST FOR RESEARCH MATERIALS

Barnabas O. Morakinyo is a doctorate student of the School of Marine Science and Engineering, University of Plymouth, Devon, United Kingdom.

His head of department has requested the Department's assistance to obtain research materials for his research project titled **"Flaring and Pollution Detection in the Niger Delta Using Remote Sensing".**

We hereby solicit your assistance to provide him access to your company's facilities to enable him gather the requisite data to successfully execute his project.

The student has been advised to treat such data as confidential and make copies of the project available to both the **Department of Petroleum Resources** and **your company** on completion of the project.

Yours faithfully,

Z.M. Aji
For: Director, Petroleum Resources

Letter E: Letter of request for research materials from Ministry of Petroleum Resources (Department of Petroleum Resources) to the Managing Director Shell Petroleum Development Company

MINISTRY OF PETROLEUM RESOURCES

DEPARTMENT OF PETROLEUM RESOURCES

7, KOFO ABAYOMI STREET, VICTORIA ISLAND, LAGOS

P.M.B. No: 12650
Telephone: 2790000
Website: www.dprnigeria.com

Ref. No: PI.EXPL/3804/REQ/V.5/322
Date: July 25, 2012

The Head
School of Marine Science and Engineering,
University of Plymouth,
Drake Circus,
Plymouth, Devon,
PL4 8AA,
United Kingdom.

Dear Sir,

RE: REQUEST FOR RESEARCH MATERIAL FOR BARNABAS O. MORAKINYO.

The attached letter on your request in respect of the above mentioned student has been forwarded to **Eleme Petrochemicals Complex** and **The Shell Petroleum Development Company** to provide him with the relevant data for the project.

Please ensure that a copy of the final project is sent to **Eleme Petrochemicals Complex, The Shell Petroleum Development Company** and **Department of Petroleum Resources** on completion of the project.

Failure to comply with the above may hinder the enthusiasm with which we respond to your requests in the future.

The transmitted data should be in the custody of the University for re-use by other students in future.

Yours faithfully,

Z.M. Aji
For: Director, Petroleum Resources.

Letter F: Letter of reply from Federal Ministry of Petroleum Resources (Department of Petroleum Resources) to Plymouth University, Plymouth, UK